IntechOpen

Induction Motors

Modelling and Control

Edited by Prof. Rui Esteves Araújo

INDUCTION MOTORS – MODELLING AND CONTROL

Edited by **Rui Esteves Araújo**

Induction Motors - Modelling and Control
http://dx.doi.org/10.5772/2498
Edited by Prof. Rui Esteves Araújo

Contributors

Raúl Igmar Gregor, Rodrigo Padilha Vieira, Cristiane Cauduro Gastaldini, Rodrigo Zelir Azzolin, Hilton Abílio Gründling, Ouahid Bouchhida, Mohamed Seghir Boucherit, Abederrezzek Cherifi, Sorin C. Musuroi, Miloje Kostic, Abdul-Ganiyu Adisa Jimoh, Pierre-Jac Venter, Edward Kofi Appiah, Marcel Janda, Ondrej Vitek, Vitezslav Hajek, Adrian Munteanu, Alecsandru Simion, Leonard Livadaru, José Luis Azcue, Alfeu J. Sguarezi Filho, Ernesto Ruppert, Erik Leandro Bonaldi, Levy Ely Oliveira, Jonas Silva, Luiz Eduardo Borges Da Silva, Germano Lambert-Torres, Marija Mirosevic, Ebrahim Amiri, Ernest Mendrela, Makbul Anwari, Houssem Bouchekara, Mohammed Simsim, Said Drid, Ivan Jaksch, Takeo Ishikawa, Marcin Morawiec, Rui Esteves Esteves Araújo, Ricardo de Castro, Pedro Melo, Malek Ghanes, Jean-Pierre Barbot, Sébastien Solvar, Leonardo Amet, Manuel Duarte-Mermoud, Venkat Krishnan, James D. McCalley

Notice

First published in Croatia, 2012 by INTECH d.o.o.
eBook (PDF) Published by IN TECH d.o.o.
Place and year of publication of eBook (PDF): Rijeka, 2019.
IntechOpen is the global imprint of IN TECH d.o.o.
Printed in Croatia

Legal deposit, Croatia: National and University Library in Zagreb

Additional hard and PDF copies can be obtained from orders@intechopen.com

Induction Motors - Modelling and Control
Edited by Prof. Rui Esteves Araújo

p. cm.

ISBN 978-953-51-0843-6

eBook (PDF) ISBN 978-953-51-6267-4

Meet the editor

Rui Esteves Araújo received the electrical engineering graduation, M. Sc. and Ph. D. degrees from the Faculty of Engineering of the University of Porto (FEUP), Portugal in 1987, 1992 and 2001, respectively. From 1987 to 1988, he was an Electrotechnical Engineer in Project Department, Adira Company, Porto, Portugal, and from 1988 to 1989, he was researcher with INESC, Porto, Portugal. Since 1989, he has been with the University of Porto, where he is an Assistant Professor with the Department of Electrotechnical and Computer Engineering at Faculty of Engineering. His research interests include energy efficiency in electric machines, design and control of power converters, industrial electronics applications to distributed power generation systems based on renewable energies and motion control applied to electric vehicles.

Contents

Preface

Induction motors research has a long and distinguished tradition stretching back to the end of the nineteenth-century with the pioneering works of Nikola Tesla. Its establishment as the main type of electric motor used in electric drives in the 1990s arose, essentially, following the early works of Blaschke and Hasse on Field-Oriented Control methods by, among others, Professors Leonhard and Lipo. All this has been increasingly underpinned by the rapid developments in computing capability and power electronics. Modern variable-speed drives rely on sophisticated control systems to meet increased performance and communication requirements. Presently, the variable-speed drives with induction motor remains the dominant market leader in a large range of industrial applications.

In broad terms, the electromechanical energy conversion can occur only by the interaction of electromagnetic fields and material bodies in motion, then it is reasonable to begin with a treatment that the task of an induction motor is to produce motive force, which can be controlled by power electronic converters with digital controllers to implement modern variable-speed drives. This unit must be controlled in harmony with the industrial processes in which the drive is applied. Historically, from the point of view of practical application, a significant amount of research on induction motor drives was motivated by industrial applications. This book aims to provide the readers with a deep discussion about relevant topics in the area of induction motor drives. There are several good books in the area of electric drives. At the same time, as a result of the increasing interest raised by the subject, a large number of technical methodological papers began to appear in the technical literature. However, this book borrows from these cited works and hopefully makes its own contribution to the literature on induction motors. The book contains twenty-one chapters, which are authored by international researchers in the field from Europe, South America, Japan and the USA. The book is organized into two parts. First part presents different views about mathematical description in terms of which transient states of an induction machine are analyzed, and explores some topics related to design of the induction motor and its applications. This part ends with a chapter on how to identify the induction motor parameters using a least-squares technique. Second part covers the control of induction motors presenting both field-oriented techniques and nonlinear control methods. The direct torque control and sensorless

methods are also presented, along with simulations results. The last chapters address the problem of how to detect induction motor faults. Particularly, the use of direct spectral analysis of stator current to find rotor faults, which has important practical applications, is presented.

In closing, I would like to express thanks to the chapter contributors for their cooperation and patience in various stages of the book. Special thanks are directed to friends and colleagues who have helped in the chapter review and selection process. These include Ângela Ferreira, André Mendes, Claudio Vergara, Pedro Melo, Ricardo Castro, Ventim Neves, and Vicente Leite. Special mention is due to my wife Manuela Araújo for the invaluable assistance, both tangible and intangible, given during the implementation of this project.

I am very grateful to all the people who were involved in the preparation of this book at Intech Europe, especially Ms. Alida Lesnjakovic and Ms. Romina Skomersic for their support and patience.

Rui Esteves Araújo
Faculdade de Engenharia da Universidade do Porto,
Portugal

Modelling

Chapter 1

Mathematical Model of the Three-Phase Induction Machine for the Study of Steady-State and Transient Duty Under Balanced and Unbalanced States

Alecsandru Simion, Leonard Livadaru and Adrian Munteanu

Additional information is available at the end of the chapter

http://dx.doi.org/10.5772/49983

1. Introduction

A proper study of the induction machine operation, especially when it comes to transients and unbalanced duties, requires effective mathematical models above all. The mathematical model of an electric machine represents all the equations that describe the relationships between electromagnetic torque and the main electrical and mechanical quantities.

The theory of electrical machines, and particularly of induction machine, has mathematical models with *distributed* parameters and with *concentrated* parameters respectively. The first mentioned models start with the cognition of the magnetic field of the machine components. Their most important advantages consist in the high generality degree and accuracy. However, two major disadvantages have to be mentioned. On one hand, the computing time is rather high, which somehow discountenance their use for the real-time control. On the other hand, the distributed parameters models do not take into consideration the influence of the temperature variation or mechanical processing upon the material properties, which can vary up to 25% in comparison to the initial state. Moreover, particular constructive details (for example slots or air-gap dimensions), which essentially affects the parameters evaluation, cannot be always realized from technological point of view.

The mathematical models with concentrated parameters are the most popular and consequently employed both in scientific literature and practice. The equations stand on resistances and inductances, which can be used further for defining magnetic fluxes, electromagnetic torque, and et.al. These models offer results, which are globally acceptable but cannot detect important information concerning local effects (Ahmad, 2010; Chiasson, 2005; Krause et al., 2002; Ong, 1998; Sul, 2011).

The family of mathematical models with concentrated parameters comprises different approaches but two of them are more popular: *the phase coordinate* model and the *orthogonal (dq)* model (Ahmad, 2010; Bose, 2006; Chiasson, 2005; De Doncker et al., 2011; Krause et al., 2002; Marino et al., 2010; Ong, 1998; Sul, 2011; Wach, 2011).

The first category works with the real machine. The equations include, among other parameters, the mutual stator-rotor inductances with variable values according to the rotor position. As consequence, the model becomes non-linear and complicates the study of dynamic processes (Bose, 2006; Marino et al., 2010; Wach, 2011).

The orthogonal (dq) model has begun with Park's theory nine decades ago. These models use parameters that are often independent to rotor position. The result is a significant simplification of the calculus, which became more convenient with the defining of the *space phasor* concept (Boldea & Tutelea, 2010; Marino et al., 2010; Sul, 2011).

Starting with the "classic" theory we deduce in this contribution a mathematical model that exclude the presence of the currents and angular velocity in voltage equations and uses total fluxes alone. Based on this approach, we take into discussion two control strategies of induction motor by principle of constant total flux of the stator and rotor, respectively.

The most consistent part of this work is dedicated to the study of unbalanced duties generated by supply asymmetries. It is presented a comparative analysis, which confronts a balanced duty with two unbalanced duties of different unbalance degrees. The study uses as working tool the Matlab-Simulink environment and provides variation characteristics of the electric, magnetic and mechanical quantities under transient operation.

2. The equations of the three-phase induction machine in phase coordinates

The structure of the analyzed induction machine contains: 3 identical phase windings placed on the stator in an 120 electric degrees angle of phase difference configuration; 3 identical phase windings placed on the rotor with a similar difference of phase; a constant air-gap (close slots in an ideal approach); an unsaturated (linear) magnetic circuit that allow to each winding to be characterized by a main and a leakage inductance. Each phase winding has W_s turns on stator and W_R turns on rotor and a harmonic distribution. All inductances are considered constant. The schematic view of the machine is presented in Fig. 1a.

The voltage equations that describe the 3+3 circuits are:

$$u_{as} = R_s i_{as} + \frac{d\psi_{as}}{dt}, \quad u_{bs} = R_s i_{bs} + \frac{d\psi_{bs}}{dt}, \quad u_{cs} = R_s i_{cs} + \frac{d\psi_{cs}}{dt} \tag{1}$$

$$u_{AR} = R_R i_{AR} + \frac{d\psi_{AR}}{dt}, \quad u_{BR} = R_R i_{BR} + \frac{d\psi_{BR}}{dt}, \quad u_{CR} = R_R i_{CR} + \frac{d\psi_{CR}}{dt} \tag{2}$$

In a matrix form, the equations become:

$$\left[u_{abcs}\right]=\left[R_s\right]\left[i_{abcs}\right]+\frac{d\left[\psi_{abcs}\right]}{dt} \tag{3}$$

$$\left[u_{ABCR}\right]=\left[R_R\right]\left[i_{ABCR}\right]+\frac{d\left[\psi_{ABCR}\right]}{dt} \tag{4}$$

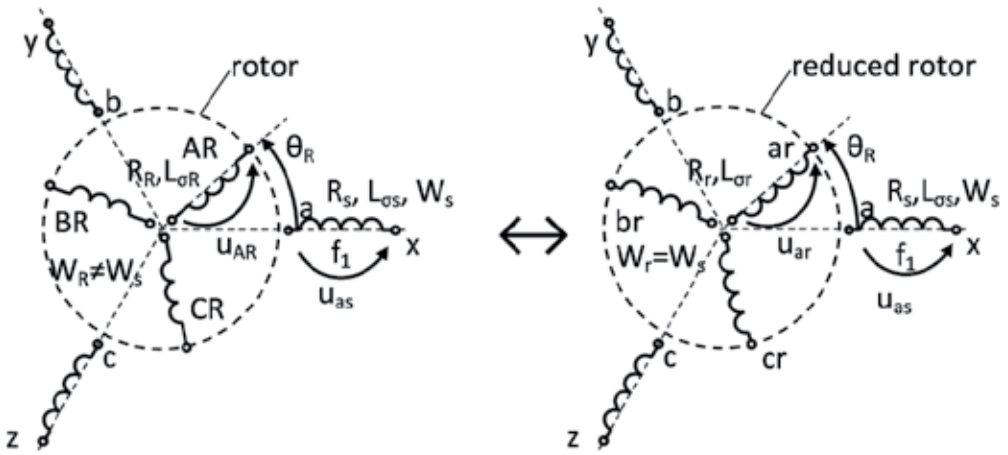

Figure 1. Schematic model of three-phase induction machine: a. real; b. reduced rotor

The quantities in brackets represent the matrices of voltages, currents, resistances and total flux linkages for the stator and rotor. Obviously, the total fluxes include both main and mutual components. Further, we define the self-phase inductances, which have a leakage and a main component: $L_{jj}=L_{\sigma s}+L_{hs}$ for stator and $L_{JJ}=L_{\Sigma R}+L_{HR}$ for rotor. The mutual inductances of two phases placed on the same part (stator or rotor) have negative values, which are equal to half of the maximum mutual inductances and with the main self-phase component: $M_{jk}=L_{jk}=L_{hj}=L_{hk}$. The expressions in matrix form are:

$$\left[L_{ss}\right]=\begin{bmatrix} L_{\sigma s}+L_{hs} & -(1/2)L_{hs} & -(1/2)L_{hs} \\ -(1/2)L_{hs} & L_{\sigma s}+L_{hs} & -(1/2)L_{hs} \\ -(1/2)L_{hs} & -(1/2)L_{hs} & L_{\sigma s}+L_{hs} \end{bmatrix} \tag{5-1}$$

$$\left[L_{RR}\right]=\begin{bmatrix} L_{\Sigma R}+L_{HR} & -(1/2)L_{HR} & -(1/2)L_{HR} \\ -(1/2)L_{HR} & L_{\Sigma R}+L_{HR} & -(1/2)L_{HR} \\ -(1/2)L_{HR} & -(1/2)L_{HR} & L_{\Sigma R}+L_{HR} \end{bmatrix} \tag{5-2}$$

$$\left[L_{sR}\right]=\left[L_{Rs}\right]_t=L_{sR}\cdot\begin{bmatrix} \cos\theta_R & \cos\left(\theta_R+u\right) & \cos\left(\theta_R+2u\right) \\ \cos\left(\theta_R+2u\right) & \cos\theta_R & \cos\left(\theta_R+u\right) \\ \cos\left(\theta_R+u\right) & \cos\left(\theta_R+2u\right) & \cos\theta_R \end{bmatrix} \tag{5-3}$$

where u denotes the angle of 120^0 (or $2\pi/3$ rad).

The analysis of the induction machine usually reduces the rotor circuit to the stator one. This operation requires the alteration of the rotor quantities with the coefficient $k=W_s/W_R$ by complying with the conservation rules. The new values are:

$$u_{abcr} = k \cdot u_{ABCR}; \quad \psi_{abcr} = k \cdot \psi_{ABCR}; \quad i_{abcr} = (1/k) \cdot i_{ABCR};$$

$$R_r = k^2 \cdot R_R; \quad L_{hr} = k^2 \cdot L_{HR} = \left(\frac{W_s}{W_R}\right)^2 \cdot \frac{W_R^2}{\Re_h} = \frac{W_s^2}{\Re_h} = L_{hs}; \tag{6}$$

$$L_{\sigma r} = k^2 L_{\Sigma R} = \left(\frac{W_s}{W_R}\right)^2 \frac{W_R^2}{\Re_{\sigma R}} = \frac{W_s^2}{\Re_{\sigma r}} \approx L_{\sigma s}; \; L_{sr} = k L_{sR} = \left(\frac{W_s}{W_R}\right)\frac{W_s W_R}{\Re_h} = L_{hs}$$

where the reluctances of the flux paths have been used. The new matrices, with rotor quantities denoted with lowercase letters are:

$$\left[L_{rr}\right] = k^2\left[L_{RR}\right] = \begin{bmatrix} L_{\sigma r}+L_{hs} & -(1/2)L_{hs} & -(1/2)L_{hs} \\ -(1/2)L_{hs} & L_{\sigma r}+L_{hs} & -(1/2)L_{hs} \\ -(1/2)L_{hs} & -(1/2)L_{hs} & L_{\sigma r}+L_{hs} \end{bmatrix} \tag{7-1}$$

$$\left[L_{sr}\right] = k\left[L_{sR}\right] = \left[L_{rs}\right]_t = L_{hs} \cdot \begin{bmatrix} \cos\theta_R & \cos(\theta_R+u) & \cos(\theta_R+2u) \\ \cos(\theta_R+2u) & \cos\theta_R & \cos(\theta_R+u) \\ \cos(\theta_R+u) & \cos(\theta_R+2u) & \cos\theta_R \end{bmatrix} \tag{7-2}$$

By virtue of these transformations, the voltage equations become:

$$\begin{cases} \left[u_{abcs}\right] = \left[R_s\right]\left[i_{abcs}\right] + \dfrac{d\left[\psi_{abcs}\right]}{dt} = \left[R_s\right]\left[i_{abcs}\right] + \left[L_{ss}\right]\dfrac{d\left[i_{abcs}\right]}{dt} + \dfrac{d\left\{\left[L_{sr}\right]\left[i_{abcr}\right]\right\}}{dt} \\ \left[u_{abcr}\right] = \left[R_r\right]\left[i_{abcr}\right] + \dfrac{d\left[\psi_{abcr}\right]}{dt} = \left[R_r\right]\left[i_{abcr}\right] + \left[L_{rr}\right]\dfrac{d\left[i_{abcr}\right]}{dt} + \dfrac{d\left\{\left[L_{sr}\right]_t\left[i_{abcs}\right]\right\}}{dt} \end{cases} \tag{8}$$

By using the notations:

$$\begin{aligned} (\Sigma L_\Pi) &= L_{\sigma r}(3L_{hs}+L_{\sigma s}) + L_{\sigma s}(3L_{hs}+L_{\sigma r}) \\ (\Pi L_s) &= L_{\sigma r}(L_{hs}+L_{\sigma s}) + L_{\sigma s}(3L_{hs}+L_{\sigma r}) \\ (\Pi L_r) &= L_{\sigma s}(L_{hs}+L_{\sigma r}) + L_{\sigma r}(3L_{hs}+L_{\sigma s}) \end{aligned} \tag{9}$$

and after the separation of the currents derivatives, (8) can be written under operational form as follows:

$$\left(\bar{s}+\frac{R_s\left(\Pi L_s\right)}{L_{\sigma s}\left(\Sigma L_\Pi\right)}\right)\bar{i}_{as}=-\frac{R_s L_{hs} L_{\sigma r}}{L_{\sigma s}\left(\Sigma L_\Pi\right)}\left(\bar{i}_{bs}+\bar{i}_{cs}\right)+\frac{2R_r L_{hs}}{\left(\Sigma L_\Pi\right)}\left[\bar{i}_{ar}\cos\theta_R+\bar{i}_{br}\cos\left(\theta_R+u\right)+\bar{i}_{cr}\cos\left(\theta_R+2u\right)\right]+$$
$$+\dot{\theta}_R\frac{L_{hs}\left(3L_{hs}+2L_{\sigma r}\right)}{\left(\Sigma L_\Pi\right)}\left[\bar{i}_{ar}\sin\theta_R+\bar{i}_{br}\sin\left(\theta_R+u\right)+\bar{i}_{cr}\sin\left(\theta_R+2u\right)\right]+$$
$$+2{,}6\dot{\theta}_R\frac{L_{hs}^2}{\left(\Sigma L_\Pi\right)}\left(\bar{i}_{bs}-\bar{i}_{cs}\right)+\frac{L_{\sigma r}L_{hs}}{L_{\sigma s}\left(\Sigma L_\Pi\right)}\left(\bar{u}_{as}+\bar{u}_{bs}+\bar{u}_{cs}\right)+\frac{3L_{hs}+2L_{\sigma r}}{\left(\Sigma L_\Pi\right)}\bar{u}_{as}-$$
$$-\frac{2L_{hs}}{\left(\Sigma L_\Pi\right)}\left[\bar{u}_{ar}\cos\theta_R+\bar{u}_{br}\cos\left(\theta_R+u\right)+\bar{u}_{cr}\cos\left(\theta_R+2u\right)\right],$$

$$\left(\bar{s}+\frac{R_s\left(\Pi L_s\right)}{L_{\sigma s}\left(\Sigma L_\Pi\right)}\right)\bar{i}_{bs}=-\frac{R_s L_{hs} L_{\sigma r}}{L_{\sigma s}\left(\Sigma L_\Pi\right)}\left(\bar{i}_{cs}+\bar{i}_{as}\right)+\frac{2R_r L_{hs}}{\left(\Sigma L_\Pi\right)}\left[\bar{i}_{br}\cos\theta_R+\bar{i}_{cr}\cos\left(\theta_R+u\right)+\bar{i}_{ar}\cos\left(\theta_R+2u\right)\right]+$$
$$+\dot{\theta}_R\frac{L_{hs}\left(3L_{hs}+2L_{\sigma r}\right)}{\left(\Sigma L_\Pi\right)}\left[\bar{i}_{br}\sin\theta_R+\bar{i}_{cr}\sin\left(\theta_R+u\right)+\bar{i}_{ar}\sin\left(\theta_R+2u\right)\right]+$$
$$+2{,}6\dot{\theta}_R\frac{L_{hs}^2}{\left(\Sigma L_\Pi\right)}\left(\bar{i}_{cs}-\bar{i}_{as}\right)+\frac{L_{\sigma r}L_{hs}}{L_{\sigma s}\left(\Sigma L_\Pi\right)}\left(\bar{u}_{as}+\bar{u}_{bs}+\bar{u}_{cs}\right)+\frac{3L_{hs}+2L_{\sigma r}}{\left(\Sigma L_\Pi\right)}\bar{u}_{bs}-$$
$$-\frac{2L_{hs}}{\left(\Sigma L_\Pi\right)}\left[\bar{u}_{br}\cos\theta_R+\bar{u}_{cr}\cos\left(\theta_R+u\right)+\bar{u}_{ar}\cos\left(\theta_R+2u\right)\right],$$

$$\left(\bar{s}+\frac{R_s\left(\Pi L_s\right)}{L_{\sigma s}\left(\Sigma L_\Pi\right)}\right)\bar{i}_{cs}=-\frac{R_s L_{hs} L_{\sigma r}}{L_{\sigma s}\left(\Sigma L_\Pi\right)}\left(\bar{i}_{as}+\bar{i}_{bs}\right)+\frac{2R_r L_{hs}}{\left(\Sigma L_\Pi\right)}\left[\bar{i}_{cr}\cos\theta_R+\bar{i}_{ar}\cos\left(\theta_R+u\right)+\bar{i}_{br}\cos\left(\theta_R+2u\right)\right]+$$
$$+\dot{\theta}_R\frac{L_{hs}\left(3L_{hs}+2L_{\sigma r}\right)}{\left(\Sigma L_\Pi\right)}\left[\bar{i}_{cr}\sin\theta_R+\bar{i}_{ar}\sin\left(\theta_R+u\right)+\bar{i}_{br}\sin\left(\theta_R+2u\right)\right]+$$
$$+2{,}6\dot{\theta}_R\frac{L_{hs}^2}{\left(\Sigma L_\Pi\right)}\left(\bar{i}_{as}-\bar{i}_{bs}\right)+\frac{L_{\sigma r}L_{hs}}{L_{\sigma s}\left(\Sigma L_\Pi\right)}\left(\bar{u}_{as}+\bar{u}_{bs}+\bar{u}_{cs}\right)+\frac{3L_{hs}+2L_{\sigma r}}{\left(\Sigma L_\Pi\right)}\bar{u}_{cs}-$$
$$-\frac{2L_{hs}}{\left(\Sigma L_\Pi\right)}\left[\bar{u}_{cr}\cos\theta_R+\bar{u}_{ar}\cos\left(\theta_R+u\right)+\bar{u}_{br}\cos\left(\theta_R+2u\right)\right],$$

$$\left(\bar{s}+\frac{R_r\left(\Pi L_r\right)}{L_{\sigma r}\left(\Sigma L_\Pi\right)}\right)\bar{i}_{ar}=\frac{2L_{hs}R_s}{\left(\Sigma L_\Pi\right)}\left[\bar{i}_{as}\cos\theta_R+\bar{i}_{bs}\cos\left(\theta_R+2u\right)+\bar{i}_{cs}\cos\left(\theta_R+u\right)\right]+2{,}6\dot{\theta}_R\frac{L_{hs}^2}{\left(\Sigma L_\Pi\right)}\left(-\bar{i}_{br}+\bar{i}_{cr}\right)-$$
$$-\frac{2L_{hs}}{\left(\Sigma L_\Pi\right)}\left[\bar{u}_{as}\cos\theta_R+\bar{u}_{bs}\cos\left(\theta_R+2u\right)+\bar{u}_{cs}\cos\left(\theta_R+u\right)\right]+\frac{L_{\sigma s}L_{hs}}{L_{\sigma r}\left(\Sigma L_\Pi\right)}\left(\bar{u}_{ar}+\bar{u}_{br}+\bar{u}_{cr}\right)+$$
$$+\frac{2L_{\sigma s}+3L_{hs}}{\left(\Sigma L_\Pi\right)}\bar{u}_{ar}+\dot{\theta}_R L_{hs}\frac{2L_{\sigma s}+3L_{hs}}{\left(\Sigma L_\Pi\right)}\left[\bar{i}_{as}\sin\theta_R+\bar{i}_{bs}\sin\left(\theta_R+2u\right)+\bar{i}_{cs}\sin\left(\theta_R+u\right)\right]-$$
$$-\frac{L_{\sigma s}L_{hs}R_r}{L_{\sigma r}\left(\Sigma L_\Pi\right)}\left(\bar{i}_{br}+\bar{i}_{cr}\right),$$

$$\left(\bar{s}+\frac{R_r\left(\Pi L_r\right)}{L_{\sigma r}\left(\Sigma L_\Pi\right)}\right)\bar{i}_{br}=\frac{2L_{hs}R_s}{\left(\Sigma L_\Pi\right)}\left[\bar{i}_{bs}\cos\theta_R+\bar{i}_{cs}\cos\left(\theta_R+2u\right)+\bar{i}_{as}\cos\left(\theta_R+u\right)\right]+2{,}6\dot{\theta}_R\frac{L_{hs}^2}{\left(\Sigma L_\Pi\right)}\left(-\bar{i}_{cr}+\bar{i}_{ar}\right)-$$
$$-\frac{2L_{hs}}{\left(\Sigma L_\Pi\right)}\left[\bar{u}_{bs}\cos\theta_R+\bar{u}_{cs}\cos\left(\theta_R+2u\right)+\bar{u}_{as}\cos\left(\theta_R+u\right)\right]+\frac{L_{\sigma s}L_{hs}}{L_{\sigma r}\left(\Sigma L_\Pi\right)}\left(\bar{u}_{ar}+\bar{u}_{br}+\bar{u}_{cr}\right)+$$
$$+\frac{2L_{\sigma s}+3L_{hs}}{\left(\Sigma L_\Pi\right)}\bar{u}_{br}+\dot{\theta}_R L_{hs}\frac{2L_{\sigma s}+3L_{hs}}{\left(\Sigma L_\Pi\right)}\left[\bar{i}_{bs}\sin\theta_R+\bar{i}_{cs}\sin\left(\theta_R+2u\right)+\bar{i}_{as}\sin\left(\theta_R+u\right)\right]-$$
$$-\frac{L_{\sigma s}L_{hs}R_r}{L_{\sigma r}\left(\Sigma L_\Pi\right)}\left(\bar{i}_{cr}+\bar{i}_{ar}\right),$$

$$\left(\bar{s}+\frac{R_r\left(\Pi L_r\right)}{L_{\sigma r}\left(\Sigma L_\Pi\right)}\right)\bar{i}_{cr}=\frac{2L_{hs}R_s}{\left(\Sigma L_\Pi\right)}\left[\bar{i}_{cs}\cos\theta_R+\bar{i}_{as}\cos\left(\theta_R+2u\right)+\bar{i}_{bs}\cos\left(\theta_R+u\right)\right]+2{,}6\dot{\theta}_R\frac{L_{hs}^2}{\left(\Sigma L_\Pi\right)}\left(-\bar{i}_{ar}+\bar{i}_{br}\right)-$$
$$-\frac{2L_{hs}}{\left(\Sigma L_\Pi\right)}\left[\bar{u}_{cs}\cos\theta_R+\bar{u}_{as}\cos\left(\theta_R+2u\right)+\bar{u}_{bs}\cos\left(\theta_R+u\right)\right]+\frac{L_{\sigma s}L_{hs}}{L_{\sigma r}\left(\Sigma L_\Pi\right)}\left(\bar{u}_{ar}+\bar{u}_{br}+\bar{u}_{cr}\right)+ \quad (10)$$
$$+\frac{2L_{\sigma s}+3L_{hs}}{\left(\Sigma L_\Pi\right)}\bar{u}_{cr}+\dot{\theta}_R L_{hs}\frac{2L_{\sigma s}+3L_{hs}}{\left(\Sigma L_\Pi\right)}\left[\bar{i}_{cs}\sin\theta_R+\bar{i}_{as}\sin\left(\theta_R+2u\right)+\bar{i}_{bs}\sin\left(\theta_R+u\right)\right]-$$
$$-\frac{L_{\sigma s}L_{hs}R_r}{L_{\sigma r}\left(\Sigma L_\Pi\right)}\left(\bar{i}_{ar}+\bar{i}_{br}\right),$$

Besides (10), the equations concerning mechanical quantities must be added. To this end, the electromagnetic torque has to be calculated. To this effect, we start from the coenergy expression, W'_m, of the 6 circuits (3 are placed on stator and the other 3 on rotor) and we take into consideration that the leakage fluxes, which are independent of rotation angle of the rotor, do not generate electromagnetic torque, that is:

$$W'_m=\frac{1}{2}\left[i_{abcs}\right]_t\left(\left[L_{ss}\right]-L_{\sigma s}\left[1\right]\right)\left[i_{abcs}\right]+\frac{1}{2}\left[i_{abcr}\right]_t\left(\left[L_{rr}\right]-L_{\sigma r}\left[1\right]\right)\left[i_{abcr}\right]+\left[i_{abcs}\right]_t\left[L_{sr}\left(\theta_R\right)\right]\left[i_{abcr}\right] \quad (11)$$

The magnetic energy of the stator and the rotor does not depend on the rotation angle and consequently, for the electromagnetic torque calculus nothing but the last term of (11) is used. One obtains:

$$T_e=\frac{1}{2}p\left[i_{abcs}\right]_t\frac{d\left[L_{sr}\left(\theta_R\right)\right]}{d\theta_R}\left[i_{abcr}\right]=$$
$$=\frac{1}{2}pL_{hs}\sin\theta_R\left[i_{as}\left(-2i_{ar}+i_{br}+i_{cr}\right)+i_{bs}\left(+i_{ar}-2i_{br}+i_{cr}\right)+i_{cs}\left(+i_{ar}+i_{br}-2i_{cr}\right)\right]+ \quad (12)$$
$$+\frac{\sqrt{3}}{2}pL_{hs}\cos\theta_R\left[i_{as}\left(i_{cr}-i_{br}\right)+i_{bs}\left(i_{ar}-i_{cr}\right)+i_{cs}\left(i_{br}-i_{ar}\right)\right]$$

The equation of torque equilibrium can now be written under operational form as:

$$\bar{\omega}_R\left(\frac{J\bar{s}+k_z}{p}\right)=\frac{1}{2}pL_{hs}\left\{\sin\theta_R\cdot\left[i_{as}\left(-2i_{ar}+i_{br}+i_{cr}\right)+i_{bs}\left(i_{ar}-2i_{br}+i_{cr}\right)+\right.\right.$$
$$\left.\left.+i_{cs}\left(i_{ar}+i_{br}-2i_{cr}\right)\right]+\sqrt{3}\cos\theta_R\cdot\left[i_{as}\left(i_{cr}-i_{br}\right)+i_{bs}\left(i_{ar}-i_{cr}\right)+i_{cs}\left(i_{br}-i_{ar}\right)\right]\right\}-T_{st}$$

$$\bar{s}\bar{\theta}_R=\omega_R=\dot{\theta}_R \quad (13)$$

where ω_R represents the *rotational pulsatance* (or *rotational pulsation*).

The simulation of the induction machine operation in Matlab-Simulink environment on the basis of the above equations system is rather complicated. Moreover, since all equations depend on the angular speed than the precision of the results could be questionable mainly for the study of rapid transients. Consequently, the use of other variables is understandable. Further, we shall use the *total fluxes* of the windings (3 motionless windings on stator and other rotating 3 windings on rotor).

It is well known that the total fluxes have a self-component and a mutual one. Taking into consideration the rules of reducing the rotor circuit to the stator one, the matrix of inductances can be written as follows:

$$\left[L_{abcabc}\right]=L_{hs}\cdot\begin{bmatrix} 1+l_{\sigma s} & -(1/2) & -(1/2) & \cos\theta_R & \cos(\theta_R+u) & \cos(\theta_R+2u)\\ -(1/2) & 1+l_{\sigma s} & -(1/2) & \cos(\theta_R+2u) & \cos\theta_R & \cos(\theta_R+u)\\ -(1/2) & -(1/2) & 1+l_{\sigma s} & \cos(\theta_R+u) & \cos(\theta_R+2u) & \cos\theta_R\\ \cos\theta_R & \cos(\theta_R+2u) & \cos(\theta_R+u) & 1+l_{\sigma r} & -(1/2) & -(1/2)\\ \cos(\theta_R+u) & L_{hs}\cos\theta_R & \cos(\theta_R+2u) & -(1/2) & 1+l_{\sigma r} & -(1/2)\\ \cos(\theta_R+2u) & \cos(\theta_R+u) & \cos\theta_R & -(1/2) & -(1/2) & 1+l_{\sigma r} \end{bmatrix} \tag{14}$$

Now, the equation system (8) can be written shortly as:

$$\left[u_{abcabc}\right]=\left[R_{s,r}\right]\left[i_{abcabc}\right]+\frac{d\left[\psi_{abcabc}\right]}{dt},\quad where:\ \left[\psi_{abcabc}\right]=\left[L_{abcabc}\right]\left[i_{abcabc}\right] \tag{15}$$

By using the multiplication with the reciprocal matrix:

$$\left[L_{abcabc}\right]^{-1}\left[\psi_{abcabc}\right]=\left[L_{abcabc}\right]^{-1}\left[L_{abcabc}\right]\left[i_{abcabc}\right],\quad or\ \left[i_{abcabc}\right]=\left[L_{abcabc}\right]^{-1}\left[\psi_{abcabc}\right] \tag{16}$$

than (15) becomes:

$$\left[u_{abcabc}\right]=\left[R_{s,r}\right]\left[L_{abcabc}\right]^{-1}\left[\psi_{abcabc}\right]+\frac{d\left[\psi_{abcabc}\right]}{dt} \tag{17}$$

This is an expression that connects the voltages to the total fluxes with no currents involvement. Now, practically the reciprocal matrix must be found. To this effect, we suppose that the reciprocal matrix has a similar form with the direct matrix. If we use the condition: $\left[L_{abcabc}\right]^{-1}\left[L_{abcabc}\right]=\left[1\right]$, than through term by term identification is obtained:

$$\left[L_{abcabc}\right]^{-1}=\frac{1}{(\Pi LD)}\cdot \begin{bmatrix} \Pi L_{s\sigma} & L_{hs}L_{\sigma r}^2 & L_{hs}L_{\sigma r}^2 & \Gamma\cos\theta_R & \Gamma\cos(\theta_R+u) & \Gamma\cos(\theta_R+2u)\\ L_{hs}L_{\sigma r}^2 & \Pi L_{s\sigma} & L_{hs}L_{\sigma r}^2 & \Gamma\cos(\theta_R+2u) & \Gamma\cos\theta_R & \Gamma\cos(\theta_R+u)\\ L_{hs}L_{\sigma r}^2 & L_{hs}L_{\sigma r}^2 & \Pi L_{s\sigma} & \Gamma\cos(\theta_R+u) & \Gamma\cos(\theta_R+2u) & \Gamma\cos\theta_R\\ \Gamma\cos\theta_R & \Gamma\cos(\theta_R+2u) & \Gamma\cos(\theta_R+u) & \Pi L_{r\sigma} & L_{hs}L_{\sigma s}^2 & L_{hs}L_{\sigma s}^2\\ \Gamma\cos(\theta_R+u) & \Gamma\cos\theta_R & \Gamma\cos(\theta_R+2u) & L_{hs}L_{\sigma s}^2 & \Pi L_{r\sigma} & L_{hs}L_{\sigma s}^2\\ \Gamma\cos(\theta_R+2u) & \Gamma\cos(\theta_R+u) & \Gamma\cos\theta_R & L_{hs}L_{\sigma s}^2 & L_{hs}L_{\sigma s}^2 & \Pi L_{r\sigma} \end{bmatrix} \tag{18}$$

where the following notations have been used:

$$\begin{gathered}(\Pi LD)=\left(3L_{hs}L_{\sigma s}+3L_{hs}L_{\sigma r}+2L_{\sigma r}L_{\sigma s}\right)L_{\sigma r}L_{\sigma s};\qquad \Gamma=-2L_{hs}L_{\sigma s}L_{\sigma r};\\ \Pi L_{s\sigma}=\left(L_{hs}L_{\sigma r}+3L_{hs}L_{\sigma s}+2L_{\sigma r}L_{\sigma s}\right)L_{\sigma r};\quad \Pi L_{r\sigma}=\left(L_{hs}L_{\sigma s}+3L_{hs}L_{\sigma r}+2L_{\sigma r}L_{\sigma s}\right)L_{\sigma s}\end{gathered} \tag{19}$$

Further, the matrix product is calculated: $\left[R_{s,r}\right]\left[L_{abcabc}\right]^{-1}\left[\psi_{abcabc}\right]$, which is used in (17). After a convenient grouping, the system becomes:

$$\frac{d\psi_{as}}{dt}+\frac{\Pi L_{s\sigma}R_s}{(\Pi LD)}\psi_{as}=u_{as}-\frac{L_{hs}L_{\sigma r}^2R_s}{(\Pi LD)}(\psi_{bs}+\psi_{cs})+\frac{L_{hs}L_{\sigma s}L_{\sigma r}R_s}{(\Pi LD)}\times \\ \times\left[(2\psi_{ar}-\psi_{br}-\psi_{cr})\cos\theta_R+\sqrt{3}(\psi_{cr}-\psi_{br})\sin\theta_R\right] \tag{20-1}$$

$$\frac{d\psi_{bs}}{dt}+\frac{\Pi L_{s\sigma}R_s}{(\Pi LD)}\psi_{bs}=u_{bs}-\frac{L_{hs}L_{\sigma r}^2R_s}{(\Pi LD)}(\psi_{cs}+\psi_{as})+\frac{L_{hs}L_{\sigma s}L_{\sigma r}R_s}{(\Pi LD)}\times \\ \times\left[(-\psi_{ar}+2\psi_{br}-\psi_{cr})\cos\theta_R+\sqrt{3}(\psi_{ar}-\psi_{cr})\sin\theta_R\right] \tag{20-2}$$

$$\frac{d\psi_{cs}}{dt}+\frac{\Pi L_{s\sigma}R_s}{(\Pi LD)}\psi_{cs}=u_{cs}-\frac{L_{hs}L_{\sigma r}^2R_s}{(\Pi LD)}(\psi_{as}+\psi_{bs})+\frac{L_{hs}L_{\sigma s}L_{\sigma r}R_s}{(\Pi LD)}\times \\ \times\left[(-\psi_{ar}-\psi_{br}+2\psi_{cr})\cos\theta_R+\sqrt{3}(\psi_{br}-\psi_{ar})\sin\theta_R\right] \tag{20-3}$$

$$\frac{d\psi_{ar}}{dt}+\frac{\Pi L_{r\sigma}R_r}{(\Pi LD)}\psi_{ar}=u_{ar}-\frac{L_{hs}L_{\sigma s}^2R_r}{(\Pi LD)}(\psi_{br}+\psi_{cr})+\frac{L_{hs}L_{\sigma s}L_{\sigma r}R_r}{(\Pi LD)}\times \\ \times\left[(2\psi_{as}-\psi_{bs}-\psi_{cs})\cos\theta_R+\sqrt{3}(\psi_{bs}-\psi_{cs})\sin\theta_R\right] \tag{20-4}$$

$$\frac{d\psi_{br}}{dt}+\frac{\Pi L_{r\sigma}R_r}{(\Pi LD)}\psi_{br}=u_{br}-\frac{L_{hs}L_{\sigma s}^2R_r}{(\Pi LD)}(\psi_{cr}+\psi_{ar})+\frac{L_{hs}L_{\sigma s}L_{\sigma r}R_r}{(\Pi LD)}\times \\ \times\left[(-\psi_{as}+2\psi_{bs}-\psi_{cs})\cos\theta_R+\sqrt{3}(\psi_{cs}-\psi_{as})\sin\theta_R\right] \tag{20-5}$$

$$\frac{d\psi_{cr}}{dt}+\frac{\Pi L_{r\sigma}R_r}{(\Pi LD)}\psi_{cr}=u_{cr}-\frac{L_{hs}L_{\sigma s}^2R_r}{(\Pi LD)}(\psi_{ar}+\psi_{br})+\frac{L_{hs}L_{\sigma s}L_{\sigma r}R_r}{(\Pi LD)}\times \\ \times\left[(-\psi_{as}-\psi_{bs}+2\psi_{cs})\cos\theta_R+\sqrt{3}(\psi_{as}-\psi_{bs})\sin\theta_R\right] \tag{20-6}$$

For the calculation of the *electromagnetic torque* we can use the principle of energy conservation or the expression of stored magnetic energy. The expression of the electromagnetic torque corresponding to a multipolar machine (p is the number of pole pairs) can be written in a matrix form as follows:

$$T_e=-\frac{p}{2}\cdot\left\{\left[\psi_{abcabc}\right]_t\cdot\frac{d\left[L_{abcabc}\right]^{-1}}{d\theta_R}\cdot\left[\psi_{abcabc}\right]\right\} \tag{21}$$

To demonstrate the validity of (21), one uses the expression of the matrix $\left[L_{abcabc}\right]^{-1}$, (18), in order to calculate its derivative:

$$\frac{d}{d\theta_R}\left[L_{abcabc}\right]^{-1} = \Lambda_3 \cdot \begin{bmatrix} 0 & 0 & 0 & \sin\theta_R & \sin(\theta_R+u) & \sin(\theta_R+2u) \\ 0 & 0 & 0 & \sin(\theta_R+2u) & \sin\theta_R & \sin(\theta_R+u) \\ 0 & 0 & 0 & \sin(\theta_R+u) & \sin(\theta_R+2u) & \sin\theta_R \\ \sin\theta_R & \sin(\theta_R+2u) & \sin(\theta_R+u) & 0 & 0 & 0 \\ \sin(\theta_R+u) & \sin\theta_R & \sin(\theta_R+2u) & 0 & 0 & 0 \\ \sin(\theta_R+2u) & \sin(\theta_R+u) & \sin\theta_R & 0 & 0 & 0 \end{bmatrix} \tag{22}$$

where the following notation has been used:

$$\Lambda_3 = \frac{1}{(3/2)(L_{\sigma s} + L_{\sigma r}) + L_{\sigma r}L_{\sigma s}/L_{hs}} \tag{23}$$

This expression defines the permeance of a three-phase machine for the mathematical model in total fluxes.

Observation: One can use the general expression of the electromagnetic torque where the direct and reciprocal matrices of the inductances (which link the currents with the fluxes) should be replaced, that is:

$$T_e = \frac{1}{2}p\left[i_{abcabc}\right]_t \frac{d\left[L_{abcabc}\right]}{d\theta_R}\left[i_{abcabc}\right] = \frac{1}{2}p\cdot\left[\psi_{abcabc}\right]_t\left[L\right]_t^{-1}\cdot\frac{d\left[L_{abcabc}\right]}{d\theta_R}\cdot\left[L\right]^{-1}\left[\psi_{abcabc}\right]$$
$$T_e = -\frac{1}{2}p\left[\psi_{abcabc}\right]_t \frac{d\left[L_{abcabc}\right]^{-1}}{d\theta_R}\left[\psi_{abcabc}\right] \tag{24}$$

A more convenient expression that depends on $\sin\theta_R$ and $\cos\theta_R$, leads to the electromagnetic torque equation *in fluxes* alone:

$$T_e = -(1/2)p\Lambda_3\left\{\left[\psi_{as}(2\psi_{ar}-\psi_{br}-\psi_{cr})+\psi_{bs}(2\psi_{br}-\psi_{cr}-\psi_{ar})+\psi_{cs}(2\psi_{cr}-\psi_{ar}-\psi_{br})\right]\sin\theta_R + \right.$$
$$\left. +\sqrt{3}\left[\psi_{as}(\psi_{br}-\psi_{cr})+\psi_{bs}(\psi_{cr}-\psi_{ar})+\psi_{cs}(\psi_{ar}-\psi_{br})\right]\cos\theta_R\right\} \tag{25}$$

Ultimately, by getting together the equations of the 6 electric circuits and the movement equations we obtain an 8 equation system, which can be written under operational form:

$$\overline{\psi}_{as}\left(\bar{s}+\frac{\Pi L_{s\sigma}R_s}{(\Pi LD)}\right) = \bar{u}_{as} - \frac{L_{hs}L_{\sigma r}^2R_s}{(\Pi LD)}\left(\overline{\psi}_{bs}+\overline{\psi}_{cs}\right)+\frac{L_{hs}L_{\sigma s}L_{\sigma r}R_s}{(\Pi LD)}\times$$
$$\times\left[\left(2\overline{\psi}_{ar}-\overline{\psi}_{br}-\overline{\psi}_{cr}\right)\cos\theta_R+\sqrt{3}\left(\overline{\psi}_{cr}-\overline{\psi}_{br}\right)\sin\theta_R\right] \tag{26-1}$$

$$\overline{\psi}_{bs}\left(\bar{s}+\frac{\Pi L_{s\sigma}R_s}{(\Pi LD)}\right) = \bar{u}_{bs} - \frac{L_{hs}L_{\sigma r}^2R_s}{(\Pi LD)}\left(\overline{\psi}_{cs}+\overline{\psi}_{as}\right)+\frac{L_{hs}L_{\sigma s}L_{\sigma r}R_s}{(\Pi LD)}\times$$
$$\times\left[\left(-\overline{\psi}_{ar}+2\overline{\psi}_{br}-\overline{\psi}_{cr}\right)\cos\theta_R+\sqrt{3}\left(\overline{\psi}_{ar}-\overline{\psi}_{cr}\right)\sin\theta_R\right] \tag{26-2}$$

$$\bar{\psi}_{cs}\left(\bar{s}+\frac{\Pi L_{s\sigma}R_s}{(\Pi LD)}\right)=\bar{u}_{cs}-\frac{L_{hs}L_{\sigma r}^2R_s}{(\Pi LD)}\left(\bar{\psi}_{as}+\bar{\psi}_{bs}\right)+\frac{L_{hs}L_{\sigma s}L_{\sigma r}R_s}{(\Pi LD)}\times$$
$$\times\left[\left(-\bar{\psi}_{ar}-\bar{\psi}_{br}+2\bar{\psi}_{cr}\right)\cos\theta_R+\sqrt{3}\left(\bar{\psi}_{br}-\bar{\psi}_{ar}\right)\sin\theta_R\right] \tag{26-3}$$

$$\bar{\psi}_{ar}\left(\bar{s}+\frac{\Pi L_{r\sigma}R_r}{(\Pi LD)}\right)=\bar{u}_{ar}-\frac{L_{hs}L_{\sigma s}^2R_r}{(\Pi LD)}\left(\bar{\psi}_{br}+\bar{\psi}_{cr}\right)+\frac{L_{hs}L_{\sigma s}L_{\sigma r}R_r}{(\Pi LD)}\times$$
$$\times\left[\left(2\bar{\psi}_{as}-\bar{\psi}_{bs}-\bar{\psi}_{cs}\right)\cos\theta_R+\sqrt{3}\left(\bar{\psi}_{bs}-\bar{\psi}_{cs}\right)\sin\theta_R\right] \tag{26-4}$$

$$\bar{\psi}_{br}\left(\bar{s}+\frac{\Pi L_{r\sigma}R_r}{(\Pi LD)}\right)=\bar{u}_{br}-\frac{L_{hs}L_{\sigma s}^2R_r}{(\Pi LD)}\left(\bar{\psi}_{cr}+\bar{\psi}_{ar}\right)+\frac{L_{hs}L_{\sigma s}L_{\sigma r}R_r}{(\Pi LD)}\times$$
$$\times\left[\left(-\bar{\psi}_{as}+2\bar{\psi}_{bs}-\bar{\psi}_{cs}\right)\cos\theta_R+\sqrt{3}\left(\bar{\psi}_{cs}-\bar{\psi}_{as}\right)\sin\theta_R\right] \tag{26-5}$$

$$\bar{\psi}_{cr}\left(\bar{s}+\frac{\Pi L_{r\sigma}R_r}{(\Pi LD)}\right)=\bar{u}_{cr}-\frac{L_{hs}L_{\sigma s}^2R_r}{(\Pi LD)}\left(\bar{\psi}_{ar}+\bar{\psi}_{br}\right)+\frac{L_{hs}L_{\sigma s}L_{\sigma r}R_r}{(\Pi LD)}\times$$
$$\times\left[\left(-\bar{\psi}_{as}-\bar{\psi}_{bs}+2\bar{\psi}_{cs}\right)\cos\theta_R+\sqrt{3}\left(\bar{\psi}_{as}-\bar{\psi}_{bs}\right)\sin\theta_R\right] \tag{26-6}$$

$$\dot{\theta}_R\left(\bar{s}+k_z/J\right)=(p/J)\left\langle-(1/2)p\Lambda_3\left\{\sin\theta_R\left[\bar{\psi}_{as}\left(2\bar{\psi}_{ar}-\bar{\psi}_{br}-\bar{\psi}_{cr}\right)+\right.\right.\right.$$
$$+\bar{\psi}_{bs}\left(2\bar{\psi}_{br}-\bar{\psi}_{cr}-\bar{\psi}_{ar}\right)+\bar{\psi}_{cs}\left(2\bar{\psi}_{cr}-\bar{\psi}_{ar}-\bar{\psi}_{br}\right)\Big]+\sqrt{3}\cos\theta_R \tag{26-7}$$
$$\left.\left.\left.\cdot\left[\bar{\psi}_{as}\left(\bar{\psi}_{br}-\bar{\psi}_{cr}\right)+\bar{\psi}_{bs}\left(\bar{\psi}_{cr}-\bar{\psi}_{ar}\right)+\bar{\psi}_{cs}\left(\bar{\psi}_{ar}-\bar{\psi}_{br}\right)\right]\right\}-T_{st}\right\rangle$$

$$\frac{d\theta_R}{dt}=\dot{\theta}_R=\omega_R \tag{26-8}$$

This equation system, (26-1)-(26-8) allows the study of any operation duty of the three-phase induction machine: steady state or transients under balanced or unbalanced condition, with simple or double feeding.

3. Mathematical models used for the study of steady-state under balanced and unbalanced conditions

Generally, the symmetrical three-phase squirrel cage induction machine has the stator windings connected to a supply system, which provides variable voltages according to certain laws but have the same pulsation. Practically, this is the case with 4 wires connection, 3 phases and the neutral. The sum of the phase currents gives the current along neutral and the homopolar component can be immediately defined. The analysis of such a machine can use the symmetric components theory. This is the case of the machine with *two unbalances* as concerns the supply. The study can be done either using

the equation system (26-1...8) or on the basis of symmetric components theory with three distinct mathematical models for each component (positive sequence, negative sequence and homopolar).

The vast majority of electric drives uses however the 3 wires connection (no neutral). Consequently, there is no homopolar current component, the homopolar fluxes are zero as well and the sum of the 3 phase total fluxes is null. This is an asymmetric condition with *single unbalance,* which can be studied by using the direct and inverse sequence components when the transformation from 3 to 2 axes is mandatory. This approach practically replaces the three-phase machine with unbalanced supply with two symmetric three-phase machines. One of them produces the positive torque and the other provides the negative torque. The resultant torque comes out through superposition of the effects.

3.1. The abc-$\alpha\beta$0 model in total fluxes

The operation of the machine with 2 unbalances can be analyzed by considering certain expressions for the instantaneous values of the stator and rotor quantities (voltages, total fluxes and currents eventually, which can be transformed from (a, b, c) to (α, β, 0) reference frames in accordance with the following procedure :

$$\begin{bmatrix} \psi_{\alpha s} \\ \psi_{\beta s} \\ \psi_{0s} \end{bmatrix} = \sqrt{\frac{2}{3}} \cdot \begin{bmatrix} 1 & -1/2 & -1/2 \\ 0 & \sqrt{3}/2 & -\sqrt{3}/2 \\ \sqrt{2}/2 & \sqrt{2}/2 & \sqrt{2}/2 \end{bmatrix} \cdot \begin{bmatrix} \psi_{as} \\ \psi_{bs} \\ \psi_{cs} \end{bmatrix} \tag{27}$$

We define the following notations:

$$\begin{aligned}
&\frac{\Pi L_{s\sigma} R_s}{(\Pi LD)} = \frac{\left(L_{hs}L_{\sigma r} + 3L_{hs}L_{\sigma s} + 2L_{\sigma r}L_{\sigma s}\right)}{\left(3L_{hs}L_{\sigma r} + 3L_{hs}L_{\sigma s} + 2L_{\sigma r}L_{\sigma s}\right)}\left(\frac{R_s}{L_{\sigma s}}\right) \cong \frac{2}{3}\left(\frac{R_s}{L_{\sigma s}}\right) = \nu_{st};\\
&\frac{L_{hs}L_{\sigma r}^2 R_s}{(\Pi LD)} = \frac{L_{hs}L_{\sigma r}R_s}{\left(3L_{hs}L_{\sigma s} + 3L_{hs}L_{\sigma r} + 2L_{\sigma r}L_{\sigma s}\right)L_{\sigma s}} \cong \frac{1}{6}\left(\frac{R_s}{L_{\sigma s}}\right) = \nu_{sr};\\
&\nu_{st} - \nu_{sr} = \frac{3 + 2\left(L_{\sigma r}/L_{hs}\right)}{3\left(L_{\sigma r}/L_{\sigma s}\right) + 3 + 2\left(L_{\sigma r}/L_{hs}\right)}\left(\frac{R_s}{L_{\sigma s}}\right) \cong \frac{1}{2}\left(\frac{R_s}{L_{\sigma s}}\right) = \nu_s
\end{aligned} \tag{28-1}$$

$$\begin{aligned}
&\frac{\Pi L_{r\sigma} R_r}{(\Pi LD)} = \frac{\left(L_{hs}L_{\sigma s} + 3L_{hs}L_{\sigma r} + 2L_{\sigma r}L_{\sigma s}\right)}{\left(3L_{hs}L_{\sigma r} + 3L_{hs}L_{\sigma s} + 2L_{\sigma r}L_{\sigma s}\right)}\left(\frac{R_r}{L_{\sigma r}}\right) \cong \frac{2}{3}\left(\frac{R_r}{L_{\sigma r}}\right) = \nu_{rt};\\
&\frac{L_{hs}L_{\sigma s}^2 R_r}{(\Pi LD)} = \frac{L_{hs}L_{\sigma s}R_r}{\left(3L_{hs}L_{\sigma s} + 3L_{hs}L_{\sigma r} + 2L_{\sigma r}L_{\sigma s}\right)L_{\sigma r}} \cong \frac{1}{6}\left(\frac{R_r}{L_{\sigma r}}\right) = \nu_{rs};\\
&\nu_{rt} - \nu_{rs} = \frac{3 + 2\left(L_{\sigma s}/L_{hs}\right)}{3\left(L_{\sigma s}/L_{\sigma r}\right) + 3 + 2\left(L_{\sigma s}/L_{hs}\right)}\left(\frac{R_r}{L_{\sigma r}}\right) \cong \frac{1}{2}\left(\frac{R_r}{L_{\sigma r}}\right) = \nu_r
\end{aligned} \tag{28-2}$$

$$\frac{3L_{hs}L_{\sigma s}L_{\sigma r}R_s}{(\Pi LD)} = \frac{3L_{\sigma s}}{\left(3L_{\sigma s}+3L_{\sigma r}+2L_{\sigma r}L_{\sigma s}/L_{hs}\right)}\left(\frac{R_s}{L_{\sigma s}}\right) \cong \frac{1}{2}\left(\frac{R_s}{L_{\sigma s}}\right) = \nu_{\sigma s}; \tag{28-3}$$

$$\frac{3L_{hs}L_{\sigma s}L_{\sigma r}R_r}{(\Pi LD)} = \frac{3L_{\sigma r}}{\left(3L_{\sigma s}+3L_{\sigma r}+2L_{\sigma r}L_{\sigma s}/L_{hs}\right)}\left(\frac{R_r}{L_{\sigma r}}\right) \cong \frac{1}{2}\left(\frac{R_r}{L_{\sigma r}}\right) = \nu_{\sigma r}; \tag{28-4}$$

By using these notations in (17) and after convenient groupings we obtain:

$$\frac{d\psi_{as}}{dt}+\nu_{st}\psi_{as} = u_{as}-\nu_{sr}\left(\psi_{bs}+\psi_{cs}\right)+\frac{1}{3}\nu_{\sigma s}\times \\ \times\left[\left(2\psi_{ar}-\psi_{br}-\psi_{cr}\right)\cos\theta_R+\sqrt{3}\left(\psi_{cr}-\psi_{br}\right)\sin\theta_R\right] \tag{29-1}$$

$$\frac{d\psi_{bs}}{dt}+\nu_{st}\psi_{bs} = u_{bs}-\nu_{sr}\left(\psi_{cs}+\psi_{as}\right)+\frac{1}{3}\nu_{\sigma s}\times \\ \times\left[\left(-\psi_{ar}+2\psi_{br}-\psi_{cr}\right)\cos\theta_R+\sqrt{3}\left(\psi_{ar}-\psi_{cr}\right)\sin\theta_R\right] \tag{29-2}$$

$$\frac{d\psi_{cs}}{dt}+\nu_{st}\psi_{cs} = u_{cs}-\nu_{sr}\left(\psi_{as}+\psi_{bs}\right)+\frac{1}{3}\nu_{\sigma s}\times \\ \times\left[\left(-\psi_{ar}-\psi_{br}+2\psi_{cr}\right)\cos\theta_R+\sqrt{3}\left(\psi_{br}-\psi_{ar}\right)\sin\theta_R\right] \tag{29-3}$$

$$\frac{d\psi_{ar}}{dt}+\nu_{rt}\psi_{ar} = u_{ar}-\nu_{rs}\left(\psi_{br}+\psi_{cr}\right)+\frac{1}{3}\nu_{\sigma r}\times \\ \times\left[\left(2\psi_{as}-\psi_{bs}-\psi_{cs}\right)\cos\theta_R+\sqrt{3}\left(\psi_{bs}-\psi_{cs}\right)\sin\theta_R\right] \tag{29-4}$$

$$\frac{d\psi_{br}}{dt}+\nu_{rt}\psi_{br} = u_{br}-\nu_{rs}\left(\psi_{cr}+\psi_{ar}\right)+\frac{1}{3}\nu_{\sigma r}\times \\ \times\left[\left(-\psi_{as}+2\psi_{bs}-\psi_{cs}\right)\cos\theta_R+\sqrt{3}\left(\psi_{cs}-\psi_{as}\right)\sin\theta_R\right] \tag{29-5}$$

$$\frac{d\psi_{cr}}{dt}+\nu_{rt}\psi_{cr} = u_{cr}-\nu_{rs}\left(\psi_{ar}+\psi_{br}\right)+\frac{1}{3}\nu_{\sigma r}\times \\ \times\left[\left(-\psi_{bs}+2\psi_{cs}-\psi_{as}\right)\cos\theta_R+\sqrt{3}\left(\psi_{as}-\psi_{bs}\right)\sin\theta_R\right] \tag{29-6}$$

Typical for the cage machine or even for the wound rotor after the starting rheostat is short-circuited is the fact that the *rotor voltages become zero*. The equations of the six circuits get different as a result of certain convenient math operations. (29-2) and (29-3) are multiplied by (-1/2) and afterwards added to (29-1); (29-3) is subtracted from (29-2); (29-1), (29-2) and (29-3) are added together. We obtain three equations that describe the stator. Similarly, (29-4), (29-5) and (29-6) are used for the rotor equations. The new equation system is:

$$\begin{cases} \dfrac{d\psi_{\alpha s}}{dt} + \nu_s \psi_{\alpha s} = u_{\alpha s} + \nu_{\sigma s}\left(\psi_{\alpha r}\cos\theta_R - \psi_{\beta r}\sin\theta_R\right) \\ \dfrac{d\psi_{\beta s}}{dt} + \nu_s \psi_{\beta s} = u_{\beta s} + \nu_{\sigma s}\left(\psi_{\alpha r}\sin\theta_R + \psi_{\beta r}\cos\theta_R\right) \\ \dfrac{d\psi_{0s}}{dt} + \left(\nu_{st} + 2\nu_{sr}\right)\psi_{0s} = u_{0s} \end{cases} \quad (30\text{-}1, 2, 3)$$

$$\begin{cases} \dfrac{d\psi_{\alpha r}}{dt} + \nu_r \psi_{\alpha r} = u_{\alpha r} + \nu_{\sigma r}\left(\psi_{\alpha s}\cos\theta_R + \psi_{\beta s}\sin\theta_R\right) \\ \dfrac{d\psi_{\beta r}}{dt} + \nu_r \psi_{\beta r} = u_{\beta r} + \nu_{\sigma r}\left(-\psi_{\alpha s}\sin\theta_R + \psi_{\beta s}\cos\theta_R\right) \\ \dfrac{d\psi_{0r}}{dt} + \left(\nu_{rt} + 2\nu_{rs}\right)\psi_{0r} = u_{0r} \end{cases} \quad (30\text{-}4, 5, 6)$$

Further, the movement equation has to be attached. It is necessary to establish the detailed expression of the electromagnetic torque in *fluxes* alone starting with (25) and using convenient transformations:

$$T_e = -\left(3/2\right)p\Lambda_3\left[\left(\psi_{\alpha s}\psi_{\alpha r} + \psi_{\beta s}\psi_{\beta r}\right)\sin\theta_R + \left(\psi_{\alpha s}\psi_{\beta r} - \psi_{\beta s}\psi_{\alpha r}\right)\cos\theta_R\right] \quad (31)$$

Ultimately, the 8 equation system under operational form is:

$$\overline{\psi}_{\alpha s}\left(\bar{s} + \nu_s\right) = \overline{u}_{\alpha s} + \nu_{\sigma s}\left(\overline{\psi}_{\alpha r}\cos\theta_R - \overline{\psi}_{\beta r}\sin\theta_R\right) \quad (32\text{-}1)$$

$$\overline{\psi}_{\beta s}\left(\bar{s} + \nu_s\right) = \overline{u}_{\beta s} + \nu_{\sigma s}\left(\overline{\psi}_{\alpha r}\sin\theta_R + \overline{\psi}_{\beta r}\cos\theta_R\right) \quad (32\text{-}2)$$

$$\overline{\psi}_{0s}\left(\bar{s} + \nu_{st} + 2\nu_{sr}\right) = \overline{u}_{0s} \quad (32\text{-}3)$$

$$\overline{\psi}_{\alpha r}\left(\bar{s} + \nu_r\right) = \overline{u}_{\alpha r} + \nu_{\sigma r}\left(\overline{\psi}_{\alpha s}\cos\theta_R + \overline{\psi}_{\beta s}\sin\theta_R\right) \quad (32\text{-}4)$$

$$\overline{\psi}_{\beta r}\left(\bar{s} + \nu_r\right) = \overline{u}_{\beta r} + \nu_{\sigma r}\left(-\overline{\psi}_{\alpha s}\sin\theta_R + \overline{\psi}_{\beta s}\cos\theta_R\right) \quad (32\text{-}5)$$

$$\overline{\psi}_{0r}\left(\bar{s} + \nu_{rt} + 2\nu_{rs}\right) = \overline{u}_{0r} \quad (32\text{-}6)$$

$$\dot{\theta}_R\left(\bar{s} + k_z / J\right) = \left(p/J\right)\cdot\left\{-\left(3/2\right)p\Lambda_3\left[\left(\overline{\psi}_{\alpha s}\overline{\psi}_{\alpha r} + \overline{\psi}_{\beta s}\overline{\psi}_{\beta r}\right)\sin\theta_R + \left(\overline{\psi}_{\alpha s}\overline{\psi}_{\beta r} - \overline{\psi}_{\beta s}\overline{\psi}_{\alpha r}\right)\cos\theta_R\right] - T_{st}\right\} \quad (32\text{-}7)$$

$$\frac{d\theta_R}{dt} = \dot{\theta}_R = \omega_R \quad (32\text{-}8)$$

These equations allow the study of three-phase induction machine for any duty. It has to be mentioned that the electromagnetic torque expression has no homopolar components of the total fluxes.

3.2. The abc-dq model in total fluxes

For the study of the single unbalance condition is necessary to consider expressions of the instantaneous values of the stator and rotor quantities (voltages, total fluxes and eventually currents in *a,b,c* reference frame) whose sum is null. The real quantities can be transformed to (d,q) reference frame (Simion et al., 2011). By using the notations (28-1), (28-2), (28-3) and (28-4) then after convenient grouping we obtain (Simion, 2010):

$$\begin{aligned}\frac{d\psi_{\alpha s}}{dt}+\nu_s\psi_{\alpha s}&=u_{\alpha s}+\nu_{\sigma s}\left(\psi_{\alpha r}\cos\theta_R-\psi_{\beta r}\sin\theta_R\right)\\ \frac{d\psi_{\beta s}}{dt}+\nu_s\psi_{\beta s}&=u_{\beta s}+\nu_{\sigma s}\left(\psi_{\alpha r}\sin\theta_R+\psi_{\beta r}\cos\theta_R\right)\end{aligned} \tag{33-1, 2}$$

$$\begin{aligned}\frac{d\psi_{\alpha r}}{dt}+\nu_r\psi_{\alpha r}&=\nu_{\sigma r}\left(\psi_{\alpha s}\cos\theta_R+\psi_{\beta s}\sin\theta_R\right)\\ \frac{d\psi_{\beta r}}{dt}+\nu_r\psi_{\beta r}&=\nu_{\sigma r}\left(-\psi_{\alpha s}\sin\theta_R+\psi_{\beta s}\cos\theta_R\right)\end{aligned} \tag{33-3, 4}$$

Further, the movement equation (31) must be attached. The operational form of the equation system (4 electric circuits and 2 movement equations) is:

$$\overline{\psi}_{\alpha s}\left(\bar{s}+\nu_s\right)=\overline{u}_{\alpha s}+\nu_{\sigma s}\left(\overline{\psi}_{\alpha r}\cos\theta_R-\overline{\psi}_{\beta r}\sin\theta_R\right) \tag{34-1}$$

$$\overline{\psi}_{\beta s}\left(\bar{s}+\nu_s\right)=\overline{u}_{\beta s}+\nu_{\sigma s}\left(\overline{\psi}_{\alpha r}\sin\theta_R+\overline{\psi}_{\beta r}\cos\theta_R\right) \tag{34-2}$$

$$\overline{\psi}_{\alpha r}\left(\bar{s}+\nu_r\right)=\nu_{\sigma r}\left(\overline{\psi}_{\alpha s}\cos\theta_R+\overline{\psi}_{\beta s}\sin\theta_R\right) \tag{34-3}$$

$$\overline{\psi}_{\beta r}\left(\bar{s}+\nu_r\right)=\nu_{\sigma r}\left(-\overline{\psi}_{\alpha s}\sin\theta_R+\overline{\psi}_{\beta s}\cos\theta_R\right) \tag{34-4}$$

$$\dot{\theta}_R\left(\bar{s}+k_z/J\right)=\left(p/J\right)\cdot\left\{-\left(3/2\right)p\Lambda_3\left[\left(\overline{\psi}_{\alpha s}\overline{\psi}_{\alpha r}+\overline{\psi}_{\beta s}\overline{\psi}_{\beta r}\right)\sin\theta_R+\left(\overline{\psi}_{\alpha s}\overline{\psi}_{\beta r}-\overline{\psi}_{\beta s}\overline{\psi}_{\alpha r}\right)\cos\theta_R\right]-T_{st}\right\} \tag{34-5}$$

$$\frac{d\theta_R}{dt}=\dot{\theta}_R=\omega_R \tag{34-6}$$

The equation sets (33-1...4) and (34-1...6) prove that a three-phase induction machine connected to the supply system by 3 wires can be studied similarly to a two-phase machine

(*two-phase* mathematical model). Its parameters can be deduced by linear transformations of the original parameters including the supply voltages (Fig. 2a).

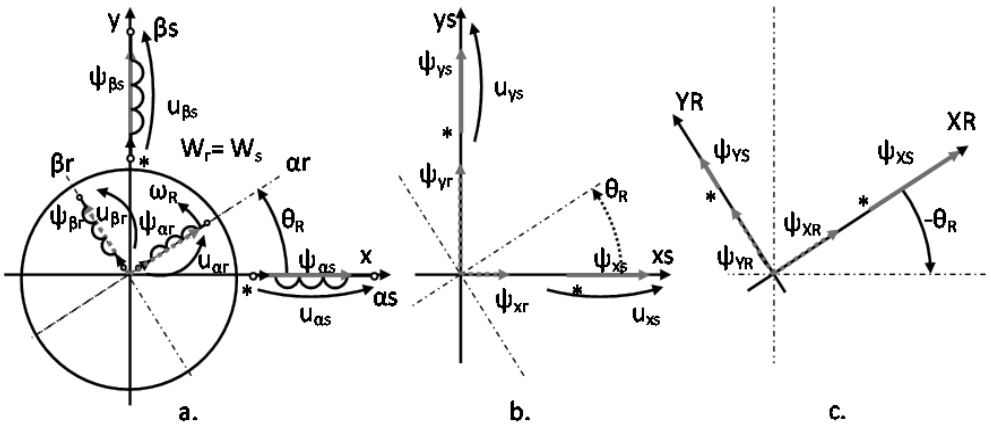

Figure 2. Induction machine schematic view: a.Two-phase model; b. Simplified view of the total fluxes in stator reference frame; c. Idem, but in rotor reference frame

The windings of two-phase model are denoted with (*αs, βs*) and (*αr, βr*) in order to trace a correspondence with the real two-phase machine, whose subscripts are (*as, bs*) and (*ar, br*) respectively. We shall use the subscripts *xs* and *ys* for the quantities that corresponds to the three-phase machine but transformed in its two-phase model. This is a rightful assumption since (*αs, βs*) axes are collinear with (*x, y*) axes, which are commonly used in analytic geometry. Further, new notations (35) for the flux linkages of the right member of the equations (33-1...4) will be defined by following the next rules:

- projection sums corresponding to rotor flux linkages from (*αr, βr*) axes along the two stator axes (denoted with *x* and *y* that is ψ_{xr}, ψ_{yr}) when they refer to the flux linkages from the right member of the first two equations, Fig. 2b.
- projection sums corresponding to stator flux linkages from (*αs, βs*) axes along the two rotor axes (denoted with *X* and *Y* that is ψ_{XS}, ψ_{YS}) when they refer to the flux linkages from the last two equations, Fig. 2c.

$$\begin{cases} \psi_{xr} = \psi_{\alpha r}\cos\theta_R - \psi_{\beta r}\sin\theta_R, & \psi_{yr} = \psi_{\alpha r}\sin\theta_R + \psi_{\beta r}\cos\theta_R \\ \psi_{XS} = \psi_{\alpha s}\cos\theta_R + \psi_{\beta s}\sin\theta_R, & \psi_{YS} = -\psi_{\alpha s}\sin\theta_R + \psi_{\beta s}\cos\theta_R \end{cases} \tag{35}$$

Some aspects have to be pointed out. When the machine operates under motoring duty, the pulsation of the stator flux linkages from (*αs, βs*) axes is equal to ω_s. Since the rotational pulsation is ω_R then the pulsation of the rotor quantities from (*αr, βr*) axes is equal to $\omega_r = s\omega_s = \omega_s - \omega_R$. The pulsation of the rotor quantities projected along the stator axes with the subscripts *xr* and *yr* is equal to ω_s. The pulsation of the stator quantities projected along the rotor axes with the subscripts *XS* and *YS* is equal to ω_r. The equations (33-1...4) become:

$$\overline{\psi}_{\alpha s}(\bar{s}+\nu_s)=\overline{u}_{\alpha s}+\nu_{\sigma s}\overline{\psi}_{xr} \tag{36-1}$$

$$\overline{\psi}_{\beta s}(\bar{s}+\nu_s)=\overline{u}_{\beta s}+\nu_{\sigma s}\overline{\psi}_{yr} \tag{36-2}$$

$$\overline{\psi}_{\alpha r}(\bar{s}+\nu_r)=\nu_{\sigma r}\overline{\psi}_{XS} \tag{36-3}$$

$$\overline{\psi}_{\beta r}(\bar{s}+\nu_r)=\nu_{\sigma r}\overline{\psi}_{YS} \tag{36-4}$$

The first two equations join the quantities with the pulsation ω_s and the other two, the quantities with the pulsation $\omega_r = s\omega_s$. The expression of the magnetic torque, in *total fluxes* and *rotor position angle* becomes:

$$T_e=-(3/2)p\Lambda_3\left(\overline{\psi}_{\alpha s}\overline{\psi}_{yr}-\overline{\psi}_{\beta s}\overline{\psi}_{xr}\right) \tag{37}$$

or a second equivalent expression:

$$T_e=(3/2)p\Lambda_3\left(\overline{\psi}_{\alpha r}\overline{\psi}_{YS}-\overline{\psi}_{\beta r}\overline{\psi}_{XS}\right) \tag{38}$$

which shows the "total symmetry" of the two-phase model of the three-phase machine regarding both stator and rotor. The equations of the four circuits together with the movement equation (37) under operational form give:

$$\overline{\psi}_{\alpha s}\left(\bar{s}+\nu_s\right)=\overline{u}_{\alpha s}+\nu_{\sigma s}\overline{\psi}_{xr} \tag{39-1}$$

$$\overline{\psi}_{\beta s}\left(\bar{s}+\nu_s\right)=\overline{u}_{\beta s}+\nu_{\sigma s}\overline{\psi}_{yr} \tag{39-2}$$

$$\overline{\psi}_{\alpha r}\left(\bar{s}+\nu_r\right)=\nu_{\sigma r}\overline{\psi}_{XS} \tag{39-3}$$

$$\overline{\psi}_{\beta r}\left(\bar{s}+\nu_r\right)=\nu_{\sigma r}\overline{\psi}_{YS} \tag{39-4}$$

$$\dot{\theta}_R\left(\bar{s}+k_z/J\right)=\left(p/J\right)\cdot\left\{\ (3/2)p\Lambda_3\left(\overline{\psi}_{\beta s}\overline{\psi}_{xr}-\overline{\psi}_{\alpha s}\overline{\psi}_{yr}\right)-T_{st}\right\} \tag{39-5}$$

$$\frac{d\theta_R}{dt}=\dot{\theta}_R=\omega_R \tag{39-6}$$

This last equation system allows the study of transients under single unbalance condition. It is similar with the frequently used equations (Park) but contains as variables only total fluxes and the rotation angle. There are no currents or angular speed in the voltage equations.

4. Expressions of electromagnetic torque

For the steady state analysis of the symmetric three-phase induction machine, one can define the simplified space phasor of the stator flux, which is collinear to the total flux of the

(αs) axis and has a $\sqrt{3}$ times higher modulus. In a similar way can be obtained the space phasors of the stator voltages and rotor fluxes and the system equation (39-1...6) that describe the steady state becomes:

$$\begin{aligned} \underline{U}_{sR3} &= \left(\nu_s + j\omega_s\right)\underline{\Psi}_{sR3} - \nu_{\sigma s}\underline{\Psi}_{rR3} = \left(\omega_s - j\nu_s\right)\Psi_{sR3}e^{j\alpha_s} + j\nu_{\sigma s}\Psi_{rR3}e^{j\alpha_r} \\ 0 &= \nu_{\sigma r}\underline{\Psi}_{sR3} - \left(\nu_r + js\omega_s\right)\underline{\Psi}_{rR3} = -j\nu_{\sigma r}\Psi_{sR3}e^{j\alpha_s} + \left(j\nu_r - s\omega_s\right)\Psi_{rR3}e^{j\alpha_r} \end{aligned} \tag{40}$$

$$T_e = \left(3/2\right)p\Lambda_3\Psi_{sR3}\Psi_{rR3}\sin\left(\alpha_s - \alpha_r\right)$$

When the speed regulation of the cage induction machine is employed by means of voltage and/or frequency variation then the simultaneous control of the two total flux space vectors is difficult. As consequence, new strategies more convenient can be chosen. To this effect, we shall deduce expressions of the electromagnetic torque that include only one of the total flux space vectors either from stator or rotor.

4.1. Variation of the torque with the stator total flux space vector

One of the methods used for the control of induction machine consists in the operation with *constant stator total flux space vector*. From (40), the rotor total flux space vector is:

$$\begin{aligned} \underline{\Psi}_{rR3} &= \frac{\nu_{\sigma r}}{\nu_r + js\omega_s}\underline{\Psi}_{sR3} = \frac{\nu_{\sigma r}\underline{\Psi}_{sR3}}{\sqrt{\omega_s^2 s^2 + \nu_r^2}}\left(\frac{\nu_r}{\sqrt{\omega_s^2 s^2 + \nu_r^2}} - j\frac{s\omega_s}{\sqrt{\omega_s^2 s^2 + \nu_r^2}}\right) = \\ &= \frac{\nu_{\sigma r}\underline{\Psi}_{sR3}}{\sqrt{\omega_s^2 s^2 + \nu_r^2}}e^{-j\theta};(\theta = \alpha_s - \alpha_r);\sin\theta = \frac{s\omega_s}{\sqrt{\omega_s^2 s^2 + \nu_r^2}};\cos\theta = \frac{\nu_r}{\sqrt{\omega_s^2 s^2 + \nu_r^2}} \end{aligned} \tag{41}$$

where θ is the angle between stator and rotor total flux space vectors. This angle has the meaning of an *internal angle of the machine*.

The expression of the magnetic torque that depends with the stator total flux space vector becomes:

$$\begin{aligned} T_e &= -\left(\frac{3}{2}\right)p\Lambda_3\,\mathrm{Re}\left(j\underline{\Psi}_{sR3}\underline{\Psi}^*_{rR3}\right) = -\left(\frac{3}{2}\right)p\Lambda_3\,\mathrm{Re}\left\{j\underline{\Psi}_{sR3}\frac{\nu_{\sigma r}}{\sqrt{\omega_s^2 s^2 + \nu_r^2}}\cdot\underline{\Psi}^*_{sR3}\left(\cos\theta + j\sin\theta\right)\right\} = \\ &= \frac{3}{2}\frac{\nu_{\sigma r}}{\nu_r}p\Lambda_3\Psi^2_{sR3}\frac{s\omega_s\nu_r}{\omega_s^2 s^2 + \nu_r^2} = \frac{3}{4}\frac{\nu_{\sigma r}}{\nu_r}p\Lambda_3\Psi^2_{sR3}\sin 2\theta. \end{aligned} \tag{42}$$

Assuming the ideal hypothesis of maintaining constant the stator flux, for example equal to the no-load value, then the pull-out torque, T_{emax}, corresponds to $\sin 2\theta = 1$ that is:

$$\begin{aligned} &2\sin\theta\cos\theta = 1 \leftrightarrow s_{cr}\omega_s = \nu_r, and\ T_{e\max} = \frac{3}{4}\frac{\nu_{\sigma r}}{\nu_r}p\Lambda_3\Psi^2_{sR3}; \\ &or\ T_{e\max} = \frac{3}{2}\nu_{\sigma r}p\Lambda_3\left(\frac{U_{sR3}}{\omega_s}\right)^2\frac{\nu_r}{\nu_s^2\left(\nu_r/\omega_s\right)^2 + 2\nu_{\sigma s}\nu_{\sigma r}\nu_r/\omega_s + \nu_{tt}^2 + 2\nu_r^2} \end{aligned} \tag{43}$$

Now an observation can be formulated. Let us suppose an ideal static converter that operates with a U/*f*=*constant*=k_1 strategy. For low supply frequencies, the pull-out torque decreases in value since the denominator increases with the pulsatance decrease, ω_s (Fig. 3). Within certain limits at low frequencies, an increase of the supply voltage is necessary in order to maintain the pull-out torque value. In other words, $U/f = k_2$, and $k_2 > k_1$.

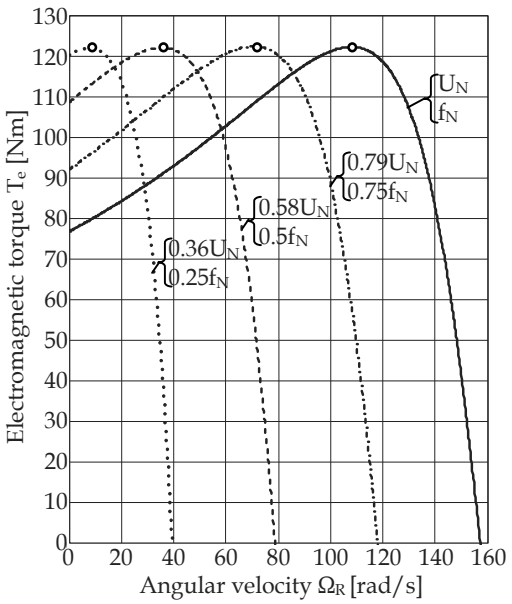

Figure 3. Mechanical characteristics, $M_e=f(\Omega_R)$ at $\Psi_{sR3}=const.$

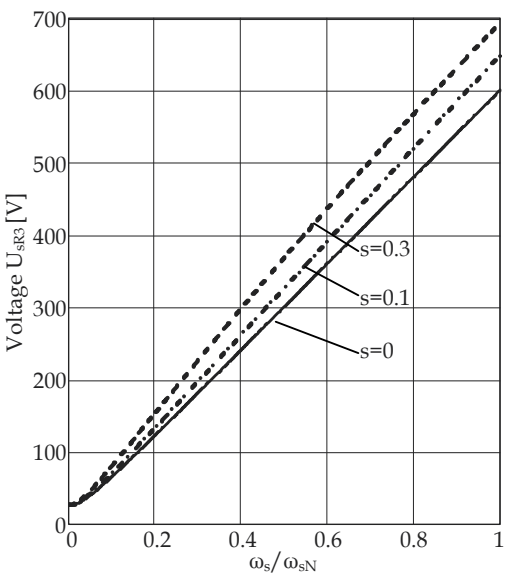

Figure 4. Resultant stator voltage vs. pulsatance $U_{sR3}=f(\omega_s)$ *at* $\Psi_{sR3}=const.$ *(1,91Wb)*

A proper control of the induction machine requires a strategy based on *U/f = variable*. More precisely, for low frequency values it is necessary to increase the supply voltage with respect to the values that result from *U/f = const.* strategy. At a pinch, when the frequency becomes zero, the supply voltage must have a value capable to compensate the voltage drops upon the equivalent resistance of the windings. Lately, the modern static converters can be parameterized on the basis of the catalog parameters of the induction machine or on the basis of some laboratory tests results.

From (40) we can deduce:

$$\underline{\Psi}_{sR3} = -j\frac{\underline{U}_{sR3}}{\omega_s}\frac{(s\omega_s - j\nu_r)}{(s\omega_s - \nu_{tt}) - j(\nu_r + s\nu_s)} \leftrightarrow U_{sR3}^2 = \frac{\Psi_{sR3}^2\omega_s^2\left(As^2 + 2Bs + C\right)}{\omega_s^2 s^2 + \nu_r^2} \tag{44}$$

and further:

$$\frac{U_{sR3}^2}{\omega_s^2} = \Psi_{sR3}^2\left[1 + \frac{\nu_s^2 s^2 + 2\nu_{\sigma s}\nu_{\sigma r}s + \nu_{tt}^2}{\omega_s^2 s^2 + \nu_r^2}\right] \leftrightarrow \Psi_{sR3} = \frac{U_{sR3}}{\omega_s}\sqrt{\frac{F(s)}{F(s) + sG(s)}} \tag{45}$$

$$where: \quad F(s) = \omega_s^2 s^2 + \nu_r^2; \quad G(s) \approx \nu_s^2 s + 2\nu_{\sigma s}\nu_{\sigma r}$$

if the term ν_{tt} was neglected. By inspecting the square root term, which is variable with the slip (and load as well), we can point out the following observations.

- Constant maintaining of the stator flux for *low pulsations* (that is low angular velocity values including start-up) can be obtained with a significant increase of the supply voltage. The "additional" increasing of the voltage depends proportionally on the load value. Analytically, this fact is caused by the predominance of the term G against F, (45). From the viewpoint of physical phenomena, a higher voltage in case of severe start-up or low frequency operation is necessary for the compensation of the leakage fluxes after which the stator flux must keep its prescribed value.
- Constant maintaining of the stator flux for *high pulsations* (that is angular speeds close or even over the rated value) requires an insignificant rise of the supply voltage. The *U/f* ratio is close to its rated value (rated values of *U* and *f*) especially for low load torque values. However, a certain increase of the voltage is required proportionally with the load degree. Analytically, this fact is now caused by the predominance of the term F against G, (45).
- In conclusion, the resultant stator flux remain constant for *U/f =constant=k*$_1$ strategy if the load torque is small. For high loads (especially if the operation is close to the pull-out point), the maintaining of the stator flux requires an increase of the *U/f* ratio, which means a significant rise of the voltage and current.

If the machine parameters are established, then a variation rule of the supply voltage can be settled in order to have a constant stator flux (equal, for example, to its no-load value) both for frequency and load variation.

Fig. 4 presents (for a machine with predetermined parameters: supply voltage with the amplitude of 490 V (U_{as}=346.5V); R_s=R_r=2; L_{hs}=0,09; $L_{\sigma s}$= $L_{\sigma r}$=0,01; J=0,05; p=2; k_z=0,02;

ω_1=314,1 (SI units)) the variation of the resultant stator voltage with the pulsatance (in per unit description) for three constant slip values. The variation is a straight line for reduced loads and has a certain inflection for low frequency values (a few Hz). For under-load operation, a significant increase of the voltage with the frequency is necessary. This fact is more visible at high slip values, close to pull-out value (in our example the pull-out slip is of 0,33).

The variation rule based on $U_{sR}=f(\omega_s)$ strategy (applied to the upper curve from Fig. 4) provide an operation of the motor within a large range of angular speeds (from start-up to rated point) under a developed torque, whose value is close to the pull-out one. Obviously, the input current is rather high (4-5 I_{1N}) and has to be reduced. Practically, the operation points must be placed within the upper and the lower curves, Fig. 4. It is also easy to notice that the operation with higher frequency values than the rated one does not generally require an increase of the supply voltage but the developed torque is lower and lower. In this case, the output power keeps the rated value.

4.2. Variation of the torque with the rotor total flux space vector

Usually, the electric drives that demand high value starting torque use *constant rotor total flux space vector* strategy. The stator total flux space vector can be written from (41) as:

$$\underline{\Psi}_{sR3}=\frac{\nu_r+js\omega_s}{\nu_{\sigma r}}\underline{\Psi}_{rR3}\Leftrightarrow\Psi_{sR3}=\Psi_{rR3}\frac{\sqrt{\omega_s^2s^2+\nu_r^2}}{\nu_{\sigma r}};\underline{\Psi}_{sR3}=\frac{\sqrt{\omega_s^2s^2+\nu_r^2}}{\nu_{\sigma r}}\underline{\Psi}_{rR3}e^{j\theta};$$
$$(\theta=\alpha_s-\alpha_r);\sin\theta=\frac{s\omega_s}{\sqrt{\omega_s^2s^2+\nu_r^2}};\cos\theta=\frac{\nu_r}{\sqrt{\omega_s^2s^2+\nu_r^2}} \tag{46}$$

and the expression of the electromagnetic torque on the basis of rotor flux alone becomes:

$$T_e=-\left(\frac{3}{2}\right)p\Lambda_3\,\mathrm{Re}\left(j\underline{\Psi}_{sR3}\underline{\Psi}^*_{rR3}\right)=\frac{3}{2}\frac{p\Lambda_3}{\nu_{\sigma r}}\Psi^2_{rR3}s\omega_s \tag{47}$$

Assuming the ideal hypothesis of maintaining constant the rotor flux, for example equal to the no-load value, then the electromagnetic torque expression is:

$$T_e=\frac{3}{2}\frac{p\Lambda_3}{\nu_{\sigma r}}\Psi^2_{rR30}s\omega_s\approx\frac{3}{2}\frac{p\Lambda_3}{\nu_{\sigma r}}\left(\frac{\nu_{\sigma r}U_{sR3}}{\nu_r\omega_s}\right)^2s\omega_s=\frac{3}{2}\frac{p\Lambda_3\nu_{\sigma r}}{\nu_r^2}\left(\frac{U^2_{sR3}}{\omega_s^2}\right)\left(\omega_s-p\Omega_R\right) \tag{48}$$

where the voltage and pulsation is supposed to have rated values. Taking into discussion a machine with predetermined parameters (supply voltage with the amplitude of 490 V (U_{as}=346.5V); R_s=R_r=2; L_{hs}=0,09; $L_{\sigma s}$= $L_{\sigma r}$=0,01; J=0,05; p=2; k_z=0,02; ω_1=314,1 (SI units)) then the expression of the mechanical characteristic is:

$$T_e=\frac{3}{2}\frac{2\cdot32,14\cdot96,43}{103,57^2}\left(\frac{U^2_{sR3N}}{\omega^2_{sN}}\right)\left(\omega_s-2\Omega_R\right)=3,17\left(\omega_s-2\Omega_R\right) \tag{49}$$

which is a straight line, A1 in Fig. 5. The two intersection points with the axes correspond to synchronism (T_e=0, Ω_R=ω_s/2=157) and start-up (T_e=995 Nm, Ω_R=0) respectively.

The pull-out torque is extremely high and acts at start-up. This behavior is caused by the hypothesis of maintaing constant the rotor flux at a value that corresponds to no-load operation (when the rotor reaction is null) no matter the load is. The compensation of the magnetic reaction of the rotor under load is *hypothetical* possible through an unreasonable increase of the supply voltage. Practically, the pull-out torque is much lower.

Another unreasonable possibility is the maintaining of the rotor flux to a value that corresponds to start-up (*s = 1*) and the supply voltage has its rated value. In this case the expression of the mechanical characteristic is (50) and the intersection points with the axes (line A2, Fig. 5) correspond to synchronism (T_e=0, Ω_R=ω_s/2=157) and start-up (T_e=78 Nm, Ω_R=0) respectively.

$$T_e = \frac{3}{2}\frac{2\cdot 32,14\cdot}{96,43}\Psi_{rRk}^2\left(\omega_s - 2\Omega_R\right) = 0,25\left(\omega_s - 2\Omega_R\right) \tag{50}$$

The supply of the stator winding with constant voltage and rated pulsation determines a variation of the resultant rotor flux within the short-circuit value (Ψ_{rRk}=0,5Wb) and the synchronism value (Ψ_{rR0}=1,78Wb). The operation points lie between the two lines, A1 and A2, on a position that depends on the load torque. When the supply pulsation is two times smaller (and the voltage itself is two times smaller as well) and the resultant rotor flux is maintained constant to the value Ψ_{rR0}=1,78Wb, then the mechanical characteristic is described by the straight line B1, which is parallel to the line A1. Similarly, for Ψ_{rRk}=0,5Wb, the mechanical characteristic become the line B2, which is parallel to A2.

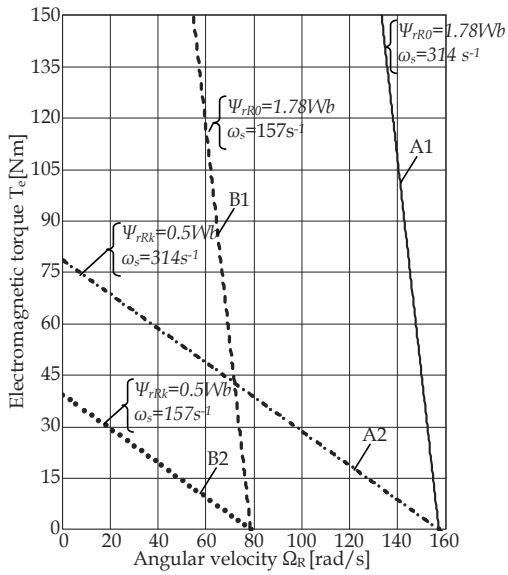

Figure 5. Mechanical characteristics $T_e=f(\Omega_R)$, $\Psi_{rR}=const.$

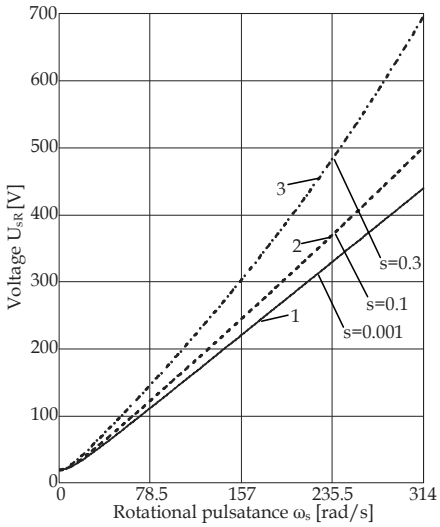

Figure 6. Resultant stator voltage vs. pulsatance, $U_{sR}=f(\omega_s)$ at $\Psi_{rR}=const.$ *(1.3Wb)*

When the applied voltage and pulsation are two times smaller regarding the rated values then the operation points lie between B1 and B2 since the rotor flux varies within Ψ_{rRk}=0,5Wb (short-circuit) and Ψ_{rR0}=1,78Wb (synchronism).

The control based on constant rotor flux strategy ensures parallel mechanical characteristics. This is an important advantage since the induction machine behaves like shunt D.C. motor. A second aspect is also favorable in the behavior under this strategy. The mechanical characteristic has no sector of unstable operation as the usual induction machine has.

The modification of the flux value (generally with decrease) leads to a different slope of the characteristics, which means a significant decrease of the torque for a certain angular speed.

The question is "what variation rule of U_{sR}/ω_s must be used in order to have constant rotor flux"? The expression of the modulus of the resultant rotor flux can be written as:

$$\frac{U_{sR3}^2}{\omega_s^2}=\Psi_{rR3}^2\frac{As^2+2Bs+C}{\nu_{\sigma r}^2}\leftrightarrow\frac{U_{sR3}}{\omega_s}=\frac{\Psi_{rR3}}{\nu_{\sigma r}}\sqrt{As^2+2Bs+C} \tag{51}$$

$$with:\quad A=\omega_s^2+\nu_s^2;B=\nu_{\sigma s}\nu_{\sigma r};C=\nu_r^2+\nu_{tt}^2;\nu_{tt}^2=(\nu_s\nu_r-\nu_{\sigma s}\nu_{\sigma r})^2/\omega_s^2\,.$$

Fig. 6 presents the variation of the stator voltage with pulsatance at constant resultant rotor flux (1,3 Wb), which are called the *control characteristics* of the static converter connected to the induction machine. The presented characteristics correspond to three constant slip values, s=0,001 (no-load)-curve 1, s=0,1 (rated duty)-curve 2 and s=0,3 (close to pull-out point)-curve 3. It can be seen that the operation with high slip values (high loads) require an increased stator voltage for a certain pulsation. As a matter of fact, the ratio U_{sR3}/ω_s must be increased with the load when the pulsatance (pulsation) and the angular speed rise as well. Such a strategy is indicated for fans, pumps or load machines with speed-dependent torque.

When the pulsation of the stator voltage is low (small angular velocities) then the torque that has to be overcame is small too, but it will rise with the speed and the frequency along a parabolic variation. Since the upper limit of the torque is given by the limited power of the machine (thermal considerations) then this strategy requires additional precautions as concern the safety devices that protect both the static converter and the supply source itself.

The analysis of the square root term from (51) generates similar remarks as in the above discussed control strategy.

Finally is important to say that a control characteristic must be prescribed for the static converter. This characteristic should be simplified and generally reduced to a straight line placed between the curves 1 and 2 from Fig. 6.

5. Study of the unbalanced duties

The unbalanced duties (generated by supply asymmetries) are generally analyzed by using the theory of symmetric components, according to which any asymmetric three-phase system with *single unbalance* (the sum of the applied instantaneous voltages is always zero) can be equated with two symmetric systems of opposite sequences: positive (+) (or direct) and negative (-) (or inverse) respectively. There are two possible ways for the analysis of this problem.

a. When the amplitudes of the phase voltages are different and/or the angles of phase difference are not equal to $2\pi/3$ then the *unbalanced three-phase* system can be replaced with an equivalent *unbalanced two-phase* system, which further is taken apart in two systems, one of *direct sequence* with higher two-phase amplitude voltages and the other of *inverse sequence* with lower two-phase amplitude voltages. Usually, this equivalence process is obtained by using an orthogonal transformation. Not only voltages but also the total fluxes and eventually the currents must be established for the two resulted systems. The quantities of the unbalanced two-phase system can be written as follows:

$$\begin{bmatrix} \underline{U}_{\alpha s} \\ \underline{U}_{\beta s} \\ \underline{U}_{0s} \end{bmatrix} = \sqrt{\frac{2}{3}} \begin{bmatrix} 1 & -1/2 & -1/2 \\ 0 & \sqrt{3}/2 & -\sqrt{3}/2 \\ 1/\sqrt{2} & 1/\sqrt{2} & 1/\sqrt{2} \end{bmatrix} \begin{bmatrix} \underline{U}_{as} \\ \underline{U}_{bs} \\ \underline{U}_{cs} \end{bmatrix} \leftrightarrow \begin{cases} \underline{U}_{\alpha s} = \sqrt{\frac{3}{2}} \underline{U}_{as}; \underline{U}_{\beta s} = \sqrt{\frac{3}{2}} \frac{\underline{U}_{bs} - \underline{U}_{cs}}{\sqrt{3}} \\ \underline{U}_{0s} = 0; \quad \underline{U}_{as} + \underline{U}_{bs} + \underline{U}_{cs} = 0 \end{cases} \tag{52}$$

Further, the unbalanced quantities are transformed to balanced quantities and we obtain:

$$\begin{bmatrix} \underline{U}_{\alpha s(+)} \\ \underline{U}_{\alpha s(-)} \end{bmatrix} = \frac{1}{2} \begin{bmatrix} 1 & j \\ 1 & -j \end{bmatrix} \begin{bmatrix} \underline{U}_{\alpha s} \\ \underline{U}_{\beta s} \end{bmatrix}, \text{ or: } \begin{cases} \underline{U}_{\alpha s(+)} = \left(\underline{U}_{as} e^{j\pi/6} + j\underline{U}_{bs} \right) / \sqrt{2}; \\ \underline{U}_{\alpha s(-)} = \left(\underline{U}_{as} e^{-j\pi/6} - j\underline{U}_{bs} \right) / \sqrt{2} \end{cases} \tag{53}$$

The quantities of the three-phase system with *single unbalance* can be written as follows:

$$u_{as} = U\sqrt{2}\cos\omega t \Leftrightarrow \underline{U}_{as} = Ue^{j0}; \underline{U}_{bs} = kUe^{-j\beta}; \underline{U}_{cs} = -U(1 + ke^{-j\beta}) \tag{54}$$

and further:

$$\underline{U}_{\alpha s(+)} = U(e^{j\pi/6} + ke^{j(\pi/2-\beta)})/\sqrt{2}; \underline{U}_{\alpha s(-)} = U(e^{-j\pi/6} - ke^{j(\pi/2-\beta)})/\sqrt{2} \tag{55}$$

Modulus of these components can be determined at once with:

$$U_{\alpha s(+)} = U\sqrt{1+k^2+2k\sin(\beta+\pi/6)}/\sqrt{2}; U_{\alpha s(-)} = U\sqrt{1+k^2-2k\sin(\beta-\pi/6)}/\sqrt{2} \tag{56}$$

For the transformation of the unbalanced two-phase quantities in balanced two-phase components (53) must be used:

$$\begin{cases} \underline{U}_{\alpha s} = \underline{U}_{\alpha s(+)} + \underline{U}_{\alpha s(-)} \\ \underline{U}_{\beta s} = -j\underline{U}_{\alpha s(+)} + j\underline{U}_{\alpha s(-)} \end{cases} \tag{57}$$

The matrix equation of the two-phase model is written in a convenient way hereinafter:

$$\begin{bmatrix} \underline{U}_{\alpha s} \\ \underline{U}_{\beta s} \\ 0 \\ 0 \end{bmatrix} = \begin{bmatrix} \nu_s + j\omega_s & 0 & 0 & -\nu_{\sigma s} \\ 0 & \nu_s + j\omega_s & -\nu_{\sigma s} & 0 \\ 0 & \nu_{\sigma r} & -(\nu_r + j\omega_s) & \omega_R \\ \nu_{\sigma r} & 0 & -\omega_R & -(\nu_r + j\omega_s) \end{bmatrix} \times \begin{bmatrix} \underline{\Psi}_{\alpha s} \\ \underline{\Psi}_{\beta s} \\ \underline{\Psi}_{yr} \\ \underline{\Psi}_{xr} \end{bmatrix} \tag{58}$$

Using elementary math (multiplications with constants, addition and subtraction of different equations) we can obtain the equations of the two-phase *direct* (M2D) and *inverse* (M2I) models:

$$\text{(M2D)} \qquad \begin{bmatrix} \underline{U}_{\alpha s(+)} \\ 0 \end{bmatrix} = \begin{bmatrix} \nu_s + j\omega_s & -\nu_{\sigma s} \\ \nu_{\sigma r} & -\left(\nu_r + js_d\omega_s\right) \end{bmatrix} \times \begin{bmatrix} \underline{\Psi}_{\alpha s(+)} \\ \underline{\Psi}_{xr(+)} \end{bmatrix} \tag{59}$$

$$\text{(M2I)} \qquad \begin{bmatrix} \underline{U}_{\alpha s(-)} \\ 0 \end{bmatrix} = \begin{bmatrix} \nu_s + j\omega_s & -\nu_{\sigma s} \\ \nu_{\sigma r} & -\left(\nu_r + js_i\omega_s\right) \end{bmatrix} \times \begin{bmatrix} \underline{\Psi}_{\alpha s(-)} \\ \underline{\Psi}_{xr(-)} \end{bmatrix} \tag{60}$$

We have defined the slip values for the direct (+) and respectively inverse (-) machines: $s_d = s = \dfrac{\omega_s - \omega_R}{\omega_s}$; $s_i = \dfrac{\omega_s + \omega_R}{\omega_s}$ with the interrelation expression: $s_i = 2 - s$.

The two machine-models create self-contained torques, which act simultaneously upon rotor. The resultant torque emerges from superposition effects procedure (Simion et al., 2009; Simion & Livadaru, 2010). The equation set (59), for M2D, gives two equations:

$$\underline{U}_{\alpha s(+)} = (\nu_s + j\omega_s)\underline{\Psi}_{\alpha s(+)} - \nu_{\sigma s}\underline{\Psi}_{xr(+)}; \quad 0 = \nu_{\sigma r}\underline{\Psi}_{\alpha s(+)} - \left(\nu_r + js\omega_s\right)\underline{\Psi}_{xr(+)} \tag{61}$$

which give further

$$\underline{\Psi}_{\alpha s(+)}=\frac{\left(\nu_r+js\omega_s\right)\underline{U}_{\alpha s(+)}}{\underline{\Delta}_{(+)}};\underline{\Psi}_{xr(+)}=\frac{\nu_{\sigma r}\underline{U}_{\alpha s(+)}}{\underline{\Delta}_{(+)}};\underline{\Delta}_{(+)}=\left(\nu_s+j\omega_s\right)\left(\nu_r+js\omega_s\right)-\nu_{\sigma s}\nu_{\sigma r} \tag{62}$$

Similarly, for M2I we obtain:

$$\underline{U}_{\alpha s(-)}=(\nu_s+j\omega_s)\underline{\Psi}_{\alpha s(-)}-\nu_{\sigma s}\underline{\Psi}_{xr(-)};\quad 0=\nu_{\sigma r}\underline{\Psi}_{\alpha s(-)}-\left[\nu_r+j(2-s)\omega_s\right]\underline{\Psi}_{xr(-)} \tag{63}$$

$$\underline{\Psi}_{\alpha s(-)}=\frac{\left[\nu_r+j\left(2-s\right)\omega_s\right]\underline{U}_{\alpha s(-)}}{\underline{\Delta}_{(-)}};\underline{\Psi}_{xr(-)}=\frac{\nu_{\sigma r}\underline{U}_{\alpha s(-)}}{\underline{\Delta}_{(-)}};\underline{\Delta}_{(-)}=\left(\nu_s+j\omega_s\right)\left[\nu_r+j\left(2-s\right)\omega_s\right]-\nu_{\sigma s}\nu_{\sigma r} \tag{64}$$

To determine the electromagnetic torque developed under unbalanced supply condition we use the symmetric components and the superposition effect. The *mean electromagnetic torque M2D* results from (25) but transformed in simplified complex quantities:

$$T_{e(+)}=-\frac{3p}{2}\Lambda_3\cdot 2\mathrm{Re}\left(j\underline{\Psi}_{\alpha s(+)}\cdot\underline{\Psi}'^{*}_{xr(+)}\right)=\frac{3p\nu_{\sigma r}\Lambda_3}{2\omega_s}\cdot\frac{2U^2_{\alpha s(+)}s}{As^2+2Bs+C} \tag{65}$$

Similarly, the expression of the *mean electromagnetic torque M2D* is:

$$T_{e(-)}=-\frac{3p}{2}\Lambda_3\cdot 2\mathrm{Re}\left(j\underline{\Psi}_{\alpha s(-)}\cdot\underline{\Psi}^{*}_{xr(-)}\right)=\frac{3p\nu_{\sigma r}\Lambda_3}{2\omega_s}\cdot\frac{2U^2_{\alpha s(-)}\left(2-s\right)}{A\left(2-s\right)^2+2B\left(2-s\right)+C} \tag{66}$$

The *mean resultant torque*, as a difference of the torques produced by M2D and M2I, can be written by using (65) and (66):

$$T_{erez}=\frac{3p\nu_{\sigma r}\Lambda_3}{2\omega_s}\left[\frac{s\cdot 2U^2_{\alpha s(+)}}{As^2+2Bs+C}-\frac{\left(2-s\right)\cdot 2U^2_{\alpha s(-)}}{A(2-s)^2+2B(2-s)+C}\right] \tag{67}$$

where we have defined the notations: $\omega_s^2+\nu_s^2=A;\quad \nu_{\sigma s}\nu_{\sigma r}=B;\quad \nu_r^2+\nu_{tt}^2=C;$ and

$$\sqrt{2}U_{\alpha s(+)}=U\sqrt{1+k^2+2k\sin(\beta+\pi/6)};\sqrt{2}U_{\alpha s(-)}=U\sqrt{1+k^2-2k\sin(\beta-\pi/6)} \tag{68}$$

Finally, the expression of the mean resultant torque with the slip is:

$$T_{erez}=\frac{3p\nu_{\sigma r}\Lambda_3U^2}{2\omega_s}\left[\frac{1+k^2+2k\sin(\beta+\pi/6)}{As^2+2Bs+C}s-\frac{1+k^2-2k\sin(\beta-\pi/6)}{A(2-s)^2+2B(2-s)+C}\left(2-s\right)\right] \tag{69}$$

The influence of the supply unbalances upon $T_e=f(s)$ characteristic are presented in Fig. 7. To this effect, let us take again into discussion the machine with the following parameters: supply voltages with the amplitude of 490 V (U_{as}=346.5V) and $2\pi/3$ rad. shifted in phase; $R_s=R_r=2$; $L_{hs}=0{,}09$; $L_{\sigma s}=L_{\sigma r}=0{,}01$; J=0,05; p=2; $k_z=0{,}02$; $\omega_1=314{,}1$ (SI units). The characteristic corresponding to the three-phase symmetric machine is the curve A (the motoring pull-out

torque is equal to 124 Nm and obviously $U_{as(-)} = 0$). If the voltage on phase *b* keeps the same amplitude as the voltage in phase *a*, for example, but the angle of phase difference changes with $\pi/24=7,5$ degrees (from $2\pi/3=16\pi/24$ to $17\pi/24$ rad.) then the new characteristic is the B curve. The pull-out torque value decreases with approx. 12% but the pull-out slip keeps its value. Other two unbalance degrees are presented in Fig. 7 as well.

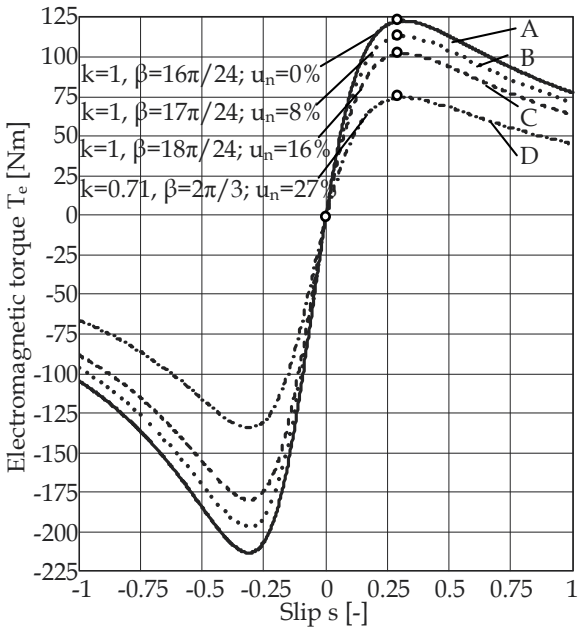

Figure 7. $T_e=f(s)$ characteristic for different unbalance degrees

Usually, the *unbalance degree* of the supply voltage is defined as the ratio of inverse and direct components:

$$u_n = \frac{U_{\alpha s(-)}}{U_{\alpha s(+)}} = \frac{\sqrt{1+k^2-2k\sin(\beta-\pi/6)}}{\sqrt{1+k^2+2k\sin(\beta+\pi/6)}} \cdot 100[\%] \tag{70}$$

The curves A, B, C, and D from Fig. 7 correspond to the following values of the unbalance degree: u_n= 0; 8%; 16% and 27%. The highest unbalance degree (27% - curve D) causes a decrease of the pull-out torque by 40%.

b. The second approach takes into consideration the following reasoning. When the amplitudes of the three-phase supply system and/or the angles of the phase difference are not equal to 2π/3 then the *unbalanced system* can be replaced by two *balanced three-phase* systems that act in opposition. One of them is the *direct sequence* system and has higher voltages and the other is the *inverse sequence* system and has lower voltages. A transformation of the unbalanced voltages and total fluxes into two symmetric systems is again necessary. In other words, there is an unbalanced voltage system ($\underline{U}_{as}$, $\underline{U}_{bs}$, $\underline{U}_{cs}$),

which is replaced by the *direct* and *inverse* symmetric systems. The mean resultant torque is the difference between the torques developed by the two symmetric machine-models. Taking into consideration their slip values ($s_d = s$ and $s_i = 2\text{-}s$) we can deduce the torque expression:

$$T_{erez} = -\left(3/2\right)p\Lambda_3 \cdot [3\mathrm{Re}\left(j\underline{\Psi}_{as1}\underline{\Psi}'^{*}_{ar1}\right) - 3\mathrm{Re}\left(j\underline{\Psi}_{as2}\underline{\Psi}'^{*}_{ar2}\right)] \tag{71}$$

$$T_{erez} = \frac{3p\nu_{\sigma r}\Lambda_3}{2\omega_s}\left[\frac{3sU_{as1}^2}{As^2 + 2Bs + C} - \frac{3\left(2-s\right)U_{as2}^2}{A(2-s)^2 + 2B(2-s) + C}\right] \tag{72}$$

and this is the same with (69) as we expected.

6. Simulation study upon some transient duties of the three-phase induction machine

6.1. Symmetric supply system

The mathematical model described by the equation system (26-1…8) allows a complete simulation study of the operation of the three-phase induction machine, which include start-up, any sudden change of the load and braking to stop eventually. To this end, the machine parameters (resistances, main and leakage phase inductances, moments of inertia corresponding to the rotor and the load, coefficients that characterize the variable speed and torque, etc.) have to be calculated or experimentally deduced. At the same time, the values of the load torque and the expressions of the instantaneous voltages applied to each stator phase winding are known, as well. The rotor winding is considered short-circuited. Using the above mentioned equation system, the structural diagram in the Matlab-Simulink environment can be carried out. Additionally, for a complete evaluation, virtual oscillographs for the visualization of the main physical parameters such as voltage, current, magnetic flux, torque, speed, rotation angle and current or specific characteristics (mechanical characteristic, angular characteristic or flux hodographs) fill out the structural diagram.

The study of the *symmetric three-phase* condition in the Matlab-Simulink environment takes into consideration the following parameter values: three identical supply voltages with the amplitude of 490 V (U_{as}=346.5V) and 2π/3 rad. shifted in phase; $u_{ar}=u_{br}=u_{cr}=0$ since the rotor winding is short-circuited; $R_s=R_r=2$; L_{hs}=0,09; $L_{\sigma s}= L_{\sigma r}$=0,01; J=0,05; p=2; k_z=0,02; ω_1=314,1 (SI units). The equation system becomes:

$$\left(\bar{s} + 135{,}71\right)\overline{\psi}_{as} = \bar{u}_{as} - 32{,}14\left(\overline{\psi}_{bs} + \overline{\psi}_{cs}\right) + 32{,}14\left(2\overline{\psi}_{ar} - \overline{\psi}_{br} - \overline{\psi}_{cr}\right)\cos\theta_R + 55{,}67(\overline{\psi}_{cr} - \overline{\psi}_{br})\sin\theta_R$$

$$\left(\bar{s} + 135{,}71\right)\overline{\psi}_{bs} = \bar{u}_{bs} - 32{,}14\left(\overline{\psi}_{cs} + \overline{\psi}_{as}\right) + 32{,}14\left(2\overline{\psi}_{br} - \overline{\psi}_{cr} - \overline{\psi}_{ar}\right)\cos\theta_R + 55{,}67(\overline{\psi}_{ar} - \overline{\psi}_{cr})\sin\theta_R$$

$$\left(\bar{s}+135,71\right)\bar{\psi}_{cs}=\bar{u}_{cs}-32,14\left(\bar{\psi}_{as}+\bar{\psi}_{bs}\right)+32,14\left(2\bar{\psi}_{cr}-\bar{\psi}_{ar}-\bar{\psi}_{br}\right)\cos\theta_R+55,67(\bar{\psi}_{br}-\bar{\psi}_{ar})\sin\theta_R$$

$$\left(\bar{s}+135,71\right)\bar{\psi}_{ar}=0-32,14\left(\bar{\psi}_{br}+\bar{\psi}_{cr}\right)+32,14\left(2\bar{\psi}_{as}-\bar{\psi}_{bs}-\bar{\psi}_{cs}\right)\cos\theta_R+55,67(\bar{\psi}_{bs}-\bar{\psi}_{cs})\sin\theta_R$$

$$\left(\bar{s}+135,71\right)\bar{\psi}_{br}=0-32,14\left(\bar{\psi}_{cr}+\bar{\psi}_{ar}\right)+32,14\left(2\bar{\psi}_{bs}-\bar{\psi}_{cs}-\bar{\psi}_{as}\right)\cos\theta_R+55,67(\bar{\psi}_{cs}-\bar{\psi}_{as})\sin\theta_R$$

$$\left(\bar{s}+135,71\right)\bar{\psi}_{cr}=0-32,14\left(\bar{\psi}_{ar}+\bar{\psi}_{br}\right)+32,14\left(2\bar{\psi}_{cs}-\bar{\psi}_{as}-\bar{\psi}_{bs}\right)\cos\theta_R+55,67(\bar{\psi}_{as}-\bar{\psi}_{bs})\sin\theta_R$$

$$\begin{aligned}\dot{\theta}_R\left(\bar{s}+0,4\right)=\left(40\right)\langle-\left(32,14\right)\{\ &\sin\theta_R\left[\bar{\psi}_{as}\left(2\bar{\psi}_{ar}-\bar{\psi}_{br}-\bar{\psi}_{cr}\right)+\bar{\psi}_{bs}\left(2\bar{\psi}_{br}-\bar{\psi}_{cr}-\bar{\psi}_{ar}\right)+\right.\\&\left.+\bar{\psi}_{cs}\left(2\bar{\psi}_{cr}-\bar{\psi}_{ar}-\bar{\psi}_{br}\right)\right]+\sqrt{3}\cos\theta_R\cdot\left[\bar{\psi}_{as}\left(\bar{\psi}_{br}-\bar{\psi}_{cr}\right)+\bar{\psi}_{bs}\left(\bar{\psi}_{cr}-\bar{\psi}_{ar}\right)+\bar{\psi}_{cs}\left(\bar{\psi}_{ar}-\bar{\psi}_{br}\right)\right]\ \}-T_{st}\rangle\end{aligned} \tag{73-1-7}$$

$$\theta_R=\omega_R\frac{1}{s} \tag{73-8}$$

$$\begin{gathered}\bar{u}_{as}\leftrightarrow\frac{490}{\sqrt{2}}e^{j(314,1t)};\bar{u}_{bs}\leftrightarrow\frac{490}{\sqrt{2}}e^{j(314,1t-2,094)};\bar{u}_{cs}\leftrightarrow\frac{490}{\sqrt{2}}e^{j(314,1t-4,188)};\\U_{as\max}=U_{bs\max}=U_{cs\max}=490\end{gathered} \tag{73-9}$$

It has to be mentioned again that the above equation system allows the analysis of the three-phase induction machine under any condition, that is transients, steady state, symmetric or unbalanced, with one or both windings (from stator and rotor) connected to a supply system. Generally, a supplementary requirement upon the stator supply voltages is not mandatory. The case of short-circuited rotor winding, when the rotor supply voltages are zero, include the wound rotor machine under rated operation since the starting rheostat is short-circuited as well.

The presented simulation takes into discussion a varying duty, which consists in a *no-load* start-up (the load torque derives of frictions and ventilation and is proportional to the angular speed and have a steady state rated value of approx. 3 Nm) followed after 0,25 seconds by a sudden loading with a constant torque of 50 Nm. The simulation results are presented in Fig. 8, 10, 12, 14 and 15 and denoted by the symbol *RS-50.* A second simulation iterates the presented varying duty but with a load torque of 120 Nm, symbol *RS-120*, Fig. 9, 11 and 13. Finally, a third simulation takes into consideration a load torque of 125 Nm, which is a value over the pull-out torque. Consequently, the falling out and the stop of the motor in t≈0,8 seconds mark the varying duty (symbol *RS-125*, Fig. 16, 17, 18 and 19).

The *RS-50* simulation shows an upward variation of the angular speed to the no-load value (in t ≈ 0,1 seconds), which has a weak overshoot at the end, Fig. 8. The 50 Nm torque enforcement determines a decrease of the speed corresponding to a slip value of s ≈ 6,5%. In the case of the *RS-120* simulation, the start-up is obviously similar but the loading torque determines a much more significant decrease of the angular speed and the slip value gets to s ≈ 25%, Fig. 9.

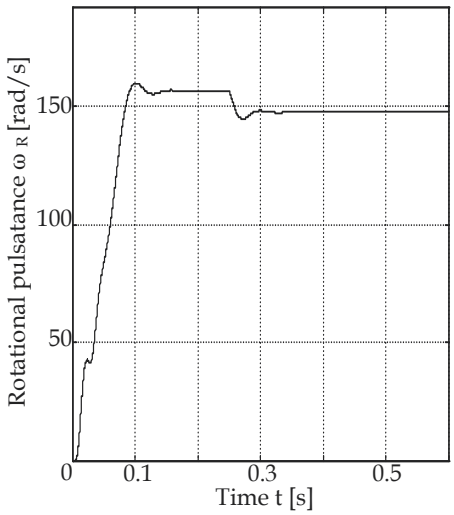

Figure 8. Time variation of rotational pulsatance – *RS-50*

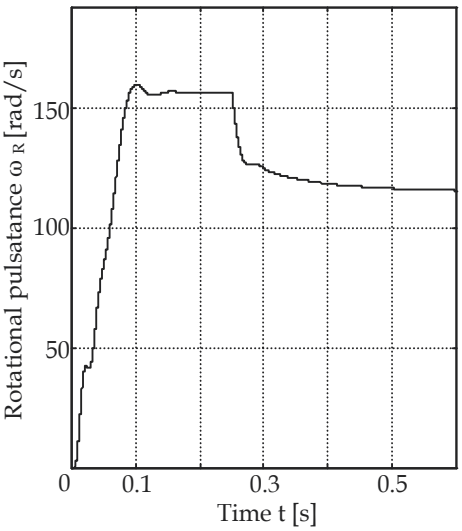

Figure 9. Time variation of rotational pulsatance – *RS-120*

In the first moments of the start-up, the electromagnetic torque oscillates around 100 Nm and after the load torque enforcement, it gets to approx. 53 Nm for *RS-50*, Fig. 10 and to approx. 122 Nm for *RS-120*, Fig. 11. The operation of the motor remains stable for the both duties.

The behavior of the machine is very interesting described by the hodograph of the resultant rotor flux (the locus of the head of the resultant rotor flux phasor), Fig. 12 and 13. With the connecting moment, the rotor fluxes start from 0 (O points on the hodograph) and track a corkscrew to the maximum value that corresponds to synchronism (ideal no-load operation), S points on the hodographs.

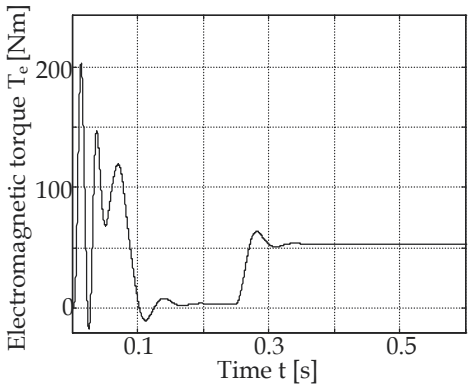

Figure 10. Time variation of electromagnetic torque – *RS-50*

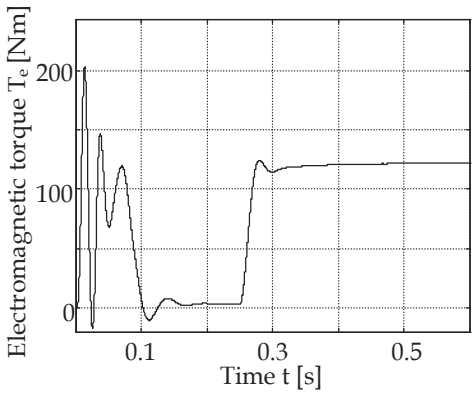

Figure 11. Time variation of electromagnetic torque – *RS-120*

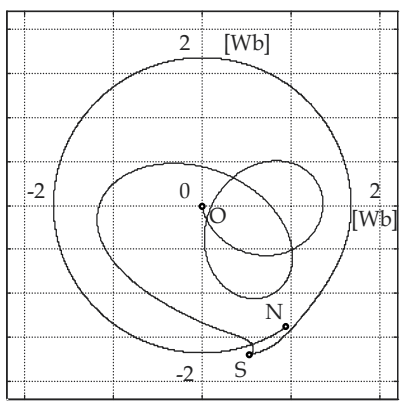

Figure 12. Hodograph of resultant rotor flux – *RS-50*

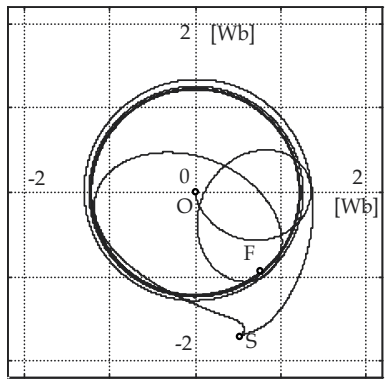

Figure 13. Hodograph of resultant rotor flux – *RS-120*

The enforcement of the load torque determines a decrease of the resultant rotor flux, which is proportional to the load degree, and is due to the rotor reaction. The locus of the head of the phasor becomes a circle whose radius is proportional to the amplitude of the resultant rotor flux. The speed on this circle is given by the rotor frequency that is by the slip value. It is interesting to notice that the load torque of 50 Nm causes a unique rotation of the rotor flux whose amplitude becomes equal to the segment ON (Fig. 12) whereas the 120 Nm torque causes approx. 4 rotations of the rotor flux and the amplitude OF is significantly smaller (Fig. 13).

If the expressions (1) and (2) are also used in the structural diagram then both stator and rotor phase currents can be plotted. The stator current corresponding to *as* phase has the frequency f_1=50 Hz and gets a start-up amplitude of approx. 70 A. This value decreases to approx. 6 A (no-load current) and after the torque enforcement (50 Nm) it rises to a stable value of approx. 14 A, Fig. 14. The rotor current on phase *ar*, which has a frequency value of $f_2 = s \cdot f_1$, gets a similar (approx. 70 A) start-up variation but in opposition to the stator current, i_{as}. Then, its value decrease and the frequency go close to zero. The loading of the machine has as result an increase of the rotor current up to 13 A and a frequency value of $f_2 \approx 3$Hz, Fig. 15. The fact that the current variations are sinusoidal and keep a constant frequency is an argument for a stable operation under symmetric supply conditions.

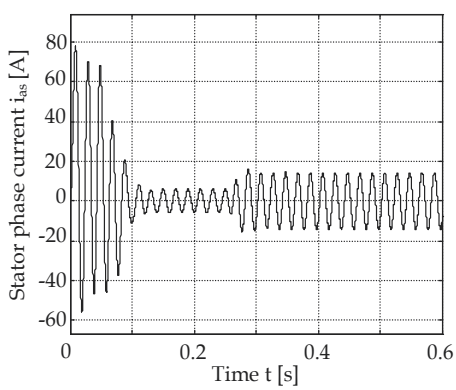

Figure 14. Time variation of stator phase current – *RS-50*

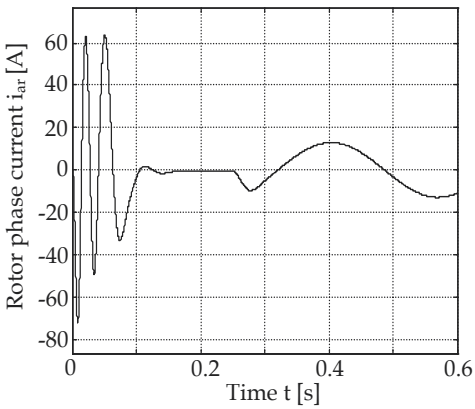

Figure 15. Time variation of rotor phase current – *RS-50*

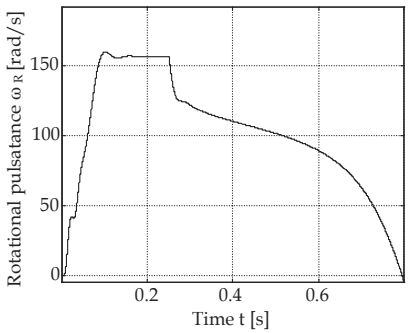

Figure 16. Time variation of rotational pulsatance – *RS-125 (start-up to locked-rotor)*

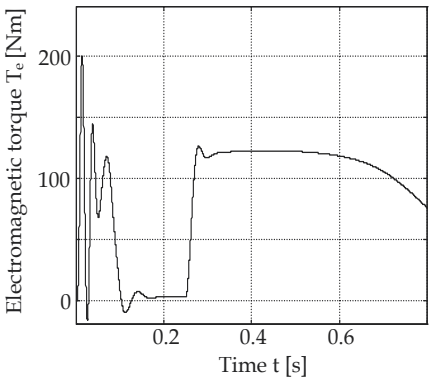

Figure 17. Time variation of electromagnetic torque – *RS-125*

The third simulation, *RS-125*, has a similar start-up but the enforcement of the load torque determines a fast deceleration of the rotor. The pull-out slip (s≈33%) happens in t≈0,5 seconds after which the machine falls out. The angular speed reaches the zero value in t≈0,8 seconds, Fig. 16, and the electromagnetic torque get a value of approx. 78 Nm. This value can be considered the locked-rotor (starting) torque of the machine, Fig. 17.

The described critical duty that involves no-load start-up and operation, overloading, falling out and stop is plotted in terms of resultant rotor flux and angular speed versus electromagnetic torque. The hodograph (Fig. 18) put in view a cuasi corkscrew section, corresponding to the start-up, characterized by its maximum value represented by the segment OS. The falling out tracks the corkscrew SP with a decrease of the amplitude, which is proportional to the deceleration of the rotor. The point P corresponds to the locked-rotor position (s=1). Fig. 19 presents the dynamic mechanical characteristic, which shows the variation of the electromagnetic torque under variable operation condition. During the no-load start-up, the operation point tracks successively the points O, M, L and S, that is from locked-rotor to synchronism with an oscillation of the electromagnetic torque inside certain limits (≈+200Nm to ≈-25Nm). The enforcement of the overload torque leads the operation point along the *downward* curve SK characterized by an *oscillation* section followed by the unstable falling out section, KP. The PKS curve, together with the marked points (Fig. 19) can be considered the *natural mechanical characteristic* under motoring duty.

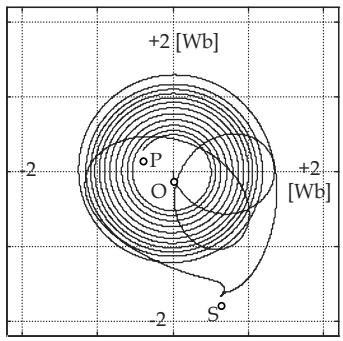

Figure 18. Hodograph of resultant rotor flux – *RS-125 (start-up to locked-rotor)*

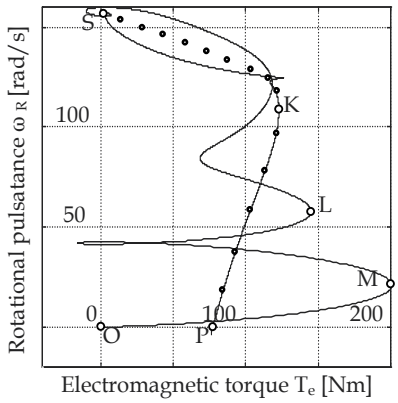

Figure 19. Rotational pulsatance vs. torque – *RS-125 (start-up to locked-rotor)*

6.2. Asymmetric supply system

A simulation study of the three-phase induction machine under unbalanced supply condition and varying duty (start-up, sudden torque enforcement and braking to stop

eventually) is possible by using the same mathematical model described by the equation system (26-1…8). The values of the resistant torques and the expressions of the instantaneous phase voltages have to be stated. Since the rotor winding is short-circuited, the supply rotor voltages are $u_{ar}=u_{br}=u_{cr}=0$. On this basis, the structural diagram has been put into effect in the Matlab-Simulink environment. As regards the unbalanced three-phase supply system, it has to be mentioned that the phase voltages are no more equal in amplitude and the angles of phase difference may have other values than $2\pi/3$ rad. In any event, the sum of the instantaneous values of the applied voltages must be zero, that is $u_{as}+u_{bs}+u_{cs}=0$. As an argument for this seemingly constraint stands the fact that the vast majority of the three-phase induction machines are connected to the industrial system via three supply leads (no neutral).

The simulation presented here takes into discussion an induction machine with the same parameters as above that is: $R_s=R_r=2$; $L_{hs}=0,09$; $L_{\sigma s}= L_{\sigma r}=0,01$; J=0,05; p=2; $k_z=0,02$; $\omega_1=314,1$ (SI units). Consequently, the equations (73-1) - (73-8) keep unchanged. The expressions (73-9) have to be modified in accordance with the asymmetry degree.

Two varying duties under unbalanced condition have been simulated. The first (denoted *RNS-1*) is characterized by an asymmetry degree, u_n = 16,5% and the following supply voltages:

$$\underline{u}_{as} \leftrightarrow \frac{490}{\sqrt{2}} e^{j(314,1t)}; \underline{u}_{bs} \leftrightarrow \frac{375}{\sqrt{2}} e^{j(314,1t-1,96)}; \underline{u}_{cs} \leftrightarrow \frac{490}{\sqrt{2}} e^{j(314,1t-3,927)}; u_n = 16,5\% \qquad (74)$$

The simulation results are presented in Fig. 20, 22, 24, 25 and 28. The second study simulation (denoted *RNS-2*) has an asymmetry degree of u_n = 27% given by the following stator voltages:

$$\underline{u}_{as} \leftrightarrow \frac{490}{\sqrt{2}} e^{j(314,1t)}; \underline{u}_{bs} \leftrightarrow \frac{346,43}{\sqrt{2}} e^{j(314,1t-2,357)}; \underline{u}_{cs} \leftrightarrow \frac{346,43}{\sqrt{2}} e^{j(314,1t-3,295)}; u_n = 27\% \qquad (75)$$

The simulation results are presented in Fig. 21, 23, 26, 27 and 29. The varying duties are similar to those discussed above and consist in a *no-load* start-up (the load torque derives of frictions and ventilation and is proportional to the angular speed and have a steady state rated value of approx. 3 Nm) followed after 0,25 seconds by a sudden loading with a constant torque of 50 Nm.

In comparison to symmetric supply, the unbalanced voltage system causes a longer start-up time with approx. 20% for *RNS-1* (Fig. 20) and with 50% for *RNS-2* (Fig. 21). Moreover, the higher asymmetry degree of *RNS-2* leads to the cancelation of the overshoot at the end of the start-up process. At the same time, significant speed oscillations are noticeable during the operation (no matter the load degree), which are higher with the increase of the asymmetry degree. These oscillations have a constant frequency, which is twice of the supply voltage frequency. They represent the main cause that determines the specific noise of the machines with unbalanced supply system.

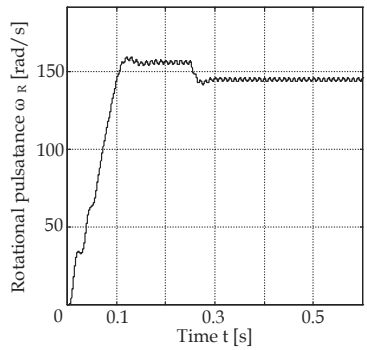

Figure 20. Time variation of rotational pulsatance – *RNS-1 (start-up + sudden load)*

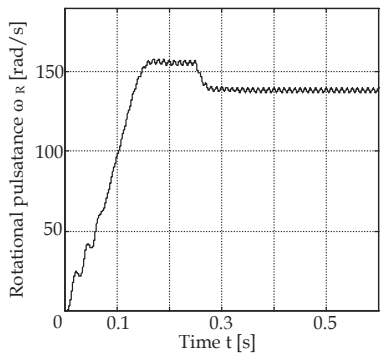

Figure 21. Time variation of rotational pulsatance – *RNS-2 (start-up + sudden load)*

The inspection of the electromagnetic torque variation (Fig. 22 and 23) shows the presence of a variable oscillating torque, whose frequency is twice the supply voltage frequency (in our case 100 Hz) and overlaps the average torque. *This oscillating component is demonstrated by the analytic expression of the instantaneous torque, which is written using nothing but total flux linkages* (25). The symmetric components theory, for example, is not capable to provide information about these oscillating torques. At the most, this theory evaluates the average torque, probably with inherent errors. Coming back to the torque variations, one can see that the amplitude oscillations increase with the asymmetry degree, but their frequency keeps unchanged.

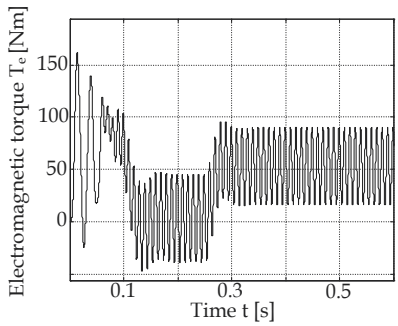

Figure 22. Time variation of electromagnetic torque – *RNS-1*

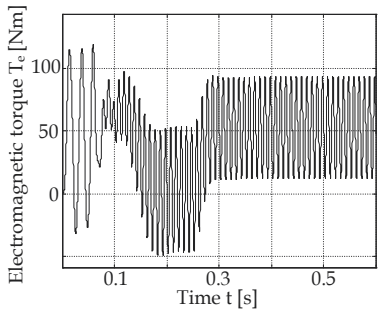

Figure 23. Time variation of electromagnetic torque – *RNS-2*

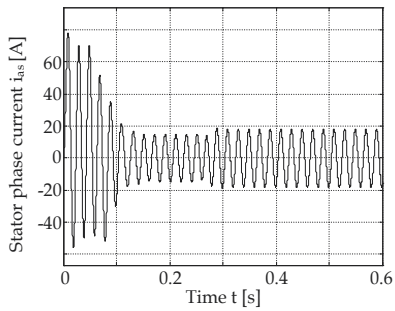

Figure 24. Time variation of stator phase current – *RNS-1*

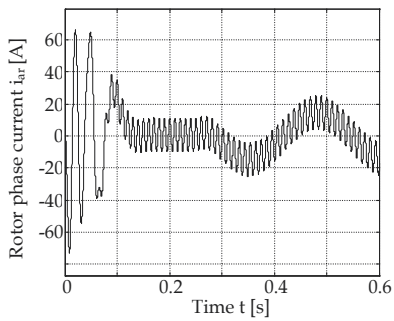

Figure 25. Time variation of rotor phase current – *RNS-1*

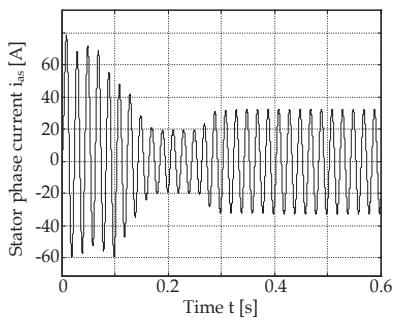

Figure 26. Time variation of stator phase current – *RNS-2*

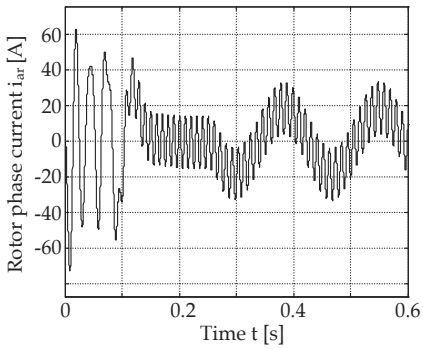

Figure 27. Time variation of rotor phase current – *RNS-2*

The stator currents variation, Fig. 24 and 26, have a sinusoidal shape and an unmodified frequency of 50 Hz. Their amplitude increases however with the asymmetry degree (approx. 18 A for *RNS-1* and approx. 32 A for *RNS-2*). As a consequence of this fact, both power factor and efficiency decrease. The rotor currents (Fig. 25 and 27) include besides the main component of $f_2=s\cdot f_1$ frequency a second oscillating component of high frequency, $f'_2=(2-s)f_1$, which is responsible for parasitic torques and vibrations of the rotor. The amplitude of these oscillating currents increases with the asymmetry degree.

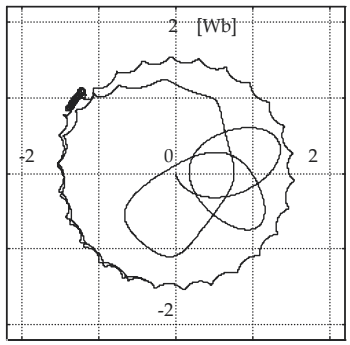

Figure 28. Hodograph of resultant rotor flux – *RNS-1*

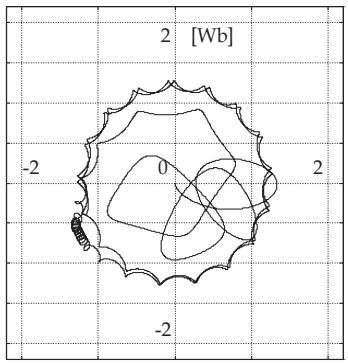

Figure 29. Hodograph of resultant rotor flux – *RNS-2*

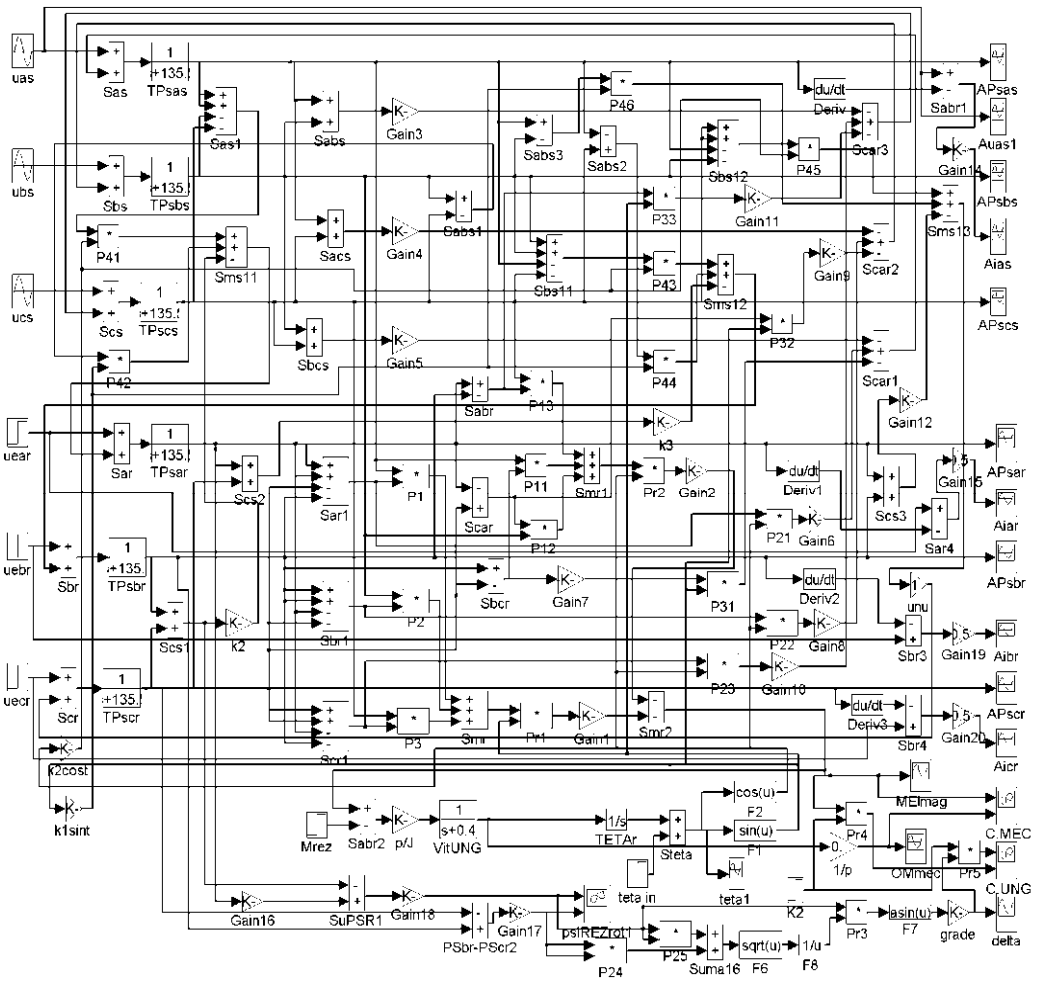

Figure 30. Structural diagram of the three-phase induction machine

The hodographs of the resultant rotor flux show a very interesting behavior of the unbalanced machines, Fig. 28 and 29. In comparison to the symmetric supply cases where the hodograph is a circle under steady state, the asymmetric system distort the curve into a „gear wheel" with a lot of teeth placed on a mean diameter whose magnitude depends inverse proportionally with the asymmetry degree. Generally, these curves do not overlap and prove that during the operation the interaction between stator and rotor fluxes is not constant in time since the rotor speed is not constant. Consequently, the rotor vibrations are usually propagated to the mechanical components and working machine.

In order to point out the superiority of the proposed mathematical model, Fig. 30 shows the structural diagram used in Simulink environment. The diagram is capable to simulate any steady-state and transient duty under balanced or unbalanced state of the induction machine including doubly-fed operation as generator or motor by simple modification of the input data. To prove this statement, a simulation of an unbalanced doubly-fed operation has been performed. The operation cycle involves: I. A no-load start-up (the wound rotor winding is short-circuited); II. Application of a supplementary output torque of (-70) Nm (at the moment t=0.4 sec.) which leads the induction machine to the generating duty (over synchronous speed); III. Supply of two series connected rotor phases with d.c. current (U_{ar}=+40V, U_{br}= −40V, U_{cr}=0V), at the moment time t=0.6 sec., which change the operation of the induction generator into a synchronized induction generator (SIG).

Fig. 31 and 32 show the dynamic mechanical characteristic, Te=f(Ω_R) and the hodograph of the resultant rotor flux respectively. The start-up corresponds to A-S1 curve, the over synchronous acceleration is modeled by S1-S curve and the operation under SIG duty corresponds to S-S2 curve. A few observations regarding Fig. 32 are necessary as well. The rotor flux hodograph is rotating in a *counterclockwise direction* corresponding to motoring duty, in a *clockwise direction* for generating duty and stands still at synchronism. The "in time" modification and the position of the hodograph corresponding to SIG duty depend on the moment of d.c. supply and the load angle of the machine.

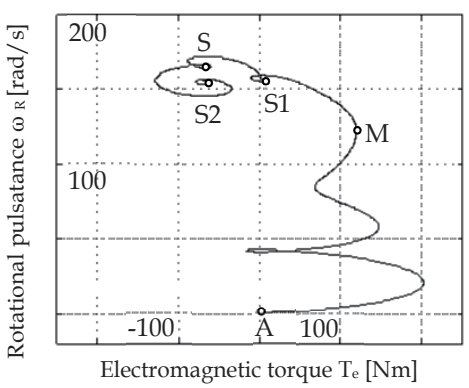

Figure 31. Dynamic mechanical characteristic

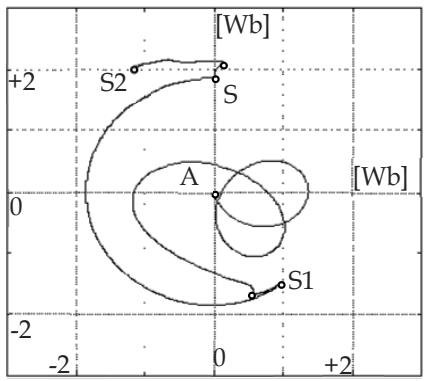

Figure 32. Hodograph of resultant rotor flux

7. Conclusion

The mathematical model presented in this contribution is characterized by the total lack of the winding currents and angular speed in the voltage equations. Since these parameters are differential quantities of other electric parameters, they usually bring supplementary calculus errors mainly for the dynamic duty analysis. Their removal assures a high accuracy of the results. If their variation is however necessary to be known then simple subsequent calculations can be performed.

The use of the mathematical model in total fluxes is appropriate for the study of the electric machines with permanent magnets where the definitive parameter is the magnetic flux and not the electric current.

The coefficients defined by (28.1-4), which depend on resistances and inductances, take into consideration the saturation. Consequently, the study of the induction machine covers more than the linear behavior of the magnetization phenomenon.

The most important advantage of the proposed mathematical model is its generality degree. Any operation duty, such as steady-state or transients, balanced or unbalanced, can be analyzed. In particular, the double feeding duty and the synchronized induction machine operation (feeding with D.C. current of a rotor phase while the other two are short-circuited) can be simulated as well.

The results obtained by simulation are based on the transformation of the equations in structural diagrams under Matlab-Simulink environment. They present the variation of electrical quantities (voltages and currents corresponding to stator and rotor windings), of mechanical quantities (expressed through rotational pulsatance) and of magnetic

parameters (electromagnetic torque, resultant rotor and stator fluxes). They put in view the behavior of the induction machine for different transient duties. In particular, they prove that any unbalance of the supply system generates important variations of the electromagnetic torque and rotor speed. This fact causes vibrations and noise.

Author details

Alecsandru Simion, Leonard Livadaru and Adrian Munteanu
"Gh. Asachi" Technical University of Iaşi, Electrical Engineering Faculty, Romania

8. References

Ahmad, M. (2010). *High Performance AC Drives. Modeling Analysis and Control,* Springer, ISBN 978-3-642-13149-3, London, UK

Boldea, I. & Tutelea, L. (2010). *Electric Machines. Steady State, Transients and Design with MATLAB*, CRC Press, ISBN 978-1-4200-5572-6, Boca Raton, USA

Bose, B. (2006). *Power Electronics and Motor Drives,* Elsevier, ISBN 978-0-12-088405-6, San Diego, USA

Chiasson, J. (2005). *Modeling and High-Performance Control of Electrical Machines,* IEEE Press, Wiley Interscience, ISBN 0-471-68449-X, Hoboken, USA

De Doncker, R.; Pulle, D. & Veltman, A. (2011). *Advanced Electrical Drives. Analysis, Modeling, Control,* Springer, ISBN 978-94-007-0179-3, Dordrecht, Germany

Krause, P.; Wasynczuk, O. & Sudhoff, S. (2002). *Analysis of Electric Machinery and Drive Systems (sec. ed.),* IEEE Press, ISBN 0-471-14326-X, Piscataway, USA

Marino, R.; Tomei, P. & Verrelli, C. (2010). *Induction Motor Control Design,* Springer, ISBN 978-1-84996-283-4, London, UK

Ong, C-M. (1998). *Dynamic Simulation of Electric Machinery using Matlab/Simulink,* Prentice Hall, ISBN 0-13-723785-5, New Jersey, USA

Simion, Al.; Livadaru, L. & Lucache, D. (2009). Computer-Aided Simulation on the Reversing Operation of the Two-Phase Induction Machine. *International Journal of Mathematical Models and Methods in Applied Sciences,* Iss. 1, Vol. 3, pp. 37-47, ISSN 1998-0140

Simion, Al. (2010). Study of the Induction Machine Unsymmetrical Condition Using In Total Fluxes Equations. *Advances in Electrical and Computer Engineering*, Iss. 1 (February 2010), pp. 34-41, ISSN 1582-7445

Simion, Al. & Livadaru, L. (2010). On the Unsymmetrical Regime of Induction Machine. *Bul. Inst. Polit. Iaşi*, Tomul LVI(LX), Fasc.4, pp. 79-91, ISSN 1223-8139

Simion, Al.; Livadaru, L. & Munteanu, A. (2011). New Approach on the Study of the Steady-State and Transient Regimes of Three-Phase Induction Machine. *Buletinul AGIR*, Nr.4/2011, pp. 1-6, ISSN-L 1224-7928

Sul, S-K. (2011). *Control of Electric Machine Drive Systems,* IEEE Press, Wiley Interscience, ISBN 978-0-470-87655-8, Hoboken, USA

Wach, P. (2011). *Dynamics and Control of Electric Drives,* Springer, ISBN 978-3-642-20221-6, Berlin, Germany

Chapter 2

The Behavior in Stationary Regime of an Induction Motor Powered by Static Frequency Converters

Sorin Muşuroi

Additional information is available at the end of the chapter

http://dx.doi.org/10.5772/38009

1. Introduction

Generally, the electric induction motors are designed for supply conditions from energy sources in which the supply voltage is a sinusoidal wave. The parameters and the functional sizes of the electric motors are guaranteed by designers only for it. If the electric motor is powered through an inverter, due to the presence in the input voltage waveform of superior time harmonics, both its parameters and its functional characteristic sizes will be more or less different from those in the case of the sinusoidal supply. The presence of these harmonics will result in the appearance of a deforming regime in the machine, generally with adverse effects in its operation. Under loading and speed conditions similar to those in the case of the sinusoidal supply, it is registered an amplification of the losses of the machine, of the electric power absorbed and thus a reduction in efficiency. There is also a greater heating of the machine and an electromagnetic torque that at a given load is not invariable, but pulsating, in rapport with the average value corresponding to the load. The occurrence of the deforming regime in the machine is inevitable, because any inverter produces voltages or printed currents containing, in addition to the fundamental harmonic, superior time harmonics of odd order. The deforming regime in the electric machine is unfortunately reflected in the supply power grid that powers the inverter. Generalizing, the output voltage harmonics are grouped into families centered on frequencies:

$$f_j = Jm_f f_c = Jm_f f_1 \quad (J = 1, 2, 3, \ ...), \tag{1}$$

and the various harmonic frequencies in a family are:

$$f_{(v)} = f_j \pm k f_c = (Jm_f \pm k) f_c = (Jm_f \pm k) f_1, \tag{2}$$

with

$$\nu = Jm_f \pm k \tag{3}$$

In the above relations, m_f represents the frequency modulation factor, f_1 is the fundamental's frequency and f_c is the frequency of the control modulating signal. Whereas the harmonic spectrum contains only ν order odd harmonics, in order that ($Jm_f \pm k$) is odd, an odd J determines an even k and vice versa. The present chapter aims to analyze the behavior of the induction motor when it is supplied through an inverter. The purpose of this study is to develop the theory of three-phase induction machine with a squirrel cage, under the conditions of the non-sinusoidal supply regime to serve as a starting point in improving the methodology of its constructive-technological design as advantageous economically as possible.

2. The mathematical model of the three-phase induction motor in the case of non-sinusoidal supply

In the literature there are known various mathematical models associated to induction machines fed by static frequency and voltage converters. The majority of these models are based on the association between an induction machine and an equivalent scheme corresponding to the fundamental and a lot of schemes corresponding to the various ν frequencies, corresponding to the Fourier series decomposition of the motor input voltage - see Fig. 1 (Murphy & Turnbull, 1988). In this model the skin effect is not considered.

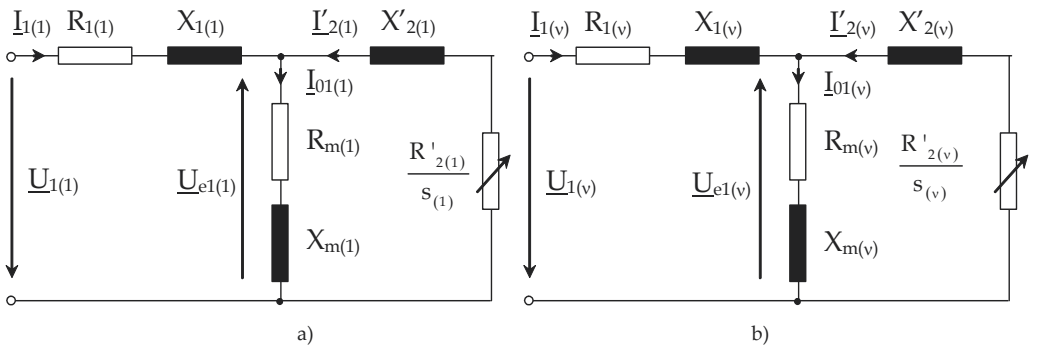

Figure 1. Equivalent scheme of the machine supplied through frequency converter: a) for the case of fundamental; b) for the ν order harmonics (positive or negative sequence).

For the equivalent scheme in Fig.1.a, corresponding to the fundamental, the electrical parameters are defined as:

$$R_{1(1)} = R_1 = R_{1n};\ X_{1(1)} = X_1 = aX_{1n};$$

$$R'_{2(1)} = R'_2 = R'_{2n};\ X'_{2(1)} = X'_2 = aX'_{2n};$$

$$R_{m(1)} = R_m = a^2 R_{mn};\ X_{m(1)} = X_m = aX_{mn}; \tag{4}$$

$$\frac{R'_{2(1)}}{s_{(1)}} = \frac{R'_2}{s} = \frac{a}{c} R'_{2n}$$

In relations (4), R_{1n}, X_{1n}, R'_{2n}, X'_{2n}, R_{mn}, X_{mn} represents the values of the parameters R_1, X_1, R'_2, X'_2, R_m and X_m in nominal operating conditions (fed from a sinusoidal power supply, rated voltage frequency and load) and

$$a = \frac{f_1}{f_{1n}} = \frac{\omega_1}{\omega_{1n}} = \frac{n_1}{n_{1n}}; \quad c = \frac{n_1 - n}{n_{1n}} = \frac{n_1 - n}{n_1} \cdot \frac{n_1}{n_{1n}} = s \cdot a \tag{5}$$

In the relations (5), f_1 and f_{1n} are random frequencies of the rotating magnetic field, and the nominal frequency of the rotating magnetic field respectively. For ν order harmonics, the scheme from Fig. 1.b is applicable. The slip $s_{(\nu)}$, corresponding to the ν order harmonic is:

$$s_{(\nu)} = \frac{\nu n_1 \mp n}{\nu n_1} = 1 \mp \frac{n}{\nu n_1} = 1 \mp \frac{1}{\nu} \pm \frac{c}{a} \frac{1}{\nu}, \tag{6}$$

where sign (-) (from the first equality) corresponds to the wave that rotates within the sense of the main wave and the sign (+) in the opposite one. For the case studied in this chapter - that of small and medium power machines – the resistances $R_{1(\nu)}$ and reactances $X_{1(\nu)}$ values are not practically affected by the skin effect. In this case we can write:

$$R_{1(\nu)} = R_{1(1)} = R_1 = R_{1n}, \tag{7}$$

$$X_{1(\nu)} = \omega_{1(\nu)} \cdot L_{1\sigma(\nu)} = \nu \omega_1 L_{1\sigma(\nu)}, \tag{8}$$

where $L_{1\sigma(\nu)}$ is the stator dispersion inductance corresponding to the ν order harmonic. If it is agreed that the machine cores are linear media (the machine is unsaturated), it results that the inductance can be considered constant, independently of the load (current) and flux, one can say that:

$$L_{1\sigma(\nu)} = L_{1\sigma(1)} = L_{1\sigma} \tag{9}$$

By replacing the inductance $L_{1\sigma(\nu)}$ expression from relation (9) in relation (8), we obtain:

$$X_{1(\nu)} = \nu \omega_1 L_{1\sigma} = \nu X_1 = \nu a X_{1n} \tag{10}$$

For the rotor resistance and rotor leakage reactance, corresponding to the ν order harmonic, both reduced to the stator the following expressions were established:

$$R'_{2(\nu)} = R'_{2(1)} = R'_2 = R'_{2n}, \tag{11}$$

$$X'_{2(\nu)} = \nu \cdot X'_2 = \nu \cdot a \cdot X'_{2n} \tag{12}$$

The magnetization resistance corresponding to the ν order harmonic, $R_{m\nu}$, is given by the relation:

$$R_{m(\nu)} = k_{K''} \cdot \nu^2 \cdot a^2 \cdot R_{mn} \tag{13}$$

$k_{K''}$ is a coefficient dependent on iron losses and on the magnetic field variation. The magnetization reluctance corresponding to the magnetic field produced by the ν order harmonic is:

$$X_{m(\nu)} = k_{K'} \nu \cdot a \cdot X_{mn} \tag{14}$$

Further the author intends to establish a single mathematical model associated to induction motors, supplied by static voltage and frequency converter, which consists of a single equivalent scheme and which describes the machine operation, according to the presence in the input power voltage of higher time harmonics. For this, the following simplifying assumptions are taken into account:

- the permeability of the magnetic core is considered infinitely large comparing to the air permeability and the magnetic field lines are straight perpendicular to the slot axis;
- both the ferromagnetic core and rotor cage (bar + short circuit rings) are homogeneous and isotropic media;
- the marginal effects are neglected, the slot is considered very long on the axial direction. The electromagnetic fields are considered, in this case plane-parallels;
- the skin effect is taken into account in the calculations only in bars that are in the transverse magnetic field of the slot. For the bar portions outside the slot and in short circuit rings, current density is considered as constant throughout the cross section of the bar;
- the passing from the constant density zone into the variable density zone occurs abruptly;
- in the real electric machines the skin effect is often influenced by the degree of saturation but the simultaneous coverage of both phenomena in a mathematical relationships, easily to be applied in practice is very difficult, even precarious. Therefore, the simplifying assumption of neglecting the effects of saturation is allowed as valid in establishing the relationships for equivalent parameters;
- the local variation of the magnetic induction and of current density is considered sinusoidal in time, both for the fundamental and for each ν harmonic;
- one should take into account only the fundamental space harmonic of the EMF.

Under these conditions of non-sinusoidal supply, the asynchronous motor may be associated to an equivalent scheme, corresponding to all harmonics. The scheme operates in the fundamental frequency $f_{1(1)}$ and it is represented in Fig. 2. According to this scheme, it can be formally considered that the motors, in the case of supplying through the power frequency converter (the corresponding parameters and the dimensions of this situation are marked with index "CSF") behave as if they were fed in sinusoidal regime at fundamental's frequency, $f_{1(1)}$ with the following voltages system:

$$u_A = \sqrt{2}\cdot U_{1(CSF)}\cdot \sin\omega_1 t\,;\; u_B = \sqrt{2}\cdot U_{1(CSF)}\cdot \sin\left(\omega_1 t - \frac{2\pi}{3}\right);\; u_C = \sqrt{2}\cdot U_{1(CSF)}\cdot \sin\left(\omega_1 t + \frac{2\pi}{3}\right), \quad (15)$$

where,

$$U_{1(CSF)} = \sqrt{U_{1(1)}^2 + \sum_{\nu\neq 1} U_{1(\nu)}^2} \quad (16)$$

$U_{1(\nu)}$ is the phase voltage supply corresponding to the ν order harmonic. Corresponding to the system supply voltages, the current system which go through the stator phases is as follows:

$$\begin{cases} i_A = \sqrt{2}\cdot I_{1(CSF)}\cdot \sin\left(\omega_1 t - \varphi_{1(CSF)}\right) \\ i_B = \sqrt{2}\cdot I_{1(CSF)}\cdot \sin\left(\omega_1 t - \varphi_{1(CSF)} - \frac{2\pi}{3}\right), \\ i_C = \sqrt{2}\cdot I_{1(CSF)}\cdot \sin\left(\omega_1 t - \varphi_{1(CSF)} - \frac{4\pi}{3}\right) \end{cases} \quad (17)$$

where $I_{1(CSF)}$ is given by:

$$I_{1(CSF)} = \sqrt{I_{1(1)}^2 + \sum_{\nu\neq 1} I_{1(\nu)}^2} \quad (18)$$

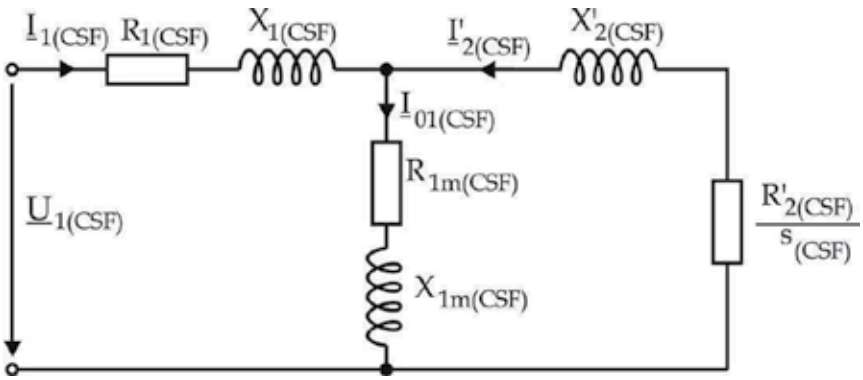

Figure 2. The equivalent scheme of the asynchronous motor powered by a static frequency converter.

Power factor in the deforming regime is defined as the ratio between the active power and the apparent power, as follows:

$$\Delta_{(CSF)} = \frac{P_{1(CSF)}}{S_{1(CSF)}} = \frac{P_{1(CSF)}}{U_{1(CSF)} I_{1(CSF)}} \quad (19)$$

If we consider the non-sinusoidal regime, the active power absorbed by the machine $P_{1(CSF)}$ is defined, as in the sinusoidal regime, as the average in a period of the instantaneous power. The following expression is obtained:

$$P_{1(CSF)} = \frac{1}{T}\int_0^T p \cdot dt = \sum_{\nu=1} U_{1(\nu)} I_{1(\nu)} \cos\varphi_{1(\nu)} = U_1 I_1 \cos\varphi_1 + \sum_{\nu\neq 1} U_{1(\nu)} I_{1(\nu)} \cos\varphi_{1(\nu)} \tag{20}$$

Therefore, the active power absorbed by the motor when it is supplied through a power static converter is equal to the sum of the active powers, corresponding to each harmonic (the principle of superposition effects is found). In relation (20), cosφ(1ν) is the power factor corresponding to the ν order harmonic having the expression:

$$\cos\varphi_{1(\nu)} = \frac{R_{1(\nu)} + \frac{R'_{2(\nu)}}{s_{(\nu)}}}{\sqrt{\left(R_{1(\nu)} + \frac{R'_{2(\nu)}}{s_{(\nu)}}\right)^2 + \left(X_{1(\nu)} + X'_{2(\nu)}\right)^2}} \tag{21}$$

The apparent power can be defined in the non-sinusoidal regime also as the product of the rated values of the applied voltage and current:

$$S_{1(CSF)} = U_{1(CSF)} \cdot I_{1(CSF)}, \tag{22}$$

Taken into account the relations (20), (21) and (22), the relation (19) becomes:

$$\Delta_{(CSF)} = \frac{U_1 I_1 \cos\varphi_1 + \sum_{\nu\neq 1} U_{1(\nu)} I_{1(\nu)} \cos\varphi_{1(\nu)}}{\sqrt{U_{1(1)}^2 + \sum_{\nu\neq 1} U_{1(\nu)}^2} \cdot \sqrt{I_{1(1)}^2 + \sum_{\nu\neq 1} I_{1(\nu)}^2}} \tag{23}$$

Because $\Delta_{(CSF)} \leq 1$, formally (the phase angle has meaning only in harmonic values) an angle $\varphi_{1(CSF)}$ can be associated to the power factor $\Delta_{(CSF)}$, as: $\cos\varphi_{1(CSF)} = \Delta_{(CSF)}$. With this, the relation (23) can be written:

$$\cos\varphi_{1(CSF)} = \frac{\cos\varphi_1 + \sum_{\nu\neq 1} \frac{U_{1(\nu)}}{U_{1(1)}} \frac{I_{1(\nu)}}{I_1} \cos\varphi_{1(\nu)}}{\sqrt{1 + \sum_{\nu\neq 1} \left(\frac{U_{1(\nu)}}{U_{1(1)}}\right)^2} \cdot \sqrt{1 + \sum_{\nu\neq 1} \left(\frac{I_{1(\nu)}}{I_{1(1)}}\right)^2}} \tag{24}$$

If one takes into account the relation (Murphy&Turnbull, 1988):

$$\frac{I_{1(\nu)}}{I_{1(1)}} = \frac{1}{\nu} \cdot \frac{1}{f_{1r} \cdot x^*_{sc}} \cdot \frac{U_{1(\nu)}}{U_{1(1)}}, \tag{25}$$

where x^*_{sc} is the reported short-circuit impedance, measured at the frequency $f_1 = f_{1n}$, relation (24) becomes:

$$\cos\varphi_{1(CSF)} = \frac{\cos\varphi_1 + \sum_{\nu\neq 1}\frac{1}{\nu}\cdot\frac{1}{f_{1r}\cdot x^*_{sc}}\cdot\left(\frac{U_{1(\nu)}}{U_{1(1)}}\right)^2\cos\varphi_{1(\nu)}}{\sqrt{\left[1+\sum_{\nu\neq 1}\left(\frac{U_{1(\nu)}}{U_{1(1)}}\right)^2\right]\cdot\left[1+\sum_{\nu\neq 1}\left(\frac{1}{\nu}\cdot\frac{1}{f_{1r}\cdot x^*_{sc}}\cdot\frac{U_{1(\nu)}}{U_{1(1)}}\right)^2\right]}} \tag{26}$$

3. The determination of the equivalent parameters of the stator winding

The equivalent parameters of the scheme have been calculated at the fundamental's frequency, under the presence of all harmonics in the supply voltage. Under these conditions, we note by $p_{Cu1(CSF)}$ the losses that occur in the stator winding when the motor is supplied through a power frequency converter. These losses are in fact covered by some active power absorbed by the machine from the network, through the converter, $P_{1(CSF)}$. According to the principle of the superposition effects, it can be considered:

$$p_{Cu1(CSF)} = p_{Cu1(1)} + \sum_{\nu\neq 1} p_{Cu1(\nu)} = 3R_{1(1)}I^2_{1(1)} + 3\sum_{\nu\neq 1} R_{1(\nu)}I^2_{1(\nu)} \tag{27}$$

Further, the stator winding resistance corresponding to the fundamental, $R_{1(1)}$ and stator winding resistances corresponding to the all higher time harmonics $R_{1(\nu)}$, are replaced by a single equivalent resistance $R_{1(CSF)}$, corresponding to all harmonics, including the fundamental. The equalization is achieved under the condition that in this resistance the same loss $p_{Cu1(CSF)}$ occurs, given by relation (27), as if considering the "ν" resistances $R_{1(\nu)}$, each of them crossed by the current $I_{1(\nu)}$. This equivalent resistance, $R_{1(CSF)}$, determined at the fundamental's frequency, is traversed by the current $I_{1(CSF)}$, with the expression given by (18). Therefore:

$$p_{Cu1(CSF)} = 3R_{1(CSF)}\cdot I^2_{1(CSF)} = 3R_{1(CSF)}\left(I^2_{1(1)} + \sum_{\nu\neq 1} I^2_{1(\nu)}\right) \tag{28}$$

Making the relations (27) and (28) equal, it results:

$$3R_{1(CSF)}\left(I^2_{1(1)} + \sum_{\nu\neq 1} I^2_{1(\nu)}\right) = 3R_{1(1)}\left(I^2_{1(1)} + \sum_{\nu\neq 1} I^2_{1(\nu)}\right) = 3R_{1(\nu)}\left(I^2_{1(1)} + \sum_{\nu\neq 1} I^2_{1(\nu)}\right), \tag{29}$$

from which:

$$R_{1(CSF)} = R_{1(1)} = R_1 . \tag{30}$$

Applying the principle of the superposition effects to the reactive power absorbed by the stator winding $Q_{Cu1\,(CSF)}$, the following expression is obtained:

$$Q_{Cu1(CSF)} = Q_{Cu1(1)} + \sum_{\nu\neq 1} Q_{Cu1(\nu)} = 3\cdot X_{1(1)}I^2_{1(1)} + 3\sum_{\nu\neq 1} X_{1(\nu)}I^2_{1(\nu)} \tag{31}$$

As in the previous case, the stator winding reactance corresponding to the fundamental, $X_{1(1)}$ (determined at the fundamental's frequency $f_{1(1)}$) and the stator winding reactances, corresponding to all higher time harmonics $X_{1(\nu)}$ (determined at frequencies $f_{1(\nu)}=\nu \cdot f_1$ where $Jm\pm k$) are replaced by an equivalent reactance, $X_{1(CSF)}$, determined at fundamental's frequency. This equivalent reactance, traversed by the current $I_{1(CSF)}$, conveys the same reactive power, $Q_{Cu1(CSF)}$ as in the case of considering "ν" reactances $X_{1(\nu)}$, (each of them determined at $f_{1(\nu)}$ frequency and traversed by the current $I_{1(\nu)}$). Following the equalization, the following expression can be written:

$$Q_{Cu1(CSF)} = 3X_{1(CSF)}I^2_{1(CSF)} = 3X_{1(CSF)}\left(I^2_{1(1)} + \sum_{\nu\neq 1} I^2_{1(\nu)}\right) \tag{32}$$

Making the relations (31) and (32) equal, it results:

$$X_{1(CSF)}\left(I^2_{1(1)} + \sum_{\nu\neq 1} I^2_{1(\nu)}\right) = X_{1(1)}I^2_{1(1)} + \sum_{\nu\neq 1} \nu X_1 I^2_{1(\nu)} = X_1\left(I^2_{1(1)} + \sum_{\nu\neq 1} \nu I^2_{1(\nu)}\right) \tag{33}$$

One can notice the following:

$$k_{X1} = \frac{X_{1(CSF)}}{X_1}$$

the factor that highlights the changes that the reactants of the stator phase value suffer in the case of a machine supplied through a power frequency converter, compared to sinusoidal supply, both calculated at the fundamental's frequency. From relations (25) and (33) it follows:

$$k_{X1} = \frac{X_{1(CSF)}}{X_1} = \frac{1 + \sum_{\nu\neq 1} \nu\left(\frac{1}{f_{1r}x^*_{sc}}\right)^2 \cdot \frac{1}{\nu^2}\left(\frac{U_{1(\nu)}}{U_{1(1)}}\right)^2}{1 + \sum_{\nu\neq 1}\left(\frac{1}{f_{1r}x^*_{sc}}\right)^2 \cdot \frac{1}{\nu^2}\left(\frac{U_{1(\nu)}}{U_{1(1)}}\right)^2} = \frac{1 + \sum_{\nu\neq 1} \frac{1}{\nu}\left(\frac{1}{f_{1r}x^*_{sc}}\right)^2\left(\frac{U_{1(\nu)}}{U_{1(1)}}\right)^2}{1 + \sum_{\nu\neq 1} \frac{1}{\nu^2}\left(\frac{1}{f_{1r}x^*_{sc}}\right)^2\left(\frac{U_{1(\nu)}}{U_{1(1)}}\right)^2} \tag{34}$$

where:

$$X^*_{sc} = \frac{X_{sc}}{Z_{(1)}}$$

- is the short circuit impedance reported, corresponding to the frequency $f_1=f_{1n}$ and f_{1r} is the reported frequency. One can notice that: $k_{X1}>1$. With the equivalent resistance given by (30) and the equivalent reactance resulting from the relationship (34) we can now write the relation for the equivalent impedance of the stator winding, $\underline{Z}_{1(CSF)}$ covering all frequency harmonics and including the fundamental:

$$\underline{Z}_{1(CSF)} = R_{1(CSF)} + jX_{1(CSF)} = R_{1(CSF)} + jk_{X1}X_1 \tag{35}$$

4. Determining the equivalent global change parameters for the power rotor fed by the static frequency converter

Further, it is considered a winding with multiple cages whose bars (in number of "c") are placed in the same notch of any form, electrically separated from each other (see Fig. 3). These bars are connected at the front by short-circuiting rings (one ring may correspond to several bars notch). This "generalized" approach, pure theoretically in fact, has the advantage that by its applying the relations of the two equivalent factors $k_{r(CSF)}$ and $k_{x(CSF)}$, valid for any notch type and multiple cages, are obtained. The rotor notch shown in Fig. 3 is the height h_c and it is divided into "n" layers (strips), each strip having a height $h_s = h_c/n$. The number of layers "n" is chosen so that the current density of each band should be considered constant throughout the height h_s (and therefore not manifesting the skin effect in the strip). The notch bars are numbered from 1 to c, from the bottom of the notch. The lower layer of each bar is identified by the index "i" and the top layer by the index "s". Thus, for a bar with index δ characterized by a specific resistance ρ_δ and an absolute magnetic permeabilityμ_δ, the lower layer is noted with $N_{\delta i}$ and the extremely high layer with $N_{\delta s}$. The current that flows through the bar δ is noted with $i_{c\delta}$ ($I_{c\delta}$ - rated value). The length of the bar, over which the skin effect occurs, is L. For the beginning, let us consider only the presence of the fundamental in the power supply, which corresponds to the supply pulsation, $\omega_{1(1)}=\omega_1=2\pi f_1$. In this case:

$$k_{r\delta(1)} = \frac{R_{\delta(1)\sim}}{R_{\delta -}} = \frac{1}{I^2_{c\delta(1)}} \cdot \sum_{\varepsilon=N_{\delta i}}^{N_{\delta s}} \frac{I^2_{\varepsilon(1)}}{b_\varepsilon} \cdot \sum_{\varepsilon=N_{\delta i}}^{N_{\delta s}} b_\varepsilon \,, \tag{36}$$

$$k_{x\delta(1)} = \frac{L_{\delta n\sigma(1)\sim}}{L_{\delta n\sigma -}} = \frac{\left|\mathrm{Re}\left[\underline{\Psi}_{\delta n\sigma(1)}\right]\right| \left(\sum_{\varepsilon=N_{\delta i}}^{N_{\delta s}} b_\varepsilon\right)^2}{\sqrt{2}\mu_\delta L h_s I_{c\delta(1)} \cdot \sum_{\lambda=N_{\delta i}}^{N_{\delta s}} \frac{1}{b_\lambda}\left[\left(\sum_{\varepsilon=N_{\delta i}}^{\lambda-1} b_\varepsilon\right)\left(\sum_{\varepsilon=N_{\delta i}}^{\lambda} b_\varepsilon\right) + \frac{b^2_\lambda}{3}\right]} \tag{37}$$

where b_λ and b_ε are the width of λ and ε order strips and $\Psi_{\delta n\sigma(1)}$ is the δ bar flux corresponding to the fundamental of the own magnetic field, assuming that for the λ order strip, the magnetic linkage corresponds to a constant repartition of the fundamental current density on the strip.

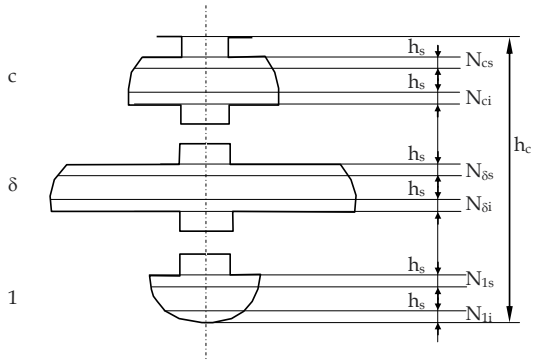

Figure 3. Notch generalized for multiple cages.

If in the motor power supply one considers only the ν order harmonic which corresponds to the supply pulsation $\omega_{1(\nu)}=\nu\omega_1$, the relations (36) and (37) remain valid with the following considerations: index "1" is replaced by index "ν" and the rotor phenomena are with the pulsation $\omega_{2(\nu)}$ given by the relation:

$$\omega_{2(\nu)} = s_{(\nu)} \cdot \omega_{1(\nu)} = \left(1 \mp \frac{1}{\nu} \pm \frac{s}{\nu}\right) \cdot \nu \cdot \omega_1 \ , \tag{38}$$

Subsequently we shall consider the real case, where in the δ bar both the fundamental and ν order time harmonics are present. For this, the equivalent d.c. global factor of the δ bar resistance modification is calculated with the relation:

$$k_{r\delta(CSF)} = \frac{p_{\delta(CSF)\sim}}{p_{\delta(CSF)-}} = \frac{R_{\delta(CSF)\sim}}{R_{\delta(CSF)-}} \ , \tag{39}$$

where $p_{\delta(CSF)\sim}$ represents the total a.c. losses in δ bar (considering the appropriate skin effect for all harmonics) and $p_{\delta(CSF)-}$ represents the bar δ total losses, without considering the repression phenomenon. The a.c. total losses in the δ bar are obtained by applying the effects superposition principle by adding all the δ bar a.c. losses caused by each ν order time, including the fundamental. Therefore one can obtain:

$$p_{\delta(CSF)\sim} = p_{\delta(1)} + \sum_{\nu\neq 1} p_{\delta(\nu)\sim} \ , \tag{40}$$

The a.c. loss in δ bar, corresponding to the fundamental, $p_{\delta(1)\sim}$, is calculated with the following relation:

$$p_{\delta(1)\sim} = I^2_{c\delta(1)} \cdot k_{r\delta(1)} \cdot R_{\delta-} \tag{41}$$

In the same way, the expression of the δ bar a.c. losses produced by some ν order time harmonic is obtained:

$$p_{\delta(\nu)\sim} = I^2_{c\delta(\nu)} \cdot R_{\delta(\nu)\sim} = I^2_{c\delta(\nu)} \cdot k_{r\delta(\nu)} \cdot R_{\delta-} \tag{42}$$

By replacing the relations (41) and (42) in relation (40), it results:

$$p_{\delta(CSF)\sim} = I^2_{c\delta(1)} \cdot k_{r\delta(1)} \cdot R_{\delta-} + \sum_{\nu\neq 1} I^2_{c\delta(\nu)} \cdot k_{r\delta(\nu)} \cdot R_{\delta-} = R_{\delta-} \left(I^2_{c\delta(1)} \cdot k_{r\delta(1)} + \sum_{\nu\neq 1} I^2_{c\delta(\nu)} \cdot k_{r\delta(\nu)} \right). \tag{43}$$

The δ bar losses without considering the repression phenomenon in the bar are calculated using the following relationship:

$$P_{\delta(CSF)-} = I^2_{c\delta(CSF)} \cdot R_{\delta-} \ , \tag{44}$$

where:

$$I_{c\delta(CSF)} = \sqrt{I^2_{c\delta(1)} + \sum_{\nu\neq 1} I^2_{c\delta(\nu)}} \tag{45}$$

is the rated value of the current which runs through the δ bar, in the case of a motor supplied by a frequency converter. By replacing the relation (45) in relation (44):

$$p_{\delta(CSF)\,-} = R_{\delta\,-}\left(I^2_{c\delta(1)} + \sum_{\nu\neq 1} I^2_{c\delta(\nu)}\right) \tag{46}$$

By replacing the relations (43) and (46) in (39) one obtains the expression for the global equivalent factor of the a.c. increasing resistance in the bar δ, $k_{r\delta\,(CSF)}$, in case of the presence of all harmonics in the motor power:

$$k_{r\delta(CSF)} = \frac{p_{\delta(CSF)\sim}}{p_{\delta(CSF)\,-}} = \frac{R_{\delta\,-}\left(I^2_{c\delta(1)}\cdot k_{r\delta(1)} + \sum_{\nu\neq 1} I^2_{c\delta(\nu)}\cdot k_{r\delta(\nu)}\right)}{R_{-}\left(I^2_{c\delta(1)} + \sum_{\nu\neq 1} I^2_{c\delta(\nu)}\right)} = \frac{k_{r\delta(1)} + \sum_{\nu\neq 1} k_{r\delta(\nu)}\left(\frac{I_{c\delta(\nu)}}{I_{c\delta(1)}}\right)^2}{1 + \sum_{\nu\neq 1}\left(\frac{I_{c\delta(\nu)}}{I_{c\delta(1)}}\right)^2} \tag{47}$$

The global equivalent change of a.c. δ bar inductance modification has the expression:

$$k_{x\delta(CSF)} = \frac{q_{\delta(CSF)\sim}}{q_{\delta(CSF)\,-}}\ , \tag{48}$$

where $q_{\delta(CSF)\sim}$ is the a.c. total reactive power, in the δ bar, and $q_{\delta(CSF)-}$ is the total reactive power for a uniform current distribution δ in the bar. Applying the superposition in the case of a.c. total reactive power, the following relationship is obtained:

$$q_{\delta(CSF)\sim} = q_{\delta(1)\sim} + \sum_{\nu\neq 1} q_{\delta(\nu)\sim}\ , \tag{49}$$

A.c. reactive power corresponding to the fundamental is calculated using the following relation:

$$q_{\delta(1)\sim} = \omega_1 \cdot k_{x\delta(1)} \cdot L_{\delta n\sigma\,-} \cdot I^2_{c\delta(1)} \tag{50}$$

In the same way, the expression of the a.c. reactive power in the δ bar corresponding to the ν order harmonic is obtained:

$$q_{\delta(\nu)\sim} = \omega_{1(\nu)} L_{\delta n\sigma(\nu)\sim} \cdot I^2_{c\delta(\nu)} = \nu \cdot \omega_1 \cdot k_{x\delta(\nu)} \cdot L_{\delta n\sigma\,-} \cdot I^2_{c\delta(\nu)} \tag{51}$$

By replacing the relations (50) and (51) in the relation (28), the expression for calculating the total a.c. reactive power in the δ bar is obtained:

$$q_{\delta(CSF)\sim} = \omega_1 \cdot k_{x\delta(1)} \cdot L_{\delta n\sigma -} \cdot I^2_{c\delta(1)} + \left(k_{x\delta(1)} \cdot I^2_{c\delta(1)} + \sum_{\nu \neq 1} \nu \cdot k_{x\delta(\nu)} \cdot I^2_{c\delta(\nu)} \right) =$$
$$= \omega_1 \cdot L_{\delta n\sigma -} \left(k_{x\delta(1)} \cdot I^2_{c\delta(1)} + \sum_{\nu \neq 1} \nu \cdot k_{x\delta(\nu)} \cdot I^2_{c\delta(\nu)} \right) \quad (52)$$

The total reactive power for an uniform current repartition in the δ bar, in the case of a motor supplied through a frequency converter, is calculated by the relation:

$$q_{\delta(CSF)-} = q_{\delta(1)-} + \sum_{\nu \neq 1} q_{\delta(\nu)-} \ , \quad (53)$$

where $q_{\delta(1)-}$ is the reactive power corresponding to the fundamental, in case of an uniform current distribution $I_{c\delta(1)}$ in the δ bar, while $q_{\delta(\nu)-}$ is the reactive power corresponding to the ν harmonic in case of a uniform current distribution $I_{c\delta(\nu)}$ in the δ bar:

$$q_{\delta(1)} = \omega_{1(1)} L_{\delta n\sigma -} \cdot I^2_{c\delta(1)} = \omega_1 \cdot L_{\delta n\sigma -} \cdot I^2_{c\delta(1)} \ . \quad (54)$$

Similarly, for the reactive power corresponding to the ν harmonic, in the case of an uniform current $I_{c\delta(\nu)}$ repartition in the δ bar, the following relation is obtained:

$$q_{\delta(\nu)-} = \omega_{1(\nu)} \cdot L_{\delta n\sigma -} \cdot I^2_{c\delta(\nu)} = \nu \cdot \omega_1 \cdot L_{\delta n\sigma -} \cdot I^2_{c\delta(\nu)} \quad (55)$$

By replacing the relations (54) and (55) in relation (53), the expression for the total reactive power for a uniform current distribution in the δ bar becomes:

$$q_{\delta(CSF)-} = \omega_1 \cdot L_{\delta n\sigma -} \cdot I^2_{c\delta(1)} + \sum_{\nu \neq 1} \nu \cdot \omega_1 \cdot L_{\delta n\sigma -} \cdot I^2_{c\delta(\nu)} = \omega_1 \cdot L_{\delta n\sigma -} \left(I^2_{c\delta(1)} + \sum_{\nu \neq 1} \nu \cdot I^2_{c\delta(\nu)} \right) \quad (56)$$

By replacing the relations (52) and (56) in relation (48), the expression for the global equivalent factor of the a.c. modifying inductance is obtained:

$$k_{x\delta(CSF)} = \frac{q_{\delta(CSF)\sim}}{q_{\delta(CSF)-}} = \frac{\omega_1 L_{\delta n\sigma -} \left(k_{x\delta(1)} \cdot I^2_{c\delta(1)} + \sum_{\nu \neq 1} \nu \cdot k_{x\delta(\nu)} \cdot I^2_{c\delta(\nu)} \right)}{\omega_1 L_{\delta n\sigma -} \left(I^2_{c\delta(1)} + \sum_{\nu \neq 1} \nu \cdot I^2_{c\delta(\nu)} \right)} = \frac{k_{x\delta(1)} + \sum_{\nu \neq 1} \left[\nu \cdot \left(\frac{I_{c\delta(\nu)}}{I_{c\delta(1)}} \right)^2 \cdot k_{x\delta(\nu)} \right]}{1 + \sum_{\nu \neq 1} \left[\nu \cdot \left(\frac{I_{c\delta(\nu)}}{I_{c\delta(1)}} \right)^2 \right]} \quad (57)$$

5. Determining the equivalent parameters of the winding rotor, considering the skin effect

The rotor winding's parameters are affected by the skin effect, at the start of the motor and also at the nominal operating regime. For establishing the relations that define these parameters, considering the skin effect, the expression of the rotor phase impedance

reduced to the stator is used. For this, the rotor with multiple bars is replaced by a rotor with a single bar on the pole pitch. Initially only the fundamental present in the power supply of the motor is considered. The rotor impedance reduced to the stator has the equation:

$$Z'_{2(1)} = \frac{R'_{2(1)}}{s_{(1)}} + jX'_{2(1)} \tag{58}$$

Knowing that the induced EMF by the fundamental component of the main magnetic field from the machine in the pole pitch bars is:

$$\underline{U}_{e(1)} = \underline{I}'_{2(1)} \cdot \underline{Z}'_{2(1)} \ , \tag{59}$$

where, for the general case of multiple cages is valid the relation:

$$\underline{I}'_{2(1)} = \sum_{\delta=1}^{c} \underline{I}'_{c\delta(1)} = \frac{\underline{U}_{e(1)}}{\underline{\Delta}_{(1)}} \sum_{\delta=1}^{c} \underline{\Delta}_{\delta(1)} \tag{60}$$

In the relation (60), the number of the cages and respectively the rotor bars/ pole pitch is equal to "c". In the case of motors with the power up to 45 [kW], c=1 (simple cage or high bars) or c=2 (double cage). $\underline{\Delta}_{(1)}$ is the determinant corresponding to the equation system:

$$\underline{U}_{e(1)} = \sum_{\varepsilon=1}^{c} \underline{R}_{\delta\varepsilon(1)} \cdot \underline{I}_{c\varepsilon(1)} \ , \ \varepsilon=1, 2, \ldots, c \ , \tag{61}$$

having the expression:

$$\underline{\Delta}_{(1)} = \begin{vmatrix} \underline{R}_{11(1)} & \cdots & \underline{R}_{1n(1)} \\ \cdot & & \cdot \\ \cdot & & \cdot \\ \underline{R}_{n1(1)} & \cdots & \underline{R}_{nn(1)} \end{vmatrix} \tag{62}$$

$\underline{\Delta}_{\delta(1)}$ is the determinant corresponding to the fundamental obtained from $\underline{\Delta}_{(1)}$, where column δ is replaced by a column of 1:

$$\underline{\Delta}_{\delta(1)} = \begin{vmatrix} \underline{R}_{11(1)} & \cdots & \underline{R}_{1,\,\delta-1(1)} & 1 & \underline{R}_{1,\,\delta+1(1)} & \cdots & \underline{R}_{1n(1)} \\ & & \cdot & & & & \cdot \\ & & \cdot & & & & \cdot \\ \underline{R}_{n1(1)} & \cdots & \underline{R}_{n,\,\delta-1(1)} & 1 & \underline{R}_{n,\,\delta+1(1)} & \cdots & \underline{R}_{nn(1)} \end{vmatrix} \tag{63}$$

Because in the first phase the steady-state regime is under focus, the phenomenon in the rotor corresponding to the fundamental has the pulsation $\omega_{2(1)}=s\omega_1$, where s is the motor slip for the sinusoidal power supply in the steady-state regime. If the relation (63) is introduced

in (60), the expression of the equivalent impedance of the rotor phase reduced to the stator, corresponding to the fundamental valid when considering the skin effect is obtained:

$$\underline{Z}'_{2(1)} = \frac{\underline{\Delta}_{(1)}}{\sum_{\delta=1}^{c} \underline{\Delta}_{\delta(1)}} \tag{64}$$

Thus, the expressions for the rotor phase resistance and inductance reduced to the stator, corresponding to the fundamental, both affected by the skin effect can be written.

$$\frac{R'_{2(1)}}{s_{(1)}} = \Re e\left[\underline{Z}'_{2(1)}\right], \tag{65}$$

$$X'_{2(1)} = \Im m\left[\underline{Z}'_{2(1)}\right] \tag{66}$$

By considering in the motor power supply the ν harmonic only, similar expressions are obtained for the corresponding rotor parameters. Thus:

$$\underline{Z}'_{2(\nu)} = \frac{\underline{\Delta}_{(\nu)}}{\sum_{\delta=1}^{c} \underline{\Delta}_{\delta(\nu)}}, \tag{67}$$

$$\frac{R'_{2(\nu)}}{s_{(\nu)}} = \Re e\left[\underline{Z}'_{2(\nu)}\right], \tag{68}$$

$$X'_{2(\nu)} = \Im m\left[\underline{Z}'_{2(\nu)}\right] \tag{69}$$

Further on we consider the real case of an electric induction machine fed by a frequency converter. For the beginning, the case of simple cage respectively high bars induction motors will be analyzed. Thus, a rotor phase resistance corresponding to the fundamental, $R'_{2(1)}$, and rotor phase resistance corresponding to higher order harmonics $R'_{2(\nu)}$ are replaced by an equivalent resistance $R'_{2(CSF)}$, which dissipates the same part of active power as in the case of "ν" resistances. This equivalent resistance is defined at the fundamental's frequency and it is traversed by the $I'_{2(CSF)}$ current:

$$I'_{2(CSF)} = \sqrt{I'^{2}_{2(1)} + \sum_{\nu\neq 1} I'^{2}_{2(\nu)}} \tag{70}$$

For the rotor phase equivalent resistance reduced to the stator, corresponding to all harmonics, defined at the fundamental's frequency, one can write:

$$R'_{2(CSF)} = k_{r(CSF)} \cdot R'_{2c} + R'_{2i}, \tag{71}$$

where: R'_{2c} is the resistance, considered at the fundamental's frequency of a part from the rotor phase winding from notches and reported to the stator, R'_{2i} is the resistance of a part of the rotoric winding, neglecting skin effect reported to the stator, $k_{r(CSF)}$ is the global modification factor of the rotor winding resistance, having the expression given by the relation (47). To track the changes that appear on the resistance of the rotor winding when the machine is supplied through a frequency converter, comparing to the case when the machine is fed in the sinusoidal regime, the $k_{R'2}$ factor is introduced:

$$k_{R'_2} = \frac{R'_{2(CSF)}}{R'_2} , \tag{72}$$

where R'_2 is the rotor winding resistance reported to the stator, when the machine is fed in the sinusoidal regime:

$$R'_2 = k_r R'_{2c} + R'_{2i} , \tag{73}$$

where k_r is the modification factor of the a.c. rotor resistance, in the case of sinusoidal: $k_r \cong k_{r(1)}$. It is obtained:

$$k_{R'_2} = \frac{k_{r(CSF)} R'_{2c} + R'_{2i}}{k_r R'_{2c} + R'_{2i}} \tag{74}$$

If both the nominator and the denominator of the second member on the relation (74) are divided by k_r and then by R'_{2c}, the following expression is obtained:

$$k_{R'_2} = \frac{\frac{k_{r(CSF)}}{k_r} + \frac{R'_{2i}}{R'_{2c}} \cdot \frac{1}{k_r}}{1 + \frac{R'_{2i}}{R'_{2c}} \cdot \frac{1}{k_r}} = \frac{k_{kr} + r_2 \cdot \frac{1}{k_r}}{1 + r_2 \cdot \frac{1}{k_r}} , \tag{75}$$

where:

$$r_2 = \frac{R'_{2i}}{R'_{2c}} \cong \text{const.} ,$$

which is constant for the same motor, at a given fundamental's frequency. For c=1, $k_{kr}>1$, it results that $k_{R'2} > 1$, which means that $R'_{2(CSF)} > R'_2$ also. The procedure is similar for the reactance. The rotor phase reactance, corresponding to the fundamental, $X'_{2(1)}$, and also the reactance corresponding to the higher harmonics, $X'_{2(v)}$, are replaced by an equivalent reactance $X'_{2(CSF)}$. As in the case of the rotor resistance, we can write:

$$k_{X'_2} = \frac{X'_{2(CSF)}}{X'_2} , \tag{76}$$

where $X'_{2(CSF)}$ is the equivalent reactance of the rotor phase, reduced to the stator, corresponding to all harmonics, including the fundamental, on the fundamental's frequency:

$$X'_{2(CSF)} = k_{X(CSF)} X'_{2c} + X'_{2i} \ , \tag{77}$$

and X'_2 is the reactance of the rotor phase reduced to the stator which characterizes the machine when it is fed in the sinusoidal regime:

$$X'_2 = k_X X'_{2c} + X'_{2i} \tag{78}$$

In relation (77) and (78), we noted: X'_{2c} -the reactance of the rotor winding part from the notches, reduced to the stator, in which the skin effect is present, X'_{2i}- the reactance of the rotor winding phase where the skin effect can be neglected. $k_{X(CSF)}$ is defined in relation (57), where $c \cong 1$. Taking into account the relations (77) and (78), the relation (76) becomes:

$$k_{X'_2} = \frac{k_{X(CSF)} X'_{2c} + X'_{2i}}{k_X X'_{2c} + X'_{2i}} = \frac{\dfrac{k_{X(CSF)}}{k_X} + \dfrac{X'_{2i}}{X'_{2c}} \cdot \dfrac{1}{k_X}}{1 + \dfrac{X'_{2i}}{X'_{2c}} \cdot \dfrac{1}{k_X}} = \frac{k_{k_X} + x_2 \dfrac{1}{k_X}}{1 + x_2 \dfrac{1}{k_X}} \ , \tag{79}$$

where:

$$x_2 = \frac{X'_{2i}}{X'_{2c}} ,$$

is a constant for the same motor at a given fundamental's frequency $k_{kX}<1$, with the consequences $k_{X'2}<1$ and $X'_{2(CSF)}<X'_2$. With this, the impedance of a rotor phase reported to the stator in the case of a machine supplied by a power converter, receives the form:

$$\underline{Z}'_{2(CSF)} = \frac{R'_{2(CSF)}}{s_{(CSF)}} + jX'_{2(CSF)} \ , \tag{80}$$

where:

$$s_{(CSF)} = \frac{R'_{2(CSF)} I'_{2(CSF)}}{U'_{e1(CSF)}} \tag{81}$$

and:

$$U_{e1(CSF)} = \sqrt{U^2_{e1(1)} + \sum_{\nu \neq 1} U^2_{e1(\nu)}} \tag{82}$$

In the case of double cage induction motors, the rotor parameters are necessary to be determined for both cages. The principle of calculation keeps its validity from the above presented case,

the induction motors with simple cage, respectively cage with high bars, with one remark: in the relations for determining $k_{r(CSF)}$ respectively $k_{x(CSF)}$,it is considered that c=2 (for δ=1 the working work cage results and for δ=c=2 the startup cage results). The complex structure of the used algorithm and its component computing relations synthetically presented in the paper, request a very high volume of calculation. Therefore the presence of a computer in solving this problem is absolutely necessary. In the Laboratory of Systems dedicated to control the electrical servomotors from the Polytechnic University of Timişoara the software calculation CALCMOT has been designed. It allows the determination and the analysis of the factors $k_{r(CSF)}$, $k_{x(CSF)}$ and the parameters of the equivalent winding machine induction in the non-sinusoidal regime. Further on, the expressions of the equivalent parameters for the magnetic circuit will be set (corresponding to all harmonics). Thus, to determine the equivalent resistance of magnetization $R_{1m(CSF)}$, we have to take into account that this is determined only by the ferromagnetic stator core losses which are covered directly by the stator power without making the transition through the stereo-mechanical power. By approximating that $I_{01(CSF)} \approx I_{\mu(CSF)}$, for $R_{1m(CSF)}$ it is obtained:

$$R_{1m(CSF)} = \frac{p_{z1(CSF)} + p_{j1(CSF)}}{3I^2_{\mu(CSF)}}, \tag{83}$$

where $p_{z1(CSF)}$ and $p_{j1(CSF)}$ are global losses occurring respectively in the stator teeth and in the yoke due to the supplying of the motor through the frequency converter. In determining the total magnetization current $I_{\mu(CSF)}$, the principle of the superposition effects is applied:

$$I_{\mu(CSF)} = \sqrt{I^2_{\mu(1)} + \sum_{\nu \neq 1} I^2_{\mu(\nu)}} \tag{84}$$

For the equivalent magnetizing reactance, corresponding to all harmonics, determined at the fundamental's magnetization frequency $f_{1(1)}$, we obtain:

$$X_{1m(CSF)} \cong \sqrt{\left(\frac{U_{1(CSF)}}{I_{\mu(CSF)}}\right)^2 - \left(R_{1(CSF)} + R_{1m(CSF)}\right)^2} \tag{85}$$

For the equivalent impedance of the magnetization circuit it can be written:

$$\underline{Z}_{1m(CSF)} = R_{1m(CSF)} + j \cdot X_{1m(CSF)} \tag{86}$$

Given these assumptions and considering that the equivalent parameters were calculated reduced to the fundamental's frequency (in the conditions of a sinusoidal regime), one may formally accept the calculation in complex quantities. Corresponding to the unique scheme shown in Fig. 2, the motor equations are:

$$\underline{U}_{1(CSF)} = \underline{Z}_{1(CSF)} \cdot \underline{I}_{1(CSF)} - \underline{U}_{e1(CSF)};$$

$$\underline{U}'_{e2(CSF)} = \underline{Z}'_{2(CSF)} \cdot \underline{I}'_{2(CSF)} = \underline{U}_{e1(CSF)};$$

$$\underline{U}_{e1(CSF)} = -\underline{Z}_{m(CSF)} \cdot \underline{I}_{01(CSF)}; \tag{87}$$

$$\underline{I}_{01(CSF)} = \underline{I}_{1(CSF)} + \underline{I}'_{2(CSF)}$$

6. Experimental validation

The induction machines which have been tested are: MAS 0,37 [kW] x 1500 [rpm] and MAS 1,1 [kW] x 1500 [rpm]. To validate the experimental studies of the theoretical work, tests were made both for the operation of motors supplied by a system of sinusoidal voltages, and for the operation in case of static frequency converter supply. In Tables 1 and 2 are presented theoretical values (obtained by running the calculation program) and the results of measurements, for $k_{R'2}$ and $k_{X'2}$, factors, respectively the calculation errors of, for both motors tested.

Nr.	$f_{1(1)}$ [Hz]	$k_{R'2} = \frac{R'_{2(CSF)}}{R'_2}$ (calculated)	$k_{R'2}$ (measured)	$\varepsilon_{kR'2}$ [%]	$k_{X'2} = \frac{X'_{2(CSF)}}{X'_2}$ (calculated)	$k_{X'2}$ (measured)	$\varepsilon_{kX'2}$ [%]
1.	25	1,048	1,11	5,58	0,863	0,894	3,6
2.	30	1,026	1,077	4,97	0,912	0,857	-6,03
3.	40	1,021	1,061	3,77	0,944	0,884	-6,35
4.	50	1,014	1,075	6,01	0,967	0,897	-7,23
5.	60	1,011	1,079	6,82	0,975	0,914	-6,25

Table 1. The theoretical and experimental values of factors $k_{R'2}$ and $k_{X'2}$, respectively the errors of calculation, corresponding to 0.37 [kW] x 1500 [rpm] MAS.

Nr.	$f_{1(1)}$ [Hz]	$k_{R'2} = \frac{R'_{2(CSF)}}{R'_2}$ (calculated)	$k_{R'2}$ (measured)	$\varepsilon_{kR'2}$ [%]	$k_{X'2} = \frac{X'_{2(CSF)}}{X'_2}$ (calculated)	$k_{X'2}$ (measured)	$\varepsilon_{kX'2}$ [%]
1.	20	1,098	1,185	7,92	0,812	0,821	1,108
2.	30	1,041	1,120	7,58	0,886	0,916	3,386
3.	40	1,034	1,106	6,96	0,926	0,891	-3,77
4.	50	1,023	1,089	6,45	0,956	0,863	-9,72
5.	60	1,018	1,082	6,28	0,966	0,871	-9,83

Table 2. The theoretical and experimental values of factors $k_{R'2}$ şi $k_{X'2}$, respectively the errors of calculation, corresponding to 1.1 [kW] x 1500 [rpm] MAS.

Parameters of the winding machine supplied by the power converter can be calculated with errors less than 10 [%]. The main cause of errors is the assumption of saturation neglect. Even in this case the results can be considered satisfactory, which leads to validate the theoretical study carried out in the paper.

7. Theoretical analysis of the magnetic losses

7.1. Statoric iron losses

7.1.1. The main stator iron losses

A. The main stator teeth losses

In the teeth, the magnetic field is alternant and generates this type of losses. In the case of the direct supplying system the total losses from the stator teeth p_{zl} are being composed by the magnetic hysteresis losses, p_{zlh} and the eddy currents losses, p_{zlw}:

$$p_{z1} = \left(k_{zh} \cdot \sigma_h \cdot f_1 + k_{zw} \cdot \sigma_w \cdot f_1^2 \cdot \Delta^2\right) \cdot B_{z1m}^2 \cdot G_{z1}\,, \tag{88}$$

where: σ_h is a material constant depending on the thickness and the quality of the steel sheet, f_1 is the supplying frequency, B_{zlm} represents the magnetic induction in the middle of the stator tooth, G_{zl} represent the weight of the stator teeth, σ_w is a material constant similar to σ_h, depending on the sheet thickness and quality and Δ represents the thickness of the sheet. k_{zh} and k_{zw} are two factors which have the mission of underlining respectively the hysteresis losses increment and the eddy currents losses increment due to the mechanical modifications of the stator's sheets. In the case of converters-mode supplying system, at the total losses from the stators teeth caused by the fundamental the losses induced by the higher time harmonics must be taken into account. For an exact analytic expression in the following it is proposed an analysis method of the iron losses based upon the equalization of the hysteresis losses with the eddy currents ones. For the start, only the fundamental is considered present in the supplying system. Distinct from the sine-mode supplying system, when in most cases the supplying frequency is $f_1=f_{1n}=50$ [Hz], is the fact that in the case of the inverter based supplying system the fundamental frequency can take values higher than 50 [Hz]. At very high magnetization frequencies the influence of the skin effect must be taken in consideration. In the following, the minimum value of the magnetization frequency is being determined and for that the skin effect must be considered. The computing relation for the magnetization frequency f_1 is the following:

$$f_1 = \left(\frac{\xi}{\Delta}\right)^2 \cdot \frac{\rho}{\mu\pi}\,, \tag{89}$$

where ξ is the refulation factor.

The minimum magnetization frequency f_{min}, computed with the relation (89), from which the skin effect must be considered is 140[Hz]. Consequently, in the fundamental - wave

supplying mode, at which usually we have f1≤120 [Hz], the principal losses from the stators teeth, can be written as following:

$$p_{z1(1)} = \left(k_{zh} \cdot \sigma_h \cdot f_1 + k_{zw} \cdot \sigma_w \cdot f_1^2 \cdot \Delta^2\right)^2 \cdot B_{z1m(1)}^2 \cdot G_{z1} \ , \tag{90}$$

where $B_{z1m(1)}$ represents the magnetic induction from the middle of the tooth, $B_{z1m(1)} = B_{z1m}$. In order to be able to apply the principle of over position effects, the machine is being considered as being ideal; therefore we neglect the hysteresis phenomenon. For this, we proposed the equalization of the hysteresis losses with the eddy current losses, an assumption that allows the linearization of the machines' equations. Through this equalization, the real machine – that is practically non-linear and in which the principal losses are made of a sum of two components: the one of eddy currents losses and the one of hysteresis losses - is being replaced with a theoretical linear machine, characterized only by its eddy currents losses. Energetically speaking, the two machines must be equivalent. As a following, if we take $p^*_{z1w(1)}$ as the eddy currents losses corresponding to the fundamental, which appear in the theoretical model of the machine adopted, than these losses must be equal to the main losses from the stator teeth characteristic to the real machine, losses given through the relation:

$$p^*_{z1w(1)} = p_{z1(1)} \tag{91}$$

We consider these equivalent losses, $p^*_{z1w(1)}$, equal to the real losses through the eddy currents corresponding to the fundamental, $p_{z1w(1)}$, multiplied with a $k_{z1e(1)}$ factor. This is an equalization factor of the real losses from the stators teeth with losses resulted only from "$p_{z1w(1)}$" – fundamental-mode supplying state:

$$p^*_{z1w(1)} = k_{z1e(1)} \cdot p_{z1w(1)} \tag{92}$$

We consider that through this equalization factor a covering value of the principal stator teeth losses is obtained. The relation (91) made explicit becomes:

$$\left(k_{zh} \cdot \sigma_h \cdot f_1 + k_{zw} \cdot \sigma_w \cdot f_1^2 \cdot \Delta^2\right) \cdot B_{z1m(1)}^2 \cdot G_{z1} = k_{z1e(1)} \cdot k_{zw} \cdot \sigma_w \cdot f_1^2 \cdot \Delta^2 \cdot B_{z1m(1)}^2 \cdot G_{z1} \ . \tag{93}$$

Because of the fact that the usually used sheets have the thickness Δ=0.5 [mm]=const, one can consider that:

$$k_{z1e(1)} = 1 + \frac{K_{z\Delta}}{f_1} \tag{94}$$

where we have

$$K_{z\Delta} = K_z / \Delta^2 \text{ with } K_z = \frac{\sigma_h \cdot k_{zh}}{\sigma_w \cdot k_{zw}}$$

In the following part we consider that only the ν order harmonic is present in the supplying wave, characterized by the magnetization frequency $f_{1(\nu)}=\nu \cdot f_1$. Therefore, the principal losses

in the stator teeth occurring in the real machine corresponding to the ν order time harmonic must be corrected through the two factors $k_{h(\nu)}$ and $k_{w(\nu)}$, which are a function of the reaction of the eddy currents:

$$p_{z1(\nu)} = \left(k_{zh} \cdot k_{h(\nu)} \cdot \sigma_h \cdot \nu \cdot f_1 + k_{zw} \cdot k_{w(\nu)} \cdot \sigma_w \cdot \nu^2 \cdot f_1^2 \cdot \Delta^2\right) \cdot B_{z1m(\nu)}^2 \cdot G_{z1} \tag{95}$$

In the relation (95), $B_{z1m(\nu)}$ represents the magnetic induction according to the ν order time harmonic from the middle of the tooth. The factors $k_{h(\nu)}$ and $k_{w(\nu)}$ have the expressions:

$$k_{h(\nu)} = \frac{\xi_{(\nu)}}{2} \cdot \frac{sh\xi_{(\nu)} + \sin\xi_{(\nu)}}{ch\xi_{(\nu)} - \cos\xi_{(\nu)}};\ k_{w(\nu)} = \frac{3}{\xi_{(\nu)}} \cdot \frac{sh\xi_{(\nu)} - \sin\xi_{(\nu)}}{ch\xi_{(\nu)} - \cos\xi_{(\nu)}}; \tag{96}$$

As in the case of the fundamental-wave supplying case, the real machine is replaced by a theoretical linear machine which has only losses given by the eddy currents. Reasoning as in the case of the fundamental, we obtain:

$$k_{z1e(\nu)} = 1 + \frac{K_z}{\Delta^2} \cdot \frac{1}{\nu \cdot f_1} \cdot \frac{k_{h(\nu)}}{k_{w(\nu)}} == 1 + \frac{K_{z\Delta}}{\nu \cdot f_1} \cdot \frac{k_{h(\nu)}}{k_{w(\nu)}}\ , \tag{97}$$

$$p_{z1(\nu)} = p^*_{z1w(\nu)} = k_{z1e(\nu)} \cdot p_{z1w(\nu)} = k_{z1e(\nu)} \cdot k_{zw} \cdot k_{w(\nu)} \cdot \sigma_w \cdot \nu^2 \cdot f_1^2 \cdot \Delta^2 \cdot B_{z1m(\nu)}^2 \cdot G_{z1} \tag{98}$$

where $p^*_{z1w(\nu)}$ are the equivalent losses corresponding to the ν harmonic. If we have $p_{z1(CSF)}$ for the losses from the stators teeth with the machine supplied by inverters, by applying the principle of over position effects for the theoretical linear model of the machine, it will be written:

$$p_{z1(CSF)} = k_{zw} \cdot \sigma_w \cdot f_1^2 \cdot \Delta^2 \cdot B_{z1m(1)}^2 \cdot G_{z1} \left[k_{z1e(1)} + \sum_{\nu \neq 1} k_{z1e(\nu)} \cdot k_{w(\nu)} \cdot \nu^2 \left(\frac{B_{z1m(\nu)}}{B_{z1m(1)}} \right)^2 \right] \tag{99}$$

In order to analyze the modifications suffered by the main losses in the stators teeth while the motor is supplied by an inverter versus the sine-mode supplying system, we analyze the ratio between the relations (99) and (88). After making the intermediary computations in which the relations (93), (94) and (99) are taken into account we obtain:

$$k_{pz1} = \frac{p_{z1(CSF)}}{p_{z1}} = 1 + \sum_{\nu \neq 1} \left(\frac{k_{z1e(\nu)}}{k_{z1e(1)}} \cdot k_{w(\nu)} \cdot \nu^2 \cdot k_{Bz1(\nu,1)}^2 \right)\ , \tag{100}$$

where $k_{Bz(\nu,1)} = B_{z1m(\nu)} / B_{z1m(1)}$.

B. The principal losses in the stator yoke

In the case of the direct – mode supplying system of the machine, the principal yoke losses consist of the hysteresis losses, p_{j1h} and eddy currents losses, p_{j1w}:

$$p_{j1} = \left(\sigma_h \cdot f_1 \cdot k_{j1h} + \sigma_w \cdot \Delta^2 \cdot f_1^2 \cdot k_{j1w}\right) \cdot B_{j1}^2 \cdot G_{j1} \tag{101}$$

where: B_{jl} is the magnetic induction in the stator yoke, G_{jl} represents the weight of the stator yoke, $k_{j1w} = k_{j1w1} \cdot k_{j1w2}$, where k_{j1w1} is a coefficient that corresponds to the non uniform repartition of the magnetic induction in the yoke and k_{j1w2} is a coefficient that corresponds to the currents closing perpendicular to the sheets, through the places with imperfections in the sheets isolation layer and also in the wholes made in the cutting process. In the case on an inverter supplying system at the total losses from the stator yoke caused by the fundamental, the superior time harmonics losses must be added. In order to apply the principle of over-position effect the method is similar to the one used in the case of the principal losses in the teeth. We equalize energetically the real machine with the linear theoretical one where we consider only the eddy currents losses. As a following, for the fundamental supplying mode, the principal losses in the stator yoke for a real machine, $p_{j1(1)}$ are:

$$p_{j1(1)} = \left(\sigma_h \cdot f_1 \cdot k_{j1h} + \sigma_w \cdot \Delta^2 \cdot f_1^2 \cdot k_{j1w}\right) \cdot B_{j1(1)}^2 \cdot G_{j1} \tag{102}$$

If we have $p^*_{j1w(1)}$ as losses in eddy currents, than these must be equalized with the principal losses from the stator yoke described with the relation (102):

$$p^*_{j1w(1)} = p_{j1(1)} \tag{103}$$

These equivalent losses, $p^*_{j1w(1)}$ are considered equal to the real eddy currents losses $p_{j1w(1)}$, multiplied with an equalizing factor of the real yoke losses with "$p_{j1w(1)}$" type losses, $k_{j1e(1)}$:

$$p^*_{j1w(1)} = k_{j1e(1)} \cdot p_{j1w(1)} \tag{104}$$

Similarly to point A, as a following of the equalization we obtain the relation:

$$k_{j1e(1)} = 1 + \frac{K_w}{\Delta^2 \cdot f_1} = 1 + \frac{K_{w\Delta}}{f_1}, \tag{105}$$

where we have:

$$K_w = \frac{\sigma_h \cdot k_{j1h}}{\sigma_w \cdot k_{j1w}} \text{ and } K_{w\Delta} = \frac{K_w}{\Delta^2}$$

As a following we consider present in the supplying system of the machine only the ν order superior time harmonic. Because of the fact that the magnetization frequency $f_{1(\nu)}$ is the fundamental one multiplied with ν, the principal losses from the stator yoke which appear in the fundamental must be adjusted with the two coefficients: $k_{h(\nu)}$ and $k_{w(\nu)}$. These factors take into account respectively the skin effect and the eddy currents reaction.

$$p_{j1(\nu)} = \left(k_{h(\nu)} \cdot \sigma_h \cdot \nu \cdot f_1 \cdot k_{j1h} + k_{w(\nu)} \cdot \sigma_w \cdot \Delta^2 \cdot \nu^2 \cdot f_1^2 \cdot k_{j1w}\right) \cdot B_{j1(\nu)}^2 \cdot G_{j1} \tag{106}$$

In the relation (106), $B_{j1(\nu)}$ represents the magnetic induction accordingly to the ν order harmonic. Through the energetically equalization realized from the replacement of the real machine with the linear model, we obtain the equalizing factor of the stator yoke losses, with the "$p_{j1w(\nu)}$" type losses:

$$k_{j1e(\nu)} = 1 + \frac{K_w}{\Delta^2} \cdot \frac{1}{\nu \cdot f_1} \cdot \frac{k_{h(\nu)}}{k_{w(\nu)}} = 1 + \frac{K_{w\Delta}}{\nu \cdot f_1} \cdot \frac{k_{h(\nu)}}{k_{w(\nu)}} \tag{107}$$

In conclusion, the principal losses in the stator yoke, corresponding to the ν order time harmonic can be written by equalizing as:

$$p_{j1(\nu)} = p^*_{j1w(\nu)} = k_{j1e(\nu)} \cdot p_{j1w(\nu)}\,, \tag{108}$$

where:

$$p_{j1w(\nu)} = k_{w(\nu)} \cdot \sigma_w \cdot \Delta^2 \cdot \nu^2 \cdot f_1^2 \cdot k_{j1w} \cdot B^2_{j1(\nu)} \cdot G_{j1} \tag{109}$$

As a following we have considered the situation of the machine supplied by the fundamental and the superior time harmonics as well. Taking $p_{j1(CSF)}$ as the global losses occurring in the stator yoke due to the converter supplying mode, by applying the over position effect principle on the theoretical linear model we can write:

$$p_{j1(CSF)} = \sigma_w \cdot f_1^2 \cdot \Delta^2 \cdot k_{j1w} \cdot B^2_{j1(1)} \cdot G_{j1} \left[k_{j1e(1)} + \sum_{\nu \neq 1} k_{j1e(\nu)} \cdot k_{w(\nu)} \cdot \nu^2 \left(\frac{B_{j1(\nu)}}{B_{j1(1)}} \right)^2 \right] \tag{110}$$

In order to analyze the changes that the principal losses from the stator yoke suffer when the machine is being supplied through an inverter versus the sine-mode supplying case, we divide the relation (110) at (101). After finishing the computations we have:

$$k_{pj1} = \frac{p_{j1(CSF)}}{p_{j1}} = 1 + \sum_{\nu \neq 1} \left(\frac{k_{j1e(\nu)}}{k_{j1e(1)}} \cdot k_{w(\nu)} \cdot \nu^2 \cdot k^2_{Bj1(\nu,1)} \right)\,, \tag{111}$$

where: $k_{Bj(\nu,1)} = B_{j1(\nu)} / B_{j1(1)}$.

7.1.2. The supplementary stator iron losses

A. Surface supplementary losses

In the case of a network supplying mode, the magnetic induction distribution curve over the polar step is not very different from a sine-curve. The surface stator losses are given by the expression:

$$P_{\sigma 1} = \frac{1}{2} \cdot l \cdot \pi \cdot D \cdot \frac{\tau_{c1} - b_{41}}{\tau_{c1}} \cdot k_o \cdot \left(N_{c2} \cdot n \right)^{1,5} \cdot \left(\tau_{c2} \cdot \beta_2 \cdot k_{\delta 2} \cdot B_\delta \right)^2 \tag{112}$$

In the relation (112) the significance of the sizes is the following: D is the inner diameter of the stator, τ_{c1} is the step of the stator slot and τ_{c2} is the step of the rotor slot, b_{41} is the opening of the stator slot, N_{c2} is the number of stator slots, n is the rotation speed, β_2 is a factor dependent on the ratio b_{42}/δ (b_{42} is the opening of the rotor slot), $k_{\delta 2}$ is an air gap factor, k_o is an adjustment factor which depends on the materials resistivity and its magnetic permeability. In the case of the inverter supplying method, due to the deforming state at the supplementary losses produced by the fundamental, the surface losses produced by the superior time harmonics must be considered. Because of the fact that the surface losses in the polar pieces are treated as the eddy current losses developed in the inductor sheets, we can apply the over position effect principle without any further parallelism. Therefore, the surface supplementary losses in the stator in the case of a machine supplied by inverters can be computed with the relation:

$$P_{\sigma 1(CSF)} = \frac{1}{2} \cdot 1 \cdot \pi \cdot D \cdot \frac{\tau_{c1} - b_{41}}{\tau_{c1}} \cdot k_o \cdot \left(N_{c2} \cdot n\right)^{1,5} \cdot \left(\tau_{c2} \cdot \beta_2 \cdot k_{\delta 2} \cdot B_{\delta(1)}\right)^2 \left[1 + \sum_{v \neq 1} \left(\frac{B_{\delta(v)}}{B_{\delta(1)}}\right)^2\right] \quad (113)$$

Dividing the supplementary losses in the stator surface when having an inverter supplying system for the machine, $P_{\sigma 1(CSF)}$, by the supplementary losses in the stator surface when we have the sine-mode supplying system for the machine, $P_{\sigma 1}$, and making the intermediary computations we obtain the increment factor of the supplementary stator surface losses in the inverter versus the sine-mode supplying case, $k_{P\sigma 1}$, as following:

$$k_{P\sigma 1} = \frac{P_{\sigma 1(CSF)}}{P_{\sigma 1}} = 1 + \sum_{v \neq 1} \left(\frac{B_{\delta(v)}}{B_{\delta(1)}}\right)^2 = 1 + \sum_{v \neq 1} k^2_{B\delta(v,1)} > 1 \ , \quad (114)$$

where $k_{B\delta(v,1)} = B_{\delta(v)} / B_{\delta(1)}$. By analyzing the relation (114) one can notice the fact that the $k_{P\sigma 1}$ factor tends to 1 because of the fact that the value is practically very low. Consequently, the surface supplementary losses increase due to the inverter supplying system to an extent that is not to be taken into consideration.

B. The pulsation supplementary losses

In the case of the sine-mode supplying system, the pulsation supplementary losses in the stator, provided that the magnetic field along the polar step is not much different from a sine-wave, has the following expression:

$$P_{P1} = \frac{1}{2} \cdot \sigma_w \cdot k_{wP1} \cdot \left(\Delta N_{c2} n\right)^2 \cdot \left(\frac{\gamma_2 \delta k_\delta}{2\tau_{c1}}\right)^2 \cdot G_{z1} \cdot B^2_{z1m} \ , \quad (115)$$

where k_{wP1} is an increment coefficient of the stator losses by eddy currents due to processing, k_δ is the total air gap factor and γ_2 is constant for the one and the same machine, depended on the opening of the stator slot and the air gap dimension. In the situation in which the

machine is supplied by inverters, by applying the over position effect principle, the following expression for the supplementary pulsation losses in the stator $P_{P1(CSF)}$ is obtained:

$$P_{P1(CSF)} = \frac{1}{2}\cdot\sigma_w\cdot k_{wP1}\cdot\left(\Delta N_{c2} n\right)^2\cdot\left(\frac{\gamma_2\delta k_\delta}{2\tau_{c1}}\right)^2\cdot G_{z1}\cdot B_{z1m(1)}^2\left[1+\sum_{\nu\neq 1}\left(\frac{B_{z1m(\nu)}}{B_{z1m(1)}}\right)^2\right] \tag{116}$$

Dividing the pulsation stator losses in the case of the inverter supplying system $P_{P1(CSF)}$, by the pulsation stator losses in the case of sine-mode supplying system P_{P1}, we obtain the increment factor of the supplementary pulsation losses in the inverter versus sine-wave supplying system, k_{Pp1}:

$$k_{Pp1} = \frac{P_{P1(CSF)}}{P_{P1}} = 1+\sum_{\nu\neq 1}\left(\frac{B_{z1m(\nu)}}{B_{z1m(1)}}\right)^2 = 1+\sum_{\nu\neq 1} k_{Bz1(\nu,1)}^2 > 1 \tag{117}$$

By analyzing the relation (117) we can state that in the case of an inverter supplied machine we have not obtained a significant increment of the pulsation losses in the stator due to the small value of the $k_{Bz1(\nu,1)}^2$.

7.2. Rotor iron losses

7.2.1. Principal losses in the rotor iron

A. The principal losses in the rotor's teeth

Firstly, only one superior time harmonic is considered present in the supplying system of the machine, of an average order ν. The real losses that this harmonic produces in the rotor teeth have the expression:

$$p_{z2(\nu)} = \left(k_{zh}\cdot k_{h(\nu)}\cdot\sigma_h\cdot s_{(\nu)}\cdot\nu\cdot f_1 + k_{zw}\cdot k_{w(\nu)}\cdot\sigma_w\cdot s_{(\nu)}^2\cdot\nu^2\cdot f_1^2\cdot\Delta^2\right)B_{z2m(\nu)}^2\cdot G_{z2} \tag{118}$$

In the relation (118), $B_{z2m(\nu)}$ represents the magnetic induction corresponding to the ν order harmonic from the middle of the rotor tooth. In the theoretical model adopted, these losses given by the relation (118) are produced only by eddy currents:

$$p_{z2(\nu)} = p_{z2w(\nu)}^* = k_{z2e(\nu)}\cdot p_{z2w(\nu)}\ , \tag{119}$$

where $k_{z2e(\nu)}$ is an equalizing factor of the real losses from the rotor teeth, only with the losses of "$p_{z2w(\nu)}$" type, corresponding to the ν order time harmonic. Developing the relation (119) by using the relation (118), after finishing the intermediary computations we obtain:

$$k_{z2e(\nu)} = 1+\frac{K_z}{\Delta^2}\cdot\frac{1}{s_{(\nu)}\cdot\nu\cdot f_1}\cdot\frac{k_{h(\nu)}}{k_{w(\nu)}} = 1+\frac{K_{z\Delta}}{s_{(\nu)}\cdot\nu\cdot f_1}\cdot\frac{k_{h(\nu)}}{k_{w(\nu)}} \tag{120}$$

Therefore, the principal losses from the rotor teeth, corresponding to the ν order time harmonic can be written by equalization as it follows:

$$p_{z2(\nu)} = k_{z2e(\nu)} \cdot k_{zw} \cdot k_{w(\nu)} \cdot \sigma_w \cdot s_{(\nu)}^2 \cdot \nu^2 \cdot f_1^2 \cdot \Delta^2 \cdot B_{z2m(\nu)}^2 \cdot G_{z2} \tag{121}$$

In the conditions in which in the supplying system of the machine all the superior time harmonics are present, the principal losses in the rotor teeth can be written as:

$$p_{z2(CSF)} = \sum_{\nu \neq 1} p_{z2(\nu)} \tag{122}$$

B. The principal losses from the rotor's yoke

In the hypotheses in which in the supplying system only the ν order harmonic is present, the real principal losses induced by it in the rotor yoke have the expression:

$$p_{j2(\nu)} = \left(k_{h(\nu)} \cdot \sigma_h \cdot s_{(\nu)} \cdot \nu \cdot f_1 \cdot k_{j1h} + k_{w(\nu)} \cdot \sigma_w \cdot s_{(\nu)}^2 \cdot \nu^2 \cdot f_1^2 \cdot \Delta^2 \cdot k_{j2w} \right) \cdot B_{j2(\nu)}^2 \cdot G_{j2} \tag{123}$$

Through the energetic equalization, due to the replacement of the real machine by a theoretical linear model we can obtain the equality:

$$p_{j2(\nu)} = p_{j2w(\nu)}^* = k_{j2e(\nu)} \cdot p_{j2w(\nu)} \tag{124}$$

Reasoning as in the previous cases, we can determine the equalizing factor of the real losses in the rotor yoke, only with losses of the type "$p_{j2w(\nu)}$" type as it follows:

$$k_{j2e(\nu)} = 1 + \frac{K_w}{\Delta^2} \cdot \frac{1}{s_{(\nu)} \cdot \nu \cdot f_1} \cdot \frac{k_{h(\nu)}}{k_{w(\nu)}} = 1 + \frac{K_{w\Delta}}{s_{(\nu)} \cdot \nu \cdot f_1} \cdot \frac{k_{h(\nu)}}{k_{w(\nu)}} \tag{125}$$

Consequently, the principal rotor yoke losses corresponding to the ν order harmonic can be written by equalization in the form:

$$p_{j2(\nu)} = k_{j2e(\nu)} \cdot k_{j2w} \cdot k_{w(\nu)} \cdot \sigma_w \cdot s_{(\nu)}^2 \cdot \nu^2 \cdot f_1^2 \cdot \Delta^2 \cdot B_{j2(\nu)}^2 \cdot G_{j2} \tag{126}$$

Disregarding all these, in the case of the inverter supplying system the total principal losses in the rotor yoke, $p_{j2(CSF)}$, are computed with the relation:

$$p_{j2(CSF)} = \sum_{\nu \neq 1} p_{j2(\nu)} \tag{127}$$

7.2.2. The supplementary losses in the rotor iron

A. The surface supplementary losses

If the machine is directly supplied from the power supply, the surface supplementary rotor losses are calculated with the relation:

$$P_{\sigma 2} = \frac{1}{2} \cdot p_{\sigma 2} \cdot l \cdot \pi \cdot \left(\Delta - 2\delta\right) \cdot \frac{\tau_{c2} - b_{42}}{\tau_{c2}} \ , \tag{128}$$

where the specific rotor surface losses $p_{\sigma 2}$ have the expression:

$$p_{\sigma 2} = k_o \left(N_{c1} \cdot n\right)^{1,5} \cdot \left(\tau_{c1} \cdot \beta_1 \cdot k_{\delta 1} \cdot B_\delta\right)^2 \tag{129}$$

In the relations (128) and (129) we noted by b_{42} the opening of the rotor slot, N_{c1} the number of rotor slots, β_1 a factor dependent on the b_{41}/δ ratio and $k_{\delta 1}$ the air gap factor. Proceeding similarly we can obtain the expression of the increment factor of the supplementary losses in the rotor surface while the machine is being supplied by inverters versus the sine-mode supplying system, $k_{P\delta 2}$:

$$k_{P\sigma 2} = \frac{P_{\sigma 2(CSF)}}{P_{\sigma 2}} = 1 + \sum_{\nu \neq 1} \left(\frac{B_{\delta(\nu)}}{B_{\delta(1)}} \right)^2 = 1 + \sum_{\nu \neq 1} k^2_{B\delta(\nu,1)} = k_{P\sigma 1} > 1 \tag{130}$$

B. The supplementary pulsation losses

The supplementary pulsation rotor losses, in the sine-mode supplying system have the following expression:

$$P_{P2} = \frac{1}{2} \sigma_w \cdot k_{wP2} \left(\Delta \cdot N_{c1} \cdot n \cdot B_{P2}\right)^2 \cdot G_{z2} \tag{131}$$

B_{P2} represents the pulsation induction in the rotor teeth. Consequently, taking into account the fact that:

$$\frac{B_{z2m(\nu)}}{B_{z2m(1)}} = \frac{B_{\delta(\nu)}}{B_{\delta(1)}} = k_{B\delta(\nu,1)}, \tag{132}$$

we obtain:

$$k_{Pp2} = \frac{P_{P2(CSF)}}{P_{P2}} = 1 + \sum_{\nu \neq 1} k^2_{B\delta(\nu,1)} > 1 \tag{133}$$

8. Conclusions

This paper aims to study the theoretical behavior of asynchronous three-phase motor in the case of supplying through a power frequency converter. This study has aimed to develop the theory of the asynchronous three-phase motor in non-sinusoidal periodic regime to serve as a starting point in optimizing the design methodology. Given that the asynchronous three-phase motor is fed through a static frequency converter, the machine operation in the presence of higher time harmonics in the supply voltage can be described by a single mathematical model. The model consists of a single equivalent scheme corresponding to all harmonics and it is defined at the fundamental frequency.

Author details

Muşuroi Sorin
Politehnica University of Timişoara, Romania

9. References

[1] Muşuroi, S.; Vătău, D.; Andea, P.; Şurianu, F.D.; Frigură, F. & Bărbulescu, C. (2007). Analysis of the Magnetic Losses from the Induction Machines Supplied by Inverters, *Proceedings of EUROCON 2007 International Conference on Computer as a Tool*, pp. 1800-1809, ISBN 978-1-4244-0812-2, Warsaw, Poland, September 9-12, 2007

[2] Muşuroi, S.; Olărescu, N.V.; Vătău, D. & Şorândaru, C. (2009). Theoretical and Experimental Determination of Equivalent Parameters of Three-Phase Induction Motor Windings in Case of Power Electronic Converters Supply, *WSEAS Transactions on Systems*, Vol.8, Issue10, (October 2009), pp. 1115-1124, ISSN 1109-2777

[3] Muşuroi, S.; Şorândaru, C.; Olărescu, N.V. & Svoboda, M. (2009) Mathematical Model Associated to Three-Phase Induction Servomotors in the Case of Scalar Control, *WSEAS Transactions on Systems*, Vol.8, Issue 10, (October 2009), pp. 1125-1134, ISSN 1109-2777

[4] Mohan, N.; Undeland, T.M. & Robbins, W.P. (1995). *Power Electronics: Converters, Applications and Design,* (2nd edition), John Wiley & Sons, ISBN 0-471-58408-8, Inc., New-York, USA

[5] Murphy, J. & Turnbull, F. (1988). *Power Electronic Control of AC Motors,* Pergarmon Press, ISBN 0-08-022683, Oxford, 1988

[6] Dordea, T. & Dordea, P.T. (1984). Ersatzläuferimpedanz einer induktionsmachine mit vielfachem käfig und in den selben nuten untergebrachten stäben, *Revue Roumaine des Sciences Techniques*, Vol.29, No.2, (December 1984), pp. 151-159, ISSN 0035-4066

Chapter 3

The Dynamics of Induction Motor Fed Directly from the Isolated Electrical Grid

Marija Mirošević

Additional information is available at the end of the chapter

http://dx.doi.org/10.5772/49973

1. Introduction

An induction motor is the most common machine used for industrial drives. It is used in variety of drives due to its robust construction, relatively low cost and reliability. In isolated electrical network, such as marine and offshore power systems and emergency generation plant, induction motors are the most power consuming loads and are used for winches, water pumps, compressors, fans and for other on-board applications, in continuous mode or intermittently.

In many applications induction motors are direct-on-line switch-started. Their dynamic characteristics have an obvious influence on the transient process of power system; however, they cause a significant disturbance in transients (significant impacts loads) that can produce disturbances in the isolated electrical network, which in turn affects the quality of electric power system and thus, on the dynamic behavior of induction motors.

Direct-on-line starting represents the simplest and the most economical system to start squirrel-cage induction motor. During starting induction motors draw high starting currents which are several times the normal full load current of the motor. This current causes a significant voltage dip on the isolated electrical grid until the induction motors reach nearly full speed. This voltage drop will cause disturbances in the torque of any other motor running on the isolated electrical grid. Significant disturbances in transients are caused by direct-on-line switch-started induction motors, especially if the load torque on the motor shaft is increased and beside that, also by the sudden change load, such as the impact load on the motor shaft (McElveen, et al., 2001; Cohen, 1995). This situation is particularly difficult because of relatively strong electrical coupling between electrical grid and loads. Besides the voltage dips, an interruption can also appear, which further affects on the fatigue of induction motors connected to the grid. When an interruption of the supply lasts longer than one voltage period, many AC contactors will switch off the motor. In some

cases, faulty contactor may produce multiple switching on and off. However, these interruptions will affect the dynamics of both electrical and mechanical variables. Therefore, it is interesting to analyze dynamics of the induction motor in case when it comes to short-term interruptions in the motor power supply.

That's why the dynamic behavior of induction motors fed directly from isolated electrical grid, as well as dynamics of aggregate is in focus of researchers. Presently, advanced modeling and digital simulation techniques can be used to analyse the dynamics behavior of electrical as well as mechanical systems.

2. Mathematical models used in isolated electrical grid

The aim is to analyze the dynamics of the induction motors fed directly from the isolated electrical grid. For this purposes the mathematical model of isolated electrical grid has been develop consisting diesel electrical aggregate and unregulated induction motors.

Diesel generators are used as the main sources of electricity in cases of isolated systems. In many applications the diesel generator can suffer significant impacts loads that can produce disturbances in the isolated grid. However, the autonomous operation of the synchronous generator is characterized by a change in steady state which causes a change in voltage and frequency, which in turn affects the quality of electric power systems.

The model of diesel electrical aggregate considered in this study consists of: a diesel engine and a speed controller, a synchronous generator and a voltage controller, a mechanical connection between engine and electrical machine shaft.

The synchronous generator is presented as a machine with three armature windings, a magnetizing winding on the rotor and damper windings. One damper winding is located along direct-axis (D), and one along the quadrature-axis (Q). The basis of the mathematical model is a set of differential equations of the synchronous generator in the standard *dq*-axis form (Kundur, 1994). The voltage equations are written in generator (source) convention system, in which synchronous machines are usually represented:

$$-u_d = r \cdot i_d + \frac{d\psi_d}{dt} - \omega \cdot \psi_q \tag{1}$$

$$-u_q = r \cdot i_q + \frac{d\psi_q}{dt} + \omega \cdot \psi_d \tag{2}$$

$$E_q = e_q + \frac{x_{1d}}{r_1} \cdot \frac{d\psi_1}{dt} \tag{3}$$

$$0 = r_D \cdot i_D + \frac{d\psi_D}{dt} \tag{4}$$

$$0 = r_Q \cdot i_Q + \frac{d\psi_Q}{dt} \tag{5}$$

where u, i, r, and ψ denote voltage, current, resistance and flux respectively.

The model of a synchronous generator is given in rotor reference frame (ω is rotor electrical speed). The equations of excitation in motor (load) convention system are written. The voltage controller, modeled as PI, is implemented in the model of the synchronous generator.

The model of the prime mover - the diesel engine assumes that the engine torque is directly proportional to the fuel consumption. In order to describe the dynamic behavior of the diesel engine it is necessary to set up a system of differential equations which includes an equation of the engine, the turbocharger, the air collector, the exhaust system, and the speed controller. Taking into account these equations requires the knowledge of characteristics of diesel engines that require complex experimental measurements, according to (Krutov, 1978; Tolšin 1977). The studies carried out in (Erceg & et al. 1996) showed that the mentioned omissions do not affect significantly the results and that the proportionality of torque to the amount of injected fuel can be assumed. This simplification is allowed when it is of interest to observe dynamics of a synchronous generator as well as induction motors. The speed controller is modeled as PI and implemented in the model.

Sudden impact load on the diesel electrical aggregate is the most difficult transition regime for units due to electricity loads and also due to torsional strains in the shaft lines. A more significant disturbance, which is at the same time very common in practice, is the direct-on-line starting of induction motors to such a grid. Starting of induction motors will cause voltage dips and will reduce engine speed depending on the time of the starting of each motor. This will also cause torsional stresses in the shaft. Thus, the mechanical coupling of a diesel engine and a synchronous generator is considered to be a rotating system with two concentrated masses. Masses are connected by flexible coupling. The flexible coupling allows these masses to rotate at a different speed in transients.

The variable angle of rotation between these masses occurs during the transient, in period when mechanical balance between diesel engine and electric generator is disturbed., The torque which appears at coupling zone between two concentrated rotational masses allows thus the analysis of the torsional dynamics in the coupling.

Induction motor as an active consumer and its parameters were analyzed in (Maljkovic, 2001; Amezquita-Brook et al., 2009). According to (Jones, 1967; Kraus 1986) three phase squirrel-cage induction motors are represented with stators and rotors voltage equations:

$$u_{dIM} = R_{sIM} \cdot i_{dIM} + \frac{d\psi_{dIM}}{dt} - \omega \cdot \psi_{qIM} \tag{6}$$

$$u_{qIM} = R_s \cdot i_{qIM} + \frac{d\psi_{qIM}}{dt} + \omega \cdot \psi_{dIM} \tag{7}$$

$$0 = R_r \cdot i_{DIM} + \frac{d\psi_{DIM}}{dt} - \left(\omega - \omega_{IM}\right) \cdot \psi_{QIM} \tag{8}$$

$$0 = R_r \cdot i_{QIM} + \frac{d\psi_{QIM}}{dt} + \left(\omega - \omega_{IM}\right) \cdot \psi_{DIM} \tag{9}$$

where: u, i, R, and ψ denote voltage, current, resistance and flux respectively of an induction motor.

All winding currents, in the transient dq axis model of induction motors as well as in a synchronous generator model, are selected as state variables. The model is completed with an equation of the rotational mass motion (Vas, 1996). All variables and parameters are in per unit (p.u.). The motor's equation of motion involves electrical torque (T_{eIM}), whereas (T_{lIM}) represents load torque on the motor's shaft.

When the induction motor starts unloaded, then the torque T_{lIMn} equals zero. Also, for this analysis the loading with a constant load was selected.

Loads, induction motors (index IM), are connected directly to a synchronous generator (index SG), what means that they are on the same voltage as the generator terminals: $-u_d=u_{dIM1}=u_{dIM2}$, $-u_q=u_{qIM1}=u_{qIM2}$. According to the Kirchhoff's law, the current relationship between supplying and receiving elements are: $i_d=i_{dIM1}+i_{dIM2}$, $i_q=i_{qIM1}+i_{qIM2}$.

The validity of the mathematical model of the generator-unit at impact load, direct-on-line starting of non-loaded induction motor, was checked in the previous work (Mirosevic, et al. 2002a, 2011b) by comparing the results of the simulation and the measurement on the generator-unit with a diesel engine of 46.4 kW, 1500 r/min and a synchronous generator of 40 kVA (3x400/231 V, cos φ=0.8; 57.7 A; 1500 r/min; 50 Hz), to which a motor drive of 7.5 kW (Δ 380 V, 14.7 A, 2905 r/min, cos φ=0.9) was connected. The results obtained by numerical calculation indicate that, the set mathematical model can be applied with sufficient certainty

The analysis of the dynamics of induction motors fed directly from the isolated electrical grid was performed by the application of program package "Matlab/Simulink". The block diagram of integral motor drives is presented in Figure 1 involves: a diesel engine (DM, SC), a three phase synchronous generator and voltage controller, their mechanical coupling and induction motors fed directly from the synchronous generator terminals.

Block diagram of Diesel engine and speed controller is presented in Figure 2 and represents subsystem of block naimed as DM SC in Fig. 1.

The Simulink is used to obtain a model of a diesel generator unit, as well as induction motors by means of basic function blocks that can be linked and edited to subsystem such as subsystems IM 1 and IM 2 in Figure 1 which representthe first and the second induction motors respectively. As one can see in Figure 3 components of the subsystem IM 1 that are used in the calculation of variables are presented.

Induction motors are connected to the network using power supply subsystem, while the load on the motor shaft is represented with subsystems: load IM1 and load IM2 in Figure 1.

Moment of switching/disconnecting on the network is controlled by means of the subsystem ON/OFF, also, the part of this subsystem is used to set the time of switching/disconnecting the load on the motor shaft.

All calculations were carried out by means of the "Variable-Step Kutta-Merson" method – an explicit method of the fourth order for solving the systems of differential equations, with variable integration increment.

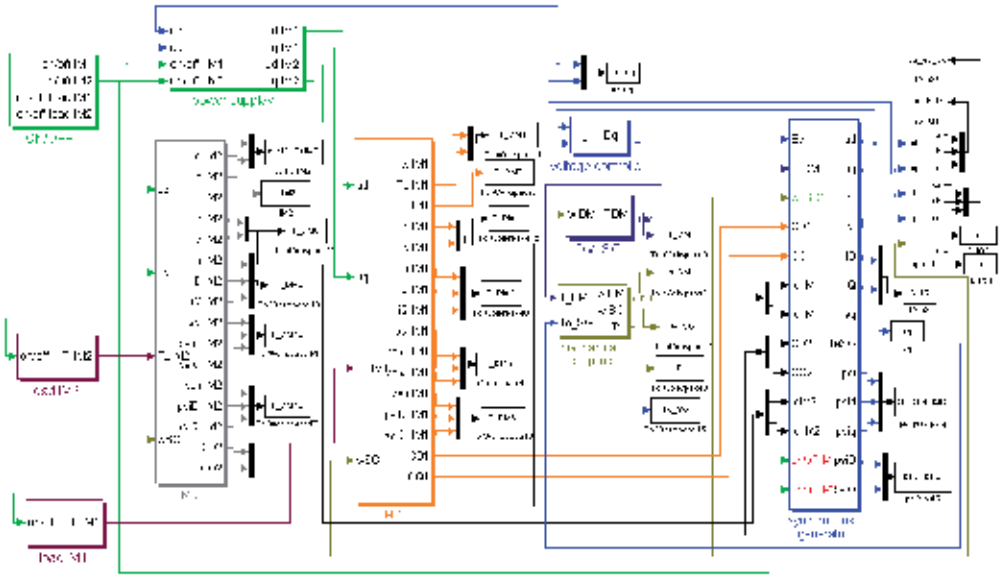

Figure 1. Simulation of the applied mathematical model

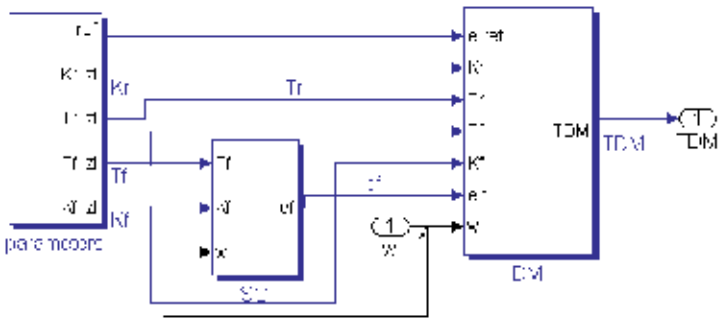

Figure 2. Diesel engine and speed controller model

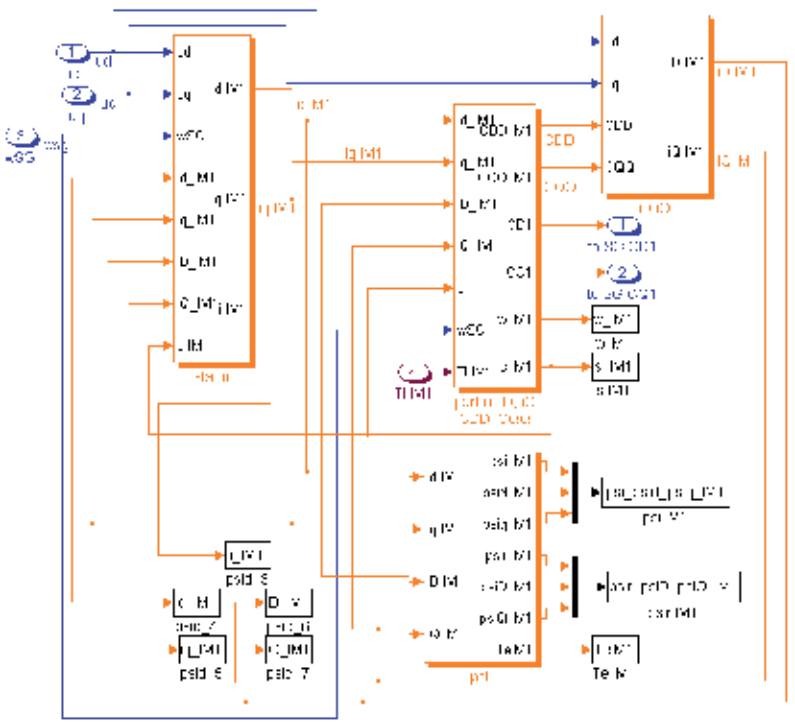

Figure 3. Induction motor model

3. Induction motor starting

At the beginning, two induction motors are connected directly to an isolated electrical grid. The first induction motor (IM1) is connected to the terminals of the aggregate and later, when the first motor has run-up successfully, the second induction motor (IM2) is connected to the grid.

The synchronous generator is initially in a steady state unloaded condition. However, in this condition stator current is zero, rated voltage is on its terminals, while rotation speed of the diesel engine (ω_{DM}) is equal to the speed of the generator (ω_{SG}) and is equal to 1 p.u.

The first observed dynamics is for the case of the starting of unloaded induction motors and in the second case dynamics of loaded induction motors are considered. Transients of: air-gap torque and speed transient of induction motors, terminal voltage, speed transient of synchronous generator and diesel engine, for both cases are presented in Figure 4.

Initially, the first induction motor is starting from rest, the rated voltage is applied on its terminals and there is no mechanical load on the motor shaft. When the induction motor is connected, the load on the aggregate is instantaneously increased, defined in the initial (sub-transient) phase of the transitional phenomenon by locked-rotor torque of the induction motor. As the motor accelerates, its torque grows and the generator load rises. When

maximum torque is achieved, the load of the synchronous generator reaches its maximum and then decreases rapidly.

At the instant of starting, as one can see in Fig. 4a, the air-gap torque is momentarily increased; reaches maximum value of 0.86 p.u. and change in it can be noticed during the whole start-up period of the first induction motor. The instantaneous torque oscillates about positive average value.

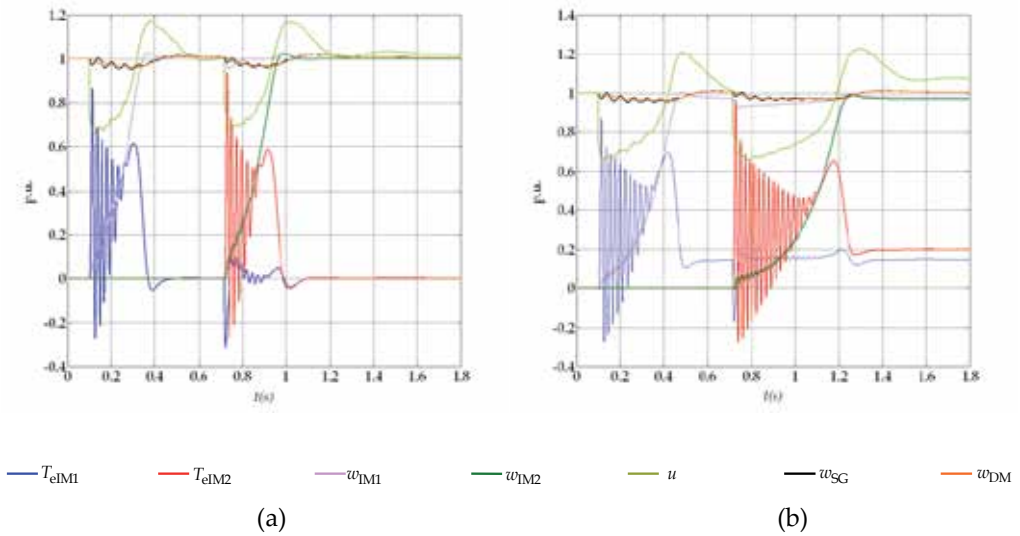

Figure 4. Transients of: air-gap torque of induction motors (T_{eIM1}, T_{eIM2}) and speed transient of induction motors (ω_{IM1}, ω_{IM2}); terminal voltage (u), speed transient of synchronous generator (ω_{SG}) and diesel engine (ω_{DM}), during direct-on-line starting of: a) unloaded b) loaded induction motors

The oscillations in the air-gap torque are caused by the interactions between the stator and rotor flux linkage. The negative oscillations in the electromagnetic torque of the induction motor are presented at the beginning of the start-up period. These are periods of momentary deceleration that occur during regeneration when the electromagnetic torque becomes negative. The rotor speed only increases when the torque is positive. The oscillations that are present in transient of air-gap torque of the first induction motor are damped at the end of start up period and finally the steady state condition is attained without oscillations.

The response of the air-gap torque is in accordance with the response of the motor currents. Transients of stator currents of induction motors and their components, for both cases, are presented in Figure 5.

Under this condition the starting current is large. The starting current of an induction motor is several times larger than the rated current since the back emf induced by Faraday's law grows smaller as the rotor speed increases. However, a large starting current tend to cause the supply voltage to dip during start-up and can cause problems for the other equipment that is connected to the same grid.

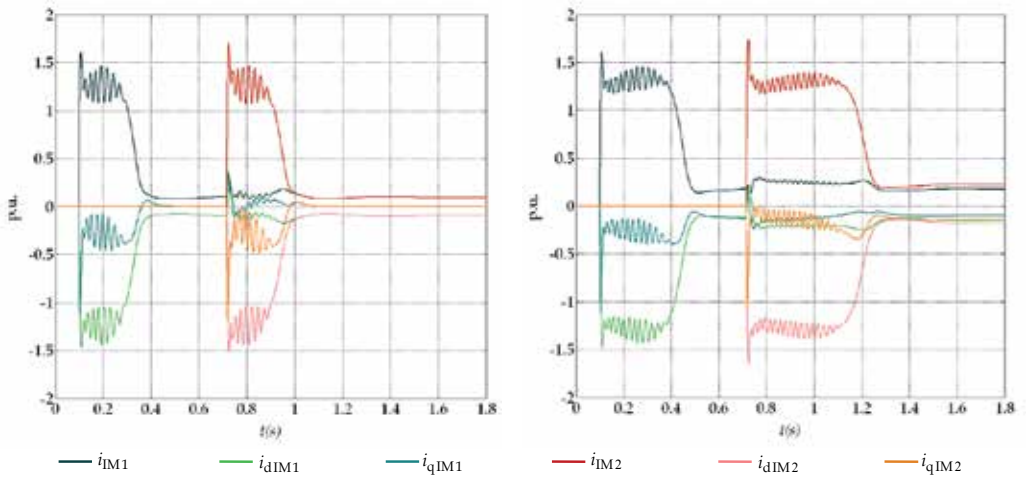

Figure 5. Transients of stator currents of induction motors (i_{IM1}, i_{IM2}) and their components in d (i_{dIM1}, i_{dIM2}) and q (i_{qIM1}, i_{qIM2}) axis during direct-on-line starting of: a) unloaded b) loaded induction motors

At the instant of starting, when the supply has just been switched on the induction motor, the first magnitude of starting current momentarily reaches maximum value of 1.61 p.u. as it is presented in Fig. 5a. The damped oscillations, that are present in stator current transients, disappear at the end of the starting period of the induction motors. When the first motor has run-up successfully, the second induction motor (IM2) is connected to the loaded synchronous generator. Involvement of the second induction motor to the isolated electrical grid the network load instantaneously increased and voltage drop occurs.

The terminal voltage is momentary decreased (Fig. 4a) and after few damped oscillations reached minimal value. However, the high starting currents are appeared. High inrush current, in the first moments, as one can see in Figure 5, reaches the magnitude of the first oscillation of 1.73 p.u. The air-gap torque of the second induction motor T_{eIM2} momentarily achieves 0.94 p.u.

At the moment of switching on to the grid, the second induction motor begins to accelerate and oscillations are present in its transients of air-gap torque during the acceleration period. At the time of the starting of second induction motor (IM2), the reverse torque impulse of 0.31 p.u. in air-gap torque of the first one (IM1) is appeared but decayed rapidly. As the torque of the first induction motor becomes negative motor speed slows down. Thereafter, damped oscillations that are present in the response of electromagnetic torque of the first motor as well as oscillations in electromagnetic torque of the second one are stifled at the end of the run-up period of the second induction motor.

At the beginning of the start-up period of the second motor, the speed of the first one decreases and afterwards recovers. Overshoot in the speed transient occurs at the end of start-up period of the second induction motor.

The starting of loaded induction motor is more difficult transition regime for the aggregate, therefore, the transients of aggregate are slower.

Thus, in the second case, the dynamics of the starting of loaded induction motors is analyzed, however, the load on the first one is T_{lIM1}=0.15 p.u. while T_{lIM2}=0.2 p.u. is applied on the second one. In this case the acceleration time is longer than in the previous case when motors are started unloaded (Fig. 4a), the voltage of synchronous generator is recovering slower, and will be lower then 80%U_n during greater part of start up period, as presented in Fig. 4b.

The initial part of the transients of electromagnetic torque is equal in both cases (load and non-load condition). At the time of the starting of the first induction motor the torque T_{eIM1} reaches a value of 0.86 (p.u.).

At the instant of connection to power supply the instantaneous torque is independent of the balanced source voltages because the machine is symmetrical, even air-gap torque depends upon the values of source voltages though the stator currents. In addition, the air-gap torque oscillates with higher magnitude, about lower average then in case of unloaded motor. These oscillations are damped at the end of the start-up period of the induction motor as presented in Figure 4b.

The component of air-gap torque, which appears because of mutual acting of free currents in stator as well as in rotor windings acts as counter torque on motors shaft and disappears before the end of the run-up. As one can see in Fig 4 the duration of the start-up of both induction motors is longer than in the previous case, in which the motors run-up unloaded. Thus, this acceleration period of second induction motor is 500 ms, while in the previous case lasted 230 ms. In Fig. 5b stator currents, in *dq* axis, and their components, during start up of loaded induction motor, are presented. As the induction motor is directly connected to the terminals of unloaded synchronous generator that means that stator current of induction motor is at the same time the armature current of synchronous generator.

At the beginning of the transient phenomena inrush current which appears during the first half period is dominating but disappears quickly. After initial damping, oscillations of free currents will continue with slightly greater magnitude than at the beginning of transients. These currents, which also can be seen during the start up period of unloaded induction motor, disappear at the end of start up. Corresponding stator flux linkage, during direct-on-line starting of unloaded and loaded induction motor are presented in Fig. 6.

The transients of the first induction motor current in *abc* coordinate system (i_{abcIM1}), in both cases, are presented in Fig. 7. The current of synchronous generator (i_{abcSG}), in both cases, is presented in Fig. 8. This is the total current that motors draw from the electrical grid.

The phenomena of voltage and frequency deviation are typical for isolated electrical grid which in turn affects the quality of electric power systems. The short-term frequency deviation, during direct-on-line starting unloaded and loaded induction motors are presented in Figure 9. There is relatively strong electrical coupling between synchronous

generator and loads as well as torsional strains in the shaft line. However, the torque in the coupling for both cases is presented in Figure 10. Oscillations in transients of torsion torque are longer present during direct-on-line starting loaded induction motor and damped at the end of start-up period.

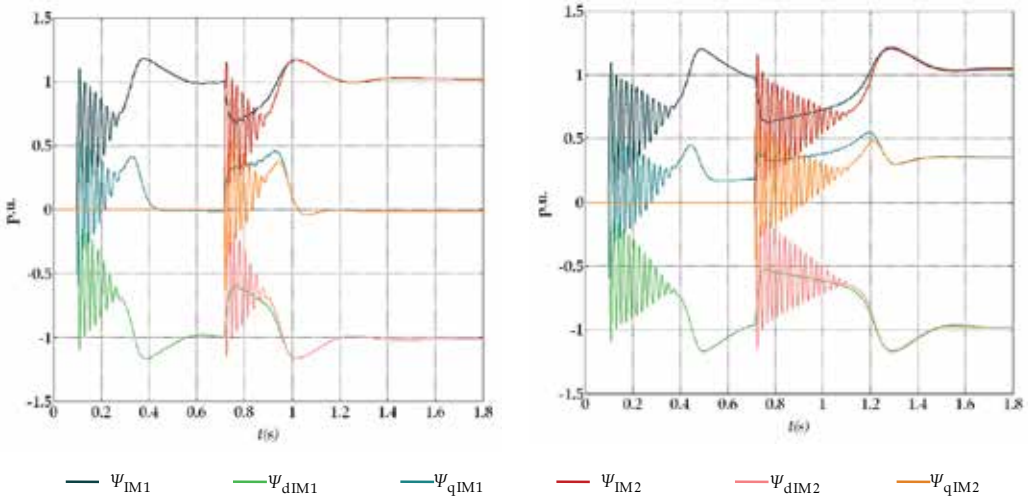

Figure 6. Transients of stator flux linkages of induction motors (Ψ_{IM1}, Ψ_{IM2}) and their components in d (Ψ_{dIM1}, Ψ_{dIM2}) and q (Ψ_{qIM1}, Ψ_{qIM2}) axis during direct-on-line starting of: a) unloaded b) loaded induction motors

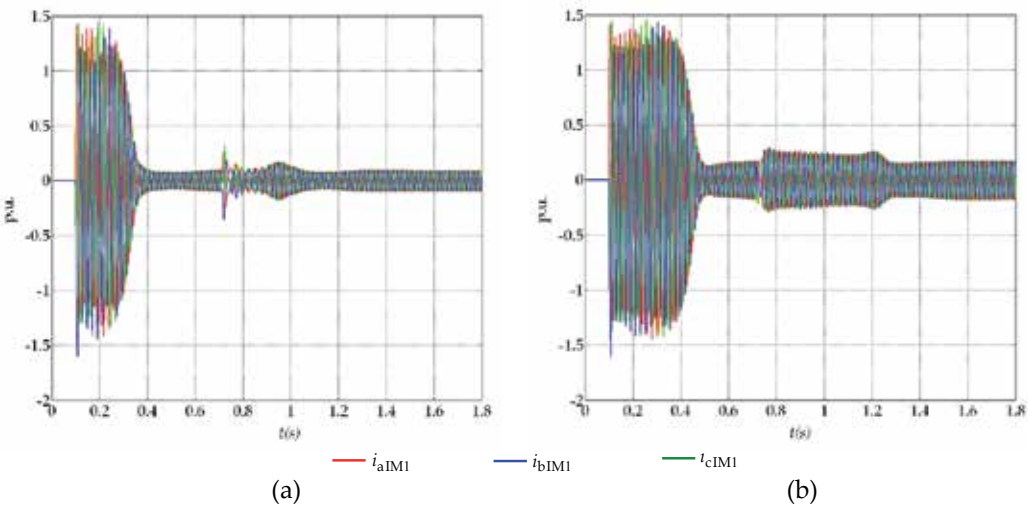

Figure 7. Stator current (i_{abcIM1}) of first induction motor, during direct-on-line starting of: a) unloaded b) loaded induction motors

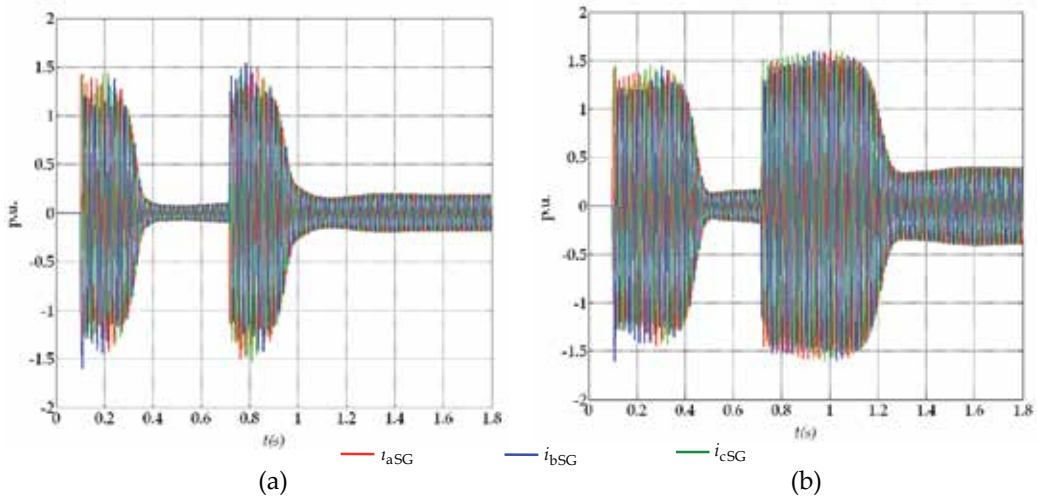

Figure 8. Stator current (i_{abcSG}) of the grid (synchronous generator), during direct-on-line starting of: a) unloaded b) loaded induction motors

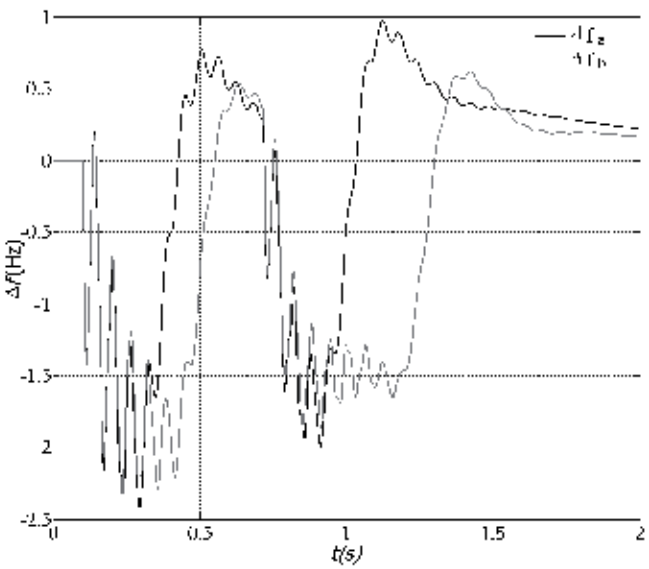

Figure 9. Frequency variations during direct-on-line starting: Δf_a-motors are unloaded, Δf_b -motors are loaded

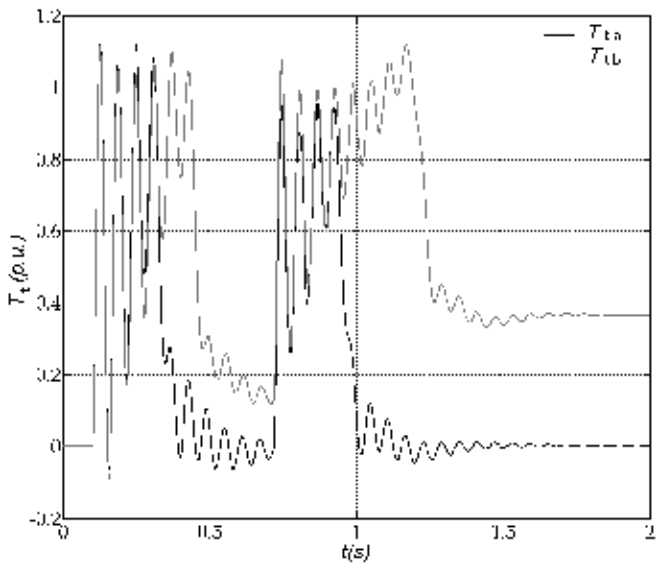

Figure 10. Torsional torque during direct-on-line starting: T_{ta}-motors are unloaded, T_{tb}-motors are loaded

4. Induction motor under sudden change load

The dynamics of sudden change load on the motor shaft is considered. Induction motors are connected directly to the grid, as in previous case, and at chosen moment the first induction motor is starting up, loaded of T_{IIM1} =0.05 p.u. When the first motor has run-up successfully, the second induction motor (IM2) is connected and it starts with T_{IIM2} =0.05 p.u. load on its shaft. Before the second induction motor is connected to the grid the aggregate was led to the steady operation conditions. During start-up of the second induction motor, sudden load change at the first induction motor shaft appeared.

Two cases are considered. In the first case, the impact load of additional 0.1 p.u. on the first induction motor IM1, is applied. While in the second case, the motor is suddenly unloaded, 0.05 p.u. is disconnected from its shaft. Thus, after disconnecting the load the first induction motor run at idle. Transients of air-gap torque and speed transient of induction motors for both cases are presented in Figure 11 and 12.

Direct on line starting of induction motors induces high strain on the power system. This strain arises when the second motor is connected, and additionally is growing up at the instant of impact 0.1 p.u. load on the first motor shaft. When the second induction motor is connected to the grid, it begins to accelerate and the torque of the first induction motor is changed. The electromagnetic torque of the first induction motor becomes negative and motor speed slows down, achieving about 0.95 p.u. Later on, the speed of the first induction motor starts recovery. At the instant of impact additional load on the motor shaft the speed

is decreasing again. The speed of the first induction motor is recovering with strongly damped oscillations at the end of start-up period of the second induction motor (Fig. 11a and Fig. 12a).

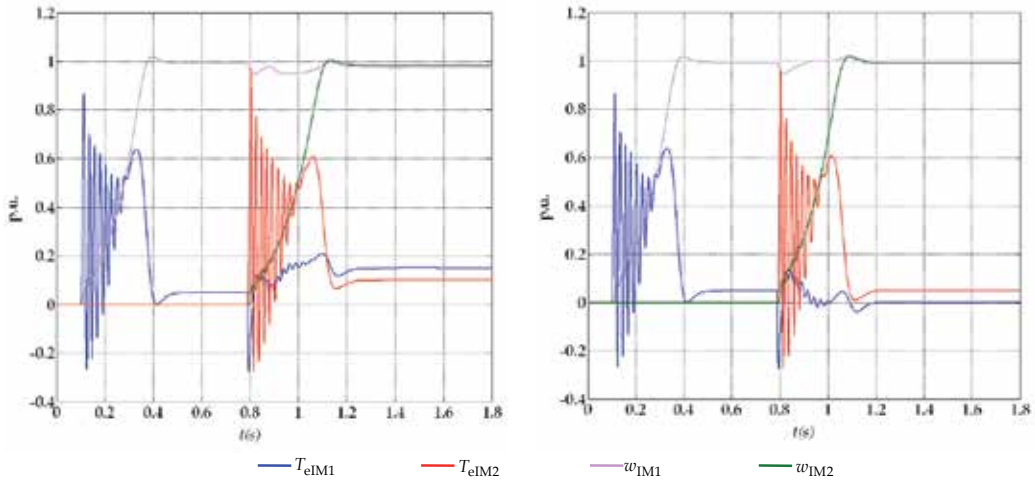

Figure 11. Transients of: air-gap torque (T_{eIM1}, T_{eIM2}) and speed transient of induction motors (ω_{IM1}, ω_{IM2}); during sudden change load: a) impact load b) load disconnected

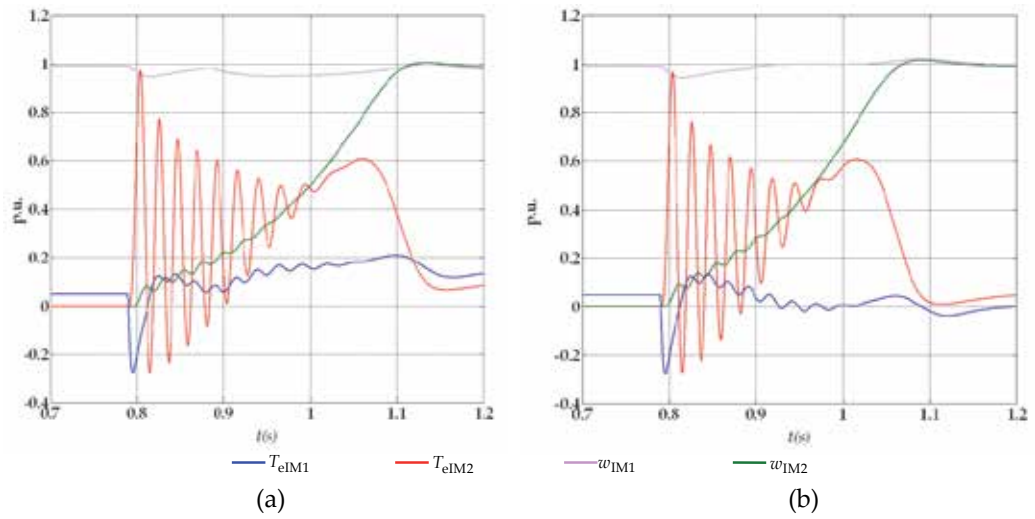

Figure 12. Transients of: air-gap torque (T_{eIM1}, T_{eIM2}) and speed transient (ω_{IM1}, ω_{IM2}); during sudden change load: a) impact load b) load disconnected, detail of Fig. 11.

Transients of stator currents of induction motors and their components, for both cases, are presented in Figure 13. The current of the first motor, at the moment of connection IM2,

momentarily increases to 0.31 p.u. and then, with damped oscillation tend to decrease. At the moment of impact additional load the current of the first induction motor is growing up (Fig. 13a). Air-gap torque of the first induction motor, after short term negative value of 0.27 p.u., oscillate about the positive average and tend to decrease.

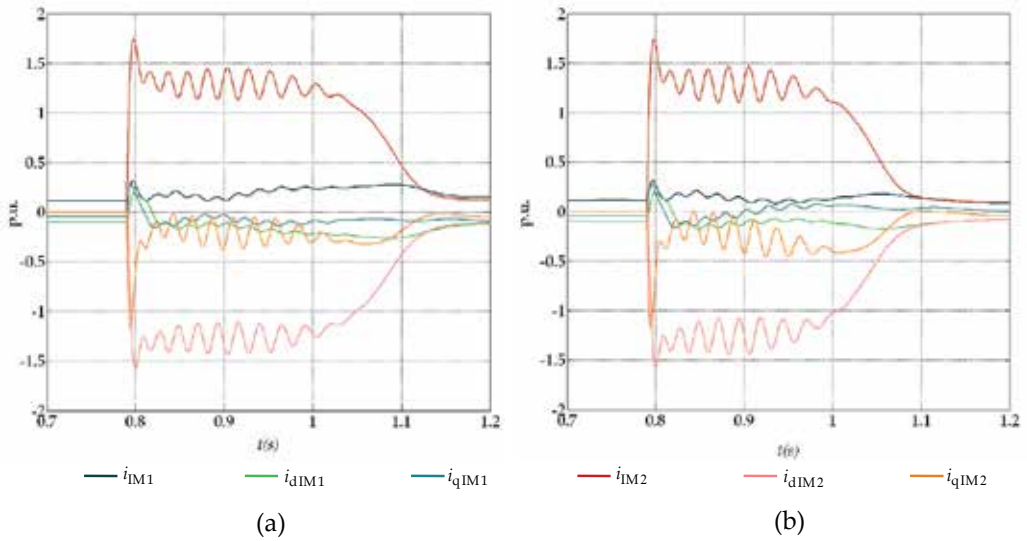

Figure 13. Transients of stator currents of induction motors (i_{IM1}, i_{IM2}) and their components in d (i_{dIM1}, i_{dIM2}) and q (i_{qIM1}, i_{qIM2}) axis during sudden change load: a) impact load b) load disconnected

Thereafter, the air-gap torque is increased, oscillates about the higher positive average then before impact additional load. The electromagnetic torque, as one can see in Fig. 12a, with damped oscillation reaches maximal value of 0.2 p.u. at the end of the start up period of the second induction motor.

The inrush current that is appeared at the beginning of the start-up period of the second induction motor reaches the magnitude of the first oscillation of 1.73 p.u. This current causes the voltage drop at the motor terminals that are connected on the same grid as the second one. The voltage drop results that the motor speed slows down. Because the motor rotor slows down the higher current is appeared on the grid and voltage are reduced even more.

As the additional load is connected the voltage is slowly recovered and start-up period of the second induction motor takes 300 ms.

In the second case, the motor is suddenly unloaded, 0.05 p.u. is disconnected from its shaft at the beginning of the start-up period of the second induction motor. After starting, the second motor begins to accelerate and the torque of the first one is changed, as mentioned before it becomes negative and motor speed slows down. Thereafter, the speed of the first

induction motor continues recovering the whole start-up period of the second induction motor (Fig. 11b). At the moment of sudden unload, the current of the first motor continues decreasing and with damped oscillation reaches steady state (Fig. 13b). Air-gap torque of the first induction motor continues decreasing reaches steady state faster than in the first case, in case of sudden impact load (Fig. 12b).

The inrush current that is appeared at the beginning of the start-up period of the second induction tends to reducing, and after the first induction motor is suddenly unloaded continues decreasing (Fig. 13b). Oscillations in transients of air-gap torque are shorter present and are damped at the end of start up period of the second induction motor, as one can see in figure (Fig. 12b). Corresponding transients of stator flux linkage, in both cases, are presented in Fig. 14. As the grid is unloaded the voltage is recovered, and start-up period of the second induction motor is now shorter, it takes about 260 ms.

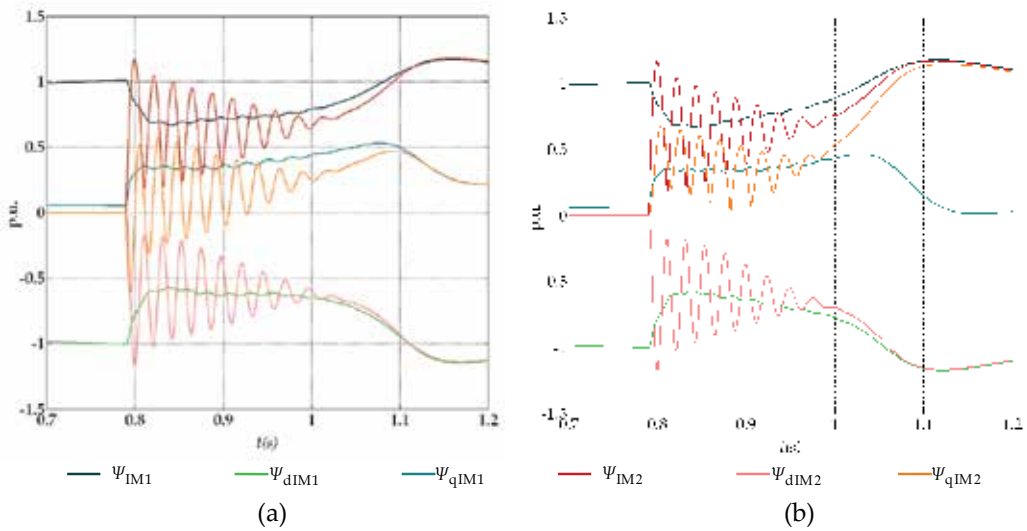

Figure 14. Transients of stator flux linkages of induction motors (Ψ_{IM1}, Ψ_{IM2}) and their components in d (Ψ_{dIM1}, Ψ_{dIM2}) and *q* (Ψ_{qIM1}, Ψ_{qIM2}) axis during sudden change load:
a) impact load b) load disconnected

The transients of the first induction motor current in *abc* coordinate system (i_{abcIM1}), in both cases, are presented in Fig. 15, while the current of synchronous generator (i_{abcSG}) is presented in Fig. 16.

Frequency variation during sudden change load is presented in Figure 17 and, as one can see, that impact load on the motor shaft results in short-term frequency decreasing. When load is switched off, short-term increase of frequency is appeared. Sudden change load affects on speed of aggregate and torque in the coupling, for both cases, is presented in Figure 18.

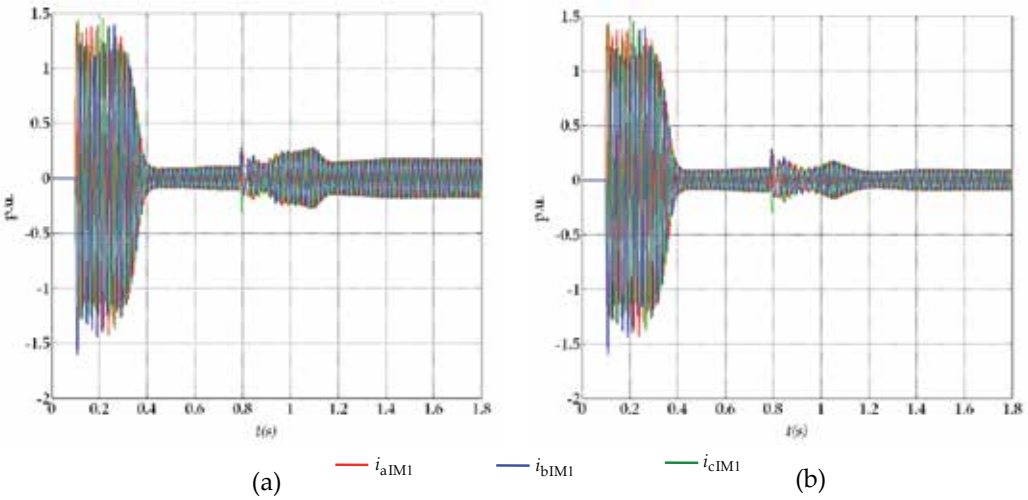

Figure 15. Stator current (i_{abcIM1}) of first induction motor, during sudden change load: a) impact load b) load disconnected

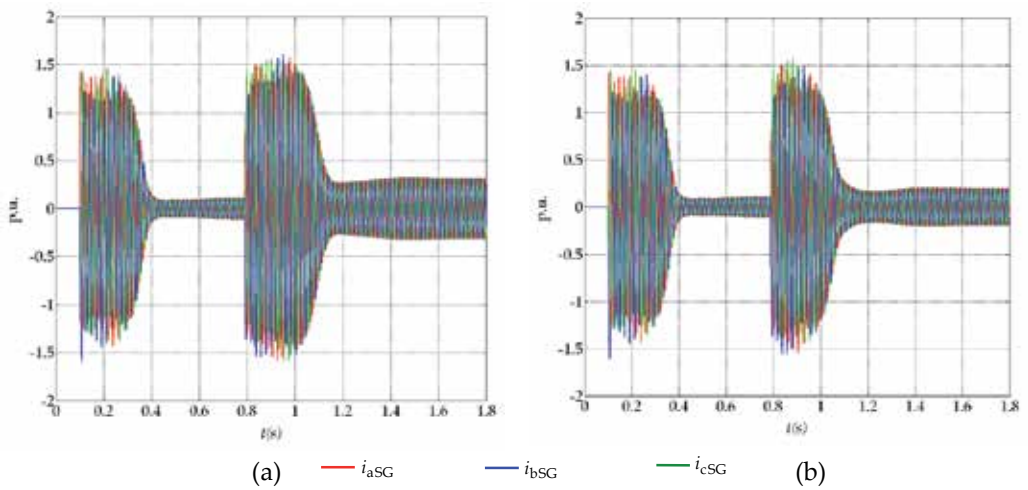

Figure 16. Stator current (i_{abcSG}) of the grid (synchronous generator), during sudden change load: a) impact load b) load disconnected

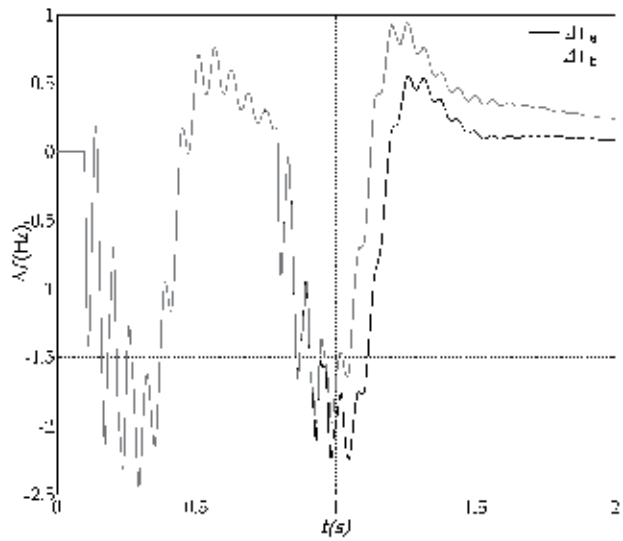

Figure 17. Frequency variations during sudden change load: Δf_a–impact load, Δf_b-load disconnected

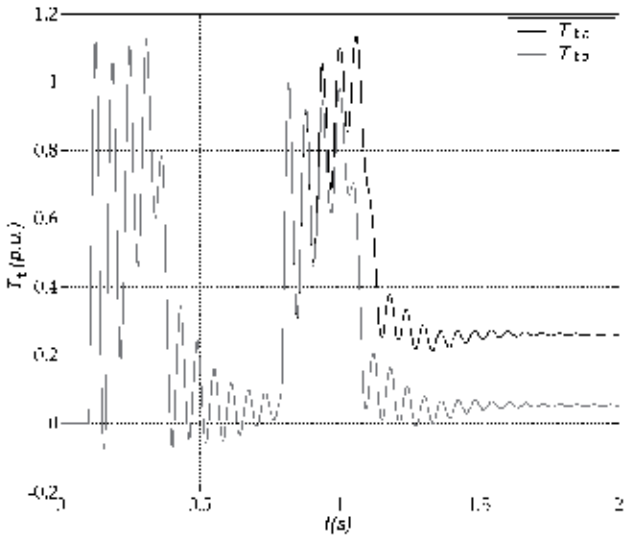

Figure 18. Torsional torque during sudden change load: T_{ta}-impact load, T_{tb}-load disconnected

5. Induction motor under short term voltage interruption

With the aim to get a better insight into the dynamics of induction motor fed directly from the isolated electrical grid the short-term interruptions in the motor power supply are considered.

Direct starting of induction motors on an isolated electrical grid produce disturbance for supply network and local consumers. This disturbance, such as voltage dips and reduction of aggregate speed, will cause decrease of network power quality. The significant voltage dips appear due to faults in power supply, and also, due to certain faults on loads connected to the isolated electrical grid. These voltage dips cause changes in transients of induction motors, as well as in transients of diesel generator unit. Besides the voltage dips, voltage interruption can also appear, which further effects the operation of the induction motor.

Two cases are considered. In the first case, a short term interruption appeared after both motors have run-up successfully. In that moment motors are in steady state condition. In the second case, interruption of power supply on the first induction motor appeared at the beginning of the start up period of the second one.

Motors are started loaded and load on the first induction motor shaft is 0.1 p.u., while the load of 0.05 p.u. is applied on the second induction motor shaft. At the beginning, the first induction motor (IM1) starts and after it has run-up successfully, the second one (IM2) is connected to the grid. At the chosen moment, as motors are in steady state condition, the first induction motor is shortly disconnected from the network, and then, after 100 ms reconnected to the power supply (Fig. 19 and 20).

At the time of voltage interruption, a large negative impulse of the torque of the first induction motor occurs. This reverse torque impulse rapidly decays and the air-gap torque (T_{eIM1}) becomes equal to zero. Changes in the electromagnetic torque of the second induction motor (T_{eIM2}) occurs at the time of disconnection of the first one.

Transients of air-gap torque and speed transient of induction motors; during the short-term interruptions that is appeared on the first induction motor, in case of steady state condition is presented in Figure 19a. However, in Figure 19b, the transients obtain in case of interruption in the first induction motor power supply that appeared at the beginning of the start up period of the second induction motor is presented. Transients of stator currents of induction motors and their components in d and q axis during the short-term interruptions, for both cases are presented in figure 20.

As one can see in Fig. 20a, at the time of voltage interruption, current of the first induction motor momentarily reaches approximately 2 p.u., while current of the second one reaches approximately 0.6 p.u. Thus, by restoring the supply, at the beginning of the transients the current of the first induction motor momentarily reaches 2 p.u., at the same time as the current of the second induction motor reaches maximal value of 0.35 p.u. A negative impulse of the torques T_{eIM1} and T_{eIM2} instantaneously appears. Thus, the speed of the first induction motor at the beginning of the transients additionally is shortly decreased, and afterwards continues recovering.

At the instant of the supply recovery air-gap torque of second induction motor suddenly reaches negative value and, as one can see in Fig. 21a, the speed of second induction motor is decreased and than rapidly recovers.

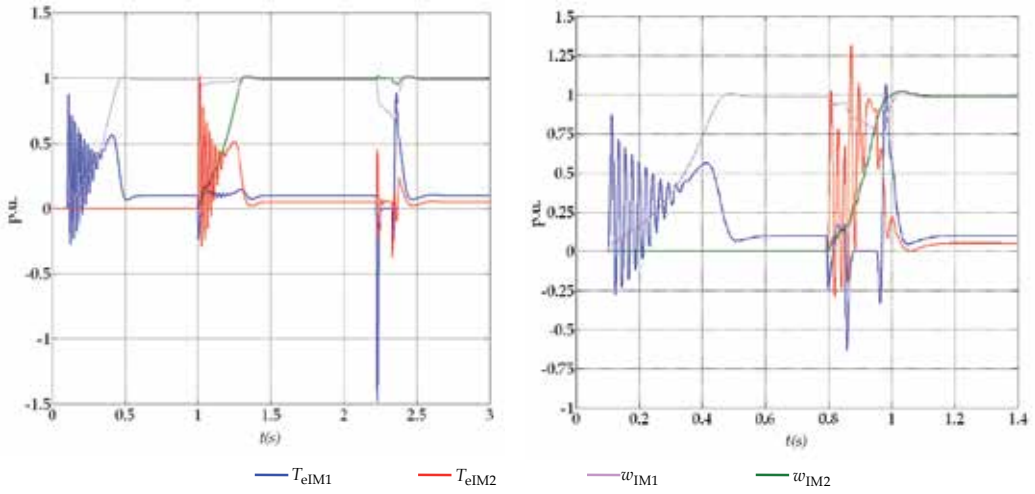

Figure 19. Transients of: air-gap torque (T_{eIM1}, T_{eIM2}) and speed transient of induction motors (ω_{IM1}, ω_{IM2}) during the short-term interruptions that is appeared on the first induction

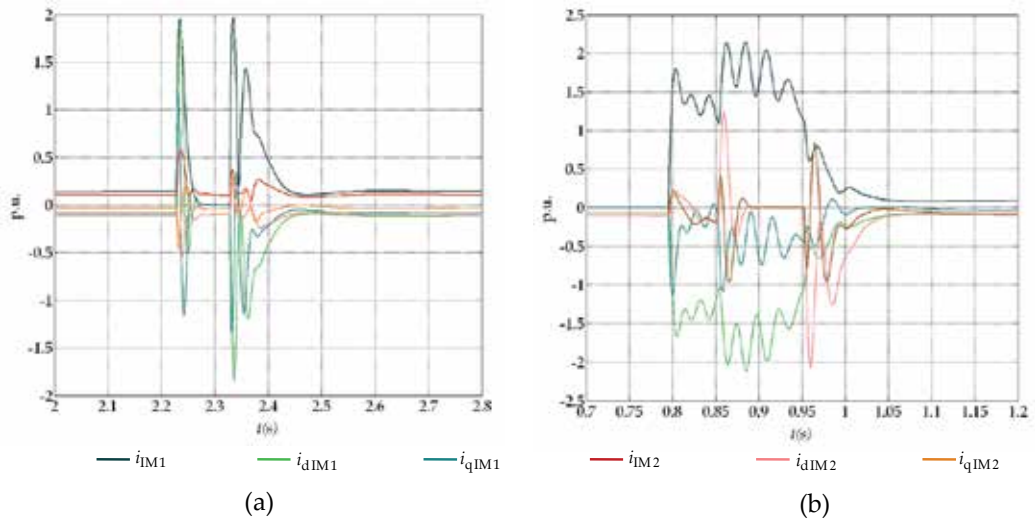

Figure 20. Transients of stator currents of induction motors (i_{IM1}, i_{IM2}) and their components in d (i_{dIM1}, i_{dIM2}) and q (i_{qIM1}, i_{qIM2}) axis during the short-term interruptions: a) motors are in steady state condition b) at the beginning of the start up period of the second one

In the second case, interruption in the first induction motor power supply appeared at the beginning of the start up period of the second induction motor.

At the time of connecting the second induction motor, the current is momentarily increased to 1.7 p.u. and has a decreasing tendency. By the time of short term power interruption on

the first induction motor, the current of the second one suddenly increases to 2.2 p.u. Further, the current oscillates around a higher average value than before and the damped oscillations are rapidly decreasing (Fig. 20b).

The transient of air-gap torque of induction motors are presented in Fig. 21. However, the air-gap torque of the first induction motor, at the time of voltage interruption occurred, momentarily reaches negative impulse of approximately 0.6 p.u. (Fig. 21b). The speed of the first induction motor (IM1) decreases at the beginning of the start up period of the second induction motor and tend to increase when fault occurs. As voltage interruption occurred the speed continuous reducing. In the speed transient of the second induction motor (IM2) one can see that is short term decreased appeared at the beginning of interruption and after that the motor continuous accelerates.

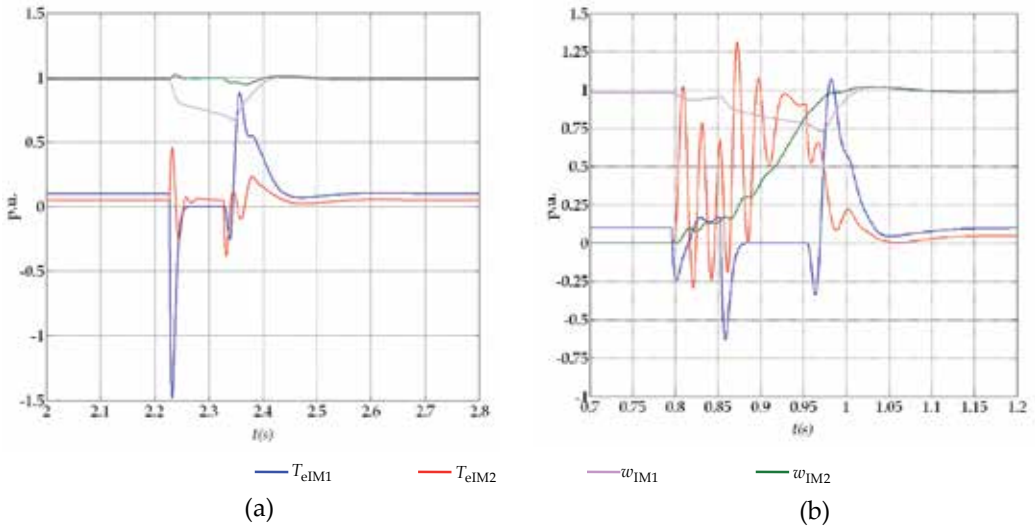

Figure 21. Transient of electromagnetic torque (T_{eIM1}, T_{eIM2}) and speed transient of induction motors (ω_{IM1}, ω_{IM2}); during the short-term interruptions: a) motors are in steady state condition b) at the beginning of the start up period of the second one detail of Fig. 20.

Terminal voltage (u_{abcIM1}) of the first induction motor, during the short-term interruptions, for the both cases is presented in Figure 22, while corresponding stator currents (i_{abcIM1}) of first induction motor are shown in Figure 23.

The voltage dips as well as voltage interruption, which further effects the operation of the induction motor, causes changes in transients of diesel generator unit. A short-term power interruption will result, as shown, in significant changes of electrical and mechanical variables and will also cause torsional strain in the shaft line. The mechanical coupling of a diesel engine and a synchronous generator is considered to be a rotating system with two concentrated masses that are connected by flexible coupling. The flexible coupling allows these masses to rotate at a different speed in transients. Thus, in Fig. 24 the speed transients of diesel engine and synchronous generator are presented, while torque at coupling zone is presented in Figure 26.

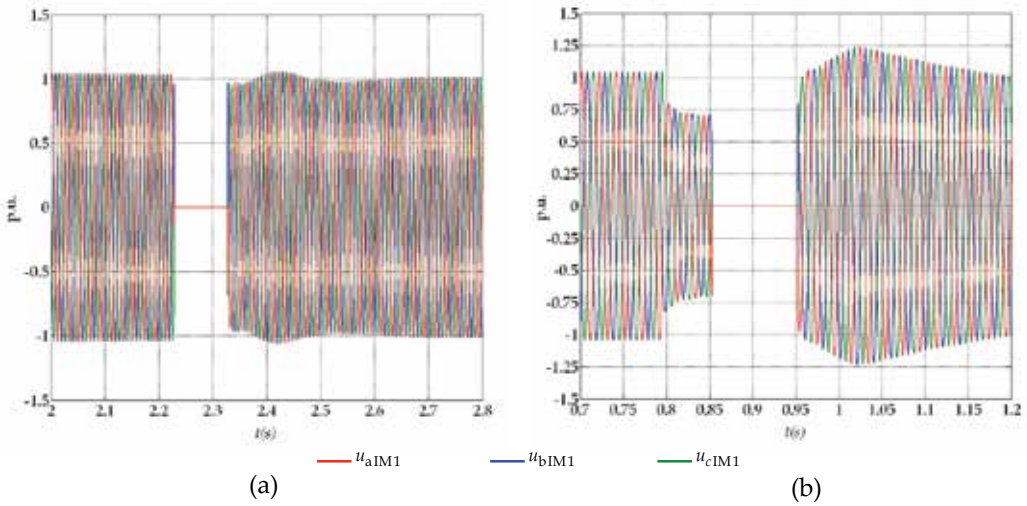

Figure 22. Voltage (u_{abcIM1}), during the short-term interruptions: a) motors are in steady state condition b) at the beginning of the start up period of the second one

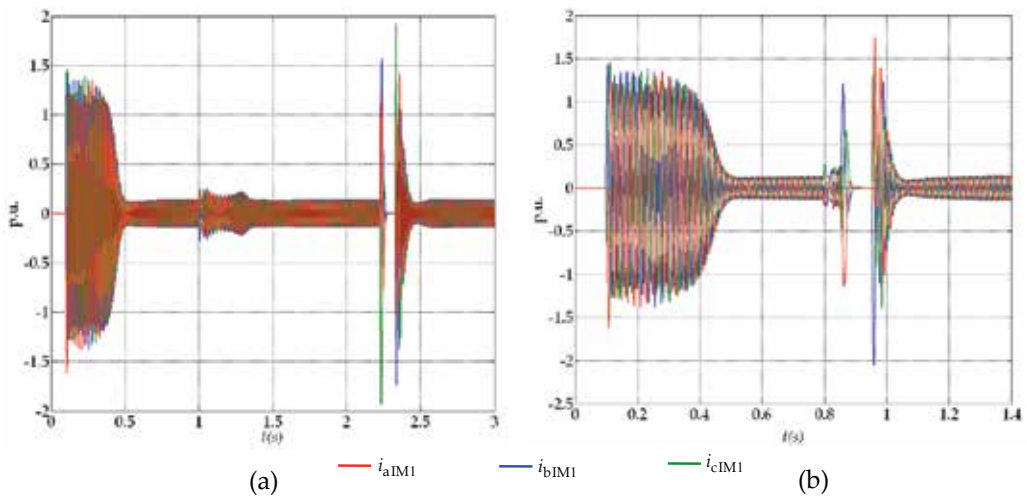

Figure 23. Stator current (i_{abcIM1}) of first induction motor, during the short-term interruptions: a) motors are in steady state condition b) at the beginning of the start up period of the second one

Sudden impact load on the isolated electrical grid induces a large strain on the diesel generator unit shaft. After the first induction motor is started, the diesel engine accepts the load and later reaches the steady speed. As a result of the starting of the loaded IM2, the speed of the diesel engine decreased and reached a minimum value of 0.97 p.u., while the speed of the synchronous generator reached a value of about 0.96 p.u. (Fig. 24a).

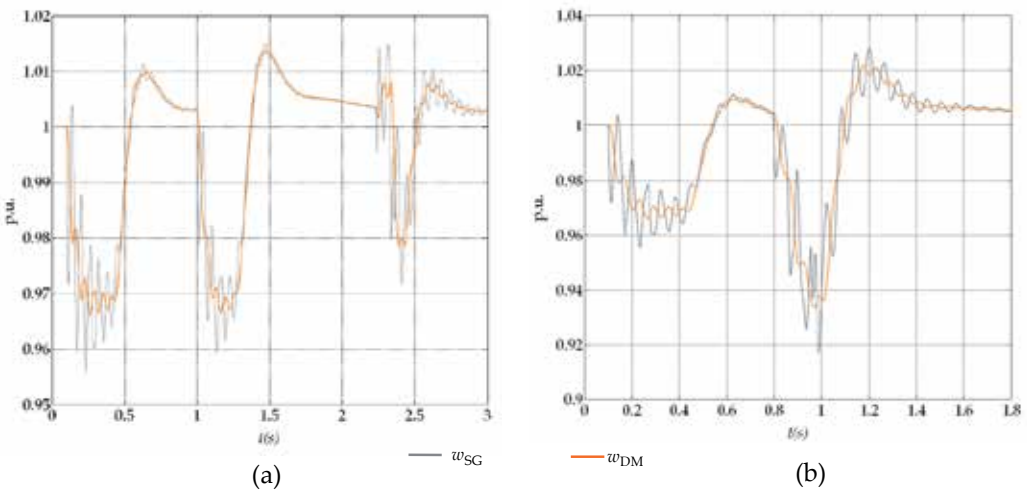

Figure 24. Speed transient of synchronous generator (ω_{SG}) and diesel engine (ω_{DM}) during the short-term interruptions: a) motors are in steady state condition b) at the beginning of the start up period of the second one

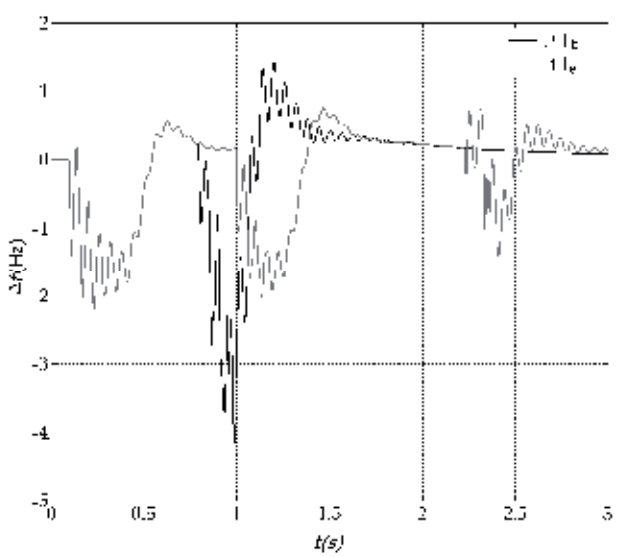

Figure 25. Frequency variations during short-term interruptions: Δf_a- motors are in steady state condition, Δf_b- at the beginning of the start up period of the second one

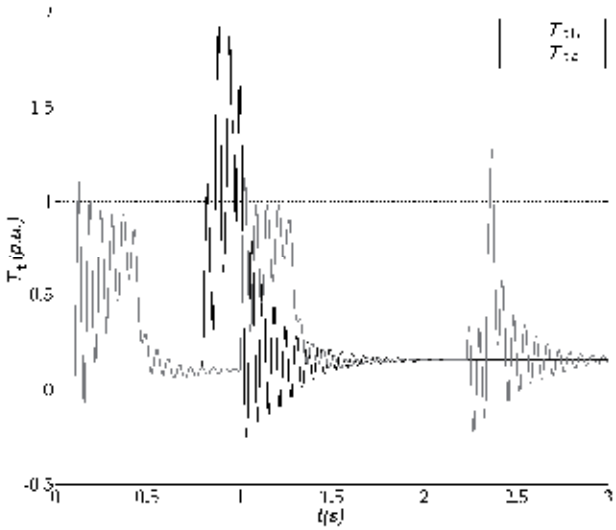

Figure 26. Transient of torsional torque during short-term interruptions:
T_{ta}-motors are in steady state condition, T_{tb}- at the beginning of the start up period of the second one

Occurrence of short-term power loss, at the time that motors are in steady state condition, speed of both machines increased. After, reconnected to the power supply the speed of synchronous generator as well as induction motor is reduced. Damped oscillations are presented during transients. In the second case, when the short-term interruption occurs at the beginning of the start up period of the second induction motor, speed of both machines continue decrease. In this case, the speed of synchronous generator is reduced to less of 0.92 p.u., while the speed of the diesel engine is reduced to less of 0.94 p.u. The oscillations appear with greater magnitude then in previous case. Speed deviation affects on frequency of grid and frequency variations during short-term interruptions, for both cases are presented in Figure 25. Significant disturbances appear in transients of torsional torque especially in case when short-term interruptions is appear at the beginning of the start up period of the second induction motor, as one can see in Figure 26.

6. Discussion

The dynamics of induction motors fed directly from the isolated electrical grid is considered in the cases of: direct-on-line starting of induction motors, sudden change load on the motor shaft and during short-term voltage interruptions. Direct on line starting of induction motors on the isolated power system is the most difficult transition regime for units due to electricity loads and also due to torsional loads on the shaft line. The autonomous operation of the synchronous generator is characterized by a change in steady state which causes a change in voltage and frequency, which in turn affects the quality of electric power systems. During starting induction motors draw high starting current, known as locked rotor current,

which are several times the normal full load current of the motor. This current causes a significant voltage dip on the isolated electrical grid, the terminal voltage is momentary decreased and after few damped oscillations reached minimal value. During this short period the voltage regulator does not affect jet. The voltage drop increases in case of starting loaded induction motor, the current momentarily reaches higher value of first magnitude and oscillates about higher average value than in previous case.

Disturbances in the system are present when the second induction motor is connected to the grid and additionally is growing up at the instant of impact additional load on the previous induction motor shaft. As load on the motor shaft grows up, the current of the motor is higher; oscillations are more damped and longer present in comparison with lightly load or no-loaded induction motor.

This current causes the voltage drop at the motor terminals that are connected on the same grid. The mutually effect between source and loads exists. The voltage drop results that the motor speed slows down. Because the motor rotor slows down the higher current is appeared on the grid and voltage are reduced even more.

At the instant of starting of induction motors the locked rotor torque appeared and as the rotor starts to rotate the air-gap torque oscillates about positive average value. Oscillations in transient of electromagnetic torque are damped at the end of start up period and finally the steady state condition is attained without oscillations. The oscillations are longer presented in case of bigger load torque on the motor shaft. Sudden change load on the motor shaft causes changes in air-gap torque. Damped oscillations are longer present in a case of impact additional load than during load disconnected. Both cases influence on the electrical grid and changes in transients of both induction motors as well as in synchronous generator are present.

The start-up period of the induction motor is longer when the bigger load torque on the motor shaft is applied. Also, decreasing the terminal voltage causes longer duration of speed transient in dynamics.

Sudden change load on a motor shaft, which occurs during operation period, results in speed change of the other motors that fed from the same grid.

Direct starting of induction motors on isolated electrical grid, as well as sudden change load, caused voltage dips and also reduces speed of aggregate. The significant voltage dips appear due to faults in power supply, as well as certain faults on loads connected to isolated electrical network. Besides the voltage dips, voltage interruption can also appear. This causes significant disturbances on the grid and affects the operation of other induction motor. If interruption of the supply lasts longer than one voltage period, many AC contactors will switch off the motor. However, in some cases, faulty contactor may produce multiple on and off switching. These interruptions affect the dynamics of both electrical and mechanical variables, which will also cause torsional stresses in the shaft line. The consequences of voltage interruption on the induction motor behavior are current and air-gap torque peaks that appear at instant of fault and recovery voltage.

Sudden changes of active power have impact on both voltage and frequency but a start-up of electric motor influences disproportionately the voltage value due to relatively low power factor during the process.

7. Conclusion

The dynamics of induction motors fed directly from the isolated electrical grid is analyzed. In isolated electrical grid, such as for example ship's electrical grid, the main source is a diesel generator and induction motors are the most common loads. Induction machine plays a very important role in that application and a significant number of induction motors are used at critical points of on board processes. The connection of large induction motors (large relative to the generator capacity) to that grid is difficult transient regime for units due to electrical loads and also due to torsional loads on the shaft line. Direct on line starting of induction motors induces high strain on the power system and this strain arises when the next induction motor is connected to the grid. Sudden impact load on the induction motors shaft is an additional strain on the network, especially when impact load on a motor shaft occurs during start up of another one. This in turn affects the quality of electric power system and thus, the dynamic behavior of induction motors. The significant voltage dips appear due to faults in power supply, and also, due to certain faults on loads connected to the isolated electrical grid. These voltage dips cause changes in transients of induction motors, as well as in transients of diesel generator unit. Besides the voltage dips, voltage interruption can also appear, which further effects the operation of the induction motor. Factory production tests demonstrate the capability of the unit to supply defined loads applied in a defined sequence. In order to make changes to the loading of an existing isolated electrical grid, it is necessary to analyze and document the effect of the additional loads on its normal and transient performance. An induction motor starting study may be of use in analyzing the performance of small power systems. Such systems are usually served by limited capacity sources that are subject to severe voltage drop problems on motor starting, especially when large motors are involved. In some cases, specific loads must be accelerated in specially controlled conditions, keeping torque values in defined limits. The results obtained by this analysis can be used as a guideline in choosing as well as setting parameters of the protection devices.

Author details

Marija Mirošević
University of Dubrovnik, Department of Electrical Engineering and Computing, Croatia

Acknowledgement

The presented results are carried out through the researches within scientific projects „New structures for hydro generating unit dynamic stability improvement“ and “Revitalization and operating of hydro generator” supported by Ministry of Science, Education and Sports in the Republic of Croatia.

8. References

Ameziquita-Brook, L., Liceaga-Castro, J., Liceaga-Castro, E., (2009). Induction Motor Identification for High Performance Control Design, *International Review of Electrical Engineering*, Vol. 4, No. 5; (October 2009), pp. (825-836) ISSN 1827-6660.

Cohen, V. (1995). Induction motors-protection and starting. *Elektron Journal-South African Institute of Electrical Engineers.12*, pp. (5-10) Citeseer.

Erceg, G., Tesnjak, S. & Erceg, R., (1996). Modelling and Simulation of Diesel Electrical Aggregate Voltage Controler with Current Sink, *Proceedings of the IEEE International conference on industrial technology*, 1996

Jones, C. V. (1967). *The Unified Theory of Electrical Machines*, Butterworths, London.

Krause, P. C. (1986). *Analysis of Electric Machinery*, McGrawHill, Inc. New York, N.Y.

Krutov, V., Dvigatelj vnutrennego sgorania kak reguliruemij objekt. (Mašinostroenie, 1978).

Kundur, P. (1994). *Power System Stability and Control*, McGraw-Hill

Maljković, Z., Cettolo, M., Pavlica, M. (2001). The Impact of the Induction Motor on Short-Circuit Current, *IEEE Industry Applications Magazine*. Vol. 7, No. 4; pp. (11-17).

McElveen, R., Toney, M., Autom, R., & Mountain, K. (2001). Starting high-inertia loads, *IEEE Transactions on Industry Applications, 37* (1), pp. (137-144).

Mirošević, M., Maljković, Z., Milković, M., (2002), Torsional Dynamics of Generator-Units for Feeding Induction Motor Drives, *Proceedings of EPE-PEMC 9th International Conference on Power Electronics and Motion Control*, Cavtat, Dubrovnik, Croatia, Sept. 2002., T8-069.

Mirošević, M., Sumina, D., & Bulić, N. (2011) Impact of induction motor starting on ship power network, *International Review of Electrical Engineering*, Vol. 6, No. 1; (February 2011), pp. (186-197) ISSN 1827-6660.

Tolšin,V. & Kovalevskij, E., Prethodnie procesi u dizel generatorov. (Mašinostroenie, 1977).

Vas, P. (1996). *Electrical Machines and Drives A Space Vector Theory Approach*, Oxford Science Publications

Chapter 4

Modelling and Analysis of Squirrel Cage Induction Motor with Leading Reactive Power Injection

Adisa A. Jimoh, Pierre-Jac Venter and Edward K. Appiah

Additional information is available at the end of the chapter

http://dx.doi.org/10.5772/50011

1. Introduction

Induction motors are by far the most used electro-mechanical device in industry today. Induction motors hold many advantages over other types of motors. They are cheap, rugged, easily maintainable and can be used in hazardous locations. Despite its advantages it has one major disadvantage. It draws reactive power from the source to be able to operate and therefore the power factor of the motor is inherently poor especially under starting conditions and under light load (Jimoh and Nicolae, 2007). Poor power factor adversely affects the economics of distribution and transmission systems and therefore may lead to higher electricity charges (Muljadi et al., 1989). At starting, power drawn by the motor is mainly reactive and it can draw up to 8 times its rated current at a power factor of about 0.2 until it reaches rated speed after which the power factor will increase to more than 0.6 if the motor is properly loaded and depending on the size of the motor.

To improve the power factor, reactive power compensation is needed where reactive power is injected. Several techniques have been suggested including synchronous compensation which is complex and expensive. Switched capacitor banks which requires expensive switchgear and may cause voltage regeneration, over voltage and high inrush currents (El-Sharkawi et al., 1985).

In this chapter another approach for power factor correction is explored where the stator of an induction motor has two sets of three phase windings which is electrically isolated but magnetically coupled. The main winding is connected to the three phase supply and the auxiliary winding connected to fixed capacitors for reactive power injection.

The first part of this chapter focuses on the development of a mathematical model for a normal three phase induction motor, the second part of the chapter focuses on the

development of the mathematical model for a dual winding three phase induction motor with reactive power injection, where the derived mathematical model is simulated using Matlab/Simulink environment and the third part of the chapter focuses on the performance analysis of both theoretical and experimental results.

2. Arbitrary reference frame theory

Arbitrary reference frame theory is mainly used in the dynamic analysis of electrical machines. Because of the highly coupled nature of the machine, especially the inductances within the winding make it rather impossible to perform dynamic simulations and analysis on electrical machines.

Arbitrary reference frame theory was discovered by Blondel, Dreyfus, Doherty and Nickle as mentioned in the classical paper (Park, 1929). This newly found theory was generalised by Park on synchronous machines and this method was later extended by Stanley to the application of dynamic analysis of induction machines (Stanley, 1938).

By using this method a poly-phase machine is transformed to a two-phase machine with their magnetic axis in quadrature as illustrated in Figure 1. This method is also commonly referred to as the *dq* method in balanced systems and to the *dq0* method in unbalanced systems with the '*0*'relating to the zero sequence or homopolar component in the Fortescue Transformation.

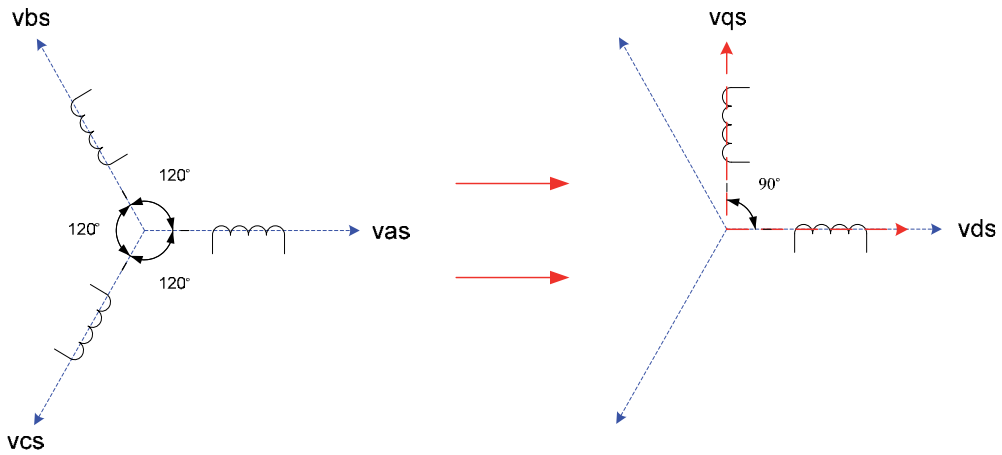

Figure 1. Park's Transform

This transformation eliminates mutual magnetic coupling between the phases and therefore makes the magnetic flux linkage of one winding independent of the current of another winding.

The transformation is done by applying a transformation matrix, Equation (1) while the inverse transformation matrix, Equation (2) will transform back to the natural reference frame. Equations (1)&(2) applies to a three phase system but can be modified to

accommodate a system with any number of phases which might be useful in the case of the machine having an auxiliary winding as proposed in this work.

$$[C] = \frac{2}{3}\begin{bmatrix} cos\theta & cos\left(\theta - \frac{2\pi}{3}\right) & cos\left(\theta - \frac{4\pi}{3}\right) \\ sin\theta & sin\left(\theta - \frac{2\pi}{3}\right) & sin\left(\theta - \frac{4\pi}{3}\right) \\ \frac{1}{2} & \frac{1}{2} & \frac{1}{2} \end{bmatrix} \quad (1)$$

$$[C]^{-1} = \begin{bmatrix} cos\theta & sin\theta & 1 \\ cos\left(\theta - \frac{2\pi}{3}\right) & sin\left(\theta - \frac{2\pi}{3}\right) & 1 \\ cos\left(\theta - \frac{4\pi}{3}\right) & sin\left(\theta - \frac{4\pi}{3}\right) & 1 \end{bmatrix} \quad (2)$$

3. Modelling of three-phase induction motor

The winding arrangement of a symmetrical induction machine is shown in Figure 2. The stator windings are identical and sinusoidally distributed, displaced 120° apart, with N_s equivalent turns and resistance r_s per winding per phase. Similarly the rotor windings are also considered as three identical sinusoidally distributed windings, displaced 120° apart, with N_r equivalent turns and resistance of r_r per winding per phase.

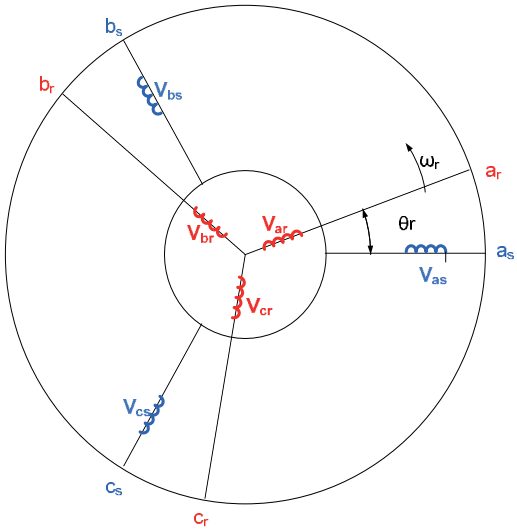

Figure 2. Three-Phase Winding Arrangement

In developing the equations which describe the behaviour of the induction machine the following assumptions are made:

1. The airgap is uniform.
2. Eddy currents, friction and windage losses and saturation are neglected.
3. The windings are distributed sinusoidally around the air gap.
4. The windings are identical

3.1. Voltage equations

Using Kirchoff's Voltage Law, the voltage equations for each winding on the stator and rotor can be determined.

Stator Windings:

$$v_{as} = r_s i_{as} + \frac{d\lambda_{as}}{dt} \tag{3}$$

$$v_{bs} = r_s i_{bs} + \frac{d\lambda_{bs}}{dt} \tag{4}$$

$$v_{cs} = r_s i_{cs} + \frac{d\lambda_{cs}}{dt} \tag{5}$$

Rotor Windings:

$$v_{ar} = r_r i_{ar} + \frac{d\lambda_{ar}}{dt} \tag{6}$$

$$v_{br} = r_r i_{br} + \frac{d\lambda_{br}}{dt} \tag{7}$$

$$v_{cr} = r_r i_{cr} + \frac{d\lambda_{cr}}{dt} \tag{8}$$

With subscript 'a','b','c' referring to the phases, subscript 's' referring to stator variables, subscript 'r' referring to rotor variables, 'v' referring to instantaneous voltage, 'i' referring to instantaneous current and 'λ' referring to flux linkage.

After obtaining the voltage equations in the natural reference frame, the transformation to the arbitrary reference frame can be done. It is very convenient to first refer all rotor variables to the stator by applying the appropriate turns ratio. Equations (9)-(11) represents all rotor variables and is expressed in a simplified way including the variables of all the rotor phases in one equation.

$$i'_{abcr} = \frac{N_r}{N_s} i_{abcr} \tag{9}$$

$$v'_{abcr} = \frac{N_s}{N_r} v_{abcr} \tag{10}$$

$$\lambda'_{abcr} = \frac{N_s}{N_r} \lambda_{abcr} \tag{11}$$

The transformation of the voltage equations to the arbitrary reference frame are dealt with in Section 3.3. It is important to determine the different inductances which will influence the flux linkage in Equations (3)-(8) and also transform it to the arbitrary reference frame.

3.2. Inductances

The flux linkages as seen in the voltage equations are functions of inductance and therefore the inductances within the motor must be determined.

The inductances within the motor consist of self inductance, leakage inductance, magnetizing inductance and mutual inductance. The flux linkage equation is shown in Equation (12) and contains the inductance matrix [L].

$$\begin{bmatrix}\lambda_{as}\\ \lambda_{bs}\\ \lambda_{cs}\\ \lambda_{ar}\\ \lambda_{br}\\ \lambda_{cr}\end{bmatrix} = \begin{bmatrix}L_{asas} & L_{asbs} & L_{ascs} & L_{asar} & L_{asbr} & L_{ascr}\\ L_{bsas} & L_{bsbs} & L_{bscs} & L_{bsar} & L_{bsbr} & L_{bscr}\\ L_{csas} & L_{csbs} & L_{cscs} & L_{csar} & L_{csbr} & L_{cscr}\\ L_{aras} & L_{arbs} & L_{arcs} & L_{arar} & L_{arbr} & L_{arcr}\\ L_{bras} & L_{brbs} & L_{brcs} & L_{brar} & L_{brbr} & L_{brcr}\\ L_{cras} & L_{crbs} & L_{crcs} & L_{crar} & L_{crbr} & L_{crcr}\end{bmatrix} \times \begin{bmatrix}i_{as}\\ i_{bs}\\ i_{cs}\\ i_{ar}\\ i_{br}\\ i_{cr}\end{bmatrix} \tag{12}$$

Where the inductance is defined by the subscript, for example L_{asas} refers to the inductance between winding *as* and winding *as,* meaning that this is self inductance in winding *as*; and L_{asbr} refers to the inductance between winding *as* and winding *br,* meaning that this is a mutual inductance.

3.2.1. Self inductance

The self inductance in the stator windings consists of magnetizing and leakage inductance. The windings are identical and therefore the self inductance of all stator windings will be identical.

$$L_{asas} = L_{bsbs} = L_{cscs} = L_{ms} + L_{ls} \tag{13}$$

The magnetizing inductance (L_{ms}) can be expressed as in Equation (14) (Lipo and Novotny, 1996).

$$L_{ms} = \frac{\mu_0 \ell r N_s^2 \pi}{4g} \tag{14}$$

The self inductance in the rotor windings is similar to that of the stator windings.

$$L_{arar} = L_{brbr} = L_{crcr} = L_{mr} + L_{lr} \tag{15}$$

And,

$$L_{mr} = \frac{\mu_0 \ell r N_r^2 \pi}{4g} \tag{16}$$

Where N_s and N_r is the effective number of turns of the stator and rotor windings, r is the radius of the motor cross-section, ℓ is the length of the motor and g is the airgap radial length.

3.2.2. Mutual inductance

Mutual inductance exists between all windings of both the stator and the rotor. There are four different types of mutual inductance which are stator-stator (mutual inductance between two different stator windings), rotor-rotor (mutual inductance between two different rotor windings), stator-rotor (mutual inductance between a stator and rotor winding) and rotor-stator (mutual inductance between a rotor and stator winding).

Stator-stator mutual inductance can be expressed as Equation (17) (Lipo and Novotny, 1996).

$$L_{xsys} = \frac{\mu_0 \ell r N_s^2 \pi}{4g} cos\theta_{xsys} \tag{17}$$

Where L_{xsys} is the inductance between any stator winding 'x' and any other stator winding 'y' and θ_{xsys} is the angle between stator winding 'x' and 'y'.

Using Equation (14), Equation (17) can be modified to be:

$$L_{xsys} = L_{ms} cos\theta_{xsys} \tag{18}$$

When considering the winding distribution in Figure 2, it can be seen that the only possible displacement between two stator windings are 120° and 240° in both directions. This implies that $cos\theta_{xsys}$ in Equation (18) can be evaluated as follows:

$$cos\theta_{xsys} = \cos(\pm 120^\circ) = \cos(\pm 240^\circ) = -\frac{1}{2} \tag{19}$$

From Equations (18)&(19) the expression describing the mutual inductance between any two stator windings can be simplified to Equation (20).

$$L_{asbs} = L_{ascs} = L_{bscs} = L_{bsas} = L_{csas} = L_{csbs} = -\frac{1}{2} L_{ms} \tag{20}$$

The rotor-rotor mutual inductances are similar to that of the stator-stator mutual inductances and can be expressed as:

$$L_{arbr} = L_{arcr} = L_{brcr} = L_{brar} = L_{crar} = L_{crbr} = -\frac{1}{2} L_{mr} \tag{21}$$

The stator-rotor mutual inductances depend on the position of the rotor according to the following relationship.

$$L_{xsyr} = L_{sr} cos\theta_{xsyr} \tag{22}$$

Where L_{xsyr} is the mutual inductance between any stator winding 'x' and any rotor winding 'y'; and θ_{xsyr} is the angle between them.

The expression for L_{sr} in Equation (22) is given by Equation (23).

$$L_{sr} = \left(\frac{N_s}{2}\right)\left(\frac{N_r}{2}\right)\frac{\mu_0 \pi r \ell}{g} \tag{23}$$

(Krause, 1986, Lipo and Novotny, 1996)

Now, using Equation (22) and Figure 2, the expressions for the stator-rotor mutual inductances can be deduced.

$$L_{asar} = L_{bsbr} = L_{cscr} = L_{sr} cos\theta_r \tag{24}$$

$$L_{asbr} = L_{bscr} = L_{csar} = L_{sr} cos\left(\theta_r + \frac{2\pi}{3}\right) \tag{25}$$

$$L_{ascr} = L_{bsar} = L_{csbr} = L_{sr}cos\left(\theta_r - \frac{2\pi}{3}\right) \tag{26}$$

Likewise it can be shown that the rotor-stator mutual inductances are:

$$L_{aras} = L_{brbs} = L_{crcs} = L_{sr}\cos(-\theta_r) \tag{27}$$

$$L_{arbs} = L_{brcs} = L_{cras} = L_{sr}cos\left(\frac{2\pi}{3} - \theta_r\right) \tag{28}$$

$$L_{arcs} = L_{bras} = L_{crbs} = L_{sr}cos\left(\frac{4\pi}{3} - \theta_r\right) \tag{29}$$

All inductances have now been quantified. The complete inductance matrix can now be constructed but to simplify the work the inductance matrix in Equation (12) is first divided into sub-matrices. The inductance matrix as in Equation (12) is repeated as Equation (30).

$$L = \begin{bmatrix} L_{asas} & L_{asbs} & L_{ascs} & L_{asar} & L_{asbr} & L_{ascr} \\ L_{bsas} & L_{bsbs} & L_{bscs} & L_{bsar} & L_{bsbr} & L_{bscr} \\ L_{csas} & L_{csbs} & L_{cscs} & L_{csar} & L_{csbr} & L_{cscr} \\ L_{aras} & L_{arbs} & L_{arcs} & L_{arar} & L_{arbr} & L_{arcr} \\ L_{bras} & L_{brbs} & L_{brcs} & L_{brar} & L_{brbr} & L_{brcr} \\ L_{cras} & L_{crbs} & L_{crcs} & L_{crar} & L_{crbr} & L_{crcr} \end{bmatrix} \tag{30}$$

The inductance matrix is divided into four sub-matrices.

$$L = \begin{bmatrix} L_s & L_{SR} \\ L_{RS} & L_r \end{bmatrix} \tag{31}$$

Where L_s is the inductance within the stator windings, L_r is the inductances within the rotor windings, L_{SR} is the inductances between stator and rotor windings and L_{RS} is the inductances between the rotor and stator windings.

Using Equation (30) and dividing according to Equation (31) and substituting inductances yield the following:

$$L_s = \begin{bmatrix} L_{ms} + L_{ls} & -\frac{1}{2}L_{ms} & -\frac{1}{2}L_{ms} \\ -\frac{1}{2}L_{ms} & L_{ms} + L_{ls} & -\frac{1}{2}L_{ms} \\ -\frac{1}{2}L_{ms} & -\frac{1}{2}L_{ms} & L_{ms} + L_{ls} \end{bmatrix} \tag{32}$$

$$L_r = \begin{bmatrix} L_{mr} + L_{lr} & -\frac{1}{2}L_{mr} & -\frac{1}{2}L_{mr} \\ -\frac{1}{2}L_{mr} & L_{mr} + L_{lr} & -\frac{1}{2}L_{mr} \\ -\frac{1}{2}L_{mr} & -\frac{1}{2}L_{mr} & L_{mr} + L_{lr} \end{bmatrix} \tag{33}$$

$$L_{SR} = L_{sr}\begin{bmatrix} cos\theta_r & \cos(\theta_r + \frac{2\pi}{3}) & \cos(\theta_r - \frac{2\pi}{3}) \\ \cos(\theta_r - \frac{2\pi}{3}) & cos\theta_r & \cos(\theta_r + \frac{2\pi}{3}) \\ \cos(\theta_r + \frac{2\pi}{3}) & \cos(\theta_r - \frac{2\pi}{3}) & cos\theta_r \end{bmatrix} \tag{34}$$

$$L_{RS=}(L_{SR})^T = L_{sr}\begin{bmatrix} cos\theta_r & \cos(\theta_r - \frac{2\pi}{3}) & \cos(\theta_r + \frac{2\pi}{3}) \\ \cos(\theta_r + \frac{2\pi}{3}) & cos\theta_r & \cos(\theta_r - \frac{2\pi}{3}) \\ \cos(\theta_r - \frac{2\pi}{3}) & \cos(\theta_r + \frac{2\pi}{3}) & cos\theta_r \end{bmatrix} \quad (35)$$

It can be proven that$L_{RS=}(L_{SR})^T$.

It is evident that θ_r exists in Equations (34)&(35) where θ_r relates to rotor position, this rotor position changes continuously which means that in the natural state the inductances are varying with time. To be able to derive a rigorous dynamic model de-coupling has to be done by using arbitrary reference frame theory as mentioned in Section 2.

Before transforming the inductances to the arbitrary reference frame all rotor parameters must be referred to the stator.

The magnetizing inductances (L_{ms}, L_{mr}) and mutual inductances (L_{sr}, L_{rs}) are from the same magnetic flux path and are therefore related. From Equations (14)&(23) it can be deduced that:

$$L_{ms} = \left(\frac{N_s}{N_r}\right) L_{sr} \quad (36)$$

By using the effective turns ratio L_{sr} can be referred to the stator.

$$L'_{sr} = \frac{N_s}{N_r}(L_{sr}) \quad (37)$$

And therefore

$$L'_{sr} = L_{ms} \quad (38)$$

The mutual inductance matrix referred to the stator can now be expressed as:

$$L'_{SR} = L_{ms}\begin{bmatrix} cos\theta_r & \cos(\theta_r + \frac{2\pi}{3}) & \cos(\theta_r - \frac{2\pi}{3}) \\ \cos(\theta_r - \frac{2\pi}{3}) & cos\theta_r & \cos(\theta_r + \frac{2\pi}{3}) \\ \cos(\theta_r + \frac{2\pi}{3}) & \cos(\theta_r - \frac{2\pi}{3}) & cos\theta_r \end{bmatrix} \quad (39)$$

Using the same approach the inductances within the rotor windings can also be simplified as:

$$L'_r = \begin{bmatrix} L'_{lr} + L_{ms} & -\frac{1}{2}L_{ms} & -\frac{1}{2}L_{ms} \\ -\frac{1}{2}L_{ms} & L'_{lr} + L_{ms} & -\frac{1}{2}L_{ms} \\ -\frac{1}{2}L_{ms} & -\frac{1}{2}L_{ms} & L'_{lr} + L_{ms} \end{bmatrix} \quad (40)$$

The flux linkage can now be expressed as:

$$\begin{bmatrix} \lambda_{abcs} \\ \lambda'_{abcr} \end{bmatrix} = \begin{bmatrix} L_s & L'_{SR} \\ (L'_{SR})^T & L'_r \end{bmatrix} \times \begin{bmatrix} i_{abcs} \\ i'_{abcr} \end{bmatrix} \quad (41)$$

Equation (41) can be transformed to the arbitrary reference frame as indicated in Equation (42) (Krause, 1986).

$$\begin{bmatrix}\lambda_{qd0s}\\ \lambda'_{qdor}\end{bmatrix}=\begin{bmatrix}K_sL_sK_s^{-1} & K_sL'_{SR}K_r^{-1}\\ K_r(L'_{SR})^TK_s^{-1} & K_rL'_rK_r^{-1}\end{bmatrix}\times\begin{bmatrix}i_{qd0s}\\ i'_{qd0r}\end{bmatrix} \tag{42}$$

Where;

$$K_s=\frac{2}{3}\begin{bmatrix}cos\theta & cos\left(\theta-\frac{2\pi}{3}\right) & cos\left(\theta-\frac{4\pi}{3}\right)\\ sin\theta & sin\left(\theta-\frac{2\pi}{3}\right) & sin\left(\theta-\frac{4\pi}{3}\right)\\ \frac{1}{2} & \frac{1}{2} & \frac{1}{2}\end{bmatrix} \tag{43}$$

$$K_s^{-1}=\begin{bmatrix}cos\theta & sin\theta & 1\\ cos\left(\theta-\frac{2\pi}{3}\right) & sin\left(\theta-\frac{2\pi}{3}\right) & 1\\ cos\left(\theta-\frac{4\pi}{3}\right) & sin\left(\theta-\frac{4\pi}{3}\right) & 1\end{bmatrix} \tag{44}$$

$$K_r=\frac{2}{3}\begin{bmatrix}cos\beta & cos\left(\beta-\frac{2\pi}{3}\right) & cos\left(\beta-\frac{4\pi}{3}\right)\\ sin\beta & sin\left(\beta-\frac{2\pi}{3}\right) & sin\left(\beta-\frac{4\pi}{3}\right)\\ \frac{1}{2} & \frac{1}{2} & \frac{1}{2}\end{bmatrix} \tag{45}$$

$$K_r^{-1}=\begin{bmatrix}cos\beta & sin\beta & 1\\ cos\left(\beta-\frac{2\pi}{3}\right) & sin\left(\beta-\frac{2\pi}{3}\right) & 1\\ cos\left(\beta-\frac{4\pi}{3}\right) & sin\left(\beta-\frac{4\pi}{3}\right) & 1\end{bmatrix} \tag{46}$$

Where;

$$\beta=\theta-\theta_r \tag{47}$$

K_s is the transformation matrix and K_s^{-1} the inverse transformation matrix for the stator parameters, K_r is the transformation matrix and K_r^{-1} the inverse transformation matrix for the rotor parameters.

Evaluating Equation (42) with Equations (43)-(46) yield the flux linkage in the arbitrary reference frame as shown in Equation (48).

Comparing Equation (48) with Equations (32)-(35), it is clear that θ_r has been eliminated from the flux linkage equations by using the arbitrary reference frame transformation. It means that the flux linkage is no longer a function of rotor position.

$$\begin{bmatrix}\lambda_{qs}\\ \lambda_{ds}\\ \lambda_{0s}\\ \lambda'_{qr}\\ \lambda'_{dr}\\ \lambda'_{0r}\end{bmatrix}=\begin{bmatrix}L_{ls}+\frac{3}{2}L_{ms} & 0 & 0 & \frac{3}{2}L_{ms} & 0 & 0\\ 0 & L_{ls}+\frac{3}{2}L_{ms} & 0 & 0 & \frac{3}{2}L_{ms} & 0\\ 0 & 0 & L_{ls} & 0 & 0 & 0\\ \frac{3}{2}L_{ms} & 0 & 0 & L'_{lr}+\frac{3}{2}L_{ms} & 0 & 0\\ 0 & \frac{3}{2}L_{ms} & 0 & 0 & L'_{lr}+\frac{3}{2}L_{ms} & 0\\ 0 & 0 & 0 & 0 & 0 & L'_{lr}\end{bmatrix}\times\begin{bmatrix}i_{qs}\\ i_{ds}\\ i_{0s}\\ i'_{qr}\\ i'_{dr}\\ i'_{0r}\end{bmatrix} \tag{48}$$

$$L_m = \frac{3}{2} L_{ms} \tag{49}$$

3.3. Voltage equations in arbitrary reference frame

Recalling and repeating the voltage equations in the natural reference frame in section 3.1, for ease of reading only, now it is presented in matrix format.

$$v_{abcs} = r_s i_{abcs} + \frac{d\lambda_{abcs}}{dt} \tag{50}$$

$$v'_{abcr} = r'_r i'_{abcr} + \frac{d\lambda'_{abcr}}{dt} \tag{51}$$

Taking only the stator voltage equations as in Equation (50) and only considering the resistive part, it can be transformed to the arbitrary reference frame as follows:

$$v_{qd0s}^{res} = K_s r_s K_s^{-1} i_{qd0s} \tag{52}$$

$$K_s r_s K_s^{-1} = \begin{bmatrix} r_s & 0 & 0 \\ 0 & r_s & 0 \\ 0 & 0 & r_s \end{bmatrix} \tag{53}$$

Therefore;

$$v_{qd0s}^{res} = r_s i_{qd0s} \tag{54}$$

Where;

$$r_s = \begin{bmatrix} r_s & 0 & 0 \\ 0 & r_s & 0 \\ 0 & 0 & r_s \end{bmatrix} \tag{55}$$

The superscript '*res*' refers to the resistive part of the voltage equation.

Now considering only the inductive part of the of the voltage equation as in Equation (50) which can be transformed to the arbitrary reference frame as follows:

$$v_{qd0s}^{ind} = K_s \frac{d}{dt} \left[K_s^{-1} \lambda_{qd0s} \right] \tag{56}$$

Expanding Equation (56) using the product rule:

$$v_{qd0s}^{ind} = K_s \frac{d}{dt} [K_s^{-1}] \lambda_{qd0s} + K_s K_s^{-1} \frac{d}{dt} \lambda_{qd0s} \tag{57}$$

Now, evaluating parts of the terms in Equation (57) separately;

Knowing that;

$$\theta = \int \omega(\xi)\, d\xi + \theta(0) \tag{58}$$

Where ξ is a dummy variable for integration.

$$\frac{d}{dt}[K_s^{-1}] = \omega \begin{bmatrix} -sin\theta & cos\theta & 0 \\ -sin\left(\theta - \frac{2\pi}{3}\right) & cos\left(\theta - \frac{2\pi}{3}\right) & 0 \\ -sin\left(\theta + \frac{2\pi}{3}\right) & cos\left(\theta + \frac{2\pi}{3}\right) & 0 \end{bmatrix} \tag{59}$$

$$K_s \frac{d}{dt}[K_s^{-1}] = \begin{bmatrix} 0 & \omega & 0 \\ -\omega & 0 & 0 \\ 0 & 0 & 0 \end{bmatrix} \tag{60}$$

$$K_s K_s^{-1} = \begin{bmatrix} 1 & 0 & 0 \\ 0 & 1 & 0 \\ 0 & 0 & 1 \end{bmatrix} \tag{61}$$

Using Equations (58)-(61) to evaluate Equation (57) yields;

$$v_{qd0s}^{ind} = \omega \begin{bmatrix} \lambda_{ds} \\ -\lambda_{qs} \\ 0 \end{bmatrix} + \frac{d}{dt} \begin{bmatrix} \lambda_{qs} \\ \lambda_{ds} \\ \lambda_{0s} \end{bmatrix} \tag{62}$$

The superscript '*ind*' refers to the inductive part of the voltage equation.

Now adding the voltage equations for the resistive and inductive parts gives the full stator voltage equations in the arbitrary reference frame.

$$v_{qd0s} = \begin{bmatrix} r_s & 0 & 0 \\ 0 & r_s & 0 \\ 0 & 0 & r_s \end{bmatrix} \begin{bmatrix} i_{qs} \\ i_{ds} \\ i_0 \end{bmatrix} + \omega \begin{bmatrix} \lambda_{ds} \\ -\lambda_{qs} \\ 0 \end{bmatrix} + \frac{d}{dt} \begin{bmatrix} \lambda_{qs} \\ \lambda_{ds} \\ \lambda_{0s} \end{bmatrix} \tag{63}$$

Using the same method the rotor voltage equation can be determined.

$$v'_{qd0r} = \begin{bmatrix} r'_r & 0 & 0 \\ 0 & r'_r & 0 \\ 0 & 0 & r'_r \end{bmatrix} \begin{bmatrix} i'_{qr} \\ i'_{dr} \\ i'_{0r} \end{bmatrix} + (\omega - \omega_r) \begin{bmatrix} \lambda'_{dr} \\ -\lambda'_{qr} \\ 0 \end{bmatrix} + \frac{d}{dt} \begin{bmatrix} \lambda'_{qr} \\ \lambda'_{dr} \\ \lambda_{0r} \end{bmatrix} \tag{64}$$

Where ω is the rotational speed of the reference frame and ω_r is the rotational speed of the rotor.

The model developed up to now is a general model in the arbitrary reference frame which means that this model can take the form of any reference frame depending the value substituted for ω , therefore called arbitrary.

Different reference frames are obtained by substituting the appropriate value of the reference frame speed into ω. Three different reference frames are commonly used, the stationary reference frame where $\omega = 0$, the synchronous reference frame where ω is set to the angular velocity of the supply voltage ($\omega = \omega_e$) and the rotor reference frame where ω is set to the angular velocity of the rotor ($\omega = \omega_r$). The use of reference frames depends on the nature of the problem to be solved.

3.4. Electromagnetic torque

The torque equation for a three phase induction machine is well known and is not derived in this section. The torque equation of the three phase machine with auxiliary winding is derived in Section 4.

$$T_e = \left(\frac{3}{2}\right)\left(\frac{P}{2}\right)\left(\lambda_{ds} i_{qs} - \lambda_{qs} i_{ds}\right) \tag{65}$$

An electric motor is an electro-mechanical device and needs an equation that couples the electrical and mechanical systems.

$$T_{em} = J\left(\frac{2}{P}\right)\frac{d\omega_r}{dt} + T_L \tag{66}$$

Where P is number of poles, J is moment of inertia, T_L is torque connected to the shaft and ω_r is the angular rotational speed of the rotor.

3.5. Equivalent circuit

The full mathematical model of the three phase induction machine is given by Equations (48),(63)&(64). These equations are used to develop the equivalent circuits for the three phase induction machine as in Figure 3

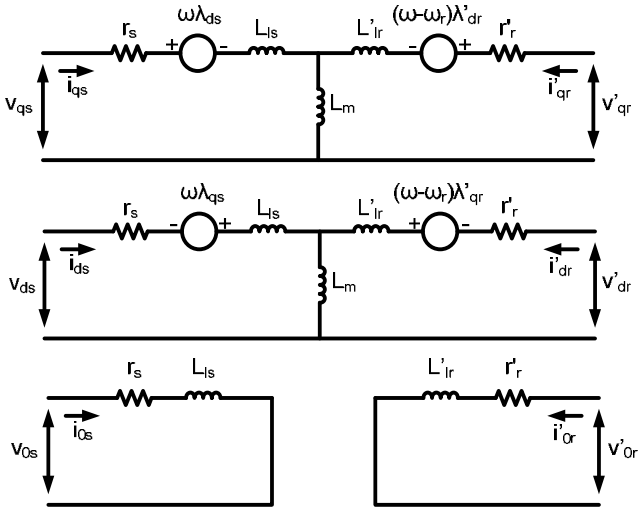

Figure 3. Equivalent Circuits

4. Modelling of three-phase with auxiliary winding

This machine consists of two three phase windings arranged on top of each other in the same slots. This means that there is no displacement between the two windings. These two windings are electrically isolated but magnetically connected. One of these windings is treated as the main winding and will be supplied with a three phase voltage. The main

winding is labelled with the subscript '*abc*'. The remaining winding is treated as the auxiliary winding. The auxiliary winding is connected to static capacitors for reactive power injection. The injection of reactive power will improve the power factor of the machine. The auxiliary winding is labelled with the subscript '*xyz*'. The winding arrangement is as shown in Figure 4.

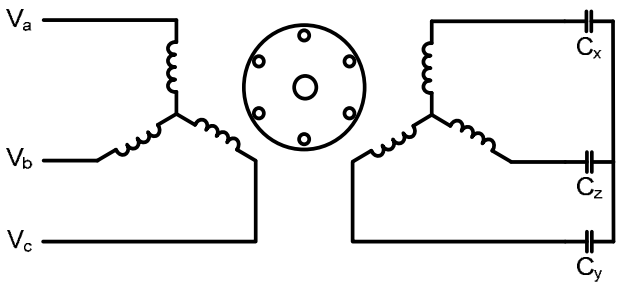

Figure 4. Winding arrangement of Main and Auxiliary Windings

The assumptions in developing the equations which describe the behaviour of this machine are the same as the assumptions mentioned in Section 3 with one addition. It is assumed that the main and auxiliary winding is identical. It has the same conductor cross section and the same number of turns.

4.1. Voltage equations

The voltage equations for this machine are developed in the same way as described in Section 3.1. There are three additional voltage equations because of the additional set of three phase windings. For simplicity the voltage equations are represented in matrix format. It is assumed that the main and auxiliary windings are identical and will therefore have the same resistance.

Main Stator Windings:

$$v_{abcs} = r_s i_{abcs} + \frac{d\lambda_{abcs}}{dt} \tag{67}$$

Auxiliary Stator Windings:

$$v_{xyzs} = r_s i_{xyzs} + \frac{d\lambda_{xyzs}}{dt} \tag{68}$$

Rotor Windings:

$$v'_{abcr} = r'_r i'_{abcr} + \frac{d\lambda'_{abcr}}{dt} \tag{69}$$

4.2. Inductances

Because of the addition of the auxiliary winding the dimensions of the inductance matrix will increase. The dimension of the inductance matrix is equal to the number of windings, in

this case a [9 x 9] matrix. The inductance matrix can again be divided into smaller more manageable sub-matrices as in Equation (70).

$$\begin{bmatrix} L_{abc\_s} \\ L_{xyz\_s} \\ L_{abc\_r} \end{bmatrix} = \begin{bmatrix} L_{abcs} & L_{abcsxyzs} & L_{abcsabcr} \\ L_{xyzsabcs} & L_{xyzs} & L_{xyzsabcr} \\ L_{abcrabcs} & L_{abcrxyzs} & L_{abcr} \end{bmatrix} \tag{70}$$

where L_{abcs}, L_{xyzs}, L_{abcr} are the inductances within the different three phase sets of windings. The other sub-matrices refer to mutual inductances between different sets of windings. This includes stator and rotor windings, for example $L_{abcsxyzs}$ refer to the mutual inductance between the main winding and the auxiliary winding on the stator. Many of the inductances in this structure are very similar to that of the conventional three phase machine. Therefore, many of the developed inductances in Section 3 can be used.

$$L_{abcs} = L_{xyzs} = \begin{bmatrix} L_{ms} + L_{ls} & -\frac{1}{2}L_{ms} & -\frac{1}{2}L_{ms} \\ -\frac{1}{2}L_{ms} & L_{ms} + L_{ls} & -\frac{1}{2}L_{ms} \\ -\frac{1}{2}L_{ms} & -\frac{1}{2}L_{ms} & L_{ms} + L_{ls} \end{bmatrix} \tag{71}$$

$$L_{abcr} = \begin{bmatrix} L_{mr} + L_{lr} & -\frac{1}{2}L_{mr} & -\frac{1}{2}L_{mr} \\ -\frac{1}{2}L_{mr} & L_{mr} + L_{lr} & -\frac{1}{2}L_{mr} \\ -\frac{1}{2}L_{mr} & -\frac{1}{2}L_{mr} & L_{mr} + L_{lr} \end{bmatrix} \tag{72}$$

$$L_{abcsabcr} = L_{xyzsabcr} = L_{ms} \begin{bmatrix} cos\theta_r & \cos(\theta_r + \frac{2\pi}{3}) & \cos(\theta_r - \frac{2\pi}{3}) \\ \cos(\theta_r - \frac{2\pi}{3}) & cos\theta_r & \cos(\theta_r + \frac{2\pi}{3}) \\ \cos(\theta_r + \frac{2\pi}{3}) & \cos(\theta_r - \frac{2\pi}{3}) & cos\theta_r \end{bmatrix} \tag{73}$$

$$L_{abcrabcs} = L_{abcrxyzs} = L^T_{abcsabcr} \tag{74}$$

All of the above was taken from Section 3 because of similar relationships between the windings. The only sub-matrices remaining are the two describing the inductances between the main and auxiliary windings on the stator. For determining the expressions of all the elements of the sub-matrices, equation (18) is used.

$$L_{abcsxyzs} = \begin{bmatrix} L_{asxs} & L_{asys} & L_{aszs} \\ L_{bsxs} & L_{bsys} & L_{bszs} \\ L_{csxs} & L_{csys} & L_{cszs} \end{bmatrix} \tag{75}$$

Where;

$$L_{asxs} = L_{bsys} = L_{cszs} = L_{ms}\cos(0^\circ) = L_{ms} \tag{76}$$

$$L_{asys} = L_{aszs} = L_{bsxs} = L_{bszs} = L_{csxs} = L_{cszs} = L_{ms}\cos(\pm 120^\circ) = -\frac{1}{2}L_{ms} \tag{77}$$

Now;

$$L_{abcsxyzs} = \begin{bmatrix} L_{ms} & -\frac{1}{2}L_{ms} & -\frac{1}{2}L_{ms} \\ -\frac{1}{2}L_{ms} & L_{ms} & -\frac{1}{2}L_{ms} \\ -\frac{1}{2}L_{ms} & -\frac{1}{2}L_{ms} & L_{ms} \end{bmatrix} \tag{78}$$

It can be shown that;

$$L_{xyzsabcs} = L_{abcsxyzs} \tag{79}$$

Mutual leakage inductance exists between the main and auxiliary windings because they are sharing the same stator slots. This mutual leakage inductance should be reflected in Equation (78) but are neglected for the purpose of this study.

Transforming the inductance matrix in the natural reference frame to the arbitrary reference frame as explained in Section 3.2 yields the following inductance matrix in the arbitrary reference frame.

$$\begin{bmatrix} L_{q1s} \\ L_{d1s} \\ L_{01s} \\ L_{q2s} \\ L_{d2s} \\ L_{02s} \\ L_{qr} \\ L_{dr} \\ L_{0r} \end{bmatrix} = \begin{bmatrix} L_{ss} & 0 & 0 & L_m & 0 & 0 & L_m & 0 & 0 \\ 0 & L_{ss} & 0 & 0 & L_m & 0 & 0 & L_m & 0 \\ 0 & 0 & L_{ls} & 0 & 0 & 0 & 0 & 0 & 0 \\ L_m & 0 & 0 & L_{ss} & 0 & 0 & L_m & 0 & 0 \\ 0 & L_m & 0 & 0 & L_{ss} & 0 & 0 & L_m & 0 \\ 0 & 0 & 0 & 0 & 0 & L_{ls} & 0 & 0 & 0 \\ L_m & 0 & 0 & L_m & 0 & 0 & L_{rr} & 0 & 0 \\ 0 & L_m & 0 & 0 & L_m & 0 & 0 & L_{rr} & 0 \\ 0 & 0 & 0 & 0 & 0 & 0 & 0 & 0 & L'_{lr} \end{bmatrix} \tag{80}$$

Where;

$$L_{ss} = L_{ls} + L_m \tag{81}$$

$$L_{rr} = L'_{lr} + L_m \tag{82}$$

Where the subscripts *'1'* refers to the main stator winding, *'2'* refers to the auxiliary stator winding and *'r'* refers to the rotor winding.

Because flux linkage appears in the voltage equations it is very convenient to represent flux linkage instead of inductance.

$$\boldsymbol{\lambda = LI} \tag{83}$$

Where Equation (83) is in matrix format and refers to any flux linkage in the system.

4.3. Voltage equation in the arbitrary reference frame

The voltage equations as developed in Section 4.1 can be transformed to the arbitrary reference frame. This is quite an easy task when the developments in Section 3 are used. The equation for the main winding on the stator and the rotor winding remains the same as that for the conventional three-phase machine as shown in Equations (84)-(85).

$$v_{qd01s} = \begin{bmatrix} r_s & 0 & 0 \\ 0 & r_s & 0 \\ 0 & 0 & r_s \end{bmatrix} \begin{bmatrix} i_{q1s} \\ i_{d1s} \\ i_{01s} \end{bmatrix} + \omega \begin{bmatrix} \lambda_{d1s} \\ -\lambda_{q1s} \\ 0 \end{bmatrix} + \frac{d}{dt} \begin{bmatrix} \lambda_{q1s} \\ \lambda_{d1s} \\ \lambda_{01s} \end{bmatrix} \tag{84}$$

$$v'_{qd0r} = \begin{bmatrix} r'_r & 0 & 0 \\ 0 & r'_r & 0 \\ 0 & 0 & r'_r \end{bmatrix} \begin{bmatrix} i'_{qr} \\ i'_{dr} \\ i'_{0r} \end{bmatrix} + (\omega - \omega_r) \begin{bmatrix} \lambda'_{dr} \\ -\lambda'_{qr} \\ 0 \end{bmatrix} + \frac{d}{dt} \begin{bmatrix} \lambda'_{qr} \\ \lambda'_{dr} \\ \lambda_{0r} \end{bmatrix} \tag{85}$$

The voltage equations of the auxiliary winding are different from the main winding because no voltage is applied directly to the winding. Capacitors are rather connected to the auxiliary winding as in Figure 4. It is therefore important to develop the voltage equation for a capacitor in the arbitrary reference frame. This is given in Equation (86).

$$Vc_{qd02s} = \frac{1}{C} \int \left[i_{qd0s2} \right] dt + \omega \begin{bmatrix} Vc_{d02} \\ -Vc_{q02} \\ 0 \end{bmatrix} \tag{86}$$

Now, the voltage equation for the auxiliary winding becomes;

$$v_{qd02s} = 0 = \begin{bmatrix} r_s & 0 & 0 \\ 0 & r_s & 0 \\ 0 & 0 & r_s \end{bmatrix} \begin{bmatrix} i_{q2s} \\ i_{d2s} \\ i_{02s} \end{bmatrix} + \omega \begin{bmatrix} \lambda_{d2s} \\ -\lambda_{q2s} \\ 0 \end{bmatrix} + \frac{d}{dt} \begin{bmatrix} \lambda_{q2s} \\ \lambda_{d2s} \\ \lambda_{02s} \end{bmatrix} + \begin{bmatrix} Vc_{q2} \\ Vc_{d2} \\ 0 \end{bmatrix} \tag{87}$$

4.4. Electromagnetic torque

The electromagnetic torque can be derived from the energy stored in the coupling system. The stored energy for a normal three-phase can be written as Equation (88) (Krause, 1986).

$$W_f = \frac{1}{2} (i_{abcs})^T (L_s - L_{ls} I) i_{abcs} + (i_{abcs})^T L'_{sr} i'_{abcr} + \frac{1}{2} (i'_{abcr})^T (L'_r - L'_{lr} I) i'_{abcr} \tag{88}$$

Where I is the identity matrix. The machine is assumed to be magnetically linear and therefore, the field energy W_f is equal to the co-energy W_c.

The change in mechanical energy in a rotational system delivering mechanical power is given as:

$$dW_m = T_{em} d\theta_{rm} \tag{89}$$

Where T_{em} is electromagnetic torque and θ_{rm} is the actual angular displacement of the rotor. The flux linkages, currents, W_f and W_c are all expressed as a function of the electrical angular displacement θ_r.

$$\theta_r = \left(\frac{P}{2} \right) \theta_{rm} \tag{90}$$

Substituting Equation (90) into Equation (89) yields:

$$dW_m = T_{em} \frac{2}{P} d\theta_r \tag{91}$$

Because W_f=W_c the electromagnetic torque can be evaluated with:

$$T_{em}(i_j, \theta_r) = \frac{P}{2}\frac{\partial W_{c(i_j,\theta_r)}}{\partial \theta_r} \tag{92}$$

Substituting Equation (88) into Equation (92) gives the electromagnetic torque of the stator side as

$$\frac{P}{2} i_S^T \frac{\partial [L_{ss}]}{\partial \theta_r} is \tag{93}$$

Where,

$$i_s = [\quad iabcs \qquad ixyzs] \tag{94}$$

$$L_s = \begin{bmatrix} L_{abcs} & L_{abcxyzs} \\ L_{xyzabcs} & L_{xyzs} \end{bmatrix} \tag{95}$$

$$L_{ss} = (L_s - L_{ls}) \tag{96}$$

Substituting Equation (95) into Equation (93) gives the torque for each of the stator currents.

$$T_{em} = \frac{P}{2}\langle (\quad iabcs)^T \frac{\partial [L_{abcs}]}{\partial \theta_r} \quad iabcs$$

$$+(\quad iabcs)^T \frac{\partial [L_{abcxyzs}]}{\partial \theta_r} \quad ixyzs + \left(\quad ixyzs\right)^T \frac{\partial [L_{xyzs}]}{\partial \theta_r} \quad ixyzs +$$

$$+\left(\quad ixyzs\right)^T \frac{\partial [L_{xyzabcs}]}{\partial \theta_r} \quad iabcs\rangle \tag{97}$$

Applying the transformation from '*abc*' to '*dq0*' yields the torque equation:

$$T_{em} = \frac{3}{2}\frac{P}{2}\left(\lambda_{d1s} i_{q1s} - \lambda_{q1s} i_{d1s} + \lambda_{d2s} i_{q1s} - \lambda_{q2s} i_{d2s}\right) \tag{98}$$

4.5. Equivalent circuit

The electrical system of this machine as described by Equations (80)&(84)-(87) can be represented with an equivalent circuit. The zero sequence circuit diagram is omitted because the system is assumed to be balanced.

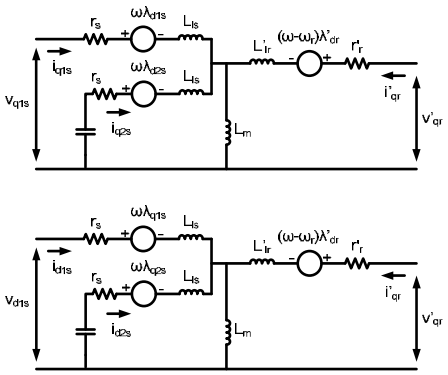

Figure 5. Equivalent *'qd'* circuit diagrams

5. Simulation results

The derived mathematical models implemented in the Matlab/Simulink environment can be used to generate steady-state and dynamic simulation results. The machine without compensation is used as reference. Capacitance is added to the auxiliary winding and compared with the behaviour of the reference machine. This will show the effect of the capacitors connected to the auxiliary winding on the performance of the modified machine. The dynamic model can be used for steady state analysis by taking readings after the transient.

5.1. Steady state analysis

The main objective of the modifications done in terms of the addition of the auxiliary winding is to improve the poor power factor an induction motor has. It is therefore important to focus on the behaviour of the machine parameters that involves power factor when introducing reactive power injection.

Figure 6 shows that the injection of reactive power in the auxiliary winding improves the power factor of the motor. The bigger the size of the capacitor, the more reactive power is injected and hence the better the power factor. For this specific machine, capacitors of 30μF connected per phase as in Figure 4 leads to a power factor very close to unity.

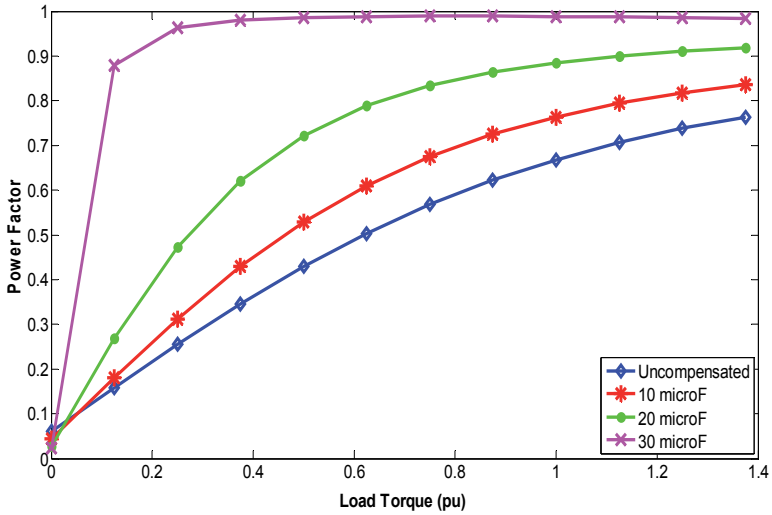

Figure 6. Torque – Power Factor waveform

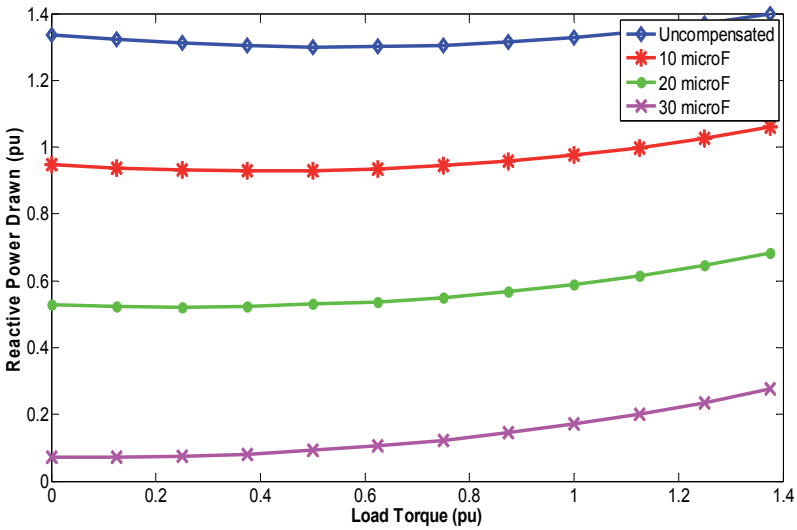

Figure 7. Torque – Reactive Power waveform

With the increase in power factor as seen in Figure 6 it is expected that less reactive power will be drawn from the source with the addition of capacitors to the auxiliary winding. Figure 7 supports this expectation. In Figure 7 the reactive power drawn from the source reduces with increasing capacitor size.

Because the reactive component of the supply current decreases with the reactive power injection, the magnitude of the supply current therefore decreases. This is shown in Figure 8.

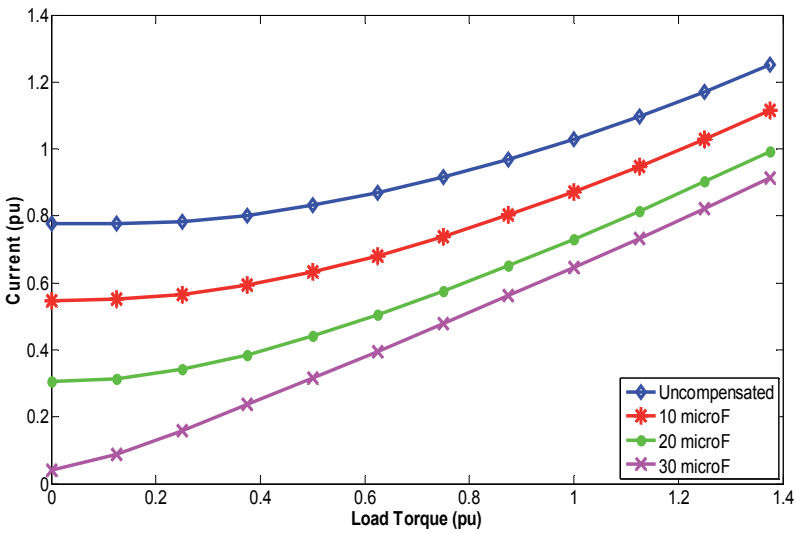

Figure 8. Torque–Current waveform

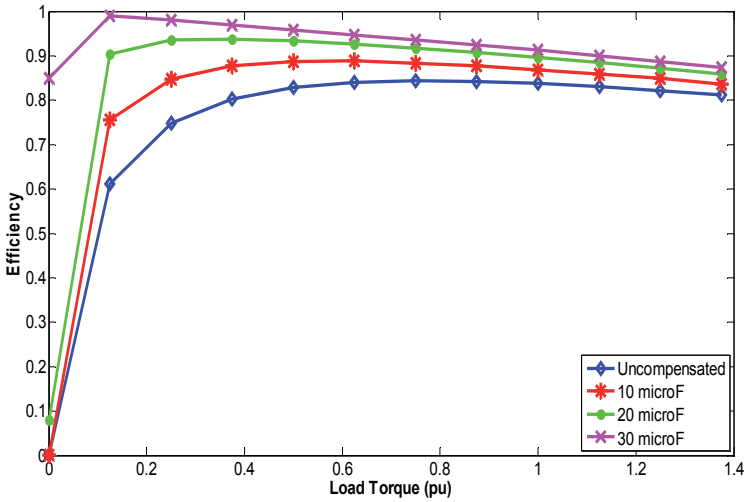

Figure 9. Torque Efficiency waveform

The active power drawn from the source consists of different components of which one is copper losses (I^2R losses). With the decrease of current shown in Figure 8, it is logical that the copper losses of the main stator winding will also decrease. This will lead to a decrease in active power drawn from the source without a change in output power and hence the improvement in the efficiency of the motor as seen in Figure 9.

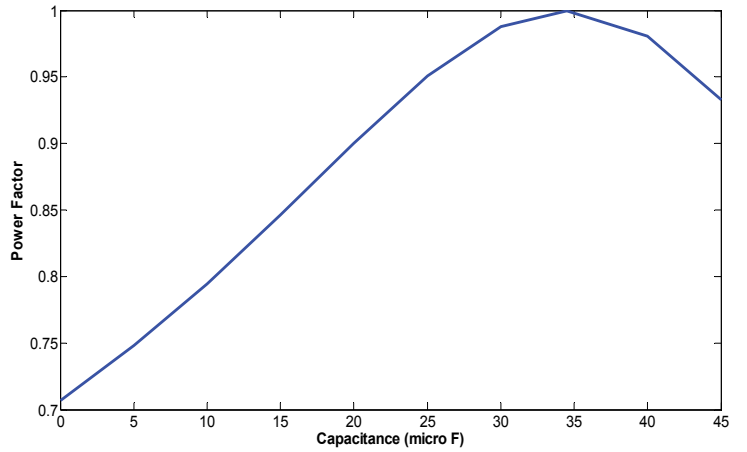

Figure 10. Capacitance-Power Factor waveform

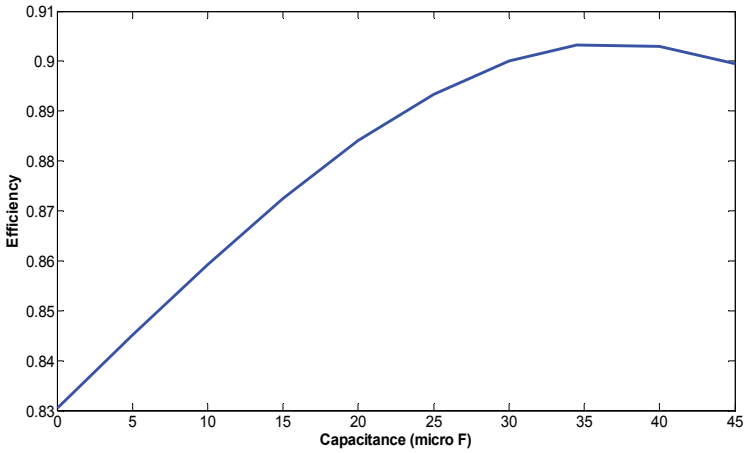

Figure 11. Capacitance-Efficiency waveform

The effect that the change of capacitance has on the performance of the machine is studied in Figures 10 and 11. Figure 10 shows that as the capacitance increase the power factor also increases. It also shows that it is possible to over-compensate the machine which will lead to a decreasing power factor. With the current machine at the current load it can be seen that the optimum value for the capacitor is slightly less than 35μF and will lead to a power factor close to unity. Figure 11 shows the improvement in efficiency as capacitance increases. The efficiency of this machine at current load can be improved with about 0.07 as seen in Figure 11.

5.2. Dynamic analysis

Steady-state analysis is not always sufficient in determining the behaviour of an electrical machine. Transient and dynamic periods are the most likely periods for harming an electrical machine. The dynamic model will show the exact behaviour of the machine during transient and or dynamic periods.

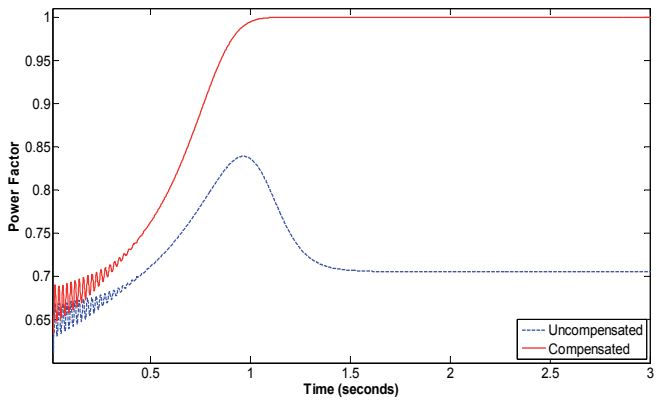

Figure 12. Power Factor

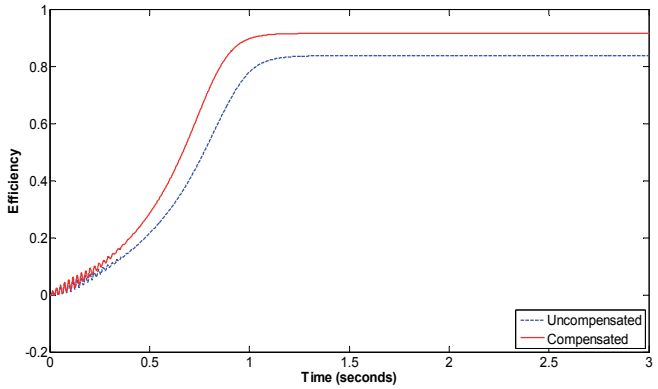

Figure 13. Efficiency

The dynamic behaviour of a compensated and uncompensated induction machine is compared in Figure 12. The uncompensated machine (dashed waveform) has a low power factor when starting and settles at a power factor of just more than 0.7. The compensated machine (solid waveform) has a higher power factor when starting and settles at a power factor close to unity. This shows how effective this concept is in power factor correction.

The earlier statement that the improvement in power factor will improve the efficiency is supported in Figure 13.

The inrush current of the machine is shown in Figure 14. This machine has a transient state when starting where the current can reach eight times rated current.

The current of the auxiliary winding is shown in Figure 15.

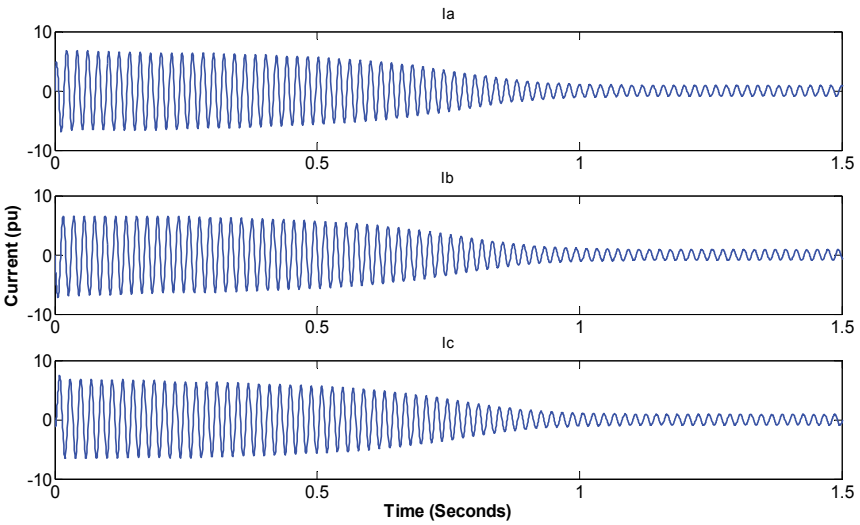

Figure 14. Phase Currents – Main Stator Winding

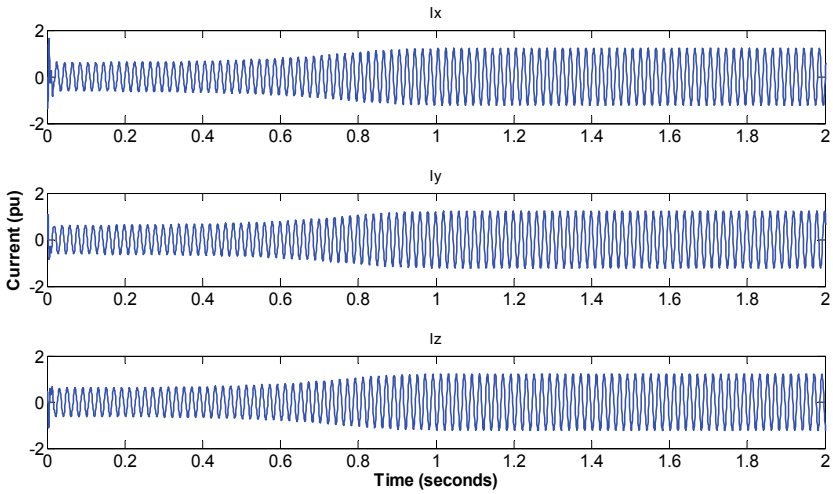

Figure 15. Phase Currents – Auxiliary Stator Winding

6. Experimental validation

In order to validate the theoretical model with the practical model, three capacitor values of 10, 20 and 30μF are used for the three phase auxiliary winding.

Figure 16. The Experimental set up

The stator current of the motor is observed for both uncompensated and compensated windings. It is seen that the starting current for the uncompensated winding is high as compared to the compensated. The current at steady state also identifies the stator current for the uncompensated to be lower as compared to the compensated. These results are shown in figures 17 and 18.

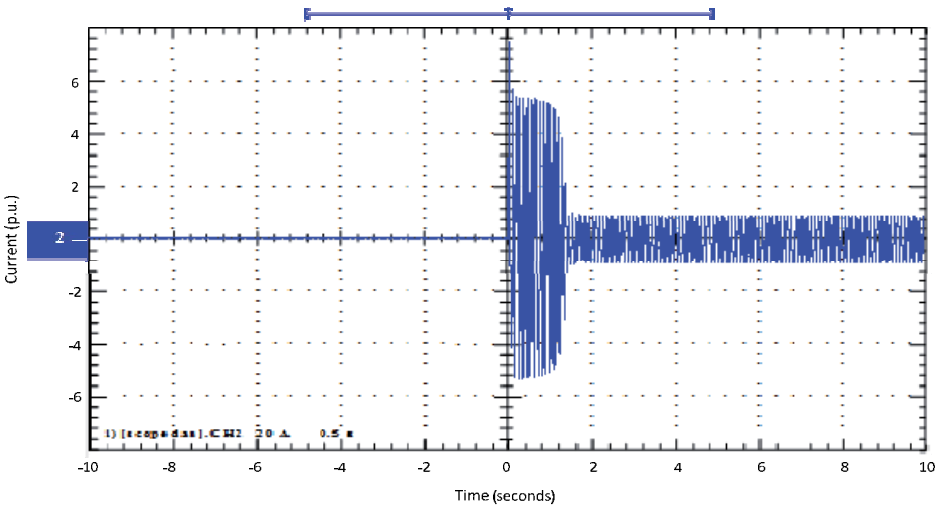

Figure 17. Stator current of uncompensated winding

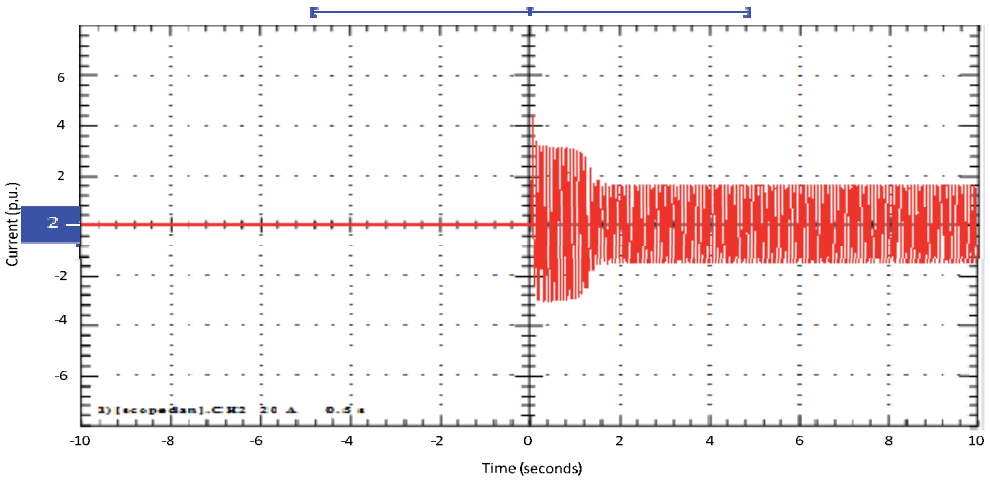

Figure 18. Phase Currents-Stator current of the compensated winding

Other experimental results such as the active power versus the capacitance and power factor versus capacitance are shown in figure 19. These results conform to the theoretical simulations.

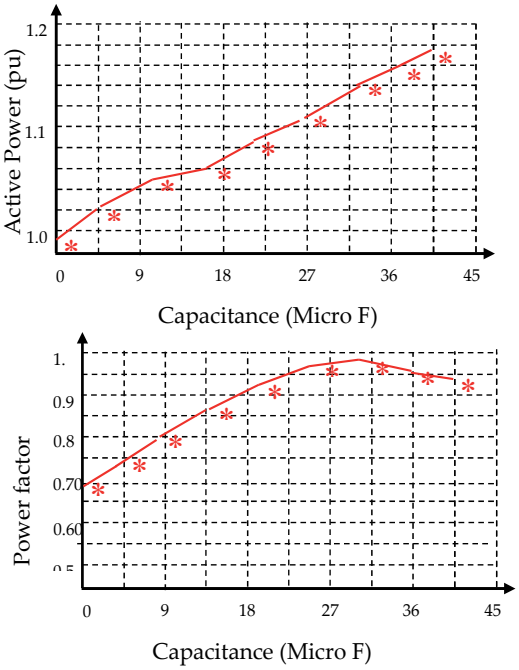

Figure 19. Experimental results of active power and power factor versus capacitance values

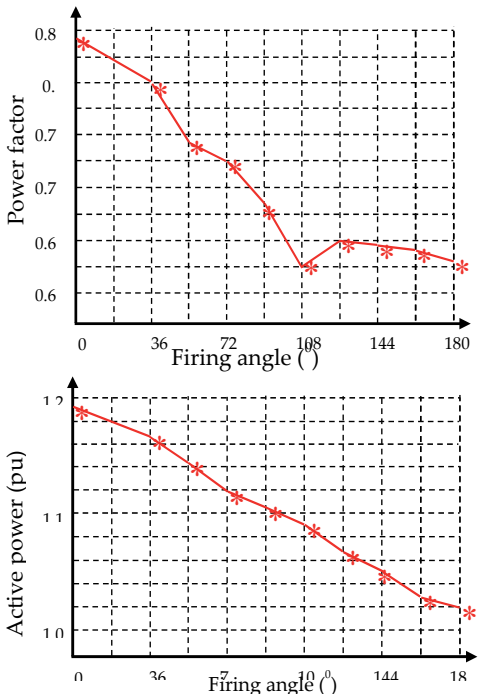

Figure 20. Experimental results of power factor and active power versus firing angle

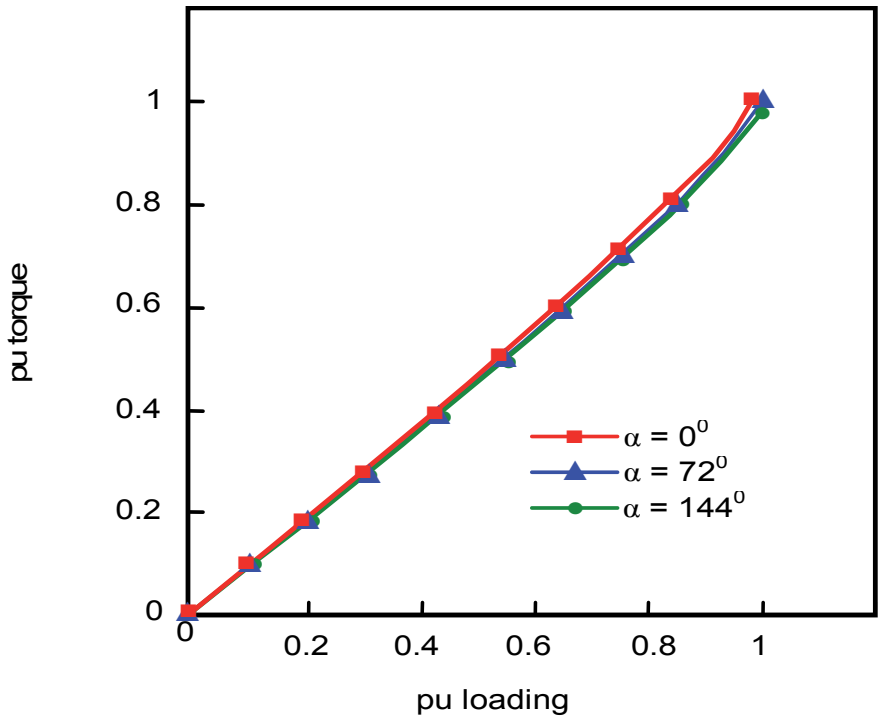

Figure 21. A p.u plot of torque versus p.u. loading for various angles

Since the effective capacitance varies with load when there is an application with varying load, the machine might not always operate at optimum power factor. A possible solution to this is to implement a thyristor controlled static switch or a PWM controller between the capacitors and the auxiliary winding; this will make the capacitance and therefore power factor controllable. Finally, further experiment is carried out on the active power per phase, the power factor versus firing angle and the per unit torque versus per unit loading where the switched series capacitor is connected to the auxiliary winding. The static switching is such that only the required level of reactive compensation is allowed. Figures 20 and 21 are the experimental results obtained based on this analysis.

7. Conclusion

A study has been conducted on a 0.75 KW machine with 380V, 50Hz supply for an effective power factor correction. This has been achieved by connecting the main winding to the three phase supply and the auxiliary winding to the fixed capacitors for reactive power injection. The modified machine with reactive power injection has potential compared to the conventional three-phase machines. It is seen from the waveform analysis that the machine has capability of reducing the starting current. Simulation results have shown a good improvement on both power factor and efficiency when introducing the reactive power injection with increase of capacitor value. Both steady-state and dynamic analysis together

with experimental set up has shown a great improvement compared to the uncompensated machine. Another very important improvement is the supply current decreasing with increasing capacitance. This is not the case with conventional power factor correction techniques because the reactive power needed is still drawn through the only stator winding set. This advantage of the modified machine may potentially reduce installation costs as smaller supply cables can be used.

Despite its good performance it has certain drawbacks. The machine would be bigger in structure than a conventional machine. More copper is needed for the additional winding and more insulating material is needed. This would make the machine much more expensive than the conventional three phase machine. Another drawback of this concept is that the capacitors have to be sized for a specific load. When there is an application with varying load, the machine might not always operate at optimum power factor. A possible solution to this is to implement a PWM controller between the capacitors and the auxiliary winding; this will make the capacitance and therefore power factor controllable.

This modified induction machine has a research potential with the recent focus on energy efficiency. Further research needs to be carried out on the performance behaviour of this machine.

Author details

Adisa A. Jimoh, Pierre-Jac Venter and Edward K. Appiah
Tshwane University of Technology, Pretoria, South Africa

8. References

el-Sharkawi, M. A., Venkata, S. S., Williams, T. J. & Butler, N. G. (1985) An Adaptive Power Factor Controller for Three-Phase Induction Generators. *Power Apparatus and Systems, IEEE Transactions on,* PAS-104**,** 1825-1831.

Jimoh, A. A. & Nicolae, D. V. (2007) Controlled Capacitance Injection into a Three-Phase Induction Motor through a Single-Phase Auxiliary Stator Winding. *Electric Machines & Drives Conference, 2007. IEMDC '07. IEEE International.*

Krause, P. C. (1986) *Analysis of Electric Machinery,* New York, Mcgraw-Hill.

Lipo, T. A. & Novotny, D. W. (1996) Vector Control and Dynamics of AC Drives. In Hammond, P., Miller, T. J. E. & Kenjo, T. (Eds.). New York, Oxford Science Publications.

Muljadi, E., Lipo, T. A. & Novotny, D. W. (1989) Power factor enhancement of induction machines by means of solid-state excitation. *Power Electronics, IEEE Transactions on,* 4**,** 409-418.

Park, R. H. (1929) Two-Reaction Theory of Synchronous Machines Generalized Method of Analysis-Part I. *American Institute of Electrical Engineers, Transactions of the,* 48**,** 716-727.

Stanley, H. C. (1938) An Analysis of the Induction Machine. *American Institute of Electrical Engineers, Transactions of the,* 57**,** 751-7.

Chapter 5

Effects of Voltage Quality on Induction Motors' Efficient Energy Usage

Miloje Kostic

Additional information is available at the end of the chapter

http://dx.doi.org/10.5772/51223

1. Introduction

Today, about 50% of electrical energy produced is used in electric drives. Electrical motors consume around 40% of total consumed electrical energy (Almeida et al., 2007) and of that thereof, induction motors account for 96% of energy consumption. Around 67% of this energy is used in induction motors with a rating below 75 kW and it can be shown that 85% of the energy losses are dissipated in these rating motors. Efficiency improvements of constant-speed drives, both constant-torque and variable-torque drives, is very important. It is usual that techniques for efficiency improvements of variable-torque drives are different from those of constant-speed and constant-torque applications. The latter is dealt with through optimization; it is very difficult to design and build a motor with high rating efficiency and rating power factor - it has been shown (Fei et al., 1989) that higher efficiencies are associated with lower power factor. It is especially difficult to design and build a drive operating at high efficiency and power factor over an entire range of loads, say from 25 - 100% of rated load (P_N), i.e. at partial load.

Electrical energy savings in the drive could be realized by improvements of power quality in the consumer network. Term power quality (Linders, 1972; Bonnett, 2000) mostly means quality of supply voltage that should meet the following requirements:

- voltage value (permissive variations are in the range of $U_N \pm 5\%$ of nominal voltage),
- permissible voltage asymmetry is 2% and has greater influence on accurate and economical motor operation,
- permissive total harmonics distortion of voltage is $THD_U \leq$ 3-8%, where higher values correspond to lower voltage networks.

Power losses and reactive loads depend from on voltage magnitude and they are further increased due to unbalanced voltage and (or) the presence of harmonics in supply voltage.

Unbalance voltage can occur due to the presence of larger single-phase consumers or asymmetrical capacitor banks with damage or capacitors that are switched off due to the fuse burning only in one phase. Nowadays, the presence of higher harmonics in the supply voltage is ever more frequent due to the growth of consumers who are supplied through the rectifiers and inverters: regulated actuators, electrothermical consumers and consumers alike.

The effect of a variation in supply voltage, wave-form or frequency on the motor's efficiency and power factor characteristics depends on the individual motor design. Typical variations of current, speed, power factor and efficiency with voltage for constant output power are given in Fink (1983). The usual characteristics of induction motors within the ±10% voltage band (U_n±10%) are well known. These are included in corresponding table for typical 30-100 kW, 1500 or 1800 1/min motors (Linders, 1972; Fink, 1983), but the effect of saturation has been largely neglected in these tables. However, it is the author's intent to show a correlation between motor characteristics and voltage level.

This proposed has three parts:

1. Study of the effect of voltage magnitude on motor losses and motor reactive loads,
2. analysis of the effect of unbalanced voltages, and
3. analysis of the effect of non sinusoidal voltages to the efficient energy use.

2. Effect of voltage magnitude on motor power losses and motor reactive loads

Voltage magnitude has a significant and different influence on motor loads and electric energy consumption, depending on types, nominal powers and load level ($p=P/P_N$) of motors. Data found in classic references (Fink, 1983) are almost identical to data from older references (Linders, 1972;), although they are not accurate enough for motors made after 1970. The main reason for disagreement is higher values of no-load current and more significant dependency of core losses on voltage magnitude for newer motors (″U″ or ″T″ shape of magnetization curve). Data for loads less than 50% are not available in Fink (1983) and Hamer et al. (1997), although more than half of motors operate in these load regimes.

The influence of voltage magnitude on energy characteristics of standard induction motors (made after 1970.) is significant, as was affirmed by the author's research and verification (Kostic, 1998). It was also ascertained that the changing of energy characteristics is more significant for smaller motors. According to newer literature, efficiency (η) and power factor ($cos\varphi$) dependency on voltage value is more significant than was shown in standard literature.

The paper by Hamer et al. (1997) analyses the effects of voltage magnitude only on two motors (10HP and 100HP) and loads from 50-100%, and the results, and results are illustrated in Fig. 1. Results for standard efficiency motors, given in Fig. 1, are almost equal to the author's results (Kostic, 1998, 2010). A brief theoretical approach for determining dependency of power losses

and reactive loads on voltage value will be presented, as well as proceedings for calculation and analysis of power losses and reactive loads on voltage value.

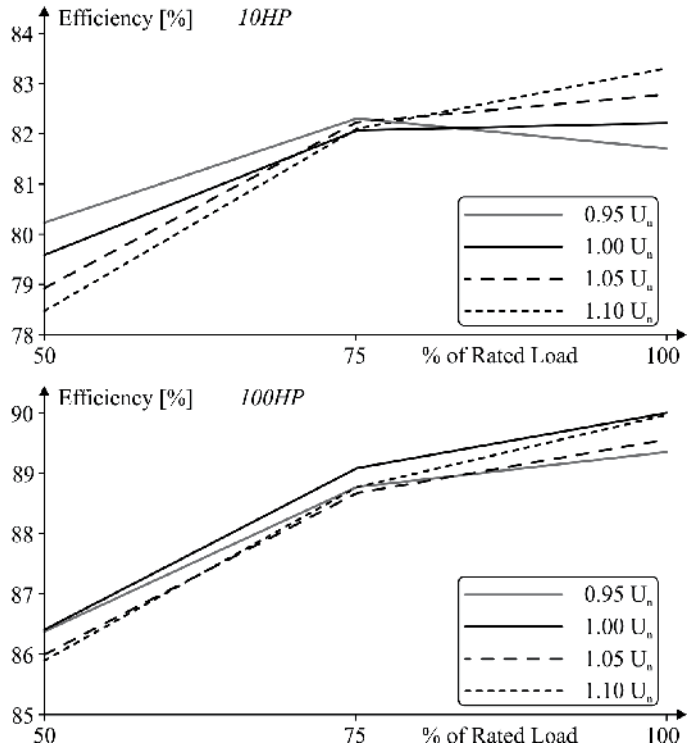

Figure 1. Efficiency versus load for various applied voltages in percent of its 460 V rating for a standard efficiency motor (10 HP and 50 HP)

2.1. Dependency of power losses and reactive loads on voltage value

In order to determine total dependence of power losses on voltage, for the load range from no-load to full load, it is necessary to determine no-load power - voltage dependency, $P_0(u)$:

$$P_0(u) = P_{Cu0}(u) + P_{Fe}(u) + P_{fw} \tag{1}$$

Where are

P_{Cu0} copper losses in no-load,
P_{Fe} core losses in no-load,
P_{fW} friction and windage losses in no-load.

Load losses component (P_{LL}) depend on relative load ($p_L=P_L/P_N$) and relative voltage values ($u=U/U_N$):

$$P_{\gamma P} = P_{LL,N} \cdot p^2 / u^2 \tag{2}$$

where are $P_{LL,N} = P_{Cu,S} + P_{Cu,R} + P_{\gamma ad}$ - a load losses in a nominal regime (P_N, U_N), and $P_{\gamma ad}$ are additional load losses. Load losses, $P_{LL,N}$, can also be calculated as a difference of full load power losses ($P_{\gamma N}$) and no-load power (P_{0N}):

$$P_{LL,N} = P_{\gamma N} - P_{0N} \tag{3}$$

or in per unit ($p_\gamma = P_\gamma / P_N$, $p_0 = P_0 / P$, and $p_{LL,N} = P_{LL,N} / P_N$) as:

$$p_{LL,N} = p_{\gamma N} - p_{0N} \tag{4}$$

Total load losses can be calculated in absolute values as:

$$P_\gamma(p,u) = P_0(u) + P_{LL,N} \cdot p^2 / u^2 \tag{5}$$

or in per unit:

$$p_\gamma(p,u) = p_0(u) + p_{LL,N} \cdot p^2 / u^2 \tag{6}$$

In order to ascertain reactive loads $Q(u)$ dependency, it is necessary to determine no-load reactive power versus voltage, in absolute values ($Q_0(u)$):

$$Q_0(u) = \sqrt{3} \cdot U_0 I_0(u) \cdot \sin\phi_0 \approx \sqrt{3} U_0 I_0(u) \tag{7}$$

Or in per unit values ($q_0(u) = Q_0 / P_N$), for the load range from no-load to full load

$$q_0(u) = \frac{\sqrt{3} \cdot u_0 i_0(u)}{\eta_N \cos\phi_N} \tag{8}$$

In the rated regime are: efficiency, $\eta_N = P_N / P_{1N}$, and power factor, $\cos\phi_N = P_N / (\sqrt{3} \cdot U_N I_N)$. Values of reactive power in the load branch, Q_{LN} and q_{LN} are calculated from the quotient of maximum and nominal torque T_m / T_N, as explained in Appendix, (Kostic, 1998, 2001):

$$Q_{LN} = 0.5 \cdot P_N / (T_m / T_N) \tag{9}$$

or in per unit as:

$$q_{LN} = 0.5 / (T_m / T_N) \tag{10}$$

Equations (9) and (10) are obtained by the procedure given in the Appendix, gained from the equivalent Γ-circuit of the induction machine (Kostic, 2001, 2010). Difference of nominal reactive power and no-load reactive power is a little bit less from calculated value of Q_{LN} and q_{LN} because of reactive power reduction on magnetization branch ($\Delta q_{\mu N} = (0.01\text{-}0.10) q_{0N}$). Total reactive load is calculated in absolute values as:

$$Q_1(u) = Q_0(u) + Q_{LN} \cdot p^2 / u^2. \tag{11}$$

or in per unit

$$q_1(u) = q_0(u) + q_{2n} \cdot p^2 / u^2 \tag{12}$$

For motors of nominal power ≤ 3kW, value of nominal reactive power is almost equal to no-load power ($Q_{1N} \approx Q_0$), because $Q_{LN} \approx \Delta Q_{\mu N}$, so $Q_1(u) \approx Q_0(u)$ and $q_1(u) \approx q_0(u)$, (Kostic, 1998, 2010). Expressions (11) and (12) are commonly in use. Instead of Q_{LN} and q_{LN}, ΔQ_N and Δq_N can be used if they are known or if they can be calculated ($\Delta Q_N = Q_{1N} - Q_{0N}$). For calculating the dependency $P_\gamma(u)$ and $Q_1(u)$, according to expressions (5) and (11), it is necessary to know:

- no-load characteristic $I_0(u)$, $Q_0(u)$, $P_0(u)$ and $P_{Fe}(u)$, for the analyzed voltage range,
- motor catalogue data: nominal power (P_N), nominal current (I_N), efficiency (η), power factor ($\cos\varphi$), slip (s_N) and the quotient of maximum and nominal torque (T_m/T_N), and
- $P_{\gamma N}$ and Q_{LN} are calculated.

2.2. Dependency of motor input power and reactive loads on voltage values

Dependencies of input power (P_1/P_{1N}) and reactive loads (Q_1/P_{1N}) versus relative voltage value (U/U_N), for $P_{LL}/P_N = 25\%$, 50%, 75% and 100%, for motors of nominal powers 1 kW, 10 kW and 100 kW, have been determined by the procedure described in chapter A; results are illustrated in the Fig. 2, (Kostic, 1998, 2010). Influence of voltage on reactive loads and power loss is notable, especially for small motors and for lower loads P_{LL}/P_N.

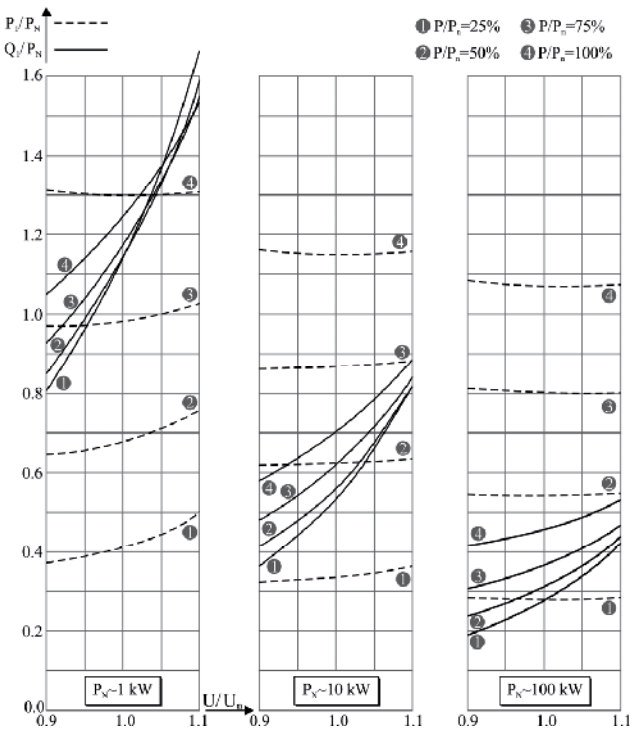

Figure 2. Dependencies of motor input power and reactive loads on supply voltage

Results of the author's research (Kostic, 1998, 2010) confirmed that there are significant possibilities for energy savings by setting voltage values within the voltage band (U_n±5%), because more then 80% of induction motors, especially small and medium power (1 - 30 kW), operate at partial load (≤70%). Dependencies of power loss $P_\gamma(u)$ and reactive loads $Q_1(u)$ for motor of nominal power 2 MW, for $P_1/P_N = 0\%$ (no-load), 25%, 50%, 75% and 100% are given in Fig. 3, (Kostic et al., 2006 and Kostic, 2010).

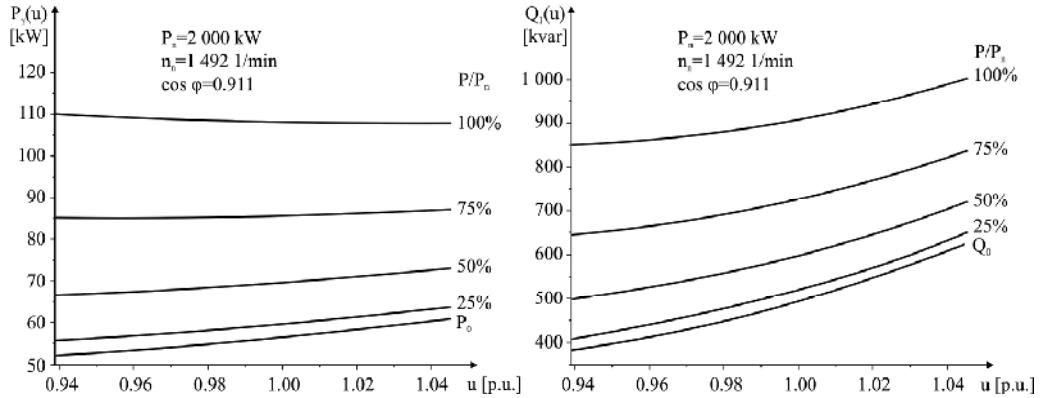

Figure 3. Dependencies of power losses and reactive loads on supply voltage

2.3. Basic reduction of electric energy own consumption of power plants by setting voltage within U_n±5%

Subject of concrete project (Kostic et al., 2006) is reduction of electric energy own consumption of thermal power plant "Nikola Tesla" B, Obrenovac (Serbia), with 2 blocks.. The own consumption of the electric energy, with motors on medium voltage (6.6 kV), is about 90% and with motors on voltage 0.4 kV is about 10%, supplied by a transformer whose primary is directly connected to the generator bus. Nominal powers of the transformers (21 kV/6.6 kV) are approximately equal to total nominal powers of all installed motors which are about 140 MW. Active and reactive loads are about 70 MW and 60 Mvar. As the load of most motors is about 35–70% of full load, reduction of electric energy own consumption could be achieved by setting the voltage magnitude in the range U_n±5%.

Application of this procedure results in reduction: of core losses (P_{Fe}), reactive loads (Q) and active power losses component $P_{CuQ}=RI_Q^2$. Thereby, both active and reactive energy consumptions are decreased. Optimal voltage values are being determined according to appropriate calculations and analysis is based on motor catalogue data and its experimental verification at actual load regimes.

According to the effects of voltage magnitude on motor power losses (P_γ) and motor reactive loads (Q_1), for overall own consumption, the following dependencies can be determined: restrictions:

- motor power losses change $\Delta P_\gamma = P_\gamma(U_i) - P_\gamma(U_N) = \Delta P_1 = P_1(U_i) - P_1(U_N)$, i.e. active loads change, and

- reactive loads change $\Delta Q_1(u) = Q_1(U) - Q_1(U_N)$,

for the voltage range U/U_N = 0.955-1.045, i.e. for U = 6300V-6900V (U_N = 6 600V), Fig. 4.

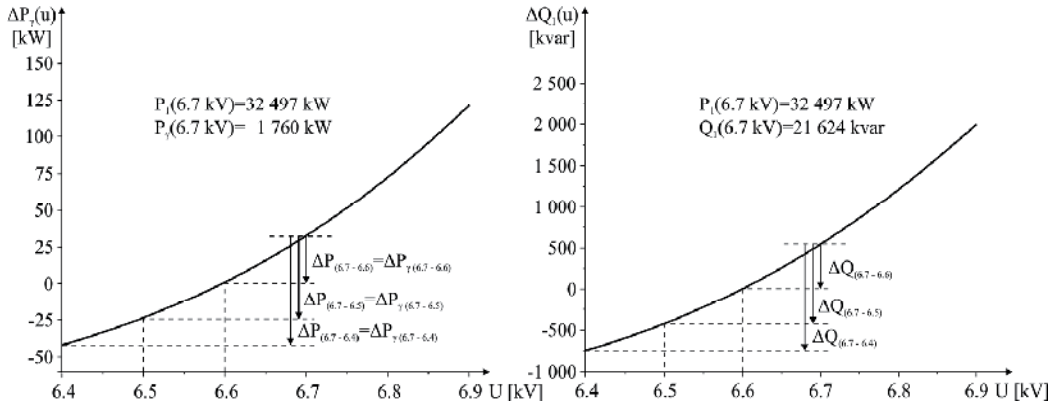

Figure 4. Dependency of total power losses and reactive loads for own consumption

As was shown in Kostic et al. (2006), application of this procedure causes reduction of the electric energy own consumption. Changing voltage value (regulation at own consumption transformers 1BT and 2BT, and at common consumption transformer OBT) from 6.8 kV (1.03 U_N) to 6.6 kV (U_N) or 6.5 kV (0.985 U_N) causes reduction of:

- Active power losses for 161 kW and 213 kW, respectively,
- Reactive loads for 3 544 knar and 4 559 knar.

Power losses addition reduction in the own consumption network for 42.4 kW and 54.7 kW, respectively, due to of the above mentioned of reactive loads' reduction in the own consumption network.

According to values of reduced power losses, reactive loads and assumed operational plan of the thermal plant (estimated 6 000 h/years), savings in active and reactive energy have been determined and given in Table I, (Kostic et al., 2006, and Kostic, 2010).

Consumption objects	Load Reduction		Consumption Energy Reduction	
	Active [kW]	Reactive [kvar]	Active Energy [kWh/year]	Reactive Energy [kvarh/year]
Block 1 Motors	161	3 544	966 000	21 264 000
Block 1 Network	42	-	252 000	-
Block 2 Motors	213	4 559	1 278 000	27 354 000
Block 2 Network	55	-	330 000	-
Total	**471**	**8 103**	**2 826 000**	**48 618 000**

Table 1. Reduction of the active and reactive energy own consumption of Power plant by voltage change, Kostic et al. (2006).

3. Motor voltage asymmetry and its influence on inefficient energy usage

Analysis of the effect of unbalanced voltages on the three-phase induction motor is presented in the paper by Bonnett (2000). Since the unbalanced voltage of 2%, 3.5% and 5% causes an increase in losses, in the same order, for 8%, 25% and 50% of nominal power losses in the motors, it is a reasonable requirement to permit voltage asymmetry ≤2%, so this is the upper limit in most national and international standards. The truth is that with less load, the motor could safely work also at higher values of unbalanced voltage. The literature (Linders, 1972) states that the information given previously is determined from measurements and that they are higher than calculated values. However, it is explained here by the fact that the rotor inverse resistance is higher by 1.41 times compared to the rotor resistance in short-circuit mode (Kostic & Nikolic, 2010), since current frequency of the negative sequence in the rotor winding is twice as high ($f_{r,NS} \approx 2f_1 = 2f_{r,SC}$), i.e. it is higher by 1.41 times than corresponding values given in the literature. Thus, it is increasingly convincing that the requirements which are given in the most appropriate standards are justified. Performed analysis shows that there are some considerations that should be included in current standards. Motor operation is not generally allowed when voltage asymmetry (U_{NS}/U_N) is higher than 5%, because in the (rare) case that the direct and inverse component of the stator currents in one phase are collinear, increase of the current in that phase would be ≥ 1.38 times, and the increase of the losses in the windings of that phase would be ≥ 90% (Linders, 1972; Kostic & Nikolic, 2010).

The effect of voltage asymmetry on the three-phase induction motor is equivalent to the appearance of negative sequence voltage system that creates a rotating field which rotates contrary to the rotation of the positive sequence field and motor rotating direction. The consequence is that small values of negative sequence voltage produce relatively high values of negative sequence currents. By definition, the coefficient of asymmetry (K_{NS}%) is the ratio of negative sequence voltage (U_{NS}) and positive sequence voltage (U_{DS}). For simplification, Standard NEMA use the following definition of voltage unbalance

Voltage unbalance=100· (maximum voltage deviation from average value)/average value

For instance, for measured voltages of 396V, 399V and 405V, average value is 400V. Then, the highest variation from average voltage is determined (405V – 400V = 5V). At the end, the coefficient (percent) of voltage asymmetry is calculated as the quotient of highest variation and average value: $K_{NS}\% = 100 \cdot (5/400) = 1.25\%$. Since percentages of negative sequence currents are 6-10 times higher than corresponding voltage asymmetry, negative sequence currents could reach 10%. This causes additional motor heating and the appearance of inverse torque that reduces starting and maximum motor torque, and causes a small increase of motor slip. Because power losses and motor heating are increased, allowed motor loading is decreased. As the percent of asymmetry rises, the derating factor of nominal power decreases, according to NEMA MG1 (Bonnett, 2000), as shown in Fig. 5.

With an increase of voltage asymmetry coefficient, motor efficiency decreases under all load levels. Dependence of motor efficiency is given in Fig. 6 for the voltage unbalance of 0.00%, 2.50%, 5.00% and 7.50% (Bonnett, 2000).

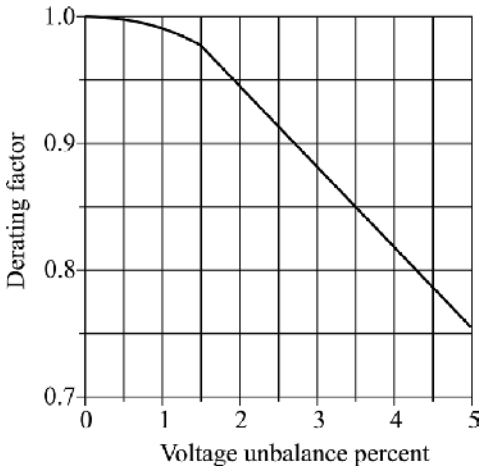

Figure 5. Relation between derating factor and voltage asymmetry

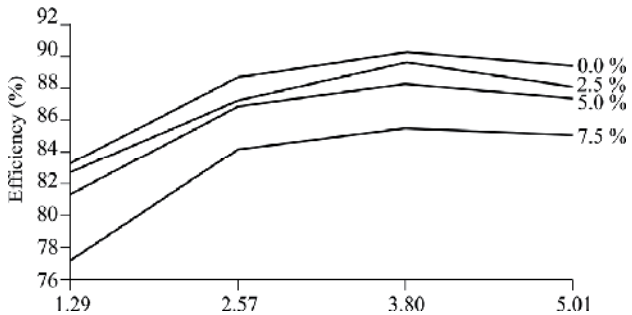

Figure 6. Motor efficiency in dependence of motor load for different voltage asymmetries

Electrical energy consumption is unnecessarily increased due to the lower motor efficiency, so maintenance of low voltage asymmetry (≤ 2%) is a measure of efficient energy usage. In that case, the influence of voltage asymmetry (negative sequence voltages) will be presented in detail in the paper as follows. At first, a procedure for calculation and analysis of negative sequence currents and corresponding power losses will be presented. Then, evaluation of voltage unbalance that could arise in the considered consumer network is presented.

3.1. Equivalent circuit of induction motor for negative sequence

When the induction motor is supplied from the network with asymmetrical voltages, then the three-phase voltage system should be decomposed to positive, negative and zero sequences. Further, using equivalent motor circuits (Boldea & Nasar, 2002; Ivanov-Smolensky, 1982) separately for positive (Fig. 7a) and for negative sequences (Fig. 7b), calculations and analyses of motor energy and operation characteristics (currents, power losses, torques) are performed. At the end, with corresponding superposition of relevance values, their overall values are obtained. Only in that way could real (overall) values of motor power losses be determined.

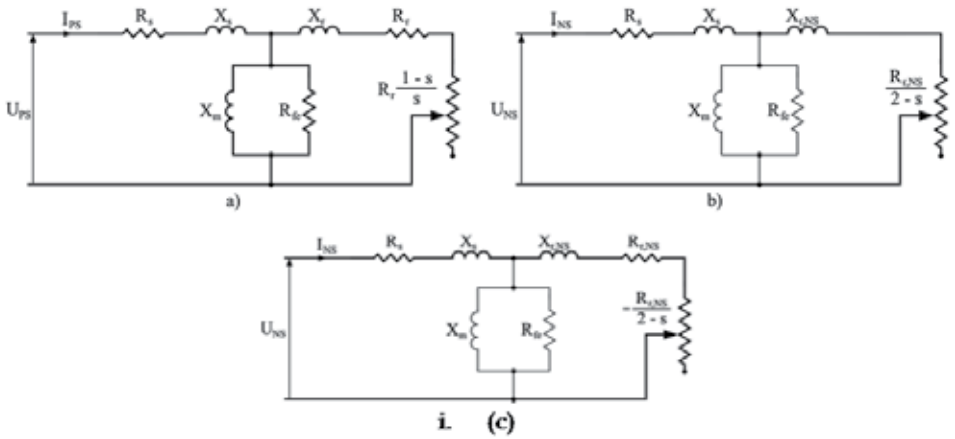

Figure 7. Equivalent circuits of induction motor a) positive and b) negative voltage sequence, and c) completely circuit for negative sequence voltage

3.2. Parameters of equivalent circuit for negative sequence

Stator winding resistance (R_s) and reactance (X_s) are almost the same for positive and negative voltage sequences. The parameters of equivalent circuits that are correlated to the rotor side and negative sequence voltage system (resistance $R_{r,NS}$ and reactance $X_{r,NS}$) are substantially different than those for positive voltage sequences, because the frequencies of the rotor currents in negative sequences are higher for 50÷100 times:

$$f_{NS} = f_1 \cdot (2 - s) \approx 2 f_1 \succ\succ s \cdot f_1 \tag{13}$$

(For example, for load slip s=0.01÷0.05: $f_{r,NS}=(1.90\div1.98)f_1 >> f_{r,PS}=s\cdot f_1=(0.01\div0.05)f_1$).

Values of resistance $R_{r,NS}$ and reactance $X_{r,NS}$ are determined from the corresponding parameters in the short-circuit regime, $R_{r,SC}$ and $X_{r,SC}$. In Boldea & Nasar (2002) and Ivanov-Smolensky (1982) it is noted that values of corresponding resistances and reactances are approximately equal to those in the short-circuit regime: $R_{r,NS} \approx R_{r,SC}$ and $X_{r,NS} \approx X_{r,SC}$.

If we look carefully, we could find that this statement is not correct. Those parameter changes are dependent on the ratio of the rotor conductor height (H_b) and field penetration depth ($\partial_{r,SC} = (2\cdot\rho/(\mu\cdot2\cdot\pi\cdot f_1))^{1/2}$, i.e. the quotient $\zeta = H_b/\partial_{r,SC}$; where: f_1 – frequency of supply voltage first order harmonic, ρ - conductor specific resistance, $\mu = \mu_0$ – magnetic permeability of conductor.

By Fig. 8 (Kostic, 2010), for $\zeta_{SC} = H_b/\partial_{SC} = 1.2\div3$ are obtained: $R_{r,SC} = 1\div3R_r$ and $L_{r,SC} = 1\div0.50L_r$, where R_r and L_r are resistance and inductance in a low slip regime, respectively, for instance in a nominal regime. Since current frequency of the negative sequence in the rotor conductor (bar) is twice as high ($f_{r,NS} \approx 2f_1 = 2f_{r,SC}$), the penetration depth of those currents is lower by √2 times then in a short-circuit regime. Corresponding values of resistance and reactance are higher by √2 times:

$$R_{r,NS} = R_{r,SC} \cdot \sqrt{2} \tag{14}$$

$$X_{r,NS} = X_{r,SC} \cdot \sqrt{2} \tag{15}$$

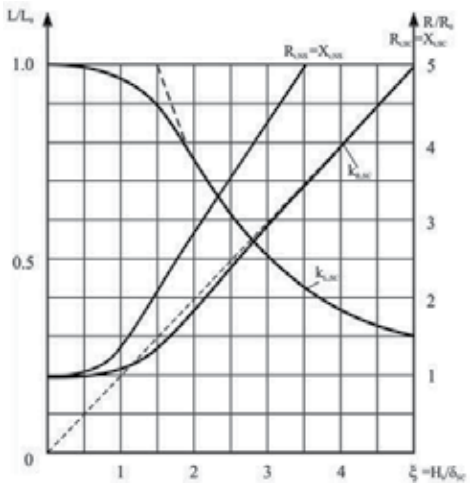

Figure 8. Dependence of rotor resistance and inductance from ratio $\zeta = H_b/\partial_{r,SC}$

The explanation is the following: for motors with powers higher than 5 kW (or with relative rotor conductor height $\xi_{SC} = H_b/\partial_{SC} \geq 1.2$), already in short-circuit mode, the rotor induced currents not the entire cross section, or rotor conductor (bar) height H_b, (Kostic, 2010). From that it could be concluded that for the negative sequence currents ($I_{r,NS}$ with frequency $f_{r,NS} \approx 2f$) it is used for $\sqrt{2}$ times lower part of the section of the rotor conductor and rotor resistance and rotor reactance are higher by √2 times, Fig. 8.

Since usually values of rotor resistance (R_r) and reactance (X_r) are known in the nominal regime, then it is necessary to know values of the coefficient of rotor resistance increase ($k_R > 1$) and the coefficient of rotor inductance decrease ($k_L < 1$), both in the short-circuit regime. From (14) and (15), the values for $R_{r,NS}$ and $X_{r,NS}$ could be calculated as:

$$R_{r,NS} = k_{R,NS} \cdot R_r = \sqrt{2} k_{R,SC} \cdot R_r \tag{16}$$

$$X_{r,NS} = k_{X,NS} \cdot X_r = \sqrt{2} k_{X,SC} \cdot X_r \tag{17}$$

where values of coefficients $k_{R,NS}$ and $k_{X,NS}$ are determined from Fig.8 for previously established ratio value $\zeta_{NS} = H_b/\partial_{NS}$, where is ∂_{NS} –penetration depth of negative sequence field in rotor conductor. In such a manner approximate values of coefficients k_R and k_X are determined, for different rotor bar height H_b (mm)= 15, 20, 30, 40, 50 and given in Tab. 2.

From the quantitative review of corresponding values for $k_{R,SC}$ and $k_{R,NS}$, and $k_{X,SC}$ and $k_{X,NS}$, it could be seen that valid relations are: $k_{R,NS} \approx 1.41 \cdot k_{R,SC}$ and $k_{X,NS} \approx k_{R,SC}/1.41$, and it could be concluded that relations (14) and (15) are correct. In that way the author's statement that **"it**

is not correct to believe that values of corresponding resistances and reactances for negative sequence currents are approximately equal to those for motor short-circuit regime" is confirmed**,** as it is quoted in the literature (Boldea & Nasar, 2002; Ivanov-Smolensky, 1982). To the contrary, it is only correct that those values are in relation by (16) and (17). It is useful to specify common values for rotor conductor (bar) height H_b (mm) and frame sizes (axial height) for standard induction motors, as given in Tab. 3. From these facts more precise calculations and analyses of negative sequence voltage (and negative sequence currents) influencing the motor operation could be performed (Kostic & Nikolic, 2010).

Rotor slot depth H [mm]	15	20	30	40	50
$K_{R,SC}$	1.30	2.00	3.00	4.00	5.00
$K_{R,NS}$	2.00	2.80	4.20	5.60	7.00
$K_{X,SC}$	0.90	0.75	0.50	0.38	0.30
$K_{X,NS}$	0.75	0.54	0.36	0.27	0.22
$\partial_{Al,SC}$ = 10 mm; $\partial_{Al,NS}$ = 7 mm					

Table 2. Coefficients k_R and k_X in short-circuit regime and negative sequence currents

Nominal power, Pn [kW]	1.1 - 2.2	3 - 7.5	11 - 18.5	22 - 45	55 - 160	200 - 355
Axial height [mm]	80 - 90	100 - 112	132 - 160	180 - 200	225 - 280	315 - 400
Rotor slot depth, H [mm]	13 - 17	18 - 22	24 - 34	35 - 44	40 - 50	40 - 50

Table 3. Usual values for rotor bar height H_b, and frame sizes for standard induction motors

3.3. Negative sequence currents and power losses

The negative effect on the motor operation due to the presence of negative sequence voltage is obvious for two reasons:

- it induces negative sequence currents that produces losses in the stator and rotor windings, i.e. on the stator (R_s) and rotor ($R_{r,NS}$) resistance, and
- inverse torque appears which is opposite to the motor operative torque.

It is useful to express the value of negative sequence current ($I_{1,NS}$) in the units of nominal positive sequence current $I_{1N,PS}$:

$$\frac{I_{1,NS}}{I_{1n}} = \frac{U_{1,NS} / Z_{M,NS}}{U_{1N} / Z_{M,n}} \approx \frac{U_{1,NS} / X_{M,NS}}{U_{1,n} / Z_{M,N}} = \frac{U_{1,NS}}{U_{1N}} \cdot \frac{1}{X_{M,NS}} \approx (6 \div 8) \cdot \frac{U_{1,NS}}{U_{1N}} \tag{18}$$

since negative sequence motor impedance $Z_{M,NS} \approx X_{M,NS} \approx$ (0.8-0.9) $X_{M,SC}$ and motor short-circuit reactance $X_{M,SC} \approx$ (0.15÷0.20) $Z_{M,N}$, where $Z_{M,N}$ is motor impedance in the nominal regime. It could be seen from (18) that negative sequence currents in stator and rotor windings are 5÷8 times higher from the values of negative sequence voltage coefficients ($U_{1,NS}/U_n$). Since negative sequence currents are not dependent on motor load and slip, and then we suggest calculating the coefficient of asymmetry in the units of nominal motor

voltage. In the following calculations and analyses the value X_{NS} =0.13 (or X_{SC} = 0.16, i.e. I_{SC}/I_N=6.25) is used, so:

$$\frac{I_{1,NS}}{I_{1n}} = 7.7 \cdot \frac{U_{1,NS}}{U_{1N}} \tag{19}$$

The value of increased losses in the phase windings of stator is proportional to the square of negative sequence currents, and then from (19) it could be calculated as:

$$\frac{P_{CuS,NS}}{P_{CuS,n}} = \left(\frac{I_{1,NS}}{I_{1N}}\right)^2 = 60 \cdot \left(\frac{U_{1,NS}}{U_n}\right)^2 \tag{20}$$

The percentage of losses in rotor conductors could be higher by up to 3-6 times (2-5 times due to the higher rotor resistance for negative sequence currents and further up to 1.2 times due to the additional increase of rotor winding temperature under such a high power losses), i.e. $R_{r,NS} \approx R_{r,SC}$=(2÷6) R_r. The equation for losses calculation in the rotor conductors for $R_{r,NS} = 5R_r$, is:

$$\frac{P_{Cur,NS}}{P_{Cur,n}} = 5 \cdot \left(\frac{I_{1,NS}}{I_{1N}}\right)^2 = 300 \cdot \left(\frac{U_{1,NS}}{U_N}\right)^2 \tag{21}$$

Assuming that negative sequence impedance is $Z_{SC,NS} \approx X_{SC,NS} = 0.13$ (or I_{SC}/I_N=7.7) and negative sequence rotor resistance is $R_{r,NS} = 5\ R_r$, the power losses values are calculated for voltage asymmetry of 2.5%, 3.5% and 5%. Such calculated values from (20) and (21), in percent of nominal losses, for particular motor parts (stator, rotor) and whole motor, are given in Tab. 4. Similar data are given in Linders (1972) where it was noted that measured values are 50% higher than calculated values. This difference was explained by an additional temperature increase of the rotor conductor, i.e. an increase of rotor resistance. Although an additional increase of rotor temperature by more than 100°C is not possible. The mentioned difference of measured and calculated values in Linders (1972) can be explained only by the fact that real rotor inverse resistance is 40% higher (based on (16) then its conventional value. Calculated values for permitted motor load are similar to those provided in NEMA standards (Fig. 5).

Negative sequence voltage [%]	0.0	2.0	3.5	5.0
Negative sequence current [%]	0.0	15.0	27.0	38.0
Stator current (RMS) [%]	100.0	101.0	104.0	107.5
Increased stator winding losses [%]	0.0	2.4	7.4	15.0
Increased rotor winding losses [%]	0.0	12.0	37.0	75.0
Increased iron losses [%], Fig. 8	0.0	2.5	7.5	15.0
Increased total motor losses [%]	0.0	5.5	17.0	34.0
Permissible motor load P/P_n [%]	100	97	91	81

Table 4. Influence of negative sequence voltage on permissible motor load ($P_N \geq 100$ kW)

Given the pessimistic assumption, especially for **smaller motors' power (up to 10 kW)** when the rotor resistance is increased only by 2-3 times (up to 1.5-2.5 times due to the higher rotor resistance for negative sequence currents and even up to 1.2 times due to additional increase in temperature of the conductor rotor in such a large loss of power, i.e. $R_{r,NS} \approx 1.4\ R_{r,SC} = (2 \div 3)\ R_r$, calculation of losses in the rotor conductors, for $R_{r,NS} = 3R_r$, was conducted by the expression:

$$\frac{P_{Cur,NS}}{P_{Cur,n}} = 60 \cdot \left(\frac{I_{1,NS}}{I_{1n}} \right)^2 = 180 \cdot \left(\frac{U_{1,NS}}{U_n} \right)^2 \tag{22}$$

since the inverse of impedance $Z_{1,NS} \approx X_{NS} \approx 0.9\ X_{SC} = 0.13$ (i.e. when the motor short-circuit reactance $X_{SC} = 0.143$, or $I_{SC} / I_n = 7$). Thus obtained data are given in Tab. 5 and they are more accurate for motors with power below 10kW. Based on these calculations, it was found that the effect of unbalanced voltage on power losses is smaller for motors with nominal power ≤ 10 kW. Thus, acceptable voltage asymmetry for these motors could be 3%.

Negative sequence voltage [%]	0.0	2.0	3.0	5.0
Negative sequence current [%]	0.0	15.0	22.0	38.0
Stator current (RMS) [%]	100.0	101.0	102.0	107.5
Increased stator winding losses [%]	0.0	2.4	5.4	15.0
Increased rotor winding losses [%]	0.0	7.0	16.0	45.0
Increased iron losses [%], Fig. 8	0.0	2.5	7.5	15.0
Increased total motor losses [%]	0.0	4.0	9.0	25.0
Permissible motor load P/P_n [%]	100	98	95	87

Table 5. Influence of negative sequence voltage on permissible motor load ($P_N \leq 10$ kW)

Based on data given in Tab. 5, it is concluded that the effects of unbalance on increased power loss is less compared to the data specified in the relevant standards for motors of nominal power ≤ 10 kW. Thus, motor total losses increase is 9% (Tab. 5) for the voltage asymmetry of 3%. As it is less then permissible 10% for these motors, for the networks with motors below 10 kW may be accept a voltage asymmetry ($U_{1,NS} / U_N$) ≤ 3%.

Although the unbalanced voltage losses in the rotor conductors are much higher than the corresponding losses in the stator winding, the increase to the losses of one phase of the stator can be the greatest. Specifically, it is unfavorable in the case where the direct and inverse current component could be in phase in one phase. Current in this phase, at the voltages' unbalance of 5%, would be:

- at nominal load $I = I_{PS} + I_{NS} = I_N + 0.38\ I_N = 1.38\ I_N$, while
- at 80% of the motor load: $I = I_{PS} + I_{NS} = 0.8\ I_N + 0.38\ I_N = 1.18\ I_N$.

These corresponding power loss values, respectively, were higher than the nominal 100% (1.38^2-1) = 90% and 100% (1.18^2-1) = 39%. Then the current increase in that phase would be 1.38 times at the negative sequence voltage $U_{1,NS} / U_N = 5\%$ and increase of the losses in the

windings of that phase could reach 90% = 100% (1.38^2-1). Otherwise, in practice it could rarely be the case when direct and inverse components of the current matching phase angle. For example, it is necessary to stress that the asymmetry is a consequence of only one phase voltage deviation of the values (not phased by the angle) and the phase angles of the direct and inverse impedance are a little different, which is rarely filled because $\tan(\phi_{NS}) = 0.3 \div 0.4$. But it is possible that the phase angle between these components is about 30^0, and a corresponding increase in this phase will be lower:

- current increase would be in the analyzed cases 1.235 I_N and 1.079 I_N, and
- corresponding increase in losses in this phase would be 52.5% and 16.4%.

respectively, for nominal load and 80% load, both for voltages' unbalance of 5%.

For these reasons the motor operation is not allowed when the values of the coefficient of negative sequence voltage is $U_{1NS} / U_N \geq 5\%$.

Experimental measurements (Boldea & Nasar, 2002) showed that the effect of unbalanced voltages on the iron losses increase more if the motor is powered with high voltage, Fig. 9:

- loss increase in iron is 25W (or 15%) and the unbalanced voltage of 5% and nominal voltage, while
- loss increase in iron is 35W (or 25%) for voltage asymmetry of 5% and the 110%voltage.

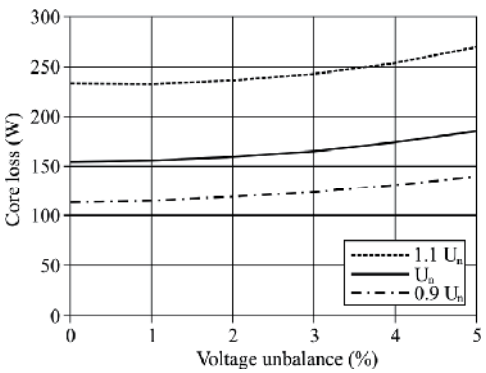

Figure 9. Dependence of iron losses on voltage asymmetry for three values of supply voltage

This additionally has an influence on reducing the coefficient of nominal power (derating factor), as well as reducing motor efficiency and increasing power consumption.

3.4. Causes and evaluation of inverse voltage values

By definition, the coefficient of asymmetry is the relationship between the inverse system voltage (U_{NS}) and direct voltage systems (U_{PS}). Thus, the percentage of unbalanced voltage is calculated using the formula:

$$K_{NS}\% = 100\frac{U_{NS}}{U_{DS}} \tag{23}$$

where the direct and inverse system voltage component are calculated using the formula

$$U_{PS} = \frac{U_{ab} + aU_{bc} + a^2U_{ca}}{3} \tag{24}$$

$$U_{NS} = \frac{U_{ab} + a^2U_{bc} + aU_{ca}}{3} \tag{25}$$

Thus, in the case of symmetrical voltages at the motor $\underline{U}_{ab} = a^2\underline{U}_{bc} = a\underline{U}_{ca}$, we get $U_{PS} = U_{ab} = U_{bc} = U_{ca}$ (24) and U_{NS}=0 (25).

Asymmetry can arise for several reasons. One is the joining of large consumers to one or two phases. Thus, if a consumer who connected to one phase, e.g. phase "a", creates a voltage drop $\Delta U = 3\%$, then it causes the asymmetry of 1% (U_{NS}= 1%), since the asymmetrical voltage system can be presented as the sum of the symmetric system voltage ($U_{ab} = U_{bc} = U_{ca}$) and the unbalanced system voltages ($U_{ab} = \Delta U = 3\%$, $U_{bc} = 0$, $U_{ca} = 0$). This second voltage system, according to (25), corresponds to unbalanced system voltage of $U_{NS} = 1\%$. If a purely inductive consumer is connected between two phases, so that the voltage levels on each phase of the impedance network is 3%, then a similar analysis leads to the conclusion that this causes asymmetry of 2% ($U_{NS} = 2\%$), at the motor connections. These cases are possible in practice and rarely exceed the specified quantitative values.

Asymmetry may be a consequence of fuse capacitor burning. The fall out of capacitors part between two phases, concerning of the voltage reduction, is equivalent to appear of inductive loads between the two the same phases. As a consequence of that is the appearance of the inverse voltage, which is value equal to 2/3 change of the phase voltages mentioned. The general assessment is that it is almost always the asymmetry coefficient $K_{NS} < 2\%$, except for the interruption of one phase in the network, or interruption in any of the motor phase windings.

3.5. Motor inverse torque

The system of negative sequence voltages leads to the appearance of the inverse torque ($T_{em,NS}$), which is opposed to the torque that drives the motor (the torque that comes from the direct system voltages and currents, $T_{em,PS}$). Resultant driving torque is reduced, $T_{em} = T_{em,PS} - T_{em,NS}$ and the direct torque must be increased to compensate that decrease. Therefore, the slip and direct current systems are increased, and also the corresponding power losses. Direct ($T_{em,PS}$) and inverse ($T_{em,NS}$) electromagnetic torques is:

$$T_{em,PS} = \frac{3U_{1PS}^2 R_r}{s\Omega\left[(R_s + R_r/s)^2 + X_{M,SC}^2\right]} \tag{26}$$

$$T_{em,NS} = \frac{3U_{1NS}^2 R_r/(2-s)}{s\Omega\left[(R_s + R_r/(2-s))^2 + X_{M,SC}^2\right]} \tag{27}$$

Where are values R_r, R_s, $Z_{M,N}$, $X_{M,SC}$, $Z_{M,SC}$ are defined in in 3.3 (page 12).

Assuming that $R_{rNS}=R_{rPS}=R_r$ and $R_r/(2-s) = R_r/2$ and with less neglect, leads to a relationship:

$$\frac{T_{em,NS}}{T_{em,PS}} \approx (\frac{U_{1NS}}{U_{1PS}})^2 \cdot \frac{Z_{PS}}{2X_{SC}} \tag{28}$$

Sometimes it is convenient to express the inverse torque in units of the nominal torque i.e.:

$$\frac{T_{em,NS}}{T_{em,N}} \approx (\frac{U_{1NS}}{U_{1N}})^2 \cdot \frac{Z_{M,N}}{2X_{SC}} \approx 3 \cdot \left(\frac{U_{1NS}}{U_{1N}}\right)^2 \tag{29}$$

This means that, for the coefficient of unbalanced voltage $U_{1,NS} / U_N = 0.04$, would be $T_{em,NS}/T_{em,N} = 3 \cdot 0.04^2 = 0.0048 = 0.48\%$. Slip and power losses will also be increased for 0.0048 times, or 0.5%. But if we assume that the inverse rotor resistance for 2-5 times higher (up to 2-4 times due to the higher rotor resistance for negative sequence currents and even up to 1.2 times due to additional increase in temperature of the conductor), then the expression for the relative values of the inverse torque is:

$$\frac{T_{em,NS}}{T_{em,N}} \approx (6 \div 15) \cdot \left(\frac{U_{1NS}}{U_{1N}}\right)^2 \tag{30}$$

The lower value of the coefficient related to the motor power up to 10 kW, and the upper value for motor power above 100 kW. When coefficient of unbalanced voltage $U_{1,NS}/ U_N = 0.05$, inverse torque in units of the nominal torque could be at $T_{em,NS}/T_{em,N} = 10 \cdot 0.05^2 = 0.025 = 2.5\%$. Slip and power losses will be increased also for 0.025 times, or 2.5% P_N. As this is a medium power motor, with $\eta_N \approx 90\%$ or with losses of $P_{\gamma N} \approx 10\%$ P_N power losses are increased by $\Delta P_\gamma = 25\%$ $P_{\gamma N}$, which is less than half of the determined value of increasing losses $\Delta P_{\gamma,NS} = 50\%$.

The explanation lies in the fact that in this way (i.e. through the power that is allocated to resistance $R_{r,NS}/2$, Fig.7c) covers only half the power losses in resistance $R_{r,,NS}$ while the remaining half of the compensated part of mechanical power (P_m), which is obtained through the axis of direct voltage system, Fig. 10. Thus, another procedure confirmed adequate accuracy of quantitative estimates given in Table 5.

4. Influence of motor non-sinusoidal voltage on efficient energy usage

Analysis of the effect of non-sinusoidal voltages on the three-phase induction motor is presented in this chapter. Power losses and reactive load are increased due to the presence of harmonics in supply voltage. Nowadays, the presence of harmonics in the supply voltage is even more frequent due to the growth of consumers which are supplied through the rectifiers and inverters.

Two interesting cases have been analyzed (Kostic M. & Kostic B., 2011).

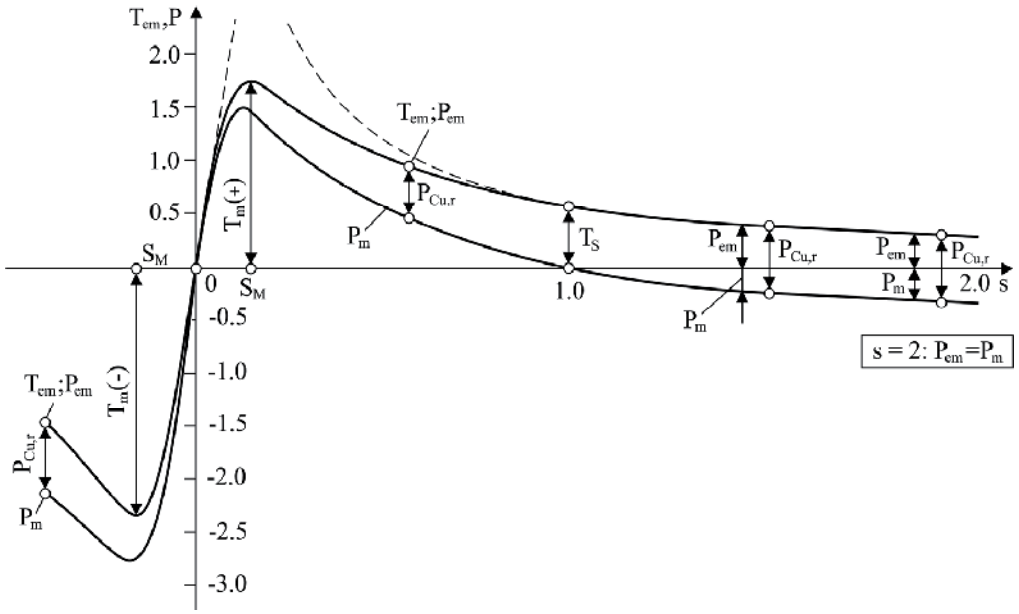

Figure 10. Electromagnetic torque characteristics (T_{em}) and the electromagnetic power (P_{em}) in the following regimes: generator (s < 0), motor (0 ≤ s ≤ 1) and braking (s> 1), as well as at point s = 2 (for the inverse voltage)

1. The case that the voltage, containing harmonics of order h = 1, 5, 7, 11, 13, 17, ..., 37, whose amplitudes are equal U_h = 5%.
2. As the induction motors are supplied by a rectangular shape of the voltage inverter with high levels of harmonic voltage ($U_{h,i} = 1/h_i$).

The reason for this (new analysis) lies in the fact that it is (wrongly) believed that the resistance of the smaller motor's rotor does not change for higher harmonic frequencies, i.e. that is identical for all harmonics ($R_{r,h} = R_{r,1} = R_r = Const.$), which brings the difference mentioned above – and error. It is shown in Kostic M. & Kostic B. (2011) that values of the rotor resistance and the rotor reactance in a short-circuit regime could be estimated on the basis of the induction motor's catalogue date. Two important conclusions are established (probably for the first time) in Kostic (2010):

1. that rotor slot resistance and the rotor slot reactance values, $R_{r\text{-}sl,SC}$ and $X_{r\text{-}sl,SC}$, are practically equally in a short-circuit regime, and
2. that they have approximately equally values, per unit, for all motors of the same series.

4.1. Equivalent circuit of induction motors for harmonics

The equivalent circuit for the harmonics is identical to the corresponding equivalent circuit for a short-circuit regime for fundamental frequency f_1. Only, instead of rotor short-circuit resistance (R_{isk}) and rotor short-circuit reactance (R_{isk}), the two rotor resistances, rotor end (R_{ah}) and rotor slot resistance ($R_{r\text{-}sl,h}$), and two rotor reactances, rotor end ($X_{r\text{-}e,h}$) and rotor slot reactance ($X_{r\text{-}sl,h}$), are used for the harmonics order (h), Fig. 11a (Kostic M. & Kostic B., 2011).

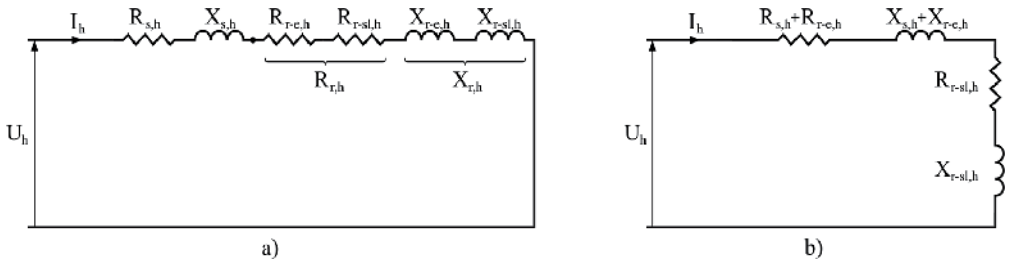

Figure 11. Motor equivalent circuit for harmonics: a) with separate rotor resistances and rotor reactances and b) with grouped motor resistances and motor reactances

Increasing the order of harmonic causes increased frequency of induced currents in rotor conductors, compared to the one in the short–circuit regime. The skin effect is practically present only in the part of the conductor in the slot of the rotor, i.e. it leads only to an increase of rotor slot resistance ($R_{r\text{-}sl,h}$) and a reduction of rotor slot inductance ($L_{r\text{-}sl,h}$). As the depth of penetration is $\partial_{Al,h=5}$ = 4.5 mm, already for the fifth harmonic, $R_{r\text{-}sl,h}$ is always equal to $X_{r\text{-}sl,h}$, Fig. 12. For this reason, similar to the corresponding scheme for short-circuit mode (Kostic, 2010), the rotor reactance ($X_{r,h}$) and resistance ($R_{r,h}$) are separated into two components in the equivalent circuit for the harmonics, Fig. 11a, i.e.:

$$R_{r,h} = R_{r-sl,h} + R_{r-e,h} \tag{31}$$

$$X_{r,h} = X_{r-sl,h} + X_{r-e,h} \tag{32}$$

where $R_{r\text{-}e,h}$ is rotor winding end resistance and $X_{r\text{-}e,h}$ is rotor winding end reactance ("e" in the index comes from the abbreviation of the word "end").

Finally, resistance and reactance of stator windings, and resistance and reactance of rotor conductors outside of slots are grouped (Fig. 11b), for which the influence of skin effects can be neglected from the nominal regime to the short–circuit regime. These are:

- grouped resistance $R_{s,h} + R_{r\text{-}e,h}$ and
- summary reactance, $X_{s,h} + X_{r\text{-}e,h}$.

The remaining resistance $R_{r\text{-}sl,h}$ and reactance $X_{r\text{-}sl,h}$, are separated (Fig 11).

4.2. Parameters of equivalent circuit for harmonics

In the paper by Caustic (2010) it is shown that values of rotor slot resistance ($R_{r\text{-}sl,SC}$) and rotor slot reactance ($X_{r\text{-}sl,SC}$) in the short-circuit mode are approximately the same for motors of all powers in a series and they are approximately equal to each other, i.e.:

$$R_{r-sl,sc} = X_{r,sc} \approx 0.030 \text{ (p.u.)} \tag{33}$$

Their values are within the narrow range of $X_{r\text{-}sl,SC} = R_{r\text{-}sl,SC} \approx 0.027 \div 0.033$ p.u., respectively for the motors of large (> 100 kW), medium (11 - 50 kW) and low power (1 - 7.5 kW).

The explanation is the following: for motors with powers higher than 5 kW (or with relative rotor conductor height $\xi_{SC} = H_b/\partial_{SC} \geq 1.5$), already in short-circuit mode, the rotor induced currents not the entire cross section, or height of rotor bars H, (Kostic, 2010). Current frequencies of individual harmonics in the rotor winding are h times higher ($f_{r,h} \approx h \cdot f_1 = h \cdot f_{r,SC}$), so the actual depth of penetration of individual harmonic currents (∂_h) is $\sqrt{h}$ times lower. Therefore, the corresponding cross section of rotor conductor is $\sqrt{h}$ times lower, so the values of rotor slot resistance are $\sqrt{h}$ times higher and the values of rotor slot inductance are $\sqrt{h}$ times lower as compared to those values for the fundamental harmonic in the short-circuit regime. In general, rotor slot resistance ($R_{r\text{-}sl,h}$), rotor slot inductance ($L_{r\text{-}sl,h}$) and rotor slot reactance ($X_{r\text{-}sl,h}$), in the function of harmonic order $h = f/f_1$, are shown in Fig. 12.

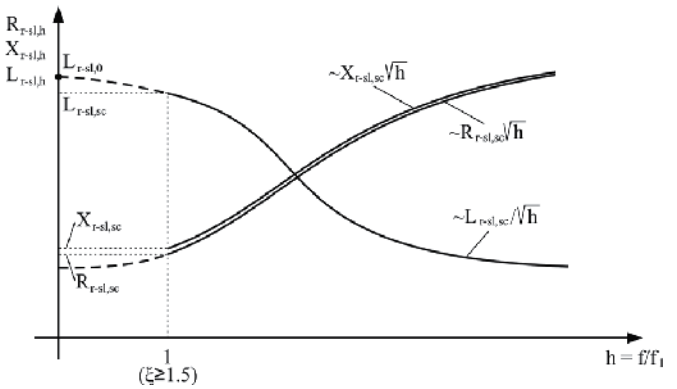

Figure 12. Dependencies of rotor slot resistance, inductance and reactance on harmonic order

If the ratio $\xi = H_b/\delta_{r,SC} \geq 1.5$, then equality $X_{r\text{-}sl,SC} = R_{r\text{-}sl,SC}$ is already true for the fundamental harmonic. As for the harmonics of order $h \geq 5$, the relative rotor conductor height is always equal to $\xi_h = H_b/\delta_h \geq 2$, then for motors of all powers is shown in Fig. 12:

$$R_{r-sl}(hf_1) / R_{r-sl,SC}(f_1) = \sqrt{h} \tag{34}$$

$$L_{r-sl}(hf_1) / L_{r-sl,SC}(f_1) = 1/\sqrt{h} \tag{35}$$

According to this, it is concluded that the following equations can be written:

$$R_{r-sl,h} = R_{r-sl,SC} \cdot \sqrt{h} \tag{36}$$

$$L_{r-sl,h} = L_{r-sl,SC} \Big/ \sqrt{h} \tag{37}$$

$$X_{r-sl,h} = X_{r-sl,SC} \cdot \sqrt{h} \tag{38}$$

This means that, based on given values of rotor slot resistance ($R_{r\text{-}sl,SC}$), rotor slot inductance ($L_{r\text{-}sl,SC}$) and rotor slot reactance ($X_{r\text{-}sl,SC}$) for fundamental frequency f_1 in short-circuit mode, the corresponding parameter values for harmonics $h = f_h/f_1$ can be calculated, i.e. values: resistance ($R_{r\text{-}sl,h}$), inductance ($L_{r\text{-}sl,h}$) and reactance ($X_{r\text{-}sl,h}$).

The values of penetration depth in the stator copper conductors are $\delta_{Cu,} \geq 1.6$ mm for frequencies $f \leq 2000$ Hz. As a rule, since the diameter of the stator winding conductors is $d_{Cu} \leq 2$ mm, it can be assumed that the value of stator windings' resistance keeps almost the same value for all harmonics of order $h \leq 40$ (or 2000 Hz/50 Hz), i.e. the following equation is valid:

$$R_{s,h} \approx R_{s,1} = R_s, \quad for \ \ h \leq 40 \tag{39}$$

The same assumption approximately applies to the rotor end resistance ($R_{r\text{-}e,h}$) and to the rotor end inductance ($L_{r\text{-}e,h}$). On this basis, the following equations can be written:

$$L_{r-e,h} \approx L_{r,e} \tag{40}$$

$$X_{s,h} + X_{r-e,h} = h \cdot \left(X_s + X_{r-e} \right) \tag{41}$$

$$R_{s,h} + R_{r-e,h} = R_s + R_{r-e} \tag{42}$$

The total value of motor resistance ($R_{M,h}$), motor reactance ($X_{M,h}$) and motor impedance ($Z_{M,h}$), for current harmonics, are given in the following expressions:

$$R_{M,h} = \left(R_s + R_{r-e} \right) + R_{r-sl,SC} \cdot \sqrt{h} \tag{43}$$

$$X_{M,h} = \left(X_s + X_{r-e} \right) \cdot h + X_{r-sl,SC} \cdot \sqrt{h} \tag{44}$$

$$Z_{M,h} = \sqrt{R_{M,h}^2 + X_{M,h}^2} \tag{45}$$

The summary value of resistance $(R_s + R_{r\text{-}e}) \approx Const$ and the summary value of inductance $(L_s + L_{r\text{-}e}) \approx Const$, retain approximately the same value in all modes: operating regime, the short-circuit regime and for regimes with harmonics. For calculation values of $R_{M,h}$ and $X_{M,h}$ by equations (43) and (44), values $(R_s+R_{r\text{-}e})$ and $(X_s+X_{r\text{-}e})$ ought to be determined from a locked rotor test, and assumed value $R_{r\text{-}sl,\,SC} = R_{r\text{-}sl,SC} = 0.030pu$.

Harmonics currents ($I_{M,h}$), due to the existence of the corresponding harmonics voltages ($U_{M,h}$), are calculated using the formula (as a percentage of nominal current, $\%I_N$):

$$I_{M,h} = 100 \cdot U_{M,h} / Z_{M,h} \ \ \left(\%I_N \right) \tag{46}$$

Harmonic losses in the motor, which are caused by harmonic currents through the windings of stator and rotor, are calculated using the formula (as a percentage of nominal motor power, $\%P_N$):

$$P_{Cu,h} = 100 \cdot \frac{R_{M,h} \cdot I_{M,h}^2}{\eta \cdot \cos\phi} \ \ \left(\%P_N \right) \tag{47}$$

Commonly, these power losses are calculated as a percentage of nominal power losses in motor windings (%P_{CuN}). Thus, assuming that losses P_{CuN} make up one half of the total power losses in the motor, their value can be determined from the formula:

$$P_{Cu,h} = 100 \cdot \frac{R_{M,h} \cdot I_{M,h}^2}{\eta \cdot \cos\phi} \cdot \frac{2\eta}{1-\eta} \left(\%P_{CuN}\right) \tag{48}$$

4.3. Current harmonics and harmonic losses in motors supplied from the network with voltage harmonics

The harmonic fields induce a current in the rotor and, as a result of interaction, are given corresponding asynchronous torques. The direction of these harmonic torques coincides with the fundamental torque direction, when h=6n+1, and harmonic torque is the opposite to the fundamental torque direction when h=6n-1. In a motor regime with slip equal to s = 0.01–0.06, in relation to the rotating fields of harmonics, the slip is approximately equal to 1, $s_h = 1 \pm 1/h \approx 1$.

In Radin et al. (1989), the following assumptions (partly wrong ones) are often listed:

- for motors of lower powers (≤ 20 kW), stator and rotor coil resistances and inductances practically do not depend on frequency, so the only values that become increased are the values of the stator and rotor leakage reactance ($X_{sh} = hX_s$, $X_{rh} = hX_r$),
- for motors of medium power (30-100 kW), rotor resistance is increased according to formula $R_{rh} \approx hR_r$, and
- for motors of high power (≥ 110 kW), both stator and rotor resistance are increased according to formula $R_{sh} \approx hR_s$ and $R_{rh} \approx hR_r$,

while the reactance values are somewhat reduced, $X_{sh} \leq hX_s$, $X_{rh} \leq hX_r$, since the values of corresponding inductances are decreased, $L_r(hf) < L_r$ and $L_s(hf) \leq L_s$.

The truth however is slightly different (Kostic, 2010):

- values of the stator resistance and inductance are practically unchanged in all low-voltage motor powers of 100–300 kW,
- the value of the slot resistance of the rotor in short-circuit mode (in relative units) is slightly changed with motor power, so it could be considered $R_{r\text{-}sl,sc} \approx 0.030$ p.u., as it is shown in Kostic (2010),
- rotor resistance on the part outside the slot is approximately given by the expression $R_{r\text{-}e\text{-}} \approx R_r/3 \approx R_s/3$.

By this and (43), an expression for determining the value of the motor resistance $R_{M,h}$ for harmonic order $h \geq 5$ is obtained:

$$R_{Mh} = \frac{4}{3} R_s + 0.03 \cdot \sqrt{h} \tag{49}$$

Example 1

For motors with power 5 kW - 400 kW, in the same order, the ranges of parameter values are given (Kravcik, 1982) for:

- efficiency factor $\eta = 0.85 - 0.95$ and power factor $cos\phi = 0.85 - 0.92$, i.e. $\eta \cdot cos\phi = 0.72 - 0.875$,
- stator resistance (R_s), for example from $R_s = 0.045Z_N$ to $R_s = 0.015Z_N$,

and the

- the corresponding values of stator harmonic resistances $R_{s,h} = R_s = 0.015Z_N \div 0.050Z_N = Const.$,
- the corresponding value of rotor resistance $R_{r,h} = 0.03\sqrt{h}$,
- the corresponding values of motor resistance $R_{M,h}$, according to (43)
- the corresponding values of motor reactance $X_{M,h}$, according to (44),
- the corresponding values of motor impedance $Z_{M,h}$, according to (45),
- harmonic currents, according to (46), and
- the value of the harmonic losses, as a percentage of nominal motor power $P_{M,h}[\%P_N]$, according to (47), and as a percentage of nominal power losses in the windings $P_{M,h}[\%P_{Cu,N}]$ according to (48).

Application of the suggested method is illustrated by Tab. 6. The results show the amounts of increase in power losses due to the presence of harmonics in a given amount ($U_i = 5\%$, $i = 5, 7, .., 37$) in the supply voltage.

$h=f/f_1$	$U_{h,i}$	R_s	$R_{r,h}$	$R_{M,h}$	$X_{M,h}$	$Z_{M,h}$	$I_{M,h}$ $[\%I_n]$	$P_{M,h}$ $[\%P_n]$	$P_{M,h}$ $[\%P_{Cun}]$
1	1.00	0.015 - 0.05	0.030	0.045 - 0.080	0.161	0.167 - 0.180			
5	0.05	0.015 - 0.05	0.067	0.072 - 0.117	0.735	0.739 - 0.744	6.748	0.039 - 0.074	1.482 - 0.839
7	0.05	0.015 - 0.05	0.079	0.094 - 0.129	1.018	1.022 - 1.053	4.822	0.026 - 0.042	0.988 - 0.476
11	0.05	0.015 - 0.05	0.099	0.114 - 0.144	1.579	1.583 - 1.586	3.157	0.014 - 0.020	0.532 - 0.227
13	0.05	0.015 - 0.05	0.108	0.123 - 0.158	2.416	2.419 - 2.421	2.066	0.006 - 0.010	0.228 - 0.113
17	0.05	0.015 - 0.05	0.124	0.129 - 0.174	2.694	2.643 - 2.646	1.891	0.006 - 0.009	0.228 - 0.102
19	0.05	0.015 - 0.05	0.131	0.146 - 0.181	3.249	3.252 - 3.254	1.537	0.004 - 0.006	0.152 - 0.068
23	0.05	0.015 - 0.05	0.144	0.159 - 0.194	3.526	3.534 - 3.536	1.414	0.004 - 0.005	0.152 - 0.057
25	0.05	0.015 - 0.05	0.150	0.165 - 0.200	3.833	3.836 - 3.838	1.303	0.003 - 0.005	0.114 - 0.057
29	0.05	0.015 - 0.05	0.212	0.177 - 0.212	4.080	4.084 - 4.086	1.224	0.003 - 0.005	0.114 - 0.057
31	0.05	0.015 - 0.05	0.167	0.182 - 0.217	4.357	4.361 - 4.362	1.147	0.003 - 0.004	0.114 - 0.045
35	0.05	0.015 - 0.05	0.177	0.192 - 0.227	4.910	4.919 - 4.920	1.016	0.002 - 0.003	0.076 - 0.034
37	0.05	0.015 - 0.05	0.182	0.197 - 0.232	5.187	5.191 - 5.192	0.963	0.002 - 0.003	0.076 - 0.034
Total	THD_u = 7.3%					THD_i =9.87%		$\Sigma P_{M,h}$ 0.112 - 0.186	$\Sigma P_{M,h}$ 4.256 - 2.109

Table 6. Values of harmonic resistances ($R_{M,h}$), reactances ($X_{M,h}$) and impedances ($Z_{M,h}$) and corresponding currents and harmonic losses for motors > 100 kW (left) and < 5 kW (right), for the given values of voltage harmonics $U_{h,i}$ (p.u.) = 5%

The results in Tab. 6 show that, at the maximum permitted content of harmonics in supply voltage ($U_{h,i}$ = 5%, i = 1–37), the percentage of harmonic losses, (in units of the nominal motor power $P_{M,h}$ [%P_N]), is relatively low:

- for motors of lower power (< 5 kW), an increase of losses is by about 0.186%P_N, so a decrease in efficiency is by about 0.2%, which is slightly less compared to 0.25% in Radin et al. (1989),
- for motors of greater power (> 100 kW), an increase of losses is by about 0.112%P_N, so a corresponding decrease in efficiency is by about 0.12%.

Increments of harmonic losses are relatively small, as a percentage of nominal power losses $P_{M,h}$ [%$P_{Cu,N}$]. Apparently:

- increase of losses is about 2.109% $P_{Cu,N}$, for motors of lower power (< 5 kW),
- increase of losses is about 4.256%$P_{Cu,N}$, for motors of greater power (> 100 kW).

By the results in Tab. 6, for $U_{h,i}$ = Const (example $U_{h,i}$ = 5%, h_i = 1–37, as in Tab. 6), the following approximate equations is confirmed:

$$\frac{P_{Cu,h2}}{P_{Cuh1}} \approx \frac{h_1}{h_2}\sqrt{\frac{h_1}{h_2}}, \quad for\ U_{h5} = U_7 = U_{hi} = Const, for h_i \le 40 \tag{50}$$

Equation (50) is derived by the following approximate assumptions: $Z_{Mh} \approx X_{Mh} \approx hX_{M,SC}$ and $R_{Mh} \approx R_{r,h} \approx R_{r,SC} \cdot \sqrt{h}$.

4.4. Harmonic losses when the motor is operating with rectangular shaped voltage

When a motor is supplied by rectangular shaped voltage $U_{h,i}$ (p.u.) = $1/h_i$, h_i = 1 to 37, it is required to calculate the correspondent approximate values of harmonic losses for motors with nominal powers from 5 kW to 400 kW (i.e. for the values of stator resistance from $R_s = 0.045Z_N$ to $R_s = 0.015Z_N$ and correspondent approximate values in a short-circuit regime, $R_{r,SC} \approx 0.03$, for each motor. For motors within the power range 3 kW-400 kW, for which parameters are given in chapter 4.3, power losses are determined.

The given results in Tab. 7 show that, in the specified harmonic content h = 1, 5, 7, 11, 13, 17, 19 ...35 and 37, the percentage of additional power losses, $P_{M,h}$ [%P_N], is relatively high:

- for motors of greater power (>100 kW), an increase of losses is by about 0.94%P_N, so a decrease in efficiency is by 1%,
- for motors of lower power (3-10 kW), an increase of losses is by about 1.68%P_N, so a decrease in efficiency is by 1.7%.

The literature (Radin et al., 1989) often states that the percentage of increase of power losses in the windings of stator and rotor is due to the harmonics in $P_{M,h}$ [%$P_{Cu,N}$]. Data from Tab. 6, column $P_{M,h}$ [%$P_{Cu,N}$], show that:

- an increase of losses is by 19.05%$P_{Cu,N}$, for motors of power (3–10 kW),
- an increase of losses is by 34.92%$P_{Cu,N}$, for motors of greater power (>100 kW).

This last figure corresponds to the values that are found in the literature, while the value of 19.05%$P_{Cu,N}$, for motors of lower power (3–10 kW), is much higher than the figure which is referred to in the literature (by about 5–10%). The reason for this lies in the fact that it is (wrongly) believed that the resistance of the rotor does not change for harmonic frequencies, i.e. that is identical for all harmonics ($R_{r,h} = R_{r,1} = R_r = Const$), which brings the difference mentioned above - and error. However, things are different because the rotor resistance is variable: $R_{r,h} > R_{r,SC} > R_{r,1}$, (Kostic, 2010; Kostic M. & Kostic B., 2011). To be precise, the values of rotor slot resistance are higher and the values of rotor slot inductance are √h times lower as compared to those values for the fundamental harmonic in short-circuit mode.

Some examples from the literature can be used as proof of the view that the rotor resistance changes for low power motors. Specifically in Vukic (1985), the influence of harmonics on the motor of low power (1.6 kW) was tested. The calculation results, which were carried out assuming that $R_r = Const$, gave an increase in power losses of 12.6%, while the experimental measurements showed that the actual increase in losses was 18.5%. Our calculations give rise to losses of 19%, which slightly differs from the measured values. The accuracy of our calculations has been increased with respect to the fact that slot reactance of the rotor increases √h times, for the harmonics of order *h*.

$h=f/f_1$	$U_{h,i}$	R_s	$R_{r,h}$	$R_{M,h}$	$X_{M,h}$	$Z_{M,h}$	$I_{M,h}$ [$\%I_n$]	$P_{M,h}$ [$\%P_n$]	$P_{M,h}$ [$\%P_{Cun}$]
1	1.00	0.015-0.05	0.030	0.045-0.080	0.161	0.167-0.180			
5	0.20	0.015-0.05	0.067	0.072-0.117	0.735	0.739-0.744	26.990	0.618-1.184	23.447-13.418
7	0.14	0.015-0.05	0.079	0.094-0.129	1.018	1.022-1.053	13.790	0.213-0.341	7.668-3.864
11	0.11	0.015-0.05	0.099	0.114-0.144	1.579	1.583-1.586	7.010	0.069-0.099	2.504-1.122
13	0.08	0.015-0.05	0.108	0.123-0.158	2.416	2.419-2.421	3.180	0.015-0.022	0.556-0.252
17	0.06	0.015-0.05	0.124	0.129-0.174	2.694	2.643-2.646	2.230	0.007-0.012	0.244-0.136
19	0.05	0.015-0.05	0.131	0.146-0.181	3.249	3.252-3.254	1.600	0.005-0.007	0.180-0.079
23	0.04	0.015-0.05	0.144	0.159-0.194	3.526	3.534-3.536	1.220	0.003-0.004	0.106-0.046
25	0.04	0.015-0.05	0.150	0.165-0.200	3.833	3.836-3.838	1.040	0.002-0.003	0.075-0.036
29	0.03	0.015-0.05	0.162	0.177-0.212	4.080	4.084-4.086	0.830	0.001-0.002	0.036-0.025
31	0.03	0.015-0.05	0.167	0.182-0.217	4.357	4.361-4.362	0.730	0.001-0.002	0.036-0.025
35	0.03	0.015-0.05	0.177	0.192-0.227	4.910	4.919-4.920	0.590	0.001-0.002	0.036-0.025
37	0.03	0.015-0.05	0.182	0.197-0.232	5.187	5.191-5.192	0.520	0.001-0.002	0.036-0.025
Total	THD_u = 30.3%					THD_i =31.5%		$\Sigma P_{M,h}$ 0.94 -1.68	$\Sigma P_{M,h}$ 34.92-19.05

Table 7. Values of harmonic resistances ($R_{M,h}$), reactances ($X_{M,h}$) and impedances ($Z_{M,h}$); as harmonic currents ($I_{M,h}$) and harmonic losses ($P_{M,h}$) for motors with power > 100 kW (left) and lower power, 3–10 kW (right), when the motor is supplied by the rectangular voltage, i.e. by voltage with harmonics $U_{hi} = 1/h_i$.

As R_s=0.050÷0.015, respectively, for motors of power 3÷200 kW, the given results are useful for the evaluation of harmonic currents ($I_{M,h}$) and harmonic losses ($P_{M,h}$) for all mentioned motors, by extrapolation.

5. Summary

The results of the analysis presented in this chapter are summarised in the following.

A) Effect of voltage magnitude on motor power losses and motor reactive loads

The results of the research show dependencies of the input power and reactive load on voltage magnitude, as given in Fig. 2.

1. Decreasing voltage magnitude by 1%, by setting voltages in range of U_n±5%, leads to:
   a. reactive loads decreasing
      - from 1% to 2%, at loads from 100% to 75%, respectively, for motors above100 kW,
      - up to 3% to 4%, at loads from 75% to 25%, respectively, for motors below 10 kW;
   b. power losses (and active input powers) decreasing/increasing (sign „ - ")
      - from (-0.1%) to 0.1%%, respectively at loads from 100% to 50%, for motors above100 kW
      - from 0% to 0.6%, respectively at loads from 100% to 25%, for motors about 10 kW,
      - from 0% to 1.6%, respectively, at loads from 100% to 25%, for motors below 1 kW.
2. On the basis of the investigation presented in this paper, it is confirmed that there are significant possibilities for energy savings by means of voltage magnitude setting, within values U_n±5%, in networks with induction motors which are light loaded (<70%).
3. Setting voltage within band $0.9\,U_n$ - $0.95\,U_n$ is not recommended, even if it leads to reduced power losses and reactive loads, because starting and maximal torque are decreased and it can also cause motor operation instability.

B) The most important conclusions regarding motor operation with the unbalanced voltage

4. It is explained that the rotor inverse resistance and rotor inverse reactance are higher for √2 times compared to the rotor resistance and rotor reactance in short-circuit mode, since current frequency of the negative sequence in the rotor winding is twice as high ($f_{r,NS} \approx 2f_1 = 2f_{r,SC}$), i.e. they are higher by 1.41 times than the corresponding values given in the literature.
5. Voltage unbalance causes increase of the motor heating, occurrence of inverse torques and a small increase in motor slip. Thus, for the voltage asymmetry of 2%, 3%, 4% and 5%, this causes an increase in power losses of 5.5%, 12%, 22% and 34% of motor nominal losses. Corresponding values of derating factors are 0.97, 0.94, 0.88 and 0.81, respectively, as noted in NEMA standards, so the acceptable voltage asymmetry is 2%.
6. Based on the actual calculation and analysis, it was found that the effects of an unbalance on power loss are smaller for motors of nominal power ≤ 10 kW. Thus, acceptable voltage asymmetry for these motors could be 3%.
7. Generally, motor operation is not allowed when voltage asymmetry is greater than 5%, because, in some cases, current and losses in one phase could be increased for 38% and 90%, respectively.

C) The most important conclusions regarding motor operation with the non-sinusoidal voltage

8. The given results show that, at the maximum permitted content of harmonics in supply voltage, $U_{h,i}$ = 5%, i = 1 to 37), the percentage of harmonic losses is relatively small:
   - about 2.109% $P_{Cu,N}$, for motors of lower power (< 5 kW), and
   - about 4.256%$P_{Cu,N}$, for motors of greater power (> 100 kW).
9. When the induction motors are supplied by rectangular shaped voltage with high levels of harmonic voltages, an increase in harmonic losses in stator and rotor windings are:
   - around 30-35% $P_{Cu,N}$, for high power motors (> 100 kW), and
   - around 15-20% $P_{Cu,N}$, for lower power motors (3–10 kW).

The increase in harmonic power losses for lower power motors is much higher than it was noted in the literature (5-10%) because it is (wrongly) believed that the resistance of the rotor does not change for higher harmonic frequencies.

Appendix

For deriving equations for electromagnetic torque and power, the equivalent Γ-circuit, shown in Fig. 13, is used (Kostic, 2010):

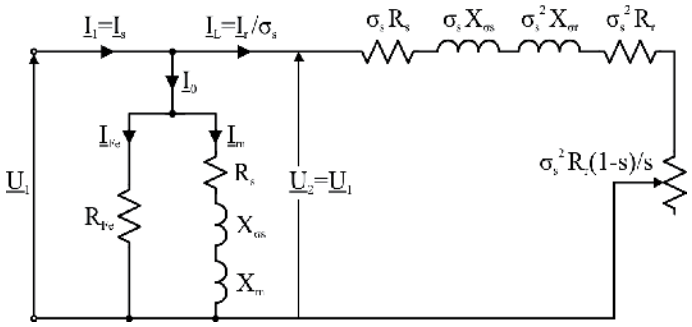

Figure 13. Equivalent Γ-circuit of induction machine

Equation (9) is completely derived in this Appendix.

1. Electromagnetic power ($P_{em,N}$) **at rated load**, i.e. at slip s=s_N, can be expressed as following:

$$P_{em,N} = T_{em,N} \cdot \Omega_1 = \frac{I_L^2 \cdot \sigma_s{}^2 R_r}{s_N} = \frac{U_1^2 \cdot \sigma_s{}^2 R_r / s_N}{(\sigma_s R_s + \sigma_s{}^2 R_r)^2 + (\sigma_s X_s + \sigma_s{}^2 R_r / s_N)^2} \tag{51}$$

For motors with power within the range of 1÷200kW, values for s_N are 0.05÷0.01, respectively, and therefore: $\sigma_s^2 R_r/s_N = (20 \div 100) \cdot \sigma_s R_s$ and $\sigma_s X_s + \sigma_s^2 X_r) \approx 0.20 \cdot \sigma_s^2 R_r/s_m$.

$$P_{em,N} = T_{em,N} \cdot \Omega_1 = \frac{I_L^2 \cdot \sigma_s{}^2 R_r}{s_N} \approx \frac{U_1^2 \cdot \sigma_s{}^2 R_r / s_N}{(1.15 \div 1.05)^2 (\sigma_s{}^2 R_r / s_N)^2} = \frac{U_1^2}{(1.15 \div 1.05)(\sigma_s^2 R_r / s_N)} \tag{52}$$

2. **Regime with maximum input power,** i.e. at $s=s_{Pm}$, accrues when resistance ($\sigma_s X_{\sigma s}+\sigma_s^2 X_{\sigma r}$) and reactance in load branch ($\sigma_s R_s+\sigma_s^2 R_r/s_m$) are equal, i.e., and when the load branch impedance is $Z_{2,m}=\sqrt{2}(\sigma_s X_{\sigma s}+\sigma_s^2 X_{\sigma r})$. Corresponding electromagnetic power ($P_{em,Pm}$) on the resistance $\sigma_s^2 R_r/s_m$ is:

$$P_{em,Pm}=T_{em,Pm}\Omega_1=I_L^2\cdot\sigma_s{}^2\frac{R_r}{s_{Pm}}=\frac{U_1^2\cdot\sigma_s{}^2R_r/s_{Pm}}{2(\sigma_\sigma X_{\sigma s}+\sigma_\sigma{}^2X_{\sigma r})^2} \tag{53}$$

Since for motors with power within the range of 1÷200kW, values for corresponding slip are s_{Pm} = 0.25÷0.05, respectively, the skin effect in the bars of the squirrel-cage is minor (the depth of penetration $\delta_r(s_m f_1)\geq H_b$-the bar (conductor rotor) height), so it is $\sigma_s^2 R_r/s_m$ = (5÷20) $\sigma_s R_s$. Consequently, it is:

$$\sigma_s^2R_rs_{Pm}=(0.8\div0.95)\cdot(\sigma_sR_s+\sigma_s^2R_r/s_{Pm})=(0.8\div0.95)\cdot(\sigma_sX_{\sigma s}+\sigma_s^2X_{\sigma r}) \tag{54}$$

and the electromagnetic power ($P_{em,m}$), in the regime with maximum input power, is:

$$P_{em,Pm}=T_{em,Pm}\cdot\Omega_1=\frac{I_L^2\cdot\sigma_s{}^2R_r}{s_{Pm}}\approx\frac{U_1^2\cdot(0.8\div0.95)(\sigma_sX_{\sigma s}+\sigma_s{}^2X_{\sigma r})}{2\cdot(\sigma_sX_{\sigma s}+\sigma_s{}^2X_{\varsigma r})^2}=\frac{U_1^2\cdot(0.8\div0.95)}{2\cdot(\sigma_sX_{\sigma s}+\sigma_s^2X_{\sigma r})} \tag{55}$$

3. If $\sigma_s^2 R_r/s_N$ is expressed from (A-4), and ($\sigma_s X_{\sigma s}+\sigma_s^2 X_{\sigma r}$) is expressed from (A-5), then it is:

$$\sigma_s{}^2R_s+\sigma_s{}^2R_r/s_N=\frac{U_1^2}{T_{em,N}\cdot\Omega_1(1.15\div1.05)} \tag{56}$$

$$\sigma_sX_{\sigma s}+\sigma_s{}^2X\sigma_r=\frac{U_1^2\cdot(0.8\div0.95)}{2T_{em,Pn}\cdot\Omega_1} \tag{57}$$

On the base of (A-6) and (A-7), it is obtained:

$$\frac{\sigma_sX_{\sigma s}+\sigma_s{}^2X_{\sigma r}}{\sigma_s{}^2R_s+\sigma_s{}^2R_r/s_N}=\frac{T_{em,N}}{2T_{em,Pm}}\cdot(0.8\div0.95)\cdot(1.15\div1.05) \tag{58}$$

Reactive power in the load branch of Γ-circuit, under rated condition, $Q_{2N}\approx Q_{LN}$ (Q_{LN} – load component of reactive power), can be expressed in terms of the electromagnetic power, $P_{em,N}$

$$Q_{2N}=P_{em,N}\cdot\frac{\sigma_sX_{\sigma s}+\sigma_s{}^2X\sigma_r}{\sigma_s{}^2R_s+\sigma_s{}^2R_r/s_N}\approx Q_{LN} \tag{59}$$

Since the relation between the electromagnetic power ($P_{em,N}$) and the rating power (P_N) is:

$$P_{em,N}=P_N\cdot\frac{\sigma_s^2R_s+\sigma_s^2R_r/s_N}{(\sigma_s^2R_r/s_N)}\cdot\frac{1}{1-s_N} \tag{60}$$

then, based on equations (A-7), (A-9) and (A-10), it follows:

$$Q_{LN} = P_N \cdot \frac{T_{em,N}}{2T_{em,Pm}} \cdot \frac{(0.08 \div 0.95) \cdot (1.15 \div 1.05)}{0.95 \div 0.99} = \frac{T_{em,N}}{2T_{em,Pm}} \cdot (0.98 \div 1.01) \approx 0.5 P_N / (T_m / T_N) \quad (61)$$

$$Q_{LN} \approx P_N \cdot \frac{T_{em,N}}{2T_{em,Pm}} = 0.5 \cdot \frac{T_{em,N}}{T_{em,Pm}} \quad (62)$$

Since the maximum torque ($T_m \approx T_{em,m}$), which is catalogue data, is greater up to 2% from mentioned torque ($T_{em,Pm}$) in the regime with maximum input power, i.e. $T_{em,Pm} \leq 1.02\, T_m$, it might be concluded that the equation (9) sufficiently accurate for calculating the rating component of reactive power in load branch, $Q_{LN}=0.5 \cdot P_N/(T_m/T_N)$.

Author details

Miloje Kostic
Electrical Engineering Institute "Nikola Tesla", Belgrade University, Belgrade, Serbia

6. References

Aníbal, T. de Almeida Fernando J. T. E. Ferreira; João Fong & Paula Fonseca (December 2007). *EUP Lot 11 Motors, Final Report*, ISR-University of Coimbra, Lot 11-8-280408.

Boldea, I.S. & Nasar, A. (2002). *The Induction Machine Handbook*, 2002 by CRC Press LLC.

Bonnett, A.H. (2000). An overview of how AC induction motors' performance has been affected by the October 24, 1997 Implementation of the Energy Policy Act of 1992, *IEEE Transaction on Industry Applications*, Vol.36, No1, 2000, pp. 242-256.

Fei, R.; Fuch, E.F.& Huang, H. (December 1989). Comparison of two optimization techniques as applied to three-phase induction motor design, *IEEE Transactions energy Conversion*, Vol.4, pp. 651-660, December 1989.

Fink, D.G. (1983). *Standard Handbook for Electrical Engineers* (1983), 11th Edition McGraw-Hill Book Company, 1983, New York, pp. 2462, ISBN 0-07-020974-X

Hamer, P. S.; Love, D. M. & Wallace, S. E. (1997). Energy Efficient Induction Motors Performance Characteristic and Life Cycle Cost Comparison for Centrifugal Loads, *IEE Trans. Ind. Applications*, No. 5, 1997, pp. 1312-1320.

IEC 60034-30 (2008). *Efficiency classes of single speed three-phase cage induction motors*.

IEC 60034-31 (2010). *Guide for selection and application of energy-efficient motors including variable-speed applications.*

Ivanov-Smolensky, A. (1982). *Electrical Machines*, Vol. 2, Mir Publishers, 1982, pp. 464.

Kostic, M (2010). *Energy Efficiency Improvement of Motors in Drives*, Electrical Engineering Institute Nicola Tesla, Belgrade, 2010, pp.325 (in Serbian), ISBN 978-86-83349-11-1.

Kostic, M. & Kostic, B. (2011). Motor Voltage High Harmonics Influence to the Efficient Energy Usage, Invited paper for *15th WSEAS International Conference on Systems, Proc. pp.* 276-281, Corfu Island, Greece, July 2011.

Kostic, M. & Nikolic, A. (August 2010). Negative Consequence of Motor Voltage Asymmetry and Its Influence on the Inefficient Energy Usage, *Wseas Transaction On Circuits And Systems*, Issue 8, Volume 9, August 2010, pp. 547-556.

Kostic, M. (1998). Reduction of loads and electric energy consumption by setting voltage magnitude, *Elektroprivreda Magazine*, *No. 3, 1998*, pp 65-78 (in Serbian).

Kostic, M. (2001). Evaluation methods for load and efficiency of induction motor in the exploitation, *11th International Symposium Ee 2001*, Novi Sad, Serbia, pp.332-336.

Kostic, M. (2010). Equivalent circuit parameters of the squirrel-cage induction motors in short circuit regime, *Tehnika*, *separate Elektrotehnika* 5/2010), pp. 7E-13E (in Serbian).

Kostic, M.; Stanisavljevic, I.; Ivanovic, M.; Jankovic, R.; Mihajlovic, Lj. & Vasic, P. (2006). The Reduction of Own Electric Energy Consumption of Thermal Power Plants, *Symposium Power Plants 2006*, Vrnjacka Banja, Serbia, 2006, No paper 59.

Kravčik. A.E. (1982). *Induction Machines Handbook* (Moscow, 1982), p. 504, (in Russian).

Linders, J.R. (July/August 1972). Effects of Power Supply Variations on AC Motor Characteristics, *IEEE Transaction on Ind. Applic.* Vol. IA-8", No 4, 1972, pp. 383-400.

Radin, I.; Bruskin & Zorohovič, A.E. (1989). *Electrical machines: Induction machines* (Moscow, 1989), p. 328 (in Russian).

Vukic, DJ. (1985). Time Harmonics Influence on Operating of Induction Motors, *Tehnika*, separate Elektrotehnika 12/1985), pp.11E-13E (in Serbian).

Chapter 6

Role of Induction Motors in Voltage Instability and Coordinated Reactive Power Planning

Venkat Krishnan and James D. McCalley

Additional information is available at the end of the chapter

http://dx.doi.org/10.5772/52480

1. Introduction

As the power system is being operated in an economic and environment friendly fashion, there is more emphasis on effective resource utilization to supply the ever increasing demand. Consequently system experiences heavy power transaction, and one of the very important stability phenomena, namely voltage stability, is capturing the attention of many power system engineers, operators, researchers, and planners. Concerns for voltage instability and collapse are prompting utilities to better understand the phenomenon so as to devise effective, efficient and economic solutions to the problem.

Past studies have investigated the intricate relationship that exist between insufficient reactive power support and unreliable system operation including voltage collapses [1, 2, 3, 4], as was observed in 2003 blackout of USA [5]. It is not just the amount of reactive support, but also the quality and placement of reactive support that matters. For instance, it is found that due to the presence of electric loads that are predominantly induction motors the voltage recovery of the system following a severe disturbance is delayed due to lack of fast responding reactive support, thereby threatening to have secondary effects such as undesirable operation of protective relays, electric load disruption, and motor stalling [6, 7]. While a number of techniques have been developed in the past to address the problems of voltage instability [8], there has been little work towards a long term reactive power (VAR) planning (RPP) tool that addresses both steady state as well as dynamic stability issues.

The available reactive power devices can be classified into static and dynamic devices [9]. The static devices include mechanically switched shunt capacitors (MSCs) and series capacitors that exert discrete open-loop control action and require more time delay for correct operation. The dynamic devices are more expensive power electronics based fast-acting devices such as static VAR compensators (SVC), Static Synchronous Compensator (STATCOM), Unified Power Flow Controller (UPFCs) that exert continuous feedback

control action and have better controllability and repeatability of operation. While MSCs are able to strengthen a power system against long term voltage instability issues [1], transient voltage dip and slow voltage recovery issues (influenced by electric load dynamics) is most effectively addressed by fast responding dynamic VAR sources [10, 11, 12]. While, past methods allocate static and dynamic VAR sources sequentially for one contingency at a time, the key to solving transmission system problems in the most cost-effective way will be to coordinate reactive power requirements simultaneously under many contingencies for both static and dynamic problems. The RPP should therefore identify the right mix of VAR devices, good locations and appropriate capacities for their installation.

In this chapter, we present a long term VAR planning algorithm, which coordinates between network investments that most effectively address steady-state voltage instability and those which most effectively address transient voltage recovery problems under severe contingencies. The study takes into account the induction motor dynamic characteristics, which influence the transient voltage recovery phenomenon. The algorithm is applied on a portion of a large scale system consisting of 16173 buses representing the US eastern interconnection. The planning method is a mixed integer programming (MIP) based optimization algorithm that uses sensitivity information of performance measures with respect to reactive devices to plan for multiple contingencies simultaneously.

The remaining parts of this chapter are organized as follows. In section 2, we discuss the very important role played by induction motor loads in the voltage stability phenomena. Section 3 sheds focus on the models used to build a base case for voltage stability assessment, and on appropriate performance criteria and solution strategies used in this chapter to devise the proposed coordinated planning. A summary of proposed RPP algorithm that considers both static as well as dynamic reactive resources in a coordinated planning framework, together with the various stages of planning are presented in Section 4. Section 5 illustrates the influence of induction motors on voltage stability phenomenon under severe contingencies, and demonstrates application of the coordinated VAR planning method on a large scale system to effectively avoid induction motor trips. Section 6 presents the conclusions.

2. Voltage instability phenomena

Several theories have been proposed to understand the mechanism of voltage instability. Voltage instability leading to collapse is system instability in that it involves many power system components and their variables at once. There are several system changes that can contribute to voltage collapse [4] such as increase in loading, SVC reaching reactive power limits, action of tap changing transformers (LTCs), load recovery dynamics, line tripping and generator outages. Most of the above mentioned system changes have a large effect on reactive power production or transmission. To discuss voltage collapse some notion of time scales is needed that accounts for fast acting variables in time scales of the order of seconds such as induction motors, SVCs to slow acting variables having long term dynamics in hours such as LTCs, load evolution etc.

2.1. Role of induction motors

A major factor contributing to voltage instability is the voltage drop that occurs when active and reactive power flow through inductive reactance of the transmission network; which limits the capability of the transmission network for power transfer and voltage support [13]. The power transfer and voltage support are further limited when some of the generators hit their field or armature current time-overload capability limits. Under such stressed conditions, the driving force for voltage instability is usually the inductive loads that try to recuperate after a disturbance. For instance, in response to a disturbance, power consumed by the induction motor loads tends to be restored by the action of motor slip adjustment, distribution voltage regulators, tap-changing transformers, and thermostats [6]. Restored loads increase the stress on the high voltage network by increasing the reactive power consumption and causing further voltage reduction. A run-down situation causing voltage instability occurs when load dynamics attempt to restore power consumption beyond the capability of the transmission network and the connected generation to provide the required reactive support.

The publication [14] corroborates this voltage instability phenomenon by means of a power-voltage (PV) curve, as shown in Figure 1. For a particular system and loads considered, the normal system can be stable with both resistive and motor loads at points where load curves and system curves intersect. However, when the system becomes stressed, with increased system reactance, it can only have a stable operating point with a resistive load. Due to lack of reactive power support that limits the transfer capability or loadability of the system, there is no intersection of system and load curves for the induction motor load since there is no stable operating point.

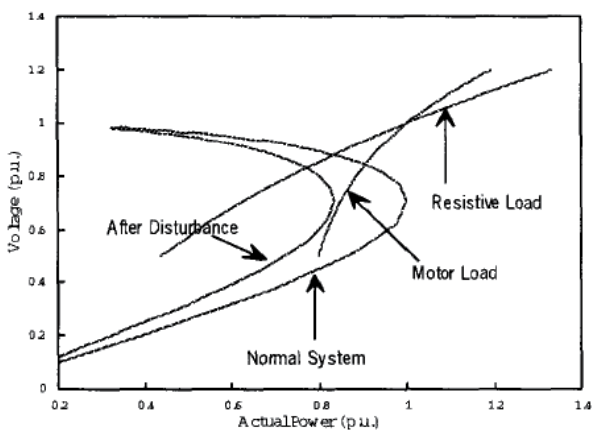

Figure 1. Stability and Load Characteristics

2.2. A typical scenario of slow voltage recovery leading to collapse

Heavily loaded transmission lines during low voltage conditions can result in operation of protective relays causing some transmission lines to trip in a cascading mode. A common

scenario is a large disturbance such as a multi-phase fault near a load center that decelerates induction motor loads. Following fault clearing with transmission outages, motors draw very high current while simultaneously attempting to reaccelerate, as discussed in previous section, thereby making slowing down the voltage recovery process. A typical slow voltage recovery phenomenon following a disturbance is indicated in Figure 2 [15]. While trying to recover, if the voltage drops to a very low point for a sustained duration due to system's inability to provide reactive support, some motors may stall. Such drastic stalling of motor further exacerbates the conditions by increasing the reactive power requirements quickly, and the rate of voltage decline can accelerate catastrophically [6, 7, 16]. Massive loss of load and possibly area instability and voltage collapse may follow.

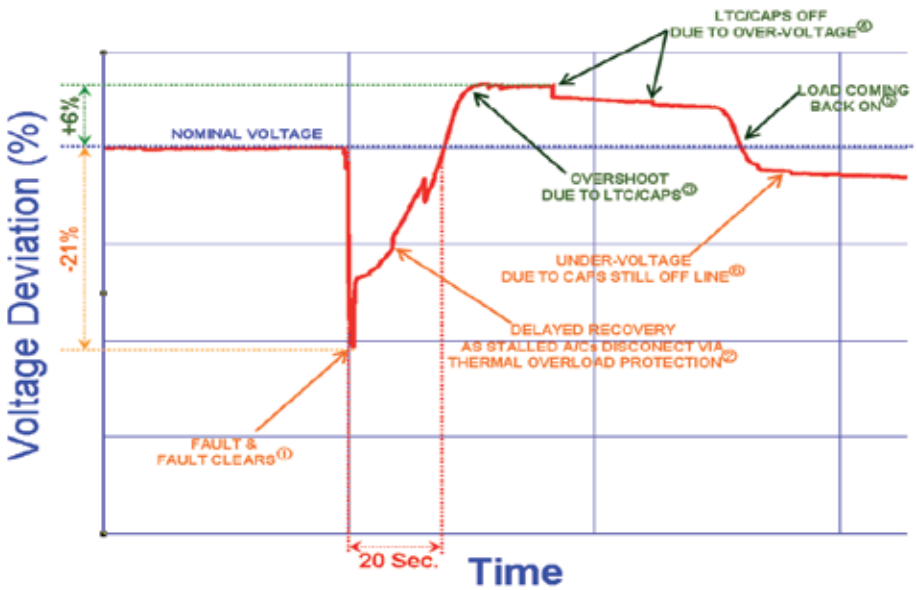

Figure 2. Post-Fault Transient Voltage Characteristics

There are several works [10] that have documented many short-term (few seconds) voltage collapse incidents with loss of load. In all cases, adequate dynamic reactive power support was not available which resulted in a large loss of load.

All the above discussions give a physical sense of how the problem of voltage instability occurs, and shed importance on the requirement of study techniques and good models, especially of induction motor dynamics as they are particularly hazardous from the viewpoint of voltage stability.

3. Voltage stability assessment and criteria

Traditionally, voltage stability investigations have been based on steady-state analyses, which involve solving conventional or modified power flow equations [17]. In such studies

system P-V curve and the sensitivity information derived from the power flow jacobian are used to assess and plan for voltage instability. But the realization that voltage stability is a dynamic phenomenon has led to dynamic formulations of the problem and application of dynamic analysis tools [18] that uses time-domain simulations to solve nonlinear system differential algebraic equations.

A pre-contingency steady state base case is required for the voltage stability study to be performed, which is usually generated from real-time sequence control (State estimator solution), or via an already recorded power flow solution. In the case of a base case for dynamics study, as discussed in previous section, the dynamic phenomenon of voltage stability is largely determined by load characteristics and the available means of voltage control. The response speeds of these loads may be comparable to the speed of response of the dynamic voltage control equipment. So in such studies involving dynamic phenomena, using static models will give forth dubious results. So it is very important to properly model dynamic behavior of such large, small and trip induction motor loads; along with that of relevant voltage controls. Investigating the post-fault dynamic system response and effective planning to prevent a voltage collapse depends on inclusion of relevant system component models.

3.1. System component models

This section presents the various components and their relevant models that are required to build a suitable base case for comprehensive voltage stability assessment and planning.

3.1.1. Static device models

1. **Transmission lines** are represented as pi-sections, possibly with unsymmetrical line charging; accompanying data include line pi-section impedances/admittances data; line thermal limit both normal and emergency.
2. **Transformers** represented as pi-sections whereby the various impedance/admittance components may be explicit functions of tap settings; three winding transformers must be properly modeled. The data also include transformer limits under normal/emergency cases. **Phase-shifting transformers** are represented by complex tap ratios, allowing both shift in angle and change in voltage magnitude;
3. **Generators** as real-power source together with a reactive power capability curve as a function of terminal voltage; The required generator static data include minimum and maximum ratings, nominal terminal voltage and reactive power capability curve as a function of terminal voltage
4. **Shunt elements** by their impedance/admittance and Static Var compensators by static gain and maximum/minimum limits
5. **Loads** by ZIP model, i.e., as a combination of constant impedance (Z), constant current (I), and constant real/reactive injection (P) components; The data necessary are default ZIP load partition ratios at nominal voltage, load limits and default power factors

3.1.2. Dynamic device models

1. **Machine** mechanical dynamic equation (swing with damping) and machine electrical dynamic equations; machine mechanical parameters such as inertia constant and damping co-efficient and machine electrical parameters such as transient/sub-transient reactances and time constants etc are required. Saturation model data is also very vital.
2. **Excitation systems** of various types; the data for each model available in standard power system stability analysis programs such as EPRI's ETMSP, PTI's PSS/E etc are used in most cases.
3. **Governor systems** of various types; Again the necessary data for each model are usually available in standard power system stability analysis programs.
4. **Load modeling** is very vital for performing a voltage stability study.
5. Models for selected prime mover, power system stabilizers, and control devices such as SVC etc. are also required.

Induction motor and SVC modeling will be discussed further in this section. In addition to all the system/device data, other system data include convergence parameters such as threshold and maximum iteration counts for static power flow studies, and also various other solution parameters used for the dynamic time domain simulation.

3.1.2.1. Induction motor modeling

As mentioned earlier large induction motor loads generally affect the voltage recovery process after voltage sag has been incepted due to system faults, and in many occasions due to extended voltage sag secondary effects such as stalling or tripping of sensitive motors might happen leading to massive load disruption. So, it is very vital to represent large, small and trip induction motor loads in various combinations in the system, so that we capture the stalling phenomenon of induction motor load, the real and reactive power requirements in the stalled state, and the tripping caused by thermal protection.

The induction motor load must be modeled such that it is sensitive to dynamic variations in voltage and frequency, and emulates the typical characteristic of consuming more power at increased speeds. Equation (1) shows the modeling of mechanical torque (T_{load}) as a function of speed deviation from nominal and motor load torque at synchronous speed (T_{nom}).

$$T_{load} = T_{nom}(1 + \Delta\omega)^{D} \tag{1}$$

Some of the primary model parameters include stator and rotor resistances and inductances, mutual inductance, saturation components, MVA base, intertia (H), per unit voltage level below which the relay to trip the motor will begin timing (V_T), time in cycles for which the voltage must remain below the threshold for the relay to trip (C_T), breaker delay time in cycles, nominal torque (T_{nom}), load damping factor (D) etc.

There are new composite load models developed by WECC LMTF [19] that improves the representation of induction motor load dynamics, and thereby more closely captures the critical role played by such loads in delayed voltage recovery events. These composite loads are represented by CMLD models in PSS/E and CMPLDW models in PSLF [20].

3.1.2.2. Static VAR compensator modeling

In the study done in this chapter we employ SVC as an effective means to mitigate transient voltage dip problem by providing fast responding dynamic reactive power support. The SVC is modeled as shown in the figure 3, with a non-windup limit B_{svc} (in MVAR) on the SVC output, which constrains the SVC output B. At its limit, SVC output is non-controllable and functions as a shunt capacitor. Hence, the ability of an SVC to provide dynamic support for mitigating the transient voltage dip problems depends on the SVC's capacitive limit (size) B_{svc}, which also increases the SVC cost. The RPP finds the optimum rating of SVC that is economical and enhances system reliability.

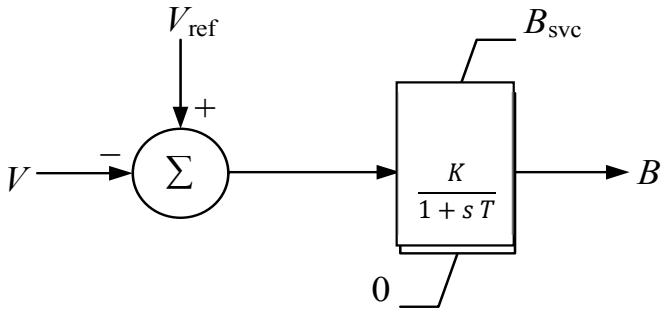

Figure 3. Static VAR compensator model

Some of the main parameters include voltage limits V_{MAX} and V_{MIN} to specify the active range of the voltage control, a time constant (of about 0.05 sec. or less) to model the delay in reactor's response, a steady-state voltage control gain K of about 100, and the time constant T of about 0.01 to provide transient gain reduction in the control loop.

Once the voltage stability base case is ready, next system analysis has to be performed to check the severity of the contingencies that need planning. So the next vital step in the planning procedure is voltage stability assessment of contingencies.

3.2. Post-contingency performance criteria for voltage stability assessment

In order to effectively plan against steady state and dynamic voltage stability problems under a certain set of contingencies, we need to identify proper performance criteria. Voltage stability of the power system should be assessed based on voltage security criteria of interest to, and accepted by, the utility.

As far as the steady state performance criteria are concerned, there are many criteria such as reactive reserve in different parts of the system, post-contingency voltage, Eigenvalues, etc. that enable to quantify the severity of a contingency with respect to voltage stability. In this work we utilize the most basic and widely accepted criteria, namely, post-contingency voltage stability margin [21, 22] for steady state performance assessments. Voltage stability margin, a steady state performance criterion, is defined as the amount of additional load in a specific pattern of load increase that would cause voltage instability. Contingencies such as

unexpected component (generator, transformer, transmission line) outages often reduce the voltage stability margin, and control actions increase it [23, 24], as shown in figure 4 [25].

The disturbance performance table within the NERC (North American Electric Reliability Corporation)/WECC (Western Electricity Coordinating Council) planning standards [26] provides the minimum acceptable performance specifications for post-contingency voltage stability margin under credible events, that it should be atleast,

- greater than 5% for N-1 contingencies,
- greater than 2.5% for N-2 contingencies, and
- greater than 0% for N-3 contingencies.

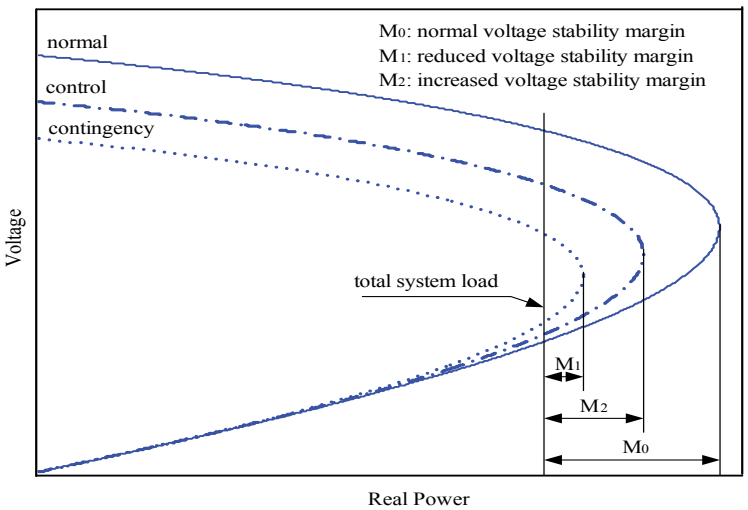

Figure 4. Voltage stability margin

As far as the performance measure for dynamic stability phenomena is concerned, in [11] it is stated that the needs of the industry related to voltage dips/sags for power system stability fall under two main scenarios. One is the traditional transient angle stability where voltage "swing" during electromechanical oscillations is the concern. The other is "short-term" voltage stability generally involving voltage recovery following fault clearing where there is no significant oscillations, for which much greater load modeling detail is required (specifically induction motor loads) with the fault applied in the load area rather than near generation. In [25], it is stated that many planning and operating engineers are insufficiently aware of potential short-term voltage instability, or are unsure on how to analyze the phenomena. In this work we focus on planning for the transient voltage recovery after a fault is cleared. For the transient voltage analysis, the minimum planning criteria is,

- **Slow voltage recovery**: The induction motor trip relay timer is actuated when the bus voltage dips below 0.7p.u and trips if voltage doesn't recover to 0.7p.u within next 20 cycles.

3.3. Sensitivities of post-contingency performance criteria

The objective of the reactive power planning problem is to satisfy these minimum performance criteria mentioned in the previous section under various credible contingencies. This is greatly dependent upon the amount, location and type of reactive power sources available in the system, which are all decision variables in the proposed coordinated RPP, as will be dealt in the next section of this chapter. If the reactive power support is far away, or insufficient in size, or too dependent on shunt capacitors (slow acting static device), a relatively normal contingency (such as a line outage or a sudden increase in load) can trigger a large system voltage drop. Hence, in order to properly allocate the reactive power support in terms of optimal type, location and amount, in this work we employ linear sensitivities of performance measure with respect to various control actions. These sensitivities enable obtaining the necessary information, i.e., the sensitivities of performance measure for the type of reactive support, the location and amount of reactive support, which are very useful to perform the proposed coordinated RPP. This section sheds light on these linear sensitivity measures.

3.3.1. Voltage stability margin sensitivity

The sensitivity of voltage stability margin refers to how much the margin changes for a small change in system parameters such as real power and reactive power bus injections, regulated bus voltages, bus shunt capacitance, line series capacitance etc [2, 27]. References [28, 29] first derived these margin sensitivities for different changing parameters.

Let the steady state of the power system satisfying a set of equations in the vector form be,

$$F(x, p, \lambda) = 0 \tag{2}$$

where x is the vector of state variables, p is any parameter in the power system steady state equations such as demand and base generation or the susceptance of shunt capacitors or the reactance of series capacitors, and λ denotes the system load/generation level called the scalar bifurcation parameter. The system reaches a state of voltage collapse, when λ hits its maximum value (the nose point of the system PV curve), and the value of the bifurcation parameter is equal to λ^*. For this reason, the system equation at equilibrium state is parameterized by this bifurcation parameter λ as shown below.

$$P_{li} = (1 + K_{lpi}\lambda)P_{li0} \tag{3}$$

$$Q_{li} = (1 + K_{lqi}\lambda)Q_{li0} \tag{4}$$

$$P_{gj} = (1 + K_{gj}\lambda)P_{gj0} \tag{5}$$

where P_{li0} and Q_{li0} are the initial loading conditions at the base case corresponding to λ=0. K_{lpi} and K_{lqi} are factors characterizing the load increase pattern (stress direction). P_{gj0} is the real power generation at bus j at the base case. K_{gj} represents the generator load pick-up

factor. For a power system model using ordinary algebraic equations, the bifurcation point sensitivity with respect to the control variable p_i evaluated at the saddle-node bifurcation point is [27]

$$\frac{\partial \lambda^*}{\partial p_i} = -\frac{w^* F_{p_i}^*}{w^* F_\lambda^*} \tag{6}$$

where w is the left eigenvector corresponding to the zero eigenvalue of the system Jacobian F_x, F_λ is the derivative of F with respect to the bifurcation parameter λ and F_{Pi} is the derivative of F with respect to the control variable parameter p_i.

The sensitivity of the voltage stability margin with respect to the control variable at location i, S_i, is

$$S_i = \frac{\partial M}{\partial p_i} = \frac{\partial \lambda^*}{\partial p_i} \sum_{i=1}^{n} K_{lpi} P_{li0} \tag{7}$$

where M is the voltage stability margin given by

$$M = \sum_{i=1}^{n} P_{li}^* - \sum_{i=1}^{n} P_{li0} = \lambda^* \sum_{i=1}^{n} K_{lpi} P_{li0} \tag{8}$$

3.3.2. Post-fault transient voltage recovery sensitivity

The sensitivity of the voltage dip time duration to the SVC capacitive limit (B_{svc}) can be defined as the change of the voltage dip time duration (voltage recovery time) for a given change in the SVC capacitive limit. Let $\tau^{(1)}$ be the time at which the transient voltage dip begins after a fault is cleared, and $\tau^{(2)}$ be the time at which the transient voltage dip ends, as shown in figure 5 [25]. Then the time duration of the transient voltage dip τ_{dip} is given by

$$\tau_{\text{dip}} = \tau^{(2)} - \tau^{(1)} \tag{9}$$

Thus, the sensitivity of the voltage dip time duration to the capacitive limit of an SVC, S_τ, is

$$S_\tau \equiv \frac{\partial \tau_{dip}}{\partial B_{\text{svc}}} = \frac{\partial (\tau^{(2)} - \tau^{(1)})}{\partial B_{\text{svc}}} = \frac{\partial \tau^{(2)}}{\partial B_{\text{svc}}} - \frac{\partial \tau^{(1)}}{\partial B_{\text{svc}}} = \tau^{(2)}_{B_{\text{svc}}} - \tau^{(1)}_{B_{\text{svc}}} \tag{10}$$

where $\tau^{(1)}_{B_{\text{svc}}}$ and $\tau^{(2)}_{B_{\text{svc}}}$ are calculated based on trajectory sensitivity computations as derived in [25]. For a large power system, this method requires computing integrals of a set of high dimension differential algebraic equations. An alternative to calculate the sensitivities is using numerical approximation [25], as shown by equation (11). This procedure of sensitivity calculation by numerical approximation requires repeated simulations of the system model for the SVC capacitive limits B_{svc} and $B_{svc}+\Delta B_{svc}$. The sensitivities are then given by the change of the voltage recovery time divided by the SVC capacitive limit change

ΔB_{svc}. This procedure is easy to implement for a large power system using available simulation tools.

$$S_\tau = \frac{\partial \tau_{dip}}{\partial B_{svc}} \approx \frac{\Delta \tau_{dip}}{\Delta B_{svc}} = \frac{\tau_{dip}(B_{svc} + \Delta B_{svc}) - \tau_{dip}(B_{svc})}{\Delta B_{svc}} \tag{11}$$

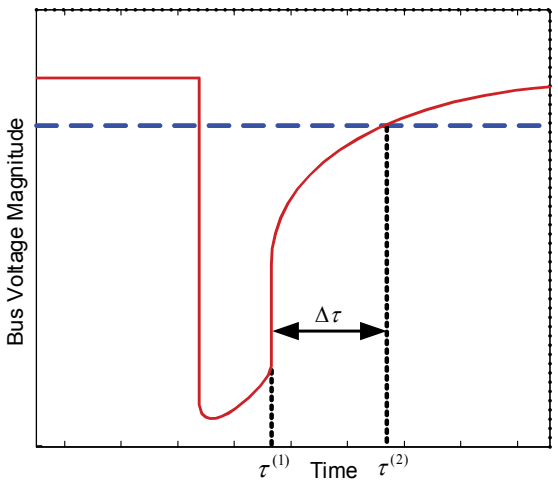

Figure 5. Post-fault clearance slow voltage recovery

4. Coordinated reactive power planning

The planning algorithm addresses the problems discussed in Table 1.

Problem	Planning Objective
A (Steady State)	To restore post-disturbance equilibrium and increase post contingency voltage stability margin beyond the minimum criteria after a severe contingency that can cause voltage instability
B (Dynamic)	To improve the characteristics of post-fault transient voltage recovery phenomenon satisfying the required minimum criteria, and prevent induction motor tripping

Table 1. Coordinated Reactive Power Planning Objectives

Figure 6 shows the general flow of the RPP procedure developed.

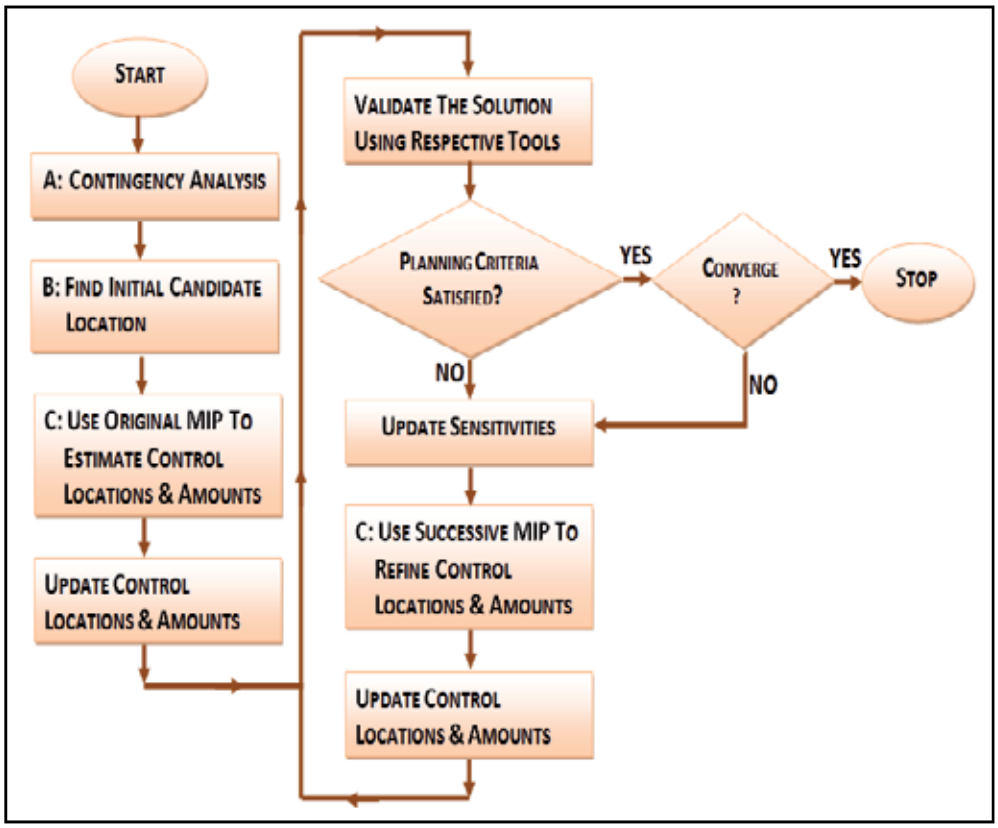

Figure 6. Flowchart of RPP procedure with successive MIP

4.1. Contingency analysis

Continuation power flow (CPF) [17] based tools and time domain simulation are used to perform the contingency analysis. The post-contingency state of the system is checked for performance criteria violations, and a list of critical contingencies is formed. In the case of steady state analysis the process of contingency screening using margin sensitivity information [29] is used to reduce the computational burden [30].

4.2. Formulation of coordinated control planning algorithm

This section presents the formulation of optimization developed to address the coordinated VAR planning problem for all the contingencies that have either one or both the planning problems shown in Table 1. The information required for the optimization algorithm are reactive device cost and maximum capacity limit at various voltage levels, performance measures and their sensitivities with respect to MSCs and SVCs under each critical contingencies, and an initial set of candidate locations for MSCs and SVCs. While many methodologies in the past determine static and dynamic VAR support sequentially, this method simultaneously determines the optimal allocation of static and dynamic VAR [31].

4.2.1. Original mixed integer programming

The objective of mixed integer program (MIP) is to minimize the total installation cost of MSCs and SVCs while satisfying the requirements of long-term voltage stability margin and short-term post-fault transient voltage characteristics.

Minimize

$$\sum_{i\in\Omega}[C_{vi\_MSC}B_{i\_MSC}+C_{fi\_MSC}q_{i\_MSC}+C_{vi\_svc}B_{i\_svc}+C_{fi\_svc}q_{i\_svc}] \tag{12}$$

Subject to

$$\sum_{i\in\Omega}S_{M,i}^{(k)}[B_{i\_MSC}^{(k)}+B_{i\_svc}^{(k)}]+M^{(k)}\geq M_{\mathrm{r}},\ \forall k \tag{13}$$

$$\sum_{i\in\Omega_{svc}}S_{\tau,n,i}^{(k)}B_{i\_svc}^{(k)}+\tau_{\mathrm{dip},n}^{(k)}\leq\tau_{\mathrm{dip},n,\mathrm{r}},\ \forall n,k \tag{14}$$

$$0\leq B_{i\_MSC}^{(k)}\leq B_{i\_MSC}\ ,\forall k \tag{15}$$

$$0\leq B_{i\_svc}^{(k)}\leq B_{i\_svc},\ \forall k \tag{16}$$

$$B_{i\min\_MSC}q_{i\_MSC}\leq B_{i\_MSC}\leq B_{i\max\_MSC}q_{i\_MSC} \tag{17}$$

$$B_{i\min\_svc}q_{i\_svc}\leq B_{i\_svc}\leq B_{i\max\_svc}q_{i\_svc} \tag{18}$$

$$q_{i\_MSC},q_{i\_svc}=0,1 \tag{19}$$

The decision variables are $B_{i}^{(k)}{}_{\_MSC}$, B_{i_MSC}, q_{i_MSC}, $B_{i}^{(k)}{}_{\_svc}$, B_{i_svc}, and q_{i_svc}.

C_{f_MSC} is fixed installation cost and C_{v_MSC} is variable cost of MSCs,

C_{f_svc} is fixed installation cost and C_{v_svc} is variable cost of SVCs,

B_{i_MSC}: size of the MSC at location i,

B_{i_svc}: size of the SVC at location i,

q_{i_MSC}=1 if the location i is selected for installing MSCs, otherwise, q_{i_MSC}=0,

q_{i_svc}=1 if the location i is selected for installing SVCs, otherwise, q_{i_svc}=0,

the superscript k represents the contingency causing insufficient voltage stability margin and/or slow voltage recovery problems,

Ω_{MSC}: set of candidate locations to install MSCs,

Ω_{svc}: set of candidate locations to install SVCs,

Ω: union of Ω_{MSC} and Ω_{svc},

$B_i^{(k)}{}_{\_MSC}$: size of the MSC to be switched at location i under contingency k,

$B_{i\_svc}^{(k)}$: size of the SVC at location i under contingency k,

$S_{M,i}^{(k)}$: sensitivity of the voltage stability margin with respect to the shunt susceptance of MSC at location i under contingency k,

$S_{\tau,n,i}^{(k)}$: sensitivity of the voltage recovery time duration at bus n with respect to the size of the SVC at location i under contingency k,

$M^{(k)}$: voltage stability margin under contingency k and without controls,

M_r: required voltage stability margin,

$\tau_{dip,n}^{(k)}$: time duration of voltage recovery at bus n under contingency k and without controls,

$\tau_{dip,n,r}$: maximum allowable time duration of voltage recovery at bus n,

B_{imin_MSC}: minimum size of the MSC at location i,

B_{imax_MSC}: maximum size of the MSC at location i,

B_{imin_svc}: minimum size of the SVC at location i, and

B_{imax_svc}: maximum size of the SVC at location i.

Note from (13) that SVCs can also be used to increase the voltage stability margin.

4.2.2. Updated successive mixed integer programming

The output of the mixed integer-programming problem in section 4.2.1 is the combined reactive compensation locations and amounts for all concerned contingencies. Now the network configuration is updated by including the identified reactive power support under each contingency. After that, the voltage stability margin is recalculated using CPF to check if sufficient margin is achieved for each concerned contingency. Also, time domain simulations are carried out to check whether the requirement of the transient voltage recovery performance is met. This step is necessary because the power system model is inherently nonlinear, and the mixed integer programming algorithm uses linear sensitivities to estimate the effect of variations of reactive support levels on the voltage stability margin and post-fault voltage recovery. So if need be, the reactive compensation locations and/or amounts can be further refined by re-computing sensitivities (with updated network configuration) under each concerned contingency, and solving a second-stage mixed integer programming problem.

This successive MIP problem based on updated sensitivity and system performance information is again formulated to minimize the total installation cost of MSCs and SVCs, subject to the constraints of the requirements of voltage stability margin and voltage

recovery. It will terminate once the post-contingency performance criteria are satisfied for all concerned contingencies, and there is no significant change in decision variables from the previous MIP solution.

5. Numerical illustration

The control planning method described in this paper was applied to a particular portion of US Eastern Interconnection system consisting of about 16173 buses. This subsystem belonging to a particular utility's control area, henceforth will be referred to as the "study area." The study area within this large system consisted of 2069 buses with 30065.2 MW of loading and 239 generators producing 37946.7 MW.

The contingencies considered for the study are the more probable ones, i.e., N-1 and N-G-T. For N-1 and N-G-T contingencies, according to the WECC/NERC performance table, minimum steady state performance criteria is to have a post-contingency voltage stability margin of at least 5% of the sub-system's base load. For the slow voltage recovery problem, the minimum performance should be such that it avoids the induction motor tripping. The trip relay timer of the trip induction motor is actuated when the bus voltage dips below 0.7p.u and trips if voltage doesn't recover to 0.7p.u within next 20 cycles. Therefore, the objective of the coordinated RPP is to identify a minimum cost mix of static and dynamic Var resources that results in satisfactory voltage stability and transient voltage recovery performance for all considered contingencies.

The study area was grouped into 6 Market Zones (MZ), representing the 6 different load increase (stress) directions required to perform CPF analysis. For a particular stress direction, the sink is characterized by the set of loads inside a MZ, and the source is characterized by generators outside of that MZ, but within the study area.

For the transient study, dynamic models for generators, exciter, governor systems, and appropriate load and SVC models are used. Loads in the focus area were partitioned as 50% induction motor load (dynamic) and 50% ZIP load (static). Induction motor was modeled using CIM5 model in PSS/E, which is sensitive to changing voltage and frequency. SVCs were modeled using CSVGN1 and CSVGN3 family of SVC models. The PSS/E manual presents the block diagram, parameters and detailed description for each of these models. The dynamic models of induction motor loads were further split equally into three different kinds, i.e., large, small, and trip motors. Table 2 shows some of the important parameters of each of these motor loads as defined in section 3.1.2.1. The ZIP load is modeled as 50% constant impedance and 50% constant current for real power load and 100% constant impedance for reactive power load.

The steady state contingency analysis using CPF is performed in Matlab, while the dynamic voltage stability analysis using time domain simulation is performed in PTI PSS/E [32]. As part of this study, which required Matlab using the input files in PSS/E's "raw" data format, a data conversion module was built that converted the system raw data to a format that was understandable by Matlab. The conversion module includes tasks such as careful modeling

of 3-winding transformer data, zero-impedance lines, switched shunt data, checking system topology, and checking for any islanding, so that the utility's base case is transported without any errors into Matlab.

	H (p.u. motor base)	V_T (p.u)	C_T (cycles)	D	T_{nom} (p.u)
Large Motor	1.5	0	20	2	1
Small Motor	0.5	0	20	2	1
Trip Motor	0.5	0.7	20	2	1

Table 2. Induction Motor Dynamic Model Parameters

Based on the pre-processing performed using these computational tools, respective sensitivity information of steady state and dynamic performance measures with respect to the reactive control device are computed, as explained in section 3.3. All the necessary input including candidate locations and control device cost information are fed as input to the coordinated planning algorithm, which is coded in Matlab and executed using CPLEX. Since candidate control locations and linear sensitivity information are used, the MIP optimization is faster even for a very large scale system. PSS/E's ability to store the results in *.csv format is utilized in post-processing the simulation results using MS Excel.

The cost is modeled as two components [24]: fixed cost and variable cost. For SVCs the fixed and variable costs were taken to be 1.5 M$ and 5 M$/100Mvar respectively. The maximum capacity limit for SVCs was fixed at 300 MVar. Table 3 shows the MSC cost information and the default maximum capacity constraints at every feasible location under different voltage levels. The maximum MSC limit at various voltage levels ensures avoiding over-deployment of MSCs at those voltage levels, which could degrade the voltage magnitude performance. At every solution validation step, if any bus has post-contingency voltage exceeding 1.06 p.u, a new maximum MSC (MVar) constraint is developed, and the optimization is re-run with the new constraint included.

Base KV	Fixed Cost (Million $)	Variable Cost (M $/100MVar)	Maximum MSC (MVar)
69	0.025	0.41	30
100	0.05	0.41	75
115	0.07	0.41	120
138	0.1	0.41	150
230	0.28	0.41	200
345	0.62	0.41	300
500	1.3	0.41	300

Table 3. MSC Cost Information and Maximum Compensation

5.1. Steady state reactive power planning and impact of induction motors

In this section we present only the steady state RPP, i.e., plan to satisfy post-contingency voltage stability margin only using MSCs, without including dynamic problem and SVCs in

the overall planning methodology. This in effect means we consider only constraints (13), (15), and (17) in original MIP of section 4.2.1, and also in updated successive MIP of section 4.2.2. We also analyze the impact of induction motors on the transient voltage recovery performance, and demonstrate the ineffectiveness of steady state planning approach to counter the ill-dynamics caused by induction motors in voltage stability phenomena. This strongly motivates the need for considering the short-term voltage performance and fast-responding dynamic reactive resource within a coordinated planning approach.

Steady state voltage stability analysis using CPF-based contingency screening was performed for all credible N-1 (2100 branches (T) and 168 generators (G)) and N-G-T (all possible combinations of G and T) contingencies under 6 different stress directions. The results indicated that only the stress direction corresponding to the MZ1 region was found to have post contingency steady state voltage stability problems, as indicated by the 56 critical N-G-T contingencies (28 line outages under 2 N-G base case, where G = {14067, 14068}) in Table 4. The total base load in MZ1 zone (sink) is 2073 MW. The collapse point for basecase was at 2393 MW, which is equivalent to a stability margin of 15.44%. All the 56 contingencies in Table 4 have stability margin lesser than 5%, with the top 14 facing instability issues. Table 4 also shows the final optimal static VAR solution that just satisfies the minimum performance criteria under every critical contingency. The final optimal investments will be the maximum amount of MSCs required at each location. The total investment cost of MSCs to solve all the steady state voltage stability problems is 2.665 M$.

Cont. No	Transmission Line		Base KV	Stability Index (Margin in %)		Capacitor Allocation (p.u Mvar)			
	From	To		Gen#1–14067	Gen#2-14068	14073	14071	14080	14160
1	14079	14083	138	Unstable	Unstable	1.5	0	1.5	0.25
2	14094	14326	230	Unstable	Unstable	1.5	1.5	0.75	0
3	14175	14319	230	Unstable	Unstable	1.2	1.5	0	0.85
4	14296	14322	500	Unstable	Unstable	1	1.2	1.25	0
5	14319	14321	230	Unstable	Unstable	1.5	1.5	0.5	0
6	14319	14326	230	Unstable	Unstable	1.5	1.5	0.9	0
7	10983	14129	345	Unstable	Unstable	1.5	1.5	1.5	1
8	14077	14080	138	1.495417	1.784853	0.3	0	0	0
9	14130	14142	138	2.411963	2.556681	0.65	0	0	0
10	14129	14162	345	2.556681	2.701399	0.85	0	0	0
11	14294	14319	230	2.990835	3.135552	0.68	0	0	0
12	14295	14302	138	2.990835	3.135552	0.65	0	0	0
13	14071	14079	138	3.28027	3.424988	0.57	0	0	0
14	14126	14142	138	3.28027	3.424988	0.55	0	0	0
15	14109	14363	138	3.617945	3.617945	0.52	0	0	0
16	14148	14232	138	3.617945	3.762663	0.45	0	0	0

17	14302	14363	138	3.617945	3.907381	0.52	0	0	0
18	14124	14126	138	3.907381	3.907381	0.5	0	0	0
19	14148	14149	138	3.907381	3.907381	0.4	0	0	0
20	14232	14328	138	3.907381	4.052098	0.5	0	0	0
21	14237	14328	138	3.907381	4.052098	0.5	0	0	0
22	14322	14494	500	3.907381	4.052098	0.5	0	0	0
23	14106	14109	138	3.95562	4.052098	0.5	0	0	0
24	14297	14311	138	4.196816	4.341534	0.47	0	0	0
25	14134	14290	138	4.245055	4.486252	0.35	0	0	0
26	14103	14130	138	4.486252	4.63097	0.4	0	0	0
27	14106	14110	138	4.486252	4.63097	0.4	0	0	0
28	14238	14297	138	4.63097	4.823927	0.4	0	0	0

Table 4. Contingency List and Optimal Allocation of MSCs by Steady State Reactive Power Planning

Even though the system is planned against steady state voltage instability using MSCs, nevertheless the effect of induction motors in transient phenomena has not been investigated.

Figure 7 shows the voltage recovery phenomenon at a certain bus with and without dynamic modeling of induction motor. The figure shows the significance of modeling induction motor properly, which has important role in ascertaining post-fault-clearance short-term voltage stability of the system. Once this phenomenon is captured by appropriate modeling, we can counter it by the proposed coordinated RPP.

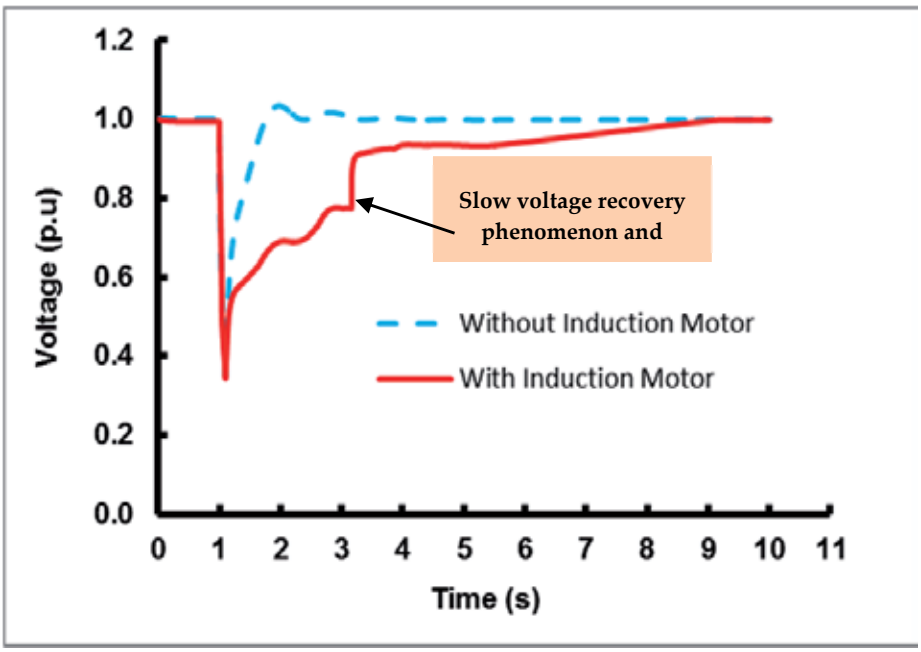

Figure 7. Voltage recovery phenomenon with and without Induction Motor modeling

With appropriate modeling of induction motor dynamics, time domain simulations were run for the top 7 contingencies by applying a 3-phase fault at t=0 at one end of the transmission circuit and then clearing the fault and the circuit at 6 cycles (t = 0.1s). All the contingencies lead to a slow voltage recovery due to the presence of induction motor loads that ultimately tripped. A list of all the buses having slow voltage recovery problem under each severe contingency was made. Table 5 shows the time domain simulation results under few of the contingencies of Table 4, wherein we notice the buses at which the minimum criteria for transient voltage recovery (more than 20 cycles below 0.7p.u) is violated. The induction motor loads connected to these buses also get tripped, in a similar manner as was shown in Figure 7. The transient voltage response under other contingencies was also very poor. For instance, under contingencies 2, 4, 5, and 6, about 76, 18, 72, 64 buses respectively violated the minimum post-fault voltage recovery criteria.

Bus Number	Contingency 1		Contingency 3	
	Recovery time	Cycles	Recovery time	Cycles
14079	0.841	50.46	0.344	20.64
14071	0.771	46.26	0.36	21.6
14084	0.694	41.64	0.36	21.6
14060	0.614	36.84	0.353	21.18

Table 5. Buses resulting in Slow Voltage Recovery and Induction Motor Tripping

Table 6 ranks the top 7 contingencies (under both gen. outages) shown in Table 4, based on their severity, which is quantified in terms of worst-case recovery times. It can be expected that the most severe contingencies will drive the amount of dynamic VARs needed.

Contingency No.	Bus Numbers		kV	Rank
	From	To		
1	14079	14083	138	**2**
2	14094	14326	230	**4**
3	14175	14319	230	**6**
4	14296	14322	500	**7**
5	14319	14321	230	**3**
6	14319	14326	230	**1**
7	10983	14129	345	**5**

Table 6. Contingency Ranking in terms of Worst-case Recovery Times

5.2. Coordinated reactive power planning

The proposed coordinated planning, as discussed in section 4.2, was performed to mitigate both transient as well as steady state problems under these contingencies. Sensitivities of post-contingency voltage stability margin and transient voltage recovery times are used as one of the inputs to find the optimal solution. The candidate locations were identified according to the following criteria:

1. Buses for which one or more contingencies result in:
   - the bus being among the top 5 worst voltage dips and
   - the bus has induction motor load that trips
2. Buses must have high steady state voltage stability margin sensitivity so that they can also efficiently address the static problems.

Table 7 shows the stage 1 MIP result, which selects two SVC locations to solve both static as well as dynamic problems. Investigation indicates the reason for this is that the transient voltage problems are so severe that the amount of SVC required to solve them is also sufficient to mitigate the steady state voltage stability problems.

N-G-T Contingencies				SVC (p.u MVAR)		Steady State Stability Margin (%)
No.	Bus Number		KV	14071	14084	
	From	To				
1	14079	14083	138	3	0.85	9.64
2	14094	14326	230	3	0.8	9.16
3	14175	14319	230	3	0.7	9.4
4	14296	14322	500	1.7	0	8.68
5	14319	14321	230	3	1.5	9.4
6	14319	14326	230	3	1.53	8.92
7	10983	14129	345	3	0.95	5.1

Table 7. Stage 1 MIP Result of Coordinated RPP and Steady State Stability Validation

When stage I MIP solution was validated for steady state voltage stability problems for the top 7 contingencies (under both gen. outages) of Table 4, it was found that they not only attained equilibrium, but also had post contingency voltage stability margin more than the minimum requirement of 5% as shown in Table 7. The remaining contingencies in Table 4 were also validated with this stage I MIP solution and were found to have sufficient post contingency voltage stability margin.

When time domain simulations were done to validate stage 1 MIP result, it was found that contingencies 1, 2, 5, 6, and 7 still had buses that violated the minimum recovery time requirement, resulting in tripping of some induction motors. Figures 8 and 9 show the voltage profiles at the most severely-affected buses under contingency 2 before and after stage 1 MIP result implementation, respectively.

Figure 9 also shows that the SVC placed after stage 1 MIP at buses 14071 and 14084, which are just sufficient to provide voltage recover within 20 cycles at some buses. For the contingencies having slow voltage recovery problems at some buses even after stage 1 MIP solution, a successive MIP is performed with updated sensitivity information using stage 1 SVC solution.

Table 8 shows the final operational solution of the coordinated planning problem, which chooses only SVCs due to the nature of problems under contingencies.

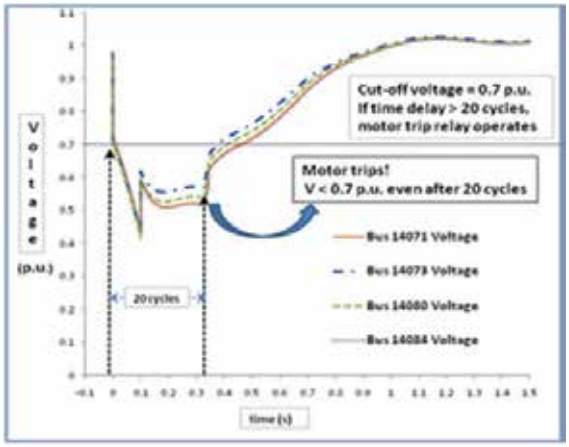

Figure 8. Voltage profiles of worst-hit buses under cont. 2 without SVC

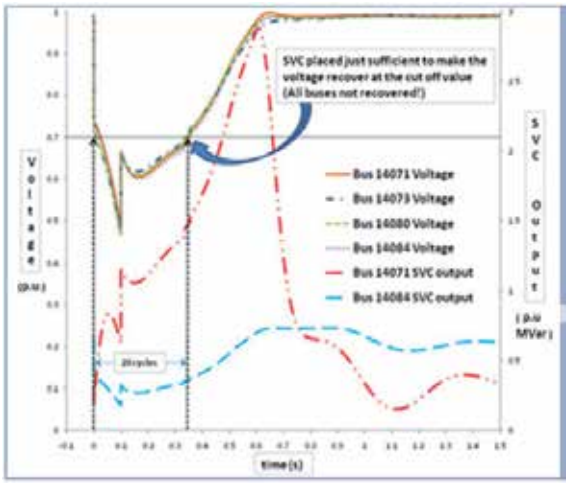

Figure 9. Voltage profiles of worst-hit buses under cont. 2 with SVC from stage 1 MIP result

No.	N-G-T Contingencies under both the N-G		KV	SVC (p.u MVAR)	
	Bus Number				
	From	To		14071	14084
1	14079	14083	138	3	2.65
2	14094	14326	230	3	2.7
3	14175	14319	230	3	0.7
4	14296	14322	500	1.7	0
5	14319	14321	230	3	2.7
6	14319	14326	230	3	2.85
7	10983	14129	345	3	2.1

Table 8. Final Solution of Coordinated Optimal Planning

Figure 10 shows the improved voltage profile at Bus 14071 under contingency 1 after implementing the final SVC solution. Figure 10 also shows the output of the two SVCs. The SVC peak output at bus 14071 is 290 MVar, and that of bus 14084 is 270 MVar.

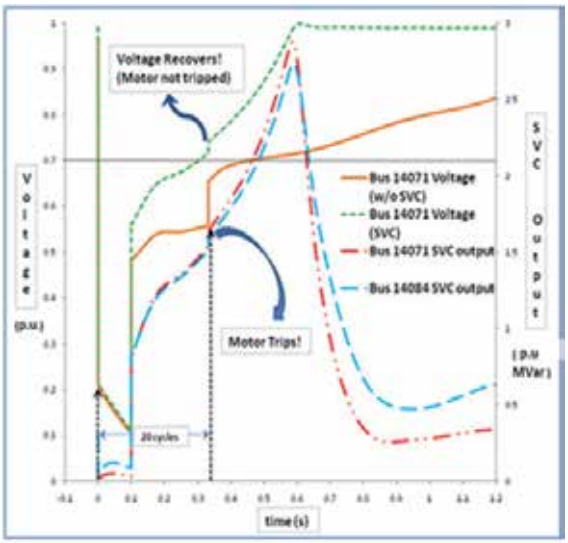

Figure 10. Bus 14071 voltage profile under cont. 1 with final allocation

The final investment solution for the coordinated planning problem includes SVC placements at buses 14071 and 14084 of maximum capacity 3.0 MVar and 2.85 MVar respectively[1]. The total cost is 32.25 M$ under the cost assumptions used for this study.

6. Conclusions

This chapter presented the critical role played by induction motors in short-term voltage stability phenomenon, and emphasizes the need for including proper dynamic models of motor loads in voltage stability related planning studies. The chapter also sheds light on the need of a coordinated framework for reactive power planning considering both static and dynamic reactive control devices, which mitigates both post-contingency steady state as well transient voltage recovery and motor stalling problems. The mixed integer optimization based VAR planning algorithm is formulated to satisfy the minimum post-contingency steady state voltage stability margin and post-fault transient voltage recovery performance criteria under many critical contingencies simultaneously. The developed method was illustrated in large-scale system with 16173 buses representing US Eastern Interconnection, wherein induction motor dynamic characteristics modeling and bus voltage magnitude limit enforcement were incorporated within the overall analysis and planning respectively. The results verify that the method works satisfactorily to plan an optimal mix of static and dynamic VAR devices under

[1] There may be cases, when the required SVC to mitigate slow voltage recovery problems might be less, and they may still not satisfy the post-contingency steady state voltage stability margin requirements. For such cases, the MIP may choose MSCs as an effective addition to the optimal solution.

many critical contingencies simultaneously and averts steady-state and dynamic voltage instability issues, including induction motor tripping.

Author details

Venkat Krishnan and James D. McCalley
Iowa State University, USA

7. References

[1] T. Van Cutsem, "Voltage instability: phenomena, countermeasures, and analysis methods," *Proc. IEEE*, vol. 88, pp. 208–227, Feb. 2000

[2] P. Kundur, *Power System Stability and Control*, EPRI Power System Engineering Series, New York: McGraw Hill, 1994

[3] NERC (North American Electric Reliability Corporation) Disturbance Analysis Working Group Database, "http://www.nerc.com/~dawg/database.html," 1984-2002

[4] Voltage Stability Assessment: Concepts, Practices and Tools, *Power systems stability subcommittee special publication*, sp101pss, IEEE-PES, Aug. 2002

[5] U.S.-Canada Power System Outage Task Force, (2004, Apr.), Final report on the August 14, 2003 blackout in the United States and Canada: Causes and recommendations. [Online]. Available: https://reports.energy.gov/BlackoutFinal-Web.pdf

[6] M. H. J. Bollen, *Understanding Power Quality Problems – Voltage Sags and Interruptions*, Wiley-IEEE Press September 24, 1999

[7] G.K. Stefopoulos and A.P. Meliopoulos, **"**Induction Motor Load Dynamics: Impact on Voltage Recovery Phenomena," *Proceedings of the 2005/2006 IEEE Transmission and Distribution Conference and Exposition*, pp.752 – 759, May 21-24, 2006

[8] "Criteria and countermeasures for voltage collapse," *CIGRE Publication*, CIGRE Task Force 38-02-12, 1994

[9] J.J. Paserba, "How FACTS controllers benefit AC transmission systems," *IEEE Power Engineering Society General Meeting, 2004.*, Vol.2, pp. 1257 – 1262, 6-10 June 2004

[10] J. A. Diaz de Leon II and C. W. Taylor, "Understanding and solving short-term voltage stability problems," *in Proc. 2002 IEEE/PES Summer Meeting*, Vol. 2, pp.745-752, July 2002

[11] D. J. Shoup, J. J. Paserba, and C. W. Taylor, "A survey of current practices for transient voltage dip/sag criteria related to power system stability," *in Proc. 2004 IEEE/PES Power Systems Conference and Exposition*, Vol. 2, pp. 1140-1147, Oct. 2004

[12] A. Hammad and M. El-Sadek, **"**Prevention of transient voltage instabilities due to induction motor loads by static VAr compensators," *IEEE Trans. Power Syst.*, Vol. 4, Issue 3, pp. 1182 – 1190, Aug. 1989

[13] IEEE/CIGRE joint task force on stability terms and definitions, "Definition and classification of power system stability," *IEEE Trans. Power Syst.*, vol. 19, pp. 1387-1401,2004

[14] Begovic. M et. al., "Summary of system protection and voltage stability", A summary of special publication prepared by Protection Aids to Voltage Stability Working Group of

the Substation Protection Subcommittee of the IEEE Power System Relaying Committee, *IEEE Trans. on Power Delivery*, Vol. 10, No. 2, April 1995

[15] NERC Transmission Issues Subcommittee, System Protection, and Control Subcommittee, "A technical reference paper fault-induced delayed voltage recovery," Technical report, NERC, June 2009

[16] P. Sakis Meliopoulos and George J. Cokkinides, "A Virtual Environment for Protective Relaying Evaluation and Testing", *IEEE Trans. of Power Syst.*, Vol. 19, pp. 104-111, 2004

[17] V. Ajjarapu and C. Christy, "The continuation power flow: A tool for steady state voltage stability analysis," *IEEE Trans. Power Syst.*, vol. 7, pp. 417-423, Feb. 1992

[18] B. Gao, G. K. Morison, and P. Kundur, "Toward the development of a systematic approach for voltage stability assessment of large-scale power systems," *IEEE Trans. Power Systems*, vol. 11, pp. 1314-1324, Aug. 1996

[19] D. Chassin et. al., "Load modeling transmission research," Technical report, CIEE, March 2010

[20] GE Positive Sequence Load Flow, User Manual Version 18.0, April 2011

[21] H. D. Chiang and H. Li, "CPFLOW for Power Tracer and Voltage Monitoring," *PSERC Publication 01-02*, May 2002

[22] C. A. Canizares and F.L. Alvarado, "Point of collapse and continuation methods for large ac/dc systems," *IEEE Trans. Power Syst.*, Vol. 8, No.1, pp. 1-8, Feb. 1993

[23] T. Van Cutsem and C. Vournas, Voltage Stability of Electric Power Systems, Boston: Kluwer Academic Publishers, 1998

[24] C. W. Taylor, *Power System Voltage Stability*, EPRI Power System Engineering Series, New York: McGraw Hill, 1994

[25] Haifeng Liu, "Planning reactive power control for transmission enhancement", PhD dissertation, Iowa State University, Ames, IA 2007

[26] Western Electricity Coordinating Council (2005, April). NERC/WECC planning standards. WECC, Salt Lake City, UT
Available: http://www.wecc.biz/documents/library/procedures/ CriteriaMaster.pdf

[27] V. Ajjarapu, *Computational Techniques for voltage stability assessment and control*, New York: Springer, 2006

[28] S. Greene, I. Dobson and F. Alvarado, "Sensitivity of the loading margin to voltage collapse with respect to arbitrary parameters," *IEEE Trans. Power Syst.*, vol. 12, 1997

[29] S. Greene, I. Dobson, and F. L. Alvarado, "Contingency ranking for voltage collapse via sensitivities from a single nose curve," *IEEE Trans. Power Syst.*, vol. 14, pp. 232-240, 1999

[30] V. Krishnan and J. D. McCalley, "Contingency assessment under uncertainty for voltage collapse and its application in risk based contingency ranking," *Int J Electr Power Energy Syst*, 43 (1), pp. 1025–1033, Dec 2012

[31] V. Krishnan, Coordinated Static and Dynamic Reactive Power Planning against Power System Voltage Stability Related Problems, M.S. Thesis, Iowa State University, Ames, 2007

[32] Siemens PTI Power Technologies Inc., PSS/E 33, Program Application Guide, Vol. II, May 2011

Chapter 7

Optimization of Induction Motors Using Design of Experiments and Particle Swarm Optimization

Houssem Rafik El-Hana Bouchekara, Mohammed Simsim and Makbul Anwari

Additional information is available at the end of the chapter

http://dx.doi.org/10.5772/38665

1. Introduction

The level of prosperity of a community is related to its ability to produce goods and services. But producing goods and services is strongly related to the use of energy in an intelligent way. Energy can be exploited in several forms such as thermal, mechanical and electrical (Boldea & Nasar, 2002). Electrical energy, measured in kWh, represents more than 30% of all used energy and it is on the rise (Boldea & Nasar, 2002). The larger part of electrical energy is converted into mechanical energy in electric motors. Among electric motors, the induction motor is without doubt the most frequently used electrical motor and is a great energy consumer. About 70% of all industrial loads on a specific utility are represented by induction motors (Maljkovic, 2001). The vast majority of induction motor drives are used for heating, ventilation and air conditioning (Blanusa, 2010; Cunkas & Akkaya 2006).

The design of an induction motor aims to determine the induction motor geometry and all data required for manufacturing to satisfy a vector of performance variables together with a set of constraints (Boldea & Nasar, 2002). Because induction motors are now a well developed technology, there is a wealth of practical knowledge, validated in industry, on the relationship between their performance constraints and their physical aspects. Moreover, mathematical modeling of induction motors using circuit, field or hybrid models provides formulas of performance and constraint variables as functions of design variables (Boldea & Nasar, 2002).

The journey from given design variables to performance and constraints is called analysis, while the reverse path is called synthesis. Optimization design refers to ways of doing efficient synthesis by repeated analysis such that some single (or multiple) objective (performance) function is maximized and/or minimized while all constraints (or part of them) are fulfilled (Boldea & Nasar, 2002). The aim of this chapter is to present an optimal

design method for induction motors using design of experiments (DOE) and particle swarm optimization (PSO) methods.

The outline of this paper is as follows. The current section is the introduction. Section 2 introduces and explains the DOE method. Section 3 gives an overview of the PSO method. In Section 4 the application of the DOE and PSO to optimize induction motors is explained and its results are also presented and discussed in detail. Finally, the conclusions are drawn in Section 5.

2. Design of Experiments (DOE)

With modern technological advances, the design and optimization of induction motors or any other electromechanical devices are becoming exceedingly complicated. As the cost of experimentation rises rapidly it is becoming impossible for the analyst, who is already constrained by resources and time, to investigate the numerous factors that affect these complex processes using trial and error methods (ReliaSoft Corporation, 2008). Computer simulations can solve partially this issue. Rather than building actual prototypes engineers and analysts can build computer simulation prototypes. However, the process of building, verifying, and validating induction motor simulation model can be arduous, but once completed, it can be utilized to explore different aspects of the modeled machine. Moreover, many simulation practitioners could obtain more information from their analysis if they use statistical theories, especially with the use of DOE.

In this section the DOE method is explained in order to make its use in this chapter understandable. The aim here is not to explain the whole method in detail (with all the mathematical developments behind), but to present the basics to demonstrate its interesting capabilities.

2.1. Why DOE?

Compared to one-factor-at-a-time experiments, i.e. only one factor is changed at a time while all the other factors remain constant, the DOE technique is much more efficient and reliable. Though, the one-factor-at-a-time experiments are easy to understand, they do not tell how a factor affects a product or process in the presence of other factors (ReliaSoft Corporation, 2008). If the effect of a factor is altered, due to the presence of one or more other factors, we say that there is an interaction between these factors. Usually the interactions' effects are more influential than the effect of individual factors (ReliaSoft Corporation, 2008). This is because the actual environment of the product or process comprises the presence of many factors together instead of isolated occurrences of each factor at different times.

The DOE methodology ensures that all factors and their interactions are systematically investigated. Therefore, information obtained from a DOE analysis is much more reliable and comprehensive than results from the one-factor-at-a-time experiments that ignore

interactions between factors and, therefore, may lead to wrong conclusions (ReliaSoft Corporation, 2008).

Let's assume, for instance, that we want to optimize an induction motor taking into account, for simplicity, only two factors: the length and the external radius. Hence, the length is the first factor and is denoted by x_1 while the external radius is the second factor and it is denoted by x_2. Each factor can take several values between two limits, i.e. $\{x_{1_{min}}, x_{1_{max}}\}$ and $\{x_{2_{min}}, x_{2_{max}}\}$. We desire to study the influence of each of these factors on the system response or output for example the torque called Y. The classical or traditional approach consists of studying the two factors x_1 and x_2, separately. First we put x_2 at the average level $x_{2_{average}}$ and study the response of the system when x_1 varies between $x_{1_{min}}$and $x_{1_{max}}$ using for example 4 steps (experiments) as shown in Fig. 1. Similarly, we repeat the same procedure to study the effect of x_2. Accordingly, the total number of tests is 8. However, we should ask a paramount question here, are these 8 experiments sufficient to have a good knowledge about the system? The simple and direct answer to this question is no. To get a better knowledge about the system, we have to mesh the validity domain of the two factors and test each node of this mesh as shown in Fig. 2. Thus, 16 experiments are needed for this investigation. In this example only two factors are taken into account. Therefore, if for example 7 factors are taken into account, the number of tests to be performed rises to $4^7 = 16384$ experiments, which is a highly time and cost consuming process.

Knowing that it is impossible to reduce the number of values for each factor to less than 2, the designer often reduces the number of factors, which leads to incertitude of results. To reduce both cost and time, the DOE is used to establish a design experiment with less number of tests. The DOE, for example, allows identifying the influence of 7 factors with 2 points per variable with only 8 or 12 tests rather than 128 tests used by the traditional method (Bouchekara, 2011; Uy & Telford, 2009).

Recently, the DOE technique has been adopted in the design and testing of various applications including automotive assembly (Altayib, 2011), computational intelligence (Garcia, 2010), bioassay robustness studies (Kutlea, 2010) and many others.

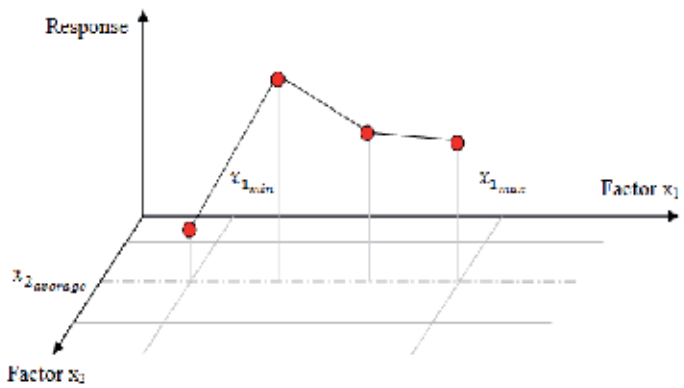

Figure 1. Traditional method of experiments.

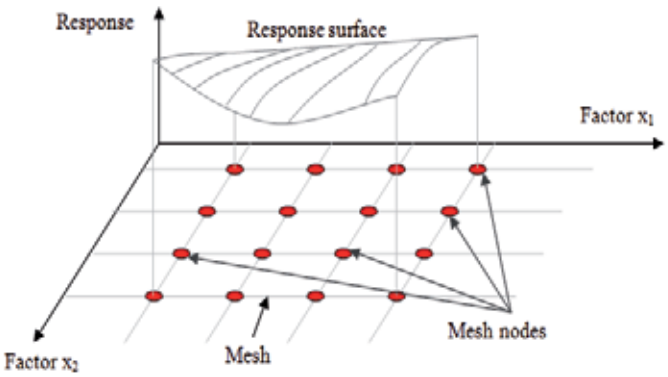

Figure 2. One experiment at each node of the mesh.

2.2. Methodology

The design and analysis of experiments revolves around the understanding of the effects of different variables on other variable(s). The dependent variable, in the context of DOE, is called the response, and the independent variables are called factors. Experiments are run at different values of the factors, called levels. Each run of an experiment involves a combination of levels of the investigated factors. The number of runs of an experiment is determined by the number of levels being investigated in the experiment (ReliaSoft Corporation, 2008).

For example, if an experiment involving two factors is to be performed, with the first factor having n_1 levels and the second having n_2 levels, then $n_1 \times n_2$ combinations can possibly be run, and the experiment is an $n_1 \times n_2$ factorial design. If all $n_1 \times n_2$ combinations are run, then the experiment is a full factorial. If only some of the $n_1 \times n_2$ combinations are run, then the experiment is a fractional factorial. Therefore, in full factorial experiments, all factors and their interactions are investigated, whereas in fractional factorial experiments, certain interactions are not considered.

2.3. Mathematical concept

Assume that y is the response of an experiment and $\{x_1, x_2, x_3, \dots, x_k\}$ are k factors acting on this experiment where each factor has two levels of variation x_{i-} and x_{i+}. The value of y, is approximated by an algebraic model given in the following equation:

$$y = a_0 + a_1x_1 + a_2x_2 + \cdots + a_kx_k + \cdots + a_1x_1x_2 + \cdots a_1x_1x_k + a_{1\dots k}x_{1\dots k} \quad (1)$$

where a_j are coefficients which represent the effect of factors and their interactions on the response of the experiment.

2.4. Full factorial design

As mentioned above, the study of full factorial design consists of exploring all possible combinations of the factors considered in the experiment (Kleijnen et al., 2005). Note that the design X^k means that this experiment concerns a system with k factors with x levels. Usually, two levels of the x's are used. The use of only two levels implies that the effects are monotonic on the response variable, but not necessarily linear (Uy & Telford, 2009). For each factor, the two levels are denoted using the "rating Yates" notation by -1 and +1 respectively to represent the low and the high levels of each factor. Hence, the number of experiments carried out by a full factorial design for k factors with 2 levels is $n = 2^k$. For example, Table 1 shows the design matrix of a full factorial design for 2 factors while, Fig. 3 shows the mesh of the experimental field where points correspond to nodes.

Run	Factor x_1	Factor x_2	Response Y
1	-1	-1	Y_1
2	-1	+1	Y_2
3	+1	-1	Y_3
4	+1	+1	Y_4

Table 1. Design Matrix for a full factorial design for 2 factors with 2 levels.

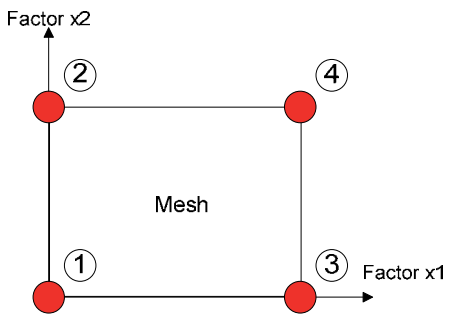

Figure 3. Strategy of experimentation; points corresponding to nodes in the mesh of the experimental field for a full factorial design for 2 factors with 2 levels.

2.5. Fractional factorial design

The advantage of full factorial designs, is their ability to estimate not only the main effects of factors, but also all their interactions, i.e. two by two, three by three, up to the interaction involving all k factors. However, when the number of factors increases, the use of such design leads to a prohibitive number of experiments. The question to be asked here is: is it necessary to perform all experiments of the full factorial design to estimate the system's response? In other words, is it necessary to conduct a test at each node of the mesh?

It is not necessary to identify the effect of all interactions because the interactions of order ≥ 2 (like $x_1x_2x_3$) are usually negligible. Therefore, certain runs specified by the full

factorial design can be used instead of using all runs. To illustrate this phenomenon, an analogy can be made with a Taylor series approximation where the information given by each term decreases when its order increases. So, fractional factorial designs can be used to estimate factors effect and interactions that influence the experiments more with a reduced number of runs (Bouchekara, 2011). Taguchi Tables (Pillet, 1997), or Box generators (Demonsant, 1996), can be used to generate the fractional factorial design matrix of experiments.

To illustrate fractional factorial designs let's take an example. If $k = 3$, the design matrix of these three factors is given by Box generators in a way that the third factor is the product of the two other factors. The factor x_3 and interaction x_1x_2 are either confused or aliased, and there is a confusion of these aliases because only their sums are reachable (Pillet, 1997; Costa, 2001).

Table 2 shows a full factorial design for 3 factors with 2 levels. The number of runs is $2^3 = 8$. This number is reduced to 4 using a fractional factorial design as shown in Table 3 where the third factor is generated using Box generator for 3 factors given in Table 4. The comparison of the 2 designs is shown in Fig. 4.

Run	**Factor x_1**	**Factor x_2**	**Factor x_3**	**Response Y**
1	-1	-1	-1	Y_1
2	-1	-1	+1	Y_2
3	-1	+1	-1	Y_3
4	-1	+1	+1	Y_4
5	+1	-1	-1	Y_5
6	+1	-1	+1	Y_6
7	+1	+1	-1	Y_7
8	+1	+1	+1	Y_8

Table 2. Design Matrix for a full factorial design for 3 factors with 2 levels.

Run	**Factor x_1**	**Factor x_2**	**Factor x_3**	**Response Y**
1	-1	-1	+1	Y_1
2	-1	+1	-1	Y_2
3	+1	-1	-1	Y_3
4	+1	+1	+1	Y_4

Table 3. Design Matrix for a fractional factorial design for 3 factors with 2 levels.

Resolution	**Design name**	**Number of Runs**	**Generators**
3	2^{3-1}	4	$x_3 = x_1 \times x_2$

Table 4. G. Box generator of fractional factorial design for 3 factors.

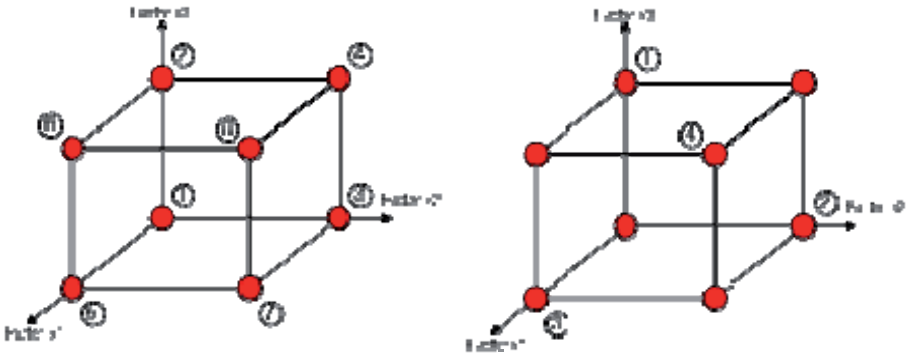

(a) (b)

Figure 4. Comparison between the design experimental field of full and fractional factorial designs with 3 factors. (a) full factorial design; (b) fractional factorial design

2.6. Estimation of model coefficients

The coefficient a_0 of (1) is estimated from the arithmetic average of all observed responses and it is given by:

$$a_0 = \bar{y} = \frac{1}{n}\sum_{i=1}^{n} y_i \tag{2}$$

where y_i is the response observed for the experiment i and n is the total number of experiments.

The effect of a factor x_j at the level x_{j+} can be calculated thus, the coefficient associated with this effect can be identified using the following equations:

$$a_j = e_{a_j} = y_{x_j}^{+} - a_0 \tag{3}$$

and

$$y_{x_j}^{+} = \frac{1}{n^{+}}\sum_{i=1}^{n} y_i^{+} \tag{4}$$

where $y_{x_j}^{+}$ is the response observed for experiment i when x_j is at level x_{j+}, n^{+} is the number of experiments when x_j is at level x_{j+} and e_{a_j} is the effect of coefficient a_j.

Once the method of how to calculate the coefficients of the model and how to identify the existing confusion between these factors has been presented, we can evaluate the contributions of contrasts (the sum of confusions) and therefore the most significant factors (affecting the response).

In (Demonsant, 1996) the identification of the significant factors has been proposed by evaluating the coefficients contribution (or contrasts, for fractional designs) on the model response from the normalization of their values compared to the sum of squared responses, such as given in the following equations:

$$C_{a_j} = \frac{SCE(a_j)}{SCE(y)} \ [\%] \tag{5}$$

with

$$SCE(y) = \sum_{i=1}^{n} (y_i - \bar{y})^2 \tag{6}$$

$$SCE(a_j) = \frac{n}{s} \sum_{j=1}^{s} \left(e_{a_j}\right)^2 \tag{7}$$

where s is the number of levels (equals to 2 in this case), e_{a_j} is the effect of coefficient a_j, and C_{aj} is the contribution of the contrast associated with the coefficient a_j.

According to (Demonsant, 1996):

- The contribution given by (5) is significant if it is higher than 5%.
- The interactions of order higher than two are negligible.
- If a contrast is negligible, all effects composing this contrast are negligible also.
- Two significant factors can generate a significant interaction. On the other side, two insignificant factors do not generate a significant interaction.

3. Particle Swarm Optimization

3.1. Introduction

PSO (Kennedy & Eberhart, 1995; Kennedy et al., 2001; Clerc, 2006) is an evolutionary algorithm for the solution of optimization problems. It belongs to the field of Swarm Intelligence and Collective Intelligence and is a sub-field of Computational Intelligence. PSO is related to other Swarm Intelligence algorithms such as Ant Colony Optimization and it is a baseline algorithm for many variations, too numerous to list (Brownlee, 2011). PSO was developed by James Kennedy and Russell Eberhart in 1995 (Kennedy & Eberhart, 1995).

PSO has similar techniques to traditional stochastic search algorithms, but the difference is that PSO is not totally stochastic. PSO can avoid trapping on suboptimal and provide a highly adaptive optimal method. Because of fast convergence, PSO has gradually been applied in identification of graphics, optimization of clustering, scheduling assignment, network optimization and multi-objective optimization. For an analysis of the publications on the applications of particle swarm optimization see (Poli, 2008).

3.2. Strategy

The goal of the algorithm is to have all the particles locate the optima in a multi-dimensional hyper-volume. This is achieved by assigning initially random positions to all particles in the space and small initial random velocities. The algorithm is executed like a simulation, advancing the position of each particle in turn based on its velocity, the best known global position in the problem space and the best position known to a particle. The objective function is sampled after each position update. Over time, through a combination of exploration and exploitation of known good positions in the search space, the particles cluster or converge together around an optimum, or several optima (Brownlee, 2011).

3.3. Procedure

The Particle Swarm Optimization algorithm is comprised of a collection of particles that move around the search space influenced by their own best past location and the best past location of the whole swarm or a close neighbor (Brownlee, 2011). In each iteration a particle's velocity is updated using:

$$v_i(t+1) = v_i(t) + \quad c_1 \times rand(\,) \times \left(p_i^{best} - p_i(t)\right) + c_2 \times rand() \times (\mathrm{p_{gbest}} - p_i(t)) \tag{8}$$

where $v_i(t+1)$ is the new velocity for the i^{th} particle, c_1 and c_2 are the weighting coefficients for the personal best and global best positions respectively, $p_i(t)$ is the i^{th} particle's position at time t, p_i^{best} is the i^{th} particle's best known position, and $\mathrm{p_{gbest}}$ is the best position known to the swarm. The $rand()$ function generates a uniformly random variable ∈ [0, 1].

Variants on this update equation consider best positions within a particles local neighborhood at time t. A particle's position is updated using:

$$p_i(t+1) = \; p_i(t) + v_i(t) \tag{9}$$

3.4. PSO algorithm

It is important to mention here that PSO has undergone many changes since its introduction in 1995. As researchers have learned about the technique, they have derived new versions, developed new applications, and published theoretical studies of the effects of the various parameters and aspects of the algorithm. (Poli, 2007) gives a snapshot of particle swarming from the authors' perspective, including variations in the algorithm, current and ongoing research, applications and open problems. Algorithm 1 provides a pseudocode listing of the Particle Swarm Optimization algorithm for minimizing a cost function used in this chapter.

Algorithm 1: Pseudocode for PSO (Brownlee, 2011).

```
Input: ProblemSize, Population_size
Output: P_g_best
Population ← ∅;
P_g_best ← ∅;
for i = 1 to Population_size do
    P_velocity ← RandomVelocity();
    P_position ← RandomPosition(Population_size);
    P_cost ← Cost(P_position);
    P_p_best ← P_position ;
    if P_cost ≤ P_g_best then
        P_g_best ← P_p_best;
    end
End
while StopCondition() do
    foreach P ∈ Population do
        P_velocity ← UpdateVelocity(P_velocity, P_g_best , P_p_best);
        P_position ← UpdatePosition(P_position, P_velocity);
        P_cost ← Cost(P_position);
        if P_cost ≤ P_p_best then
            P_p_best ← P_position ;
            if P_cost ≤ P_g_best then
                P_g_best ← P_p_best ;
            end
        end
    end
end
return P_p_best;
```

According to (Brownlee, 2011):

- The number of particles should be low, around 20-40
- The speed a particle should be bounded.
- The learning factors (biases towards global and personal best positions) should be between 0 and 4, typically 2.
- A local bias (local neighborhood) factor can be introduced where neighbors are determined based on Euclidean distance between particle positions.
- Particles may leave the boundary of the problem space and may be penalized, be reflected back into the domain or biased to return back toward a position in the

problem domain. Alternatively, a wrapping strategy may be used at the edge of the domain creating a loop, torrid or related geometrical structures at the chosen dimensionality.

- An inertia coefficient can be introduced to limit the change in velocity.

4. Induction motor design: An optimization problem

Induction motors with power below 100 kW (Fig. 5) constitute a sizable portion of the global electric motor markets (Boldea & Nasar, 2002). The induction motor design optimization is a nature mixture of art and science. Detailed theory of design is not given in this chapter. Here we present what may constitute the main steps of the design methodology. For further information, see (Vogt, 1988; Boldea & Nasar, 2002; Murthy, 2008). The suitability of the DOE and the PSO techniques in induction motor design optimization will be demonstrated in this section.

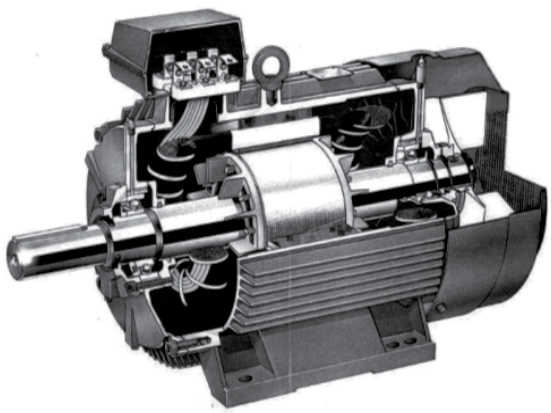

Figure 5. Low power 3 phase induction motor with cage rotor (Boldea & Nasar, 2002).

4.1. The algorithm

The main steps in induction motor design optimization are shown in Fig. 6.

Step (1): Initialization

The design process may start with design specifications and assigned values of: rated power, nominal voltage, frequency, power factor, type (squirrel Cage or slip-ring), connection (star or delta), ventilation, ducts, iron factor, insulation, curves like B/H, losses, Carter coefficient, tables like specific magnetic loading, specific electric loading, density etc. Then, design constraints for flux densities, current densities are specified. After that, the computer program is formulated with imposing max & min limits for rotor peripheral speed, length/pole pitch, stator slot-pitch, number of rotor slots. Finally, suitable values for certain parameters are assumed and objective functions are defined.

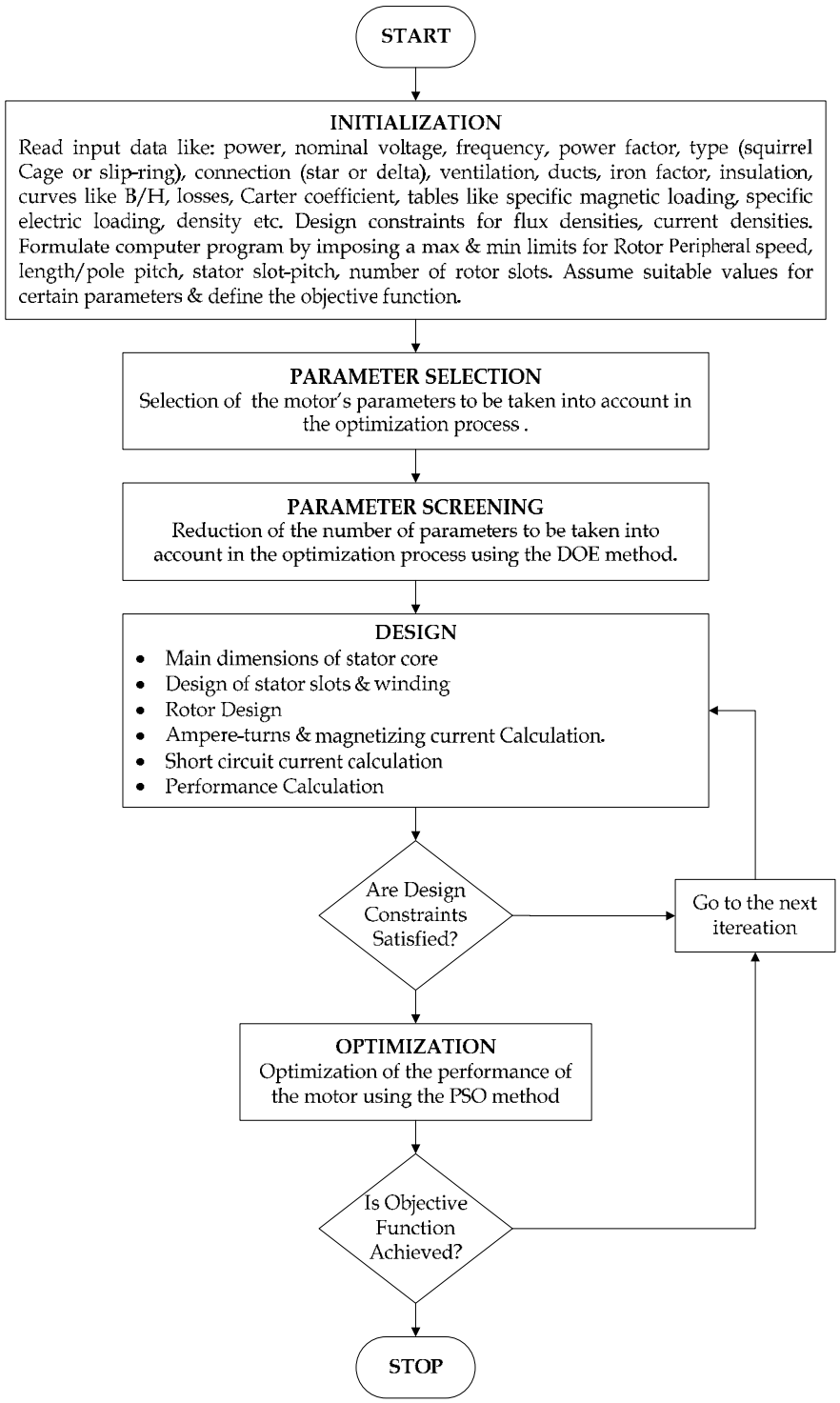

Figure 6. Flowchart for computer-aided optimal design of 3-ph induction motor.

Step (2): Parameter selection

In this step the parameters to be taken into account in the optimization process are selected. The selection of parameters may be chosen by the designer or imposed by the user (for specific application for instance).

Step (3): Parameter screening

While there are potentially many parameters (factors) that affect the performance (objective functions) of the induction motor, some parameters are more important, *viz,* have a greater impact on the performance. The DOE provides a systematic & efficient plan of experimentation to compute the effect of factors on the performance of the motor, so that several factors can be studied simultaneously (Bouchekara, 2011). As said earlier, the DOE technique is an effective tool for maximizing the amount of information obtained from a study while minimizing the amount of data to be collected (Bouchekara, 2011). The DOE technique is used here to reduce the number of parameters (screening) to be taken into account in the optimization process. This goal is achieved by identifying the effect of each parameter on the objective function to be optimized. Only significant parameters (with contribution higher than 5%) are considered in the optimization step.

Step (4): Design

Total design is split into six parts in a proper sequence as shown in Fig. 6. The sequential steps for design of each part are briefly describes in the following sub sections. For more details see (Murthy, 2008).

Part I: Design of magnetic frame

In this part the output coefficient (C0) is calculated by:

$$C0 = 11 \times kW \times Bav \times q \times EFF \times pf \times 10^{-3} \tag{10}$$

where: kW is the rating power, Bav is the specific magnetic loading, q is the specific electric loading, EFF is the efficiency and pf is the power factor.

Then the rotor volume that is (rotor diameter D)^2 × (rotor length L) is computed using the following formula:

$$D^2L = \frac{kW}{C0 \times ns} \tag{11}$$

where: ns is the synchronous speed measured in rps.

Finally, the flux per pole ϕ is calculated by:

$$\phi = \frac{\tau_p \times L \times Bav}{10^6} \tag{12}$$

where: τ_p is the pole pitch and its is given by:

$$\tau_p = \frac{\pi \times D}{P} \tag{13}$$

Part II: Design of stator winding

The first step of this part consists of calculating the size of slots using the following equations:

$$\text{Slot Width(Ws)} = [\text{Zsw} \times (\text{Tstrip} + \text{insS}) + \text{insW}] \tag{14}$$

$$\text{Slot Height (Hs)} = [\text{Zsh} \times (\text{Hstrip} + \text{insS}) + \text{Hw} + \text{HL} + \text{insH}] \tag{15}$$

where: Zsw is the width-wise number of conductors, Tstrip is the assuming thickness of strip/conductor, insS is the strip insulation thickness, insW is the width-wise insulation, Zsh is the number of strips/conductors height-wise in a slot, Hstrip is the height of the strip, HL is height of lip, Hw is the height of wedge and insH is the height-wise insulation.

Then, the copper losses and the weight of copper are calculated by:

$$\text{Copper Losses (Pcus)} = 3 \times \text{Iph}^2 \times \text{Rph} \tag{16}$$

$$\text{Weight of Copper (Wcus)} = \text{Lmt} \times \text{Tph} \times 3 \times \text{As} \times 8.9 \times 10^{-3} \tag{17}$$

where: Iph is the current per phase, Rph is the resistance at 20°C, Lmt is the mean length of turn, Tph represents the turns per phase and As is the area of strip/conductor.

Finally, the iron losses are calculated by multiplying the coefficient deduced from the curve giving the losses in (W/kg) in function of the flux density in (T) by the core weight.

Part III: Design of Squirrel Cage Rotor

First, the air gap length is calculated by:

$$\text{Air} - \text{Gap Length (Lg)} = 0.2 + 2 \times \sqrt{\text{D} \times \text{L} \times 10^6} \tag{18}$$

Then, the rotor diameter is calculated using the following formula:

$$\text{Rotor Diameter (Dr)} = \text{D} - 2 \times \text{Lg} \tag{19}$$

Finally, the copper losses and the rotor weight are calculated using equations (20), (21) and (22).

$$\begin{aligned}&\text{Total Rotor Copper Loss (Pcur)}\\ &= \text{Copper Loss in the Bars} + \text{Copper Losses in the 2 End Rings}\end{aligned} \tag{20}$$

$$\text{Weight of Rotor Copper (Wcur)} = \text{Lb} \times \text{Sr} \times \text{Ab} \times 8.9 \times 10^{-6} \tag{21}$$

$$\text{Weight of Rotor End} - \text{Rings (Weue)} = \pi \times \text{Dme} \times 2 \times \text{Ae} \times 8.9 \times 10^{-6} \tag{22}$$

where: Lb is the length of bar, Sr is the number of Rotor Slots, Ab is the rotor bar area, Ae the area of cross sectional of end ring and Dme is mean diameter of end-ring.

Part IV: Total ampere turns and magnetizing current

First, the total ampere turns (ATT) for the motor are calculated using (23). Then, the magnetizing current (Im) is calculated using (24). Finally, the no load phase current (I0) and the no load power factor (pf0) are calculated using respectively (25) and (26).

$$\text{ATT} = \text{ATS} + \text{ATR} + \text{ATg} \tag{23}$$

$$\text{Im} = \frac{\text{P} \times \text{ATT}}{2 \times 1.17 \times \text{kW} \times \text{Tph}} \tag{24}$$

$$\text{I0} = \sqrt{\text{Iw}^2 + \text{Im}^2} \tag{25}$$

$$\text{pf0} = \frac{\text{Iw}}{\text{I0}} \tag{26}$$

where: ATS, ATR and ATg are the total ampere turns for the stator, the rotor and the air gap and Iw is the Wattful current.

Part V: Short-circuit current calculation

In this part the total reactance per phase, short-circuit current, and short-circuit power factor are calculated using the following formulas:

$$\text{Total Reactance/ph} = \text{Xs} + \text{X0} + \text{Xz} \tag{27}$$

$$\text{Short Circuit Current (Isc)} = \frac{\text{Vph}}{\text{Z}} \tag{28}$$

$$\text{Short Circuit pf} = \frac{\text{R}}{\text{Z}} \tag{29}$$

where: Xs is the slot reactance, X0 is the overhang reactance , Xz is the zig-zag reactance, R is the resistance and Z is the impedance.

Part VI: Performance calculation

In this last part of the design the performance of the induction motor are evaluated. The efficiency, the slip, the starting torque, the temperature rise and the total weight per kilo watt are calculated using the following formulas:

$$\text{Efficiency (EFF)} = \frac{\text{kW}}{\text{KW} + \text{Total Losses}} \tag{30}$$

$$\text{Slip at Full Load (SFL)} = \text{Total Rotor copper loss} \times \text{Rotor Input} \times 100 \tag{31}$$

$$\text{Starting Torque (Tst)} = \left(\frac{\text{Isc}}{\text{Ir}}\right)^2 \times \text{Slip at Full Load} \tag{32}$$

$$\text{Temperature Rise (Tr)} = 0.03 \times \frac{\text{Total Stator Losses}}{\text{Total Cooling Area}} \tag{33}$$

$$\text{kg/kW} = \frac{\text{Total Weight}}{\text{kW}} \tag{34}$$

where: Isc is the short circuit current and Ir is the equivalent rotor current.

At the end of step (4) an automatic check is performed. If the design constraints are satisfied we move to step (5) otherwise step (4) is restarted with new values of parameters.

Step (5): Optimization

In this step the motor's performances are checked and if found unsatisfactory, the process is restarted in step (4) with new values of parameters. The decision is made based on the PSO optimization method.

4.2. Design specifications

Design calculations are done for a given rating of an induction motor. Standard design specifications are:

- Rated power: P [kW] = 30.
- Line supply voltage: V [V] = 440.
- Supply frequency: f [Hz] = 50.
- Number of phases: 3.
- Phase connections: delta.
- Rotor type (squirrel cage or sling-ring): squirrel cage.
- Insulation class: F;
- Temperature rise: class B.
- Protection degree: IP55 – IC411.
- Environment conditions: standard (no derating).
- Configuration (vertical or horizontal shaft etc.): horizontal shaft.
- NEMA class: B.

4.3. Problem formulation

A very important problem in the induction motor design is to select the independent variables otherwise the problem would have been very much complicated using too many

variables (Thanga, 2008). Therefore variables selection is important in the motor design optimization. A general nonlinear programming problem can be stated in mathematical terms as follows.

Find X = $(x_1, x_2 \ldots . x_n)$ such that
$F_i(x)$ is a minimum or maximum
$g_i(x) \leq 0,\ i = 1, 2, \ldots m$

F_i is known as objective function which is to be minimized or maximized; g_i's are constants and x_i's are the variables. The following variables and constraints (Thanga, 2008) are considered to get optimal values of objective functions.

4.3.1. Variables

The variables considered are given in Table 5.

Name	Description	Minimum Value	Maximum Value	Type
P	Number of poles	4	6	Discrete
CDSW	Stator winding current density	3 [A/mm²]	5 [A/mm²]	Continuous
cdb	Current density in rotor bar	4 [A/mm²]	6 [A/mm²]	Continuous
Spp	Slots/pole/phase	3	4	Discrete
Tstrip	Stator conductor thickness	1 [mm]	2 [mm]	Continuous
Zsw	Number of conductors width-wise	1	2	Discrete

Table 5. Design optimization parameters with their domains.

4.3.2. Objective functions

Five different objective functions are considered while designing the machine using optimization algorithm. The objective functions are,

1. Maximization of efficiency; $F_1(x) = \max(EFF)$.
2. Minimization of kg/kW; $F_2(x) = \min(kg/kW)$.
3. Minimization of temperature rise in the stator; $F_3(x) = \min(Tr)$.
4. Minimization of I0/I ratio; $F_4(x) = \min(I0/I)$.
5. Maximization of starting torque; $F_5(x) = \max(Tst)$.

4.4. Fractional 2 levels factorial design

Here, the DOE is applied to analyze the objective functions. The proposed approach uses tools of the experimental design method: fractional designs, notably of Box generators to estimate the performance of the induction motor. The interest is to save calculation time and to find a near global optimum. The saving of time can be substantial because the number of simulations needed is significantly reduced.

Since six parameters define the shape of the motor, it is advisable to determine the effect of each parameter on the objective functions. Thus, it is very important to provide proper parameter ranges. The considered parameters are listed in Table 5. There are two types of parameters; continuous parameters and discrete parameters.

4.4.1. Results

Using two-level full factorial design needs 2^6=64 runs (simulations) to evaluate objective functions. However, using a 2^{6-2} fractional factorial design will significantly reduce the number of runs from 64 to 16. The 2^{6-2} design matrix and the simulation results obtained for this design are given in Table 6. This design has been generated using Box generators given in Table 7. The choice of a 2^{6-2} means that we have a 2 levels design with 6 factors where 2 of these factors are generated using the other 4 factors as shown in Table 7. Thus:

- The factor (5) will be generated using the product of factors (1), (2) & (3).
- The factor (6) will be generated using the product of factors (2), (3) & (4).

The contributions of obtained contrasts are given in Table 8. It shows in its first column contrasts and in the other columns their contribution or influences on objective functions. Keep in mind that a contribution is significant if it is higher than 5% and high order interactions (higher than 2) are considered negligible while only interactions of significant parameters are also significant.

N°	P	CDSW [A/mm²]	Cdb [A/mm²]	Spp	Tstrip [mm]	Zsw	EFF	Kg/kW	Tr [°]	I0/I	Tst [pu]
1	4	3	4	3	1	1	86.09	16.94	69.25	0.30	0.07
2	4	3	4	4	1	2	88.98	8.07	55.06	0.29	0.42
3	4	3	6	3	2	2	89.40	7.02	50.15	0.27	0.37
4	4	3	6	4	2	1	88.46	8.20	55.30	0.29	0.52
5	4	5	4	3	2	2	89.30	5.94	54.81	0.26	0.30
6	4	5	4	4	2	1	88.69	6.55	58.44	0.28	0.48
7	4	5	6	3	1	1	86.34	10.95	69.06	0.28	0.15
8	4	5	6	4	1	2	88.33	6.17	57.99	0.28	0.70
9	6	3	4	3	2	1	87.73	9.58	60.22	0.30	0.22
10	6	3	4	4	2	2	89.35	6.26	51.54	0.39	0.94
11	6	3	6	3	1	2	87.29	9.04	59.93	0.30	0.32
12	6	3	6	4	1	1	85.96	11.06	69.10	0.35	0.36
13	6	5	4	3	1	2	87.38	7.15	64.56	0.29	0.31
14	6	5	4	4	1	1	86.49	8.19	70.80	0.35	0.42
15	6	5	6	3	2	1	86.78	7.18	65.09	0.29	0.38
16	6	5	6	4	2	2	87.99	5.18	58.95	0.40	1.30

Table 6. Design matrix generated by the 2^{6-2} Box-Wilson fractional factorial design and the simulation results.

Resolution	Design name	Number of Runs	Generators
4	2^{6-2}	16	$x_5 = x_1 \times x_2 \times x_3$ $x_6 = x_2 \times x_3 \times x_4$

Table 7. Box generator of the fractional factorial design 2^{6-2}.

Contrasts	EFF	kg/kW	Tr	I0/I	Tst
P	13	2	9	45	7
CDSW	1	18	8	0	3
Cdb	3	1	0	0	5
Spp	4	10	2	25	41
Tstrip	34	24	36	0	14
Zsw	38	29	39	0	19
P × CDSW + Cdb × Tstrip	1	0	1	0	0
P × cdb + CDSW × Tstrip	2	2	1	0	0
P × Spp + Tstrip × Zsw	2	5	3	18	1
P × Tstrip + CDSW × Cdb + Spp × Zsw	1	3	0	4	5
P × Zsw + Spp × Tstrip	1	3	0	4	5
CDSW × Spp + Cdb × Zsw	0	1	0	0	1
Cdb × Spp + CDSW × Zsw	1	2	1	0	0

Table 8. Contrasts and contribution obtained.

The application of DOE identifies the effect of each parameter on each objective function. We can notice that for the efficiency Zsw, Tsrip, and P are the most significant factors with respectively 38% 34% and 13% of contribution on the objective function. Moreover, Fig. 7 gives more details. When P is low the efficiency is high and vice versa when P is high.

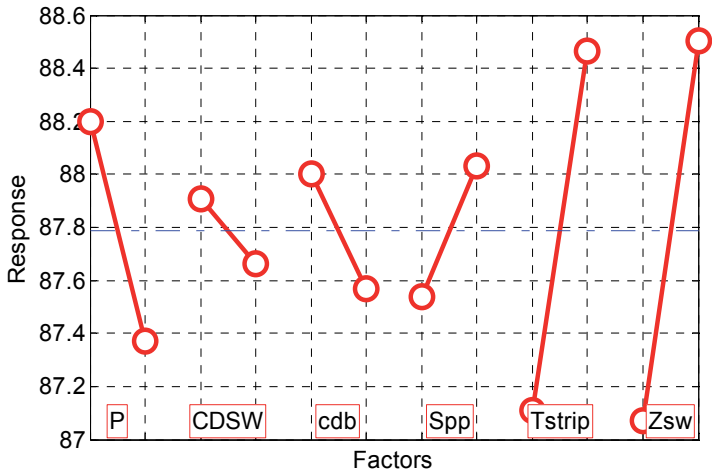

Figure 7. Plot of effects for the efficiency.

Contrariwise, when Tstrip and Zsw are low the efficiency is low, while it is high when Tstrip and Zsw are high.

For the objective function kg/kW the most important parameters are respectively Zsw (29%), Tstrip (24%), CDSW (18%) and Spp (10%). Fig. 8 shows that when each one of these parameters is low the kg/kW is high and inversely when they are high. Furthermore, for this objective function there is a significant interaction between some factors 'P × Spp + Tstrip × Zsw' (5%). Note that we have isolated all of the main effects from every 2-factors interaction. The two largest effects are Zsw and Tstrip, hence it seems reasonable to attribute this to the Tstrip × Zsw interaction.

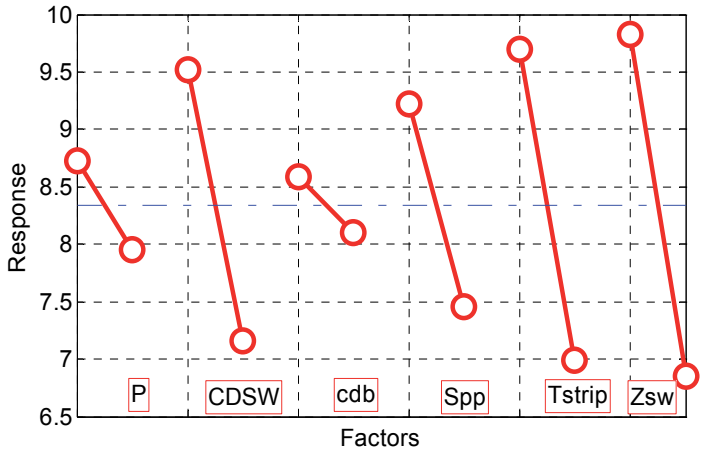

Figure 8. Plot of effects for kg/kW.

Concerning the temperature rise we can observe that, Zsw (39%), Tstrip (36%), P(9%) and CDSW (8%) are the most significant parameters. On the contrary, no significant interaction is discerned. Fig. 9 shows that the temperature rise is low when P and CDSW are low and it

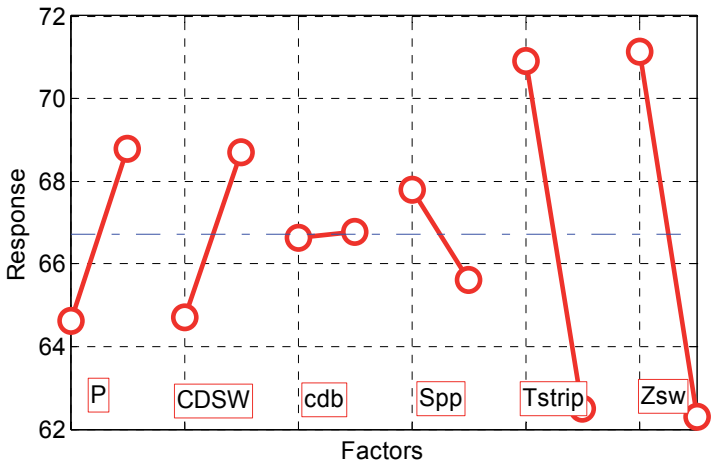

Figure 9. Plot of effects for temperature rise.

is high when they are high. Inversely, for Tstrip and Zsw the temperature rise is low when they are high.

For the objective function I0/I the significant parameters are P (45%) and Spp (25)%. Furthermore, there is a significant interaction between P and Spp included in the contrast 'P × Spp + Tstrip × Zsw'. Fig. 10 shows that I0/I is low when each parameter is low and vise versa.

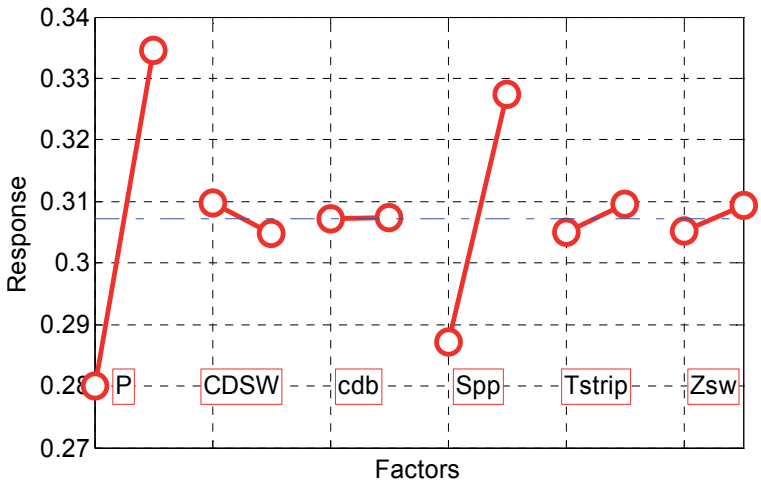

Figure 10. Plot of effects for I0/I.

Finally, for the starting torque the most significant parameters are given in this order: Spp (4%), Zsw (19%), Tstrip (14%), P (7%) and Cdb (5%). From Fig. 11 we can notice that when

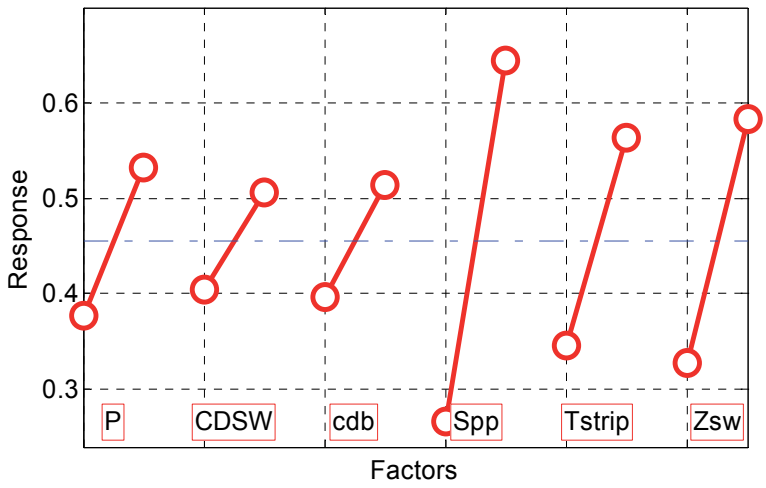

Figure 11. Plot of effects for starting torque.

each one of these parameters is low the starting torque is low. Likewise, when these parameters are high, the starting torque is high. Furthermore, for this objective function there is two significant interaction between some factors 'P × Tstrip + CDSW × Cdb + Spp × Zsw' (5%) and 'P × Zsw + Spp × Tstrip' (5%). Note that we have isolated all of the main effects from every 2-factor interaction. For the first contrast the two largest effects are Spp and Zsw. Thus, it seems reasonable to attribute this to the Spp × Zsw interaction. While, for the second contrast the two largest effects are Spp and Tstrip. Hence, it is appropriate to attribute this to the Spp × Tstrip interaction.

4.5. Optimization

Two optimization approaches can be achieved. The first one is to treat 1 of the 5 objective functions (defined in the Objective Function section) at a time. Thus, every time a single objective function is taken into account regardless of the 4 others. The second approach is to consider a multi objective function where the 5 objective functions are taken into account at the same time. The resulted complicated multiple-objective function can be converted into a simple and practical single-objective function scalarization. Among scalarization methods we can find the weighting method. In this method, the problem is posed as follows:

$$\mathrm{F_{objective}} = \sum_{\mathrm{i=1}}^{5} \mathrm{w_i}\, f_i \tag{35}$$

where: $f_1 = \mathrm{EFF}$, $f_2 = -\mathrm{kg}/\mathrm{kW}$, $f_3 = -\mathrm{Tr}$, $f_4 = -\mathrm{I0}/\mathrm{I}$, $f_5 = \mathrm{Tst}$ and w_i is a constant indicating the weight (and hence importance) assigned to f_i. By giving a relatively large value to w_i it is possible to favor f_i over other objective functions. Note that the condition $\sum_{\mathrm{i=1}}^{\mathrm{k}} w_i = 1$ can be posed in Eq.(35).

Nevertheless, since the 5 functions of the multi-objective function have different ranges, for instance f_1 varies from 85 to 91 and f_5 varies from 0.07 to 1.3. Thus, the values of these functions must be normalized between 0 and 1. The minimum of a given function is equal to 0 and the maximum is equal to 1. The normalization operation is given by:

$$\mathrm{Normalized_{Value}} = \frac{\left(\mathrm{Actual_{Value}} - \min(f_i)\right)}{\max(f_i) - \min(f_i)} \tag{36}$$

and (35) becomes:

$$\mathrm{F_{objective}} = \sum_{\mathrm{i=1}}^{5} \mathrm{w_i}\, f_{i_{\mathrm{Normalized}}} \tag{37}$$

For this chapter we have chosen the first approach i.e. the single objective one.

The PSO algorithm is implemented to optimize the design of induction motor whose specifications are given above. The results of PSO algorithm for the optimized motor are given in the Table 9. The algorithm has returned an acceptable solution every time, which is indicated by a good value for objective with no constraint violations.

Parameters	EFF	Kg/KW	Tr	I0/I	Tst
P	4	4	4	4	6
CDSW	3	5	3	5	5
Cdb	4	6	4	6	6
Spp	4	4	4	3	4
Tstrip	2	2	2	2	2
Zsw	2	2	2	2	2
Existing Motor	89.7	5.36	53.8	0.27	0.5
Optimized Motor	90.1	5.15	48.5	0.26	1.3

Table 9. Optimum design results for efficiency maximization, minimization of kg/kW, minimization of temperature rise, minimization of the ratio I0/I and starting torque maximization.

According to the results presented in Table 9, when the efficiency of the motor is considered as the objective function, we can see that it increased from 89.7 to 90.1 compared to the existing motor. We can notice also that the when Kg/KW is minimized, it reduced from 5.36 to 5.15. Moreover, the optimization process allowed to the temperature rise to decrease form 53.8 to 48.5 which is a important reduction. Likewise, the I0/I is slightly reduced from 0.27 to 0.26 when it is the objective function. Finally, Table 9, shows that the starting torque is higher for the optimized motor (1.3) compared to the existing one (0.5).

According to these results, we can say that PSO is suitable for motor design and can reach successful designs with better performances than the existing motor while satisfying almost every constraint.

5. Conclusion

This chapter investigated the optimal design of induction motor using DOE and PSO techniques with five objective functions namely, maximization of efficiency, minimization of kg/kW, minimization of temperature rise in the stator, minimization of I0/I ratio, maximization of starting torque. It has been shown that DOE and PSO based algorithms constitute a viable and powerful tool for the optimal design of induction motor. The main objective of the DEO here is to identify the effect of each parameter on the objective functions. This is of a paramount importance mainly because of two reasons. The first one and also the obvious one is the reduction of the number of parameters to be taken into

consideration in the optimization stage called screening. This can be achieved by neglecting the parameters with less effect. This will reduce the computing time burden and simplify the analysis of the designed motor. The second reason is that among the influent parameters themselves we can classify the parameters in function of their calculated effect. This will help the designer to have a clear picture of the importance of each parameter. For instance, if two parameters having respectively 45% and 5% of influence on a given objective function are compared; it is obvious that even if both parameters have an effect on the given objective function, the first one is greatly more important than the second one.

The approach developed here is universal and, although demonstrated here for induction motor design optimization, it may be applied to the design optimization of other types of electromagnetic device. It can be used also to investigate new types of motors or more generally electromagnetic devices. MATLAB code was used for implementing the entire algorithm. Thus, another valuable feature is that the developed approach is implementable on a desktop computer.

Author details

Houssem Rafik El-Hana Bouchekara
Department of Electrical Engineering, College of Engineering and Islamic Architecture, Umm Al-Qura University, Makkah, Saudi Arabia
Electrical Laboratory of Constantine "LEC", Department of Electrical Engineering, Mentouri University – Constantine, Constantine, Algeria

Mohammed Simsim and Makbul Anwari
Department of Electrical Engineering, College of Engineering and Islamic Architecture, Umm Al-Qura University, Makkah, Saudi Arabia

6. References

Altayib K., Ali, A. (2011). Improvement for alignment process of automotive assembly plant using simulation and design of experiments. International Journal of Experimental Design and Process Optimization, vol.2, no.2, pp.145-160.

Blanusa, B. (2010). New Trends in Efficiency Optimization of Induction Motor Drives, New Trends in Technologies: Devices, Computer, Communication and Industrial Systems, Meng Joo Er (Ed.), ISBN: 978-953-307-212-8, InTech.

Boldea, I. Nasar, S.A. (2002). The Induction Machine Handbook. CRC Press LLC, ISBN 0-8493-0004-5.

Bouchekara, H., Dahman, G., Nahas, M. (2011). Smart Electromagnetic Simulations: Guide Lines for Design of Experiments Technique. Progress in Electromagnetics Research B, Vol. 31, 357-379.

Brownlee, J. (2011). Clever Algorithms: Nature-Inspired Programming Recipes, lulu.com; 1ST edition, ISBN-10: 1446785068.

Clerc, M. (2006). Particle Swarm Optimization, Hermes Science Publishing Ltd., ISBN 1905209045, London.

Costa, M. C. (2001). Optimisation De Dispositifs Electromagnétiques Dans Un Contexte D'analyse Par La Méthode Des Eléments Finis. PhD thesis, National polytechnic institute of Grenoble.

Cunkas, M. Akkaya, R. (2006). Design Optimization of Induction Motor by Genetic Algorithm and Comparison with Existing Motor. Mathematical and Computational Applications, Vol. 11, No. 3., pp. 193-203.

Demonsant, J. (1996). Comprendre et Mener des Plans d'Expériences. Afnor, ISBN 2-124-75032-1.

Kennedy, J. Eberhart, R. C. (1995). Particle swarm optimization. Proceedings IEEE international conference on neural networks, Vol. IV, pp. 1942– 1948.

Kennedy, J., Eberhart, R. C., Shi, Y. (2001). Swarm Intelligence, San Francisco: Morgan Kaufmann Publishers.

Kleijnen, J. P. C., Sanchez S. M, T.W. Lucas, Cioppa, T. M. (2005). State-of-the-Art Review: A User's Guide to the Brave New World of Designing Simulation Experiments. Journal on Computing 17(3): 263–289.

Kutlea, L., Pavlovića, N., Dorotića, M., Zadroa, I., Kapustića, M., Halassy, B. (2010). Robustness testing of live attenuated rubella vaccine potency assay using fractional factorial design of experiments. Vaccine, vol.28, no.33, 2010, pp.5497-5502.

Maljkovic, Z., Cettolo, M. (2001). The Impact of the Induction Motor on Short-Circuit Current", IEEE Ind. Application Magazine, pp. 11-17.

Murthy, K.M.V. (2008). Computer-Aided Design of Electrical Machines', ISBN: 978-81-7800-146-3, Bs Publications/bsp Books.

Pillet, M. (1997). Les Plans d'Expériences par la Méthode TAGUCHI. Les Editions d'Organisation, ISBN 2-70-812031-X.

Poli, R. (2008). Analysis of the publications on the applications of particle swarm optimisation. Journal of Artificial Evolution and Applications, 1:1–10.

Poli, R., Kennedy, J., Blackwell, T. (2007). Particle swarm optimization an overview. Swarm Intelligence, 1:33–57.

ReliaSoft Corporation, 2008, Chapter 2: Overview. Available from: http://www.weibull.com/DOEWeb/experiment_design_and_analysis_reference.htm#introduction.htm>.

Thanga Raj, C., Srivastava, S. P., Agarwal, P. (2008). Realization on Particle Swarm Optimized Induction Motor Via SPEED/PC-IMD", IAENG Int. J. of Computer Science, Vol. 16, No. 4, pp. 486-492.

Uy, M., Telford, J.K. (2009). Optimization by Design of Experiment techniques. Aerospace conference, IEEE, pp.1-10, 7-14.

Vogt. V. (1988). Electrical Machines. Design of Rotary Electric Machines, Fourth edition (in German), VEB Verlag Technik Berlin.

Chapter 8

Noise of Induction Machines

Marcel Janda, Ondrej Vitek and Vitezslav Hajek

Additional information is available at the end of the chapter

http://dx.doi.org/10.5772/38152

1. Introduction

Diagnostics of electric machines is very interesting and extensive. There are many methods used to detect properties of electrical machines. Between diagnostic methods include too the measurement and analyze of noise, which generates electrical machines.

Itself the noise of electric machines is byproduct of the machine operation. The generation of noise is involved in many physical principles.

Noise of electrical machinery is generated by the vibration of machine parts. Gradual spread of vibration from the engine to the surroundings causes pulses of air with certain frequencies. This creates a sound wave generator, which can be within a certain frequency range, audible to humans.

The main sources of noise in electrical machines are time change of the electromagnetic fields, noise of bearings and other mechanical sources. Finally, the unwanted noise is creating too due to coolant flow or parts that come into contact with coolant in electric machines. Level of noise sources in electrical machines depends on the structural arrangement and the accuracy of engine design.

A major problem in measurement noise is interference environment. For a perfect suppression ambient noise is necessary to have a specialized laboratory. It should be also measured machine have isolated from vibration, which it may be transferred from storage.

2. Basic concepts of noise

The sound wave is generated by vibrating objects and can be defined as mechanical interference with the finite speed of advancing through the media. These waves have small amplitude, adiabatic oscillation are characterized by a wave speed, wavelength, frequency and amplitude. Sound has the character of longitudinal sound waves in the direction of propagation in the environment. In other words, it is the movement of individual particles

of the medium in a direction parallel to the transmission of energy. Sound waves spread in three-dimensional environment from the source. It is same in all directions, if is the environment homogeneous. Sound waves can be polarized, they cannot have orientation. Non-polarized waves can oscillate in any direction in the plane perpendicular to the direction of propagation.

Sound amplitude can be measured as sound pressure level (SPL), sound intensity (SIL), sound power level (SWL) and the intensity of the acoustic energy (SED). The human ear can perceive sound waves of sufficient intensity and frequencies are ranging from 20 to 20,000 Hz. The Minimum sound intensity is different for different frequency and it is called the threshold of audibility. Range of sound intensity, which can capture the human ear, is 10-12 to 1 W/m^2corresponding sound pressure of 20 MPa. Maximum sound level in which humans feel pain is called threshold of pain. Amplitude of sound about pressure 100 Pa is very loud.

2.1. Acoustic pressure

Concentration of particle of vibrating environment corresponds with increase or decrease pressure inside gasses and liquids. This means that the total pressure in the environment is changing and therefore fluctuates around the initial static value or barometric pressure. The acoustic pressure is then considered deviation of the total pressure from the static pressure. For acoustic pressure is valid relationship

$$p_c = p_\mathrm{b} + p(t) \tag{1}$$

$$p(t) = p_0.cos(\omega.t + \varphi) = \mathrm{p}_0.cos(2.\pi.f.t + \varphi) \tag{2}$$

$$p_c = p_0 + p_0.cos(2.\pi.f.t + \varphi) \tag{3}$$

Where

- $\mathrm{p_c}$… Acoustic Pressure [Pa]
- p_b… Barometric pressure [Pa]
- $\mathrm{p_0}$…Amplitude of sound pressure [Pa]
- f… Frequency [Hz]
- t… Time [s]
- φ…phase shift

For effective sound pressure value is valid relationship

$$\mathrm{p_{ef}}\frac{p_0}{\sqrt{2}} \tag{4}$$

Acoustic pressure is a variable and it describing the noise source quantitatively. The measured level depends on the observer's distance from the source and the quality of the transmission environment Acoustic pressure level gives us information on the total sound pressure across a entire audible band. For sound pressure level is valid relationship

$$L\_p = 20.log(p/p\_0) \tag{5}$$

Where

- p ... Static pressure [Pa]
- p_0 ...Minimum value of static pressure, which is able to capture the human ear [Pa]

2.2. Sound power level

Mechanical vibrations are transmitted in form of mechanical energy from the source through acoustic waves. Sound power level is called the energy that passes per unit time over surface. For sound output, we can write the relationship

$$P_{ac} = p_c . v . A \tag{6}$$

Where

P_{ac}… Sound power level [W]
p_c… Acoustic pressure [Pa]
v… Vibration velocity of particles[m/s]
A… Area [m^2]

The sound power level depend on the the environment parameters and distance from the measurement point. The sound power level can be expressed as

$$L_{Pac} = 20 . \log\left(\frac{v}{10^{-9}}\right) + k \tag{7}$$

Where

k… constant

2.3. Acoustic intensity

Acoustic intensity is a vector quantity that describes the amount and direction of flow of acoustic energy in the environment. Vector of acoustic intensity is time-change of instantaneous sound pressure and it is corresponding instantaneous speed of vibrating particle environment in the same place

$$I = \overline{p(t) . v(t)} \tag{8}$$

Where

I… Acoustic intensity[W/m^2]

3. Noise sources

From the physical point of view, mechanical sound is waves in a flexible environment. The Frequency range of sound audibly for human ear is from 20 Hz to 20 kHz. The sound spreads in all directions from resources by transmitting acoustic wave energy. Division by frequencies of sound waves:

- Infrasound - up to 20Hz
- Low frequency - 20Hz to 40Hz
- RF - 8kHz to 16kHz
- Ultrasound - 20kHz over

Dividing the sound by timing:

- Steady
- variable
- intermittent
- pulse

The interest noise frequency is over 1000 Hz for induction machines. Noise of Electrical Machines is characterized as a set of sounds that are caused by rapid changes in air pressure. These changes cause most commonly:

- Vibration of machine parts or the whole of its surface
- Aerodynamic phenomena that lead to pulsation of pressure near the machine

Basic sources of noise are induction motors (see diagram):

- Electromagnetic source
- The mechanical source
- The aerodynamic source

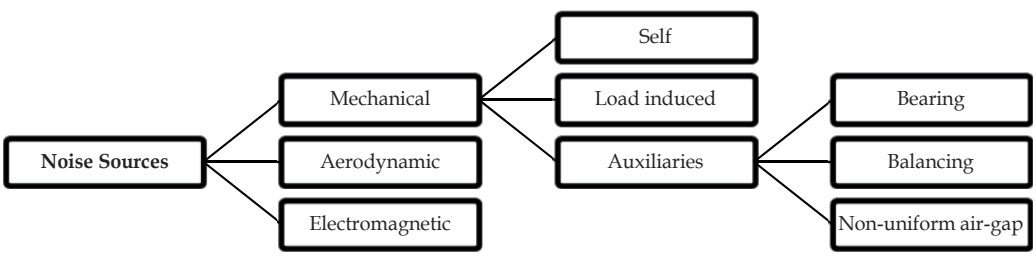

Figure 1. Division of noise sources in electrical machines

The noise from electromagnetic source is the most typical component noise of electrical machine. Its cause is the vibration of motor body, or other parts of the machine on which work the electromagnetic forces. Frequency Spectrum noise of the electromagnetic source has discrete character, while there is very distinct directional radiation characteristics of this component in many cases.

Determining the influence of this component on the overall noise of electric machine is often simply done so, that after switching off the machine from the network is observed decline in

the acoustic signal in time. If is this decline immediately, then it is obviously a component of the noise of electromagnetic origin. Another method of investigation is the measurement of electromagnetic noise spectrum for different values of power - or even frequency.

Noise origin of ventilation is crucial observe especially in machines with high rotational speed. Detailed analysis of the fan noise shows that the main source in this case is very fan with its nearest surroundings. It is the decisive exceeds other sources of noise, which can be, for example rotor wings, radial or axial cooling channels in the machine, input and output caps and the like.

Frequency analysis of noise ventilation origin shows that the spectrum has a broadband character, either discrete or vice versa. In the first case, the aerodynamic noise is created from turbulent airflow near fan blade and near the entrance, but also the output edges of blades. These pulsations are uneven both in space and in time, so the frequency spectrum created of wind noise is broadband and contains all components of the audible band.

In contrast, discrete nature of the spectrum, sometimes the siren phenomenon can arise. This phenomenon arise if the fan or behind obstacles (such as a blade with these obstacles) is not profile of velocity uniform air flow around the wheel circumference, leading to periodic pulsation of pressure. Then the siren noise is produced naturally.

The noise of mechanical origin is primarily inflicted on roller bearings and unbalance of rotating machine parts. Rolling bearings can create multiple frequency components, which have their origin mainly in inequality as part of rolling paths of the bearing rings. In principle, the noise of mechanical origin has a mixed character.

3.1. Electromagnetic noise

The influence of magnetic induction in the air gap formed magnetic forces; these forces operate across various directions. They may also have various amplitude and frequency. Their work is split between the rotor and stator of electric machine. Their characteristics depend on the size and shape of the air gap and a number of other factors.

The construction of the rotor is the main radiator noise machine. If the frequency is close to the radial force or equal to one natural frequency of the stator system, resonance occurs which leads distorted stator system with vibration and noise. Magnetostriction noise electric machine can be neglected in most cases due low and high frequency 2f arrangement r = 2p of radial forces, where f is the fundamental frequency and p is the number of pole pairs. However, the radial forces due magnetostriction can reach up to 50% the radial forces produced in the air gap magnetic field.

Magnetic flux density wave

$$\text{Stator: } B_{m1}.cos(\omega_1.t + k.\alpha + \Phi_1) \tag{9}$$

$$\text{Rotor: } B_{m2}.cos(\omega_2.t + l.\alpha + \Phi_2) \tag{10}$$

Where

- B_{m1} … Amplitude of magnetic flux density in stator [T]
- B_{m2}… Amplitude of magnetic flux density in rotor [T]
- ω_{Φ_1} … Angular frequency of stator magnetic fields
- ω_{Φ_1} … Angular frequency of rotor magnetic fields
- k,l … Variable (values 1,2,3,4,….)

For total wave of magnetic flux density can be write relationship

$$P_{mr} = 0{,}5.B_{m1}.B_{m2}.cos[(\omega_1+\omega_2).t+(k+l).\alpha+(\Phi_1+\Phi_2)]+$$
$$+0{,}5.B_{m1}.B_{m2}.cos[(\omega_1+\omega_2).t+(k-l).\alpha+(\Phi_1-\Phi_2)] \quad (11)$$

The magnetic stress wave has worked in radial directions on the stator and on active surfaces of rotor. This causing the deformation and subsequently cause the vibration and noise.

The mixed product of stator and rotor winding space harmonic create forces at frequencies

$$f_r = f_1.\left[\frac{n.Z_r}{p}.(1-s)+2\right]$$
$$f_r = f_1.\left[\frac{n.Z_r}{p}.(1-s)\right] \quad (12)$$

Where

- f_1… Supply frequency [Hz]
- n…. value n=0, ±1, ±2,… [-]
- p… number of pole pairs [-]
- N_{rs}…Number of rotor slots [-]
- s… slip

The mixed product of stator winding and rotor eccentricity space harmonics create forces with frequencies

$$f_r = f_1.\left[\frac{n.N_{rs}}{p}.(1-s)+2\right]$$
$$f_r = f_1.\left[\frac{n.N_{rs}}{p}.(1-s)\right]$$
$$f_r = f_1.\left[\frac{n.N_{rs}}{p}.(1-s)+\frac{1-s}{p}\right]$$
$$f_r = f_1.\left[\frac{n.N_{rs}}{p}.(1-s)+2+\frac{1-s}{p}\right] \quad (13)$$

The mixed product of stator winding and rotor saturation harmonics create forces at frequencies

$$f_r = f_1.\left[\frac{n.N_{rs}}{p}.(1-s)+4\right] \tag{14}$$

$$f_r = f_1.\left[\frac{n.N_{rs}}{p}.(1-s)+2\right] \tag{15}$$

3.2. Rotor eccentricity

The air gap width depends only on position (no on time) in the static eccentricity. We conclude that the magnetic field in the air gap is rotating synchronous speed. That is given by the mains frequency and with the number of pole pair's induction machine. Modulation of magnetic field in one period is function, which is represented by a variable air gap, i.e. a function of its conductivity. Static eccentricity is defined as the rotor axis offset from the axis of the stator. The air gap has a variable character. There is stronger interaction of stator and rotor magnetic field at the point where the gap is smaller. Influence of the static eccentricity manifests as the emergence of side frequency bands, which are shifted from the mains frequency f_1 of the synchronous frequency f. For static eccentricity is the angular frequency $\Omega_\varepsilon = 0$.

Static eccentricity is straight-line. The frequency for static eccentricity is twice power frequency

$$f_{stat} = 2.f_1 \tag{16}$$

The relative eccentricity ε is defined as

$$\varepsilon = \frac{e}{g} = \frac{e}{R-r} \tag{17}$$

Where

- R… Inner stator core radius
- r… Outer rotor radius
- e… Rotor eccentricity
- g… Ideal uniform air-gap for e=0

Dynamic eccentricity occurs when the rotor failure or its affiliates. Ratios are complicated by the fact that the width of air gap is not just a function of position, but is also a function of time. The variable air gap is changing at the rotation of the rotor. There is emergence of side bands that appears in the frequency range of vibrations of electric machine.

Angular frequency for dynamic eccentricity

$$\Omega_\varepsilon = \Omega.(1-s) = \frac{\omega}{p}.(1-s) = 2.\pi.\frac{f}{p}.(1-s) \tag{18}$$

The frequency generated by the dynamic eccentricity

$$f_{DYN} = f_1 \pm (1-s).f_{SO} \tag{19}$$

For frequency generated by eccentricity is true also relationship

$$f_{exc}\left[(n_{rt}.R \pm n_d).\frac{1-s}{p}.n_{\omega s}\right].f \tag{20}$$

Where

- R…Number of grooves engine
- s… Chute
- p… Number of pole pairs

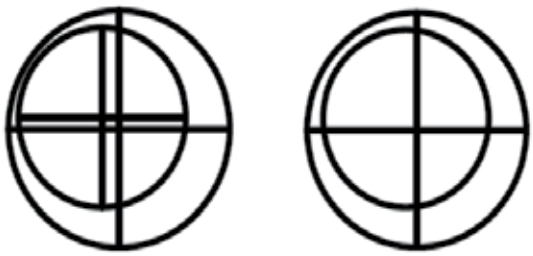

Static eccentricity Dynamic eccentricity

Figure 2. Rotor eccentricity

3.3. Aerodynamic noise

Aerodynamic noise arises most often around the fan, or in the vicinity of the machine that behaves like a fan. Noise can be created too on the necks stator slot windings or rotor. The aerodynamic noise sources can also include the noise produced by air flow inside and outside the design of electrical machines.

The main reason for the fan noise is formation of turbulent air flow around the blades. This noise is characterized by spectrum in a wide range, which has continuous character. Acoustic performance is increasing with the square of velocity. Siren noise can be eliminated by increasing the distance between the impeller and the stationary obstacle.

For the fan noise can write the relationship

$$L_A = 60.logU_2 + 10.logD_2.b_2 + \sum k_1 \tag{21}$$

Where

- U_2…Outer speed of fan on the circuit $[m.s^{-1}]$
- D_2…Outer diameter of the fan [m]
- B_2… Fan width [m]
- k_1… Constants for the correction

The vortex frequency is expressed by

$$f_v = 0{,}185.\frac{v}{D_2} \tag{22}$$

The frequency of the pure tone due to the fan blades is given by relationship

$$f_f = N_b . \frac{N}{60} \tag{23}$$

Where

- N…speed [rev/min.]
- N_b… Number of fan blades [-]

Sound power level of aerodynamic noise is

$$L_w = 67 + 10. log_{10}(P_{out}) + 10. log_{10}(p) \tag{24}$$

$$L_w = 40 + 10. log_{10}(Q) + 20. log_{10}(p) \tag{25}$$

$$L_w = 94 + 20. log_{10}(P_{out}) - 10. log_{10}(Q) \tag{26}$$

Where

- P_{out}… Motor rated power [kW]
- p… Fan static pressure [Pa]
- Q…Flow rate [$m^3 . s^{-1}$]

Reducing aerodynamic noise in electrical machines can be use the following ways:

- Reducing the required amount of coolant used for ventilation of electrical machines
- Optimal design of fan. Especially the number and shape of the fan blades has an impact on the noise generated by the electric machine.
- To minimize the noise is needed to prevent vibration machine parts, which come into contact with a cooling medium.

3.4. Mechanical noise sources

Mechanical noise is mainly due with bearings, their defects, ovality, sliding contacts, bent shaft, rotor unbalance, shaft misalignment, couplings, U-joints, gears etc. In principle, the mechanical source of noise has a mixed character. The noise caused by unbalance of rotating parts and noise of bearing is spread after machine constructions very well. Dynamic balancing in production serves to reducing the noise of mechanical source. Especially for machines with high speed is necessary to perfect balance. Also, compliance with the manufacturing tolerances and technological processes, especially in the manufacture of small machines is the best solution to reduce the noise of mechanical source. Any change in noise from this source can mean failure of the mechanical parts inside the motor. For example, the bearings failure (damaged ball) is appear in the noise spectrum. There are specific frequencies by individual damage. The very faults of bearings and their effect on the noise spectrum of the electric machines are now well mapped.

Design of bearings can be either a sliding or rolling bearings. Rolling bearings can create multiple vibration frequencies, which have their origin mainly in the uneven parts or rolling themselves paths to the bearing rings. If bearing has mechanical damage, there is uneven

movement of the whole system and thus increasing vibration and noise of the electric machine.

The main mechanical sources of the noise

- Alignment
- Inaccurate machining of parts
- Running speed
- Number of rolling elements carrying the load
- Mechanical resonance frequency of the outer ring
- Lubrication conditions
- Temperature

3.4.1. Rolling bearings

The noise of rolling bearings depends on the type of bearing and its construction and accuracy of bearing parts. The increase in vibration and noise level of bearings, when the rotational speed changes from $n_1$ton_2 can be expressed as

$$\Delta L_v = 20.log\frac{n_2}{n_1} \tag{27}$$

Ball pass frequency – outer race

$$f_{or} = \frac{N_b}{2}.n_m.\left(1 - \frac{d_b}{D}.cos\alpha\right) \tag{28}$$

Where

- D…Pitch diameter [m]
- n_m… Rotation speed [rev/s]
- N_b…Number of balls [-]
- d_b…Diameter of balls]m]
- α…Contact angle of balls

Ball pass frequency – inner race

$$f_{ir} = \frac{N_b}{2}.n_m.\left(1 + \frac{d_b}{D}.cos\alpha\right) \tag{29}$$

3.4.2. Sleeve bearings

- Uneven journal

$$f_{ov} = k.n_m \tag{30}$$

k=1, 2, 3, …

- Axial groves

$$f_{gr} = N_g.n_m \tag{31}$$

N_g…number of groove

3.4.3. Load induced noise

In certain cases, the vibrations and thus noise transmitted from the load, which is connected to the induction motor. In most cases, this occurs with wrong balance or bad connects of couplings. Uneven distribution load acting on the motor shaft or inappropriate use of gears may also affect noise machine. The only possible protection against these effects is the perfect balance of the whole set and if possible an even distribution of forces acting on the connecting elements. Noise arises too due to coupling of the machine with a load, e.g., shaft misalignment. Next noise arises from belt transmission, from cogwheels and couplings. It may also arise to noise due to mounting the machine on foundation or other structure.

4. Noise measurement

For measurement noise of induction machines can be used several techniques. The basic method for the measurement noise is the sound meter. It is a device which measures sound pressure.

4.1. Measurement process

Measurement of noise can be divided into three main parts. The first part is data capture. For this purpose, the most commonly used microphones, or specialized equipment to measure noise (sound level meter). Their output is usually an analog signal, which must be further processed. When choosing of microphone is needed careful heed on certain parameters that can affect measurement accuracy. One of the most important parameter is the sensitivity of frequency. Worse microphones not recorded of the entire spectrum of the measured noise. Thanks to this complicates achieve it of accurate analysis results. Other parameters include the microphone sensitivity, which indicates the size of the output voltage (mV / Pa), depending on the pressure acting on the membrane. In addition, the structural dimensions of the measurement microphone and also the type of sound field that which is measured. Computers are most frequently use for Signal processing. For this reason it is necessary to convert from analog signal to digital form.

Large numbers of types A/D converters is on the market. Some are stand-alone converters; others are integrated to the specialized measurement cards. In both cases, the measurement depends on the three main parameters. The first is the measuring range of the converter. It gives the minimum, respectively maximum, measurable value. Because the signal is weak from a microphone, there should be used an amplifier for its amplification. Another parameter of the A/D converter is the bit depth conversion. This parameter defines the limitations of this device.

Figure 3. Block diagram of measurement process

Factors to selecting a suitable type of microphone are as follows

Characteristics of sound field	Required accuracy	Environmental conditions
Freely field for a closed chamber	Tolerance sensitivity	Noise level background
An important range of sound pressure levels	Frequency distortion tolerance	Humidity
An important frequency range	Phase distortion tolerance	Atmospheric pressure
	Tolerance of non-linear distortion	wind
	Own noise tolerance	Strong electromagnetic fields
		Mechanical shock

Table 1. Selecting factors of microphone

4.2. Sound level meter

Sound level meter is an essential instrument for measuring sound pressure levels. This device consists of the following components: Microphone, preamp, overload detector, central Unit, weighing Network, filters, amplifier, RMS detector, Output and Display.

One of the basic parameters of sound level meter is range of frequency. The sound intensity I has broad frequency range. The dispersion of the frequencies is from lower f_1 to higher f_2 . The immediate value is indicated by I (f). For sound intensity is valid the relationship

$$I = \int_{f_1}^{f_2} I(f)df \tag{32}$$

Where $I(f) = \frac{\Delta I}{\Delta f}$ is intensity in the frequency interval f = 1 Hz.

Spectral intensity level (ISL) L_{Is} is defined

$$L_{Is} = 10log\left[\frac{I(f)}{I_{ref}}\right] \tag{33}$$

Where I_{ref} is the reference intensity levels (for air $\frac{10^{-12}W}{m^2}$).

$$L_I = L_{Is} + 10log(\Delta f) \tag{34}$$

Similarly, the sound pressure level L_p is related to the level of spectral noise L_{ps}as follows:

$$L_p = L_{ps} + 10log(\Delta f) \tag{35}$$

$$\Delta f = f_u - f_l \tag{36}$$

Where f_l and f_u are the lower and upper frequency to half power.

5. Fast Fourier Transformation (FFT)

Fast Fourier Transformation is one of the most common mathematical functions, which is used for noise analysis of electrical machines. The Fast Fourier Transformation is applied in an increasing scale in science, engineering, and technology. The use of complex exponentials has often been convenient rather than fundamental. Most signals and functions used in real applications are real rather than complex. In areas such as digital filtering, convolution, correlation, image processing, and partial differential equations, the actual signals or functions, are real, but they are considered to be the real part of a complex quantity in order to be able to use the complex formulation of Fourier series and transforms. The complex Fourier transform (CFT) of a signal$x(t) - \infty \leq t \leq -\infty$ with finite energy, is defined as

$$x_c(f) = \int_{-\infty}^{\infty} x(t).e^{-j2.\pi.f.t}dt \tag{37}$$

The inverse complex Fourier transform (ICFT) is given by

$$x(t) = \int_{-\infty}^{\infty} x_c(f).e^{j.2.\pi.f.t}dt \tag{38}$$

The real Fourier transform (RFT) of $x(t)$ can be defined as

$$x(f) = 2\int_{-\infty}^{\infty} x(t).cos\big(2.\pi.f.t + \Theta(f)\big)dt \tag{39}$$

$$\text{Where: } \Theta(f) = \begin{cases} 0, & f \geq 0 \\ \frac{\pi}{2}, & f < 0 \end{cases}$$

The inverse real Fourier transform (IRFT) is given by

$$x(t) = \int_{-\infty}^{\infty} x(f).cos\big(2.\pi.f.t + \Theta(t)\big)df \tag{40}$$

Equation (3) and (5) can be written for $f \geq 0$ as follows

$$x_1(f) = 2\int_{-\infty}^{\infty} x(t).cos(2.\pi.f.t)dt \tag{41}$$

$$x_0(f) = 2\int_{-\infty}^{\infty} x(t).sin(2.\pi.f.t)dt \tag{42}$$

And

$$x(t) = \int_{-\infty}^{\infty}[x_1(t).cos(2.\pi.f.t) + x_0(t).sin(2.\pi.f.t)]df \tag{43}$$

Thus $x(f)$ equals $x_1(f)$for$f \geq 0$, and $x_0(f)$ for$f < 0.x_1(f)$and$x_0(f)$ will be referred toas the cosine and the sine parts. The relationship between the CFT and the RFT can be expressed for $f \geq 0$ as$x_c(0) = x_1(0)$

$$\begin{bmatrix} x_c(f) \\ x_c(-f) \end{bmatrix} = \frac{1}{2}.\begin{bmatrix} 1 & -j \\ 1 & j \end{bmatrix}.\begin{bmatrix} x_1(f) \\ x_{10}(f) \end{bmatrix}, f \neq 0 \tag{44}$$

Equation (44) reflects the fact that $x_1(f)$ and $x_0(f)$are even and odd functions, respectively.

The inverse of (44) for $x_1(f)$ and $x_0(f)$ is

$$\begin{bmatrix} x_1(f) \\ x_0(-f) \end{bmatrix} = \begin{bmatrix} 1 & 1 \\ 1 & -j \end{bmatrix} . \begin{bmatrix} x_c(f) \\ x_c(-f) \end{bmatrix} \tag{45}$$

Equations (44) and (45) are very useful to convert from one representation to the other. When $x(t)$is real, $x_1(f)$ and $x_0(f)$are also real. Then, (44) shows that $x_c(f)$ and $x_c(-f)$ are complex conjugates of each other. Equations (44) and (45) are also valid in the case of the discrete time Fourier transformation. In addition, they are valid for Fourier series and the discrete Fourier transforms with the replacement of fby the frequency index n. The RFT relations given by (43) can be proven by using (44), and writing (38) as

$$x(t) = \int_0^{\infty} \frac{1}{2} . [x_1(f) - jx_0(f)] . e^{j.2.\pi.f.t} df + \int_0^{-\infty} \frac{1}{2} . [x_1(-f) - jx_0(-f)] . e^{j.2.\pi.f.t} df \tag{46}$$

Then

$$x(t) = \int_0^{\infty} [x_1(f) . cos(2.\pi.f.t) + x_0(f) . sin(2.\pi.f.t)] df \tag{47}$$

6. Measurement noise of induction machines

6.1. Disturbed surroundings

Surrounding noise sources have an impact on the measurement of electrical machinery. It is not always possible to perform measurements in specialized laboratories, which are perfectly sound-insulated. To laboratory measurement can penetrate the noise from nearby sources (see Fig. 4), which is inaudible to the human ear. The interference from other sources can be created undesirable frequencies in the frequency band.

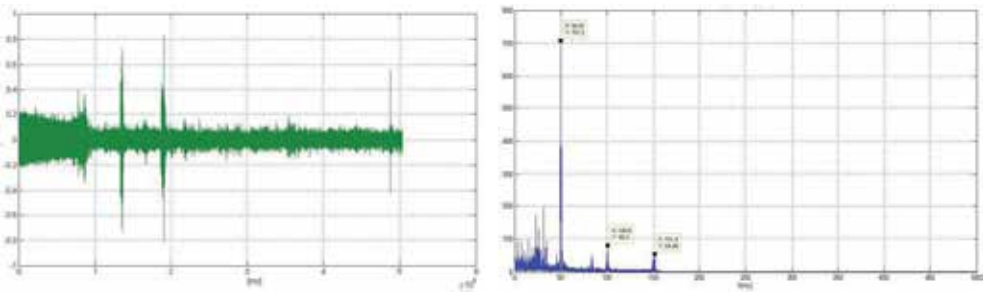

a) Noise detected in the laboratory b)Fast Fourier Transformation of laboratory noise

Figure 4. Noise measurement in the laboratory when the machine is switched off

Interference of other sources in the neighborhood of workplace cannot be directly prevented, but you can minimize their impact on analysis of the measured signal. Before the measurements it must be made measurement ambient noise before the main measurements. It is necessary to determine whether the background noise is random, or it is periodically repeated. In the case of random noise is preferable to wait to other time of measurement or it must count with errors in the measurement. In the event that can be measurement of noise repeated. Can be recorded the extent of spectral interference with which will be calculate when evaluating the measured results. From Spectral analyses of interference is possible to

determine the proportion of individual harmonics. These harmonic then they can be the "subtracted" from the noise levels of electrical machines.

The next part of the measurement was performed on the induction motor which worked without a load. The electric motor was loosely placed on a foam board. This board was for suppression the transmission of vibrations from the surroundings. External vibrations are not desirable for accurate measurements.

Measurement noise of electric machine, that is run, is shown in Fig. 5. As seen from the measured values, that the noise level is constantly fluctuating.

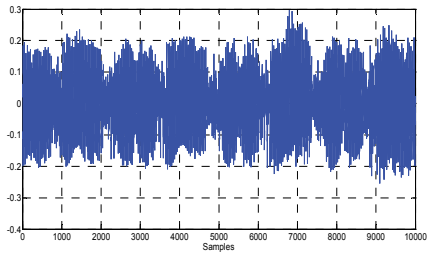

Figure 5. Noise of induction machines - no load

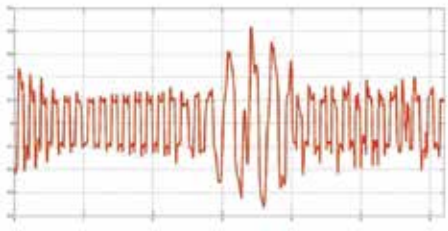

Figure 6. Noise of induction machine – 1 rotation

6.2. Noise of induction machine

On Fig. 7 is an analysis of the measured noise using MATLAB. Specifically, was carried Fast Fourier Transform (FFT). Dominant frequency is 600 Hz. This frequency is multiple of power supply frequency. It is a frequency of radial forces. In measurement signal can be involved many harmonics frequencies of radial forces. Than we can write equation

$$f_v = 6.k.f \tag{48}$$

Where

- f_v … Frequency of radial force [Hz]
- f … Power supply frequency [Hz]
- k … Number (k=1, 2, 3, …..)

For $f = 50Hz$ are frequencies of radial forces $f_v = 300, 600, 900, \ldots Hz$.

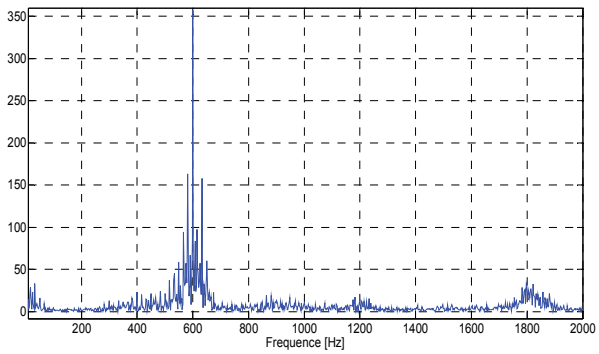

Figure 7. Fast Fourier Transformation of induction machine noise

It was done measurements eccentricity of rotor. Eccentricity of rotor is shown in Fig. 9. From the measured values it was found that the largest deviations occur in the range of approximately 120 degrees.

When comparing the noise of induction machines recorded on one rotation and values of rotor eccentricity can see a connection. In both cases (Fig. 8 and Fig. 9) appeared larger deflection in the range of 120 degrees. Extreme deviation is in a different quadrant in each graph. This is due to the different measurement principles. Noise measurements done digitally, while measuring the eccentricity was used mechanical method. It was therefore not possible to accurately determine the initial rotor position in both measurements.

it can be argued that the noise of induction machines is generated of the rotor who has eccentricity. Given that the, that machine is equipped with a ventilator, there are two sources of noise. The influence of the fan but will not cause displacement of only a specific part of one rotation.

Given that the measured induction motor was not equipped with cooling system (fan) can be assumed, that the vibration and thus the noise are produced only by electromagnetic source and mechanical source.

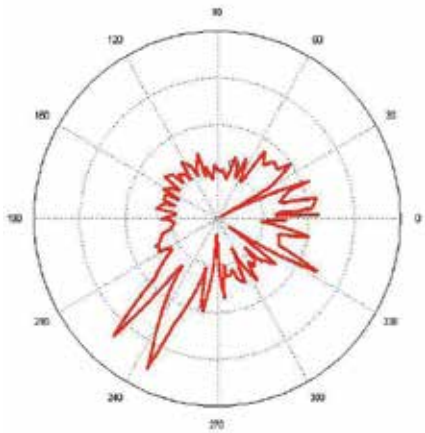

Figure 8. Noise envelope – 1 rotation

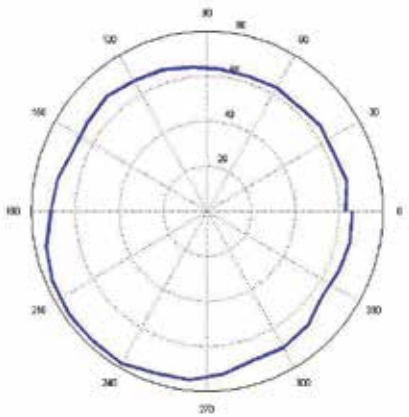

Figure 9. Rotor Eccentricity - Mechanical measurement

Analyze of noise was performed on the one rotation of rotor. The Fig 5 shows the noise levels depending on the position of the rotor. As the graph shows it is to generate greater levels of noise in the position of the rotor from 300 to 60 degrees (about 120 degrees).

7. Conclusion

Diagnosis of induction motors is a very complex issue that has many components. One of them is the analysis of motor noise. Noise measurement asynchronous machines are the commonly used diagnostic method. This method is relatively simple. You need to be near an electrical machine quality microphone and recording equipment. Analysis itself can be the performed on specialized software, either on the spot or later in laboratory.

Subsequent analysis of the signal can then indicate whether the machine operates as required, or whether there was damage to electrical equipment. Based on the fast Fourier analysis of noise can be determined which components of the signal are dominant. Based on knowledge of layout design of the engine is then possible to determine what is causing individual harmonics. According to the frequency it is possible to determine which there the main sources of noise are.

A major problem in measuring the noise may be interference from nearby sources. To avoid the external influence of external noise is possible only in specialized laboratories.

During measurements realized appeared possible link between noise and rotor eccentricity of electrical machinery. In the analysis of noise is dominant skew in the range of 120 ° in one rotation. In the same range (120 °) was measured the dominant deflection of rotor eccentricity this rotor machine. Given that the machine has not a cooling system, there is not source of aerodynamic noise; there are only two possible causes of this deviation. Source of electromagnetic noise would not cause deviation only at certain rotor position, but in the whole rotation. Displacement of noise in a certain position the rotor it cannot assign too resources source of mechanical noise. This group includes vibration bearings. During the measurement was verified that the bearings are not damaged. There are not larger deviations of movement in rotation of bearing.

As a source of noise is impact of rotor eccentricity on the running of the induction motor. Unfortunately, the verification of this theory would require accurate measurement with recording of the rotor position and size of air gap. This measurement is very difficult.

Author details

Marcel Janda, Ondrej Vitek and Vitezslav Hajek
Brno University of Technology, Czech Republic

Acknowledgement

Research described in this paper was financed by the Ministry of Education of the Czech Republic, under project FR-TI3/073 Research and development of small electric machines; and the project of the Grant agency CR No. 102/09/1875 - – Analysis and Modeling of Low Voltage Electric Machines Parameters. The work was supported by Centre for Research and utilization of renewable energy - CZ.1.05/2.1.00/01.0014

8. References

Vijayraghavan, P.; Krishnan, R.; "Noise in electric machines: a review," Industry Applications Conference, 1998. Thirty-Third IAS Annual Meeting. The 1998 IEEE ,vol.1, no., pp.251-258 vol.1, 12-15 Oct 1998 doi: 10.1109/IAS.1998.732298

Ellison, A.J.; Yang, S.J.; "Effects of rotor eccentricity on acoustic noise from induction machines," Electrical Engineers, Proceedings of the Institution of, vol.118, no.1, pp.174-184, January 1971doi: 10.1049/piee.1971.0028

Hamata, Václav. Hluk elektrických strojů.Praha : Academia, 1987. 176 s.

Mišun, Vojtěch. Vibrace a hluk. 2. Brno :CERM, s.r.o., 2005. 176 s. ISBN 80-216-3060-5.

Gieras, Jacek F.; Wang, Chong; Cho Lai, Joseph. Noise of Polyphase Electric Motors. [s.l.] :CRC Press, 2005. 392 s. ISBN 978-0824723811.

Srinivas, K.N.; Arumugam, R.; "Analysis and characterization of switched reluctance motors: Part II. Flow, thermal, and vibration analyses", IEEE Transactions on Magnetics, vol.41, no.4, pp. 1321- 1332, April 2005 doi: 10.1109/TMAG.2004.843349. ISSN: 0018-9464

Srinivas, K.N.; Arumugam, R.; "Static and dynamic vibration analyses ofs witched reluctance motors including bearings, housing, rotor dynamics, and applied loads", IEEE Transactions on Magnetics, vol.40, no.4, pp. 1911- 1919, July 2004 doi: 10.1109/TMAG.2004.828034. ISSN: 0018-9464.

Ersoy, O.K.; "A comparative eview of real and complex Fourier-related transforms" Proceedings of the IEEE , vol.82, no.3, pp.429-447, Mar 1994 doi: 10.1109/5.272147. ISSN: 0018-9219

Chapter 9

Analysis of Natural Frequency, Radial Force and Vibration of Induction Motors Fed by PWM Inverter

Takeo Ishikawa

Additional information is available at the end of the chapter

http://dx.doi.org/10.5772/49950

1. Introduction

Lately, as engineers have recognized the importance of having a high-quality working place, the effect of the noise and vibration emitted by inverter-fed induction machines has become a subject to study. Economic considerations force to use less active material. Since the encasing is less stiff, the machine becomes more sensitive to vibrations and noise. Less use of iron in the stator not only yields to a weaker structure but also higher field levels, thus causing higher magnetic forces, which yields to increased vibrations. Then the first aim of this work is to reach a wide knowledge how the levels of noise and vibration generated by the induction motor vary under different working conditions.

Electromagnetic noise is generated when the natural frequencies of vibration of induction motors match or are close to the frequencies present in the electromagnetic force spectrum. In order to avoid such noise and vibration, it is necessary to estimate the amplitude of the radial electromagnetic forces as well as the natural frequencies of the structure. For this reason, several papers have been published to analyze the natural frequencies, electromagnetic force, vibration and acoustic noise. For the analysis of the natural frequencies, a lot of papers have analyzed the stator core without winding. However, it is known that it is difficult to estimate the Young's modulus of winding. For the analysis of the radial force, vibration and acoustic noise, several papers have been published (Ishibashi et al., 2003, Shiohata et al., 1998, Munoz et al., 2003). They gave the amplitudes as well as the frequencies of the radial electromagnetic force. However, they mainly treated the case when the slip was 0. Ishibashi et al. did not consider the rotor current (Ishibashi et al., 2003), and Munoz et al. specified stator currents calculated by MATLAB/Simulink as input data not stator voltages (Munoz et al., 2003).

This paper investigates the vibration of induction motors fed by a Pulse Width Modulation (PWM) inverter. First we analyze the natural frequencies of the stator by considering the stator coil, and compare with the measured ones. Next, we analyze the radial electromagnetic force by using two-dimensional (2D) non-linear finite element method (FEM) which is considering the rotor current and is coupled with voltage equations, and discuss the calculated result with the measured vibration velocity. We clarify the influence of slip, the distributed stator winding and the PWM inverter on the radial force. Moreover, it is well known that a random PWM reduces the acoustic noise emitted from an inverter drive motor (Trzynadlowski et al., 1994). Then, we investigate the radial force of the motor fed by two types of random PWM method, namely, a randomized pulse position PWM and a randomized switching frequency PWM.

2. Natural frequencies

2.1. Analysis method of natural frequencies

The mechanical equation for the stator model with the free boundary condition is expressed as

$$[\mathbf{M}]\{\ddot{x}\}+[\mathbf{K}]\{\mathbf{x}\}=\{\mathbf{0}\} \tag{1}$$

where, $\{\mathbf{x}\}$ is the node displacement, $[\mathbf{M}]$ and $[\mathbf{K}]$ are the global mass matrix and stiffness matrix. In the two-dimensional (2D) case, the plate is assumed to have constant mass density ϱ, area A, uniform thickness h, and motion restricted to the {x, y} plane. The element mass matrix is expressed as a 6 × 6 matrix

$$\mathbf{M}^e=\frac{\rho Ah}{12}\begin{bmatrix}2&0&1&0&1&0\\0&2&0&1&0&1\\1&0&2&0&1&0\\0&1&0&2&0&1\\1&0&1&0&2&0\\0&1&0&1&0&2\end{bmatrix} \tag{2}$$

The element stiffness matrix for plane strain is given by

$$\mathbf{K}^e=\frac{E}{(1+\nu)(1-2\nu)}\begin{bmatrix}1-\nu&\nu&0\\\nu&1-\nu&0\\0&0&(1-2\nu)/2\end{bmatrix} \tag{3}$$

where E is Young's modulus and ν is Poisson's ratio.

Equation (1) leads to the eigenvalue problem,

$$([\mathbf{K}]-\omega_i^2[\mathbf{M}])\{\Phi\}_i=\{\mathbf{0}\} \tag{4}$$

where, $\{\Phi\}_i$ is eigenvector representing the mode shape of the i-th natural angular frequency ω_i. We solve (4) by discretizing the stator into a finite element mesh and using an eigenvalue subroutine utilized in International Mathematics and Statistics Library (IMSL).

In the calculation of natural frequencies using FEM, the most important but unknown constant is Young's modulus of winding which is composed of the enameled wires, insulation films and vanish. Itori et al. has given the equivalent Young's modulus of winding in slot by the experimental investigation (Itori et al., 2002)

$$E = (0.0319S - 1.05) \times 10^9 \left[\mathrm{N/m^2} \right] \tag{5}$$

where, S is the space factor of winding.

2.2. Experimental motors

This chapter investigates the vibration characteristics of two motors, hereafter K-model and M-model, whose properties and characteristics are as follows. For M-model, 1.5 kW, 200 volt, 50 Hz, 6.8 A, 4 poles, number of stator slots: 36, number of rotor slots: 44, and one slot-pitch skewing, see Fig.1 (Mori et al., 2005, 2005). For K-model, 100 volt, 50 Hz, 4 poles, number of stator slots: 24, number of rotor slots: 34, stator winding: 66 turns, rotor bar: aluminium, and no skewing, see Fig. 2 (IEEJ, 2002).

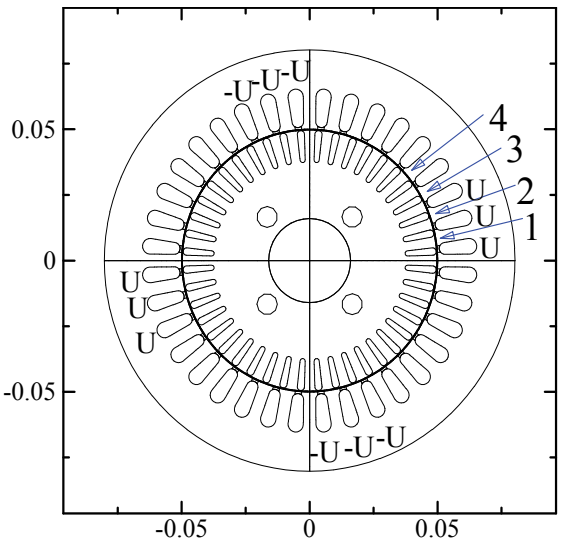

Figure 1. Experimental motor, M-model.

2.3. Measurement of natural frequencies

Natural frequencies are obtained by measuring the transfer function of the stator core. Fig. 3 shows an experimental setup to measure the natural frequencies. A piezoelectric accelerometer PV08A is placed at the top of the stator and is connected to one channel of a

charge amplifier UV-06. An impulse hammer PH-51 is connected to the other channel. The charge amplifier is connected to a signal analyzer SA-01A4, and then to a PC where a software for SA-01A4 is installed.

The transfer function is measured by hammering the stator surface. First, the natural frequencies of the stator core only of M-model are measured. We have removed the stator windings from the stator. Table 1 shows the four lowest measured natural frequencies.

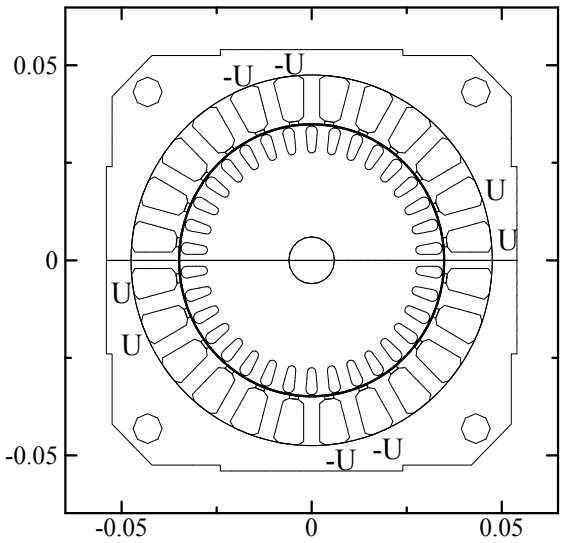

Figure 2. Experimental motor, K-model.

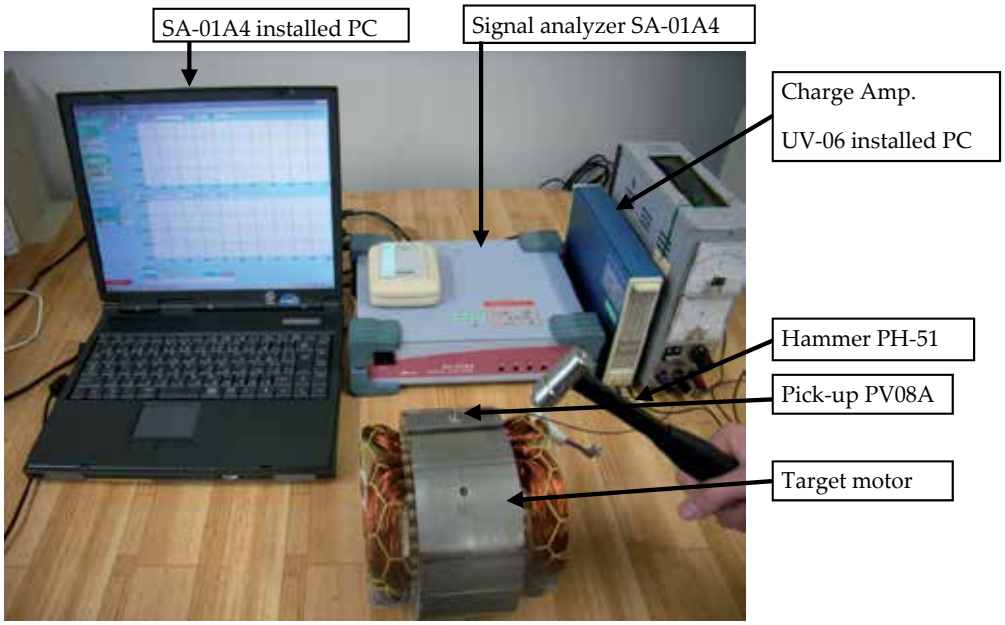

Figure 3. Experimental setup for measurement of natural frequencies.

Mode	Frequency [Hz]
2	1,325
2	1,337
3	3,425
3	3,875

Table 1. Measured natural frequencies of the stator core of M-model motor.

Next, the natural frequencies of the stator with winding of M-model are measured as shown in Fig. 4. The natural frequencies around 1,200Hz are generated from rotor. Three lowest natural frequencies except around 1,200Hz are shown in Table 2.

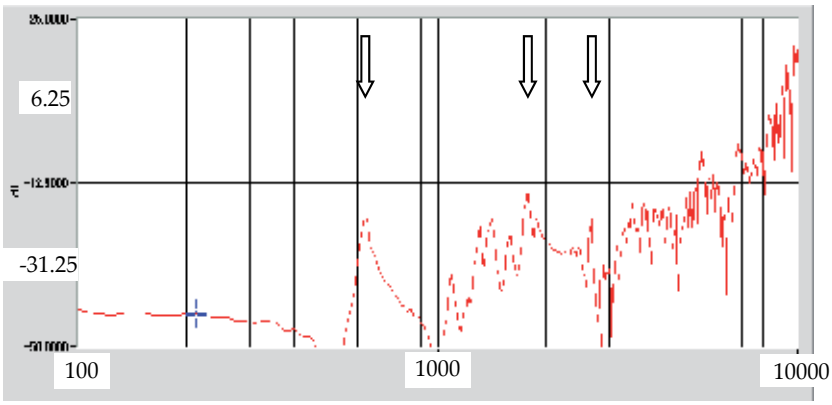

Figure 4. Natural frequencies measured for the whole motor M-model.

Mode	Frequency [Hz]
2	637
3	1,770
4	2,694

Table 2. Three lowest natural frequencies of the M-model motor with stator winding.

2.4. Calculation of natural frequencies

First, we calculate the natural frequencies for the stator core only of the M-model motor, whose mechanical properties include mass density of 7,850kg/m^3, Young's modulus of 2.1× 10^{10}N/m^2 and Poisson's ratio of 0.3. Table 3 shows the comparison of the calculated natural frequencies with the measured ones. It shows a good agreement between the measured values and the calculated ones. In this calculation, we use 18,811 finite element nodes. If we calculate the natural frequencies with a rough mesh, they become higher values. Fig. 5 shows the modes of stator due to each harmonic. The natural frequencies of 1,369 and 1,425Hz have mode 2, and 3,446 and 3,926Hz have mode 3.

Mode	Measured [Hz]	Calculated [Hz]
2	1,325	1,369
2	1,337	1,425
3	3,425	3,446
3	3,875	3,926

Table 3. Comparison of the calculated natural frequencies with the measured ones for the stator core only.

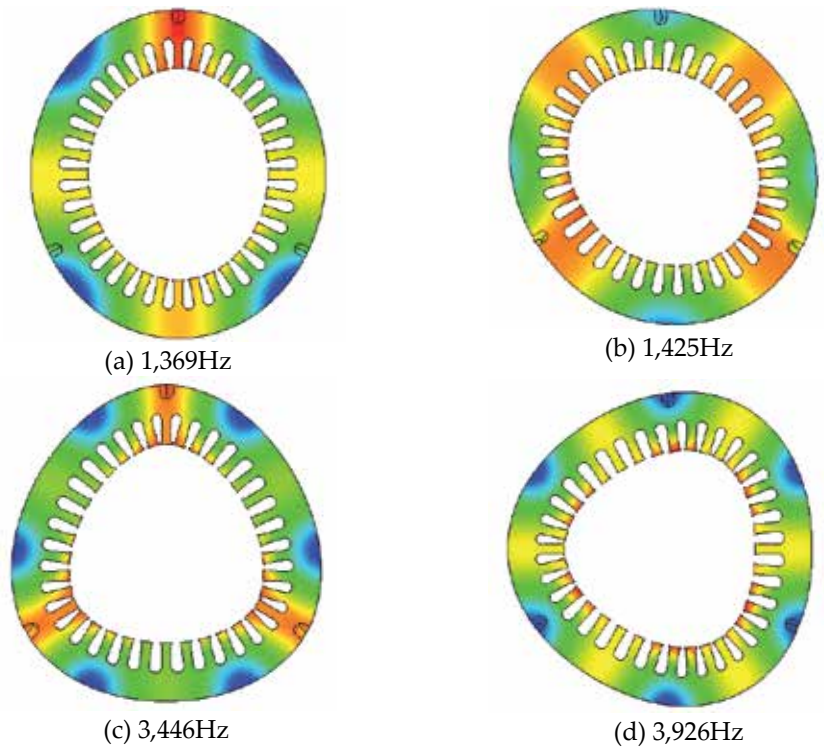

Figure 5. Natural vibration modes for stator core only.

Next, we calculate the natural frequencies of the stator with winding, where the space factor of winding is chosen to be 0.43 by considering the enameled wires. Three lowest natural frequencies and the natural vibration modes are shown in Table 4 and Fig. 6. The natural frequencies of 587, 1,545 and 2,739Hz have mode 2, 3 and 4, respectively.

Mode	Measured [Hz]	Calculated [Hz]
2	637	587.0
3	1,770	1,544.6
4	2,694	2,739.0

Table 4. Comparison of the calculated natural frequencies with the measured ones for the stator with winding.

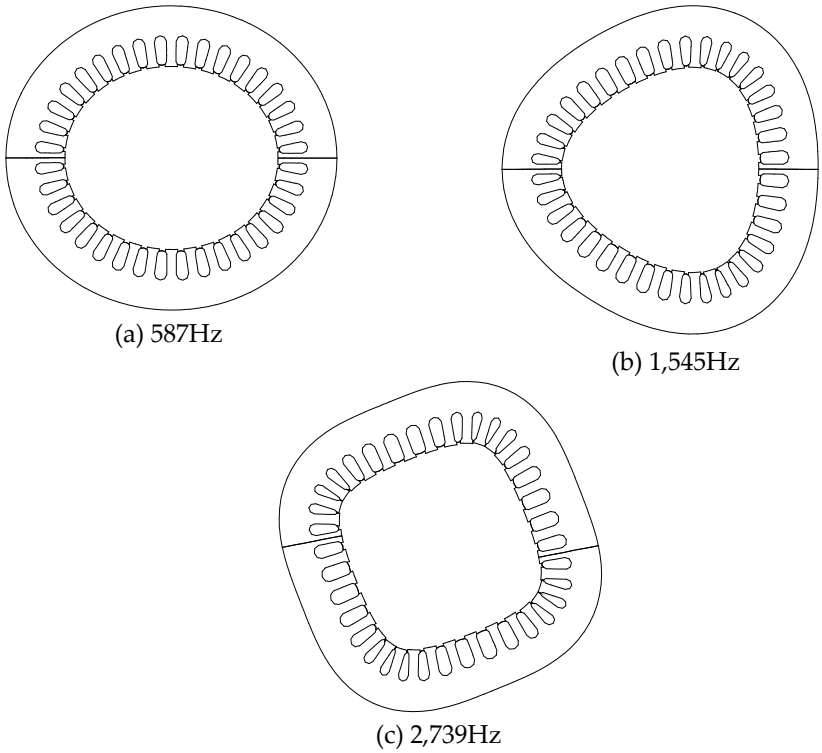

Figure 6. Natural vibration modes for stator with winding.

As the natural frequencies around 1,200Hz are generated from rotor. Three smallest natural frequencies except around 1,200Hz are shown in Table 4 as well as the measured ones. It is shown that the calculated natural frequencies are a little smaller than the measured ones. This is because we calculate the space factor of winding composed of the enameled wires only. If the insulation films and vanish are taken into account, the space factor is larger. Fig. 7 shows the lowest natural frequency by changing the space factor. Therefore, if the insulation films and vanish are taken into account, the smallest natural frequency becomes large, that is, close to the measured one.

3. Radial magnetic force

3.1. Analysis method of radial magnetic force

The simulation of the electromagnetic force is implemented by using a 2D non-linear finite element method considering the rotor current coupled with voltage equations. As we consider the force and vibration at a steady state, the rotating speed is assumed to be constant. Then, the government equations are as follows,

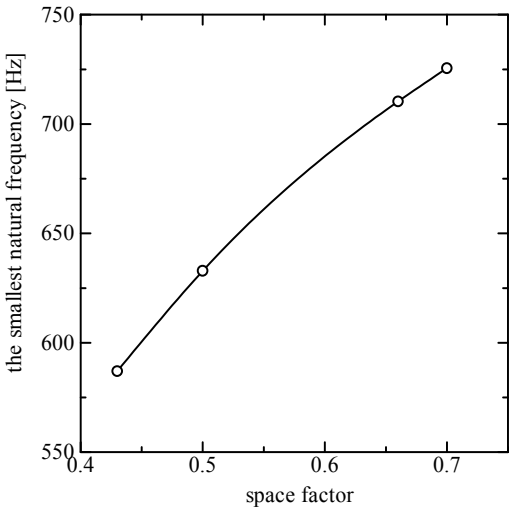

Figure 7. Relationship between the smallest natural frequency and space factor.

$$\frac{\partial}{\partial x}(\nu\frac{\partial A}{\partial x})+\frac{\partial}{\partial y}(\nu\frac{\partial A}{\partial y})=-\sum_k J_{0k}+\sigma\frac{\partial A}{\partial t}\ , \tag{6}$$

$$V_k=r\ i_k+l\frac{d\ i_k}{d\ t}+\frac{d\Phi_k}{d\ t}\quad , \qquad (k=a,b,c) \tag{7}$$

$$\text{where}\ \ \Phi_k=\frac{n}{S_k}\iint_{S_k} AL\ dxdy\ , \qquad J_{0k}=\frac{n}{S_k}i_k\ , \tag{8}$$

where, $A,\nu,J_0,\sigma,V,i,r,l,\Phi,n,S,L$ are magnetic vector potential, reluctivity, current density, conductivity, stator phase voltage, stator current, resistance of the stator winding, leakage inductance of the stator end winding, flux linkage, number of turns of stator winding, cross section area of the stator winding, and stack length, respectively. We solve equations (6) and (7) by using the time-stepping FEM. In the case where the motor is driven by the line voltage, the time step Δt is constant so that the step of rotation $\Delta\theta$ is about $2\pi/500$ at slip=0. In the case of PWM inverter, Δt is calculated from the intersection point of a sine wave and a jagged wave with a carrier frequency of 5 kHz. The transient state converged at about five cycles of the input voltage on our simulation. The radial electromagnetic force is calculated by the Maxwell's stress tensor method,

$$F_n=\frac{1}{2\mu_0}(B_n^2-B_t^2) \tag{9}$$

where, μ_0 is the permeability of air, B_n and B_t are the normal and tangential component of the flux density in the air gap. In order to take into account the 3D effects, the resistance of the end ring of the rotor is considered in the 2D model by modifying the conductivity of the rotor bars. Resistances of bar and end ring can be written as

$$R_b = \frac{1}{\sigma}\frac{l_b}{S_b}$$
$$R_r = \frac{2}{\sigma}\frac{l_r}{S_r}\frac{N_2}{(p\pi)} \tag{10}$$

where, σ, l_b, S_b, l_r, S_r, N_2, and p are the conductivity of aluminium, the longitude of the rotor bar, the cross section area of rotor bar, the longitude of the end ring, the cross section area of end ring, the number of rotor slots, and the number of poles, respectively. It is assumed that the rotor resistance is expressed by an equivalent bar with a modified conductivity

$$R_b' = \frac{1}{\sigma'}\frac{l_b}{S_b} = R_b + R_r \tag{11}$$

Therefore, the modified conductivity is obtained by using the next formula (IEE Japan, 2000)

$$\sigma' = \frac{\frac{l_b}{S_b}}{\frac{l_b}{S_b} + 2 \times \frac{l_r}{S_r} \times \frac{N_2}{(p\pi)^2}}\sigma \tag{12}$$

Stator end leakage inductance l is also taken into account and given by a traditional method (Horii, 1978)

$$l = \frac{2.3}{2\pi}\mu_0 N^2 l_f \left(\log_{10}\frac{l_f}{d_s} - 0.5 \right) \tag{13}$$

where, N, l_f, and d_s are number of stator windings, total length of coil end, and diameter of an equivalent circle whose area equals to the cross section of stator coils. If the motor has skewed slots, we should use one of the multi-slice model, the coupled method of 2D and 3D models (Yamasaki, 1996) and the full 3D model (Kometani et al., 1996). The influence that the skewing has on the radial force and vibration is not taken into account in this paper.

3.2. Steady state characteristics

Electromagnetic force is calculated by the 2D non-linear finite element method coupled with voltage equations. The models are created using a triangular mesh with 13,665 elements and 6,907 nodes for the M-model see Fig. 8. One fourth of the motor is calculated because of symmetry. For the M-model these numbers are 14,498 elements and 7,333 nodes, and half of the motor is calculated, see Fig. 9. The values obtained for the aluminium relative conductivity are $\sigma' = 0.737\sigma$ for the K-model, and $\sigma' = 0.351\sigma$ for the M-model.

To corroborate the validity of the model, the measured and calculated values of the output torque and current are compared, and the results are presented in Figs. 10 and 11. The

graphic shows a good agreement between the measured values and the calculated values for both models. This paper does not consider the effect of skewing, then this produces some error around 1400min^{-1} rotating speed in the M-model.

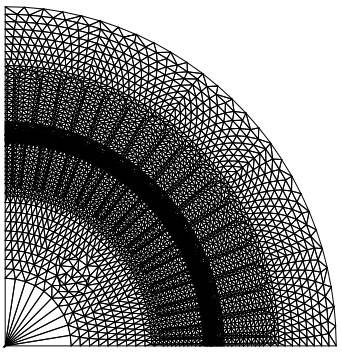

Figure 8. Mesh partition for M-model motor

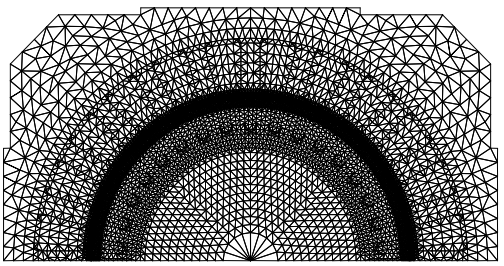

Figure 9. Mesh partition for K-model motor

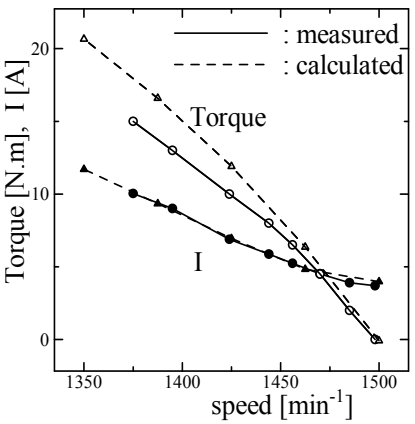

Figure 10. Steady state characteristic for M-model motor

3.3. Radial magnetic force under line source

The space variation of the radial electromagnetic force is presented in Fig. 12. It is shown that the radial force is big at the position where the flux density is big as shown in Fig. 13,

and is approximately flat in the teeth and becomes a small value at the positions where the rotor slot exists.

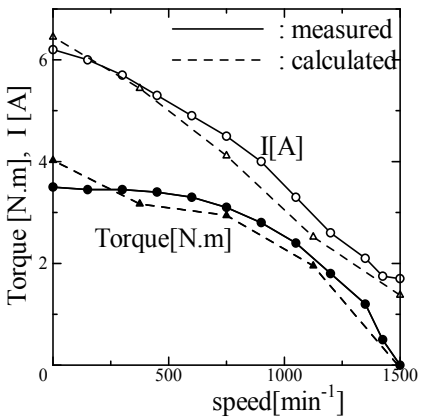

Figure 11. Steady state characteristic for K-model motor

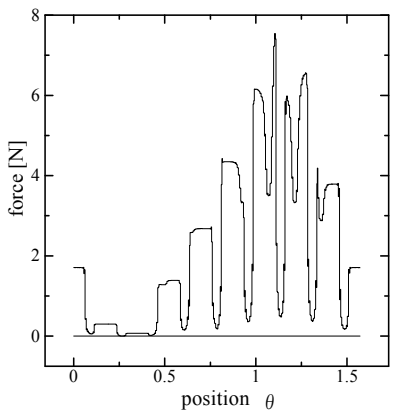

Figure 12. Space variation of radial force.

Fig. 14 shows the time variation of the force at the different teeth. It is shown that the force at tooth 1 is the same as that at tooth 4 and is bigger than those at teeth 2 and 3, because the stator winding is distributed in three slots as shown in Fig. 1.

Figs. 15 and 16 show the radial force and its spectrum at slip=0. It is shown that the force at the teeth is bigger than that at the slots and has a fundamental frequency of 2 times the line frequency of 50Hz. Figs. 17 and 18 show the radial force and its spectrum at slip=0.05. It is shown that the radial force at the slip of 0.05 is very different from that at 0.

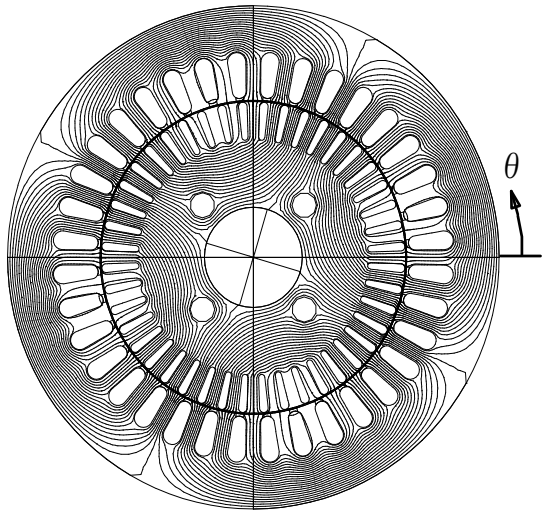

Figure 13. Flux distribution at slip=0.

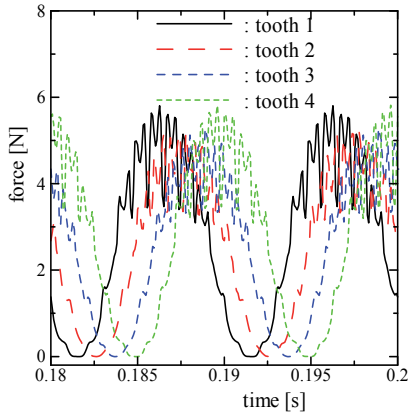

Figure 14. Radial magnetic force at different teeth.

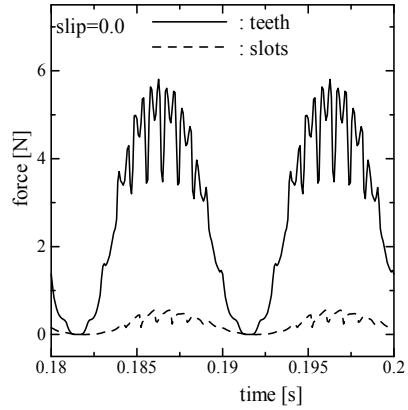

Figure 15. Waveform of radial magnetic force of M model motor at slip=0.

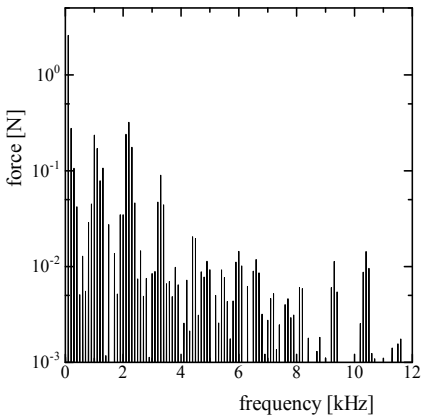

Figure 16. Spectrum of radial magnetic force of M model motor at slip=0.

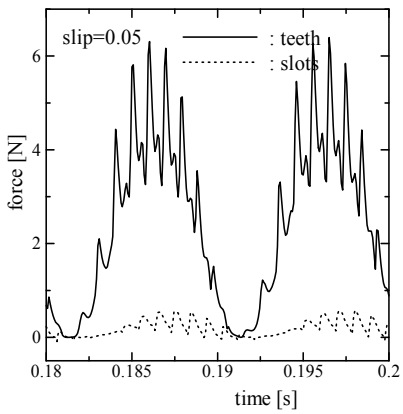

Figure 17. Waveform of radial magnetic force of M model motor at slip=0.05.

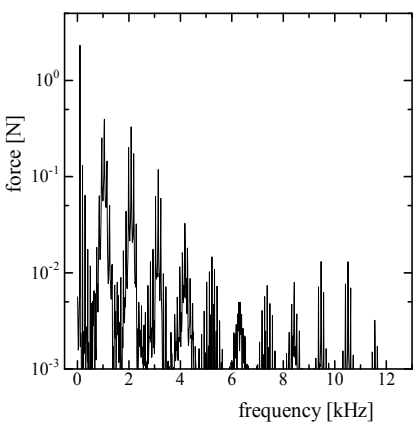

Figure 18. Spectrum of radial magnetic force of M model motor at slip=0.05.

Here we discuss the frequencies of radial force. The electromagnetic flux harmonics are produced due to the relative movement between the rotor and stator. Seeing it from the

stator's side where the main flux is generated, the permeance varies periodically due to the presence of the slots in the rotor. Following this reason, the frequency of the harmonics in the electromagnetic flux is obtained by the product of the fundamental stator magnet-motive force (MMF) and the rotor slot permeance. The fundamental stator MMF F is proportional to $\cos(p/2\cdot\theta - 2\pi ft)$, where θ is the stator angle. The permeance P is proportional to $1+\Sigma A_k \cos kN_2\left(\theta - \frac{2}{p}(1-s)2\pi ft\right)$, where N_2, s and k are the number of rotor slots, slip and the order of space harmonics, respectively. Considering that the radial electromagnetic force is proportional to $(F\cdot P)^2$, the next three frequencies are obtained,

$$2f,\ \frac{2kN_2}{p}(1-s)f,\ \frac{2kN_2}{p}(1-s)f \pm 2f \tag{14}$$

Since the rotor has 44 slots, when slip is 0, the combination of the slot permeance and the fundamental stator MMF produces the peaks at 100, {1000, 1100, 1200}, {2100, 2200, 2300}, and so on, see Fig. 16. When the slip is 0.05, the frequencies are 100, {945, 1045, 1145}, {1190, 2090, 2190}, see Fig. 18.

In the vibration problems, small space harmonics, namely, small modes are important. Then, we calculate the space and time spectrum of the radial electromagnetic force in the air gap, and show the time spectrum for several space harmonics in Figs. 19 and 20. It is shown that time harmonics of mode 4 are 100, 200, 400, and so on, and the mode of harmonics of 300, 600 and 900Hz is 12.

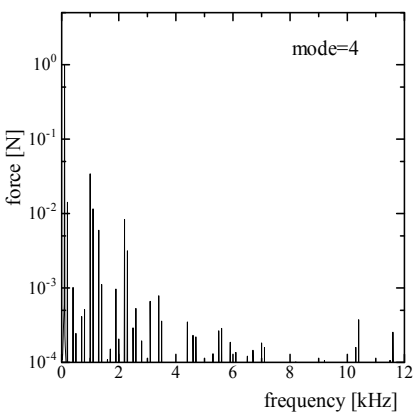

Figure 19. Frequency spectrum for different mode.

For the K-model the rotor has 34 slots, when slip is 0, the combination of the slot permeance and the fundamental stator MMF produces the peaks at 100, {750, 850, 950}, {1600,1700,1800}, {2450,2550,2650}, and so on, see Fig. 21. When the slip is 0.5, the frequencies are 100, {325,425,525}, {750,850,950}, see Fig. 22. When slip=1.0, only the first frequency remains and this is appreciated in Fig. 23.

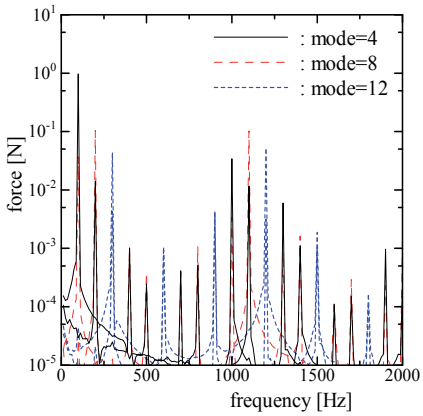

Figure 20. Enlarged one of Fig. 19.

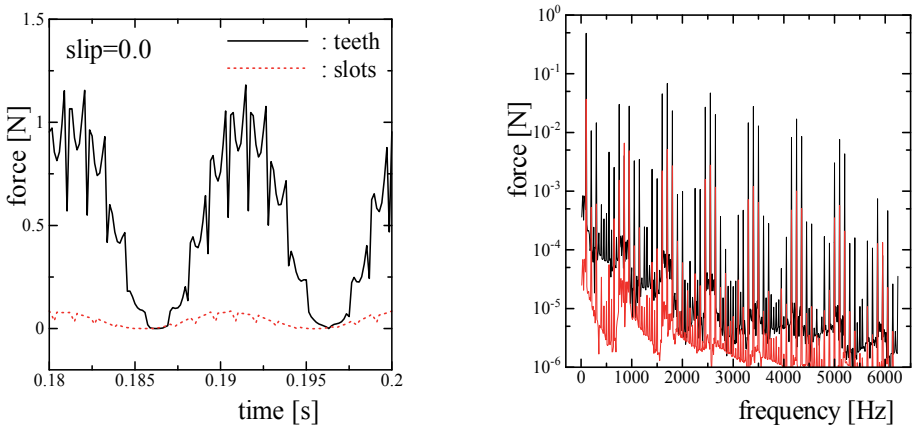

Figure 21. Radial force and its spectrum of K model motor at slip=0.

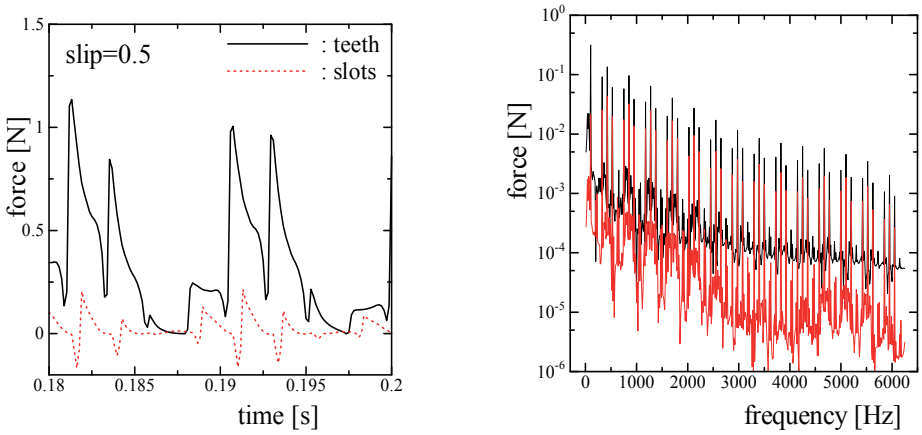

Figure 22. Radial force and its spectrum of K model motor at slip=0.5.

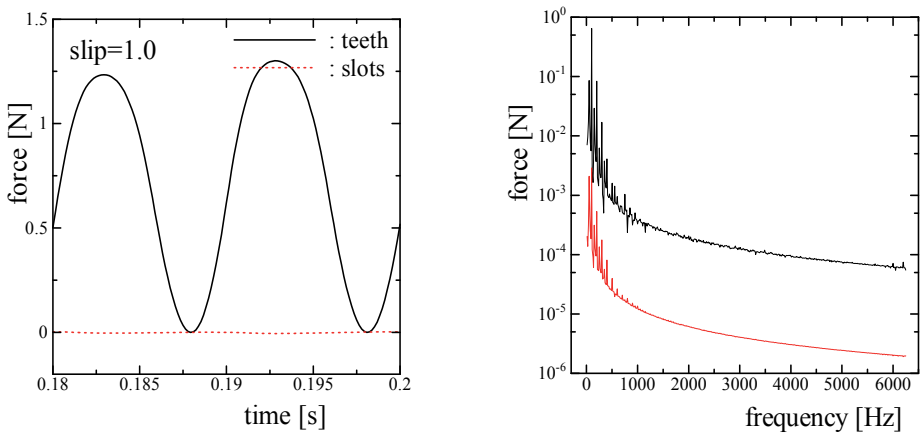

Figure 23. Radial force and its spectrum of K model motor at slip=1.00.

3.4. Radial magnetic force under PWM inverter source

Next, to clarify the difference between the line source and the PWM inverter, Figs. 24 and 25 show the waveforms of torque and stator current at slip=0 and 0.5 for the K-model. The PWM inverter has a currier frequency of 5kHz and the fundamental amplitude is equal to the line source. It is shown that the current and torque contain the component of the carrier frequency.

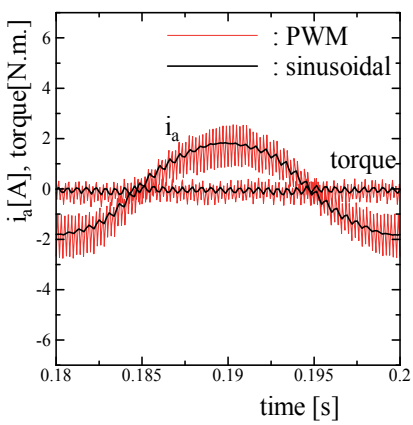

Figure 24. Torque and stator current waveforms of K model driven by PWM inverter, slip=0.

Fig. 26 shows the radial force and its spectrum at slip=0.5 for the K-model. The waveform of radial force driven by the PWM inverter is approximately the same as that driven by the line source. We can find a small noise in the waveform, and find that the amplitude around 5 kHz, that is, carrier frequency is bigger than that of the line source in the spectrum.

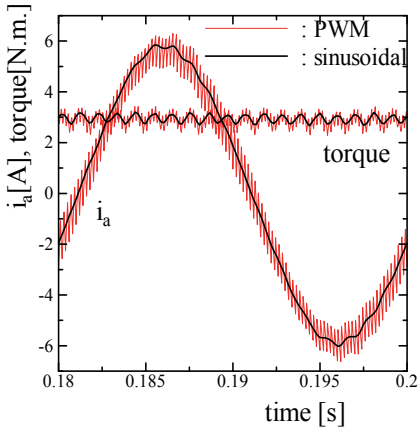

Figure 25. Torque and stator current waveforms of K model driven by PWM inverter, slip=0.5

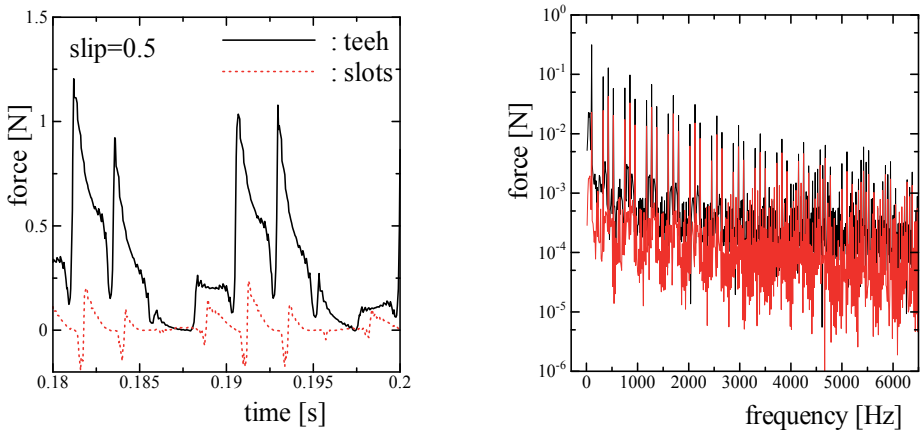

Figure 26. Radial force and frequency spectrum of K-model driven by PWM inverter at slip = 0.5.

3.5. Vibration velocity

Fig. 27 shows the vibration velocity measured at the centre of stator surface, when the motor is running at no-load. The vibration of 600 through 650 Hz is mainly emitted from the natural frequency, and 100, 200, 400, 500, 700, 1000 and 1200 Hz are corresponding to the frequency of the radial force with mode 4. We think that the vibration of 25Hz is emitted by the eccentricity of the rotor. Fig. 28 shows the vibration velocity emitted from the inverter-fed induction motor. We can see the vibration at around nf_c, where n is an integer and f_c is the carrier frequency.

3.6. Radial magnetic force under randomized PWM inverter source

It is well known that a random PWM method reduces the acoustic noise emitted from an inverter drive motor. Then, we analyze the radial force of the motor fed by two types of

random PWM method, namely, a randomized pulse position PWM and a randomized switching frequency PWM. The randomized pulse position PWM changes the pulse width as

$$duty = \frac{v + V_{\max}}{2V_{\max}} + (x - 0.5) * k \tag{15}$$

where, $v, V_{\max}, x$ and k are the voltage reference, the amplitude of the jagged wave with 5 kHz carrier frequency, a random number and the maximum variation of pulse position, respectively. This means that the interval of switching signals is changed by DT, where $-0.5k / 5000 < DT < 0.5k / 5000$ [sec]. The randomized switching frequency PWM changes the switching frequency as

$$f_c = 5000 + (x - 0.5) * (\alpha - 1) * 50 \tag{16}$$

Fig. 29 shows the time spectrum of the radial force of the motor fed by the randomized pulse position PWM, where the end of the interval of switching signals is changed by DT, $-0.2 / 5000 < DT < 0.2 / 5000$ [sec]. Fig. 30 shows the time spectrum by the randomized switching frequency PWM, where the switching frequency is change by DF, $-500 < DF < 500$ [Hz]. The time spectrum shown in Figs 29 and 30 are approximately the same as that under line source, except for the reduction of radial forces at around nf_c. The reduction of radial forces is summarized in Tables 5 and 6.

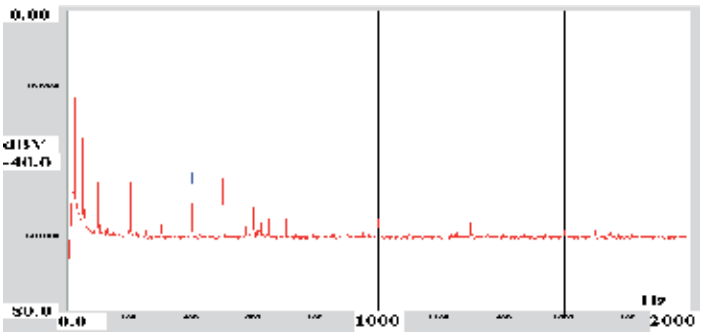

Figure 27. Vibration velocity emitted from M model driven by the line source (measured)

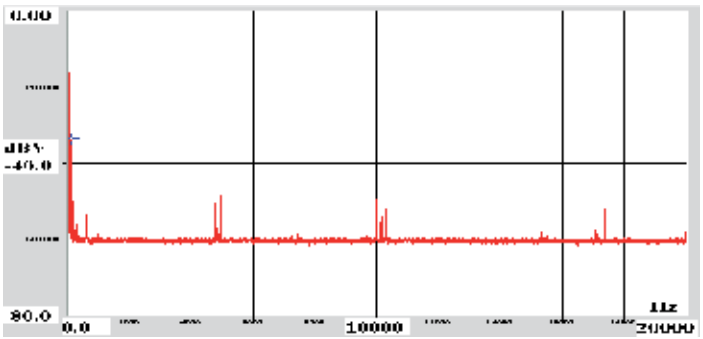

Figure 28. Vibration velocity emitted from M model driven by the PWM inverter source (measured)

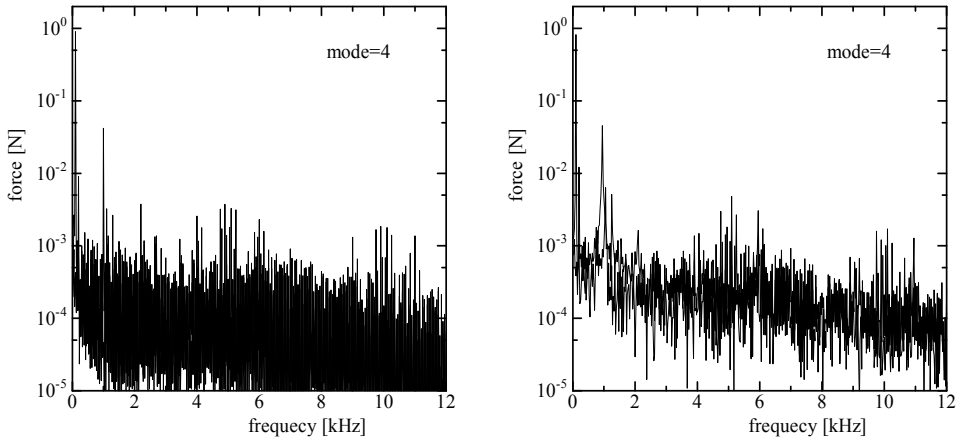

Figure 29. Spectrum of radial force for the randomized pulse position PWM.

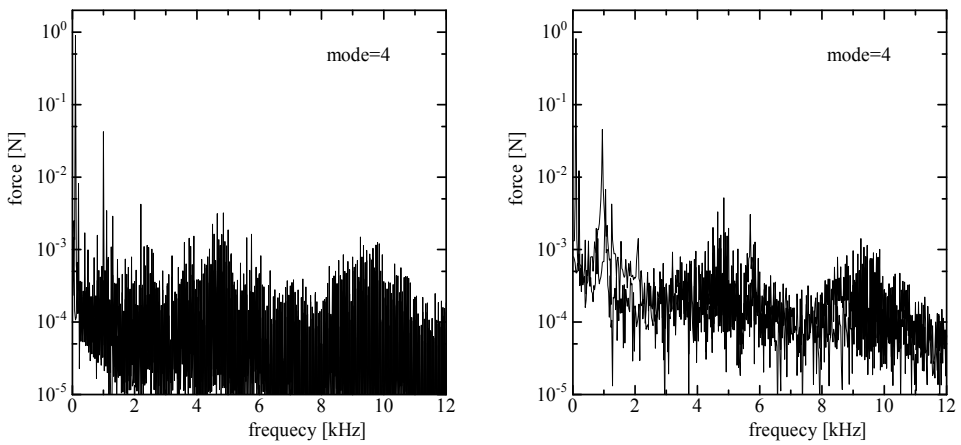

Figure 30. Spectrum of radial force spectrum for the randomized switching frequency PWM.

Frequency	100Hz	400Hz	f_c	2 f_c
Line	0.897	0.0437	--	--
PWM	0.896	0.0423	0.00366	0.00260
P PWM	0.904	0.0418	0.00375	0.00185
F PWM	0.899	0.0423	0.00321	0.00125

P PWM: Randomized pulse position PWM,
F PWM: Randomized switching frequency PWM

Table 5. Comparison of radial force at slip=0.0.

Frequency	100Hz	400Hz	f_c	$2f_c$
Line	0.815	0.0467	--	--
PWM	0.813	0.0455	0.00560	0.00263
P PWM	0.821	0.0455	0.00480	0.00171
F PWM	0.815	0.0454	0.00516	0.00142

Table 6. Comparison of radial force at slip=0.05.

3.7. Discussions

The steady state characteristics of the induction motor can be calculated by the 2D FEM considering the modified conductivity in the rotor slot by (12) and the leakage inductance of stator coil end by (13). However, for the motor with one-slot skewing there is some error in the low speed range, that is, high torque region.

In the section 3.3, it is shown that the space variation of the radial force is approximately flat in the teeth and becomes a small value at the positions where the rotor slot exists. The radial force at one tooth is bigger than that at the other two teeth, when the stator winding is distributed in three slots as shown in Fig. 14. It is also shown that the radial force has a fundamental frequency of 2 times the line frequency of 50Hz, because this motor is two pole pairs machine. Moreover, some frequencies of the radial force are obtained by considering the stator magnet-motive force and the rotor slot permeance.

In the section 3.4, when the motor is driven by the PWM inverter, the current and torque contain the component of the carrier frequency as well known. As a result, the waveform of the radial force also includes small noise. The Fourier analysis shows that the fundamental component is almost same as that driven by line source, and that the amplitude around 5 kHz, that is, carrier frequency is bigger than that of the line source as shown in Figs. 22 and 26.

In the section 3.5, the measurement of vibration velocity shows that there are vibration at around natural frequency and some frequencies corresponding to the radial force. However, there are the other frequencies corresponding to the harmonics of line frequency and the frequency produce by the eccentricity of the rotor

In the section 3.6, the effect of the randomized PWM inverter on the radial force is calculated. Two types of random PWM method, namely, a randomized pulse position PWM and a randomized switching frequency PWM are taken into account.

However, the time spectrum shown in Figs 29 and 30 are approximately the same as that under line source, except for the reduction of radial forces at two times carrier frequency. The calculation was carried out for about five cycles of the fundamental frequency. If a very long period is calculated, the reduction of radial force at the carrier frequency becomes larger.

4. Conclusion

The natural frequencies of the motor can be estimated by considering the equivalent Young's modulus of the stator windings. For example, the lowest measured and calculated natural frequencies are 1,325 and 1,369 Hz for the stator core only, and are 637 and 587 Hz for the stator core with winding. They agree well with each other.

The steady state characteristics of the induction motor can be calculated by the 2D FEM considering the modified conductivity in the rotor slot and the leakage inductance of stator coil end. Using this simulation model, the radial force of the induction motor fed by the line source has been analyzed. It is shown that the frequencies are explained by the product of the fundamental stator MMF and the rotor slot permeance, and that the radial force is different at each tooth because of the distributed stator winding.

When the motor is driven by the PWM inverter, the fundamental component of radial force is almost same as that driven by line source and the amplitude around the carrier frequency is bigger than that of the line source. Moreover, the effect of the randomized PWM inverter on the radial force is calculated. The radial forces at two times carrier frequency can be reduced by using the randomized pulse position PWM or by the randomized switching frequency PWM.

Author details

Takeo Ishikawa
Gunma University, Japan

5. References

F. Ishibashi, K. Kamimoto, S. Noda, and K. Itomi, Small induction motor noise calculation, IEEE Trans. on Energy Conversion, vol.18, no.3 pp.357-361, 2003.

K. Shiohata, K. Nemoto, Y. Nagawa, S. Sakamoto, T. Kobayashi, M. Itou, and H. Koharagi, A method for analyzing electromagnetic-force-induced vibration and noise analysis, (in Japanese) Trans. IEE Japan, vol.118-D, no.11 pp.1301-1307, 1998.

D. M. Munoz, J. C. S. Lai, Acoustic noise prediction in a vector controlled induction machine, 2003 IEEE international Electric Machines and Drives Conference, pp.104-110, 2003.

Technical Report on Computational method of Electromagnetics for Virtual Engineering of Rotating Machinery, (in Japanese) IEE Japan, vol. 776, March, 2000.

D. Mori and T. Ishikawa, Force and Vibration Analysis of Induction Motors, IEEE Transactions on Magnetics, Vol. 41, No.5, pp. 1948-1951, 2005.

D. Mori and T. Ishikawa, Force and Vibration Analysis of a PWM Inverter-Fed Induction Motor, The 2005 International Power Electronics Conference,pp.644-650, Niigata, 2005

T. Horii, Electrical Machines Outline, Corona, publishing Co., Ltd., 1978

K. Yamasaki, Modification of 2D Nonlinear time-stepping analysis by limited 3D analysis for induction machines, IEEE Trans. on Magnetics, vol.33, no.22, 1997

H. Kometani, S. Sakabe, and N.Nakanishi, 3-D Electromagnetic analysis of a cage induction motor with rotor skew, IEEE Trans. on Energy Conversion, vol.11, no.2, 1996

A. M. Trzynadlowski, F. Blaabjerg, J. K. Pedersen, R. L. Kirlin, and S. Legowski, Random Pulse Width Modulation Techniques for Converter-Fed Drive Systems - A Review, IEEE Trans. on Industry Applications, vol. 30, No.5, pp.1166-1175, 1994.

K. Itori, S. Noda, F. Ishibashi, and H. Yamawaki, Young's modulus of windings on finite element method for natural frequency analysis of stator core in induction motor, (in Japanese) Trans. of the Japan Society of Mechanical Engineers, Series C, vol. 68, no.669, pp.1-6, 2002.

Chapter 10

Induction Motors with Rotor Helical Motion

Ebrahim Amiri and Ernest Mendrela

Additional information is available at the end of the chapter

http://dx.doi.org/10.5772/48056

1. Introduction

A demand for sophisticated motion control is steadily increasing in several advanced application fields, such as robotics, tooling machines, pick-and-place systems, etc. These kinds of applications require implementation of at least two or more conventional motors/actuators, often operating with different type of mechanical gear. Electric motors/actuators that are able directly perform complex motion (with multiple degrees of mechanical freedom – multi-DoMF) may provide appreciable benefits in terms of performances, volume, weight and cost.

This chapter is organized as follows. Section 2 provides a brief overview of the main typologies of induction motors with two degrees of mechanical freedom (IM-2DoMF) structure. Section 3 introduces the mathematical model for helical-motion induction motors. Section 4 discusses the phenomenon known end effect caused by finite length of the armature and its negative influences on the motor performance. Section 5 presents a construction of a twin-armature rotary-linear induction motor with solid double layer rotor, its design data and the performance prediction of the motor. The results obtained from FEM modeling are then verified by the test carried out on experimental model of the motor what validates the theoretical modeling of the motor.

2. Topologies of induction motors with two degrees of mechanical freedom

Several topologies of electromagnetic motors featuring a multi-DoMF structure were investigated in the technical literatures (Mendrela et al., 2003, Krebs, et al., 2008). Considering the geometry, three classes of motors can be distinguished:

- X-Y motors – flat structure
- Rotary-linear motor – cylindrical geometry
- Spherical motors – spherical geometry

2.1. X-Y motors

X-Y motors, also called planar motors, are the machines which are able to translate on a plane, moving in the direction defined by two space co-ordinates. They may be usefully employed for precision positioning in various manufacturing systems such as drawing devices or drive at switch point of guided road/e.g. railway. The representative of X-Y motors is shown schematically in Fig. 1. Primary winding consist of two sets of three phase windings placed perpendicularly to one another. Therefore, magnetic traveling fields produced by each winding are moving perpendicularly to one another as well. Secondary part can be made of non-magnetic conducting sheet (aluminum, copper) backed by an iron plate. The motor with a rotor rectangular grid-cage winding is another version that can be considered.

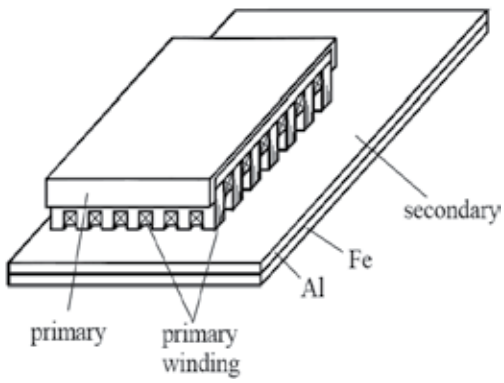

Figure 1. Construction scheme of X-Y induction motor (Mendrela et al., 2003).

The forces produced by each of traveling fields can be independently controlled contributing to the control of both magnitude and direction of the resultant force. This in turn controls the motion direction of the X-Y motor.

2.2. Rotary-linear motors

Mechanical devices with multiple degrees of freedom are widely utilized in industrial machinery such as boring machines, grinders, threading, screwing, mounting, etc. Among these machines those which evolve linear and rotary motion, independently or simultaneously, are of great interest. These motors, which are able effectively generate torque and axial force in a suitably controllable way, are capable of producing pure rotary motion, pure linear motion or helical motion and constitute one of the most interesting topologies of multi-degree-of freedom machines (Bolognesi et al., 2004). Some examples of such actuators have already been the subject of studies or patents (Mendrela et al., 2003, Giancarlo & Tellini, 2003, Anorad, 2001). A typical rotary-linear motor with twin-armature is shown in Fig. 2. A stator consists of two armatures; one generates a rotating magnetic field, another traveling magnetic field. A solid rotor, common for the two armatures is applied. The rotor consists of an iron cylinder covered with a thin copper layer. The rotor cage winding that looks like grid placed on cylindrical surface is another version that can be applied. The direction of the rotor motion depends on two

forces: linear (axially oriented) and rotary, which are the products of two magnetic fields and currents induced in the rotor. By controlling the supply voltages of two armatures independently, the motor can either rotate or move axially or can perform a helical motion.

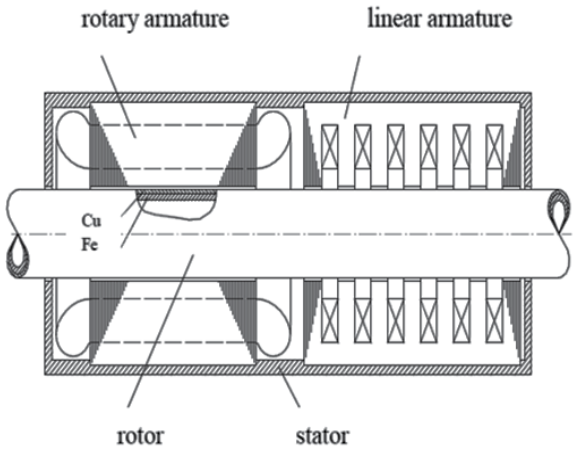

Figure 2. Scheme of twin armature rotary-linear induction motor (Mendrela et al., 2003).

2.3. Spherical motors

The last class of multi-DoMF motors has spherical structure. The rotor is able to turn around axis, which can change its position during the operation. Presently, such actuators are mainly proposed for pointing of micro-cameras and laser beams, in robotic, artificial vision, alignment and sensing applications (Bolognesi et al., 2004). In larger sizes, they may be also used as active wrist joints for robotic arms. Fig. 3 shows one of the designs in which the rotor driven by two magnetic fields generated by two armatures moving into two directions perpendicular to one another. This design is a counterpart of twin-armature rotary-linear motor.

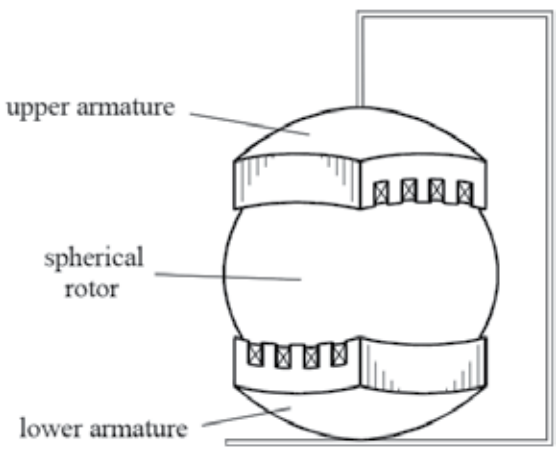

Figure 3. Construction scheme of twin-armature induction motor with spherical rotor (Mendrela et al., 2003).

3. Mathematical model of induction motor with magnetic field moving helically

The basic and most comprehensive research on IM-2DoMF is contained in the book (Mendrela et al., 2003). The analysis of these motors is based on theory of the induction motors whose magnetic field is moving in the direction determined by two space coordinates. According to this theory the magnetic field of any type of motor with 2DoMF can be represented by the sum of two or more rotating-traveling field what allows to consider the complex motion of the rotor as well as end effects caused by the finite length of stator. In the next subsections a sketch of theory of the motor with the rotating-traveling magnetic field whose rotor is moving with helical motion is presented.

3.1. Definition of magnetic field and rotor slip

3.1.1. Magnetic field description

The magnetic field moving helically in the air-gap is represented by the magnetic flux density B wave moving in the direction placed between two co-ordinates z and θ (Fig. 4).

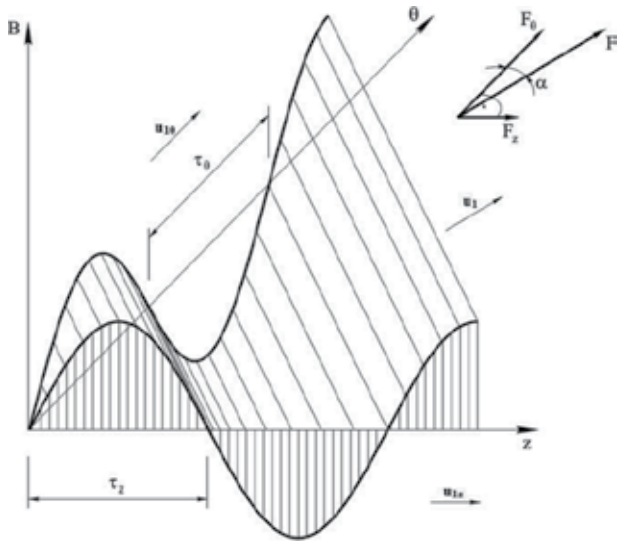

Figure 4. Magnetic field wave moving into direction between two spaces coordinates (Mendrela et al., 2003).

It can be expressed by the following formula (Mendrela et al., 2003):

$$B = B_m \exp\left[j\left(\omega t - \frac{\pi}{\tau_\theta}\theta - \frac{\pi}{\tau_z} z \right) \right] \tag{1}$$

where B_m - amplitude of travelling wave of magnetic flux density, ω - supply pulsation, τ_θ and τ_z - pole-pitch length along θ and z axes.

The physical model of the motor which could generate such a field is shown in Fig. 5.

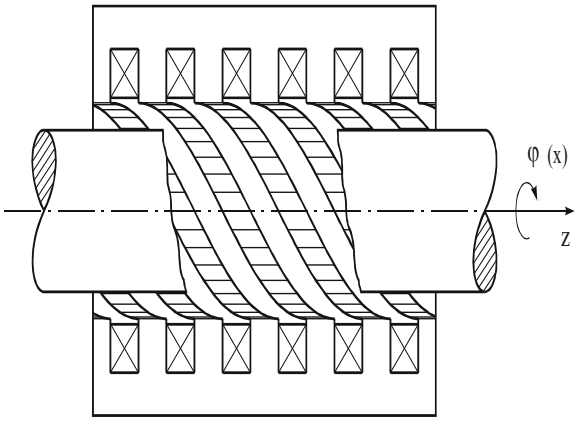

Figure 5. Rotary-linear induction motor with rotating-traveling magnetic field (Mendrela et al., 2003).

The electromagnetic force that exerts on the rotor is perpendicular to the wave front and can be divided into two components: F_z – linear force, F_θ - rotary component (Fig. 4). The relationships between force components are:

$$\frac{F_\theta}{F_z} = ctg\,\alpha\ , \qquad F_\theta = F\cos\alpha \tag{2}$$

where,

$$ctg\alpha = \frac{\tau_z}{\tau_\theta} \tag{3}$$

3.1.2. Rotor slip

To derive a formula for the rotor slip the motor is first considered to operate at asynchronous speed. Meaning, an observer standing on the rotor surface feels a time variant magnetic field. Therefore, magnetic field for a given point $P(\theta_1 z_1)$ (Fig. 6) on the rotor surface is varying in time and expressed by the following equation:

$$B(t,\theta_1,z_1) = B_m \exp\left[j\left(\omega t - \frac{\pi}{\tau_\theta}\theta_1 - \frac{\pi}{\tau_z}z_1\right)\right] = var \tag{4}$$

Eqn. (4) is true if:

$$\omega t - \frac{\pi}{\tau_\theta}\theta_1(t) - \frac{\pi}{\tau_z}z_1(t) = \psi(t) \tag{5}$$

where $\psi(t)$ is the angle between point P and the wave front of the magnetic field wave. Differentiating Eqn. (5) with respect to time t yields:

$$\omega - \frac{\pi}{\tau_\theta}\omega_\theta - \frac{\pi}{\tau_z}u_z = \omega_2 \tag{6}$$

where ω_2 (slip speed) is the angular speed of point P with respect to the stator field and ω_θ and u_z are the angular and linear speeds of the rotor, respectively.

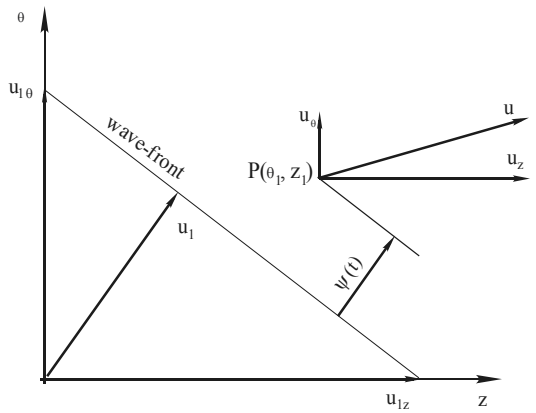

Figure 6. Rotary-linear slip derivation (Mendrela et al., 2003).

The, field velocities along θ and z axes are expressed by the equations:

$$\omega_{1\theta} = 2\tau_\theta f \quad , \qquad u_{1z} = 2\tau_z f \tag{7}$$

Inserting (7) to (6), it takes the form:

$$\omega - \frac{\omega}{\omega_{1\theta}}\omega_\theta - \frac{\omega}{u_{1z}}u_z = \omega_2 \tag{8}$$

Similarly, as in the theory of conventional induction motors, it can be written:

$$\omega_2 = \omega s \tag{9}$$

From (8) and (9) the following equation for the rotor slip is finally derived:

$$s_{\theta z} = 1 - \frac{\omega_\theta}{\omega_{1\theta}} - \frac{u_z}{u_{1z}} \tag{10}$$

The two dimensional rotor slip obtained in Eqn (10) is a function of rotary and linear rotor speed components as well as the speeds of the magnetic field moving along two space coordinates. If the motion of rotor is blocked along one of the coordinates, this slip takes the form known for motors with one degree of freedom. For example: if the rotor is blocked in the axial direction, the u_z component drops to zero and the slip takes the form:

$$s_\theta = 1 - \frac{\omega_\theta}{\omega_{1\theta}} \tag{11}$$

which is the form of rotor slip in the theory of conventional induction motor.

3.2. Motor equivalent circuit

For the induction motor with rotating-travelling field the equivalent circuit is shown in Fig. 7, which corresponds to the well-known circuit of rotary induction motor. The only

difference is in the rotor slip, which for rotary-linear motor depends on both rotary and linear rotor speeds.

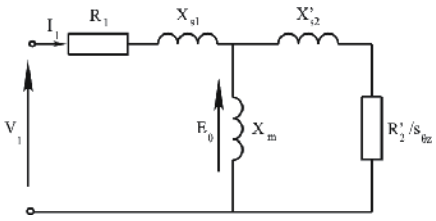

Figure 7. Equivalent circuit of induction motor with rotating-travelling magnetic field.

Similarly to the conventional rotary motors, the secondary resistance can be split into two resistances as shown in Fig. 8. R_2' represents the power loss in the rotor windings and the second part $(R_2' \frac{1-s_{\theta z}}{s_{\theta z}})$ contributes to mechanical power P_m.

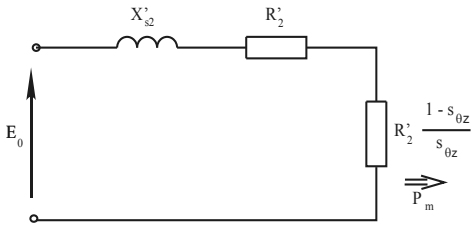

Figure 8. Equivalent circuit of rotor of rotary-linear induction motor.

The mechanical power of the resultant motion between θ and z axis is proportional to the resistance $R_2' \frac{1-s_{\theta z}}{s_{\theta z}}$ and is equal to:

$$P_m = mR_2' \frac{1-s_{\theta z}}{s_{\theta z}} I_2'^2 \tag{12}$$

where m is the number of phases.

Inserting Eqn (10) into Eqn (12), it takes the form:

$$P_m = mI_2'^2 \frac{R_2'}{s_{\theta z}} \left(\frac{\omega_\theta}{\omega_{1\theta}} + \frac{u_z}{u_{1z}}\right) \tag{13}$$

The resultant mechanical power P_m can be expressed in the form of its component in θ and z direction:

$$P_m = P_{m\theta} + P_{mz} \tag{14}$$

From (11), (13) and (14):

$$P_{m\theta} + P_{mz} = mR_2' \frac{1-s_\theta}{s_{\theta z}} I_2'^2 + mR_2' \frac{1-s_z}{s_{\theta z}} I_2'^2 \tag{15}$$

Therefore, Fig. 8 can be redrawn in terms of the resistance split into two components as shown in Fig. 9.

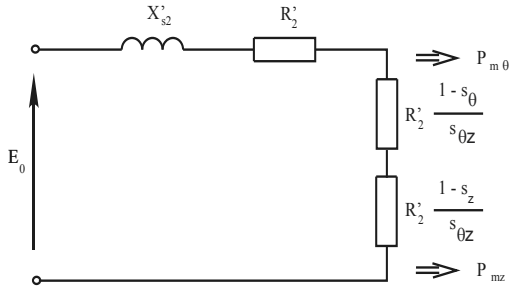

Figure 9. Equivalent circuit of rotor of rotary-linear induction motor with mechanical resistance split into two components.

3.3. Electromechanical characteristics

Unlike conventional rotary motors with the curvy characteristics of electromechanical quantities versus slip, electromechanical quantities in rotary-linear motor cannot be interpreted in one dimensional shape and should be plotted in a surface profile as a function of either slip $s_{\theta z}$ or speed components u_θ and u_z. The circumferential speed u_θ is expressed as follows:

$$u_\theta = R_r \,.\, \omega_\theta \tag{16}$$

where R_r is the rotor radius.

As an example, the force-slip characteristic of a typical rotary-linear motor is plotted in Fig. 10.

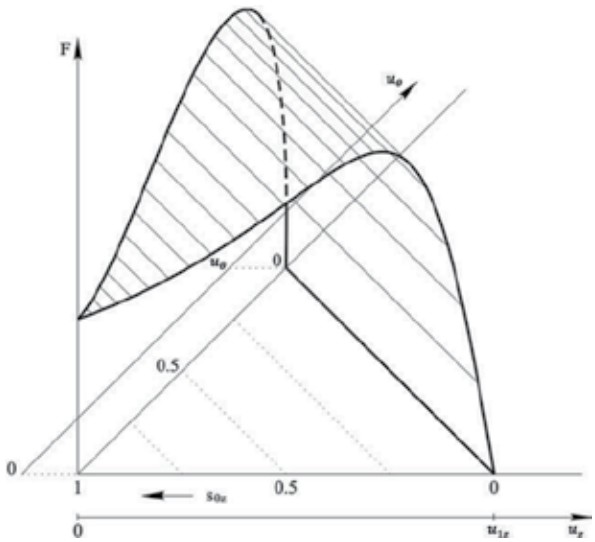

Figure 10. Fig. 10. Electromechanical characteristic of the induction motor with a rotating-travelling field (Mendrela et al., 2003).

In order to determine the operating point of the machine set, let the rotor be loaded by two machines acting independently on linear (axial) and rotational directions with the load force characteristics shown in Fig. 11.

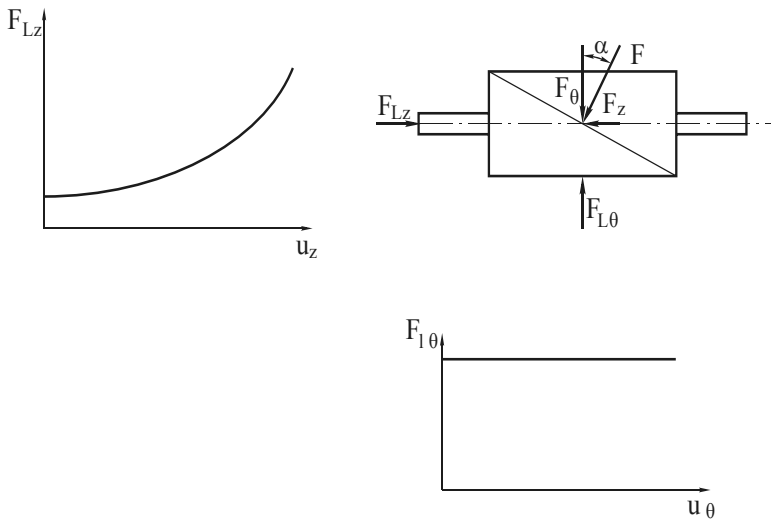

Figure 11. Load characteristics for IM-2DoMF, F_{lz}: load force in axial direction, $F_{l\theta}$: load force in rotary direction.

The equilibrium of the machine set takes place when the resultant load force is equal in its absolute value and opposite to the force developed by the motor. The direction of the electromagnetic force F of the motor is constant and does not depend on the load. Thus, at steady state operation both load forces $F_{l\theta}$ and F_{lz} acts against motor force components F_θ and F_z in the same direction if the following relation between them takes place:

$$\frac{F_\theta}{F_z} = \frac{F_{l\theta}}{F_{lz}} = ctg\alpha = \frac{\tau_z}{\tau_\theta} \tag{17}$$

To draw both load characteristics on a common graph, the real load forces $F_{l\theta}$ and F_{lz} acting separately on rotational and linear directions should be transformed into $F'_{l\theta}$ and F'_{lz}, forces acting on the direction of the motor force *F*. These equivalent forces are:

$$F'_{l\theta} = \frac{F_{l\theta}}{\cos\alpha} \quad , \quad F'_{lz} = \frac{F_{lz}}{\sin\alpha} \tag{18}$$

The transformed load characteristics drawn as a function of u_θ and u_z, as shown in Fig. 12, are the surfaces intersecting one another along the line segment $\overline{KA}$. This line segment that forms the $F_l(u)$ characteristic is a set of points where the following equation is fulfilled:

$$F'_{l\theta} = F'_{lz} \tag{19}$$

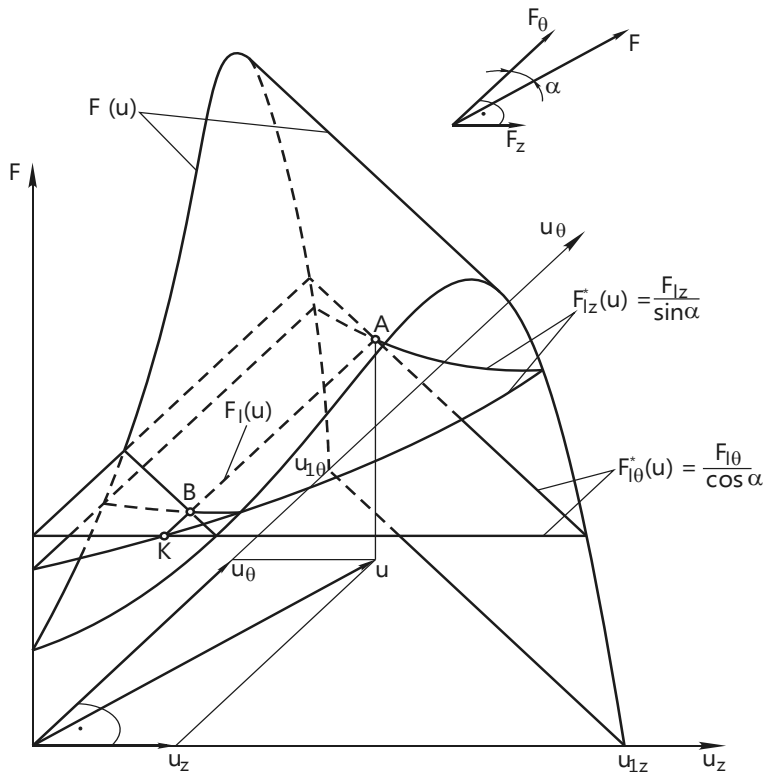

Figure 12. Determination of the operating point A of the machine set with IM-2DoMF (Mendrela et al., 2003).

The load characteristic $F_l(u)$ intersects with the motor characteristic at points A and B, where the equilibrium of the whole machine set takes place. To check if the two points are stable the steady state stability criterion can be used, which is applied to rotary motors in the following form:

$$\frac{dF}{du} < \frac{dF_l(u_\theta, u_z)}{du} \tag{20}$$

$$\frac{dF_{l\theta}}{du_\theta} > 0, \quad \frac{dF_{lz}}{du_z} > 0 \tag{21}$$

Applying this criterion, point A in Fig. 12 is stable and point B is unstable.

3.4. Conversion of mathematical model of IM-2DoMF into one of IM-1DoMF

The mathematical model of IM-2DoMF presented in previous subsections is more general than the one for linear or rotating machines. The rotating magnetic field wave of rotating

machines and the traveling field of linear motors are in the mathematical description special cases of the rotating–traveling field. If the wave length remains steady, pole pitches along both axis (τ_θ and τ_z) will vary by changing the motion direction of field waves. For example: if the wave front (see Fig. 4) turns to θ axis, then $\tau_z = \infty$. This makes the formula (1) changes to:

$$B = B_m \exp\left[j\left(\omega t - \frac{\pi}{\tau_\theta}\theta \right) \right] \tag{22}$$

which is the flux density function for rotary motor. The $\alpha = 0$ and according to Eqn (2) the force $F = F_\theta$ what is the case for rotary motors. On the other hand, turning the wave completely toward z axis leads to infinity pole pitch value along θ axis ($\tau_\theta = \infty$). By inserting this into Eqn (1) and (10) the description of both field and slip expressed by two space coordinates turns to the description of such quantities in linear motors.

In other word, the mathematical model of the rotary-linear motor is a general form of conventional, one dimensional motors and can be reduced at any time to the model either of rotary or linear motors.

4. Edge effects in rotary-linear induction motors

The twin-armature rotary-linear induction motor, which is the object of this chapter consists of two armatures what makes this machine a combination of two motors: rotary and tubular linear, whose rotor are coupled together. This implies that the phenomena that take place in each set of one-degree of mechanical freedom motors also occur in the twin armature rotary-linear motor in perhaps more complex form due to the complex motion of the rotor. One of these phenomena is called end effects and occurs due to finite length of the stator at rotor axial motion. This phenomenon is not present in conventional rotating induction machines, but play significant role in linear motors.

These effects are the object of study of many papers (Yamamura, 1972, Greppe et all, 2008, Faiz & Jafari, 2000, Turowski, 1982, Gierczak & Mendrela, 1985, Mosebach et all, 1977, Poloujadoff et all, 1980). In the literature, end effects are taken into account in various ways. In the circuit theory a particular parameter can be separated from the rest of equivalent circuit elements, and it represents the only phenomena that are caused by finite length of primary part of linear motor. This approach has been done in (Pai et all, 1988, Gieras et all, 1987, Hirasa et all, 1980, Duncan & Eng, 1983, Mirsalim et all, 2002). Kwon et al, solved a linear motor (LIM) with the help of the FEM, and they suggested a thrust correction coefficient to model the end effects (Kwon et all., 1999). Fujii and Harada in (Fujii & Harada, 2000) modeled a rotating magnet at the entering end of the LIM as a compensator and reported that this reduced end effect and thrust was the same as a LIM having no end effects. They used FEM in their calculations. Another application of FEM in analysing LIMs is reported by (Kim & Kwon, 2006). A d-q axis equivalent model for dynamic simulation purposes is obtained by using nonlinear transient finite element analysis and dynamic end effects are obtained.

The end effect has been also included in the analysis of rotary-linear motors in the literature (Mendrela et al., 2003, Krebs et all, 2008, Amiri et all, 2011). This inclusion was done by applying Fourier's harmonic method when solving the Maxwell's equations that describe motor mathematically (Mendrela et al., 2003). This approach was also applied to study the linear motor end effects (Mosebach et all, 1977, Poloujadoff et all, 1980).

The edge effects phenomena caused by finite length of both armatures can be classified into two categories as follows:

- End effects: which occurs in the tubular part of the motor.
- Transverse edge effects: which exists in the rotary part.

4.1. End effects

One obvious difference between LIM and conventional rotary machines is the fact that in LIM the magnetic traveling field occurs at one end and disappears at another. This generates the phenomena called end effects. End effects can be categorized into two smaller groups called: static end effects and dynamic end effects.

4.1.1. Static end effects

This is the phenomenon which refers to the generation of alternating magnetic field in addition to the magnetic traveling field component. The process of generation of alternating magnetic field at different instances is shown in Fig. 13.

Instant $t_1 = 0$: The 3-phase currents are of the values shown by phasor diagram in Fig. 13.b and 13.c with maximum in phase A. The current distribution in the primary winding relevant to these values is shown in Fig. 13.a and its first space harmonic is represented by curve J in Fig. 13.b. The distribution of magneto-motive force F_m in the air-gap corresponding to this linear current density has the cosine form with the maximum value at both edges of the primary part shown in Fig. 13.b. This mmf generates the magnetic flux which consists of two components: alternating flux Φ_a shown in Fig. 13.a and traveling flux component. The distribution of these two components B_a and B_t as well as the resultant flux density ($B_a + B_t$) are shown in Fig. 13.c.

Instant $t_2 = ¼$ T (where T is sine wave period): The 3-phase currents are of value shown by phasor diagram in Fig. 13.d with zero in phase A. These currents make the distribution of the first harmonic of mmf F_m as shown in Fig. 13.d. Since there is no mmf at primary edges, the alternating flux component Φ_a does not occur and the traveling flux B_t is the only available component.

Instant $t_3 = ½$ T: After a half period, the currents are of values shown by phasor diagram in Fig. 13.e with the maximum negative value in phase A. The relevant mmf distribution reveals its maximum negative value at primary edges which generates the magnetic flux Φ_a represented by its flux density B_a (see Fig. 13.e) which adds to the traveling flux component B_t.

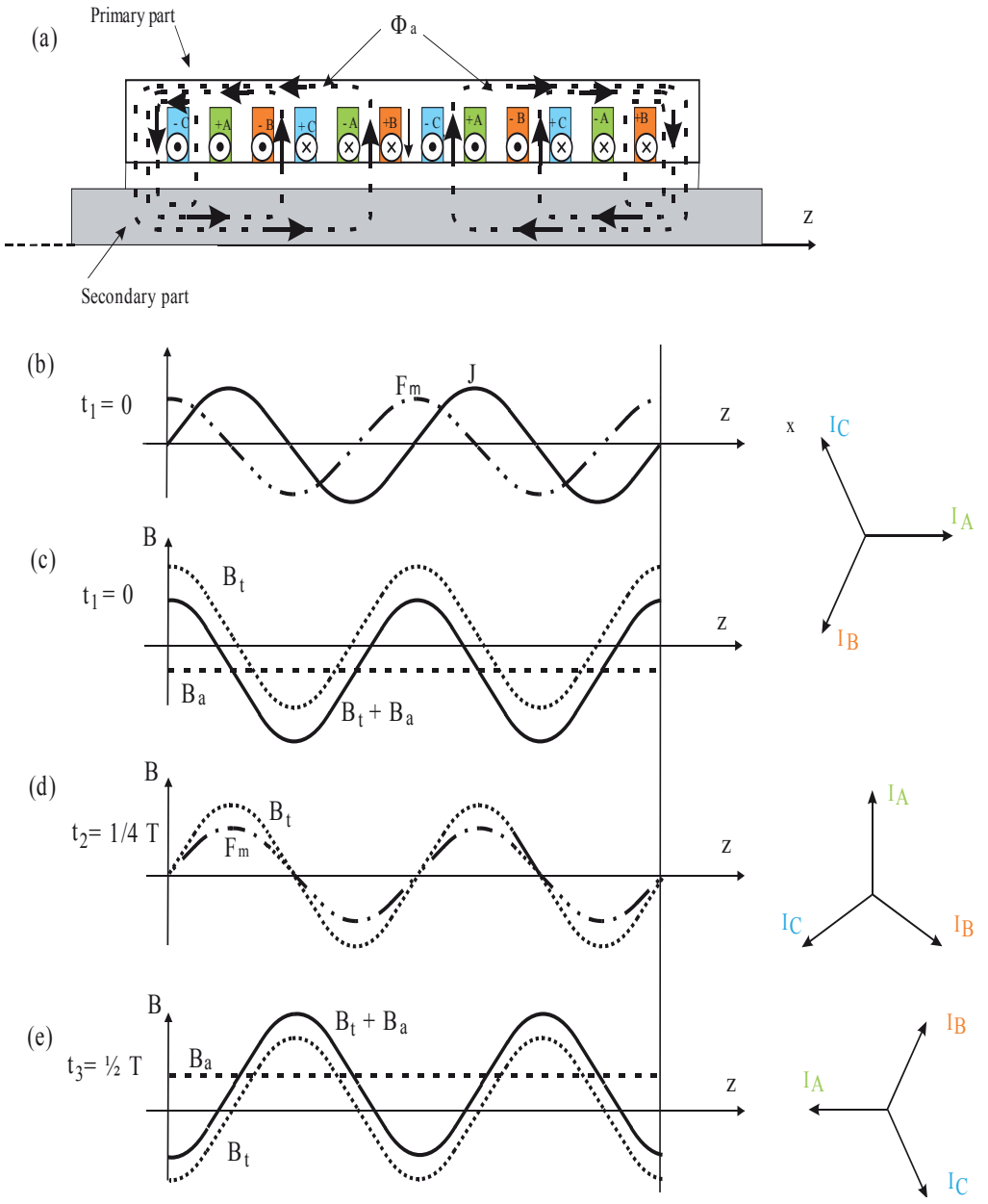

Figure 13. The process of generation of alternating magnetic field at different instances in 4-pole tubular motor: (Φ_a) – alternating component of magnetic flux, (B_a) – alternating component of magnetic flux density in the air-gap, (B_t) - travelling component of magnetic flux density in the air-gap, (J) – linear current density of the primary part, (F_m) – magneto-motive force of primary part in the air-gap.

Analysing the above phenomenon in time, one may find that magnetic flux density has two components: B_a which does not move in space but changes periodically in time called alternating component and B_t which changes in time and space is called traveling

component. The first component B_a does not exist in motors with infinity long primary part, which is the case in conventional rotary machines.

Summarizing, the resultant magnetic flux density distribution is a combination of the traveling wave component $B_t(t)$ and alternating magnetic field $B_a(t)$ denoted by:

$$B(t,z) = B_t \cos\left(\omega t - \frac{\pi}{\tau_p} z + \delta_m\right) + B_a \sin\left(\omega t - \frac{\pi}{\tau_p} + \delta_a\right) \tag{23}$$

where τ_p is pole pitch and δ_m is phase angle.

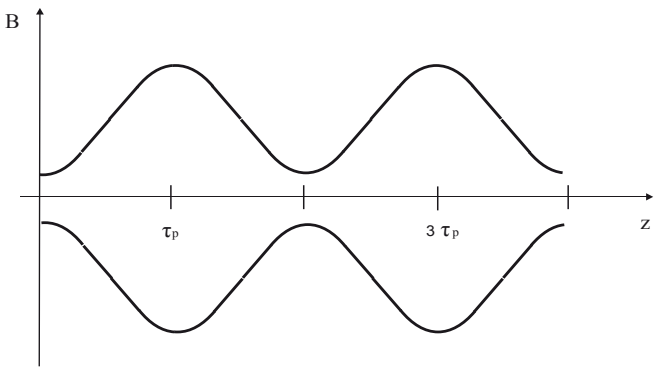

Figure 14. The envelope of the resultant magnetic flux density in the air-gap of four pole linear motor due to presence of the alternating magnetic field (τ_p - pole pitch).

When only the travelling wave exists, the envelop of flux density distribution in the air gap is uniform over the entire length of the primary core but the second term deforms the air gap field distribution to the shape shown in Fig. 14. The alternating flux contributes to the rising of additional power losses in the secondary and to producing of braking force when one part of LIM motor is moving with respect to the other one (Mosebach et all, 1977, Poloujadoff, et all, 1980, Amiri, et all, 2011). This component occurs no matter what is the value of the speed of the secondary part (Poloujadoff, 1980). The envelope of the resultant magnetic flux density for the four-pole motor is no longer uniform as shown in Fig. 14.

4.1.2. Dynamic end effects

The dynamic end effects are the entry and exit effects that occur when the secondary moves with respect to the primary part. This phenomenon will be explained in two stages:

Stage I: secondary part moves with synchronous speed

There are no currents induced in the rotor (within the primary part range) due to traveling magnetic field component (since the secondary moves synchronously with travelling field). However, the observer standing on the secondary (see Fig. 15) feels relatively high change of magnetic flux when enters the primary part region and when leaves this region at exit edge. This change contributes to rising of the eddy currents at both the entry and exit edges. These

currents damp the magnetic field in the air-gap at entry in order to keep zero flux linkage for the secondary circuit. At the exit edge the secondary eddy currents tries to sustain the magnetic flux linkage outside the primary zone the same as it was before the exit. This leads to damping magnetic flux at the entry edge and to appearance of magnetic flux tail beyond the exit edge (Fig. 16.a). The distribution of the primary current J_1 is uniform over the entire region. The envelop of the eddy currents induced in the secondary J_2 shown in Fig. 16.a is relevant to the magnetic flux density distribution in the air-gap.

The eddy currents at the entry and exit edges attenuate due to the fact that the magnetic energy linked with these currents dissipate in the secondary resistance. Thus, the lower is the secondary resistance the more intensive is damping at entry and the longer is the tail beyond the exit.

Stage II: rotor (secondary part) moves with a speed less than the synchronous speed

The currents are induced in the secondary over the entire primary length due to slip of the secondary with respect to the travelling component of primary magnetic flux. These currents superimpose the currents that are due to the entry and exit edges. The resultant eddy current envelop is shown schematically in Fig. 16.b. The flux density distribution in the air-gap and current density in the primary windings are also shown in Fig. 16.b. As it is illustrated the primary current density is uniformly distributed along the primary length only if the coils of each phase are connected in series and the symmetry of 3-phase currents is not affected by the end effects. The magnetic flux density distribution has the same shape and changes in a same pattern in both stages, but due to the rotor current reaction, the second stage has a lower magnetic flux density (B). However, primary current density is higher at the second stage if the primary winding is supplied in these two cases with the same voltage.

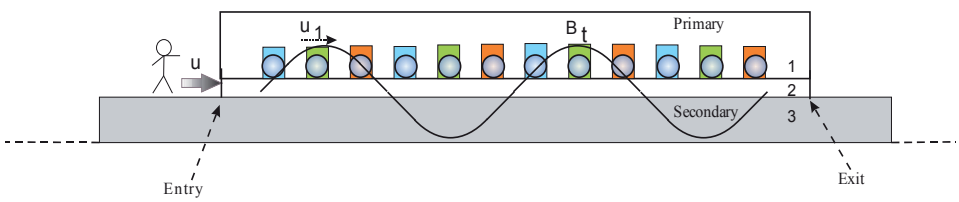

Figure 15. End effect explanation: (B_t) - travelling component of magnetic flux density in the air-gap (u_1) speed of traveling magnetic field (u) speed of the rotor.

In general, end effect phenomena leads to non-uniform distribution of:

- magnetic field in the air-gap,
- current in the secondary,
- driving force density,
- power loss density in the secondary.

Thus, this contributes to:

- lower driving force,
- higher power losses,

- lower motor efficiency,
- lower power factor.

Due to dynamic end effects, the resultant magnetic flux density in the air-gap can be expressed as a summation of three flux density components as follows (Greppe, et all, 2008):

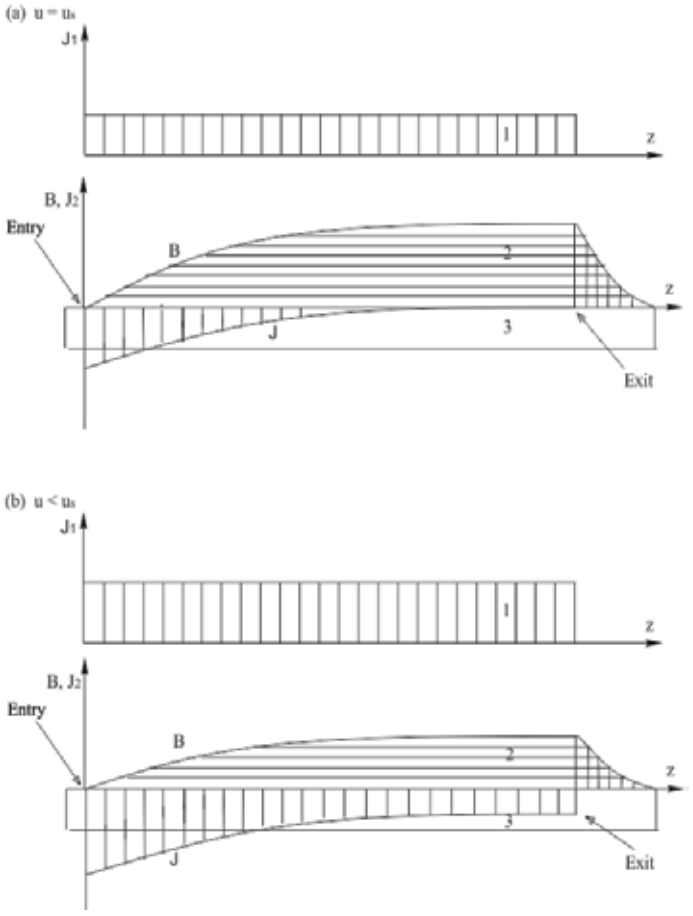

Figure 16. Distribution of primary current (J_1), secondary current (J_2) and magnetic flux density in the air-gap (B): (a) $u = u_1$ (b) $u < u_s$.

$$B(t,z) = B_t \cos\left(\omega t - \frac{\pi}{\tau_p} z + \delta_m\right) + B_1 e^{-z/\alpha_1} \cos\left(\omega t - \frac{\pi}{\tau_{pe}} z + \delta_1\right) + B_2 e^{+z/\alpha_2} \cos\left(\omega t + \frac{\pi}{\tau_{pe}} z + \delta_2\right) \quad (24)$$

All the three terms of this equation have the same frequency and are steady with respect to time t. The first term is the traveling wave moving forward at synchronous speed. The second term is an attenuating traveling wave generated at the entry end, which travels in the positive direction of z and whose attenuation constant is $1/\alpha_1$ and its half-wave length is τ_{pe}. The third term of Eqn (24) is an attenuating traveling wave generated at the exit end, which travels in the negative direction and whose attenuation constant is $1/\alpha_2$ and

half-wave length is τ_{pe}. The B_1 wave is caused by the core discontinuity at the entry end and the B_2 wave is caused by the core discontinuity at the exit end, hence, both are called end effect waves. Both waves have an angular frequency ω, which is the same as that of power supply. They have the same half wave-length, which is different from half-wave length (equal to pole pitch) of the primary winding. The traveling speed of the end waves is given by $v_e = 2\,f\,\tau_{pe}$ and is the same as the secondary speed if high speed motors is studied. However, in low speed motors, the speed of the end waves can be much higher than that of secondary (Yamamura, 1972). The length of penetration of entry end wave α_1 depends on motor parameters such as gap length and secondary surface resistivity. The impact of these parameters on α_1 are quiet different at high speed motors and low speed motors. As a result, α_1 is much longer at high speed motors with respect to low speed motors. Also, in the high-speed motors, half wave length τ_{pe} is almost linearly proportional to the speed of secondary and is independent from gap length and secondary surface resistivity while it is dependent to such parameters at low speed motors (Yamamura, 1972). Therefore, the speed of the end waves is equal to the secondary speed at high speed motors regardless the value of parameters such as supply frequency, gap length and surface resistivity, while in low speed motors, end wave's speed depends on such parameters and may reach to even higher than synchronous speed at low slip region. The super-synchronous speed of the end-effect wave at motor speed lower and close to synchronous speed occurs only in low speed motors (Yamamura, 1972).

The entry-end-effect wave decays relatively slower than the exit-end-effect wave and unlike exit-end-effect wave, is present along the entire longitudinal length of the air-gap and degrades the performance of the high speed motor. The exit-end-effect wave attenuates much faster due to the lack of primary core beyond the exit edge. Therefore, the influence of the exit field component B_2 on motor performance is less than that of the entry component B_1, and it may be disregarded for many applications Gieras et all, 1987, Hirasa et all, 1980, Greppe, et all, 2008).

For the motors with the number of magnetic pole pairs greater than 2 if the synchronous speed is below 10 m/s the end effects can be ignored. For the motors with higher synchronous speeds the influence of end effects can be seen even for the motors with higher number of pole-pairs (Mendrela, 2004).

4.2. Transverse edge effects

The transverse edge effect is generally described as the effect of finite width of the flat linear motor and is the result of x component of eddy current flowing in the solid plate secondary (Fig. 17.b). Since, there are no designated paths for the currents, as it is in cage rotors of rotary motors, the currents within the primary area are flowing in a circular mode (Fig. 17.b). These currents generate their own magnetic field, whose distribution is shown schematically in Fig. 17.a. This magnetic field shown schematically as B_r in Fig. 18 subtracts from the magnetic field B_s generated by the primary part winding. The resultant field has non-uniform distribution in transverse direction (x axis) (Fig. 19). This

non-uniform distribution of the magnetic field and circular pattern of the secondary currents contribute to the increase of power losses, decrease of motor efficiency and reduction of maximum electromagnetic force (Boldea & Nasar, 2001).

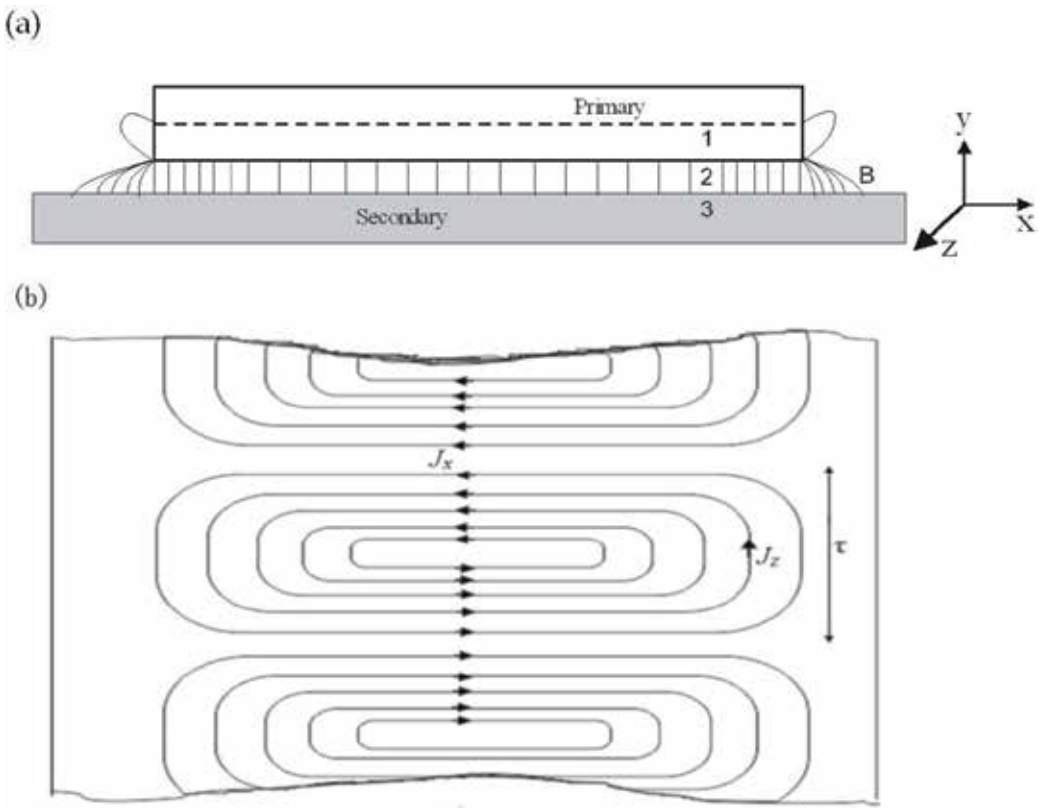

Figure 17. Transverse edge effect explanation: (a) The resultant magnetic flux distribution, (b) eddy current induced in the secondary.

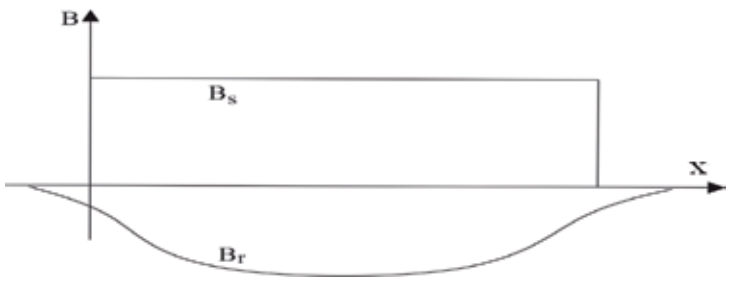

Figure 18. The distribution of magnetic flux density B_s produced by the primary current and B_r by the secondary currents.

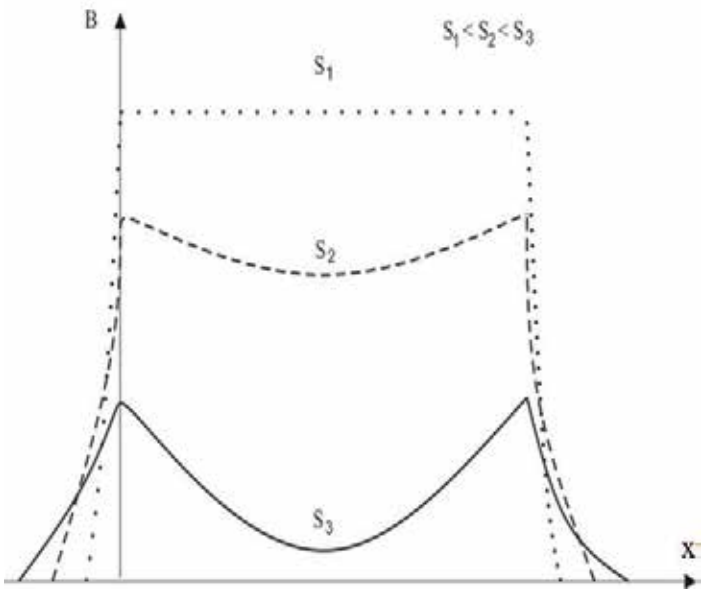

Figure 19. The resultant magnetic flux density distribution in the air-gap at different secondary slips.

As the rotary-linear motor is concerned, the transverse edge effect occurs for rotary armature. This effect has here more complex form due to the additional axial motion of the rotor. The above transverse edge effects superimpose on entry and exit effects whose nature is the same as discussed earlier for linear part of the rotary-linear motor. This motion makes the flux density distribution distorted as shown in Fig. 20. At the entry edge the flux density in the air-gap is damped, but at the exit edge it increases.

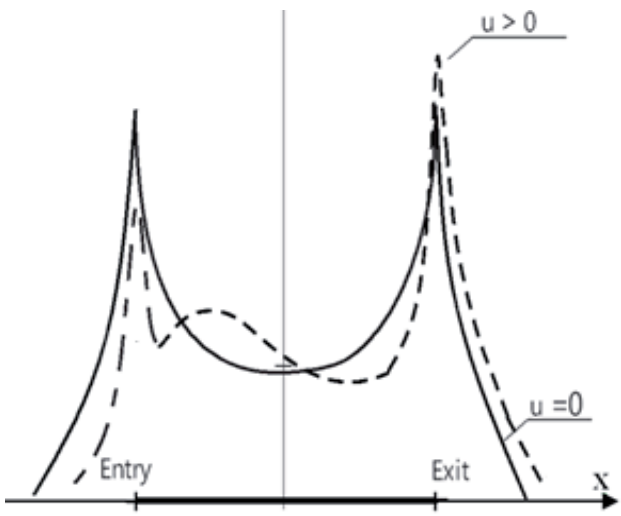

Figure 20. Resultant magnetic flux density in the air-gap of rotary part of the IM-2DoMF motor with linear speed greater than zero (u > 0).

5. Performance of twin-armature rotary-linear induction motor

5.1. Design parameter of the motor

One of a few design versions of rotary-linear motors is a Twin-Armature Rotary-Linear Induction Motor (TARLIM) shown schematically in Fig. 21. The stator consists of a rotary and linear armature placed aside one another. One generates a rotating magnetic field, another traveling magnetic field. A common rotor for these two armatures is applied. It consists of a solid iron cylinder covered with a thin copper layer. The direction of the rotor motion depends on two forces; linear and rotary, which are the products of two magnetic fields and currents induced in the rotor.

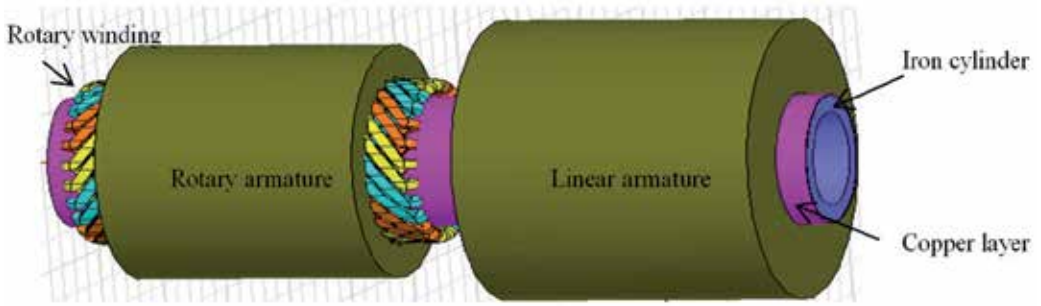

Figure 21. Schematic 3D-view of twin-armature rotary-linear induction motor.

The TARLIM in its operation can be regarded as a set two independent motors: a conventional rotary and tubular linear motor with the rotors joined stiffly. This approach can be applied only if there is no magnetic link between the two armatures, what practically is fulfilled due to the relatively long distance between the armatures and the low axial speed of the rotors. In case of the motor analysed here both conditions are satisfied and the analysis of each part of the TARLIM can be carried out separately as the analysis of IM 3-phase rotary and linear motors. The only influence of one motor on the other is during the linear motion of the rotor which will be considered at the end of this chapter.

To study the performance of TARLIM the exemplary motor has been chosen with the dimensions shown in Fig. 22. The dimensions of rotary armature are presented in details in Fig. 23.

The core of both armatures is made of laminated steel. The common rotor is made of solid steel cylinder covered by copper layer. Both armatures possess a 3-phase winding. The rotary and linear winding diagrams are shown in Figs. 24.a and 24.b, respectively. The winding parameters and the data of stator and rotor core material are enclosed in Table 1.

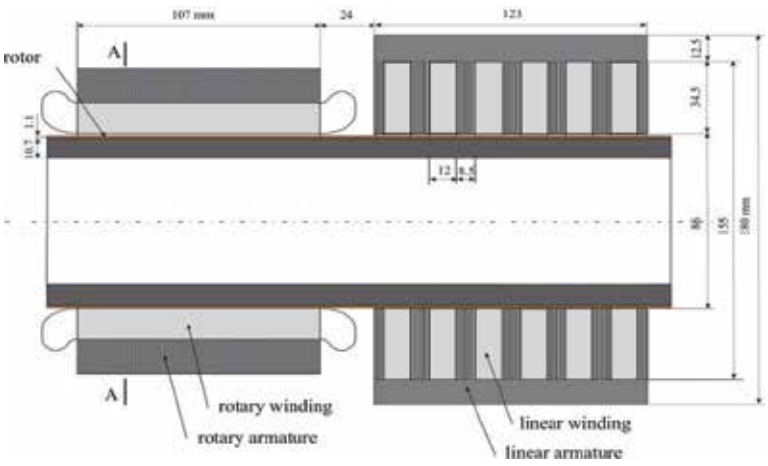

Figure 22. Dimensions of TARLIM chosen for analyse.

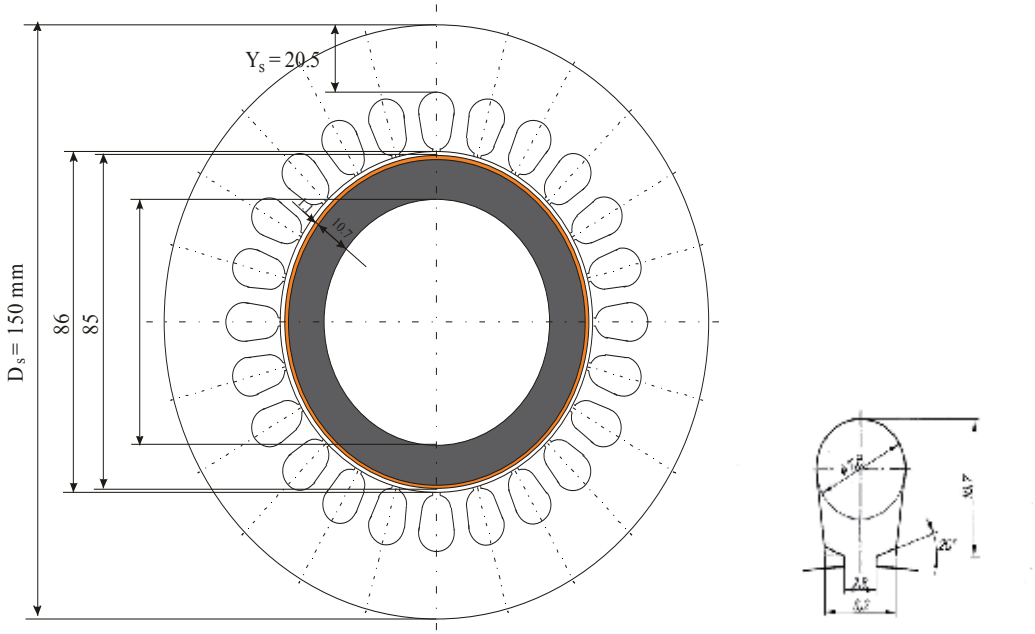

Figure 23. Rotary armature dimensions.

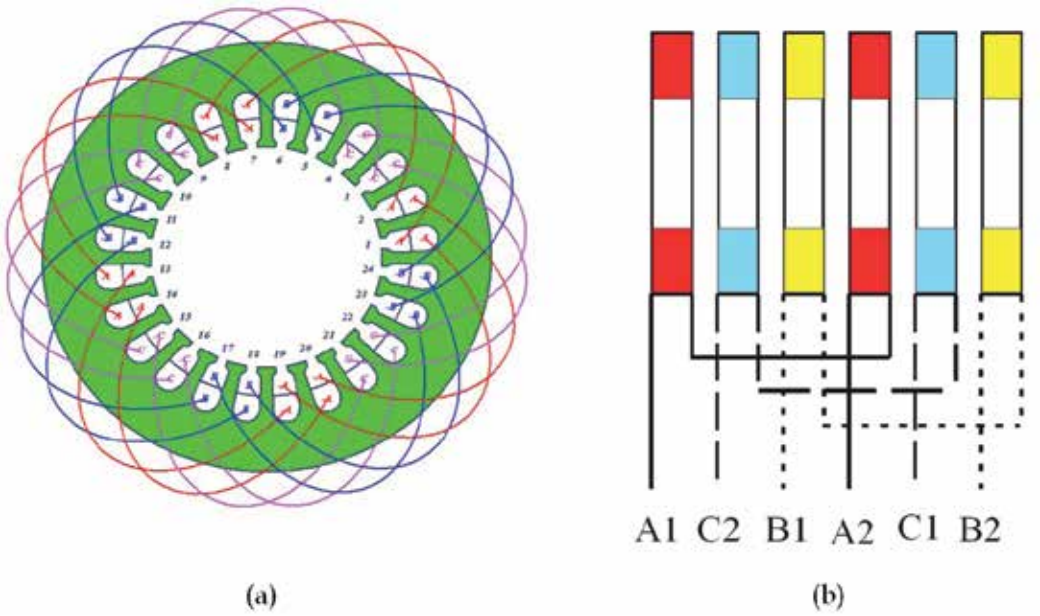

Figure 24. Winding diagram of the TARLIM, (a) rotary winding, (b) linear winding.

Linear winding data:	
Number of phases	3
Number of poles	2
Number of slots per pole per phase	1
Number of wires per slot, N_w	215
Copper wire diameter	1.29 mm
Rotary winding data:	
Number of phases	3
Number of poles	4
Number of slots per pole per phase	2
Number of wires per slot, Nw	96
Copper wire diameter	0.7 mm
Armature Core	Laminated steel
Air gap length, mm	0.5
Rotor	
Copper layer	
Thickness mm	1.1 mm
Conductivity ($\gamma_{Cu,\ @\ 20C}$)	57.00x106 S/m
Solid iron cylinder	
Thickness mm	10.7 mm
Conductivity ($\gamma_{Fe\ ,\ @\ 20C}$)	5.91x106 S/m

Table 1. Winding and materials data for TARLIM.

5.2. Experimental model

To verify the modeling results, a real prototype of the motor was built (see Figs. 25 and 26) and tested. The laboratory model of TARLIM has a relatively short secondary length. Therefore, measuring motor performances at linear speed greater than zero was practically difficult so the test was carried out only at zero linear speed. The TARLIM operates practically at low rotary slip and at linear slip close to one. Thus the dynamic end effects does not influence much the motor performance but the static end effect caused by finite length of each of the armatures has a large impact on the linear motor performance.

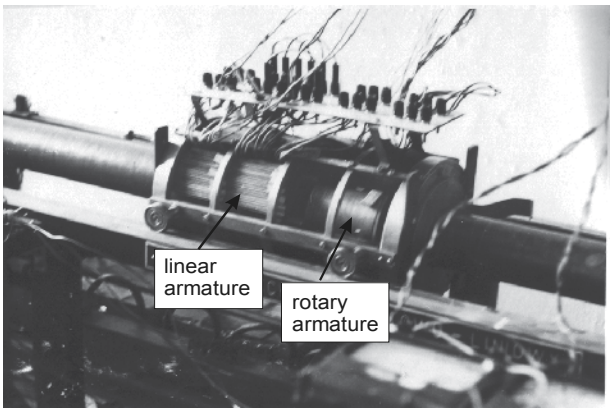

Figure 25. Laboratory model of twin-armature rotary-linear induction motor.

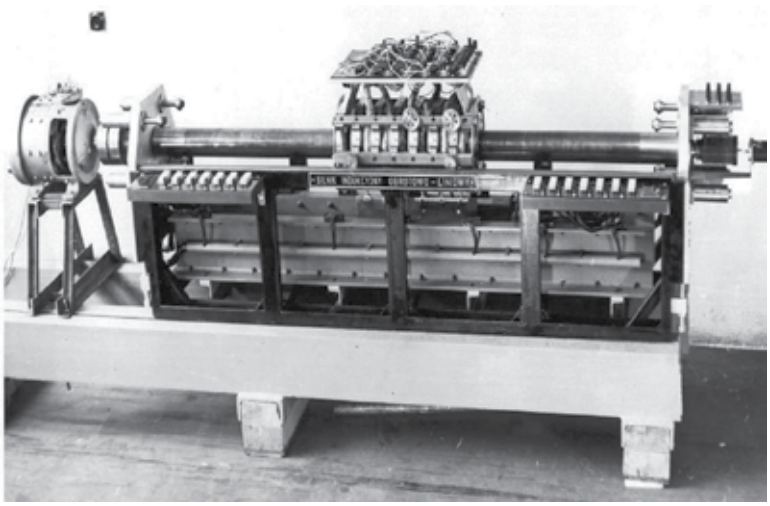

Figure 26. Measurement stand for testing of rotary-linear motors.

5.3. Motor performance

The analysis of each part of TARLIM performance is carried out separately as an independent tubular linear and rotary motor by 3-D FEM modelling.

The linear armature is being supplied from the constant voltage source of 86.6 V (rms), 50 Hz frequency. The results of simulation are shown in Figs. 27, 28 and 29 in form of the electromechanical force (F_{em}), mechanical power (P_m) and efficiency, respectively, versus linear slip of the rotor. These characteristics illustrate a significant impact of end effects on motor performance and are drawn as dashed line curves for the infinitely long motor when no end effects are considered, circles for the actual motor of finite armature length, when both static and dynamic end effects are taken into account and triangular sign for the experimental result.

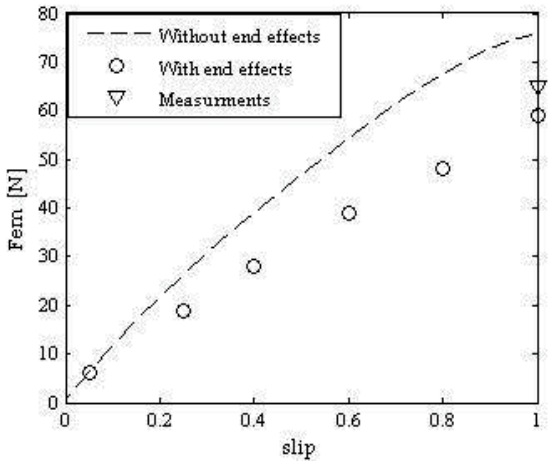

Figure 27. Characteristic of force vs linear slip.

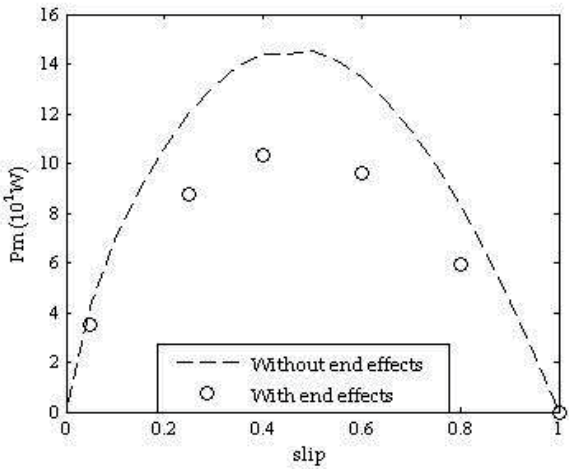

Figure 28. Characteristic of output power vs linear slip.

The motor under study has a linear synchronous speed equal to 6.15 m/s and is considered as low-speed motor. In low-speed motors, the speed of the end effect wave can be higher than the motor speed and even much higher than the synchronous speed, while in high-speed motors the speed of the end effect wave is about the same as the motor speed and

cannot be higher the synchronous speed. In low-speed motors, the attenuation of the entry end-effect wave is quick, while in high-speed motors the attenuation is very slow and the entry-end-effect wave presents over the entire longitudinal length of the air-gap. As a consequence of the difference, the influence of the end-effect wave on motor performance is also quite different at high-speed motors and low-speed motors. In low-speed motors, the end effect wave may improve motor performance in low-slip region, the important motor-run region, increasing thrust, power factor and efficiency, and allowing net thrust to be generated even at synchronous and higher speeds. On the contrary, in high speed motors, thrust, power factor and efficiency are reduced to a large extent in the low-slip region, and it is not an over statement to say that high-speed applications of linear induction motors may not be feasible if the end effect is overlooked and is allowed to remain as an influence.

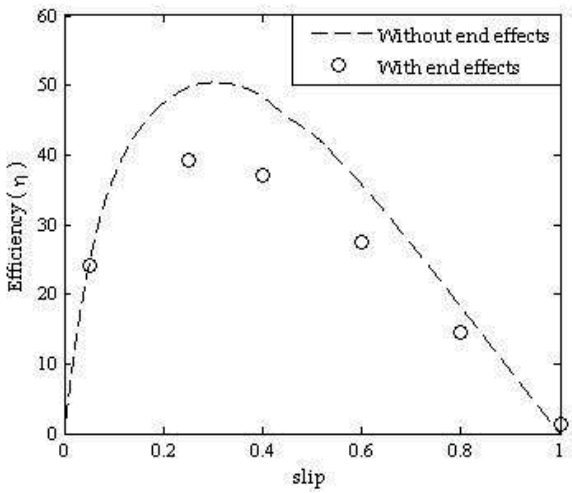

Figure 29. Characteristic of efficiency vs linear slip.

To study the performance of the motor at higher speeds, let us change the supply frequency to 3 times higher (synchronous speed, v_s= 3 * 6.15 m/s) and then recalculate the forces acted on rotor when all end effects are taken into account. Table 2 compares the output forces of the low-speed and high-speed motor at relatively low operational slip region.

Synchronous speed	Operational slip region	
	S=0.25	S=0.05
v_s= 6.15 m/s	19 N	6 N
v_s= 3*6.15 m/s	6 N	0 N

Table 2. Electromechanical force of low speed and high speed LIM.

The simulation of rotary part of the motor is done for the winding being supplied by the three-phase voltage of 150 V (rms), 50 Hz frequency.

Due to closed magnetic circuit in rotary armature, static end effect does not exist in rotational direction. However, the performance of rotary armature might be affected by dynamic end

effects during rotor axial motion. This is the only influence of linear part of TARLIM on rotary motion and, as stated earlier, both armatures have no more influence on one another due to the relatively long distance and the lack of magnetic interaction in between. To determine the influence of rotor axial motion on the performance of rotary armature, the characteristics of electromagnetic torque (T_{em}) and mechanical power (P_m) versus rotary slip at three different linear speeds (u = 0 m/s, u =3 m/s and u =6 m/s) along with experimental results at zero linear speed (u = 0 m/s) are plotted in Figs. 30 and 31. These effects contribute to diminishing of torque and all other rotary motor performances. One can observe that, the higher axial speed leads to lower rotary torque and mechanical power.

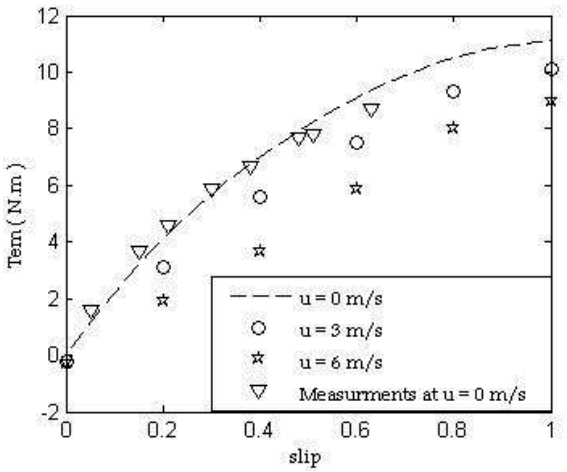

Figure 30. Characteristic of Torque vs rotary slip with and without linear motion.

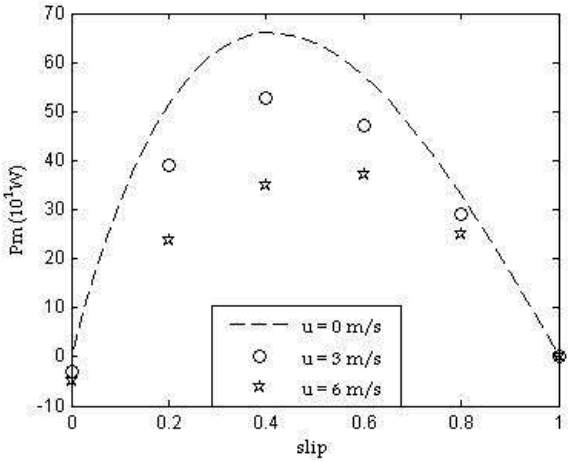

Figure 31. Characteristic of output power vs linear slip with and without linear motion.

Note, that the output quantities are extremely dependent on the property of materials. The conductivity of the materials used in 3D FEM analysis is kept constant, but in reality it might be influenced by the temperature. Therefore, minimal mismatch between

experimental measurements, where the temperature changes during the experiment and FEM results is expected. On the other hand, FEM needs as dense mesh as possible to compute quantities accurately, but the execution time of such a complicated model is enormous. Therefore, some trade-off between accuracy and execution time is required to obtain a good solution at reasonable cost. However, the discrepancies between test and simulation results are relatively small which validates the simulation models.

6. Conclusion

Rotary-linear induction motor is one of a few types of motors with two degrees of mechanical freedom. It may find application in robotics and special types of drives like machine tools and drilling machines. One of its representatives, the TARLIM, with two solid layer rotor was modelled in 3-D FEMM and its performance has been determined. The operation of the motor does not differ from the operation of machine set consisting rotary and tubular linear motor of which rotors are firmly coupled. The electromechanical performances of the motor are affected by the end effects which are familiar phenomena in linear machines. Practically, the impact of these phenomena is not significant in low axial speed of the rotor, what is expected for these types of motors.

The results obtained from the test carried out on the experimental model do not differ much from the ones got from simulations. Thus they validate the theoretical modeling of the motor.

Motor with the rotor cage made in form of grid placed on the cylindrical core is another version of TARLIM and is expected to have a better performance with respect to the solid two layer rotor.

Author details

Ebrahim Amiri and Ernest Mendrela
Louisiana State University, USA

7. References

Mendrela, E, Fleszar, J, Gierczak, E. (2003). *Modeling of Induction Motors With One and Two Degrees of Mechanical Freedom*, Norwell, MA: Kluwer Academic Publishers.

Krebs, G, Tounzi, A, Pauwels, B and Willemot, D. (2008). *General overview of integrated linear rotary actuators, in Proc. ICEM Conf.*

Bolognesi P, Bruno O, Landi A, Sani L, Taponecco L. (2004). *Electromagnetic actuators featuring multiple degrees of freedom:* a survey. In: ICEM conference, Krakow (Poland), 5–8 September.

Giancarlo, B and Tellini, B. (2003). *Helicoidal electromagnetic field for coilgun armature stabilization, IEEE Trans. Magn.*, vol. 39, no. 1, pp. 108–111, Jan. 2003.

Anorad Corp., New York, USA. (2001). *Rotary linear actuator*, U.S. Patent 6 215 206.

Yamamura, S. (1972). *Theory of Linear Induction Motors*, John Wiley & Sons.

Creppe, R. C, Ulson, J. A. C, Rodrigues, J. F. (2008). *Influence of Design Parameters on Linear Induction Motor End Effects*, *IEEE* Trans. Energy Convers., vol. 23, no. 2, pp. 358–362 June. 2008.

Faiz, J Jafari, H. (2000) *Accurate Modelling of Single-Sided Linear Induction Motor Considers End Effect and Equivalent Thickness,* IEEE Transactions on Magnetics, vol. 36, No. 5, September 2000, pp. 3785-3790.

Turowski, J. (1982). *Electromagnetic calculations of machine elements and electro mechanics*. WNT Warsaw, (in Polish).

Gierczak, E, Mendrela, E. (1985). *Magnetic flux, current, force and power loss distribution in twin-armature rotary-linear induction motor*, Scientia Electrica, Vo. 31, pp. 65-74, 1985.

Mosebach, H, Huhns, T, Pierson, E.S, Herman, D. (1977). *Finite Length Effects in Linear Induction Machines with Different Iron Contours*, IEEE Trans. On PAS-96, 1977, pp. 1087-1093.

Poloujadoff, M, Morel, B, Bolopion, A (1980). *Simultaneous Consideration of Finite Length and Finite Width of Linear Induction Motors,* IEEE Trans. On PAS, Vol. PAS-99, No. 3, 1980, pp. 1172-1179.

Pai, R.M., Boldea, I., and Nasar, S.A. (1988). *A complete equivalent circuit of a linear induction motor with sheet secondary*, IEEE. Trans., 1988, MAG-24, (1), pp. 639–654.

Gieras, J. F. , Dawson, G. E. and Eastham, A. R. (1987). *A new longitudinal end effect factor for linear induction motors, IEEE Trans. Energy Convers.*, vol. 2, no. 1, pp. 152–159, Mar. 1987.

Hirasa, T, Ishikawa, S and Yamamuro, T. (1980). *Equivalent circuit of linear induction motors with end effect taken into account*, *Trans. IEE Jpn.*, vol. 100, no. 2, pp. 65–71, 1980.

Duncan, J., and Eng, C. (1983) *Linear induction motor-equivalent circuit model'*, IEE Proc., Electr. Power Appl., 1983, 130, (1), pp. 51–57.

Mirsalim, M, Doroudi, A and Moghani, J. S. (2002). *Obtaining the operating characteristics of linear induction motors: A new approach*, IEEE Trans. Magn., vol. 38, no. 2, pp. 1365–1370, Mar. 2002.

Kwon, B. I, Woo, K. I. and Kim, S (1999). *Finite element analysis of direct thrust controlled linear induction motor*, IEEE Trans. Magn., vol. 35, no. 3, pp. 1306–1309, May 1999.

Fujii, N and Harada, T. (2000). *Basic consideration of end effect compensator of linear induction motor for transit*, in Industry Applications Conf., Oct. 8–12, 2000, pp. 1–6.

Kim, D.-k. and Kwon, B.-I. (2006). *A novel equivalent circuit model of linear induction motor based on finite element analysis and and its coupling with external circuits*, IEEE Trans. Magn., vol. 42, no. 10, pp. 3407–3409, Oct. 2006.

Krebs, G, Tounzi, A, Pauwels, B, Willemot, D and Piriou, F. (2008). *Modeling of a linear and rotary permanent magnet actuator*, IEEE Trans. Magn., vol. 44, no. 10, pp. 4357-4360, Nov. 2008.

Amiri, E, Gottipati, P, Mendrela, E. (2011). *3-D Space Modeling of Rotary-Linear Induction Motor With Twin-Armature* The 1st IEEE International Conference on Electrical Energy Systems, Chennai, Tamil Nadu, India, Jan 2011.

Poloujadoff, M. (1980). *The Theory of Linear Induction Machinery*, Oxford University Press, 1980.

Mendrela, E. (2004) *Electric Machines", Course Pack "Advanced Electric Machine*, Louisiana State University.

Boldea, I, Nasar, S.A.. (2001). *Linear Motion Electromagnetic Devices*, Taylor and Francis, 2001.

Chapter 11

Electrical Parameter Identification of Single-Phase Induction Motor by RLS Algorithm

Rodrigo Padilha Vieira, Rodrigo Zelir Azzolin, Cristiane Cauduro Gastaldini and Hilton Abílio Gründling

Additional information is available at the end of the chapter

http://dx.doi.org/10.5772/37664

1. Introduction

This chapter addresses the problem of the electrical parameter identification of Single-Phase Induction Motor (SPIM). The knowledge of correct electrical parameters of SPIM allows a better representation of dynamic simulation of this machine. In addition, the identified parameters can improve the performance of the Field Oriented Control (FOC) and sensorless techniques used in these systems.

Controlled induction motor drives have been employed on several appliances in the last decades. Commonly, the control schemes are based on the FOC and sensorless techniques. These methods are mainly applied to three-phase induction machine drives, and a wide number of papers, such as [5, 9, 10, 15, 19, 23, 26] have described such drives. On the other hand, for several years the SPIM has been used in residential appliances, mainly in low power and low cost applications such as in freezers and air conditioning, consuming extensive rate of electrical energy generated in the world. In most of these applications, the SPIM operates at fixed speed and is supplied directly from source grid. However, in the last few years several works have illustrated that the operation with variable speed can enhance the process efficiency achieved by the SPIM ([1, 4, 8, 31]). Furthermore, some other studies have presented high performance drives for SPIM using vector control and sensorless techniques, such as is presented in [7, 12, 18, 24] and [29]. However, these schemes applied on single-phase and three-phase induction motor drives need an accurate knowledge of all electrical parameters machine to have a good performance.

As a consequence of the parameter variation and uncertainties of the machine, literature presents algorithms for computational parameter estimation of induction machines, mainly about three-phase induction machines ([3, 13, 20, 21, 27]). Some authors proposed an on-line

parameter estimation, for adaptive systems and self-tuning controllers due to the fact that the parameters of induction machine change with temperature, saturation, and frequency ([22]).

Differently from the three-phase induction motors, the SPIM is an asymmetrical and coupled machine; these features make the electrical parameter estimation by classical methods difficult, and these characteristics complicate the use of high performance techniques, such as vector and sensorless control. Thus, the use of Recursive Least Square (RLS) algorithm can be a solution for the parameter estimation or self-tuning and adaptive controllers, such as presented in [28] and [30]. Other studies have also been reported in literature describing the parameter estimation of SPIM ([2, 11, 17, 25]).

The aim of this chapter is to provide a methodology to identify a set of parameters for an equivalent SPIM model, and to obtain an improved SPIM representation, as consequence it is possible to design a high performance sensorless SPIM controllers. Here, from the machine model, a classical RLS algorithm is applied at *q* and *d* axes based on the current measurements and information of fed voltages with a standstill rotor. The automatized test with standstill rotor can be a good alternative in some applications, such as hermetic compressor systems, where the estimation by conventional methods is a hard task due the fact of the machine is sealed.

An equivalent SPIM behavior representation is obtained with this methodology in comparison with the SPIM model obtained by classical tests. However, some types of SPIM drives, for instance a hermetic system, it is impossible to carried out classical tests. In addition, the proposed methodology has a simple implementation.

This chapter is organized as follows: Section 2 presents the SPIM model, Section 3 gives the RLS parameter algorithm, Section 4 presents and discusses the experimental results obtained with the proposed methodology, and Section 5 gives the main conclusions of this study.

2. Single-phase induction motor model

The commercial SPIM commonly used in low power applications is usually a two-phase induction machine with asymmetrical windings, whose equivalent circuit without the permanent split-capacitor can be represented as in Fig. 1.

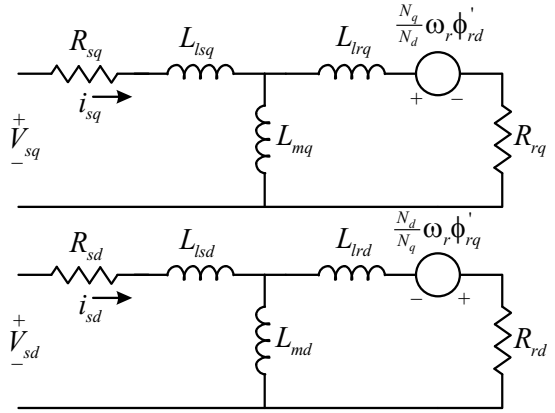

Figure 1. Equivalent circuit of SPIM.

As in [14], in this chapter the squirrel cage SPIM mathematical model is described in a stationary reference-frame by the following equations

$$\begin{bmatrix} V_{sq} \\ V_{sd} \end{bmatrix} = \begin{bmatrix} R_{sq} & 0 \\ 0 & R_{sd} \end{bmatrix} \begin{bmatrix} i_{sq} \\ i_{sd} \end{bmatrix} + \frac{d}{dt} \begin{bmatrix} \phi_{sq} \\ \phi_{sd} \end{bmatrix} \tag{1}$$

$$\begin{bmatrix} V_{rq} \\ V_{rd} \end{bmatrix} = \begin{bmatrix} R_{rq} & 0 \\ 0 & R_{rd} \end{bmatrix} \begin{bmatrix} i_{rq} \\ i_{rd} \end{bmatrix} + \frac{d}{dt} \begin{bmatrix} \phi_{rq} \\ \phi_{rd} \end{bmatrix} + \omega_r \begin{bmatrix} 0 & -1/n \\ n & 0 \end{bmatrix} \begin{bmatrix} \phi_{rq} \\ \phi_{rd} \end{bmatrix} = \begin{bmatrix} 0 \\ 0 \end{bmatrix} \tag{2}$$

$$\begin{bmatrix} \phi_{sq} \\ \phi_{sd} \end{bmatrix} = \begin{bmatrix} L_{sq} & 0 \\ 0 & L_{sd} \end{bmatrix} \begin{bmatrix} i_{sq} \\ i_{sd} \end{bmatrix} + \begin{bmatrix} L_{mq} & 0 \\ 0 & L_{md} \end{bmatrix} \begin{bmatrix} i_{rq} \\ i_{rd} \end{bmatrix} \tag{3}$$

$$\begin{bmatrix} \phi_{rq} \\ \phi_{rd} \end{bmatrix} = \begin{bmatrix} L_{mq} & 0 \\ 0 & L_{md} \end{bmatrix} \begin{bmatrix} i_{sq} \\ i_{sd} \end{bmatrix} + \begin{bmatrix} L_{rq} & 0 \\ 0 & L_{rd} \end{bmatrix} \begin{bmatrix} i_{rq} \\ i_{rd} \end{bmatrix} \tag{4}$$

$$T_e = p(L_{mq} i_{sq} i_{rd} - L_{md} i_{sd} i_{rq}) \tag{5}$$

$$p(T_e - T_L) = J \frac{d\omega_r}{dt} + B_n \omega_r \tag{6}$$

where, the indexes q and d represent the main winding and auxiliary winding, respectively, the indexes sq and sd represent the stator variables, and the indexes rq and rd are used for the rotor variables. V_{sq}, V_{sd}, V_{rq}, V_{rd}, i_{sq}, i_{sd}, i_{rq}, i_{rd}, ϕ_{sq}, ϕ_{sd}, ϕ_{rq}, and ϕ_{rd} are the stator and rotor voltages, currents, and flux; R_{sq}, R_{sd}, R_{rq}, and R_{rd} are the stator and rotor resistances; L_{lsq}, L_{lsd}, L_{lrq}, and L_{lrd} are the leakage inductances; L_{mq} and L_{md} are the mutual inductances; L_{sq}, L_{sd}, L_{rq}, and L_{rd} are the stator and rotor inductances, and are given by: $L_{sq} = L_{lsq} + L_{mq}$, $L_{sd} = L_{lsd} + L_{md}$, $L_{rq} = L_{lrq} + L_{mq}$, and $L_{rd} = L_{lrd} + L_{md}$; N_q and N_d represent the number of turns for the main and auxiliary windings, respectively; p is the pole pair number and ω_r is the rotor speed, and n is the relationship between the number of turns for auxiliary and for main winding N_d/N_q. T_e is the electromagnetic torque, T_L is the load torque, B_n is the viscous friction coefficient, and J is the inertia coefficient.

From (1) - (4) it is possible to obtain the differential equations that express the dynamical behavior of the SPIM, as follows,

$$\frac{d}{dt} i_{sq} = -\frac{R_{sq} L_{rq}}{\overline{\sigma}_q} i_{sq} - \omega_r \frac{1}{n} \frac{L_{mq} L_{md}}{\overline{\sigma}_q} i_{sd} + \frac{R_{rq} L_{mq}}{\overline{\sigma}_q} i_{rq} - \omega_r \frac{1}{n} \frac{L_{rd} L_{mq}}{\overline{\sigma}_q} i_{rd} + \frac{L_{rq}}{\overline{\sigma}_q} V_{sq} \tag{7}$$

$$\frac{d}{dt} i_{sd} = \omega_r n \frac{L_{md} L_{mq}}{\overline{\sigma}_d} i_{sq} - \frac{L_{rd} R_{sd}}{\overline{\sigma}_d} i_{sd} + \omega_r n \frac{L_{rq} L_{md}}{\overline{\sigma}_d} i_{rq} + \frac{R_{rd} L_{md}}{\overline{\sigma}_d} i_{rd} + \frac{L_{rd}}{\overline{\sigma}_d} V_{sd} \tag{8}$$

$$\frac{d}{dt} i_{rq} = \frac{L_{mq} R_{sq}}{\overline{\sigma}_q} i_{sq} + \omega_r \frac{1}{n} \frac{L_{sq} L_{md}}{\overline{\sigma}_q} i_{sd} - \frac{L_{sq} R_{rq}}{\overline{\sigma}_q} i_{rq} + \omega_r \frac{1}{n} \frac{L_{sq} L_{rd}}{\overline{\sigma}_q} i_{rd} - \frac{L_{mq}}{\overline{\sigma}_q} V_{sq} \tag{9}$$

$$\frac{d}{dt} i_{rd} = -\omega_r n \frac{L_{sd} L_{mq}}{\overline{\sigma}_d} i_{sq} + \frac{L_{md} R_{sd}}{\overline{\sigma}_d} i_{sd} - \omega_r n \frac{L_{sd} L_{rq}}{\overline{\sigma}_d} i_{rq} - \frac{L_{sd} R_{rd}}{\overline{\sigma}_d} i_{rd} - \frac{L_{md}}{\overline{\sigma}_d} V_{sd} \tag{10}$$

where $\overline{\sigma}_q = L_{sq}L_{rq} - L_{mq}^2$, $\overline{\sigma}_d = L_{sd}L_{rd} - L_{md}^2$.

The transfer functions in the axes q and d at a standstill rotor ($\omega_r = 0$) are obtained from (7)-(10), where these functions are decoupled and presented in (11) and (12).

$$H_q(s) = \frac{i_{sq}(s)}{V_{sq}(s)} = \frac{s\overline{\sigma}_q^{-1}L_{rq} + \overline{\sigma}_q^{-1}\tau_{rq}^{-1}L_{rq}}{s^2 + sp_q + \overline{\sigma}_q^{-1}R_{rq}R_{sq}} \tag{11}$$

$$H_d(s) = \frac{i_{sd}(s)}{V_{sd}(s)} = \frac{s\overline{\sigma}_d^{-1}L_{rd} + \overline{\sigma}_d^{-1}\tau_{rd}^{-1}L_{rd}}{s^2 + sp_d + \overline{\sigma}_d^{-1}R_{rd}R_{sd}} \tag{12}$$

where $p_q = \left(R_{sq}L_{rq} + R_{rq}L_{sq}\right)/\overline{\sigma}_q$ and $p_d = \left(R_{sd}L_{rd} + R_{rd}L_{sd}\right)/\overline{\sigma}_d$.

3. Parameter identification of single-phase induction machine

In section 2, the decoupled transfer functions of the SPIM were obtained assuming a standstill rotor ($\omega_r = 0$). Thus, in this section the parameter identification is achieved with SPIM at a standstill rotor by a RLS algorithm. The identification with a standstill rotor is appropriated in some cases such as hermetic refrigeration compressors ([28]). The RLS identification algorithm requires the plant model in a discrete time linear regression form. Assuming the actual sampling index k, the regression model is given by

$$\hat{\mathbf{Y}}(k) = \phi^T(k)\theta(k) \tag{13}$$

The recursive algorithm is achieved with the equations (14)-(17).

$$e(k) = \mathbf{Y}(k) - \hat{\mathbf{Y}}(k) \tag{14}$$

$$\mathbf{K}(k) = \frac{\mathbf{P}(k-1)\phi(k)}{1 + \phi^T(k)\mathbf{P}(k-1)\phi(k)} \tag{15}$$

$$\theta(k) = \theta(k-1) + \mathbf{K}(k)e(k) \tag{16}$$

$$\mathbf{P}(k) = \left(I - \mathbf{K}(k)\phi^T(k)\right)\mathbf{P}(k-1) \tag{17}$$

where $dim\ \mathbf{Y} = \bar{M} \times \bar{N}$, $dim\ \phi^T(k) = \bar{M} \times \bar{r}$

$dim\ \theta(k) = \bar{r} \times \bar{N}$, $dim\ e(k) = \bar{M} \times \bar{N}$

$dim\ \mathbf{K}(k) = \bar{r} \times \bar{M}$, $dim\ I = dim\ \mathbf{P}(k) = \bar{r} \times \bar{r}$

From the equations (11) and (12) it is possible to reformulate the estimation parameter problem based on a linear regression model. Here, the parameter estimation method is divided into two steps:

***First step**: estimation of (18) and (19) vide equations (20) and (21) :*

This step consists into obtaining a linear-time-invariant model of the SPIM. The identification of b_1, b_0, a_1 and a_0 is done by performing a standstill test. The coefficients presented in (11) and (12) are functions of the machine parameters. For simplicity, the transfer functions given in (11) and (12) are rewritten in two transfer functions given by (18) and (19).

$$H_q(s) = \frac{i_{sq}^s(s)}{V_{sq}^s(s)} = \frac{sb_{1q} + b_{0q}}{s^2 + sa_{1q} + a_{0q}} \tag{18}$$

and

$$H_d(s) = \frac{i_{sd}^s(s)}{V_{sd}^s(s)} = \frac{sb_{1d} + b_{0d}}{s^2 + sa_{1d} + a_{0d}} \tag{19}$$

where

$$b_{1q} = \frac{L_{rq}}{\overline{\sigma}_q},\ b_{0q} = \frac{L_{rq}}{\overline{\sigma}_q \tau_{rq}},\quad a_{1q} = \frac{R_{sq}L_{rq} + R_{rq}L_{sq}}{\overline{\sigma}_q},\ a_{0q} = \frac{R_{sq}R_{rq}}{\overline{\sigma}_q} \tag{20}$$

and

$$b_{1d} = \frac{L_{rd}}{\overline{\sigma}_d},\ b_{0d} = \frac{L_{rd}}{\overline{\sigma}_d \tau_{rd}},\quad a_{1d} = \frac{R_{sd}L_{rd} + R_{rd}L_{sd}}{\overline{\sigma}_d},\ a_{0d} = \frac{R_{sd}R_{rd}}{\overline{\sigma}_d} \tag{21}$$

In order to obtain the regression linear model the transfer functions of (18) and (19) can be generalized and rewritten as,

$$\frac{d^2 i_{sq}}{dt^2} + a_{1q}\frac{di_{sq}}{dt} + a_{0q} i_{sq} = b_{1q}\frac{dV_{sq}}{dt} + b_{0q} V_{sq} \tag{22}$$

and

$$\frac{d^2 i_{sd}}{dt^2} + a_{1d}\frac{di_{sd}}{dt} + a_{0d} i_{sd} = b_{1d}\frac{dV_{sd}}{dt} + b_{0d} V_{sd} \tag{23}$$

Solving for the second derivative of the stator current,

$$\frac{d^2 i_{sq}}{dt^2} = \begin{bmatrix} -\frac{di_{sq}}{dt} & -i_{sq} & \frac{dV_{sq}}{dt} & V_{sq} \end{bmatrix} \begin{bmatrix} a_{1q} \\ a_{0q} \\ b_{1q} \\ b_{0q} \end{bmatrix} \tag{24}$$

and

$$\frac{d^2 i_{sd}}{dt^2} = \begin{bmatrix} -\frac{di_{sd}}{dt} & -i_{sd} & \frac{dV_{sd}}{dt} & V_{sd} \end{bmatrix} \begin{bmatrix} a_{1d} \\ a_{0d} \\ b_{1d} \\ b_{0d} \end{bmatrix} \tag{25}$$

The estimation of coefficients b_{1q}, b_{0q}, a_{1q}, a_{0q}, b_{1d}, b_{0d}, a_{1d} and a_{0d} is done by using RLS estimation algorithm described in the equations (13)-(17). The linear regression model form (13) is given for the q axis by the following equations,

$$\mathbf{Y}_q(k) = \frac{d^2 i_{sq}}{dt^2} \tag{26}$$

$$\phi_q^T(k) = \begin{bmatrix} -\frac{di_{sq}}{dt} & -i_{sq} & \frac{dV_{sq}}{dt} & V_{sq} \end{bmatrix} \tag{27}$$

$$\theta_q^T(k) = \begin{bmatrix} a_{1q} & a_{0q} & b_{1q} & b_{0q} \end{bmatrix} \tag{28}$$

And, for the d axis,

$$\mathbf{Y}_d(k) = \frac{d^2 i_{sd}}{dt^2} \tag{29}$$

$$\phi_d^T(k) = \begin{bmatrix} -\frac{di_{sd}}{dt} & -i_{sd} & \frac{dV_{sd}}{dt} & V_{sd} \end{bmatrix} \tag{30}$$

$$\theta_d^T(k) = \begin{bmatrix} a_{1d} & a_{0d} & b_{1d} & b_{0d} \end{bmatrix} \tag{31}$$

where, let us assume that the derivatives presented in (26)-(27) and (29)-(30) are measurable quantities. In the implementation, these quantities are obtained by State Variable Filters (SVF) such as in [6]. Four SVF filters were developed by discretization of the continuous-time transfer function given by,

$$\frac{V_{sqf}}{V_{sq}} = \frac{V_{sdf}}{V_{sd}} = \frac{i_{sqf}}{i_{sq}} = \frac{i_{sdf}}{i_{sd}} = G_{svf}(s) = \frac{\omega_{svf}^3}{(s+\omega_{svf})^3} \tag{32}$$

where, ω_{svf} is the filter bandwidth defined at around 5 to 10 times the input frequency signal. Here, $\omega_{svf} = \omega$, and ω is signal frequency, and the signals V_{sq}, V_{sd}, i_{sq}, and i_{sd} are used to obtain the filtered signals V_{sqf}, V_{sdf}, i_{sqf} and i_{sdf}.

The discretized transfer function, using the Euler method and sampling time of T_s, can be performed in state-space as

$$\mathbf{x}_{svf(k+1)} = \left(1 + \mathbf{A}_{svf}T_s\right)\mathbf{x}_{svf(k)} + T_s\mathbf{B}_{svf}u_{svf(k)} \tag{33}$$

where, $\mathbf{A}_{svf} = \begin{bmatrix} 0 & 1 & 0 \\ 0 & 0 & 1 \\ -\omega_{svf}^3 & -3\omega_{svf}^2 & 3\omega_{svf} \end{bmatrix}$, $\mathbf{B}_{svf} = \begin{bmatrix} 0 \\ 0 \\ \omega_{svf}^3 \end{bmatrix}$, $x_{svf} = \begin{bmatrix} x_1 \\ x_2 \\ x_3 \end{bmatrix}$ The variable u_{svf} represents the input signal, while the state variables x_1, x_2 and x_3 represent the input filtered signal, first derivative signal and second derivative signal, respectively.

With the SVF it is possible to avoid the use o low-pass filters in signals of the currents and the voltages, due the fact of the SVF has behavior of a low-pass filter. In addition, due this characteristic the SVF atenues the impact of pulsed and noise signals on the measurements of stator currents. For instance, to demonstrate the response of SVF Figure 2 presents the Module and the Phase Bode diagram with bandwidth of $\omega_{svf} = 5 * 2\pi * 30Hz \ [rad/s]$. It is possible to observer that the high frequency signals are attenuated.

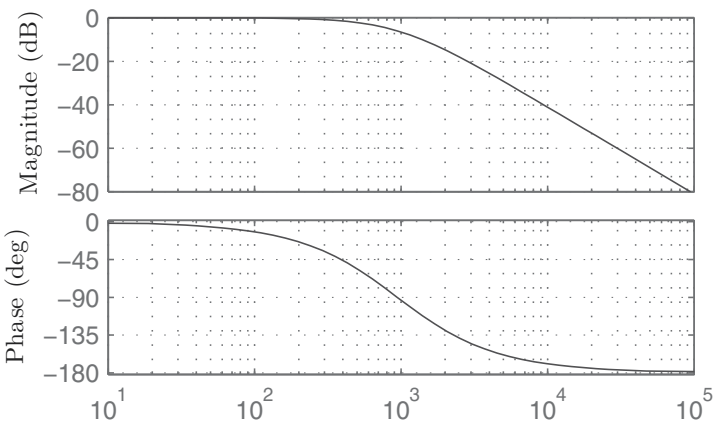

Figure 2. Bode diagram of the State Variable Filter.

***Second step**: identification of machine parameters, R_{sq}, R_{sd}, R_{rq}, R_{rd}, L_{mq}, L_{md}, L_{sq}, L_{sd}, L_{rq} and, L_{rd}:*

The electrical parameters of the SPIM are obtained combining the identified coefficients of $\theta_q(k)$ and $\theta_d(k)$ in (28) and (31) with the coefficients of the transfer functions (20) and (21), respectively, after the convergence of the RLS algorithm by the equations (34) and (35). In the numerical solution, the stator and rotor inductances are considered to have the same values in each winding.

$$\begin{aligned}
\hat{R}_{sq} &= \frac{a_{0q}}{b_{0q}} \\
\hat{R}_{rq} &= \frac{a_{1q}}{b_{1q}} - \hat{R}_{sq} \\
\hat{L}_{mq} &= \frac{\sqrt{\hat{R}_{rq}\left(b_{1q}^2\hat{R}_{rq} - b_{0q}\right)}}{b_{0q}} \\
\hat{L}_{sq} &= \hat{L}_{rq} = \hat{R}_{rq}\frac{b_{1q}}{b_{0q}}
\end{aligned} \tag{34}$$

$$\begin{aligned}
\hat{R}_{sd} &= \frac{a_{0d}}{b_{0d}} \\
\hat{R}_{rd} &= \frac{a_{1d}}{b_{1d}} - \hat{R}_{sd} \\
\hat{L}_{md} &= \frac{\sqrt{\hat{R}_{rd}\left(b_{1d}^2\hat{R}_{rd} - b_{0d}\right)}}{b_{0d}} \\
\hat{L}_{sd} &= \hat{L}_{rd} = \hat{R}_{rd}\frac{b_{1d}}{b_{0d}}
\end{aligned} \tag{35}$$

4. Results and discussions

The RLS parameter identification algorithm presented in this chapter is implemented in a DSP based platform using TMS320F2812 DSP and a three-leg voltage source inverter. Figure 3 shows the diagram of the system to obtain the experimental results. The machine used for the validation of this methodology is a SPIM of a commercial hermetic refrigeration compressor of an air conditioning. The SPIM was removed from the hermetic compressor to achieve classical tests. The machine is two-pole, 220 V type. In the implementation of RLS identification parameter algorithm, the DC bus was limited in 177V/5A, and the sampling time of $400\mu s$ was used.

As described in Sections 2 and 3, the experiment for the parameter identification is achieved with a standstill rotor. In the first step, a square wave with variable frequency and reduced voltage supplies the main winding, while the auxiliary winding is opened. The stator current in the main winding is measured using hall effect sensor. The voltage used in this algorithm is estimated by the product of modulation and DC bus indexes. After the identification for the main winding, the same procedure is repeated for the auxiliary winding. The square wave is used for better excitation of the plant.

The frequency of the supply voltage is 5 Hz in the estimation of resistances to minimize the skin effect, and it is 30 Hz for the estimation of inductances.

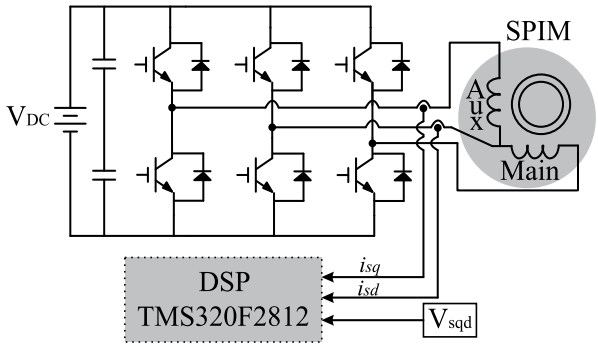

Figure 3. System diagram for the experimental results.

The first test for the identification of stator and rotor resistances is achieved in the main winding. The convergence of coefficients θ_q for this winding is presented in Fig. 4. Fig. 4 (a) presents the coefficients a_{1q} and a_{0q}, while Fig. 4 (b) gives the coefficients b_{1q} and b_{0q}. In this experiment the frequency of the supply voltage is selected on 5 Hz. As presented in figures, the coefficient convergence is fast and it is excited by the reset of the covariance matrix (**P**). Here, the reset of the covariance matrix (**P**) is used to avoid that this matrix reach zero and consequently loses the ability of to update the parameter matrix ($\theta_q(k)$). Some oscillations are introduced every time that the covariance matrix (**P**) is reset, but the convergence of coefficients $\theta_q(k)$ is stable around a region.

The aim of the algorithm (13)-(17) is to identify a set of parameters that produce a good dynamic response such as real dynamic response of the induction machine. If it is necessary to ensure the parameter convergence to the true values the Lemma 12.5.2 (Persistent Excitation) of [16] must be satisfied. However, in practical implementations the designer normally unknown the exactly parameter values due the assumptions and approximations made to develop the mathematical model of the plant, and due the presence of unmodulated dynamics in the system, such as the measurement and drive systems.

The coefficients used in the electrical parameter calculation are the final values of Fig 4. The coefficient convergence for d axis has behavior similar to coefficient convergence for q axis in Fig. 4.

Table 1 shows the final obtained coefficients a_{1q}, a_{0q}, b_{1q}, and b_{0q} in a q axis when the voltage frequency is 5 Hz and 30 Hz. Table 2 shows the final obtained coefficients a_{1d}, a_{0d}, b_{1d}, and b_{0d} in a d axis when the voltage frequency is 5 Hz and 30 Hz. From Fig. 4 it can be observed that the coefficient convergence is fast.

	5 Hz	30 Hz
a_{1q}	244.27	707.64
a_{0q}	447.96	8084.14
b_{1q}	24.82	27.73
b_{0q}	128.58	2913.7

Table 1. Final convergence for coefficients of the main winding.

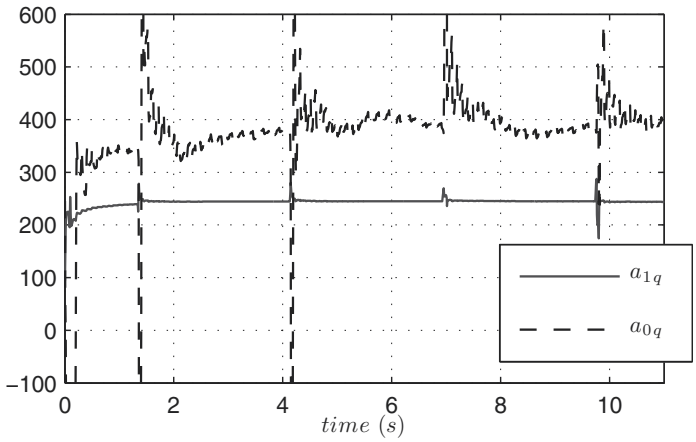

(a)

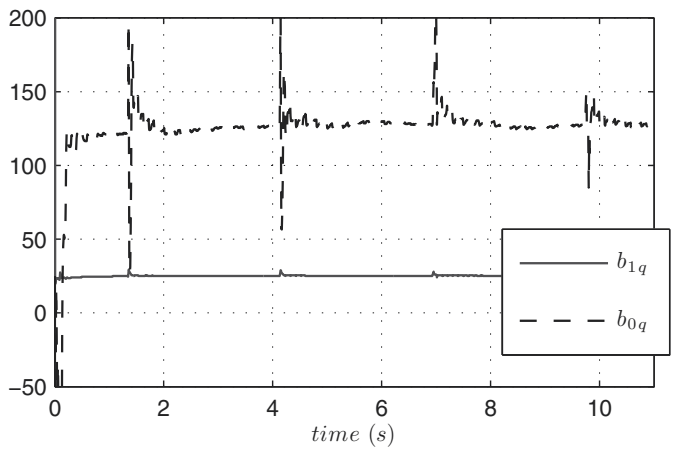

(b)

Figure 4. Coefficients convergence.

	5 Hz	30 Hz
a_{1d}	246.15	779.65
a_{0d}	559.4	3304.5
b_{1d}	9.83	17.62
b_{0d}	43.67	2448.17

Table 2. Final convergence for coefficients of the auxiliary winding.

The electrical parameters of the induction machine are obtained combining the final value of coefficients in Table 1 and Table 2 with the equations (34) and (35), respectively. Table 3 presents the identified electrical parameters of SPIM. In this study we also make a comparison with the results obtained by classical methods, thus, the SPIM identified by RLS algorithm is

also tested using no-load and standstill classical methods. The electrical parameters estimated when the SPIM is tested by classical methods are shown in Table 4.

	R_{sq}	R_{rq}	L_{mq}	$L_{sq} = L_{rq}$
Identified	3.62Ω	6.27Ω	0.2186H	0.2376H
	R_{sd}	R_{rd}	L_{md}	$L_{sd} = L_{rd}$
Identified	12.79Ω	12.23Ω	0.2849H	0.3142H

Table 3. Experimental identified electrical parameters by RLS algorithm.

	R_{sq}	R_{rq}	L_{mq}	$L_{sq} = L_{rq}$
Estimated	3.95Ω	5.1506Ω	0.2149H	0.2292H
	R_{sd}	R_{rd}	L_{md}	$L_{sd} = L_{rd}$
Estimated	11.95Ω	8.6463Ω	0.382H	0.401H

Table 4. Electrical parameters estimated by classical tests.

Aiming the model validation, two experiments are carried out. In the first experiment, the SPIM is driven by a *v/f* strategy at no-load operation, thus, the main and the auxiliary windings are supplied by controlled voltages varying the frequency from zero until a steady-state condition. The rotor speed and the stator currents are also measured. These measurements are recorded for posterior comparison with simulated values.

The model of single-phase induction machine presented in equations (7)-(10) is simulated using the estimated parameters of the machine by RLS algorithm given in Table 3. The model is also simulated using the parameters estimated by the classical methods presented in Table 4. The simulated stator currents are compared with the measured stator currents. The induction motor model equations (7)-(10) are discretized using the Euler Method in the same frequency of the experimental commutation for this test at 5 kHz. The recorded rotor speed is used in the simulated model to make it independent of the mechanical parameters.

In the first experimental result, the frequency of stator voltages varies from zero until 25 Hz and it is fixed in 25 Hz, by the *v/f* method. The recorded voltage values are used to supply the SPIM model in the simulation. Thus, from the same input voltages, Fig. 5 shows currents simulated and measured for the main winding in the first experiment. Fig. 5 (a) presents the comparison between the simulation of i_{sq} current with parameters estimated by RLS algorithm, and the experimental measurement of i_{sq} current, and Fig 5 (b) presents the comparison of the i_{sq} current when the simulations is carried out with parameters estimated by classical tests.

Fig. 6 presents a detail of the comparison between the measured and the simulated currents in steady-state condition for the main winding. In Fig. 6 (a) the comparison between experimental current and simulated current is presented when the SPIM parameters are estimated by RLS algorithm, while Fig. 6 (b) presents the comparison between experimental current and simulated current when the SPIM parameters are estimated by classical tests.

Fig. 7 presents a comparison among i_{sd} currents on the first experiment. Fig. 7 (a) shows the simulated current using parameters estimated by RLS algorithm in the SPIM model and the

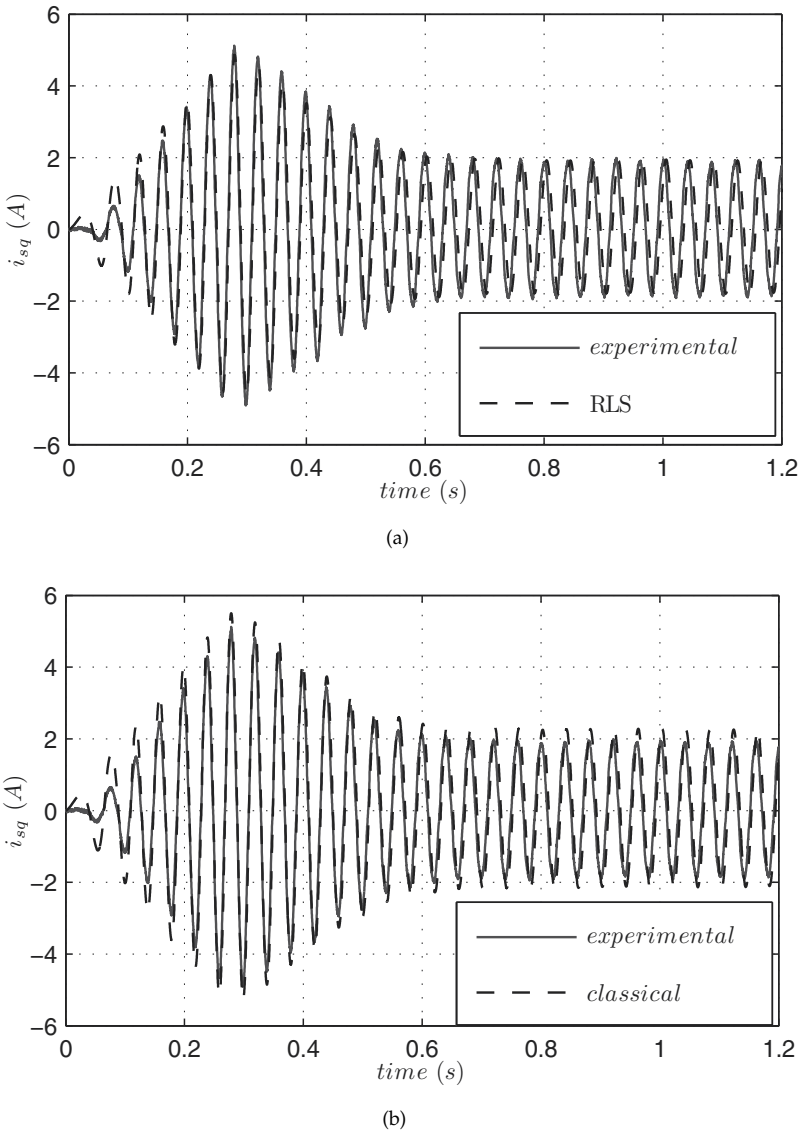

Figure 5. Comparison among measured and simulated currents for the first test. (a) Simulated i_{sq} using parameters estimated with RLS algorithm and measured i_{sq} current. (b) Simulated i_{sq} current using parameters estimated by classical tests and measured i_{sq} current.

measured i_{sd} current. Fig. 7 (b) gives the simulated current using parameters estimated by classical tests and the measured current.

Fig. 8 shows the comparison between i_{sd} currents in steady-state condition, Fig. 8 (a) gives the comparison between the measured i_{sd} current and the simulated i_{sd} current using SPIM parameters estimated by the RLS algorithm, whereas, Fig. 8 (b) presents the comparison

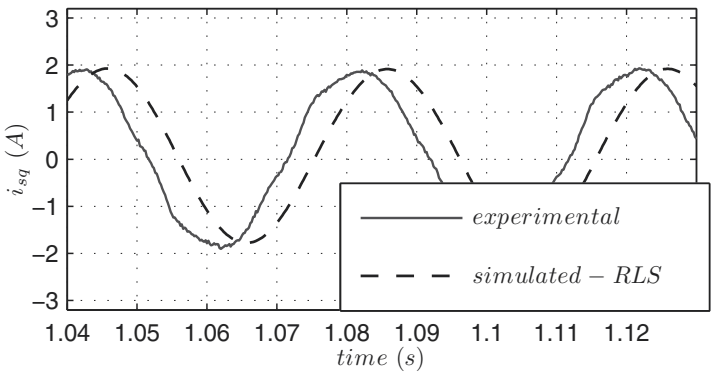

(a)

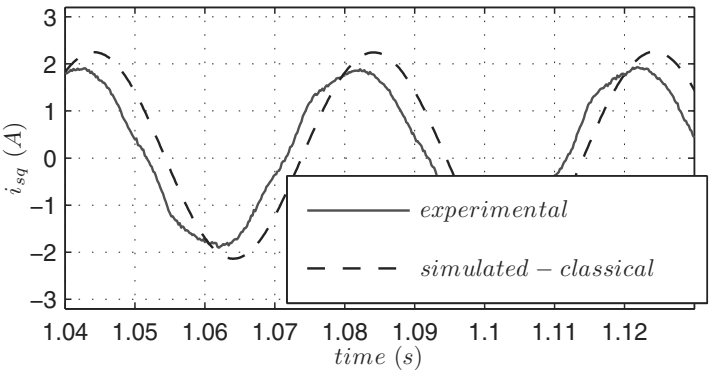

(b)

Figure 6. Comparison between measured and simulated currents at 25 Hz. (a) Simulated (RLS - Parameters) and measured i_{sq} currents. (b) Simulated (Classical - Parameters) and measured i_{sq} currents.

between the measured i_{sd} current and the simulated i_{sd} current using classical method for parameter estimation.

From Figures 5-8 it is possible to observer the good matching between the simulated and experimental currents for the q and d axes. In addition, some small discrepancies are found in these figures due the parameter inaccuracies and unmodulated effects (for instance the measurement and drive systems).

The advantage of the methodology presented in this chapter employing the RLS algorithm is that some types of applications, such as hermetic compressor, it is impossible carried out classical tests for estimation of the electrical parameters of the SPIM. In addition, the methodology has simplicity in implementation.

In the second experiment, the frequency of the supplied voltages of SPIM varies from zero until 30 Hz, and it is fixed at 30 Hz. As in the previous test, this is a no-load test and the SPIM is driven by a *v/f* strategy. The stator currents and rotor speed are measured and recorded.

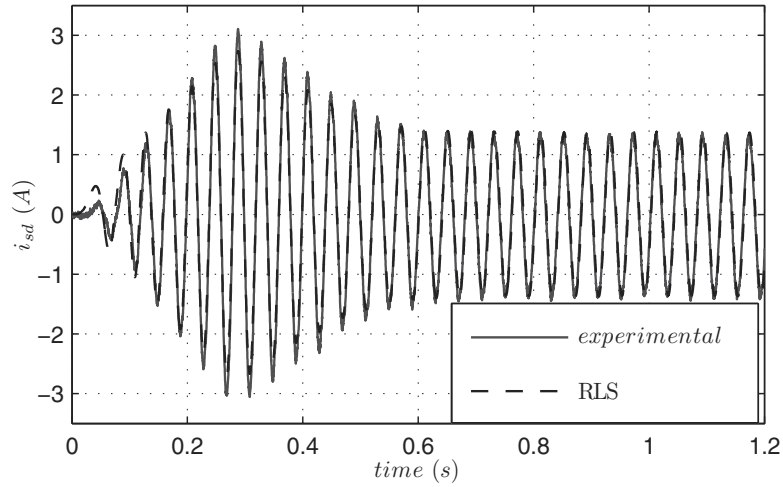

(a)

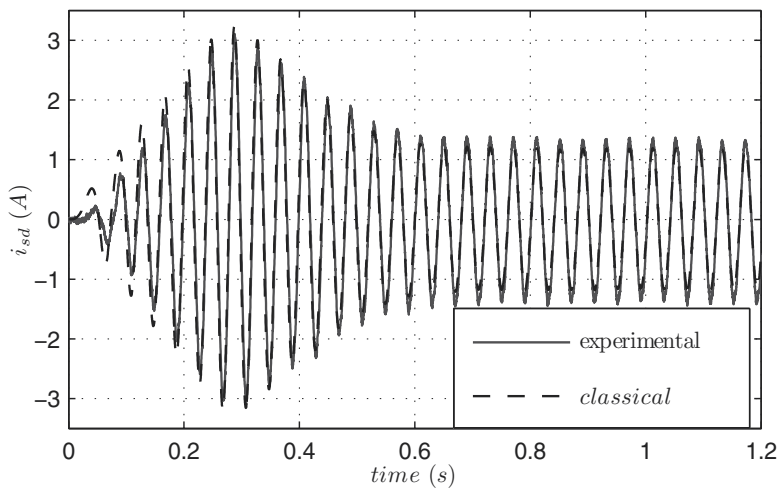

(b)

Figure 7. Comparison among i_{sd} currents in first test. (a) Simulated i_{sd} current by RLS parameter estimation and measured i_{sd} current. (b) Simulated i_{sd} current by classical tests and measured i_{sd} current.

Fig. 9 presents a comparison between measured and simulated i_{sq} currents in steady-stead condition. In Fig. 9 (a) shows the measured i_{sq} current and the simulated i_{sq} current using parameters estimated by RLS algorithm on the SPIM model, while Fig. 9 (b) gives the measured i_{sq} and the simulated i_{sq} current using parameters estimated by classical tests.

Fig. 10 presents a comparison between i_{sd} currents in steady-state condition for the second test.

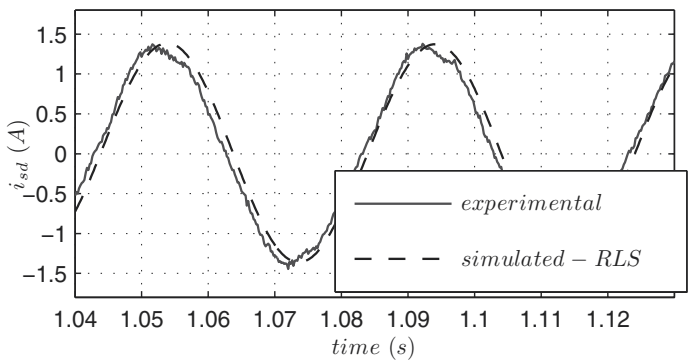

(a)

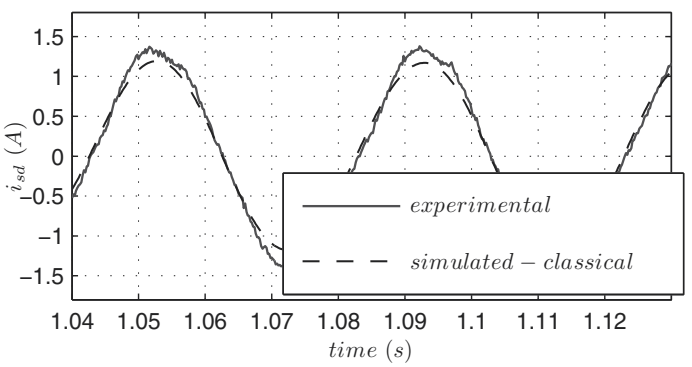

(b)

Figure 8. Comparison between i_{sd} currents at 25 Hz. (a) Simulated (RLS - parameter) and measured i_{sd} currents. (b) Simulated (classical tests) and measured i_{sd} currents.

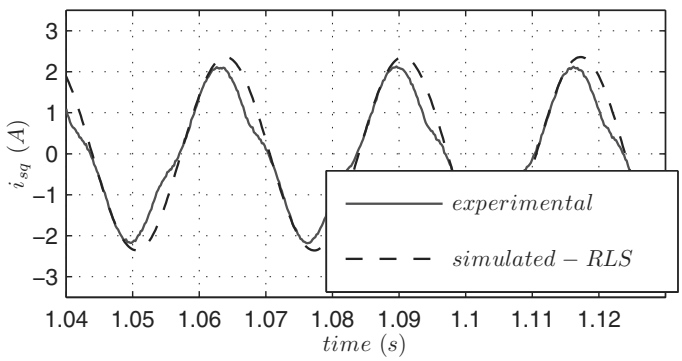

(a)

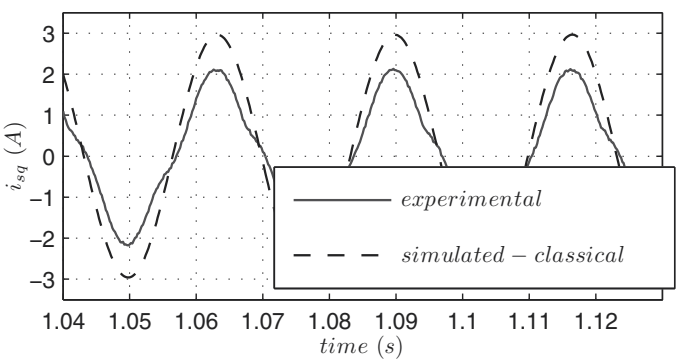

(b)

Figure 9. Comparison between i_{sq} currents at 30 Hz in steady-state condition. (a) Simulated (RLS - parameter) and measured i_{sq} currents. (b) Simulated (classical tests) and measured i_{sq} currents.

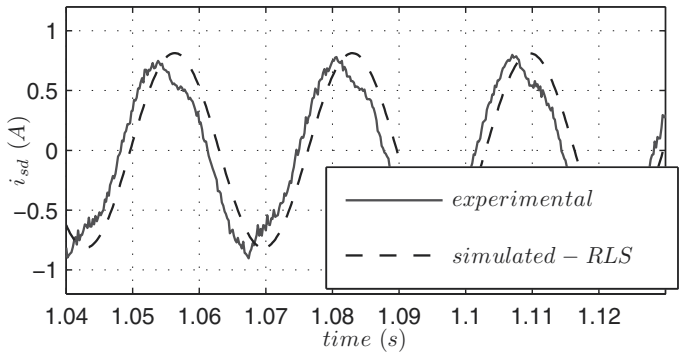

(a)

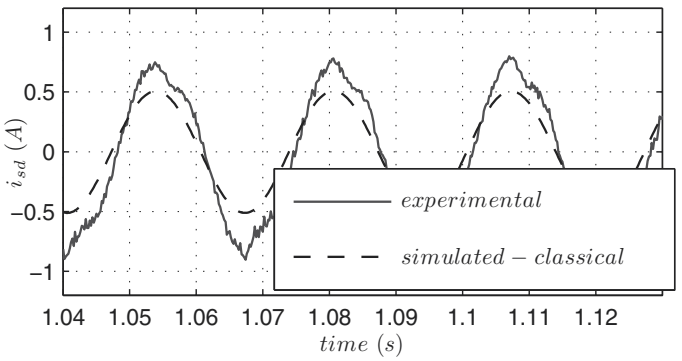

(b)

Figure 10. Comparison between i_{sd} currents at 30 Hz. (a) Simulated (RLS - parameter) and measured i_{sd} currents. (b) Simulated (classical tests) and measured i_{sd} currents.

5. Conclusion

A methodology for single-phase induction machine parameter identification was presented and discussed in this chapter. The machine tested was a SPIM used in a hermetic compressor of air conditioning. Using the proposed methodology it is possible to obtain all electrical parameters of SPIM for simulation and design of high performance vector control and sensorless SPIM drives. The main contribution of this study is the development of an automatized procedure for the identification of all electrical parameters of SPIM, such as the SPIM used in hermetic conditioning compressor. Experimental results demonstrate the effectiveness of the method. Some experimental comparisons among measurements and simulations using parameters estimated by classical tests and simulations using parameters obtained by RLS algorithm are presented. From Table 3 and Table 4 it is possible to observe that the parameters obtained with RLS algorithm converge to different values compared to classical tests. However, the results in Fig. 5 - 10 show that the parameters estimated with RLS algorithm present equivalent dynamical behavior compared with parameters estimated by classical methods. The methodology proposed in this chapter can be extended to be applied in other SPIM drives and three-phase induction motor drives.

Author details

Rodrigo Padilha Vieira
Federal University of Pampa - UNIPAMPA, Federal University of Santa Maria - UFSM, Power Electronics and Control Research Group - GEPOC, Brazil

Rodrigo Zelir Azzolin
Federal University of Rio Grande - FURG, Federal University of Santa Maria - UFSM, Power Electronics and Control Research Group - GEPOC, Brazil

Cristiane Cauduro Gastaldini
Federal University of Pampa - UNIPAMPA, Federal University of Santa Maria - UFSM, Power Electronics and Control Research Group - GEPOC, Brazil

Hilton Abílio Gründling
Federal University of Santa Maria - UFSM, Power Electronics and Control Research Group - GEPOC, Brazil

6. References

[1] Amin, A., El Korfally, M., Sayed, A. & Hegazy, O. [2009]. Efficiency optimization of two-asymmetrical-winding induction motor based on swarm intelligence, *IEEE Transactions on Energy Conversion* 24(1): 12 –20.

[2] Azzolin, R. Z., Gastaldini, C. C., Vieira, R. P. & Gründling, H. A. [2011]. *A RMRAC Parameter Identification Algorithm Applied to Induction Machines, Electric Machines and Drives, Miroslav Chomat (Ed.)*, InTech.

[3] Azzolin, R. Z. & Gründling, H. A. [2009]. A MRAC parameter identification algorithm for three-phase induction motors, *IEEE International Electric Machines and Drives Conference, IEMDC '09.*, pp. 273 –278.

[4] Blaabjerg, F., Lungeanu, F., Skaug, K. & Tonnes, M. [2004]. Two-phase induction motor drives, *IEEE Industry Applications Magazine* 10(4): 24–32.

[5] Bose, B. [2009]. Power electronics and motor drives recent progress and perspective, *IEEE Transactions on Industrial Electronics* 56(2): 581 –588.

[6] Câmara, H. T., Cardoso, R. C., Azzolin, R. Z., Pinheiro, H. & Gründling, H. A. [2006]. Low-cost sensorless induction motor speed control, *IEEE 32nd Annual Conference on Industrial Electronics, IECON 2006*, pp. 1200 –1205.

[7] de Rossiter Corrêa, M., Jacobina, C., Lima, A. & da Silva, E. [2000]. Rotor-flux-oriented control of a single-phase induction motor drive, *IEEE Transactions on Industrial Electronics* 47(4): 832–841.

[8] Donlon, J., Achhammer, J., Iwamoto, H. & Iwasaki, M. [2002]. Power modules for appliance motor control, *IEEE Industry Applications Magazine* 8(4): 26–34.

[9] Finch, J. & Giaouris, D. [2008]. Controlled AC electrical drives, *IEEE Transactions on Industrial Electronics* 55(2): 481 –491.

[10] Holtz, J. [2005]. Sensorless control of induction machines: With or without signal injection?, *IEEE Transactions on Industrial Electronics* 53(1): 7 – 30.

[11] Hrabovcova, V., Kalamen, L., Sekerak, P. & Rafajdus, P. [2010]. Determination of single phase induction motor parameters, *International Symposium on Power Electronics Electrical Drives Automation and Motion (SPEEDAM)*, pp. 287 –292.

[12] Jemli, M., Ben Azza, H., Boussak, M. & Gossa, M. [2009]. Sensorless indirect stator field orientation speed control for single-phase induction motor drive, *IEEE Transactions on Power Electronics* 24(6): 1618–1627.

[13] Koubaa, Y. [2004]. Recursive identification of induction motor parameter, *Simulation Modelling Practice and Theory* 12(5): 368–381.
[14] Krause, P. C., Wasynczuk, O. & Sudhoff, S. D. [2002]. *Analysis of Electric Machinery and Drive Systems*, 2 edn, Wiley-IEEE Press.
[15] Lascu, C., Boldea, I. & Blaabjerg, F. [2005]. Comparative study of adaptive and inherently sensorless observers for variable-speed induction-motor drives, *IEEE Transactions on Industrial Electronics* 53(1): 57 – 65.
[16] Middleton, R. H. & Goodwin, G. C. [1990]. *Digital Control and Estimation - A Unified Approach*, 1 edn, Prentice Hall.
[17] Myers, M., Bodson, M. & Khan, F. [2011]. Determination of the parameters of non-symmetric induction machines, *Annual IEEE Applied Power Electronics Conference and Exposition (APEC)*, pp. 1028 –1033.
[18] Nied, A., de Oliveira, J., de Farias Campos, R., Jr., S. I. S. & de Souza Marques, L. C. [2011]. *Space Vector PWM-DTC Strategy for Single-Phase Induction Motor Control, Electric Machines and Drives, Miroslav Chomat (Ed.)*, InTech.
[19] Orlowska-Kowalska, T. & Dybkowski, M. [2010]. Stator-current-based mras estimator for a wide range speed-sensorless induction-motor drive, *IEEE Transactions on Industrial Electronics* 57(4): 1296 –1308.
[20] Rao, S., Buss, M. & Utkin, V. [2009]. Simultaneous state and parameter estimation in induction motors using first- and second-order sliding modes, *IEEE Transactions on Industrial Electronics* 56(9): 3369 –3376.
[21] Ribeiro, L. A. S., Jacobina, C. B. & Lima, A. M. N. [1995]. Dynamic estimation of the induction machine parameters and speed, *26th Annual IEEE Power Electronics Specialists Conference, PESC '95.* 2: 1281–1287 vol.2.
[22] Toliyat, H., Levi, E. & Raina, M. [2003]. A review of RFO induction motor parameter estimation techniques, *IEEE transactions on Energy conversion* 18(2): 271–283.
[23] Utkin, V. [1993]. Sliding mode control design principles and applications to electric drives, *IEEE Transactions on Industrial Electronics* 40(1): 23 –36.
[24] Vaez-Zadeh, S. & Reicy, S. [2005]. Sensorless vector control of single-phase induction motor drives, *Proceedings of the Eighth International Conference on Electrical Machines and Systems, 2005. ICEMS 2005* 3: 1838–1842 Vol. 3.
[25] van der Merwe, C. & van der Merwe, F. [1995]. A study of methods to measure the parameters of single-phase induction motors, *IEEE Transactions on Energy Conversion* 10(2): 248 –253.
[26] Vas, P. [1998]. *Sensorless Vector and Direct Torque Control*, Oxford Univ. Press.
[27] Velez-Reyes, M., Minami, K. & Verghese, G. [1989]. Recursive speed and parameter estimation for induction machines, *Conference Record of the Industry Applications Society Annual Meeting, 1989.* pp. 607–611 vol.1.
[28] Vieira, R. P., Azzolin, R. Z., Gastaldini, C. C. & Gründling, H. [2010]. Electrical parameters identification of hermetic refrigeration compressors with single-phase induction machines using RLS algorithm, *International Conference on Electrical Machines, 2010. ICEM 2010.*
[29] Vieira, R. P., Azzolin, R. Z. & Gründling, H. A. [2009]. A sensorless single-phase induction motor drive with a MRAC controller, *35st Annual Conference of IEEE Industrial Electronics Society, 2009.*, pp. 1003 –1008.
[30] Vieira, R. P., Azzolin, R. Z. & Gründling, H. A. [2009]. Parameter identification of a single-phase induction motor using RLS algorithm, *Brazilian Power Electronics Conference, 2009. COBEP '09.*, pp. 517 –523.
[31] Zahedi, B. & Vaez-Zadeh, S. [2009]. Efficiency optimization control of single-phase induction motor drives, *IEEE Transactions on Power Electronics* 24(4): 1062 –1070.

Control and Diagnosis

Chapter 12

Advanced Control Techniques for Induction Motors

Manuel A. Duarte-Mermoud and Juan C. Travieso-Torres

Additional information is available at the end of the chapter

http://dx.doi.org/10.5772/50237

1. Introduction

The design of suitable control algorithms for induction motors (IM) has been widely investigated for more than two decades. Since the beginning of field oriented control (FOC) of AC drives, seen as a viable replacement of the traditional DC drives, several techniques from linear control theory have been used in the different control loops of the FOC scheme, such as Proportional Integral (PI) regulators, and exact feedback linearization (Bose, 1997, 2002; Vas, 1998). Due to their linear characteristics, these techniques do not guarantee suitable machine operation for the whole operation range, and do not consider the parameter variations of the motor-load set.

Several nonlinear control techniques have also been proposed to overcome the problems mentioned above, such as sliding mode techniques (Williams & Green, 1991; Al-Nimma & Williams, 1980; Araujo & Freitas, 2000) and artificial intelligence techniques using fuzzy logic, neuronal networks or a combination of them (Vas, 1999; Al-Nimma & Williams, 1980; Bose, 2002). All these techniques are based on complex control strategies differing of the advanced control techniques described here.

In this chapter we present a collection of advanced control strategies for induction motors, developed by the authors during the last ten years, which overcome some of the disadvantages of the previously mentioned control techniques. The techniques studied and presented in this chapter are based on equivalent passivity by adaptive feedback, passivity by interconnection and damping assignment (IDA-PCB) and fractional order proportional-integral controller (FOPIC) in the standard field oriented control scheme (FOC).

All of the control strategies described here guarantee high performance control, such as high starting torque at low speed and during the transient period, accuracy in steady state, a wide range of speed control, and good response under speed and load changes. For all of

the control strategies developed throughout the chapter, after a brief theoretical description of each one of them, simulation as well as experimental results of their application to control IM are presented and discussed.

The main contribution of this Chapter is to show that IM control techniques based on passivity, IDA-PCB and FOPIC can be successfully used in a FOC scheme, presenting some advantages over the classical techniques.

2. Adaptive passivity based control for the IM

Four novel adaptive passivity based control (APBC) techniques were first developed by the main author and his collaborators. As explained in Sections 2.1 and 2.2, these are the adaptive approach of feedback passive equivalence controllers, which were developed for SISO (Castro-Linares & Duarte-Mermoud, 1998; Duarte-Mermoud et al, 2001) and MIMO systems (Duarte-Mermoud et al 2003; Duarte-Mermoud et al, 2002), including controllers with fixed adaptive gains (CFAG) as well as controllers with time-varying adaptive gains (CTVAG). The nonlinear model characteristics were considered in the controller design and they are adaptive in nature, guaranteeing robustness under all model parameter variations.

These techniques were developed for systems parameterized in the so called normal form with explicit linear parametric dependence, which are also locally weakly minimum phase. It can be verified that the IM can be expressed in that particular form and therefore these strategies can be readily applied to them.

Based on the APBC control techniques developed for SISO systems, previously presented, two novel control strategies for induction motors were proposed in Travieso-Torres & Duarte-Mermoud (2008) as described in Section 2.3. Besides, a MIMO version, based on the MIMO techniques already mentioned, was applied to the IM in Duarte-Mermoud & Travieso-Torres (2003) and described here in Section 2.4. Results from SISO and MIMO controllers are similar, however the SISO controllers present only two adjustable parameters by means of simple adaptive laws, being simpler than the solution for the MIMO case, since the MIMO controllers have a larger number of adjustable parameters.

These controllers are applied to the IM considering the scheme presented in Figure 1. In both cases, SISO and MIMO controllers were suitably simplified using the Principle of Torque-Flux Control (PTFC) proposed in Travieso (2002). This principle is applicable to strategies working under a FOC scheme. Based on the PTFC, the design of the SISO and MIMO controllers do not require flux estimations.

For the SISO and the MIMO approaches, the proposed CFAG is simpler, but better transient behaviour was obtained when CTVAG was used. The results were compared with the classical basic control scheme (BCS) shown in Figure 2 (Chee-Mun, 1998), concluding that the proposed adaptive controllers showed a better transient behaviour. In addition, CFAG and CTVAG do not need the knowledge of the set motor–load parameters and robustness under variations of such parameters is guaranteed.

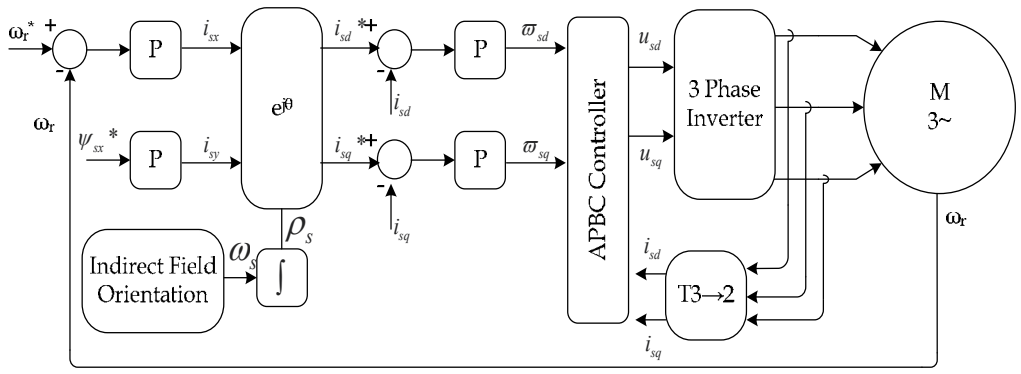

Figure 1. Proposed control scheme with field oriented block (APBC)

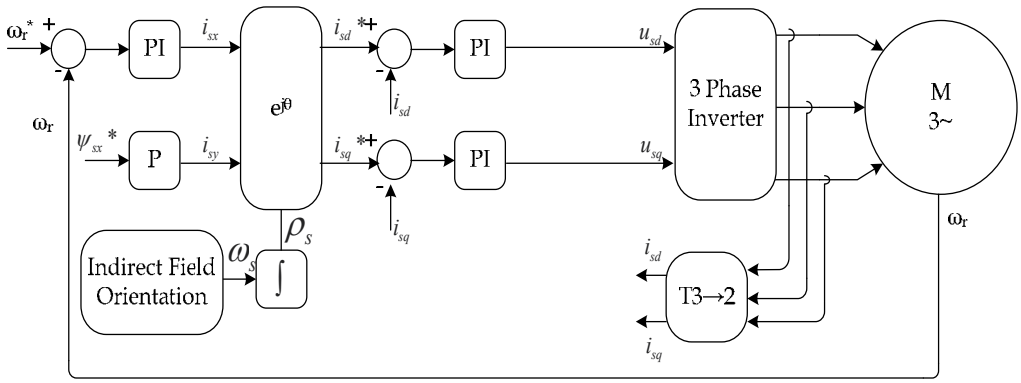

Figure 2. Basic control scheme with field oriented block (BCS)

2.1. SISO Adaptive Passivity Based Control (ABPC) theory

The SISO APBC approach was proposed in Castro-Linares & Duarte-Mermoud (1998) and Duarte-Mermoud et al (2001), for systems parameterized in the following normal form (Byrnes et al, 1991), with explicit linear parametric dependence

$$\begin{aligned} \dot{y} &= \Lambda_a^T A(y,z) + \Lambda_b B(y,z) u \\ \dot{z} &= \Lambda_0 f_o(z) + \Lambda_p P(y,z) y \end{aligned} \tag{1}$$

with $z \in \Re^n$, $y \in \Re$, $u \in \Re$, $A(y, z) \in \Re^m$, $B(y, z) \in \Re$, $f_0 \in \Re^n$, $P(y, z) \in \Re^n$; and the parameters $\Lambda_a \in \Re^m$, $\Lambda_b \in \Re$, $\Lambda_0 \in \Re^{nxn}$, $\Lambda_p \in \Re^{nxn}$. The function $\dot{z} = \Lambda_0 f_0(z)$ is known as zero dynamics (Isidori, 1995; Nijmiejer & Van der Shaft, 1996). Besides, it is necessary to check that the system is locally weakly minimum phase by finding a positive definite differentiable function $W_0(z)$ satisfying $\left(\partial W_0(z)/\partial z\right)^T \Lambda_0 f_0(z) \le 0, \forall \Lambda_0$ (Byrnes et al, 1991). According to the theory presented in the original papers, for locally weakly minimum phase systems of the form (1) with matrix $B(y,z)$ being invertible, there exist two adaptive controllers guaranteeing stability described in the following section.

2.1.1. SISO controller with fixed gains

A SISO controller with fixed adaptive gains (CFAG) was proposed in Castro-Linares & Duarte-Mermoud (1998) for SISO systems of the form (1). This controller has the following form

$$u(y,z,\theta_h)=\frac{1}{B}\left[\theta_1^T(t)A(y,z)-\theta_2(t)P(y,z)\frac{\partial W_0(z)}{\partial z}+\theta_3(t)\varpi\right] \tag{2}$$

with $z \in \Re^2$, $y \in \Re$, $u \in \Re$, $A(y, z) \in \Re$, $B(y, z) \in \Re$, $f_0 \in \Re^2$, $P(y, z) \in \Re^2$ and the adjustable parameters $\theta_1(t) \in \Re^p$ and $\theta_2(t), \theta_4(t) \in \Re$ updated with the adaptive laws

$$\begin{aligned}\dot{\theta}_1(t)&=-sign(\Lambda_b)A(y,z)y\\ \dot{\theta}_2(t)&=-sign(\Lambda_b)yP(y,z)\left(\frac{\partial W_0(z)}{\partial z}\right)\\ \dot{\theta}_3(t)&=-sign(\Lambda_b)y\varpi\end{aligned} \tag{3}$$

that applied to system (1) make it locally feedback equivalent to a C²-passive system from the new input ϖ to the output y. The parameters $\Lambda_a \in \Re$, $\Lambda_b \in \Re$, $\Lambda_0 \in \Re$, $\Lambda_p \in \Re^{2x2}$ represent constant but unknown parameters from a bounded compact set Ω.

2.1.2. SISO controller with time-varying gains

Another adaptive controller approach but with time-varying gains (Duarte-Mermoud et al, 2001) was also proposed for a SISO system of the form (1). This controller has the same control law shown in (2), but updated with the following adaptive laws

$$\begin{aligned}\dot{\theta}_1(t)&=-sign(\Lambda_b)\left(\gamma_1^{-1}(t)\Big/\sqrt{1+\frac{1}{\gamma(t)^T\gamma(t)}}\right)A(y,z)y\\ \dot{\theta}_2(t)&=-sign(\Lambda_b)\left(\gamma_2^{-1}(t)\Big/\sqrt{1+\frac{1}{\gamma(t)^T\gamma(t)}}\right)P(y,z)\left(\frac{\partial W_0(z)}{\partial z}\right)y\\ \dot{\theta}_3(t)&=-sign(\Lambda_b)\left(\gamma_3^{-1}(t)\Big/\sqrt{1+\frac{1}{\gamma(t)^T\gamma(t)}}\right)\varpi y\end{aligned} \tag{4}$$

where $\gamma_1(t) \in \Re^{4\times4}$ and $\gamma_2(t), \gamma_3(t), \gamma_4(t) \in \Re$ are time-varying adaptive gains defined by

$$\begin{aligned}\dot{\gamma}_1(t)&=-\left[\gamma_1 A(y,z)A^T(y,z)\gamma_1\right],\\ \dot{\gamma}_2(t)&=\left[\gamma_2(t)P(y,z)\left(\frac{\partial W_0(z)}{\partial z}\right)\right]^2, \qquad \gamma(t)=\left[Trace\{\gamma_1(t)\}\quad \gamma_2(t)\quad \gamma_3(t)\right]\in\Re^3\\ \dot{\gamma}_3(t)&=\left[\gamma_3(t)\varpi\right]^2.\end{aligned} \tag{5}$$

2.2. MIMO Adaptive Passivity Based Control (ABPC) theory

The MIMO APBC approach was proposed in Duarte-Mermoud et al (2002) and Duarte-Mermoud et al (2003), for systems parameterized in the following normal form (Byrne et al, 1991), with explicit linear parametric dependence

$$\begin{aligned} \dot{y} &= \Lambda_a A(y,z) + \Lambda_b B(y,z)u \\ \dot{z} &= \Lambda_0 f_0(z) + P^T(y,z)\Lambda_p y \end{aligned} \tag{6}$$

with $z \in \Re^2$, $y \in \Re^2$, $u \in \Re^2$, $A(y,z) \in \Re^8$, $B(y,z) \in \Re^{2x2}$, $f_0 \in \Re^2$, $P(y,z) \in \Re^{2x2}$. The parameters $\Lambda_a \in \Re^{2x8}$, $\Lambda_b \in \Re^{2x2}$, $\Lambda_0 \in \Re^{2x2}$ and $\Lambda_p \in \Re^{2x2}$ represent constant but unknown parameters from a bounded compact set Ω. The term $\dot{z} = \Lambda_0 f_0(z)$ is the so called zero dynamics (Isidori, 1995; Nijmiejer & Van der Shaft, 1996). In this case it is also necessary to check that system (6) is locally weakly minimum phase by finding a positive definite differentiable function $W_0(z)$ satisfying $\left(\partial W_0(z)/\partial z\right)^T \Lambda_0 f_0(z) \le 0, \forall \Lambda_0$ (Byrnes et al, 1991). According to the theory presented in the original papers, for locally weakly minimum phase systems of the form (11) with matrix $B(y,z)$ being invertible, there exist two type of adaptive controllers guaranteeing stability which are described in the following section.

2.2.1. MIMO controller with fixed gains

According to Duarte-Mermoud et al (2002) there exists an adaptive controller of the form

$$u(t) = \left[\theta_1(t)A(y,z) - \theta_2(t)P(y,z)\frac{\partial W_0(z)}{\partial z} + \theta_3(t)\varpi(t) \right] \tag{7}$$

with the adaptive laws

$$\begin{aligned} \dot{\theta}_1(t) &= -yA^T(y,z) \\ \dot{\theta}_2(t) &= -y\left(\frac{\partial W_0(z)}{\partial z}\right)^T P^T(y,z) \\ \dot{\theta}_3(t) &= -y\varpi^T(t) \end{aligned} \tag{8}$$

that applied to system (6) make it locally feedback equivalent to a C^2-passive system from the input $\varpi(t)$ to the output $y(t)$. The parameters $\theta_1(t) \in \Re^{2x8}$, $\theta_2(t) \in \Re^{2x2}$ and $\theta_3(t) \in \Re^{2x2}$ represent adjustable controller parameters whose ideal values are $\theta^*_1 = -\Lambda_b^{-1}\Lambda_a \in \Re^{2x8}$, $\theta^*_2 = -\Lambda_b^{-1}\Lambda_p^T \in \Re^{2x2}$ and $\theta^*_3 = \Lambda_b^{-1} \in \Re^{2x2}$.

2.2.2. MIMO controller with time-varying gains

On the other hand, CTVAG was proposed in Duarte-Mermoud et al (2003). This controller has the same form (7), but with adaptive laws given by

$$\dot{\theta}_1(t) = -yA^T(y,z)\frac{\Gamma_1^{-1}}{\sqrt{1+Trace\left(\Gamma_1^{-2}+\Gamma_2^{-2}+\Gamma_3^{-2}\right)}}$$
$$\dot{\theta}_2(t) = -\frac{\Gamma_2^{-1}}{\sqrt{1+Trace\left(\Gamma_1^{-2}+\Gamma_2^{-2}+\Gamma_3^{-2}\right)}}y\left(\frac{\partial W_0(z)}{\partial z_1}\right)^T P^T(y,z) \tag{9}$$
$$\dot{\theta}_3(t) = -\frac{\Gamma_3^{-1}}{\sqrt{1+Trace\left(\Gamma_1^{-2}+\Gamma_2^{-2}+\Gamma_3^{-2}\right)}}y\varpi^T(t)$$

and time-varying adaptive gains defined by

$$\dot{\Gamma}_1 = -\Gamma_1 A(y,z)A^T(y,z)\Gamma_1, \qquad \Gamma_1(t_0) > 0$$
$$\dot{\Gamma}_2 = -\Gamma_2 P(y,z)\left(\frac{\partial W_0(z)}{\partial z}\right)\left(\frac{\partial W_0(z)}{\partial z}\right)^T P^T(y,z)\Gamma_2, \qquad \Gamma_2(t_0) > 0 \tag{10}$$
$$\dot{\Gamma}_3 = -\Gamma_3\varpi(t)\varpi^T(t)\Gamma_3, \qquad \Gamma_3(t_0) > 0$$

According to Duarte-Mermoud et al (2002), this controller applied to system (6) will convert it to an equivalent C²-passive system from the input $\varpi(t)$ to the output $y(t)$. The parameters $\theta_1(t) \in \Re^{2x8}$, $\theta_2(t) \in \Re^{2x2}$ and $\theta_3(t) \in \Re^{2x2}$ represent adjustable controller parameters whose ideal values are $\theta^*_1 = -\Lambda_b^{-1}\Lambda_a \in \Re^{2x8}$, $\theta^*_2 = -\Lambda_b^{-1}\Lambda_p{}^T \in \Re^{2x2}$ and $\theta^*_3 = \Lambda_b^{-1} \in \Re^{2x2}$

2.3. SISO ABPC applied to the IM

In this Section the design of SISO CFAG and SISO CTVAG for IM is explained, based on the SISO theories previously described.

2.3.1. SISO IM modeling

In order to apply the controllers described in Section 2.1 the IM model was expressed as SISO subsystems parameterized in the following locally weakly minimum phase normal form with explicit linear parametric dependence. For Subsystem 1 we have

$$\Lambda_{a1} = \left[-\frac{R'_s}{\sigma L_s} \quad 1 \quad \frac{L_m R_r}{\sigma L_s L_r^2} \quad \frac{L_m}{\sigma L_s L_r}\right]^T, \quad A_1(y_i,z) = \begin{bmatrix} e_{i_{sx}} \\ \omega_g e_{i_{sy}} \\ e_{\psi_{rx}} \\ \omega_r e_{\psi_{ry}} \end{bmatrix}, \quad \Lambda_{b1} = \frac{1}{\sigma L_s}, \quad B_1(y_i,z) = 1,$$
$$\Lambda_{p1} = \begin{bmatrix} \frac{L_m}{T_r} & 0 \\ 0 & \frac{L_m}{T_r} \end{bmatrix}, \quad y_1 = e_{i_{sx}}, \quad P_1(y_i,z) = \begin{bmatrix} P_{11} \\ P_{21} \end{bmatrix} = \begin{bmatrix} 1 \\ \frac{\dot{e}_{i_{sy}}}{\dot{e}_{i_{sx}}} \end{bmatrix}, \quad u_1 = e_{u_{sx}}. \tag{11}$$

For Subsystem 2 we can write

$$\Lambda_{a2}=\left[-\frac{R'_s}{\sigma L_s}\quad -1\quad \frac{L_m R_r}{\sigma L_s L_r^2}\quad -\frac{L_m}{\sigma L_s L_r}\right]^T,\quad A_2(y_i,z)=\begin{bmatrix} e_{i_{sy}} \\ \omega_g e_{i_{sx}} \\ e_{\psi_{ry}} \\ \omega_r e_{\psi_{rx}} \end{bmatrix},\quad \Lambda_{b2}=\frac{1}{\sigma L_s},\quad B_2(y_i,z)=1,$$
$$\Lambda_{p2}=\begin{bmatrix} \frac{L_m}{T_r} & 0 \\ 0 & \frac{L_m}{T_r} \end{bmatrix},\quad y_2=e_{i_{sy}},\quad P_2(y_i,z)=\begin{bmatrix} P_{12} \\ P_{22} \end{bmatrix}=\begin{bmatrix} \frac{\dot{e}_{i_{sx}}}{\dot{e}_{i_{sy}}} \\ 1 \end{bmatrix},\quad u_2=e_{u_{sy}}. \tag{12}$$

2.3.2. Principle of torque – Flux control

The PTFC, proposed in Travieso (2002), states that in controlling the torque and flux for IM, the controllers design can be focused only to control the stator currents. This is true for the case when a scheme with coordinate transformation block $e^{j\rho_g}$ (Field Oriented Scheme), to transform from a stationary to a rotating coordinate system, is considered. Therefore, it is pointless to make efforts to directly control rotor flux or rotor current components. It is proven in Travieso (2002) that the controller still guarantees suitable control of the torque and flux and making it possible to discard all the terms concerning the rotor current or rotor flux components in its design.

2.3.3. SISO CFAG applied to the IM

In Travieso-Torres & Duarte-Mermoud (2008) a simplified controller for IM was proposed based on the theories from Castro-Linares & Duarte-Mermoud (1998). After applying the PTFC and considering the controller directly feeding the IM in the stator coordinate system, this means that ωg = 0, this SISO controller has the following form

$$\left.\begin{aligned} u_i(y_i,z,\theta_{hi}) &= \theta_{1i}y_i+\theta_{4i}\varpi_i \\ \dot{\theta}_{1i} &= -y_i^2 \\ \dot{\theta}_{4i} &= -y_i\varpi_i \end{aligned}\right\}\quad \begin{aligned} i &= 1,2 \\ h &= 1,4 \end{aligned} \tag{13}$$

2.3.4. SISO CTVAG applied to the IM

Another adaptive controller but with time-varying gains was also proposed in Travieso-Torres & Duarte-Mermoud (2008), based on the results of Duarte-Mermoud & Castro-Linares (2001). This controller, after applying the PTFC and considering the controller directly feeding the motor in the stator coordinate system, has the following form

$$\left.\begin{aligned} u_i(y_i,z,\theta_{hi}) &= \theta_{1i}y_i + \theta_{4i}\varpi_i \\ \dot{\theta}_{1i} &= -sign(\Lambda_{bi}^*)\left(\gamma_1^{-1}\Big/\sqrt{1+\frac{1}{\gamma_i^T\gamma_i}}\right)y_i^2, \\ \dot{\theta}_{4i} &= -sign(\Lambda_{bi}^*)\left(\gamma_4^{-1}\Big/\sqrt{1+\frac{1}{\gamma_i^T\gamma_i}}\right)\varpi_i y_i, \end{aligned}\right\} \text{with} \quad \begin{aligned} \dot{\gamma}_{1i} &= -\left(\gamma_{1i}y_i\right)^2 \\ \dot{\gamma}_{4i} &= -\left(\gamma_{4i}\varpi_i\right)^2 \end{aligned} \quad \text{and} \quad \begin{aligned} i &= 1,2 \\ h &= 1,4 \end{aligned} \tag{14}$$

2.4. MIMO ABPC applied to the IM

In this Section the design of the MIMO CFAG and the MIMO CTVAG for the IM are presented, based on the MIMO theories previously stated.

2.4.1. MIMO model of the IM

In order to apply controllers from Duarte-Mermoud et al (2002) and Duarte-Mermoud et al (2003), the IM model was expressed in form (6) as follows

$$\dot{y} = \begin{bmatrix} -\frac{R'_s}{\sigma L_s} & 0 & 0 & 1 & \frac{L_m R_r}{\sigma L_s L_r^2} & 0 & 0 & -\frac{L_m}{\sigma L_s L_r} \\ 0 & -\frac{R'_s}{\sigma L_s} & -1 & 0 & 0 & \frac{L_m R_r}{\sigma L_s L_r^2} & \frac{L_m}{\sigma L_s L_r} & 0 \end{bmatrix} \begin{bmatrix} e_{i_{sx}} \\ e_{i_{sy}} \\ \omega_g e_{i_{sx}} \\ \omega_g e_{i_{sy}} \\ e_{\psi_{rx}} \\ e_{\psi_{ry}} \\ \omega_r e_{\psi_{rx}} \\ \omega_r e_{\psi_{ry}} \end{bmatrix} + \begin{bmatrix} \frac{1}{\sigma L_s} & 0 \\ 0 & \frac{1}{\sigma L_s} \end{bmatrix} I_2 u,$$

$$\dot{z} = \begin{bmatrix} -\frac{R_r}{L_r} & \left(\omega_g - \omega_r\right) \\ -\left(\omega_g - \omega_r\right) & -\frac{R_r}{L_r} \end{bmatrix} \begin{bmatrix} e_{\psi_{rx}} \\ e_{\psi_{ry}} \end{bmatrix} + I_2 \begin{bmatrix} \frac{L_m}{T_r} & 0 \\ 0 & \frac{L_m}{T_r} \end{bmatrix} y, \tag{15}$$

$$\text{with} \quad z = \begin{bmatrix} e_{\psi_{rx}} \\ e_{\psi_{ry}} \end{bmatrix}, \quad y = \begin{bmatrix} e_{i_{sx}} \\ e_{i_{sy}} \end{bmatrix}, \quad u = \begin{bmatrix} e_{u_{sx}} \\ e_{u_{sy}} \end{bmatrix}$$

with $T_r = L_r/R_r$

2.4.2 MIMO CFAG applied to the IM

According to Duarte-Mermoud and Travieso-Torres (2003) there exist an adaptive controller of the form

$$
\begin{aligned}
u(t) &= \theta_1(t) y^T + \theta_3(t)\varpi(t) \\
\dot{\theta}_1(t) &= -yy^T \\
\dot{\theta}_3(t) &= -y\varpi^T(t)
\end{aligned}
\tag{16}
$$

that applied to system (6) makes it locally feedback equivalent to a C^2-passive system from the input $\varpi(t)$ to the output $y(t)$. The parameters $\theta_1(t) \in \Re^{2x8}$, $\theta_2(t) \in \Re^{2x2}$ and $\theta_3(t) \in \Re^{2x2}$ represent adjustable controller parameters whose ideal values are $\theta^*_1 = -\Lambda_b^{-1}\Lambda_a \in \Re^{2x8}$, $\theta^*_2 = -\Lambda_b^{-1}\Lambda_p^T \in \Re^{2x2}$ and $\theta^*_3 = \Lambda_b^{-1} \in \Re^{2x2}$.

2.4.3. MIMO CTVAG applied to the IM

Finally a CTVAG was proposed in Duarte-Mermoud and Travieso-Torres (2003). This controller has the following form

$$
\begin{aligned}
&u(t) = \theta_1(t) y + \theta_3(t)\varpi(t) \\
&\dot{\theta}_1(t) = -\left(\Gamma_1^{-1} / \sqrt{1 + Trace\left(\Gamma_1^{-2} + \Gamma_3^{-2}\right)}\right) yy^T, \qquad \dot{\Gamma}_1 = -\Gamma_1 yy^T \Gamma_1, \qquad \Gamma_1(t_0) > 0 \\
&\dot{\theta}_3(t) = -\left(\Gamma_3^{-1} / \sqrt{1 + Trace\left(\Gamma_1^{-2} + \Gamma_3^{-2}\right)}\right) y\varpi^T(t), \qquad \dot{\Gamma}_3 = -\Gamma_3 \varpi(t)\varpi^T(t)\Gamma_3, \qquad \Gamma_3(t_0) > 0
\end{aligned}
\tag{17}
$$

This controller will convert system (6) to an equivalent C^2-passive system from the input $\varpi(t)$ to the output $y(t)$. The parameters $\theta_1(t) \in \Re^{2x8}$ and $\theta_3(t) \in \Re^{2x2}$ represent adjustable controller parameters whose ideal values are $\theta^*_1 = -\Lambda_b^{-1}\Lambda_a \in \Re^{2x8}$ and $\theta^*_3 = \Lambda_b^{-1} \in \Re^{2x2}$.

2.5. Simulation results of APBC for the IM

In order to verify the advantages of the proposed controllers a comparison with a traditional current regulated PWM induction motor drive from Chee-Mun (1998) with PI loop controllers (see Figure 2), was carried out. In the simulations a squirrel-cage induction motor whose nominal parameters are: 15 [kW] (20 [HP), 220 [V], fp= 0.853, 4 poles, 60 [Hz], R_s = 0.1062 [Ω], X_{ls}=X_{lr} = 0.2145 [Ω], x_m = 5.8339 [Ω], R_r = 0.0764 [Ω], J = 2.8 [kg m^2] and B_p = 0 were considered (Chee-Mun, 1998). All the simulations were made using the software package SIMULINK/MATLAB with ODE 15s (stiff/NDF) integration method and a variable step size.

The obtained control schemes only need the exact values or the estimates of parameters Xm and T_r for the field orientation block. No other parameters or state estimations are used. The PI speed controller is tuned as P=30 and I= 10 according to Chee-Mun (1998).

Figure 3 shows the information used to compare both control schemes. The variations of the reference speed ω^*_r (Figure 3(a)), the variations in load torque (Figure 3(b)), the variation of about 30% in the stator and rotor resistance (Figure 3(c) and Figure 3(d)), the linear increase up to double the load inertia during the motor operation (Figure 3(e)) and the variations in the viscous friction coefficient (Figure 3(f)). For both proposed control strategies (CFAG and

CTVAG) and the classical FOC control (BCS), five comparative tests considering the variations shown in Figure 3 were carried out.

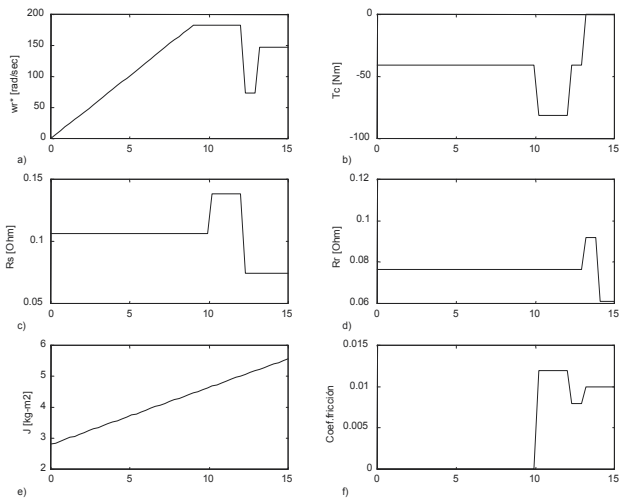

Figure 3. Parameter and reference variations used in the set of comparative tests

These tests allow us to study the behavior of the schemes under the situations described next.

- ***Test 1:*** The reference of speed is increased as a ramp from 0 to 190 [RPM] in 0.5 [s] and the load torque is fixed at the nominal value 69.5 [Nm].
- ***Test 2:*** Variations on load torque, as indicated in Figure 3(b).
- ***Test 3:***Variations on speed reference, as shown in Figure 3(a).
- ***Test 4:*** Variation of the motor resistances, as shown in Figures 3(c) and 3(d).
- ***Test 5:*** Variation of the load parameters, as indicated in Figures 2(e) and 2(f).
- ***Test 6:*** Changes in the controller parameters (P and I) of the control loops.

In all the simulation results of the proposed controllers shown in Figure 4 through 9, the initial conditions of all the controller parameters and adaptive gains were set equal to zero, that is to say, $\theta_{ik}(0) = \gamma_{ih}(0) = 0$, for *i=1,2* y *h=1,4*.

Figure 4 shows the comparative results obtained for the proposed controllers under normal conditions (i.e. according to Test 1), without considering variations of any type. APBC controllers present better transient behavior than traditional PI controllers. CFAG presents a quite accurate stationary state (with a velocity error less than 0.5 %). And CTVAG is equally accurate as the CFAG, but with better transient behavior.

Let us observe next in Figure 5, how the different schemes behave under variations of the load torque, as described in Figure 3(b). In the case of the CFAG shown, the error values are 0.5 % for a nominal load torque and of 0.22% for a half nominal load torque. The **CTVAG** presents a similar response to that of CFAG, but the transient response is slightly better. APBC controllers have better transient behavior than BCS.

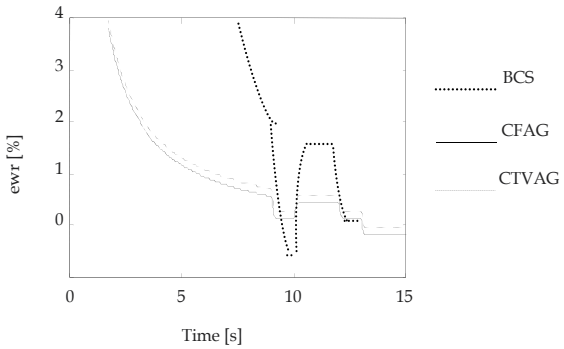

Figure 4. Results for the initial situation

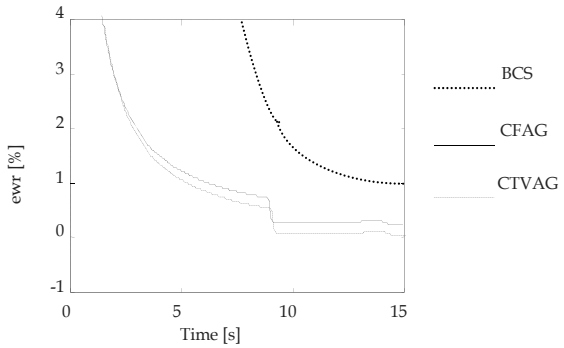

Figure 5. Results under load torque variations

In Figure 6, the effects of speed reference variations at nominal load torque, according to the variations indicated in Figure 3, are presented. The results for the proposed CFAG and CTVAG are similar rendering similar velocity errors whereas the rest of the variables present a suitable behavior. In these cases we have an error of about 0.5 % for nominal speed and of approximately 1.1 % at half the nominal speed.

When analyzing Test 4 (Figures 3(c) and 3(d)) both controllers present good behavior under changes on the stator resistance (see Figure 7). Nevertheless, under changes of the rotor resistance the field orientation is lost and the speed response is affected considerably. Notice how the flow of the machine diminishes considerably when the rotor resistance is decreased. We can also claim that the response in both cases (CFAG and CTVAG)is much more robust than the traditional PI controller of BCS. Both controllers present lesser speed errors in steady state than the classical PI scheme.

Considering now the variations of the load parameters according to Test 5 (Figures 3(e) and 3(f)), neither of the two controllers under study were affected, as is shown in Figure 8. For the proposed controllers, the differences found in the general behavior still remain. CFAG presents a similar error in the steady state than the CTVAG, but with slightly better transient behavior.

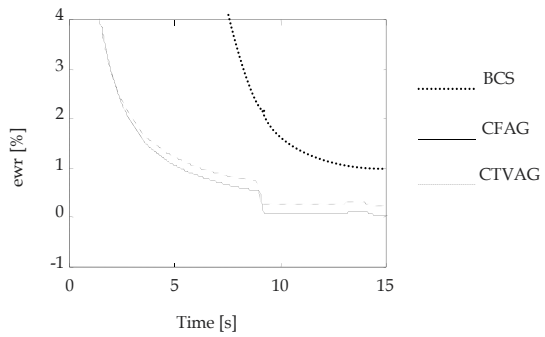

Figure 6. Results for speed reference variations

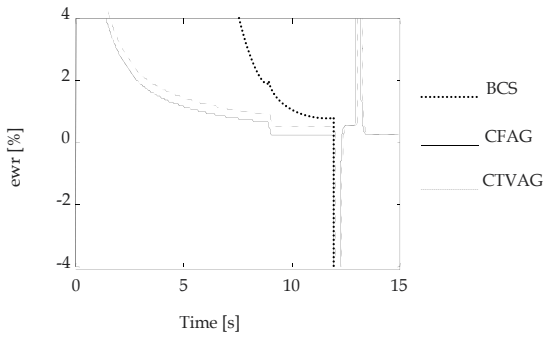

Figure 7. Results for Test 4.

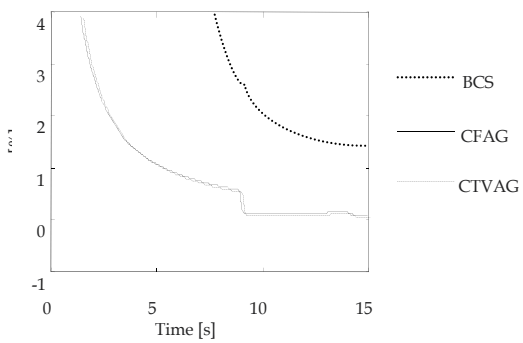

Figure 8. Results under for variations of load parameters

In Figure 9, the proportional gains of all control loops were changed. For CFAG and CTVAG, variations for the speed loop control parameter of 37.5 % were applied (P varies from 80 to 50). The flux loop was varied by 13 %, (P changes from 69 to 60). The current loops were varied by 33.3 % (P varies from 30 to 20). In Figure 9 it can be seen how in spite of these simultaneous gain variations, the speed error continues being less than 1% and the transient response after 0.5 sec. was practically not affected. CFAG as well as CTVAG guarantees good results for a wide range of variations of the proportional gains.

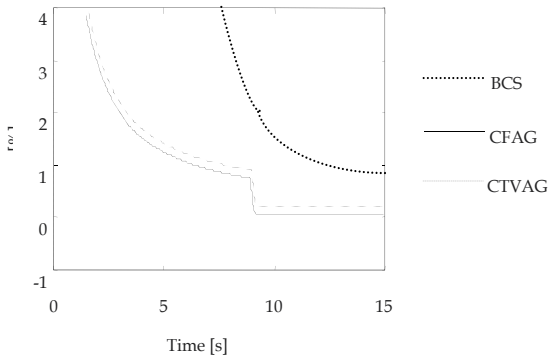

Figure 9. Results under changes in the tuning of the proportional gains

3. Control of IM using IDA-PCB techniques

In this section we will present a brief summary of the *Interconnection and Damping Assignment – Passivity-Based Control (IDA-PBC)* technique and the main ideas on which this method is based. This method provides a novel technique for computing the control necessary for modifying the storage function of a dynamical system assigning a new internal topology (in terms of interconnections and energy dissipation). Further details on the method can be found in Ortega et al. (2002) and Ortega & García-Canseco (2004). Next we will apply this technique to the control of an IM and compare it with BCS and APBC already described in Section 2.

3.1. Foundations of IDA-PCB control

Let us consider a system described in the form called Port-Controlled Hamiltonian (PCH) (Van der Shaft, 2000)

$$\Sigma_{PCH}: \begin{cases} \dot{x} = \left[J(x) - R(x) \right] \nabla H + g(x) u \\ y = g^T(x) \nabla H \end{cases} \tag{18}$$

where $x \in \Re^n$ is the state, and $u, y \in \Re$ are the input and the output of the system. H represents the system's total stored energy, $J(x)$ is a skew-symmetric matrix ($J(x) = -J^T(x)$) called *Interconnection Matrix* and $R(x)$ is a symmetric positive definite matrix ($R(x) = R(x)^T \geq 0$) called *Damping Matrix*. Let us assume (Ortega et al., 2002; Ortega & García-Canseco, 2004) that there exist matrices $g^{\perp}(x)$, $J_d(x) = -J_d^T(x)$, $R_d(x) = R_d^T(x) \geq 0$ and a function $H_d : \Re^n \to \Re$, such that

$$g^{\perp}(x)\left[J(x) - R(x) \right] \nabla H = g^{\perp}(x)\left[J_d(x) - R_d(x) \right] \nabla H_d \tag{19}$$

where $g^{\perp}(x)$ is the full-rank left annihilator of $g(x)$ ($g^{\perp}(x) g(x) = 0$) and $H_d(x)$ is such that $x^* = \arg\min_{x \in \Re^n} (H_d)$. Then, applying the control $\beta(x)$ defined as

$$\beta(x)=\left[g^T(x)g(x)\right]^{-1}g^T\left\{\left[J_d(x)-R_d(x)\right]\nabla H_d-\left[J(x)-R(x)\right]\nabla H\right\} \tag{20}$$

the overall system under control can be written as

$$\dot{x}=\left[J_d(x)-R_d(x)\right]\nabla H_d \tag{21}$$

where x^* is a locally Lyapunov stable equilibrium. That is to say applying control (20) to (18) the dynamic of the system is changed to that shown in (21). x^* is a locally Lyapunov asymptotically stable equilibrium if it is an isolated minimum of H_d and the largest invariant inside the set $\left\{x\in R^n\middle|\nabla H_d^T(x)R_d(x)\nabla H_d(x)\right\}$ is equal to $\{x^*\}$.

There are two ways to find control (20). The first one consists of fixing the topology of the system (by fixing J_d, R_d and $g^{\perp}$) and solving the differential equation (19). The second method consists of fixing H_d (the initial geometrical form of the desired energy) and then (19) becomes an algebraic system that has to be solved for J_d, R_d and $g^{\perp}$ (Ortega et al., 2002; Ortega & García-Canseco, 2004).

For the IDA-PBC scheme developed in Section 3.2, the model of the IM should be expressed in the PCH form previously stated, which has the general form shown in (18). In this study the load torque will be assumed proportional to rotor speed ($T_c=B\omega_r$) which typically represents fan load type. In this particular case the PCH model of the induction motor (see (22)), assuming also that the speed of the *x-y* reference system is synchronized to electrical frequency ($\omega_s=\omega_s$), has the form (González, 2005, González& Duarte-Mermoud, 2005; González et al., 2008)

$$\begin{aligned}
\dot{x}&=\begin{bmatrix}-R_s & 0 & 0 & 0 & 0\\ 0 & -R_r & 0 & 0 & -x_4\\ 0 & 0 & -R_s & 0 & 0\\ 0 & 0 & 0 & -R_r & x_2\\ 0 & x_4 & 0 & -x_2 & -B'\end{bmatrix}\nabla H+\begin{bmatrix}1 & 0 & x_3\\ 0 & 0 & x_4\\ 0 & 1 & -x_1\\ 0 & 0 & -x_2\\ 0 & 0 & 0\end{bmatrix}\begin{pmatrix}u_{sx}\\ u_{sy}\\ \omega_s\end{pmatrix},\\
y&=\begin{bmatrix}1 & 0 & 0 & 0 & 0\\ 0 & 0 & 1 & 0 & 0\\ x_3 & x_4 & -x_1 & -x_2 & 0\end{bmatrix}\nabla H=\begin{bmatrix}i_{sx}\\ i_{sy}\\ 0\end{bmatrix}\\
x&=\begin{bmatrix}\psi_{sx} & \psi_{rx} & \psi_{sy} & \psi_{ry} & J\omega_r\end{bmatrix}^T=\begin{bmatrix}x_{12}{}^T & x_{34}{}^T & x_5\end{bmatrix}^T,\\
H&=\frac{1}{2}x_{12}{}^TL^{-1}x_{12}+\frac{1}{2}x_{34}{}^TL^{-1}x_{34}+\frac{1}{2}J^{-1}x_5{}^2\\
u&=\begin{bmatrix}u_{sx} & u_{sy} & \omega_s\end{bmatrix}^T,\qquad y=\begin{bmatrix}i_{sx} & i_{sy} & 0\end{bmatrix}^T,\\
&with\qquad L=\begin{bmatrix}L_s & L_m\\ L_m & L_r\end{bmatrix}
\end{aligned} \tag{22}$$

where $\psi_{sx}, \psi_{sy}, \psi_{rx}, \psi_{ry}$ are the stator and rotor fluxes, respectively, and $B' = B_p + B$. In general, when using PCH representation, the obtained state variables are not necessarily the best choice for analysis and additional measurement/estimation may be needed in the controller implementation. Other types of load torque may also be considered in this analysis (e.g. constant, proportional to squared speed, etc.), in which case a slightly different PCH model will be obtained.

3.2. IDA-PBC strategy applied to the IM

The IDA-PBC strategy (Ortega et al., 2002; Ortega & García-Canseco, 2004) consists basically of assigning a new storage function to the closed-loop system, changing the topology of the system, in terms of interconnections and energy transfers between states. In the case of IM (González, 2005, González& Duarte-Mermoud, 2005; González et al., 2008), the controller is defined by some feasible solution for k_1, k_2 and k_3 of the following algebraic equation

$$L^{-1}x_{12} + \left(\begin{array}{c} k_1 \\ \dfrac{x_4}{x_2^{\,2} + x_4^{\,2}} k_3 \end{array} \right) = 0, \quad L^{-1}x_{34} + \left(\begin{array}{c} k_2 \\ \dfrac{x_4}{x_2^{\,2} + x_4^{\,2}} k_3 \end{array} \right) = 0, \quad J^{-1}x_5 + k_3 = 0 \tag{23}$$

From the third equation in (23), it is observed that an equilibrium point $x_5^* = \omega_r^*$ exists for ω_r defined as $\omega_r^* = -k_3$. For the other parameters (k_1, k_2) the solutions are given by the following relationship $(k_1^2 + k_2^2)L_m^{\,2} \geq 2k_3 L_r B$ (González, 2005; González et al., 2008).
With the previous results, according to (20), the IDA-PBC controller is defined as

$$\begin{aligned} u_{sx}(x) &= -R_s k_1 + \left(1 + \frac{R_r B'}{x_2^{\,2} + x_4^{\,2}}\right) x_3 k_3, \\ u_{sy}(x) &= -R_s k_2 - \left(1 + \frac{R_r B'}{x_2^{\,2} + x_4^{\,2}}\right) x_3 k_3, \\ \omega_s(x) &= -\left(1 + \frac{R_r B'}{x_2^{\,2} + x_4^{\,2}}\right) k_3 \end{aligned} \tag{24}$$

States x_2 and x_4 correspond to rotor flux expressed in orthogonal coordinates (ψ_{rx}, ψ_{ry}). The rotor flux will be zero if and only if the motor is at rest and without voltage applied. At t=0, some tension has to be applied to control the motor and therefore ψ_r becomes different from zero at t=0. Thus, no undetermined values of the controller are obtained.

The IDA-PBC scheme used in this paper was slightly modified. In principle, this strategy was developed to control the motor speed, not being robust with respect to load perturbations on the motor axis. This means that permanent errors in the mechanical speed were obtained. In order to solve this problem, a simple proportional integral loop was added for the speed error loop modifying the original IDA-PBC, scheme as is shown in Figure 10.

In general the rotor flux cannot be measured in the majority of IM's, which is why it was necessary to implement a rotor flux observer for the experimental implementation of this strategy. The observer was implemented based on the voltage-current model of the induction motor, developed in Marino et al (1994), Jansen et al (1995) and Martin (2005).

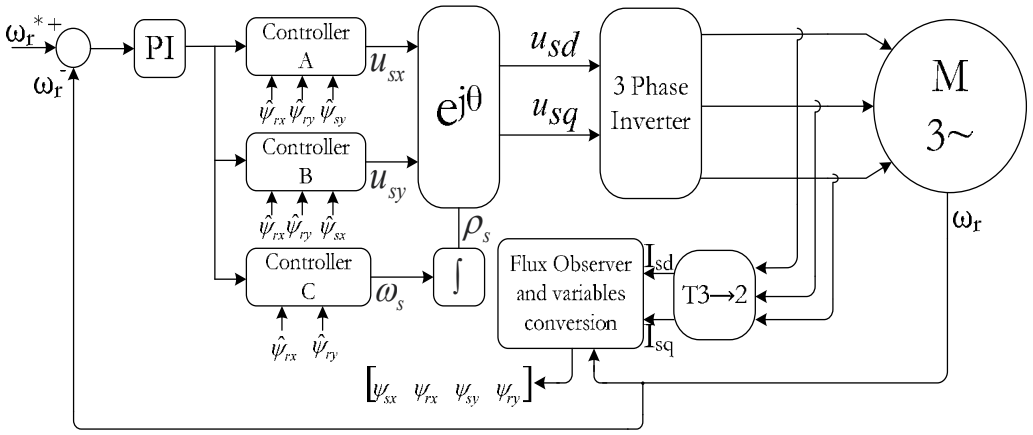

Figure 10. The IDA-PBC control scheme

3.3. Simulation results using IDA-PCB

In this section we present simulation results of applying the IDA-PBC technique for the speed control of an IM (Pelisssier, 2006; Pelisssier & Duarte-Mermoud, 2007). These results are compared with the basic control strategy (BCS) described in Figure 2 and with APBC strategies with fixed and time varying adaptive gains described in Section 2 (Figure 1). The results were obtained using Matlab/Simulink and the IM considered is that described in Chee-Mun (1998). The following two tests were performed on the simulated IM.

Test 1 (Regulation): Speed ramp from zero to nominal speed in 20 seconds with load torque proportional to speed, staring from zero. Then in t=25[s] a load torque of 50% magnitude of the nominal torque value is applied; in t=40[s] the magnitude of the load torque is increased to 100%; in t=60[s] the magnitude of the load torque is decreased to 50% and finally in t=120[s] the load torque is set to zero.

Test 2 (Tracking): Speed ramp from zero to nominal speed in 20 seconds with load torque proportional to speed, staring from zero. Between t=50[s] and 100[s] a pulse train of amplitude $0.1\omega_{r_{nom}}$ and frequency $2\pi/20$ is added to the constant speed reference. Between t=120[s] and 160[s] a sinusoidal speed reference of amplitude $0.1\omega_{r_{nom}}$ and frequency $2\pi/20$ is added to the constant nominal speed reference. The load torque is kept constant in 50% of the nominal torque during the whole test.

The PI controller parameters were first determined using the Ziegler-Nichols criteria and modified later by simulations, until a good response was obtained. For the APB scheme the controllers 'constants were chosen as follows: K_P=0.3 and K_I=0.1 for the external loop and

K_P=500*76.82 for the internal loop. For the IDA-PBC scheme, the values of the parameters were chosen so that equation (23) is satisfied. The values found were k_1=k_2=-7. For the external loop the values were chosen as K_p=K_i=0.5. The results were compared with the BCS described in Figure 2 and the APBC shown in Figure 1.

The simulations results obtained for Test 1 and Test 2 are shown in Figures 11 and 12.

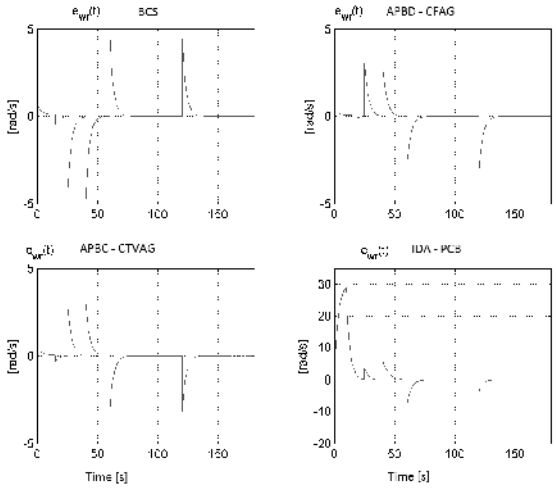

Figure 11. Simulation results for Test 1

The results obtained from Test 1 (Figure 11) show that the smaller errors are obtained by APBC strategies (CFAG and CTVAG) with a maximum error around 3 [rad/s]. This error is less than those obtained from the BCS and the IDA-PBC strategies which are around 5 and 30 [rad/s] respectively. However, the settling time of all four strategies is similar.

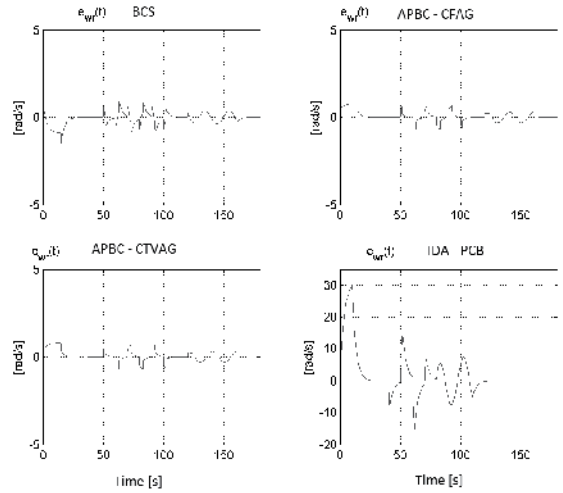

Figure 12. Simulation results for Test 2

From the results obtained for Test 2 (Figure12) a faster stabilization is obtained by the APBC strategies (CFAG and CTVAG), followed by the BCS strategy which was better than the IDA-PBC. The later is strongly dependant on the dynamics of the external loop introduced for controlling the mechanical torque.

3.4. Experimental results using IDA-PBC

In this section the experimental results obtained by applying APBC (CFAG and CTVAG) described in Figure 2 and IDA-PBC strategies described in Figure 10, are presented and compared with the BCS described in Figure 3. The experimental set up as well as the tests carried out for each strategy are described in what follows.

The three phase inverter used in the experiments was that designed and built by González (2005). Communication to PC was done though the software Matlab-Simulink using a customized S-Function. The IM used in the experiments was a Siemens 1LA7080, 0.55KW, cos(ϕ)=0.82, 220V, 2.5A, 4 poles and 1395RPM. From motor tests (no load and locked rotor) the estimated motor parameters used in the study the following: Rs=14.7Ω, Rr=5.5184Ω, Xs=11.5655Ω, Xr=11.5655Ω and Xm=115.3113Ω.

In order to apply resistive torque on motor axis, the induction motor was mechanically coupled to a continuous current generator, Briggs & Stratton ETEK, having a permanent magnet field. The load to the generator was applied using a cage of discrete resistances connected to generator stator and manually controlled by switches. The magnitudes of the resistances were chosen such that maximum values of induction motor operation were not exceeded under any circumstances. The experimental assembly including the motor-generator group used in the experimental tests is shown in Figures 13 (a) and (b).

Test 1 (Basic Behavior): The speed reference was a ramp starting from zero at t=0 to the nominal speed (146.08 rad/s) in 9s. The load torque was kept constant and equal to the nominal value (100%) during the whole test. Initial conditions (IC) for controller parameters were all set to zero, except for the time-varying gains which were chosen as $\Gamma_1(0) = \Gamma_3(0) = I$, where I is the 2x2 identity matrix.

Test 2 (Tracking): A ramp speed referenced was considered, starting from rest at zero and reaching the nominal speed (146.08 [rad/s]) in 9[s]. Between t=40[s] and t=70[s] a pulse train reference of amplitude $0.1\omega_{r_{nom}}$ and frequency $\pi/10$ [rad/s] was added on top of the constant nominal value. Between t=80[s] and t=110[s] a sinusoidal reference of amplitude $0.1\omega_{r_{nom}}$ and frequency $\pi/10$ was added on top of the constant nominal value. Additionally, the load torque (proportional to the speed) was kept at 50% of the nominal during the whole test. The IC of the controller parameters were all set to zero, except for time-varying gains initial values that were chosen as $\Gamma_1(0) = \Gamma_3(0) = I$, where I is the 2x2 identity matrix.

Test 3 (Regulation): The speed reference was a ramp starting from rest at zero reaching the nominal value(146.08 [rad/s]) in 9s, where the reference was kept constant. Initial load torque was equals to 0% of the nominal value. Between t=40[s] and t=80[s] a torque perturbation equal to 50% of the nominal value is added.

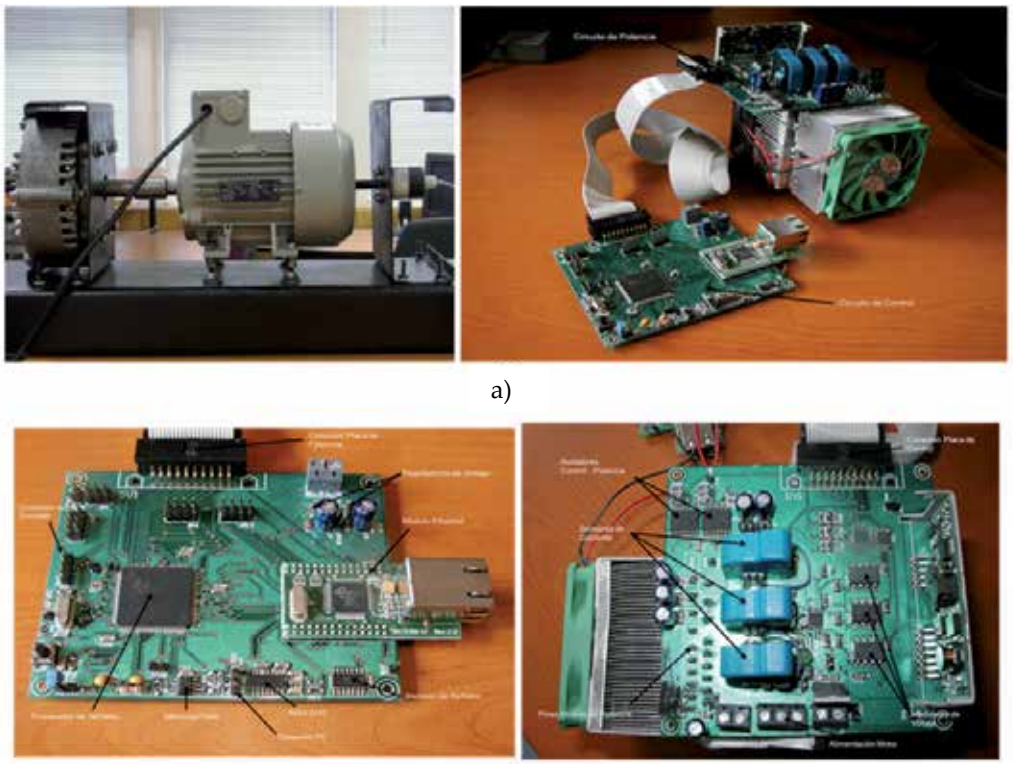

a)

(b)

Figure 13. (a). Experimental assembly. Motor-generator and inverter. (b). Experimental assembly. Control circuit and power circuit.

For the experimental tests, the best values of PI controller parameters for inner and outer loops were chosen based on those obtained from the simulation results of Section 3.2 (González, 2005; González& Duarte-Mermoud, 2005; Pelissier & Duarte-Mermoud, 2007). Later, these values were adjusted during the experiments performing a small number of trial tests. The final values chosen for the constants of control loops used in the BCS and in APBC scheme are as follows: K_P=0.403 and K_I=0.0189 for the outer loop and K_P=45 for the inner loop. For the IDA-PBC strategy, the values of constants k_1 and k_2 were determined based on simulations results reported in Pelissier & Duarte-Mermoud (2007). The chosen values were k_1=k_2=-30 and for the proportional integral loop it K_P=3 and K_I=0.5 were chosen.

For the experimental tests the control strategies were implemented in Matlab/Simulink, using a fixed step of 10[micro s] and the solver ODE5 (Dormand-Prince). In the electronics, a vector modulation with a carrier frequency of 20[kHz] was used. All IC were set to zero except time-varying gains initial values which were chosen as $\Gamma_1(0) = \Gamma_3(0) = I$, where I is the 2x2 identity matrix.

The experimental results obtained after applying the techniques under study for Test 1, Test 2 and Test 3 already described, are shown next. In Figures 14 through 16 the evolution of the speed errors are plotted for each strategy for each one of the tests.

In Figure 14 it is observed the following results: the fastest convergence of control error to zero, with a constant nominal load torque applied (Test 1), was achieved by the IDA-PBC strategy, with about 40[s]. Then 60[s] and 80[s] were obtained by BCS and APBC strategies, respectively. However, in the IDA-PBC strategy an important oscillatory behavior of the control error is observed at the beginning. For more information about the behavior of other variables see González (2005), Pelissier & Duarte-Mermoud (2007) and González et al (2008).

From the tracking viewpoint (Test 2), the best results were achieved for the APBC strategies, which follow reference changes better than the BCS (See Figure 15). The IDA-PBC strategy is not able to follow reference changes properly, presenting an oscillatory behavior of speed error. Convergence of the control error to zero for the IDA-PBC is influenced by rotor flux observer convergence, which necessarily adds a dynamic to the system affecting the global behavior of the overall system. For information about the evolution of other variables see González (2005), Pelissier & Duarte-Mermoud (2007) and González et al (2008).

When applying torque perturbations on the motor axis (Test 3), it is observed that fastest stabilization was attained by APBC strategies, without large oscillations (see Figure 16). The IDA-PBC strategy, although perturbations are quickly controlled, has an oscillatory control error. The BCS case is the slowest with a larger error in stationary state. This last strategy is not robust in the presence of perturbations on the mechanical subsystem. The evolution of other variables can be seen in (González, 2005; Pelissier & Duarte-Mermoud, 2007; González et al., 2008).

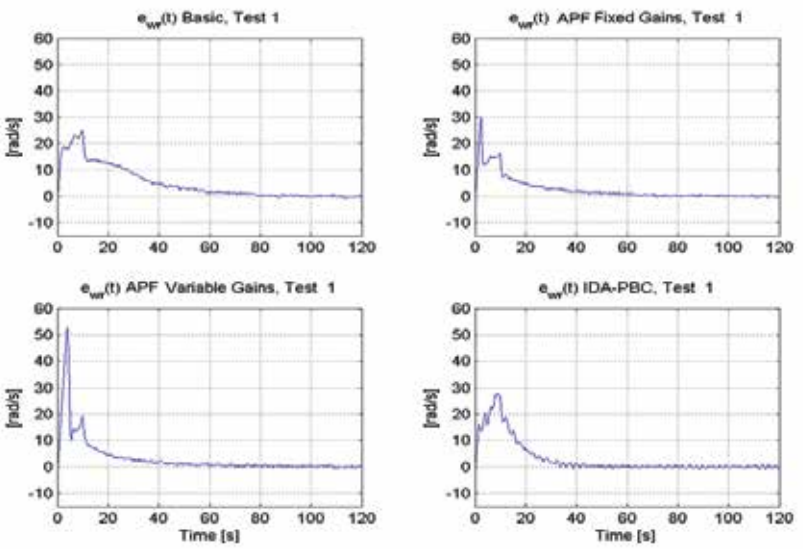

Figure 14. Speed errors for experimental Test 1 with constant load torque

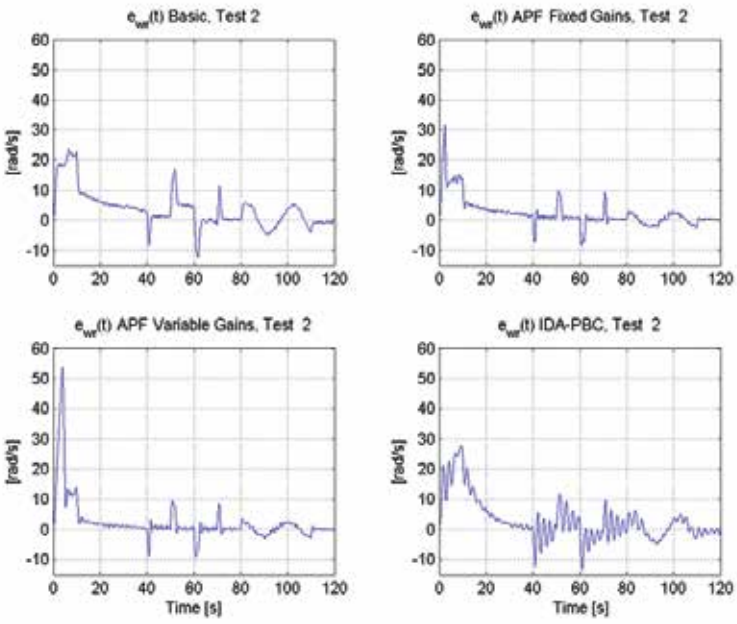

Figure 15. Speed errors for experimental Test 2 for reference tracking

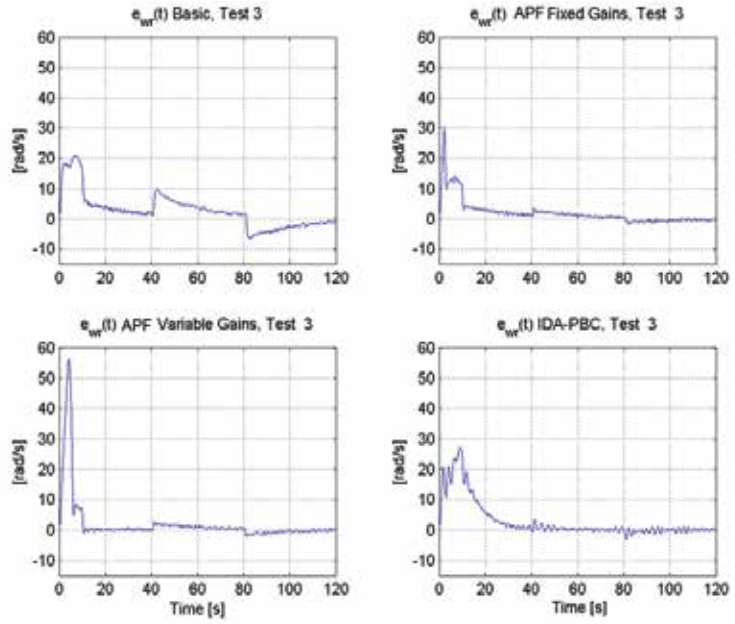

Figure 16. Speed errors for experimental Test 3 for load torque perturbations

Numerous other experiments and simulations, not shown here for the sake of space, were carried out to analyze the influence of several other parameters on the BCS, APBC and IDA-

PBC strategies (Travieso, 2002; Pelisssier, 2006). In particular the effects of initial conditions on APBC strategies, as well as the effects of using fixed and time-varying adaptive gains were analyzed. It was observed, in general, that time-varying gains improve transient behavior and diminish initial control error. In simulations, a small noise was added on these signals and the performance of the method were not affected significantly (González, 2005). At the experimental level, the influence of the normal noise present in the measurement of current signals during the test did not affect the behavior of the APBC. For higher noise levels some deterioration of the control system behavior was observed. In this case, more robust adaptive laws should be used. For instance the σθ-modification (Narendra & Annaswamy, 1989) could be used.

4. Induction motor speed control using fractional order PI controllers

In this section we present a field oriented control scheme like the one shown in Figure 2, where the PI controller used in the speed loop is changed to a PI controller in which the integral order is not unity (fractional integral effect). The main idea to explore is that fractional order integrals are of benefit in this kind of IM controllers.

4.1. Fractional order PI controllers

The FOPI controller is based on the same principles as the classical PI controller, with the difference that in this case the control action is calculated by means of fractional order integrals. The transfer function of a FOPI controller is given by

$$H_{FOPI}(s) = k_p + k_i / s^{\nu} \tag{25}$$

where ν denotes the integration order, k_p is the proportional constant and k_i is the integral constant. The detailed computation of fractional integrals is shown (Valério, 2005). Expression (8) allows computing fractional integrals $\nu < 0$ and fractional derivatives $\nu > 0$, corresponding to Caputo's definition (Oldham & Spanier, 1974; Kilbas et al., 2006; Sabatier et al., 2007).

$$\frac{d^{\nu}}{dx^{\nu}} = \begin{cases} \dfrac{1}{\Gamma(-\nu)} \displaystyle\int_{x_0}^{x} (x-t)^{-\nu-1} f(t)dt, & \nu < 0 \\ f(x), & \nu = 0 \\ \dfrac{1}{\Gamma(-\nu)} \displaystyle\int_{x_0}^{x} (x-t)^{-\nu-1} \left[D^m f(t) \right] dt, & \nu > 0 \end{cases} \tag{26}$$

In this equation x corresponds to the integration variable, Γ corresponds to Gamma function, m denotes the integer immediately greater than ν, and D denotes the integer derivative with respect to x. The Laplace Transform of fractional order derivatives and integrals (according to Caputo's definition) is shown in (9), where $F(s) = \mathcal{L}\{f(x)\}$.

$$L\left\{\frac{d^{\nu}}{dx^{\nu}}f(x)\right\}=\begin{cases} s^{\nu}F(s), & \nu \le 0 \\ s^{\nu}F(s)-\sum_{k=0}^{n-1}s^{k}\left({}_{0}^{x}D^{\nu-k-1}\right)f(0), & \nu > 0 \end{cases} \tag{27}$$

Other definitions commonly used in fractional calculus can be found in Oldham & Spanier (1974), Valério (2005), Kilbas et al (2006) and Sabatier et al (2007).

In this study the FOC scheme shown in Figure 2 (changing the PI controllers by FOPI controllers in the spped control block) is used to control the speed of an IM. The "Speed Controller" block shown in Figure 2 corresponds to a FOPI controller, in which the parameter ν will be modified to analyze its effects on the controlled system. This strategy will be denoted as FOC-FOPI and will be compared with the classical strategy using a standard PI controller (BCS), which will be denoted as FOC-PI. Notice that this case corresponds to the FOC-FOPI strategy when ν = 1. "Current Controller" block and "Flux Controller" block in Figure 2 correspond to proportional controllers. All these controller parameters (proportional constants) will be kept constant at values indicated in Section 4.2.

4.2. Simulation set up

The controlled system corresponds to the Siemens 3-phase IM, model 1LA7080 descrbed in Section 3.3. All the simulations shown in this study were performed using MATLAB/Simulink. The following describes the tests performed on the IM, in simulation analysis. These tests were used to determine the general features of FOC-FOPI scheme, and will be compared with FOC-PI scheme. For the sake of space only results concerning the regulation of the controlled system (capacity of the system reject external perturbations at different levels of load) are shown. Although the tracking study (capacity of the system to reach and follow a pre-specified speed reference at different levels of load) was also done (Mira, 2008; Mira & Duarte-Mermoud, 2009; Duarte-Mermoud et al, 2009) the simulated results are not shown here.The simulation results will be analyzed and discussed including stabilization time, rise time and control effort, among other aspects.

Test 1(Regulation): The speed reference increases from zero at a rate of 16 $[rad/s^2]$) until nominal speed ($146.08[rad/s] = 1395[rpm]$) in 9.33$[s]$. Then the reference is kept constant at the nominal speed until the end of the test (315$[s]$). (See Figure 4). The mechanical load varies during the test as shown in Table 2 and Figure 17.

The FOPI controller has the transfer function shown in (7). In all tests, parameters k_p and k_i were kept fixed at 0.5 and 0.05 respectively. These values were chosen after performing a series of preliminary simulation tests, analyzing the stabilization time and the control effort for different values. The values of the proportional constant used in current and flux proportional controllers were chosen to be 45. This value was also determined after a series of preliminary tests. The integration order was changed to explore the system's sensitivity with respect to parameter ν. The results shown in the next section include orders 0.7, 1.0 (Classical PI), 1.7 and 2.0. Theoretically the limit of stability is at ν = 2, a fact verified at the

simulation level (Mira & Duarte-Mermoud, 2009). See also Figure 21. Many other integration orders have been analyzed at the simulation level but they are not shown here for the sake of space. The reader is referred to Mira (2008) for more details.

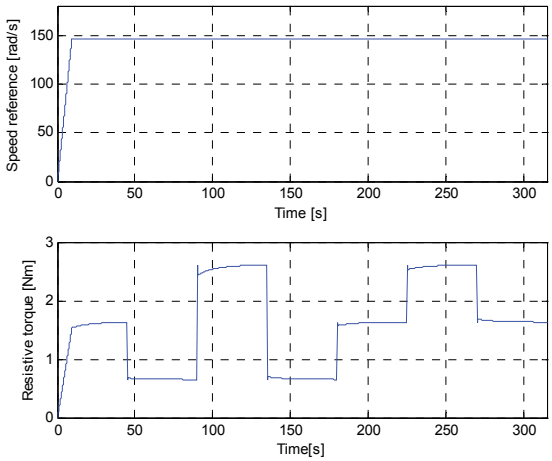

Figure 17. Description of Test 1 (Regulation)

Interval [s]	Level of load
0 – 45	50%
45 – 90	0%
90 – 135	100%
135 – 180	0%
180 – 225	50%
225 – 270	100%
270 – 315	50%

Table 1. Variation of load torque

4.3. Simulation results (regulation)

In this section the simulated behavior of IM control under the FOC-FOPI scheme, when Test 1 is applied, is shown in Figs. 18 to 21, for different values of the integration order ν of the integral part of PI controller (ν = 0.7, ν = 1.0, ν = 1.7 and ν = 2.0). Note that the classical FOC-PI scheme is obtained from the FOC-FOPI strategy by setting ν = 1. In all the figures, only the controlled variable (motor speed) is shown. The results obtained are quite satisfactory, as can be seen from Figures 18 to 21. The evolution of the controlled variable tries to follow the speed reference at all times, in spite of the perturbation being applied.

From Figure 18 it can be observed that for integration orders less than 1.0 the response presents no overshoot although the response is slower. It can be concluded, from information contained in Figure 20, that the response is faster when the integration order is greater than 1.0 but an overshoot is observed. When ν is chosen as 2.0 critically stable behavior is attained, as shown in Figure 21

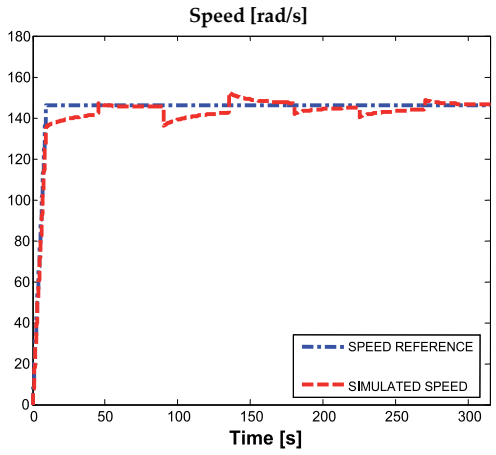

Figure 18. Simulation results for $\nu = 0.70$

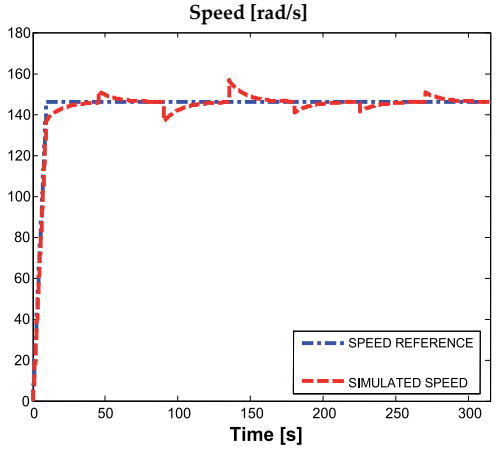

Figure 19. Simulation results for $\nu = 1.00$

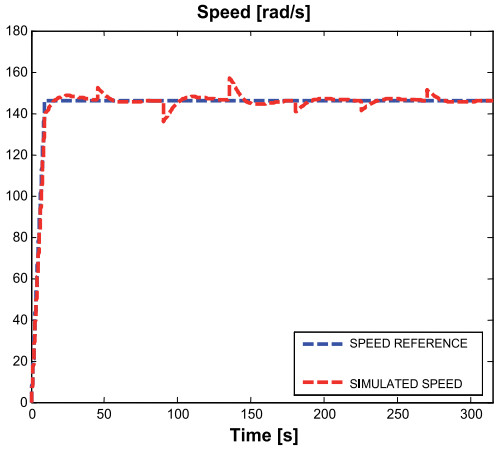

Figure 20. Simulation results for $\nu = 2.00$

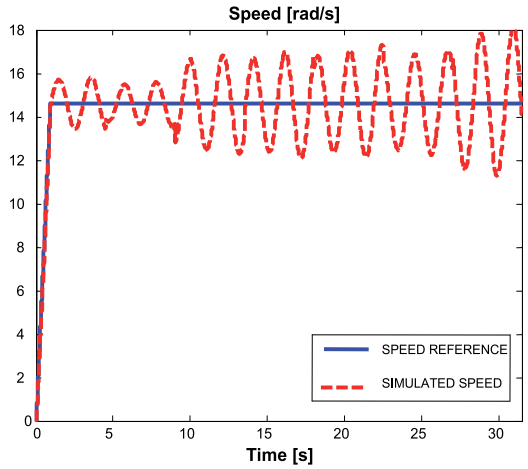

Figure 21. Simulation results for $\nu = 1.30$

Experimental analysis of the FOC-FOPI scheme is currently underway. These results will be reported, compared and discussed in the near future.

5. Conclusions

From simulation and experimental analysis performed on induction motor control some interesting conclusions can be drawn. In APBC strategies an important simplification of control scheme based on FOC principle can be attained when using the TFCP, allowing an effective control of the system without the necessity of having a rotor flux sensor or implementing a rotor flux observer to orientate the field. For APBC strategy the use of time-varying adaptive gains noticeably improves the transient behavior of controlled system, both for tracking as well as for regulation, when compared with the APBC strategy with fixed adaptive gains and also when compared with classical control strategies. Results are very similar for both the SISO and the MIMO approaches when using APBC. Compared with other control schemes proposed in the literature such as those based on traditional PI (Chee-Mun, 19998), sliding modes (Chan & Wang, 1996 ; Dunningan et al, 1998 ; Taoutaou & Castro-Linares, 2000; Araujo & Freitas, 2000), artificial intelligence (Bose, 1997 ; Vas, 1999) and non adaptive passivity (Taoutaou & Castro-Linares, 2000; Espinosa & Ortega, 1995), we have been able to develop four simple and novel controllers. They have adaptive characteristics, being robust in the presence of load parameter variations. Simple proportional controllers are used for the rotor speed, rotor flux and stator current control loops. They are also robust for a large range of proportional gain variations.

In the case of energy shaping strategy, IDA-PBC, a novel control scheme was studied and implemented. Since the original strategy was only designed for speed control, the addition of an outer speed loop of proportional-integral type, allowed obtaining certain robustness with respect to torque perturbations. In this strategy was necessary the design and implementation of a rotor flux observer, adding certain complexity to the complete system.

Since the BCS has fixed controller parameters its behavior is not as good as the adaptive strategies studied and presented here.

From simulation results obtained in this study it is possible to state that the integration order of FOPI controller plays a central role in speed control of an IM, when compared with the BCS. Choosing a suitable value of the integration order allows obtaining fast/slow responses and over/under damped responses. For this particular case of IM speed control , it was observed that for integration orders lesser than 1 the stabilization time is rather large and the controlled variable may not present overshoot. On the contrary, for values over 1 the stabilization time is small (and diminishes as integration order increases); the overshoot increases as the integration order does, reaching instability for integration order equal to 2. It was observed that the best results obtained from this study correspond to integration orders near to 1.40, presenting small rise and stabilization times, though with certain degree of overshoot.

In conclusion, the adaptive strategies studied present clear advantages with respect to the BCS used as basis of comparison. Amongst the adaptive schemes the APBC with time-varying adaptive gains is the one that behaves better.

Author details

Manuel A. Duarte-Mermoud & Juan C. Travieso-Torres
Department of Electrical Engineering, University of Chile, Santiago, Chile

Acknowledgement

The results reported here have been supported by CONICYT-Chile under grants Fondecyt 1061170, Fondecyt 1090208 and FONDEF D05I-10098.

6. References

Al-Nimma, D.A. and Williams, S. (1980). Study of rapid speed-changing methods on A.C. motor drives. *IEE Proceedings, Part B, Electric Power Applications*, Vol.127, No.6, pp. 382 – 385, ISSN: 0143-7038

Araujo, R. E. & Freitas, D. (2000), "Non-linear control of an induction motor : sliding mode theory leads to robust and simple solution ". *International Journal of Adaptive Control and Signal Processing*, Vol.14, No. 2, pp. 331-353, MES, ISSN: 0890-6327.

Bose, B.K. (1997). *Power Electronics and Variable Frequency Drives; Technology and Applications*. IEEE Press Marketing, ISBN-13: 978-0780310841, New York, USA

Bose, B.K. (2002). *Modern Power Electronics and AC Drives*, Prentice Hall PTR, ISBN-13: 978-0130167439, Upper Saddle River, USA

Byrnes, C.I., Isidori, A. & Willems, J.C. (1991), "Passivity, feedback equivalence, and the global stabilization of minimum phase nonlinear systems". *IEEE Transactions on Automatic Control*, Vol. 36, No. 11, pp. 1228-1240, November, ISSN: 0018-9286.

Castro-Linares, R. & Duarte-Mermoud, M.A. (1998), "Passivity equivalence of a class of SISO nonlinear systems via adaptive feedback". *Proceedings of VIII Latinamerican Congress on Automatic Control*, 9 – 13 November, Vol. 1, pp. 249-254.

Chan, C.C. & Wang, H.Q. (1996), "New scheme of sliding-mode control for high performance induction motor drives". *IEE Proceedings on Electrical Power Applications*, Vol. 143, pp. 177-185, ISSN: 1350-2352.

Chee-Mun, O. (1998), *Dynamic Simulation of Electric Machinery, using Matlab/Simulink*. Prentice Hall PTR, ISBN-10: 0137237855, ISBN-13: 978-0137237852, USA.

Duarte-Mermoud M.A., Castro-Linares R. and Castillo-Facuse A. (2001), "Adaptive passivity of nonlinear systems using time-varying gains". *Dynamics and Control*, Vol. 11, No. 4, December, pp. 333-351, ISSN: 0925-4668.

Duarte-Mermoud, M.A. & Travieso-Torres, J.C. (2003), "Control of induction motors: An adaptive passivity MIMO perspective". *International Journal of Adaptive Control and Signal Processing*, Vol. 17, No. 4, May, pp. 313-332, ISSN: 0890-6327.

Duarte-Mermoud, M.A., Castro-Linares, R. & Castillo-Facuse, A. (2002), "Direct passivity of a class of MIMO nonlinear systems using adaptive feedback". *International Journal of Control*. Vol.75, No. 1, January, pp. 23-33, ISSN: 0020-7179.

Duarte-Mermoud, M.A., Méndez-Miquel, J.M., Castro-Linares, R. & Castillo-Facuse, A. (2003), "Adaptive passivation with time-varying gains of MIMO nonlinear systems". *Kybernetes*, Vol. 32, Nos. 9/10, pp. 1342-1368, ISSN: 0368-492X.

Duarte-Mermoud, M.A., Mira, F.J., Pelissier, I.S. & Travieso-Torres, J.C., "Evaluation of a fractional order PI controller applied to induction motor speed Control". *Proceedings of the 8th IEEE International Conference on Control & Automation (ICCA2010)*, June 9-11, 2010, Xiamen, China. Proc. in CD, Paper No. 790, ThA4.5, ISBN: 978-1-4244-5195-1.

Dunnigan, M.W., Wade, S., Williams, B.W. & Yu, X. (1998), "Position control of a vector controlled induction machine using Slotine's sliding mode control approach". *IEE Proceedings on Electrical Power Applications*, Vol. 145, pp. 231-248, ISSN: 1350-2352.

Espinosa, G. and Ortega, R. (1995), "An output feedback globally stable controller for induction motors". *IEEE Transaction on Automatic Control*, Vol. 40, pp. 138-143, ISSN: 0018-9286.

González, H. (2005). *Development of Control Schemes based on Energy Shaping for a Class of Nonlinear Systems and Design of an Open Three Phase Inverter for on-line Applications in Induction Motors*. (In Spanish). M.Sc. Thesis, Department of Electrical Engineering, University of Chile

González, H., Duarte-Mermoud, M.A., Pelissier, I., Travieso J.C. & Ortega, R. (2008). A novel induction motor control scheme using IDA-PBC. *Journal of Control Theory and Applications*. Vol. 6, No. 1, January 2008, pp. 123-132, ISSN: 1993-0623.

González, H.A. & Duarte-Mermoud, M.A. (2005a). Induction motor speed control using IDA-PCB". (In Spanish). *Anales del Instituto de Ingenieros de Chile (Annals of the Chilean Institute of Engineers)*, Vol.117, No.3, December 2005, pp. 81-90 ISSN 0716-3290.

Isidori, A. (1995), *Nonlinear Control Systems*. Springer Verlag, Third Ed, ISBN-10: 3540199160, ISBN-13: 978-3540199168, USA.

Jansen, P.L.; Lorenz, D. & Thompson, C.O. (1995). Observer-based direct field orientation for both zero and very high speed operation. *IEEE Ind. Applic. Society Magazine*, Vol.1, No.4, (Jul. 1995), pp. 7-13, ISSN 1077-2618.

Kilbas, A. A.; Srivastava, H. M. & Trujillo, J. J. (2006). *Theory and Applications of Fractional Differential Equations.* Elsevier Science Inc., North-Holland Mathematics Studies, Vol.204, ISBN 978-0-444-51832-3, New York, USA

Marino, R.; Peresada, S. & Tomei, P. (1994). Adaptive observers for induction motors with unknown rotor resistance. *Proceeding of the 33rd Conf. on Decision and Control*, Vol.1, pp. 4018-4023, ISBN 0-7803-1968-0, Orlando, Florida, USA, December 1994

Martin, C. (2005). *A Comparative Analysis on Magnetic Flux Observers for Induction Motor Control Schemes*. (In Spanish). E.E. Thesis, Department of Electrical Engineering, University of Chile

Mira, F. (2008). *Design of a Three Phase Inverter and its Application to Advanced Control of Electrical Machines*. (In Spanish), E. E. Thesis, Dept. Elect. Eng., University of Chile

Mira, F.J. & Duarte-Mermoud, M.A. (2009). "Speed control of an asynchronous motor using a field oriented control scheme together with a fractional order PI controller. (In Spanish). *Annals of the Chilean Institute of Engineers*, Vol.121, No.1, pp. 1-13, ISSN 0716-3290.

Narendra, K.S. & Annaswamy, A.S. (1989). *Stable Adaptive Systems*. Prentice Hall, ISBN 0-13-839994-8, Englewood Cliffs, New Jersey, USA

Nijmeijer, H. & Van der Schaft, A. (1990), *Nonlinear Dynamical Control Systems*. Springer Verlag, ISBN-10: 038797234X, ISBN-13: 978-0387972343, USA.

Oldham, K. B. & Spanier, J. (1974). *The Fractional Calculus: Theory and Applications of Differentiation and Integration to Arbitrary Order.* Academic Press, Inc., Mathematics in Science and Engineering, Vol.111, ISBN 0-12-558840-2, New York, USA.

Ortega, R. & García-Canseco, E. (2004). Interconnection and damping assignment passivity-based control: A survey. *European Journal of Control*, Vol.10, No.5, pp. 432-450, ISSN 0947-3580.

Ortega, R., van der Schaft, A., Maschke, B. & Escobar, G. (2002). Interconnection and damping assignment passivity-based control of port-controlled Hamiltonian systems. *Automatica*, Vol.38, pp. 585-596, ISSN 0005-1098.

Pelissier, I. & Duarte-Mermoud, M.A. (2007). Simulation comparison of induction motor schemes based on adaptive passivity and energy shaping. (In Spanish). *Anales del Instituto de Ingenieros de Chile (Annals of the Chilean Institute of Engineers)*, Vol.119, No.2, August 2007, pp. 33-42, ISSN 0716-3290.

Pelissier, I. (2006). *Advanced strategies for induction motor control*. (In Spanish). E.E. Thesis, Department of Electrical Engineering, University of Chile

Sabatier, J.; Agrawal, O. P. & Machado, J. A. Eds. (2007). *Advances in Fractional Calculus: Theoretical Developments and Applications in Physics and Engineering.* Springer Verlag, ISBN ISBN 978-90-481-7513-0, New York, USA.

Taoutaou, D. & Castro-Linares, R. (2000), "A controller-observer scheme for induction motors based on passivity feedback equivalence and sliding modes". *International Journal of Adaptive Control and Signal Processing*, Vol. 14, No. 2-3, pp. 355-376, ISSN: 0890-6327.

Travieso, J.C. (2002). *Passive equivalence of induction motors for control purposes by means of adaptive feedback*. (In Spanish). Ph.D. Thesis, Electrical Engineering Department, Universidad de Santiago de Chile

Travieso-Torres, J.C. & Duarte-Mermoud, M.A. (2008), "Two simple and novel SISO controllers for induction motors based on adaptive passivity". *ISA Transactions*, Vol. 47, No. 1, January, pp.60-79, ISSN 0019-0578.

Valério, D. (2005). *Fractional Robust System Control.* Ph.D. Dissertation, Instituto Superior Técnico, Universidade Técnica de Lisboa, Portugal

Van der Schaft, A. (2000). *L2-Gain and Passivity Techniques in Nonlinear Control*. 2nd Edition. Springer-Verlag, ISBN: 1-85233-073-2, London, GB

Vas, P. (1998). *Sensorless Vector and Direct Torque Control.* Oxford University Press, ISBN-10: 0198564651, N-13: 978-0198564652, New York, USA

Vas, P. (1999). *Artificial-Intelligence-Based Electrical Machines and Drives*. Oxford University Press, ISBN-10: 019859397X, ISBN-13: 978-0198593973, USA.

Williams, B.W. & Green, T.C. (1991). Steady state control of an induction motor by estimation of stator flux magnitude. *IEE Proceedings, Part B, Electric Power Applications*, Vol.138, No.2, pp. 69 -74, ISSN: 0143-7038

Chapter 13

Tuning PI Regulators for Three-Phase Induction Motor Space Vector Modulation Direct Torque Control Using Complex Transfer Function Concept

Alfeu J. Sguarezi Filho, José L. Azcue P. and Ernesto Ruppert

Additional information is available at the end of the chapter

http://dx.doi.org/10.5772/39006

1. Introduction

The dynamics of induction motor (IM) is traditionally represented by differential equations. The space-vector concept [13] is used in the mathematical representation of IM state variables such as voltage, current, and flux.

The concept of complex transfer function derives from the application of the Laplace transform to differential equations in which the complex coefficients are in accordance with the spiral vector theory which has been presented by [24]. The complex transfer function concept is applied to the three-phase induction motor mathematical model and the induction motor root locus was presented in [10]. Other procedures for modeling and simulating the three-phase induction motor dynamics using the complex transfer function concept are also presented in [4].

The induction machine high performance dynamics is achieved by the field orientation control (FOC) [1, 17]. The three-phase induction motor field orientation control using the complex transfer function concept to tune the PI controller by using the frequency-response function of the closed-loop complex transfer function of the controlled induction machine was presented in [2]. This strategy has satisfactory current response although stator currents had presented cross-coupling during the induction machine transients. An interesting solution was presented in [11] in which it was designed a stator-current controller using complex form. From this, the current controller structure employing single-complex zeros is synthesized with satisfactory high dynamic performance although low-speed tests had not been shown in mentioned strategies.

An alternative for induction motor drive is the direct torque control (DTC), which consists of the direct control of the stator flux magnitude λ_1 and the electromagnetic torque T_e. DTC controllers generate a stator voltage vector that allows quick torque response with the smallest

variation of the stator flux. The principles of the DTC using hysteresis controllers and variable switching frequency have been presented by [22] and [6]. It has disadvantages such as low speed operation [19].

The PI-PID controllers are widely used in control process in industry [18]. The PI controller was applied to the IM direct torque control has been presented by [23]. Some investigations to tune the PI gains of speed controller have been presented using genetic-fuzzy [20] and neural networks [21]. These strategies have satisfactory torque and flux response although a method to tune the PI controllers for stator flux and electromagnetic torque loop and low-speed tests had not been shown.

To overcome low speed operation shortcomings, various approaches for DTC applying flux vector acceleration method [9, 14] and deadbeat controller [5, 12, 15] have been reported. These strategies aim the induction motor control at low speed. In this case, the complex transfer function was not used to tune PI controllers for such strategy when the induction motor operates at any speed.

The aim of this book chapter is to provide the designing and tuning method for PI regulators, based on the three-phase induction motor mathematical model complex transfer function to be used in induction motor direct torque control when the machine operates at low speed which is a problem so far. This methods is in accordance with the present state of the art. The PI controller was designed and tuned by frequency-response function of the closed loop system. The controller also presents a minor complexity to induction motor direct torque control implementation. Experimental results are carried out to validate the controller design.

2. The complex model of the induction motor

The three-phase induction motor mathematical model in synchronous reference frame (dq) is given by [16]

$$\vec{v}_{1dq} = R_1\vec{i}_{1dq} + \frac{d\vec{\lambda}_{1dq}}{dt} + j\omega_1\vec{\lambda}_{1dq} \tag{1}$$

$$0 = R_2\vec{i}_{2dq} + \frac{d\vec{\lambda}_{2dq}}{dt} + j\left(\omega_1 - P\omega_{mec}\right)\vec{\lambda}_{2dq} \tag{2}$$

the relationship between fluxes and currents

$$\vec{\lambda}_{1dq} = L_1\vec{i}_{1dq} + L_M\vec{i}_{2dq} \tag{3}$$

$$\vec{\lambda}_{2dq} = L_M\vec{i}_{1dq} + L_2\vec{i}_{2dq} \tag{4}$$

The electromagnetic torque is expressed in terms of the cross-vectorial product of the stator flux and the stator current space vectors.

$$T_e = \frac{3}{2}P\frac{L_M}{L_2L_1\sigma}\vec{\lambda}_{2dq} \times \vec{\lambda}_{1dq} \tag{5}$$

$$T_e = \frac{3}{2}P\frac{L_M}{L_2L_1\sigma}\left|\vec{\lambda}_{2dq}\right|\left|\vec{\lambda}_{1dq}\right|\sin(\alpha_r - \delta) \tag{6}$$

$$T_e = \frac{3}{2}P\frac{L_M}{L_2L_1\sigma}\left|\vec{\lambda}_{2dq}\right|\left|\vec{\lambda}_{1dq}\right|\sin(\alpha) \tag{7}$$

Equation (7) shows that variations in stator flux will reflect variations on rotor flux.

Where δ and α_r are the angle of the stator flux and rotor flux space vector with respect to the direct-axis of the synchronous reference frame respectively as is shown in Fig. 1, $\alpha = \alpha_r - \delta$ is the angle between the stator and rotor flux space vectors, P is a number of pole pairs and $\sigma = 1 - L_M^2/(L_1 L_2)$ is the dispersion factor.

Combining equations (1), (2), (3) and (4), after some manipulations, the induction machine model can be written as a complex space state equation in the synchronous reference frame (dq) and the state variables are stator current $\vec{i}_{1dq} = i_{1d} + j i_{1q}$ and stator flux $\vec{\lambda}_{1dq} = \lambda_{1d} + j\lambda_{1q}$ and it is shown in equation (9).

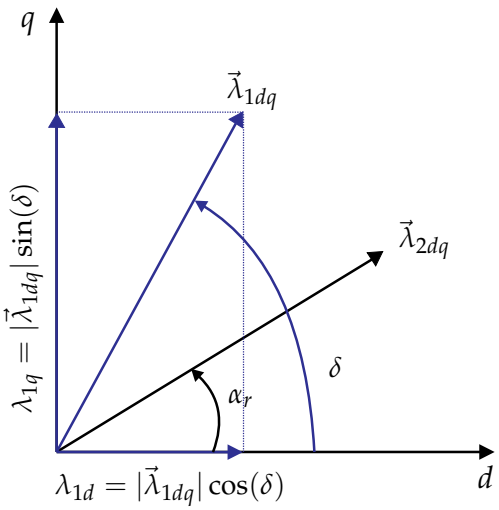

Figure 1. stator and rotor fluxes space vectors in synchronous reference frame.

$$\frac{d\vec{\lambda}_{1dq}}{dt} = -j\omega_1 \vec{\lambda}_{1dq} - R_1 \vec{i}_{1dq} + \vec{v}_{1dq} \tag{8}$$

$$\frac{d\vec{i}_{1dq}}{dt} = a_3\, \vec{\lambda}_{1dq} + a_4\, \vec{i}_{1dq} + \frac{\vec{v}_{1dq}}{\sigma L_1} \tag{9}$$

$$a_3 = \left(\frac{R_2}{\sigma L_1 L_2} - \frac{jP\omega_{mec}}{\sigma L_1} \right) \tag{10}$$

$$a_4 = -\left[\frac{R_1}{\sigma L_1} + \frac{R_2}{\sigma L_2} + j\,(\omega_1 - P\omega_{mec}) \right] \tag{11}$$

The machine mechanical dynamics is given by

$$J\frac{d\omega_{mec}}{dt} = \frac{3}{2} P \frac{L_M}{L_2 L_1 \sigma} \vec{\lambda}_{2dq} \times \vec{\lambda}_{1dq} - T_L \tag{12}$$

The ω_1 is the synchronous speed, ω_{mec} is the machine speed, R_1 and R_2 are the estator and rotor windings per phase electrical resistance, L_1 , L_2 and L_m are the proper and mutual inductances of the stator and rotor windings, $\vec{v}$ is the voltage vector , P is the machine number

of pair of poles, J is the load and rotor inertia moment, the symbol "*" represents the conjugate of the complex number and T_L is the load torque.

In order to obtain the induction motor complex transfer function the Laplace transform is applied to the equations (8) and (9) in accordance with the complex transfer function concept [24], [10]. Thus, the equation (8) complex transfer function is shown in Figure 2.

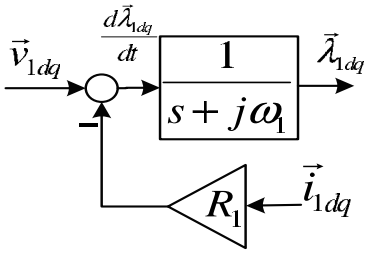

Figure 2. Equation (8) complex transfer function.

And the equation (9) complex transfer function complex transfer function is shown in Figure 3. Thus, the induction motor block diagram originated by use of the equations (8)

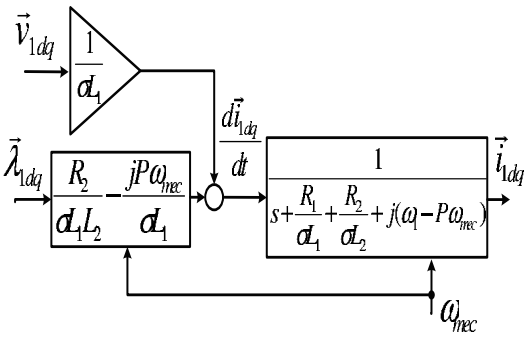

Figure 3. Equation (9) complex transfer function.

and (9) complex transfer functions shown in Figures 2 and 3 and the machine mechanical dynamics (12) is shown in Figure 4. When designing the DTC control system through the

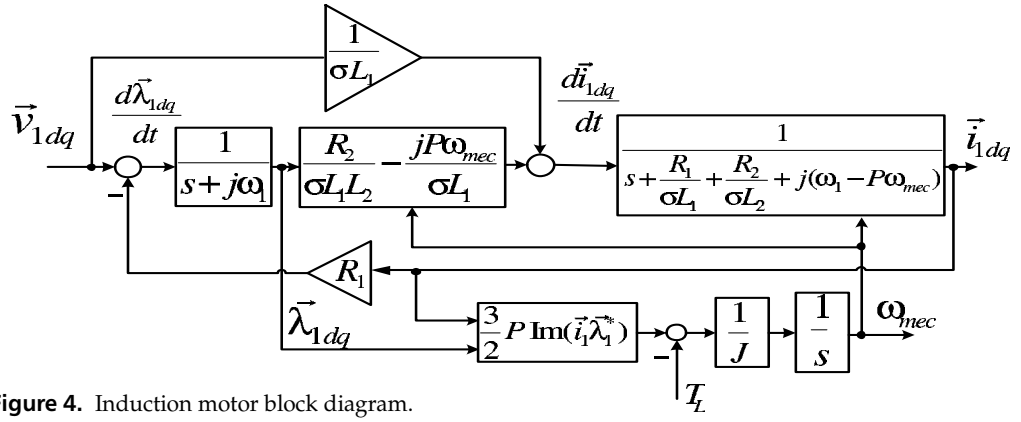

Figure 4. Induction motor block diagram.

IM complex transfer function, $\vec{v}_{1dq}$ is considered as the input and the $\vec{i}_{1dq}$ is considered as the output. For this purpose it is assumed that the mechanical time constant of the motor is much larger than the transient electromagnetic time constants and the saturation effects is neglected. Thus, $\omega_{mec} =$ constant is a valid approximation [24], [11]. Therefore the induction machine complex transfer function $H(s)$ is derived from application of the Laplace transform in equations (8) and (9) and it is the closed loop system of Figure 4 without machine mechanical dynamics. Thus, it has the form given in 13.

$$H(s) = \frac{I_{1dq}}{V_{1dq}} = \frac{\left(\frac{s + j\omega_1}{\sigma L_1}\right) + a_3}{(s + j\omega_1)\ (s + a_4) + R_1\, a_3} \tag{13}$$

where $I_{1dq} = \mathcal{L}\left\{\vec{i}_{1dq}\right\}$ and $V_{1dq} = \mathcal{L}\left\{\vec{v}_{1dq}\right\}$.

3. Direct torque control

If the sample time is short enough, such that the stator voltage space vector is imposed to the motor keeping the stator flux constant at the reference value. The rotor flux will become constant because it changes slower than the stator flux.

The electromagnetic torque (14) can be quickly changed by changing the angle α in the desired direction. The angle α can be easily changed when choosing the appropriate stator voltage space vector.

$$T_e = \frac{3}{2} P \frac{L_M}{L_2 L_1 \sigma} \left|\vec{\lambda}_{2\alpha\beta}\right| \left|\vec{\lambda}_{1\alpha\beta}\right| \sin(\alpha) \tag{14}$$

For simplicity, let us assume that the stator phase ohmic drop could be neglected in $\vec{v}_{1\alpha\beta} = R_1 \vec{i}_{1\alpha\beta} + \frac{d\vec{\lambda}_{1\alpha\beta}}{dt}$. Therefore $d\vec{\lambda}_{1\alpha\beta}/dt = \vec{v}_{1\alpha\beta}$. During a short time Δt, when the voltage space vector is applied it has:

$$\Delta\vec{\lambda}_{1\alpha\beta} \approx \vec{v}_{1\alpha\beta} \cdot \Delta t \tag{15}$$

Thus, the stator flux space vector moves by $\Delta\vec{\lambda}_{1\alpha\beta}$ in the direction of the stator voltage space vector at a speed which is proportional to the magnitude of the stator voltage space vector. By selecting step-by-step the appropriate stator voltage vector, it is possible to change the stator flux in the required direction.

3.1. Stator flux oriented direct torque control

The stator flux oriented direct torque control (SFO-DTC) have two PI regulators. The outputs of the PI flux and torque controllers can be interpreted as the stator voltage components in the stator flux oriented coordinates as shown in Fig. 5 [23], [3]. The control strategy relies on a simplified description of the stator voltage components, expressed in stator-flux-oriented coordinates as:

$$v_{1d} = R_1 i_{1d} + \frac{d\lambda_1}{dt} \tag{16}$$

$$v_{1q} = R_1 i_{1q} + \omega_1 \lambda_1 \tag{17}$$

Where ω_1 is the angular speed of the stator flux vector. The above equations show that the component v_{1d} has influence only on the change of stator flux magnitude, and the component v_{1q}, if the term $\omega_1\lambda_1$ is decoupled, can be used for torque adjustment. Therefore, after coordinate transformation $dq/\alpha\beta$ into the stationary frame, the command values $v_{1d_{ref}}, v_{1q_{ref}}$, are delivered to SVM module.

This SFO-DTC scheme requires the flux and the torque estimators, which can be performed as it is proposed in Fig. 5. Therefore, the control signals are fed to the power electronics drive.

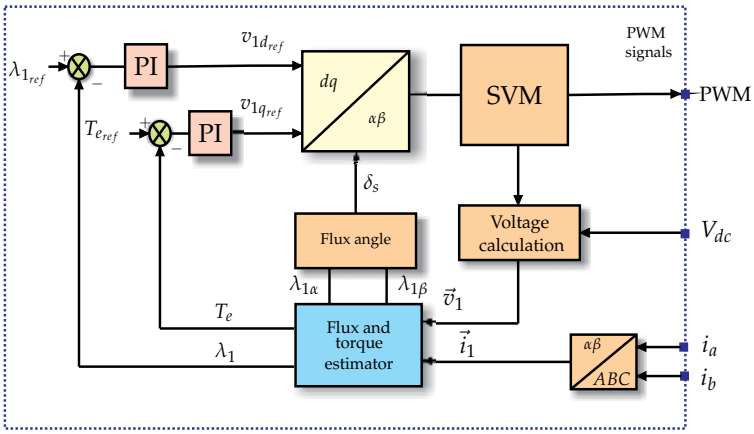

Figure 5. Stator flux oriented direct torque control scheme.

4. Design and tuning PI gains

By using stator field orientation, the torque and stator flux must become parts of a complex number, where the magnitude of the stator flux λ_1 is the real component and the torque T_e is the imaginary component. Hence, the reference signals and the error become a complex number. Thus, the PI regulators presented in the before section [23] has the function to generate a voltage reference space vector using the stator flux-torque error vector $(\varepsilon_\lambda + j\varepsilon_T)$. This way the stator-voltage vector in this control strategy is given by

$$\vec{v}_{1dq_{ref}} = (\varepsilon_\lambda + j\varepsilon_T)\left(Kp + \frac{Ki}{s}\right) \tag{18}$$

Which means that the direct and quadrature axis of the voltage vector are

$$v_{1d_{ref}} = (\varepsilon_\lambda)\left(Kp + \frac{Ki}{s}\right) \tag{19}$$

$$v_{1q_{ref}} = (\varepsilon_T)\left(Kp + \frac{Ki}{s}\right) \tag{20}$$

Where kp is the proportional gain, ki is the integral gain, ε_λ is the flux error signal and ε_T is the torque error signal.

The block diagram of the strategy with the PI regulators is shown in Figure 6.

The reference stator voltage vector $\vec{v}_{1dq_{ref}}$ is transformed by using stator flux angle δ_s to obtain the stator voltage at stationary reference frame $\alpha\beta$.

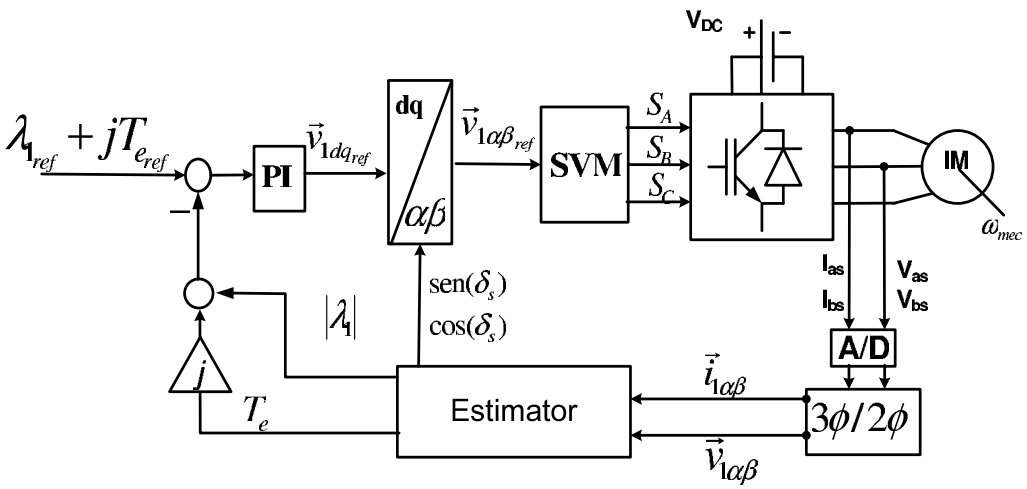

Figure 6. DTC strategy with PI regulators and complex signals.

4.1. Stator flux estimation

The stator flux estimation is done by

$$\vec{\lambda}_{1\alpha\beta} = \int (\vec{v}_{1\alpha\beta} - R_1 \vec{i}_{1\alpha\beta}) dt \tag{21}$$

A satisfactory flux estimation for induction motor at low speed using Equation (21) is obtained by using the integration method presented in [8] and the block diagram for the flux stimation is presented in Figure 7

The stator flux angle is estimated by using the trigonometric transfer function

$$\delta_s = \arctan\left(\frac{\lambda_{1\beta}}{\lambda_{1\alpha}}\right) \tag{22}$$

4.2. Design of the PI regulator gains

In order to tune the PI regulator it is necessary the closed-loop complex transfer function of the controlled induction motor. The complex transfer function of the controlled induction motor was also used to tune a complex gain controller in which has been presented in [7].

In accordance with the DTC control strategy the induction motor output has to be the stator flux magnitude λ_1 and the torque T_e. Therefore the H(s) (13) outputs have to become the stator flux magnitude λ_1 and the torque T_e. The expression to obtain the stator flux by using the stator current i_{1d} is given by

$$\lambda_1 = \lambda_{1d} \cong G\,\sigma\,L_1\,i_{1d} \tag{23}$$

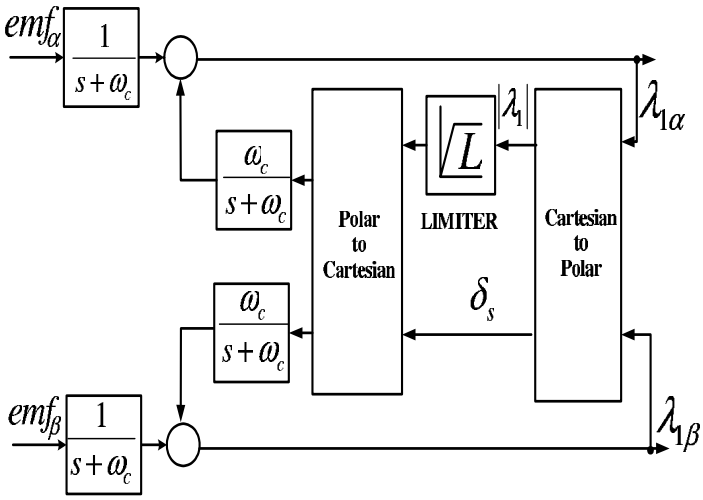

Figure 7. Block diagram for the stator flux stimation.

and to obtain the electromagnetic torque in the dq reference frame one may use the expression:

$$T_e = \frac{3}{2} P \lambda_1 \, i_{1q} \tag{24}$$

As the stator flux magnitude λ_1 is assumed to be essentially constant through of the equations (13), (23) and (24) the new transfer function is achieved with torque and flux as output and it is given by

$$\frac{X_{\lambda T}}{V_{1dq}} = H(s) \left(G\sigma L_1 + jP\frac{3}{2}\lambda_1 \right) \tag{25}$$

where $X_{\lambda T} = \mathcal{L}\{\lambda_1 + jT_e\}$.

The low speeds utilized in this book chapter are 60 rpm ($6.25 rad/s$), 125 rpm ($13 rad/s$), 150 rpm ($16 rad/s$) , 180 rpm ($17 rad/s$) that corresponds to 2Hz, 4.16Hz, 5Hz and 6Hz respectively. The frequency-response function of Equation (25) is presented in Figure 8 at frequencies 2Hz, 4.16Hz, 5Hz and 6Hz in accordance with the induction motor desired speed.

Then, from Equations (18) and (25) one obtain the control system block diagram and it is shown in Figure 9.

The expression of the closed loop transfer function of the system to design the PI regulators showed in Figure 9 is given by

$$\frac{X_{\lambda T}}{X_{\lambda T_{ref}}} = \frac{\left(Kp + \frac{Ki}{s} \right) H(s) \left(G\sigma L_1 + jP\frac{3}{2}\lambda_1 \right)}{1 + \left(Kp + \frac{Ki}{s} \right) H(s) \left(G\sigma L_1 + jP\frac{3}{2}\lambda_1 \right)} \tag{26}$$

where $X_{\lambda T_{ref}} = \mathcal{L}\left\{ \lambda_{1_{ref}} + jT_{e_{ref}} \right\}$.

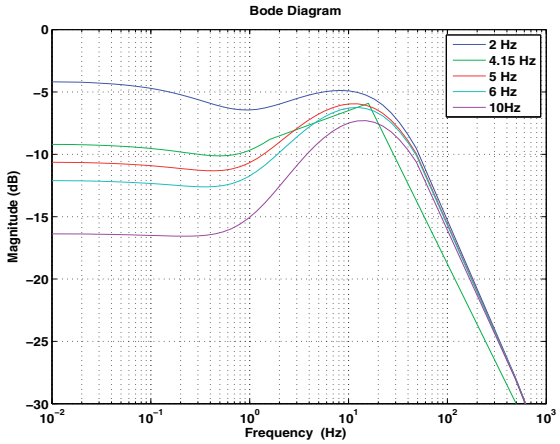

Figure 8. Equation (25) frequency-response function.

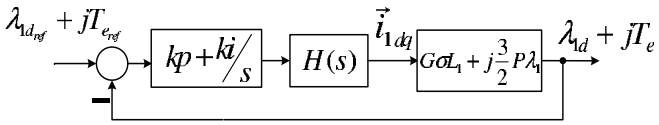

Figure 9. System to design the PI regulator.

As the variables at synchronous referential are constants the angle of output $X_{\lambda T}$ is neglected. At the frequency of 2Hz, 4.16Hz and 6Hz the kp and ki gains are chosen by using simulations, considering slip approximately null and the 0 dB magnitude. Them values are $kp = 155$ and $ki = 15$. The frequency-response function of Equation (26) is shown in Figure 10 and its magnitude is near 0 dB.

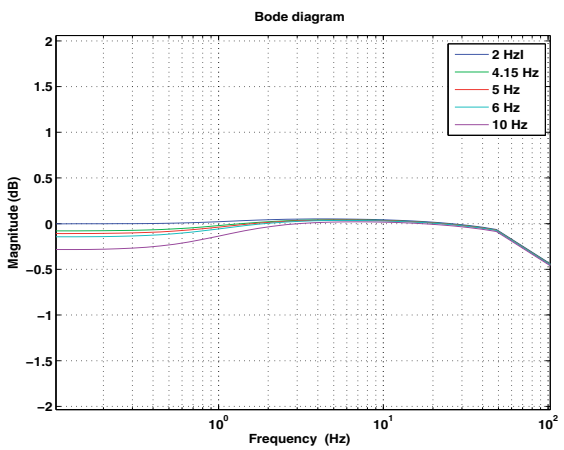

Figure 10. Frequency-response function of the equation (26)

5. Experimental results

The DTC strategy were implemented using a Texas Instruments DSP TMS320F2812 platform. The system consists of a three-phase voltage source inverter with insulated-gate bipolar transistors (IGBTs) and the three-phase induction motor parameters are shown in the appendix. The stator voltage commands are modulated by using symmetrical space vector PWM, with switching frequency equal to 2.5 kHz. The DC bus voltage of the inverter is 226 V. The stator voltages and currents are sampled in the frequency of 2.5 kHz. A conventional PI regulators generates a torque reference by using the speed error. The flux and torque estimation, and the flux and torque PIs regulators and speed controller have the same sampling frequency of 2.5 kHz. The encoder resolution is 1500 pulses per revolution. The algorithm of the DTC strategy was programmed on the Event Manager 1 of the Texas Instruments DSP TMS320F2812 platform and its flowchart is presented in Figure 11 and the schematic of implemention is presented in Figure 12.

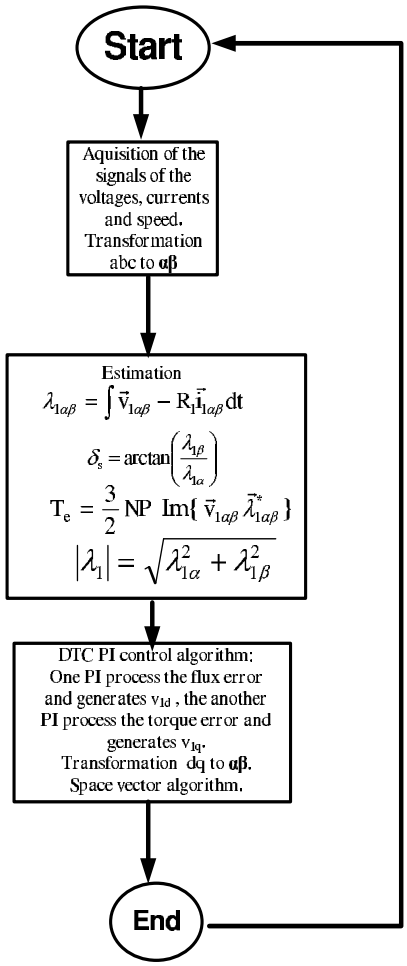

Figure 11. The flowchart of the DSP program.

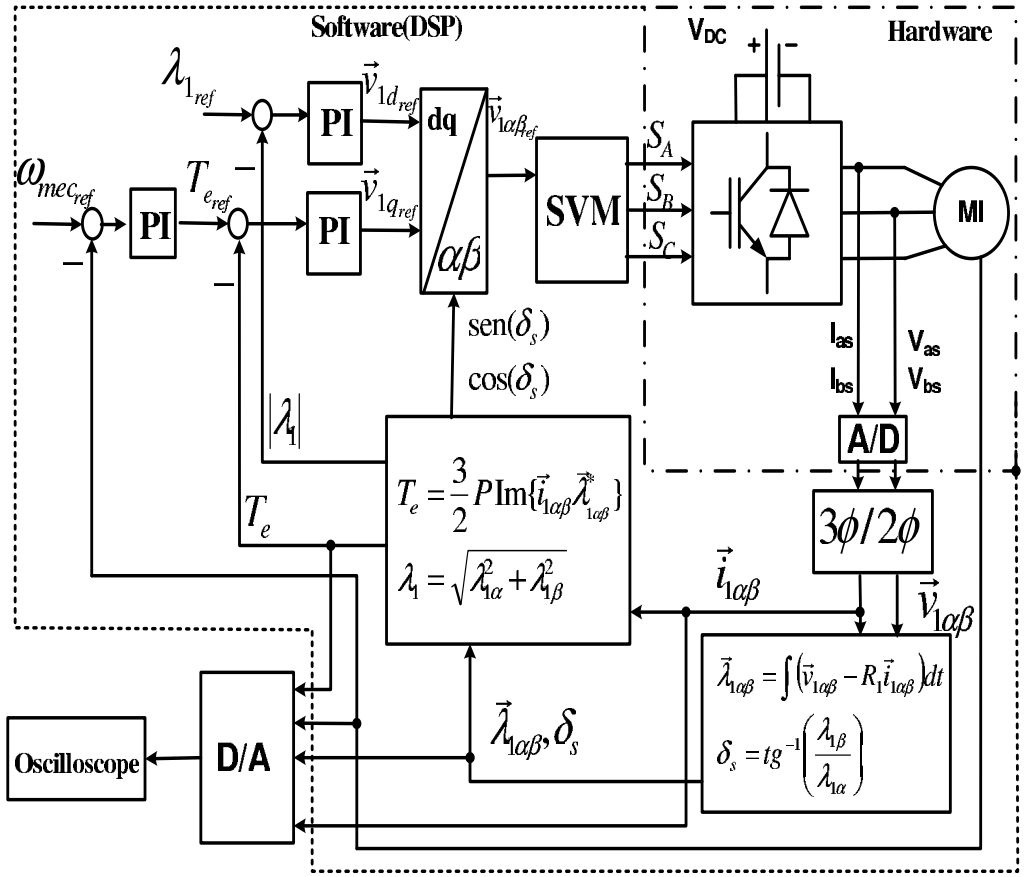

Figure 12. Schematic of implemention.

Five no-load induction motor tests were made. The first one was the response to a torque step of 12.2 Nm which is shown in Figure 13. It can be seen the satisfactory response of torque although it has oscillation. This oscillation occurs due to the natural lack of accuracy in the measurements of currents, voltages and parameters variations.

Figure 14 shows when the speed varies from 6.28 rad/s to 18.85 rad/s in 200 ms. This result confirms the satisfactory performance of the controller due to the fact that the the speed reaches the reference in several conditions although the gains of PI are designed for induction motor speed operation at 2 Hz and 6 Hz.

In the third test the speed varies in forward and reversal operation and the result are presented in Figures 15(a) and 15(b). The speed changes from 13 rad/s to -13 rad/s in 1 s and the gains of PI regulator are not changed during the test. This result confirms the satisfactory performance of the controller due to the fact that the the speed reaches the reference in several conditions and the PI regulator was designed for induction motor speed operation at 4.15 Hz. The small error occurs due the natural lack of accuracy in the measurement of the speed.

Figure 16 presents the speed response when the speed varies from 6.28 rad/s to -6.28 rad/s. The result confirms the satisfactory performance of the PI regulator again due to the fact that

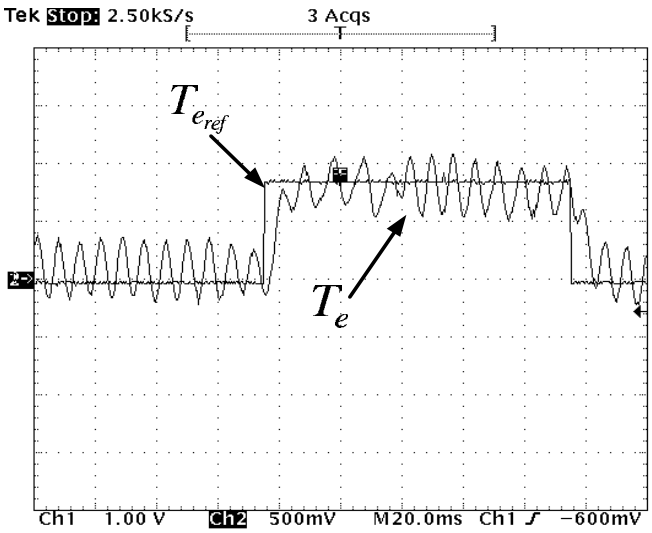

Figure 13. Responses to step torque operation (9 Nm/div).

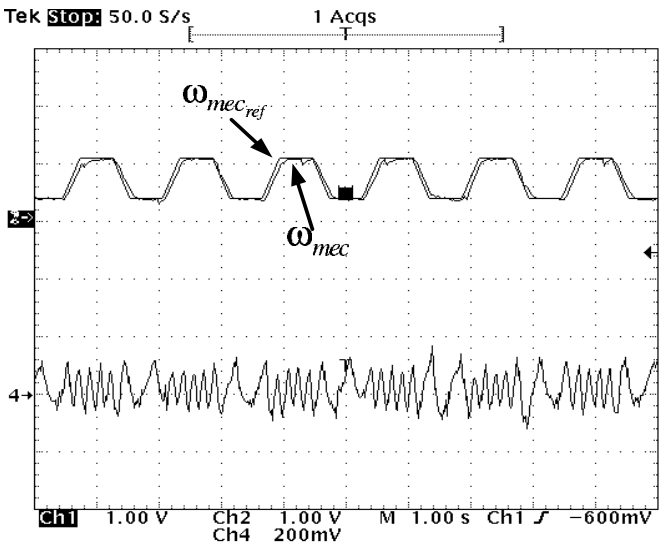

Figure 14. Speed forward and reversal operation (15.7 ras/s.div) and *a* phase current (10 A/div).

the speed reaches the reference value and the gains of PI are designed for induction motor speed operation at 2 Hz.

In load test the speed reference was 36.6 rad/s and a load torque of 11.25N.m was applied to the motor. In this test a dc generator is coupled to the rotor of induction motor. So the generated voltage of the DC generator is conected to the load with variable resistance. The test is shown in Figure 17 and the steady state error is 4.5%.

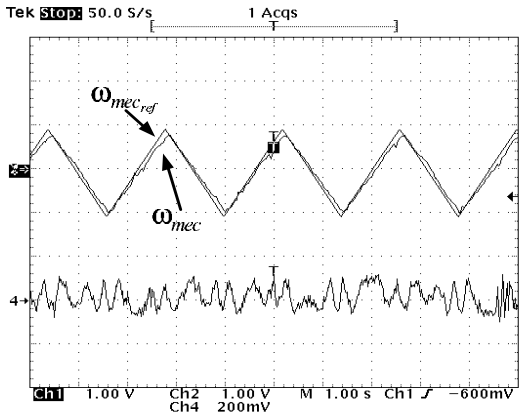

(a) Speed reversal operation (12.57 rad/s.div).

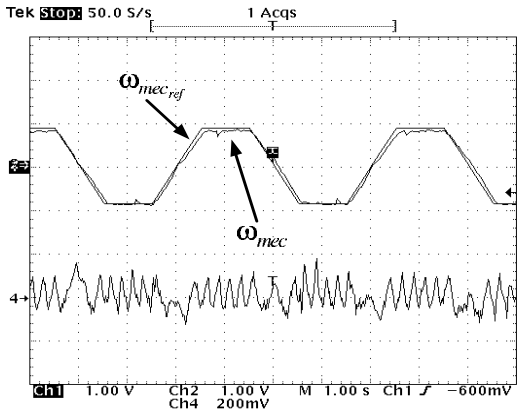

(b) Speed forward and reversal (13 rad/s.div).

Figure 15. Speed forward and reversal operation and *a* phase current (10 A/div)

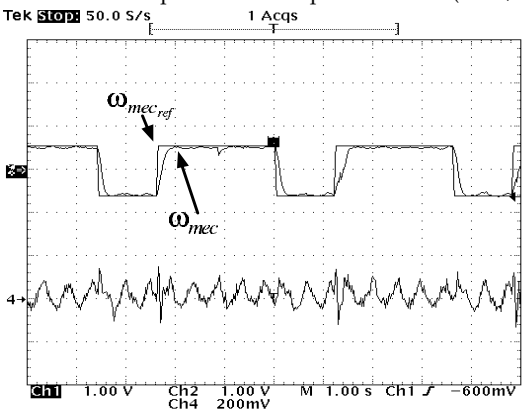

Figure 16. Speed response to step operation (12.57 rad/s.div) and *a* phase current (10 A/div).

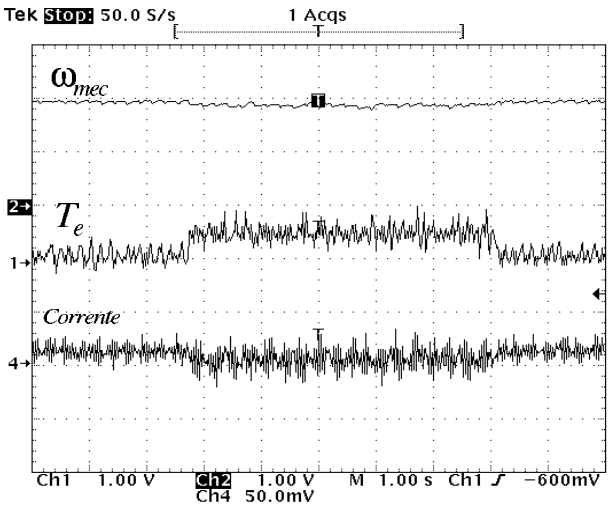

Figure 17. Load test (18,3 rad/s.div) and *a* phase current (20 A/div).

6. Conclusion

In this book chapter was presented a method to design and tune the PI regulators for the three-phase IM DTC-SVM strategy using the mathematical model complex transfer function when the machine operates at low speed. The concept of complex transfer function allows to obtain the PI regulator gains by using the closed loop system frequency response function of the controlled induction motor.

The experimental results shown the satisfactory performance of the regulator due to the fact that the speed reaches the reference value in several conditions although the complex gain was designed for a limited points of induction motor operation. Thus, the design of PI regulator has an acceptable performance although an detailed analysis considering parameters variations and other several speed operations has to be done. Due to the variable speed operation maybe it will be necessary to construct a table with PI gains designed for each desired speed or to an each speed range. The PI regulator overcomes the low speed operations shortcomings to the IM DTC-SVM strategy with a minor complexity. Thus, the complex transfer function becomes an interesting tool for design and tune PI regulator for IM drives.

Appendix

Three-phase induction motor variables and parameters: $PN = 2.3kW; V_N = 220\ V$; $Poles = 4$ $R_1 = 2.229\ \Omega$; $R_2 = 1.522\ \Omega$; $L_m = 0.238485\ H$; $L_1 = 0.2470\ H$; $L_2 = 0.2497\ H$; $J = 0.0067\ Kgm^2$.

Acknowledgment

The authors are grateful to CAPES, CNPq and FAPESP for the financial support for this research.

Author details

Alfeu J. Sguarezi Filho
Universidade Federal do ABC, Brazil

José Luis Azcue and Ernesto Ruppert
School of Electrical and Computer Engineering, University of Campinas, Brazil

7. References

[1] Blaschke, F. [1977]. The principle of field orientation control as applied to the new transvector closed loop control system for rotating machines, *Siemens Review* 39(5): 217–220.

[2] Briz, F., degener, M. W. & Lorenz, R. D. [2000]. Analysis and design of current regulators using complex vectors, *IEEE Trans. Ind. Applicat.* 32: 817–825.

[3] Buja, G. & Kazmierkowski, M. [2004]. Direct torque control of pwm inverter-fed ac motors - a survey, *Industrial Electronics, IEEE Transactions on* 51(4): 744–757.

[4] Cad, M. M. & de Aguiar, M. L. [2000]. The concept of complex transfer functions applied to the modeling of induction motors, *IEEE Winter Meeting 2000 of the IEEE Power Engineering Society* .

[5] Casadei, D., Serra, G. & Tani, A. [2001]. Steady-state and transient performance evaluation of a dtc scheme in the low speed range, *IEEE Trans. on Power Electronics* 16(6): 846–851.

[6] Depenbrock, M. [1988]. Direct self-control(dsc) of inverter-fed induction machine, *IEEE Trans. Power Electronics* 3(4): 420–429.

[7] Filho, A. J. S. & Filho, E. R. [2008]. The complex controller applied to the induction motor control, *IEEE Applied Power Electronics Conference and Exposition - APEC* pp. 1791–1795.

[8] Filho, A. J. S. & Filho, E. R. [2009]. The complex controller for three-phase induction motor direct torque control, *Sba Controle e Automação* 20(2).

[9] Gataric, S. & Garrigan, N. R. [1999]. Modeling and design of three-phase systems using complex transfer functions, *IEEE Trans. Ind. Electron.* 42: 263–271.

[10] Holtz, J. [1995]. The representation of ac machine dynamics by complex signal flow graphs, *IEEE Trans. Ind. Electron.* 42: 263–271.

[11] Holtz, J., Quan, J., Pontt, J., Rodríguez, J., newman, P. & Miranda, H. [2004]. Design of fast and robust current regulators for high-power drives based on complex state variables, *IEEE Trans. Ind. Applications* 40: 1388–1397.

[12] Kenny, B. H. & Lorenz, R. D. [2001]. Stator and rotor flux based deadbeat direct torque control ofinduction machines, *IEEE Industry Applications Conference* 1: 133–139.

[13] Kovács, P. K. & Rácz, E. [1984]. *Transient Phenomena in Electrical Machines*, Amsterdam, The Netherlands: Elsevier.

[14] Kumsuwana, Y., Premrudeepreechacharna, S. & Toliyat, H. A. [2008]. Modified direct torque control method for induction motor drives based on amplitude and angle control of stator flux, *Electric Power Systems Research* 78: 1712–1718.

[15] Lee, K.-B., Blaabjerg, F. & Yoon, T.-W. [2007]. Speed-sensorless dtc-svm for matrix converter drives with simple nonlinearity compensation, *IEEE Transactions on Industry Applications* 43(6): 1639–1649.

[16] Leonhard, W. [1985]. *Control of Electrical Drives*, Springer-Verlag Berlin Heidelberg New York Tokyo.
[17] Novotny, D. W. & Lipo, T. A. [1996]. *Vector Control and Dynamics of AC Drives*, Clarendon Press OXFORD.
[18] Phillips, C. [2000]. *Feedback Control Systems*, Pretince Hall.
[19] Ryu, J. H., Lee, K. W. & Lee, J. S. [2006]. A unified flux and torque control method for dtc-based induction-motor drives, *IEEE Trans. on Power Electronics* 21(1): 234–242.
[20] Shady M. Gadoue, D. G. & Finch, J. W. [2005]. Tuning of pi speed controller in dtc of induction motor based on genetic algorithms and fuzzy logic schemes, *International Conference on Technology and Automation* .
[21] Sheu, T.-T. & Chen, T.-C. [1999]. Self-tuning control of induction motor drive using neural network identifier, *IEEE Transactions on Energy Conversion* 14(4).
[22] Takahashi, I. & Noguchi, T. [1986]. A new quick-response and high-efficiency control strategy of an induction motor, *Industry Applications, IEEE Transactions on* IA-22(5): 820 –827.
[23] Xue, Y., Xu, X., Habetler, T. G. & Divan, D. M. [1990]. A low cost stator flux oriented voltage source variable speed drive, *Conference Record of the 1990 IEEE Industrial Aplications Society Annual Meetting* 1: 410–415.
[24] Yamamura, S. [1992]. *Spiral Vector Theory of AC Circuits and Machines*, Clarendon Press OXFORD.

Chapter 14

The Takagi-Sugeno Fuzzy Controller Based Direct Torque Control with Space Vector Modulation for Three-Phase Induction Motor

José Luis Azcue, Alfeu J. Sguarezi Filho and Ernesto Ruppert

Additional information is available at the end of the chapter

http://dx.doi.org/10.5772/48044

1. Introduction

The Direct Torque Control (DTC) has become a popular technique for three-phase Induction Motor (IM) drives because it provides a fast dynamic torque response without the use of current regulators [23][9], however, nowadays exist some other alternative DTC schemes to reduce the torque ripples using the Space Vector Modulation (SVM) technique [11][14]. In general the use of fuzzy systems does not require the accurate mathematic model of the process to be controlled. Instead, it uses the experience and knowledge of the involved professionals to construct its control rule base. Fuzzy logic is powerful in the motor control area, e.g., in [1] the PI and Fuzzy Logic Controllers (FLC) are used to control the load angle which simplifies the IM drive system.

In [8] the FLC is used to obtain the reference voltage vector dynamically in terms of torque error, stator flux error and stator flux angle. In this case both torque and stator flux ripples are remarkably reduced. In [15] the fuzzy PI speed controller has a better response for a wide range of motor speed. Different type of adaptive FLC such as self-tuning and self-organizing controllers has also been developed and implemented in[20][4].

In [18], [13] and [10] are proposed fuzzy systems which outputs are a specific voltage vector numbers, similarly to the classic DTC scheme[23]. On the other hand, in [26] is proposed a fuzzy inference system to modulate the stator voltage vector applied to the induction motor, but it consider the stator current as an additional input.

In [19] two fuzzy controllers are used to generate the two components of the reference voltage vector instead of two PI controllers, similarly, in [7] flux and torque fuzzy controllers are designed to substitute the original flux and torque PI controllers, but these schemes use two independent fuzzy controllers, one for the flux control and another one for the torque control.

Unlike the schemes mentioned before, the aim of this chapter is to design a Takagi-Sugeno (T-S) Fuzzy controller to substitute flux and torque PI controllers in a conventional DTC-SVM scheme. The T-S fuzzy controller calculates the quadrature components of the stator voltage vector represented in the stator flux reference frame. The rule base for the proposed controller is defined in function of the stator flux error and the electromagnetic torque error using trapezoidal and triangular membership functions. The direct component of the stator voltage takes a linear combination of the inputs as a consequent part of the rules, however, the quadrature component of the stator voltage takes the similar linear combination used in the first output but with the coefficients interchanged, not to be necessary another different coefficients values for this output.

The simulation results shown that the proposed T-S fuzzy controller for the DTC-SVM scheme have a good performance in terms of rise time (t_r), settling time (t_s) and torque ripple when it was tested at different operating conditions validating the proposed scheme. The chapter is organized as follows. In section 2 the direct torque control principles of the DTC for three-phase induction motor is presented. In section 3 the topology of the proposed control scheme is analyzed and in section 4 the proposed T-S fuzzy controller is described in detail mentioning different aspects of its design. Section 5 presents the simulations results of T-S fuzzy controller, and in the end, the conclusion is given in Section 6.

2. Direct Torque Control principles

2.1. Dynamical equations of the three-phase induction motor

By the definitions of the fluxes, currents and voltages space vectors, the dynamical equations of the three-phase induction motor in stationary reference frame can be put into the following mathematical form [25]:

$$\vec{u}_s = R_s\vec{i}_s + \frac{d\vec{\psi}_s}{dt} \tag{1}$$

$$0 = R_r\vec{i}_r + \frac{d\vec{\psi}_r}{dt} - j\omega_r\vec{\psi}_r \tag{2}$$

$$\vec{\psi}_s = L_s\vec{i}_s + L_m\vec{i}_r \tag{3}$$

$$\vec{\psi}_r = L_r\vec{i}_r + L_m\vec{i}_s \tag{4}$$

Where $\vec{u}_s$ is the stator voltage space vector, $\vec{i}_s$ and $\vec{i}_r$ are the stator and rotor current space vectors, respectively, $\vec{\psi}_s$ and $\vec{\psi}_r$ are the stator and rotor flux space vectors, ω_r is the rotor angular speed, R_s and R_r are the stator and rotor resistances, L_s, L_r and L_m are the stator, rotor and mutual inductance, respectively.

The electromagnetic torque is expressed in terms of the cross-vectorial product of the stator and the rotor flux space vectors.

$$t_e = \frac{3}{2}P\frac{L_m}{L_rL_s\sigma}\vec{\psi}_r \times \vec{\psi}_s \tag{5}$$

$$t_e = \frac{3}{2}P\frac{L_m}{L_rL_s\sigma}\left|\vec{\psi}_r\right|\left|\vec{\psi}_s\right|\sin(\gamma) \tag{6}$$

Where γ is the load angle between stator and rotor flux space vector, P is a number of pole pairs and $\sigma = 1 - L_m^2/(L_s L_r)$ is the dispersion factor.

The three-phase induction motor model was implemented in MATLAB/Simulink as is shown in [3], the code source of this implementation is shared in MATLAB CENTRAL [2].

2.2. Direct Torque Control

In the direct torque control if the sample time is short enough, such that the stator voltage space vector is imposed to the motor keeping the stator flux constant at the reference value. The rotor flux will become constant because it changes slower than the stator flux. The electromagnetic torque (6) can be quickly changed by changing the angle γ in the desired direction. This angle γ can be easily changed when choosing the appropriate stator voltage space vector.

For simplicity, let us assume that the stator phase ohmic drop could be neglected in (1). Therefore $d\vec{\psi}_s/dt = \vec{u}_s$. During a short time Δt, when the voltage space vector is applied it has:

$$\Delta\vec{\psi}_s \approx \vec{u}_s \cdot \Delta t \tag{7}$$

Thus the stator flux space vector moves by $\Delta\vec{\psi}_s$ in the direction of the stator voltage space vector at a speed which is proportional to the magnitude of the stator voltage space vector. By selecting step-by-step the appropriate stator voltage vector, it is possible to change the stator flux in the required direction.

2.2.1. Stator-flux-oriented direct torque control

The stator-flux-oriented direct torque control (SFO-DTC) based on space vector modulation scheme have two PI controllers as is shown in Fig. 2. This control strategy relies on a simplified description of the stator voltage components expressed in stator-flux-oriented coordinates

$$u_{ds} = R_s i_{ds} + \frac{d\psi_s}{dt} \tag{8}$$

$$u_{qs} = R_s i_{qs} + \omega_s \psi_s \tag{9}$$

Therefore, in this reference frame the stator flux quadrature component is zero as is shown in Fig. 1 that means $\psi_s = \psi_{ds}$ and $\psi_{qs} = 0$. Also, in this reference frame the electromagnetic torque is calculated by

$$T_{em} = \frac{3P}{2}\psi_s i_{qs} \tag{10}$$

$$i_{qs} = \frac{2}{3P}\frac{T_{em}}{\psi_s} \tag{11}$$

However, if the equation (11) is substitute in the equation (9), we can obtain the expression to control the electromagnetic torque applying and appropriate stator voltage quadrature

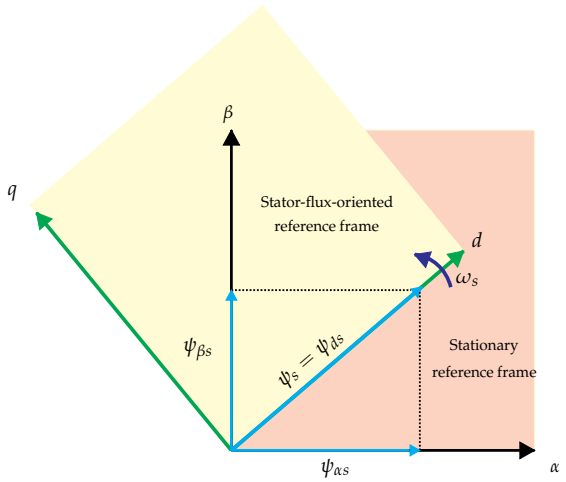

Figure 1. Stator-flux-oriented reference frame.

component, it is:

$$u_{qs} = \frac{2}{3P} R_s \frac{T_{em}}{\psi_s} + \omega_s \psi_s \tag{12}$$

From equation (8), the stator flux is controlled with the stator voltage direct component u_{ds}. For every sampled period T_s, the equation (8) is approximated by

$$u_{ds} = R_s i_{ds} + \Delta\psi_s / T_s \tag{13}$$

When the three-phase IM operates at high speeds the term $R_s i_{ds}$ can be neglected and the stator voltage can to become proportional to the stator flux change with a switching frequency $1/T_s$. However, at low speeds the term $R_s i_{ds}$ is not negligible and with the aim to correct this error is used the PI controller, it is:

$$u_{ds}^* = (K_{P\psi} + K_{I\psi}/s)(\psi_s^* - \hat{\psi}_s) \tag{14}$$

From the equation (12), the electromagnetic torque can be controlled with the stator voltage quadrature component if the term $\omega_s \psi_s$ is decoupled. A simple form to decoupled it is adding the term $\omega_s \psi_s$ to the output of the controller as is shown in Fig. 2. Then, the PI controller is used to control the electromagnetic torque, it is:

$$u_{qs}^* = (K_{PT_{em}} + K_{IT_{em}}/s)(T_{em}^* - \hat{T}_{em}) + \omega_s \psi_s \tag{15}$$

Finally, the outputs of the PI flux and PI torque controllers can be interpreted as the stator voltage components in the stator-flux-oriented coordinates [6].

Where ω_s is the angular speed of the stator flux vector. The equations (12) and (13) show that the component u_{ds} has influence only on the change of stator flux magnitude, and the component u_{qs}, if the term $\omega_s \psi_s$ is decoupled, can be used for torque adjustment. Therefore, after coordinate transformation $dq/\alpha\beta$ into the stationary reference frame, the command values u_{ds}^*, u_{qs}^* are delivered to SVM. In [3] this scheme is analyzed in detail.

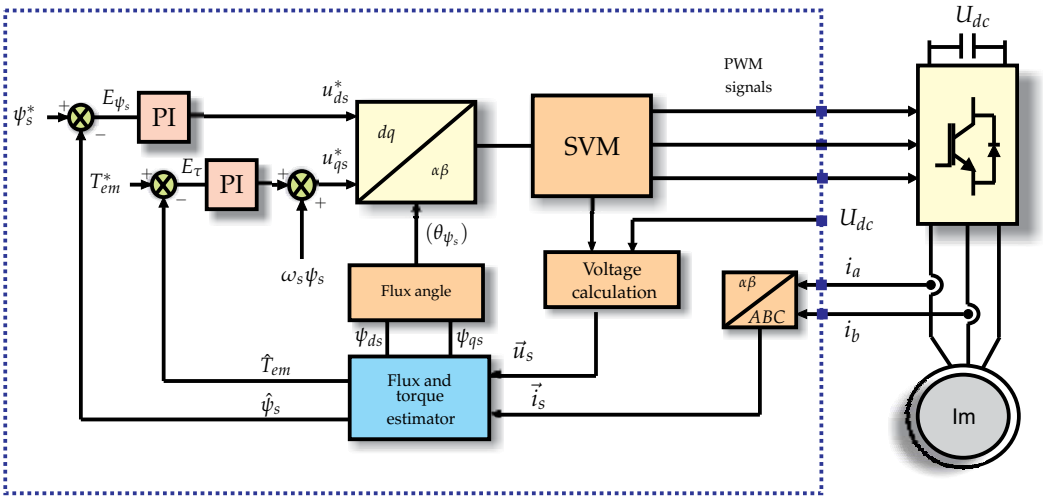

Figure 2. Conventional stator-flux-oriented direct torque control scheme.

The SFO-DTC based on space vector modulation scheme requires the flux and the torque estimators, which can be performed as it is proposed in this chapter, this scheme is used to implement the T-S fuzzy controller proposed.

3. The proposed direct torque control scheme

The Figure 3 shows the proposed DTC-SVM scheme, this scheme only needs sense the DC link and the two phases of the stator currents of the three-phase induction motor. In the DTC-SVM scheme the electromagnetic torque error (E_τ) and the stator flux error (E_{ψ_s}) are the inputs and the stator voltage components are the outputs of the Takagi-Sugeno fuzzy controller, these outputs are represented in the stator flux reference frame. Details about this controller will be presented in the next section.

3.1. Stator voltage calculation

The stator voltage calculation use the DC link voltage ($\mathbf{U_{dc}}$) and the inverter switch state (S_{Wa}, S_{Wb}, S_{Wc}) of the three-phase two level inverter. The stator voltage vector $\vec{u}_s$ is determined as in [5]:

$$\vec{u}_s = \frac{2}{3}\left[(S_{Wa} - \frac{S_{Wb}+S_{Wc}}{2}) + j\frac{\sqrt{3}}{2}(S_{Wb} - S_{Wc})\right] U_{dc} \tag{16}$$

3.2. Space vector modulation technique

In this work is used the space vector modulation (SVM) technique with the aim to reduce the torque ripple and total harmonic distortion of the current, is therefore necessary to understand the operation and fundamentals that governing their behavior. This concept was discussed in publications such as [24], [12] and [27]. For our purpose the basic ideas are summarized. In Fig. 4 and Fig. 5 are shown the three-phase two level inverter diagram, where the state of the

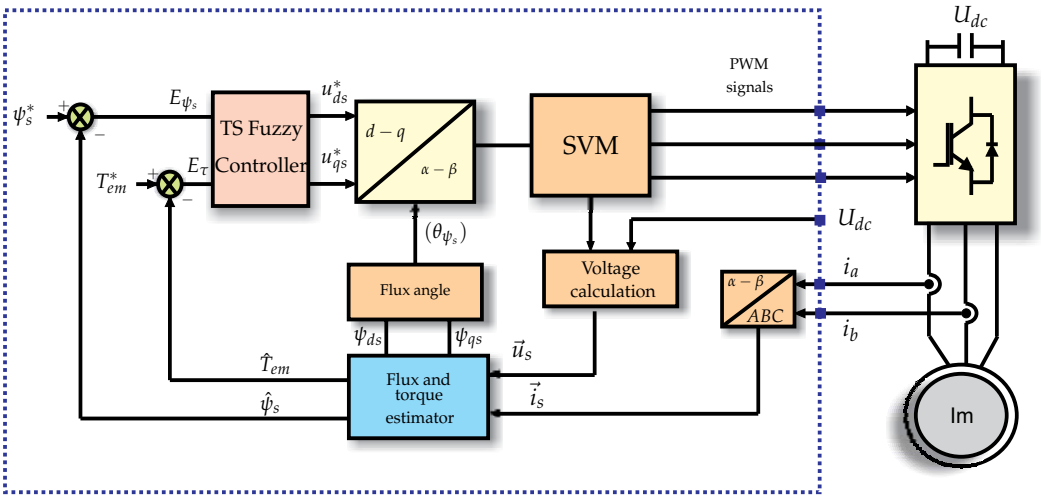

Figure 3. Takagi-Sugeno fuzzy controller in the direct torque control with space vector modulation scheme.

switches follow the following logic.

$$S_{Wi} = \begin{cases} 1, \text{ the switch } S_{Wi} \text{ is ON and the switch } \bar{S}_{Wi} \text{ is OFF} \\ 0, \text{ the switch } S_{Wi} \text{ is OFF and the switch } \bar{S}_{Wi} \text{ is ON} \end{cases} \tag{17}$$

Where i=a,b,c and considering that the switch $\bar{S}_{Wi}$ is the complement of S_{Wi} is possible to resume all the combinations only considering the top switches as is shown in Table 1.

Vector	S_{Wa}	S_{Wb}	S_{Wc}
$\vec{S}_0$	0	0	0
$\vec{S}_1$	1	0	0
$\vec{S}_2$	1	1	0
$\vec{S}_3$	0	1	0
$\vec{S}_4$	0	1	1
$\vec{S}_5$	0	0	1
$\vec{S}_6$	1	0	1
$\vec{S}_7$	1	1	1

Table 1. Switching vectors

Where $\vec{S}_0$, $\vec{S}_1$, $\vec{S}_2$, $\vec{S}_3$, $\vec{S}_4$, $\vec{S}_5$, $\vec{S}_6$ and $\vec{S}_7$ are switching vectors. These switching vectors generate six active voltage vectors ($\vec{U}_1$, $\vec{U}_2$, $\vec{U}_3$, $\vec{U}_4$, $\vec{U}_5$ and $\vec{U}_6$) and two zero voltage vectors ($\vec{U}_0$ and $\vec{U}_7$) as are shown in the Figures 6 and 7. The generalized expression to calculate the active and zero voltage vectors is:

$$\vec{U}_n = \begin{cases} \frac{2}{3}\sqrt{3}U_{dc} \cdot e^{j(2n-1)\frac{\pi}{6}} & , n = 1, ..., 6 \\ 0 & , n = 0, 7 \end{cases} \tag{18}$$

Where U_{dc} is the DC link voltage.

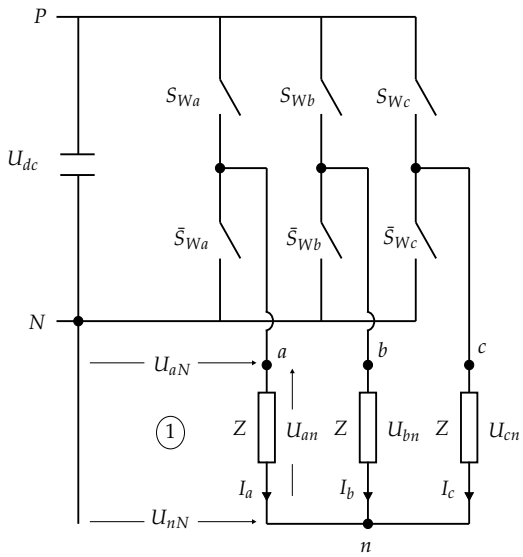

Figure 4. Three-phase two level inverter with load

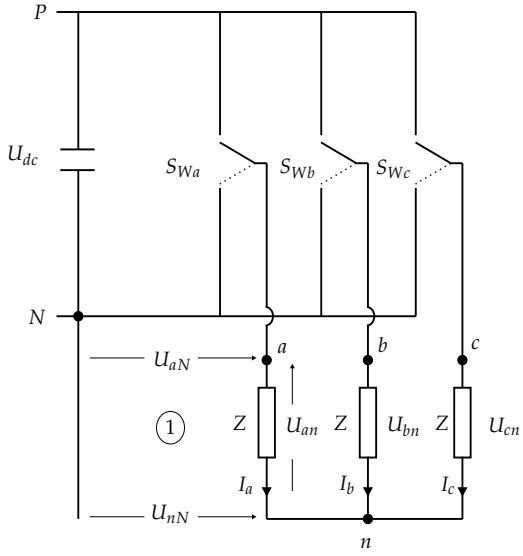

Figure 5. Simplified three-phase two level inverter with load

In Fig. 6 the hexagon is divided in six sectors, and any reference voltage vector is represented as combination of adjacent active and zero voltage vectors, e.g. the voltage vector $\vec{U}^*$ is localized in sector I between active vectors $\vec{U}_1$ and $\vec{U}_2$, as is shown in Fig. 8, and considering a enough short switching period, it is:

$$\begin{aligned} \vec{U}^* \cdot T_z &= \vec{U}_1 \cdot T_1 + \vec{U}_2 \cdot T_2 \\ \vec{U}^* &= \vec{U}_1 \frac{T_1}{T_z} + \vec{U}_2 \frac{T_2}{T_z} \end{aligned} \tag{19}$$

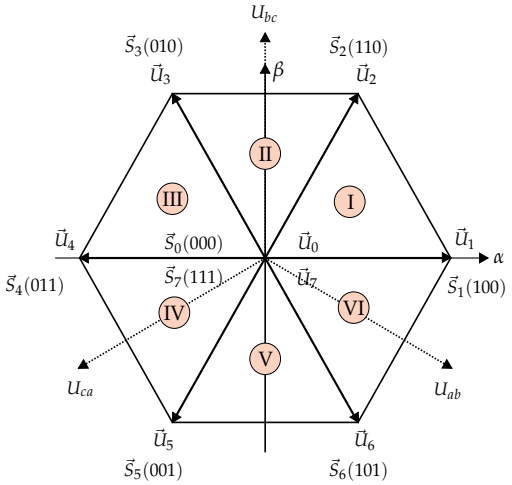

Figure 6. Switching and voltage vectors

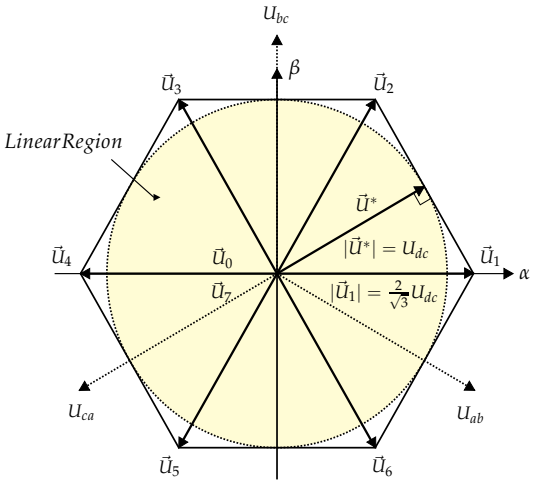

Figure 7. Linear region to work without overmodulation

The times T_1 and T_2 are calculated using trigonometric projections as is shown in Fig. 8, it is:

$$T_1 = \frac{|\vec{U}^*|}{|\vec{U}_1|} \cdot T_z \frac{\sin(\frac{\pi}{3} - \phi)}{\sin(\frac{2\pi}{3})} \tag{20}$$

$$T_2 = \frac{|\vec{U}^*|}{|\vec{U}_2|} \cdot T_z \frac{\sin(\phi)}{\sin(\frac{2\pi}{3})} \tag{21}$$

Where T_1 and T_2 are the times of application of the active vectors in a switching period, T_Z is the switching period and ϕ is the angle between the reference voltage vector and the adjacent active vector ($\vec{U}_1$). If the sum of times T_1 and T_2 is minor of the switching period, the rest of the time is apply the zero vectors, it is:

$$T_0 = T_7 = T_Z - T_1 - T_2 \tag{22}$$

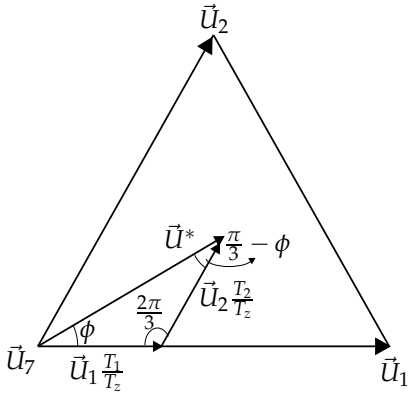

Figure 8. Voltage vector $\vec{U}^*$ and its components in sector I

Where T_0 and T_7 are the times of applications of zero vectors in a switching period. Once calculated the times of applications of each adjacent voltage vectors the next step is to follow a specific switching sequence for the symmetrical space vector modulation technique, this one depends if the reference vector is localized in an even or odd sector, e.g. in Fig. 9 is observed the optimum switching sequence and the pulse pattern for odd sector ($\vec{S}_0$,$\vec{S}_1$,$\vec{S}_2$ and $\vec{S}_7$), however for even sector the switching sequence is contrary to the case for odd sector as is shown in Fig. 10.

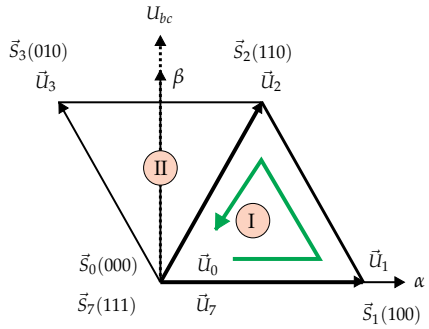

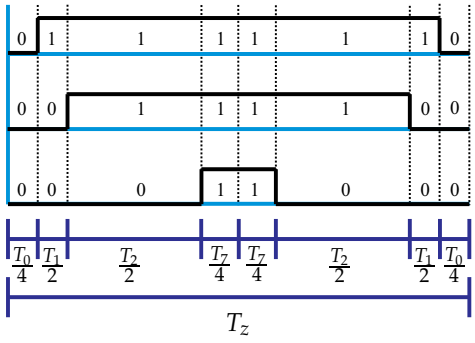

Figure 9. Switching sequence for odd sector.

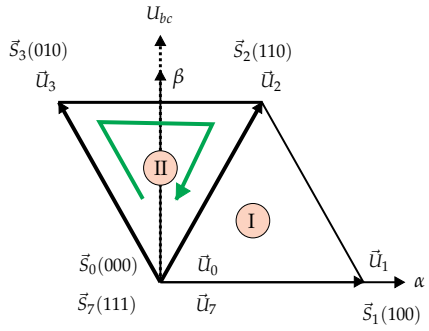

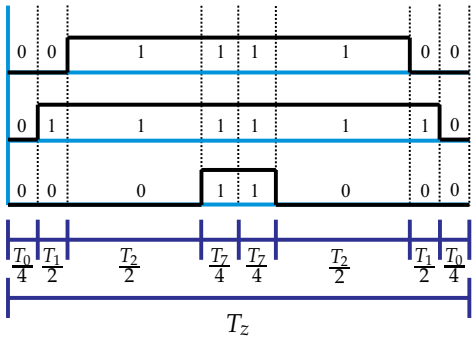

Figure 10. Switching sequence for even sector.

The details about the implementation of SVM algorithm in MATLAB/Simulink are presented in [3] in page 97.

3.3. Electromagnetic torque and stator flux estimation

The Figure 3 shows that the electromagnetic torque and the stator flux estimation depends of the stator voltage and the stator current space vectors, therefore:

$$\vec{\psi}_s = \int (\vec{u}_s - R_s \cdot \vec{i}_s) dt \tag{23}$$

The problem in this type of estimation is when in low speeds the back electromotive force (emf) depends strongly of the stator resistance, to resolve this problem is used the current model to improve the flux estimation as in [17]. The rotor flux represented in the rotor flux reference frame is:

$$\vec{\psi}_{rdq} = \frac{L_m}{1 + sT_r}\vec{i}_{sdq} - j\frac{(\omega_{\psi_r} - \omega_r)T_r}{1 + sT_r}\vec{\psi}_{rdq} \tag{24}$$

Where $T_r = L_r/R_r$ is the rotor time constant. In this reference frame $\psi_{rq} = 0$ and substituting this expression in the equation (24), it is:

$$\psi_{rd} = \frac{L_m}{1 + sT_r} i_{sd} \tag{25}$$

In the current model the stator flux is represented as:

$$\vec{\psi}_s^i = \frac{L_m}{L_r}\vec{\psi}_r^i + \frac{L_s L_r - L_m^2}{L_r}\vec{i}_s \tag{26}$$

Where $\vec{\psi}_r^i$ is the rotor flux estimated in the equation (25). The voltage model is based in the equation (1) and from there the stator flux in the stationary reference frame is:

$$\vec{\psi}_s = \frac{1}{s}(\vec{v}_s - R_s\vec{i}_s - \vec{U}_{comp}) \tag{27}$$

With the aim to correct the errors associated with the pure integration and the stator resistance variations with temperature, the voltage model is adapted through the PI controller.

$$\vec{U}_{comp} = (K_p + K_i\frac{1}{s})(\vec{\psi}_s - \vec{\psi}_s^i) \tag{28}$$

The K_p and K_i coefficients are calculated with the recommendation proposed in [17]. The rotor flux $\vec{\psi}_r$ in the stationary reference frame is calculated as:

$$\vec{\psi}_r = \frac{L_r}{L_m}\vec{\psi}_s - \frac{L_s L_r - L_m^2}{L_m}\vec{i}_s \tag{29}$$

The estimator scheme shown in the Figure 11 works with a good performance in the wide range of speeds.

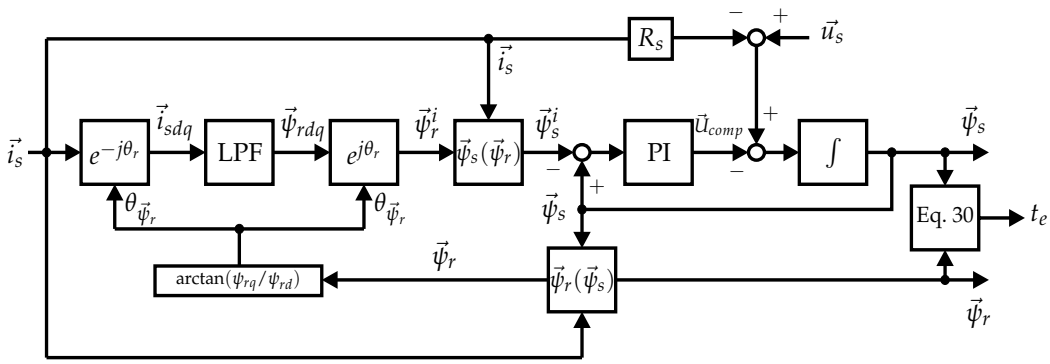

Figure 11. Stator and rotor flux estimator, and electromagnetic torque estimator.

Where LPF means low pass filter. In the other hand, when the equations (27) and (29) are replaced in (5) it is estimated the electromagnetic torque.

$$t_e = \frac{3}{2} P \frac{L_m}{L_r L_s \sigma} \vec{\psi}_r \times \vec{\psi}_s \tag{30}$$

4. Design of Takagi-Sugeno fuzzy controller

The Takagi-Sugeno Fuzzy controller takes as inputs the stator flux error E_{ψ_s} and the electromagnetic torque error E_τ, and as outputs the quadrature components of the stator voltage vector, represented in the stator flux reference frame. The first output (u_{ds}^*) takes a linear combination of the inputs as a consequent part of the rules, similarly, the second output (u_{qs}^*) takes the similar linear combination used in the first output but with the coefficients interchanged how is shown in the Figure 12.

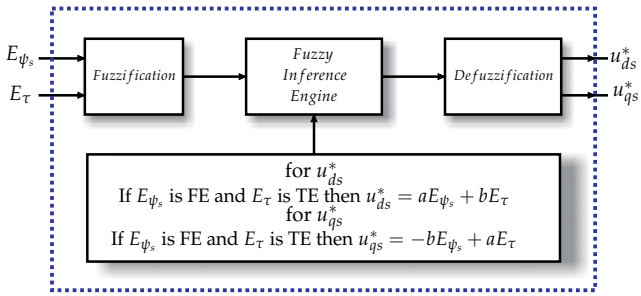

Figure 12. The structure of a fuzzy logic controller.

4.1. Membership functions

The Membership Functions (MF) for T-S fuzzy controller are shown in Figure 13 and in Figure 14, for the stator flux error and the electromagnetic torque error, respectively. These MF's shape and parameters was found through trial and error method with multiple simulations and with the knowing of the induction motor response for every test. This method is know as subjective approach [22].

The universe of discourse for the stator flux error input is defined in the closed interval [-0.5, 0.5]. The extreme MFs have trapezoidal shapes but the middle one takes triangular shape as is shown in Figure 13. However, the universe of discourse for electromagnetic torque error input is defined in the closed interval [-20, 20] but with the objective to see the shape of the MFs only is shown the interval [-5, 5] in Figure 14, the shapes of these MF are similar to the first input. For both inputs the linguistic labels N, Ze and P means Negative, Zero and Positive, respectively.

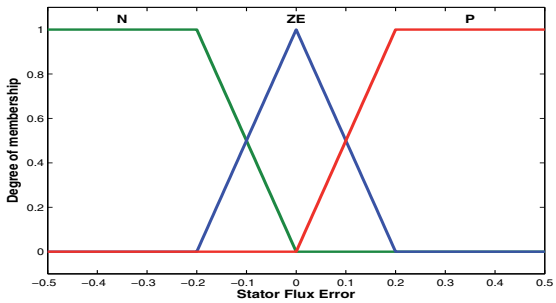

Figure 13. Membership function for stator flux error input (E_{ψ_s})

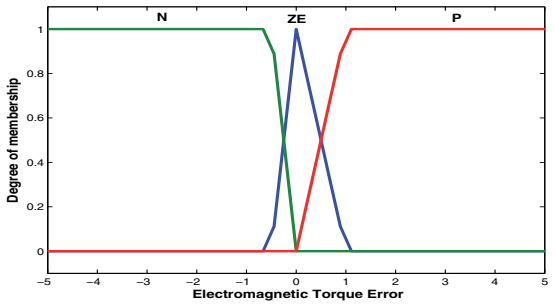

Figure 14. Membership function for electromagnetic torque error input (E_τ)

4.2. The fuzzy rule base

The direct component of the stator voltage u^*_{ds} is determined by the rules of the form:

$$R_x: \text{ if } E_{\psi_s} \text{ is } FE \text{ and } E_\tau \text{ is } TE \text{ then } u^*_{ds} = aE_{\psi_s} + bE_\tau$$

However, the quadrature component of the stator voltage u^*_{qs} is determined by the rules of the form:

$$R_y: \text{ if } E_{\psi_s} \text{ is } FE \text{ and } E_\tau \text{ is } TE \text{ then } u^*_{qs} = -bE_{\psi_s} + aE_\tau$$

Where $FE = TE = \{N, ZE, P\}$ are the fuzzy sets of the inputs and, **a** and **b** are coefficients of the first-order polynomial function typically present in the consequent part of the firs-order Takagi-Sugeno fuzzy controllers.

For instance, when the consequent function of the rule R_i is a real number, the consequent function is a zero-order polynomial and we have a zero-order controller. If the consequent function is a linear we have first-order controller [21].

$$R_i : \text{ if } X \text{ is } A_i \text{ and } Y \text{ is } B_i \text{ then } z = f_i(X, Y)$$

The rule base to calculate u^*_{ds} and u^*_{qs} is shown in Table 2. The **product** is the conjunction operator and the weighted average (**wtaver**) is the defuzzification method used to set the controller in the MATLAB fuzzy editor.

E_{Ψ_s} / E_σ	N	ZE	P
N	$u^*_{ds} = aF_e + bT_e$ $u^*_{qs} = -bF_e + aT_e$	$u^*_{ds} = aF_e + bT_e$ $u^*_{qs} = -bF_e + aT_e$	$u^*_{ds} = aF_e + bT_e$ $u^*_{qs} = -bF_e + aT_e$
ZE	$u^*_{ds} = aF_e + bT_e$ $u^*_{qs} = -bF_e + aT_e$	$u^*_{ds} = aF_e + bT_e$ $u^*_{qs} = -bF_e + aT_e$	$u^*_{ds} = aF_e + bT_e$ $u^*_{qs} = -bF_e + aT_e$
P	$u^*_{ds} = aF_e + bT_e$ $u^*_{qs} = -bF_e + aT_e$	$u^*_{ds} = aF_e + bT_e$ $u^*_{qs} = -bF_e + aT_e$	$u^*_{ds} = aF_e + bT_e$ $u^*_{qs} = -bF_e + aT_e$

Table 2. Fuzzy rules for computation of u^*_{ds} and u^*_{qs}

5. Simulation results

The simulations were performed using MATLAB simulation package which include Simulink block sets and fuzzy logic toolbox. The switching frequency of PWM inverter was set to be $10kHz$, the stator reference flux considered was 0.47 Wb and the coefficients considered were $a = 90$ and $b = 2$. In order to investigate the effectiveness of the proposed control system and in order to check the closed-loop stability of the complete system, we performed several tests.

We used different dynamic operating conditions such as: step change in the motor load (from 0 to 1.0 pu) at fifty percent of rated speed, no-load sudden change in the speed reference (from 0.5 pu to -0.5 pu), and the application of an arbitrary load torque profile at fifty percent of rated speed. The motor parameters are given in Table 3.

Rated voltage (V)	220/60Hz
Rated Power (HP)	3
Rated Torque (Nm)	11.9
Rated Speed (rad/s)	179
R_s, $R_r(\Omega)$	0.435, 0.816
L_{ls}, L_{lr} (H)	0.002, 0.002
L_m (H)	0.0693
$J(K_g m^2)$	0.089
P (pole pairs)	2

Table 3. Induction Motor Parameters [16]

The Figure 15 illustrates the torque response of the DTC-SVM scheme with T-S fuzzy controller when the step change in the motor load is apply. The electromagnetic torque tracked the reference torque and in this test is obtained the following good performance measures: rise time $t_r = 1.1ms$, settling time $t_s = 2.2ms$ and torque ripple $ripple = 2.93\%$. Also is observed that the behavior of the stator current is sinusoidal.

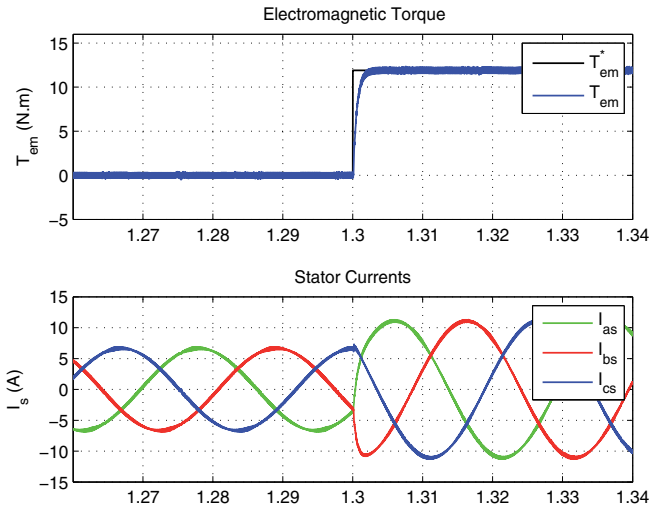

Figure 15. Electromagnetic torque and stator current response for step change in the motor load at fifty percent of rated speed

The Figure 16 presents the results when an arbitrary torque profile is imposed to DTC-SVM scheme with T-S fuzzy controller. In the first sub-figure the electromagnetic torque tracked the reference torque as expected, and in the next one the sinusoidal waveforms of the stator currents is shown. The Figure 17 shows space of the quadrature components of the stator flux and it shows the circular behavior of the stator flux when the torque profile is applied, and in consequence the proposed controller maintain the stator flux constant.

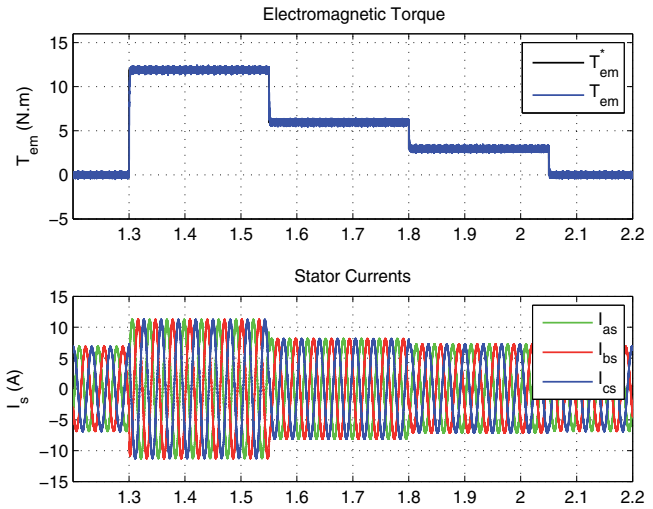

Figure 16. Electromagnetic torque and stator current response when is apply the load torque profile at fifty percent of rated speed

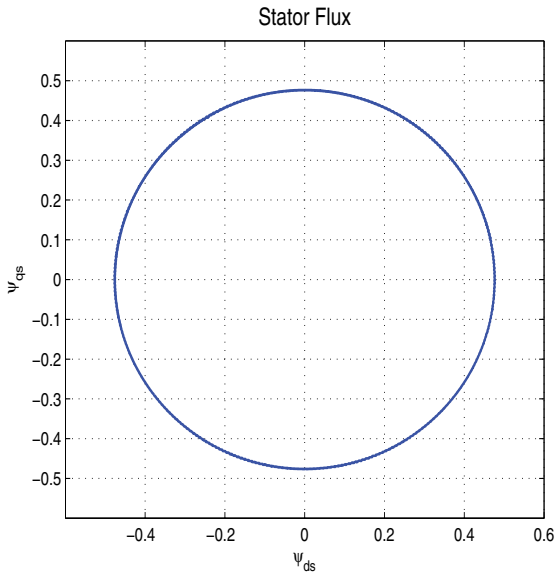

Figure 17. Space of the stator flux quadrature components.

The Figure 18 shows the behavior of the rotor angular speed ω_r, the electromagnetic torque and the phase **a** stator current waveform when a step change in the reference speed from 0.5 pu to -0.5 pu is imposed, with no-load. The torque was limited in 1.5 times the rated torque how it was projected and the sinusoidal waveforms of the stator current shown that this control technique allowed also a good current control because it is inherent to the algorithm control

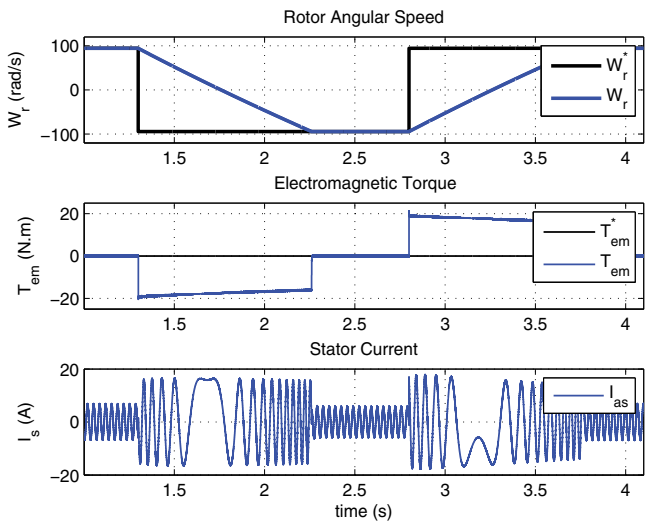

Figure 18. Rotor angular speed, electromagnetic torque and phase **a** stator current when was apply the no-load sudden change in the speed reference at fifty percent of rated speed

proposed in this chapter. All the test results showed the good performance of the proposed DTC-SVM scheme with T-S fuzzy controller.

6. Conclusion

This chapter presents the DTC-SVM scheme with T-S fuzzy controller for the three-phase IM. The conventional DTC-SVM scheme takes two PI controllers to generate the reference stator voltage vector. To improve the drawback of this conventional DTC-SVM scheme is proposed the Takagi-Sugeno fuzzy controller to substitute both PI controllers. The proposed controller calculates the quadrature components of the reference stator voltage vector in the stator flux reference frame. The rule base for the proposed controller is defined in function of the stator flux error and the electromagnetic torque error using trapezoidal and triangular membership functions. The direct component of the stator voltage takes a linear combination of its inputs as a consequent part of the rules, however, the quadrature component of the stator voltage takes the similar linear combination used in the first output but with the coefficients interchanged, not to be necessary another different coefficients values for this output. Constant switching frequency and low torque ripple are obtained using space vector modulation technique.

Simulations at different operating conditions have been carried out. The simulation results verify that the proposed DTC-SVM scheme with T-S fuzzy controller achieved good performance measures such as rise time, settling time and torque ripple as expected, It shown the fast torque response and low torque ripple in a wide range of operating conditions such as step change in the motor load, no-load sudden change in the speed reference, and the application of an arbitrary load torque profile. These results validate the proposed scheme.

Author details

José Luis Azcue and Ernesto Ruppert
University of Campinas (UNICAMP), Brazil

Alfeu J. Sguarezi Filho
CECS/UFABC, Santo André - SP, Brazil

7. References

[1] Abu-Rub, H., Guzinski, J., Krzeminski, Z. & Toliyat, H. [2004]. Advanced control of induction motor based on load angle estimation, *Industrial Electronics, IEEE Transactions on* 51(1): 5 – 14.

[2] Azcue P., J. L. [2009]. Modelamento e simulação do motor de indução trifásico. URL: *http://www.mathworks.fr/matlabcentral/fileexchange/24403-modelamento-e-simulação-do-motor-de-indução-trifásico*

[3] Azcue P., J. L. [2010]. *Three-phase induction motor direct torque control using self-tuning pi-type type fuzzy controller.*, Master's thesis, University of Campinas (UNICAMP). URL: *http://cutter.unicamp.br/document/?code=000777279*

[4] Azcue P., J. & Ruppert, E. [2010]. Three-phase induction motor dtc-svm scheme with self-tuning pi-type fuzzy controller, *Fuzzy Systems and Knowledge Discovery (FSKD), 2010 Seventh International Conference on*, Vol. 2, pp. 757 –762.

[5] Bertoluzzo, M., Buja, G. & Menis, R. [2007]. A direct torque control scheme for induction motor drives using the current model flux estimation, *Diagnostics for Electric Machines, Power Electronics and Drives, 2007. SDEMPED 2007. IEEE International Symposium on* pp. 185 –190.

[6] Buja, G. & Kazmierkowski, M. [2004]. Direct torque control of pwm inverter-fed ac motors - a survey, *Industrial Electronics, IEEE Transactions on* 51(4): 744–757.

[7] Cao, S., Liu, G. & Cai, B. [2009]. Direct torque control of induction motors based on double-fuzzy space vector modulation technology, *Information Engineering and Computer Science, 2009. ICIECS 2009. International Conference on*, pp. 1 –4.

[8] Chen, L., Fang, K.-L. & Hu, Z.-F. [2005]. A scheme of fuzzy direct torque control for induction machine, *Machine Learning and Cybernetics, 2005. Proceedings of 2005 International Conference on*, Vol. 2, pp. 803 –807 Vol. 2.

[9] Depenbrock, M. [1988]. Direct self-control (dsc) of inverter-fed induction machine, *Power Electronics, IEEE Transactions on* 3(4): 420 –429.

[10] Ding, X., Liu, Q., Ma, X., He, X. & Hu, Q. [2007]. The fuzzy direct torque control of induction motor based on space vector modulation, *Natural Computation, 2007. ICNC 2007. Third International Conference on*, Vol. 4, pp. 260 –264.

[11] Habetler, T., Profumo, F., Pastorelli, M. & Tolbert, L. [1992]. Direct torque control of induction machines using space vector modulation, *Industry Applications, IEEE Transactions on* 28(5): 1045 –1053.

[12] Holtz, J. [1992]. Pulsewidth modulation-a survey, *Industrial Electronics, IEEE Transactions on* 39(5): 410 –420.

[13] Jiang, Z., Hu, S. & Cao, W. [2008]. A new fuzzy logic torque control scheme based on vector control and direct torque control for induction machine, *Innovative Computing Information and Control, 2008. ICICIC '08. 3rd International Conference on*, p. 500.

[14] Kang, J.-K. & Sul, S.-K. [1999]. New direct torque control of induction motor for minimum torque ripple and constant switching frequency, *Industry Applications, IEEE Transactions on* 35(5): 1076 –1082.

[15] Koutsogiannis, Z., Adamidis, G. & Fyntanakis, A. [2007]. Direct torque control using space vector modulation and dynamic performance of the drive, via a fuzzy logic controller for speed regulation, *Power Electronics and Applications, 2007 European Conference on*, pp. 1 –10.

[16] Krause, P. C., Wasynczuk, O. & Sudhoff, S. D. [2002]. *Analysis of Electric Machinery and Drive Systems*, IEEE Press.

[17] Lascu, C., Boldea, I. & Blaabjerg, F. [2000]. A modified direct torque control for induction motor sensorless drive, *Industry Applications, IEEE Transactions on* 36(1): 122–130.

[18] Lin, G. & Xu, Z. [2010]. Direct torque control of induction motor based on fuzzy logic, *Computer Engineering and Technology (ICCET), 2010 2nd International Conference on*, Vol. 4, pp. V4–651 –V4–654.

[19] Pan, Y. & Zhang, Y. [2009]. Research on direct torque control of induction motor based on dual-fuzzy space vector modulation technology, *Fuzzy Systems and Knowledge Discovery, 2009. FSKD '09. Sixth International Conference on*, Vol. 6, pp. 383 –388.

[20] Park, Y.-M., Moon, U.-C. & Lee, K. [1995]. A self-organizing fuzzy logic controller for dynamic systems using a fuzzy auto-regressive moving average (farma) model, *Fuzzy Systems, IEEE Transactions on* 3(1): 75 –82.

[21] Pedrycz, W. & Gomide, F. [2007]. *Fuzzy Systems Engineering Toward Human-Centric Computing*, Wiley-IEEE Press.

[22] Reznik, L. [1997]. *Fuzzy Controllers Handbook: How to Design Them, How They Work*, Newnes.

[23] Takahashi, I. & Noguchi, T. [1986]. A new quick-response and high-efficiency control strategy of an induction motor, *Industry Applications, IEEE Transactions on* IA-22(5): 820 –827.

[24] van der Broeck, H., Skudelny, H. & Stanke, G. [1988]. Analysis and realization of a pulsewidth modulator based on voltage space vectors, *Industry Applications, IEEE Transactions on* 24(1): 142–150.

[25] Vas, P. [1998]. *Sensorless vector and Direct Torque Control*, Oxford University Press.

[26] Viola, J., Restrepo, J., Guzman, V. & Gimenez, M. [2006]. Direct torque control of induction motors using a fuzzy inference system for reduced ripple torque and current limitation, *Power Electronics and Motion Control Conference, 2006. EPE-PEMC 2006. 12th International*, pp. 1161 –1166.

[27] Zhou, K. & Wang, D. [2002]. Relationship between space-vector modulation and three-phase carrier-based PWM: a comprehensive analysis [three-phase inverters], *Industrial Electronics, IEEE Transactions on* 49(1): 186–196.

Chapter 15

Industrial Application of a Second Order Sliding Mode Observer for Speed and Flux Estimation in Sensorless Induction Motor

Sebastien Solvar, Malek Ghanes, Leonardo Amet,
Jean-Pierre Barbot and Gaëtan Santomenna

Additional information is available at the end of the chapter

http://dx.doi.org/10.5772/52910

1. Introduction

Recently, considerable research efforts are focused on the sensorless Induction Motors (*IM*) control problem. We refer the reader to [12] for a tutorial account on the topic. Indeed, industries concerned by sensorless *IM* drives are continuously seeking for cost reductions in their products. The main drawback of *IM* is the mechanical sensor. The use of such direct speed sensor induces additional electronics, extra wiring, extra space, frequent maintenance, careful mounting and default probability. Moreover, the sensor is vulnerable for electromagnetic noise in hostile environments and has a limited temperature range.

To avoid mechanical sensor (speed, position and load torque) of *IM*, several approaches for the so-called "sensorless control" have attracted a great deal of attention recently (see for example [21], [15], [22], [16], [11], [14], [6], [10], [1], [8], [19]. These methods can be classified into three main strategies.

- Artificial intelligence strategies [22], [19].
- Strategies based on IM spatial saliency methods with fundamental excitation and high frequency signal injection [16], [12].
- Fundamental motor model strategies: adaptive observer [21], Luenberger observe [15], Kalman filter observer [11], high gain observer [14], [6], sliding mode observer [10], [1], interconnected high gain observer [8].

This chapter belongs to the third strategy using mainly observer methods.

First and second strategies have been a subject of growing interest in recent years. For example the second strategy based on IM spatial saliency with extra converters is a robust and physical method. But artificial intelligence and spatial saliency algorithms are quite heavy for basic microprocessors.

The third strategy that is a powerful observer that can estimate simultaneously variables and parameters of a large class of nonlinear systems doesn't require a very high performance processor for real time implementation but they are often tested at high speed in sensorless *IM* whereas the main difficulties are mainly at very low frequencies [10], [8].

However for our best of knowledge, examination of the literature on the third strategy shows that the real time computation constraints with a cheapest microprocessors or microprocessors not specially allowed to this task[1] are not taken into account to deal with industrial applications of sensorless *IM* including very low frequencies drives.

Meanwhile, compared with other observers, sliding mode technic [20] have attractive advantages of robustness against matching disturbances and, insensitivity to some specific variation of parameters in sliding mode behavior. However, the chattering effect (that is inherent to standard first sliding mode technic) is often an obstacle for practical applications. Higher-Order Sliding Modes (see for example [2], [18] and [5]) are one of the solutions which does not compromise robustness and avoid filtering of estimated variables as considered by other methods.

In this chapter, a second order sliding mode observer for the *IM* without mechanical sensor is presented for the open problem of sensorless *IM* drives at very low frequency. This observer converges in finite time and is robust to the variation of parameters. To illustrate the proposed observer, firstly a very simple case is presented in order to exemplified the tuning parameters. Then, to highlight the technological interest of the proposed method and also show the difficulties due to real time computation constraints when a basic microprocessors are used, an industrial application is proposed.

This paper is organized as follows: the section 2 recalls both *IM* model and unobservability phenomena of *IM*. In section 3 the super twisting algorithm (second sliding mode observer) is first presented in a simple case and then applied for sensorless *IM*. After that the section 4 proposes a discrete version of the super twisting observer. In section 5 the experimental results of the proposed observer carried out in an industrial framework are presented. Some conclusions and remarks are drawn in section VII.

2. Technical background

2.1. *IM* model

In [4] the following *IM* model is proposed, in the fixed (α,β) frame:

$$\begin{cases} \dot{i}_{s\alpha} &= -\dfrac{R_s L_r^2 + R_r M_{sr}^2}{\sigma L_s L_r^2}\, i_{s\alpha} + \dfrac{M_{sr}}{\sigma L_s L_r}\,(\dfrac{R_r}{L_r}\,\phi_{r\alpha} + p\,\Omega\phi_{r\beta}) + \dfrac{1}{\sigma L_s}\,v_{s\alpha} \\ \dot{i}_{s\beta} &= -\dfrac{R_s L_r^2 + R_r M_{sr}^2}{\sigma L_s L_r^2}\, i_{s\beta} + \dfrac{M_{sr}}{\sigma L_s L_r}\,(\dfrac{R_r}{L_r}\,\phi_{r\beta} - p\,\Omega\phi_{r\alpha}) + \dfrac{1}{\sigma L_s}\,v_{s\beta} \\ \dot{\phi}_{r\alpha} &= \dfrac{M_s r R_r}{L_r}\, i_{s\alpha} - \dfrac{R_r}{L_r}\,\phi_{r\alpha} - p\,\Omega\phi_{r\beta} \\ \dot{\phi}_{r\beta} &= \dfrac{M_s r R_r}{L_r}\, i_{s\beta} - \dfrac{R_r}{L_r}\,\phi_{r\beta} + p\,\Omega\phi_{r\alpha} \\ \dot{\Omega} &= \dfrac{p M_s r}{J L_r}\,(\phi_{r\alpha} i_{s\beta} - \phi_{r\beta} i_{s\alpha}) - \dfrac{f}{J}\,\Omega - \dfrac{1}{J}\,T_l \end{cases} \tag{1}$$

[1] The microprocessors may be dedicated to many process tasks as supervision process, communication process in addition to the considered task

As the mechanical position and magnetic variables are unknown, $d-q$ frame is well appropriate for sensorless observer based control design.

***IM* parameters:**

- R_S: Stator resistance ($Ohms$).
- R_R: Rotor resistance ($Ohms$).
- L_S: Stator inductance ($Ohms$).
- L_R: Rotor inductance (H).
- L_M: Mutual inductance (H).
- p: number of pole pairs.
- f: viscous friction coefficient ($Nm.s/rad$).
- J: inertia ($Kg.m^2$).

***IM* variables :**

- $v_{s\alpha,\beta}$: Stator voltage (V).
- $i_{s\alpha,\beta}$: Stator current (A).
- $\phi_{r\alpha,\beta}$: Rotor flux (Wb).
- Ω: Mechanical speed (rad/s).
- T_l: Load torque (Nm).

In order to construct the proposed observer for an industrial application, we work with a per unit model, under the following equations :

$$\begin{cases} \dot{x}_1 = -\gamma\, x_1 + \theta\,(b\, x_3 + c\, x_5 x_4) + \xi\, v_1 \\ \dot{x}_2 = -\gamma\, x_2 + \theta\,(b\, x_4 - c\, x_5 x_3) + \xi\, v_2 \\ \dot{x}_3 = a\, x_1 - b\, x_3 - c\, x_5 x_4 \\ \dot{x}_4 = a\, x_2 - b\, x_4 + c\, x_5 x_3 \\ \dot{x}_5 = h\,(x_3 x_2 - x_4 x_1) - d\, x_5 - e\, T_l \end{cases} \tag{2}$$

With the following parameters:

$$\begin{array}{llllll} x_1 = \dfrac{i_{s\alpha}}{I_{ref}} & x_2 = \dfrac{i_{s\beta}}{I_{ref}} & x_3 = \dfrac{\omega_{ref}\phi_{r\alpha}}{V_{ref}} & x_4 = \dfrac{\omega_{ref}\phi_{r\beta}}{V_{ref}} & x_5 = \dfrac{p\,\Omega}{\omega_{ref}} \\ a = \dfrac{M_{sr} I_{ref}\,\omega_{ref}}{T_r V_{ref}} & b = \dfrac{1}{\tau_r} & c = \omega_{ref} & d = \dfrac{f_v}{J} & \\ e = \dfrac{p}{J\,\omega_{ref}} & h = \dfrac{p^2\, M_{sr} I_{ref} V_{ref}}{J\omega_{ref}^2 L_r} & \theta = \dfrac{K V_{ref}}{I_{ref}\omega_{ref}} & \xi = \dfrac{V_{ref}}{\sigma\ L_s I_{ref}} & \\ \sigma = 1 - \dfrac{M_{sr}^2}{L_s L_r} & \gamma = \dfrac{R_s L_r^2 + R_r M_{sr}^2}{\sigma L_s L_r^2} & \tau_r = \dfrac{L_r}{R_r} & K = \dfrac{M_{sr}}{\sigma L_s L_r} & \end{array}$$

Thus for the sake of homogeneity, hereafter experimental results will be given in per-unit (p.u.).

2.2. Observability

The *IM* observability has been studied by several authors (see for example [3], [13], [9]). In [9], it is proved that the IM observability cannot be established in the particular case when fluxes $\Phi_{r\alpha}$, $\Phi_{r\beta}$ and speed Ω are constant, even if we use the higher derivatives of currents. This is a sufficient and necessary condition for lost of observability.

This operating case match to the following physically interpretation:

Constant fluxes $(\dot{\phi}_{r\alpha} = \dot{\phi}_{r\beta} = 0)$

With ω_s the stator voltage pulsation and T_{em} the electromagnetic torque.

$$\omega_s = p\Omega + \frac{R_r T_{em}}{p\Phi_{rd}^2} = 0 \tag{3}$$

where $\Phi_{rd}^2 = \phi_{r\alpha}^2 + \phi_{r\beta}^2$ is the square of the direct flux in (d, q) frame.

Constant speed $(\dot{\Omega} = 0)$

$$T_{em} = f\Omega + T_l \tag{4}$$

Thanks to previous equations, we obtain:

$$T_l = -\left(f + \frac{p^2\Phi_{rd}^2}{R_r}\right)\Omega \tag{5}$$

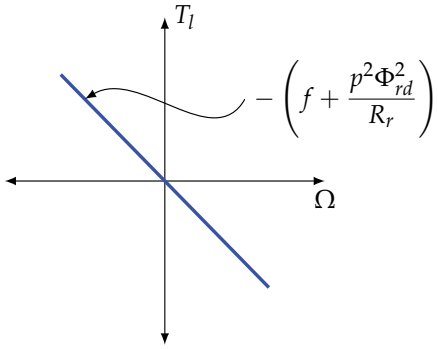

Figure 1. Inobservability curve

The unobservability curve in the map (T_l, Ω) is shown in figure (1).

Obviously, the observability is lost gradually when we approach this curve [9].

3. Second order sliding mode observer

3.1. Super twisting algorithm: An academic example

Sliding modes were used at first, as a control technique, but in the recent years it presented as a very good tool for observer design [17], [17], [5].

Considering the following system:

$$\begin{cases} \dot{x}_1 = x_2 \\ \dot{x}_2 = f(x,t) \\ y \ = h(x) = x_1 \end{cases} \tag{6}$$

With $f(x,t)$ a bounded function.

For system (6), a second order sliding mode observer is designed in the following way:

$$\begin{cases} \dot{\hat{x}}_1 = \hat{x}_2 + \lambda |e_1|^{\frac{1}{2}} sign(e_1) \\ \dot{\hat{x}}_2 = \alpha sign(e_1) \end{cases} \tag{7}$$

$$\text{With } \lambda, \alpha > 0 \quad \text{ and } \quad e_1 = x_1 - \hat{x}_1.$$

The efficiency of the this strategy depends on coefficients α and λ. For second order system (6)we show convergence of estimated variables ($\hat{x}_1$,$\hat{x}_2$) to (x_1,x_2) by studying dynamics errors $\dot{e}_1$ and $\dot{e}_2$.

Thus

$$\begin{cases} \dot{e}_1 = \dot{x}_1 - \dot{\hat{x}}_1 = e_2 - \lambda |x_1 - \hat{x}_1|^{\frac{1}{2}} sign(x_1 - \hat{x}_1) \\ \dot{e}_2 = \dot{x}_2 - \dot{\hat{x}}_2 = f(x,t) - \alpha sign(x_1 - \hat{x}_1) \end{cases} \tag{8}$$

With

$$f(x,t) \in [-f^+, f^+], \quad e_2 = x_2 - \hat{x}_2$$

And

$$\ddot{e}_1 = f(x,t) - \alpha sign(e_1) - \frac{1}{2}\lambda |e_1|^{-\frac{1}{2}} \dot{e}_1$$

Thus

$$\ddot{e}_1 \in [-f^+, f^+] - \alpha sign(e_1) - \frac{1}{2}\lambda |e_1|^{-\frac{1}{2}} \dot{e}_1$$

Where

$$f^+ = max\{f(x,t)\}$$

Conditions on λ and α that permit a convergence in finite time of ($\dot{e}_1$,e_1) to (0,0) are derived hereafter according to figure 2.

Proposition: For any initial conditions $x(0)$, $\hat{x}(0)$, there exists a choice of λ and α such that the error dynamics $\dot{e}_1$ and $\dot{e}_2$ converge to zero in finite time and by consequence $\hat{x}_1 \longmapsto x_1$ and $\hat{x}_2 \longmapsto x_2$.

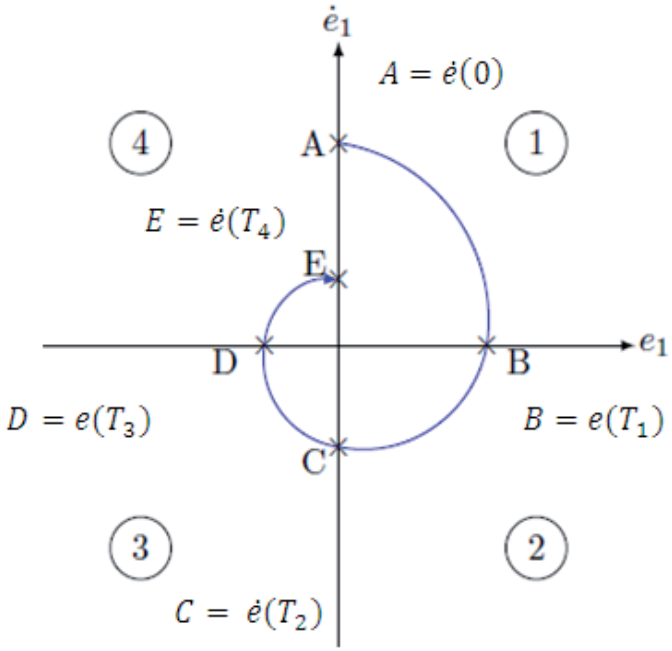

Figure 2. Upper bound of finite time convergence curve.

Proof: Consider system (6). To show the convergence of $(\hat{x}_1, \hat{x}_2)$ to (x_1, x_2) (ie., $(e_1, e_2) \rightarrow (0,0)$), we need to show that

$$\frac{|\dot{e}_1(T_2)|}{|\dot{e}_1(0)|} < 1 \tag{9}$$

of figure 2, where $\dot{e}_1(T_2) = C$ and $\dot{e}_1(0) = A$.

Figure 2 illustrates the finite time convergence behavior of the proposed observer for system 6. In what follows we will give the error trajectory for each quadrant in the worst cases.

Let consider the system's dynamic $\ddot{e}_1$

$$\ddot{e}_1 = f(x,t) - \alpha sign(e_1) - \frac{\lambda}{2}|e_1|^{-\frac{1}{2}}\dot{e}_1 \tag{10}$$

with $\frac{d|x|}{dt} = \dot{x}sign(x)$.

Equation (10) leads to

$$\ddot{e}_1 \in \left[-f^+, f^+\right] - \alpha sign(e_1) - \frac{\lambda}{2}|e_1|^{-\frac{1}{2}}\dot{e}_1 \tag{11}$$

where

$$f^+ = max(f(t,x)),$$

First quadrant: $e_1 > 0$ and $\dot{e}_1 > 0$

Starting from point A of figure 2 the trajectory of $\dot{e}_1 = f(e_1)$ is in the first quadrant $e_1 \geq 0$ and $\dot{e}_1 \geq 0$. The rising trajectory is given by $\ddot{e}_1 = -(\alpha - f^+)$.

By choosing

$$\alpha > f^+ \tag{12}$$

we ensure that $\ddot{e}_1 < 0$ and hence $\dot{e}_1$ decreases and tends towards the y-axis, corresponding to $\dot{e}_1 = 0$ (point B in figure 2).

Computing of $e_1(T_1)$

From (10), we have

$$\ddot{e}_1 = -(\alpha - f^+)$$

Which implies that

$$\dot{e}_1(t) = -(\alpha - f^+)t + \dot{e}_1(0) \tag{13}$$

And

$$e_1(t) = -(\alpha - f^+)\frac{t^2}{2} + \dot{e}_1(0)t$$

From (13), since $\dot{e}_1(T_1) = 0$, we obtain the necessary time for going from A to B with $B = e_1(T_1)$.

$$T_1 = \frac{\dot{e}_1(0)}{(\alpha - f^+)} \tag{14}$$

Then we can compute $e(T_1)$ as follows

$$\begin{aligned} e_1(T_1) &= -(\alpha - f^+)\frac{\dot{e}_1^2(0)}{2(\alpha - f^+)} + \frac{\ddot{e}_1^2(0)}{(\alpha - f^+)} \\ &= \frac{\dot{e}_1^2(0)}{2(\alpha - f^+)} \end{aligned} \tag{15}$$

Second quadrant: $e_1 > 0$ and $\dot{e}_1 < 0$

In this case, $\ddot{e}_1 = -f^+ - \alpha sign(e_1) - \frac{\lambda}{2}|e_1|^{-\frac{1}{2}}\dot{e}_1$

becomes negative $(\ddot{e}_1 < 0)$ on making a good choice of α which leads to

$$(\alpha + f_1^+) > -\frac{\lambda_1}{2}|e_1|^{-\frac{1}{2}}\dot{e}_1 \tag{16}$$

Since $\dot{e}_1$ is negative, then

$$|\dot{e}_1(t)| \leq \frac{2(\alpha + f_1^+)}{\lambda}|e_1(t)|^{\frac{1}{2}} \tag{17}$$

Considering by the sake of simplicity (17), $e_1 > 0$ and $\dot{e}_1 < 0$.

Integrating (17) with $e_1(0) = 0$ gives

$$\sqrt{e_1(t)} = \frac{(\alpha + f^+)}{\lambda} t \tag{18}$$

At $t = T_2$, we should make the inverse of function (18) from point B to C in figure 2. This leads to

$$e_1(T_2) = e_1(T_1). \tag{19}$$

Then (18) becomes

$$\sqrt{e_1(T_1)} = \frac{(\alpha + f^+)}{\lambda} T_2 \tag{20}$$

By replacing $e_1(T_1)$ coming from (15) in equation (20), we get the necessary time for going from B to C

$$T_2 = \frac{\lambda}{(\alpha + f^+)} \frac{\dot{e}_1(0)}{\sqrt{2}(\alpha - f^+)} \tag{21}$$

After that, by using the argument of (19) in equation (17) evaluated at $t = T_2$ in the worth case, we get

$$|\dot{e}_1(T_2)| = \frac{2(\alpha + f_1^+)}{\lambda} |e_1(T_1)|^{\frac{1}{2}} \tag{22}$$

By replacing $e_1(T_1)$ by its expression given by (15) in (22), we get

$$|\dot{e}_1(T_2)| = \frac{2(\alpha + f_1^+)}{\lambda} \frac{|\dot{e}_1(0)|}{\sqrt{2}\sqrt{(\alpha - f^+)}} \tag{23}$$

Thus, by satisfying inequality (9) in equation (23) λ should be chosen as

$$\lambda > (\alpha + f_1^+) \sqrt{\frac{2}{(\alpha - f^+)}} \tag{24}$$

Finally, conditions (12) and (24) of the observer parameters are sufficient conditions guaranteeing the state convergence (i.e. the states $(e_1, \dot{e}_1)$ tend towards $e_1 = \dot{e}_1 = 0$ (Figure 2).

This ends the proof.

Moreover the convergence is in finite time, because from (14) and 21 we obtain

$$T_\infty \leq (\sum_{i=0}^{+\infty} (\frac{\sqrt{2}(\alpha + f^+)}{\lambda\sqrt{\alpha - f^+}})^i)(\frac{\lambda}{\sqrt{2}(\alpha + f^+)} + 1) \frac{\dot{e}_1(0)}{(\alpha - f^+)}$$

as

$$|\frac{\sqrt{2}(\alpha + f^+)}{\lambda\sqrt{\alpha - f^+}}| < 1$$

we obtain a bounded limit

$$T_\infty \leq \left(\frac{1}{1-\frac{\sqrt{2}(\alpha+f^+)}{\lambda\sqrt{\alpha-f^+}}}\right)\left(\frac{\lambda}{\sqrt{2}(\alpha+f^+)}+1\right)\frac{\dot{e}_1(0)}{(\alpha-f^+)}$$

Here we give simulations of a very simple example. The function $f(t,x)$ in system (6) is set equal to $sin(t)$ with $f^+ = max\{sin(t)\} = 1$. We get

$$\begin{cases} \dot{x}_1 = x_2 \\ \dot{x}_2 = sin(t) \\ y = x_1 \end{cases} \tag{25}$$

The associated observer is:

$$\begin{cases} \dot{\hat{x}}_1 = \tilde{x}_2 + \lambda|e_1|^{\frac{1}{2}} sign(e_1) \\ \dot{\tilde{x}}_2 = \alpha sign(e_1) \end{cases} \tag{26}$$

The simulation results are shown in figure 3. It can be seen that figure (3) spotlight *two* steps into Super Twisting Algorithm, which are convergence step in finite time, and sliding mode. Indeed observer is working on $t = 1s$ with $\hat{x}_1(0) = 1$ and $\tilde{x}_2(0) = 1$. $\hat{x}_1$ converges under $1s$ to x_1, and then slides along x_1 path, and equal to $\tilde{x}_2$.

3.2. Application to *Induction Motor*

At first, due to the nonlinearity of flux and speed product, the *IM* model (2) is not written in a suitable form allowing to apply the super twisting algorithm presented in previous section. To overcome this difficulty, we make the following change of variables in order to rewrite the *IM* model (2) (without $\dot{x}_5$ equation) into a form 6:

$$\begin{cases} z_1 = x_1 \\ z_2 = x_2 \\ z_3 = b\, x_3 + c\, x_5 x_4 \\ z_4 = b\, x_4 - c\, x_5 x_3 \\ z_5 = \dot{z}_3 \\ z_6 = \dot{z}_4 \end{cases} \tag{27}$$

Equation 27 is not a diffeomorphism, not an homeomorphism but only an immersion, because the dimension of x is 5 and the dimension of z is 6. Nevertheless, this immersion is used in order to avoid some singularities in a speed estimation as this will be pointed out in the next.

From the *IM* model (2) and (27), we obtain a new dynamical system as following:

$$\begin{cases} \dot{z}_1 = -z_1 + \theta z_3 + \xi v_1 \\ \dot{z}_2 = -\gamma z_2 + \theta z_4 + \xi v_2 \\ \dot{z}_3 = z_5 \\ \dot{z}_4 = z_6 \end{cases} \tag{28}$$

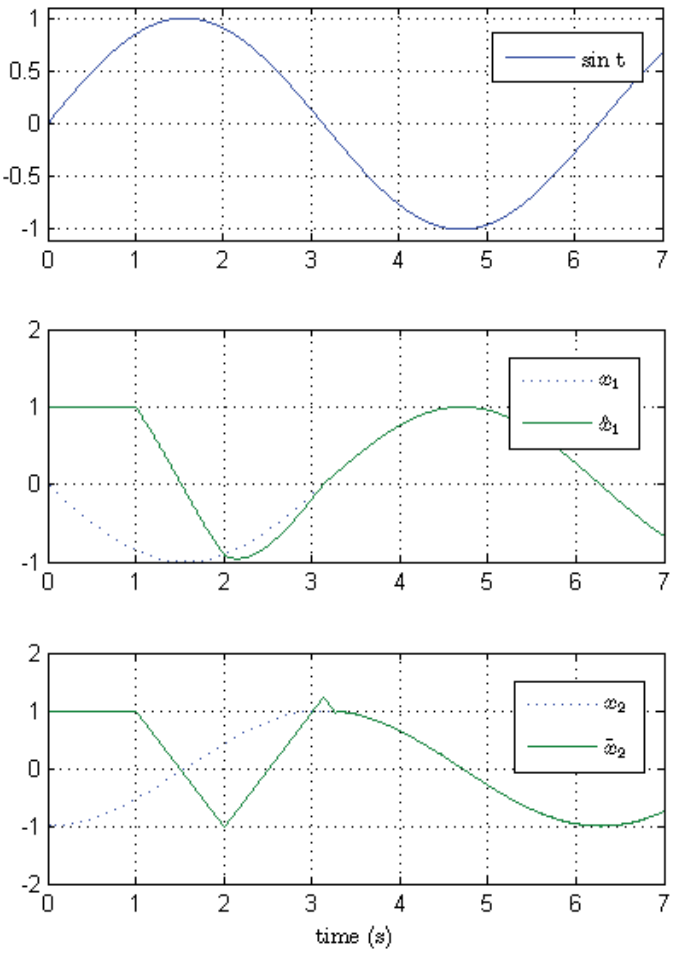

Figure 3. Super Twisting Algorithm example.

Thus, we can propose a new observer structure for dynamical system (28):

$$\begin{cases} \dot{\hat{z}}_1 = \theta\,\tilde{z}_3 - \gamma\,z_1 + \xi\,v_1 + \lambda_1\,|e_1|^{\frac{1}{2}}\,sign(e_1) \\ \dot{\tilde{z}}_3 = \alpha_1\,sign(e_1) \\ \dot{\hat{z}}_2 = \theta\,\tilde{z}_4 - \gamma\,z_2 + \xi\,v_2 + \lambda_2\,|e_2|^{\frac{1}{2}}\,sign(e_2) \\ \dot{\tilde{z}}_4 = \alpha_2\,sign(e_2) \\ \dot{\hat{z}}_3 = E_1\,E_2\,(\tilde{z}_5 + \lambda_3\,|e_3|^{\frac{1}{2}}\,sign(e_3)) \\ \dot{\tilde{z}}_5 = E_1\,E_2\,\alpha_3\,sign(e_3) \\ \dot{\hat{z}}_4 = E_1\,E_2\,(\tilde{z}_6 + \lambda_4\,|e_4|^{\frac{1}{2}}\,sign(e_4)) \\ \dot{\tilde{z}}_6 = E_1\,E_2\,\alpha_4\,sign(e_4) \end{cases} \tag{29}$$

$$\text{with } E_i \begin{cases} 1 \text{ if } e_i = z_i - \hat{z}_i = 0, i = 1,2 \\ 0 \text{ if not} \end{cases} \tag{30}$$

This observer structure depends on Super Twisting Algorithm presented in previous section and Step by Step proficiencies [7]. We propose to put in multiples-series observers with functions (E_i).

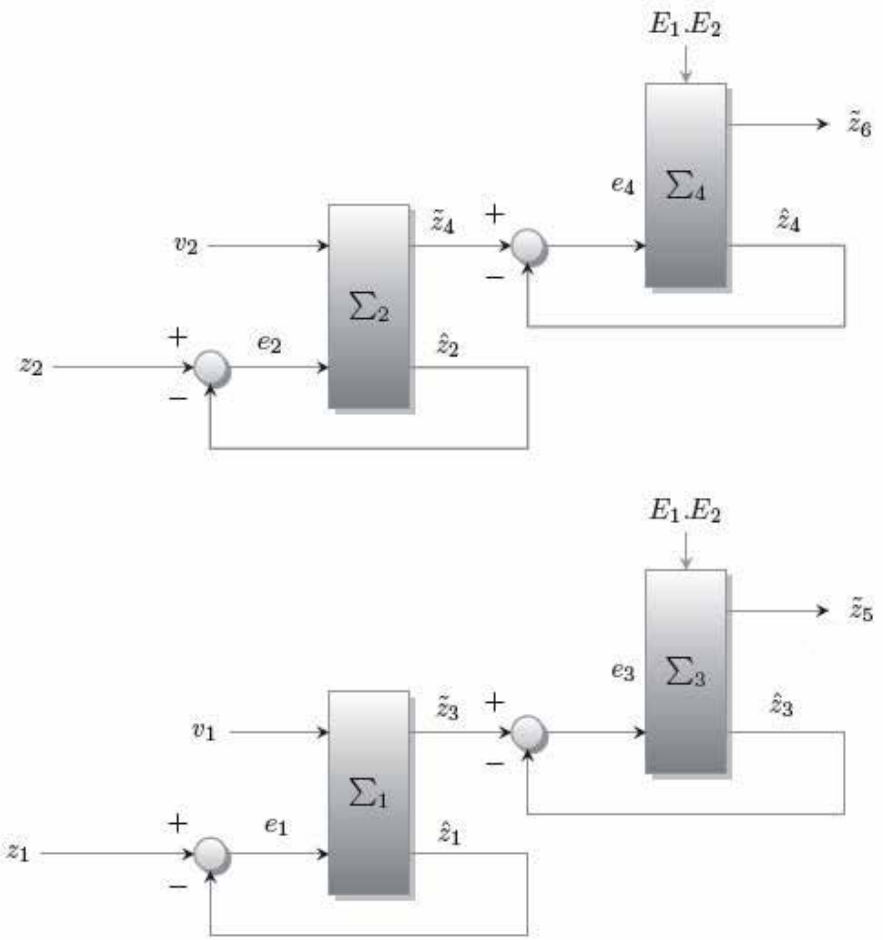

Figure 4. General *IM* Observer Structure.

The functions E_i ensure that the next steps errors do not escape too far before one has the convergent of the last step error.

The gains α_i, λ_i are chosen which respect to the reachability condition of the Super Twisting algorithm as stated in inequalities (12) and (24) of previous section. By choosing

$$\alpha_1 > max(\theta z_3), \quad \lambda_1 > (max(\theta z_3) + \alpha_1)\sqrt{\frac{2}{\alpha_1 - max(\theta z_3)}} \tag{31}$$

$$\alpha_2 > max(\theta z_4), \quad \lambda_2 > (max(\theta z_4) + \alpha_2)\sqrt{\frac{2}{\alpha_2 - max(\theta z_4)}} \tag{32}$$

$$\alpha_3 > max(z_5), \quad \lambda_3 > (max(z_5) + \alpha_3)\sqrt{\frac{2}{\alpha_3 - max(z_5)}} \tag{33}$$

$$\alpha_4 > max(z_6), \quad \lambda_4 > (max(z_6) + \alpha_4)\sqrt{\frac{2}{\alpha_4 - max(z_6)}} \tag{34}$$

and we get

$$e_1 = e_2 = e3 = e_4 = 0$$

i.e.

$$\begin{aligned} \hat{z}_1 &= z_1, \quad \hat{z}_2 = z_2 \\ \hat{z}_3 &= \tilde{z}_3, \quad \hat{z}_4 = \tilde{z}_4 \\ \tilde{z}_5 &= z_5, \quad \tilde{z}_6 = z_6 \end{aligned}$$

Consequently all variables z_1, z_2, $\hat{z}_3$, $\hat{z}_4$, $\tilde{z}_5$, $\tilde{z}_6$ are available and then we can deduce *IM* variables.

We propose to treat this problem in two different cases: $\dot{x}_5 \neq 0$, and $\dot{x}_5 = 0$

CASE A : $\dot{x}_5 \neq 0$

Firstly we propose to express fluxes x_3 and x_4, from equation (27) we obtain:

$$\begin{aligned} \hat{z}_3 &= bx_3 + cx_5x_4 \\ \hat{z}_4 &= bx_4 - cx_5x_3 \end{aligned}$$

We deduce

$$x_3 = \frac{\hat{z}_3 - cx_5x_4}{b} \tag{35}$$

$$x_4 = \frac{\hat{z}_4 + cx_5x_3}{b} \tag{36}$$

By substituting x_4 by its expression in (35) and x_3 in (36) we have:

$$\begin{aligned} x_3 &= \frac{\hat{z}_4 + \frac{c}{b} z_3 x_5}{b + \frac{c^2 x_5^2}{b}} \\ x_4 &= \frac{\hat{z}_3 - \frac{c}{b} z_4 x_5}{b + \frac{c^2 x_5^2}{b}} \end{aligned} \tag{37}$$

Now let us express x_5. From (2) we know

$$\begin{aligned} \dot{x}_3 &= ax_1 - bx_3 - cx_5x_4 \\ \dot{x}_4 &= ax_2 - bx_4 + cx_5x_3 \end{aligned} \tag{38}$$

Firstly we propose to write $\dot{x}_3$ and $\dot{x}_4$ as a function of variables z. By using (27) in (38), we get:

$$\begin{aligned} \dot{x}_3 &= az_1 - \hat{z}_3 \\ \dot{x}_4 &= az_2 - \hat{z}_4 \end{aligned} \tag{39}$$

By Replacing (39) in (38) and using the two first equations in (27), it follows

$$\hat{z}_3 = bx_3 + cx_5x_4 \tag{40}$$

$$\hat{z}_4 = bx_4 - cx_5x_3 \tag{41}$$

Taking the time derivative of (41) and using third-fourth equations in (27) yields to

$$\dot{z}_3 = \tilde{z}_5 = b\dot{x}_3 + c\dot{x}_5x_4 + c\dot{x}_4x_5 \tag{42}$$

$$\dot{z}_4 = \tilde{z}_6 = b\dot{x}_4 - c\dot{x}_5x_3 - c\dot{x}_3x_5 \tag{43}$$

From (42) we have:

$$\dot{x}_5 = \frac{\tilde{z}_5 - b\dot{x}_3 - cx_5\dot{x}_4}{cx_4} \tag{44}$$

By substituting (44) in (43), we get

$$\tilde{z}_6 = b\dot{x}_4 - cx_5\dot{x}_3 - x_3\frac{\tilde{z}_5 - b\dot{x}_3 - cx_5\dot{x}_4}{x_4} \tag{45}$$

Then we can deduce the motor speed x_5 by replacing in (45) expressions of x_3-x_4 and $\dot{x}_3$-$\dot{x}_4$ coming from (37) and (39), respectively.

After a straightforward computations, we obtain a second order expression of x_5:

$$\pi_1 x_5^2 + \pi_2 x_5 + \pi_3 = 0 \tag{46}$$

where

$$\begin{aligned} \pi_1 &= \frac{c}{b}\left[(az_2 - \hat{z}_4)\hat{z}_3 - (az_1 - \hat{z}_3)\hat{z}_4\right] \\ \pi_2 &= \frac{c}{b}\left[b(az_1 - \hat{z}_3)\hat{z}_3 - b(az_2 - \hat{z}_4)\hat{z}_4 - \tilde{z}_5\hat{z}_3 + \hat{z}_4\tilde{z}_6\right] \\ \pi_3 &= \hat{z}_3\left[-\tilde{z}_6 + b(az_2 - \hat{z}_4)\right] - \hat{z}_4\left[\tilde{z}_5 - b(az_1 - \hat{z}_3)\right] \end{aligned}$$

CASE B : $\dot{x}_5 = 0$

We propose this hypothesis because of dynamical gap evolution between electrical and mechanical variables, in fact speed evolves much more slowly than currents or fluxes.

Thus with this hypothesis we simplify (42) and (43), and obtain two expressions of x_5 :

$$x_5 = \frac{\tilde{z}_5 - b\dot{x}_3}{c\dot{x}_4} \tag{47}$$

or

$$x_5 = \frac{b\dot{x}_4 - \tilde{z}_6}{c\dot{x}_3} \tag{48}$$

we change $\dot{x}_3$ by expression (35) and $\dot{x}_4$ by expression(36)

$$x_5 = \frac{\tilde{z}_5 - baz_1 + b\hat{z}_3}{caz_2 - c\hat{z}_4} \tag{49}$$

or

$$x_5 = \frac{\tilde{z}_6 + baz_2 - b\hat{z}_4}{caz_1 - c\hat{z}_3} \tag{50}$$

Equations (49) and (50) are true only if :

$$caz_2 - c\hat{z}_4 \neq 0 \text{ for (49) and } caz_1 - c\hat{z}_3 \neq 0 \text{ for (50)}$$

Speed estimation

In order to avoid singularities of speed estimation in (49) and (50), we use the fact that (49) and (50) are in quadrature and thus we get the estimation of speed x_5 as follows :

$$x_5 = \frac{(\tilde{z}_5 - baz_1 + b\hat{z}_3)(caz_2 - c\hat{z}_4) + (\tilde{z}_6 + baz_2 - b\hat{z}_4)(caz_1 - c\hat{z}_3)}{(caz_2 - c\hat{z}_4)^2 + (caz_1 - c\hat{z}_3)^2} \tag{51}$$

Flux estimation

The rotor flux are obtained by replacing the estimation speed (51) in (37)

Flux position estimation

Having the rotor flux estimation (37), we can obtain rotor flux position ρ

$$\rho = atan(\frac{x_4}{x_3}) \tag{52}$$

4. Discrete time implementation

4.1. Explicit Euler method

For the industrial application in real time, the discrete time observer is designed. The explicit Euler's method is chosen to transform continuous observer to discrete observer. This is due to the simplicity of computation. Considering a differential equation :

$$\dot{x} = f(x)$$

The explicit Euler's method with a sampling time T_e gives:

$$x(k) = x(k-1) + T_e f(x(k-1))$$

the data acquisition period T_e is also the computation period.

Applying the explicit Euler's method for the second order sliding mode observer, the discrete observer is obtained:

$$\begin{cases} \hat{z}_1(k) = \hat{z}_1(k-1) + T_e \left[\theta\, \tilde{z}_3(k-1) - \gamma\, z_1(k-1) + \xi\, v_1(k-1) \right. \\ \qquad\qquad \left. + \lambda_1\, |e_1(k-1)|^{\frac{1}{2}}\, sign(e_1(k-1))\right] \\ \tilde{z}_3(k) = \tilde{z}_3(k-1) + T_e \;\; \alpha_1\, sign(e_1(k-1)) \\ \hat{z}_2(k) = \hat{z}_2(k-1) + T_e \left[\theta\, \tilde{z}_4(k-1) - \gamma\, z_2(k-1) + \xi\, v_2(k-1) \right. \\ \qquad\qquad \left. + \lambda_2\, |e_2(k-1)|^{\frac{1}{2}}\, sign(e_2(k-1))\right] \\ \tilde{z}_4(k) = \tilde{z}_4(k-1) + T_e\, \alpha_2\, sign(e_2(k-1)) \\ \hat{z}_3(k) = \tilde{z}_3(k-1) + T_e\, E_1\, E_2 \left[\tilde{z}_5(k-1) + \lambda_3\, |e_3(k-1)|^{\frac{1}{2}}\, sign(e_3(k-1))\right] \\ \tilde{z}_5(k) = \tilde{z}_5(k-1) + T_e\, E_1\, E_2\, \alpha_3\, sign(e_3(k-1)) \\ \hat{z}_4(k) = \hat{z}_4(k-1) + T_e\, E_1\, E_2 \left[\tilde{z}_6(k-1) + \lambda_4\, |e_4(k-1)|^{\frac{1}{2}}\, sign(e_4(k-1))\right] \\ \tilde{z}_6(k) = \tilde{z}_6(k-1) + T_e\, E_1\, E_2\, \alpha_4\, sign(e_4(k-1)) \end{cases} \tag{53}$$

4.2. Oversampling

To achieve good accuracy, a small sample period and fast DSP are needed. In the industrial application, the DSP clock frequency is only $150MHz$, which does not allow a small enough sample period. So in experimentation an over-sample technique is proposed. In the following paragraphs we show that, under a few low restrictive conditions, it is possible to reduce the error of Euler's method, seen in the previous subsection (4.1).

Hereafter we first present the oversampling method in a very simple use, where $f \in C^{\infty}$. Assume a continuous autonomous system of the form:

$$\dot{x} = f(x); \quad x(t_0) = x_0 \tag{54}$$

Assume in addition that the system is discretized at a sampling time T_e. Then the system ((54)) can be approximated by the explicit Euler's method:

$$x(t_{k+1}) = x(t_k) + T_e\, \dot{x}(t_k) + O(T_e^2) \tag{55}$$

For small values of T_e, $O(T_e^3)$ is neglected and the truncation error is approximately proportional to T_e^2.

Suppose now that the system (54) is discretized at two different sample rates resulting in two discrete time systems: H_1 sampled at frequency $f_{s1} = \dfrac{1}{T_e}$ and H_2 sampled at frequency $f_{s2} = \dfrac{N}{T_e}$; and let us compare the truncation error of each one after T_e seconds for N large enough. The discrete time is given by $t_{H1} = nT_e$ for H_1 and $t_H 2 = k\dfrac{T_e}{N}$ for H_2, with $n, k \in \mathbb{N}$. Assume that the initial times and the initial conditions are the same for both of them, that is: $nT_e = k\dfrac{T}{T_e} = t_0$ and $x(nT_e) = x\left(k\dfrac{T_e}{N}\right) = x(t_0) = x_0$, The dynamics of the discrete time system H_1 can be written as:

$$x\left((n+1)T_e\right) = x\left(nT_e\right) + T_e f\left(x(nT_e)\right) + O(T_e^2) \tag{56}$$

H_2, sampled at $f_{s2} = \dfrac{N}{T_e}$, evolves as follows:

$$\begin{aligned}
x((k+1)\frac{T_e}{N}) &= x(k\frac{T_e}{N}) + \frac{T_e}{N} f\left(x(k\frac{T_e}{N})\right) + O\left(\frac{T_e}{N}\right)^2 \\
x((k+2)\frac{T_e}{N}) &= x((k+1)\frac{T_e}{N}) + \frac{T_e}{N} f\left(x((k+1)\frac{T_e}{N})\right) + O(\frac{T_e}{N})^2 \\
&= x(k\frac{T_e}{N}) + \frac{T_e}{N} f\left(x(k\frac{T_e}{N})\right) \\
&\quad + \frac{T_e}{N} f\left(x(k\frac{T_e}{N}) + \frac{T_e}{N} f\left(x(k\frac{T_e}{N})\right) + O\left(\frac{T_e}{N}\right)^2\right) + 2O\left(\frac{T_e}{N}\right)^2
\end{aligned} \tag{57}$$

For N large enough we can consider the influence of the error term $O\left(\dfrac{T_e}{N}\right)^2$ over the function $\dfrac{T_e}{N} f(\cdot)$ as a term in $O\left(\dfrac{T_e}{N}\right)^3$, then:

$$\begin{aligned}
x((k+2)\frac{T_e}{N}) &\approx x(k\frac{T_e}{N}) + \frac{T_e}{N} f\left(x(k\frac{T_e}{N})\right) + \frac{T_e}{N} f\left\{x\left(k\frac{T_e}{N}\right) + \frac{T_e}{N} f\left(x\left(k\frac{T_e}{N}\right)\right)\right\} \\
&\quad + 2O\left(\frac{T_e}{N}\right)^2 \\
&= x(k\frac{T_e}{N}) + \frac{T_e}{N} f\left(x(k\frac{T_e}{N})\right) + \frac{T_e}{N} f(x((k+1)\frac{T_e}{N})) + 2O\left(\frac{T_e}{N}\right)^2
\end{aligned} \tag{58}$$

So, in a general way, we have:

$$x((k+N)\frac{T_e}{N}) \approx x(k\frac{T_e}{N}) + \frac{T_e}{N} \sum_{i=k}^{k+N-1} f(x(i\frac{T_e}{N})) + N\,O\left(\frac{T_e}{N}\right)^2 \tag{59}$$

As we can see from (56) and (59), the truncation errors of the discrete systems H_1 and H_2 are

$$\varepsilon_1 = O\left(T_e^2\right) \tag{60}$$

and

$$\varepsilon_2 = N\,O\left(\left(\frac{T_e}{N}\right)^2\right) \tag{61}$$

The truncation errors ε_1 and ε_2, given by (60) and (61) respectively give

$$N\,O\left(\left(\frac{T_e}{N}\right)^2\right) \approx \frac{O\left(T_e^2\right)}{N} \tag{62}$$

$$\varepsilon_2 \approx \frac{\varepsilon_1}{N} \tag{63}$$

Then the oversampled system H_2 reduces the truncation error about N times.

In practice, to achieve the benefits of oversampling, we emulate this technique based on the assumption that between two consecutive samples of an input signal, its derivative is nearly constant. In this way the new" samples are obtained by linear interpolation between consecutive "measured" samples. This technique is shown in figure 5. On the top the

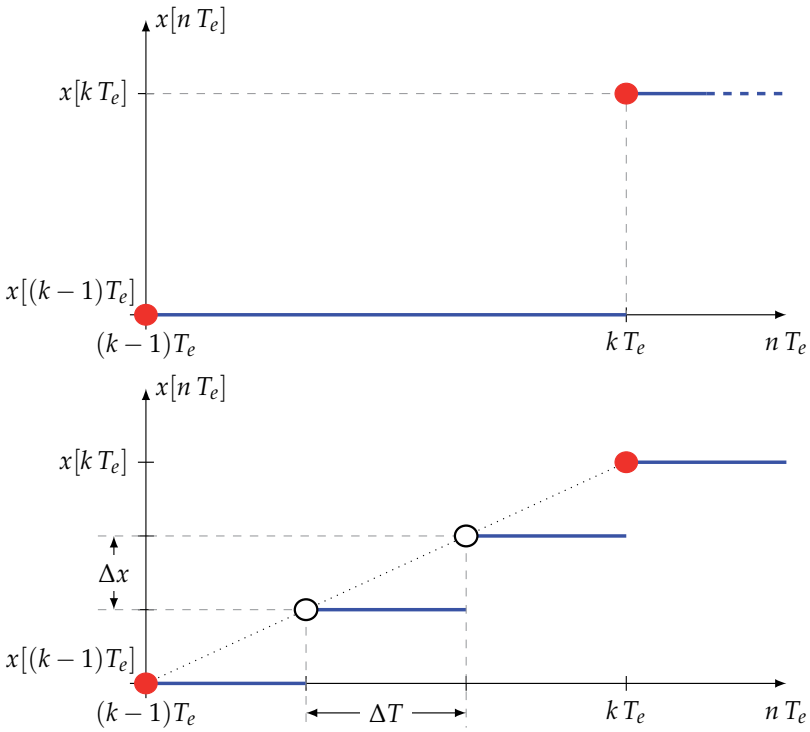

Figure 5. Comparison between sampling and oversampling implementation.

"classical sampling" is shown and on the bottom, the oversampling technique is depicted. As we can see, the sample period is reduced three times its original value, that is, $\frac{T_e}{N} = \frac{T_e}{3}$. This technique reduces the truncation error, inherent to Euler's method, three times. The benefits of this technique are exposed and validated by experimental tests.

5. Experimentations

5.1. Test bench

Table (1) presents all electrical and mechanical parameters of Induction machine used in practice, and in Table (2) main VAR-CNTRL card features are presented.

The tunning parameters α_i, λ_i, $i = 1, ..., 4$ of the proposed observer are chosen according to inequalities (31), 32, 33 and 34 to satisfy convergence conditions.

P_N	rated power	1.5KW
V_N	rated voltage	230V
I_N	rated current	3.2A
F_N	rated frequency	50Hz
N_N	rated speed	2998tr/min
p	number of pair of poles	1
R_S	stator resistance	4.2Ω
R_R	rotor resistance	2.8Ω
L_S	stator inductance	0.522 H
L_R	stator inductance	0.537 H
M_{SR}	mutual inductance	0.502 H
f	viscous coefficient	1N.s/rad
α_1, λ_1	tunning parameters	$\alpha_1 = 1500, \lambda_1 = 2500$
α_2, λ_2	tunning parameters	$\alpha_2 = \alpha_1, \lambda_2 = \lambda_1$
α_3, λ_3	tunning parameters	$\alpha_3 = 1500, \lambda_3 = 2000$
α_4, λ_4	tunning parameters	$\alpha_4 = \alpha_3, \lambda_4 = \lambda_3$

Table 1. Induction machine and observer parameters.

Figure 6. VAR-CNTRL card a product of GS Maintenance.

1	Analog Input/Output connectors. (3 Inputs /3 0utputs)
2	Communication port. (1 $RS232$)
3	Logical Output connector. (6 Outputs)
4	QEP connector. (A-B-Z)
5	Logical Input connector. (8 Isolated Inputs)
6	Supply voltage connector. (3.3V- 5V - (±15V) - 24V)
7	Measurements connector. (V_{DC}, I_A, I_B)
8	DSP $TMS320F2812$
9	PWM connector. (6 Output signals).

Table 2. VAR-CNTRL card main elements.

VAR-CNTRL is a electronic card designed by **GS Maintenance** and dedicated to motor control (Synchronous, Induction machine, Brushless, and DC motor). Equipped with a **DSP TMS320F2812** from **Texas Instrument**,this component is a fixed point; data are represented under 32 bits.

Practicals tests have been done under the following configurations:

- Fe , Sampling frequency of 8KHZ.
- Fcyc, **DSP** clock frequency of 150MHZ.
- 1024 points encoder, as speed sensor.
- **ADC**'s (Analog-to-Digital Coder) of 12 bits provide bus voltage (V_{DC}), and phase currents (I_A,I_B) frames under 12 bits.

In addition to the **VAR-CNTRL**, a **MMI** (Man Machine Interface) permits to visualize **DSP** data registers in representation format 8.8 that means possible variations are from [-127.996 to 128].

To summarize our Bed Test description, we have :

- An **IM**.
- A two-level **VSI** (Voltage Source Inverter).
- A control card , **VAR-CNTRL**.
- A **MMI**.
- A speed sensor, a voltage sensor, and two current sensors.

5.2. Results

In this section we propose some experimentation results, that allow the following points:

- Validate Super Twisting Algorithm convergence.
- Evaluate Oversampling method efficiency.
- Evaluate Motor variables estimation.

In section 4.1 we introduced Euler Explicit Sampling Method to discretize a continuous system. Some technical limits about sampling frequency Fe lead us to introduce Oversampling strategy (c.f. section 4.2) . At first glance we propose to validate Super Twisting Observer strategy (c.f. system 7), we will take account of subsystem Σ_1 in figure 4 with the following entries : (v_1 , z_1), and outputs : ($\hat{z}_1$, $\tilde{z}_3$).

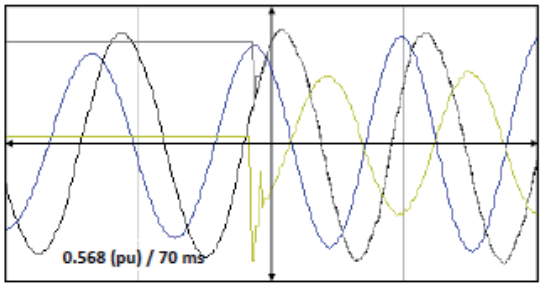

Figure 7. MMI capture : (z_1,v_1) and ($\hat{z}_1$, $\tilde{z}_3$) on convergence phase.

On figure 7 we validate the convergence of Σ_1 in figure 4, we can see that under some initials values $\hat{z}_1$ converge to z_1 in a finite time.

Figures 8 and 9 permit to assume that oversampling method is efficient, in fact we see that signals estimated by the observer (53) of the subsystem Σ_1 in figure 4 are much more better with an oversampling than without.

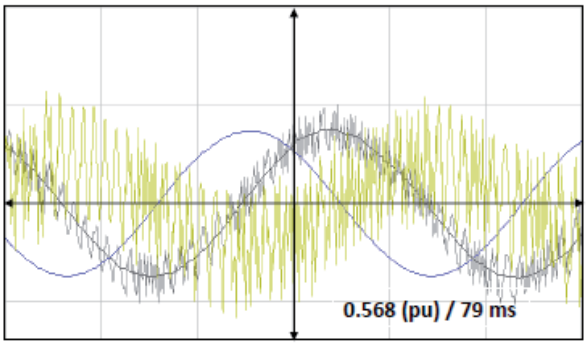

Figure 8. MMI capture : (z_1,v_1) and ($\hat{z}_1$, $\tilde{z}_3$) without oversampling method.

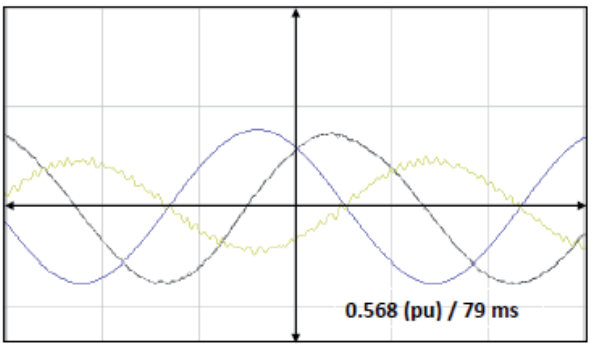

Figure 9. MMI capture : (z_1,v_1) and ($\hat{z}_1$, $\tilde{z}_3$) with oversampling method. ($N = 10$.)

Thus at the same operating point, we assume that with oversampling method we improve efficiency of the algorithm. With this validated data we can now abort estimation of *IM* magnetic (x_3, x_4) and mechanical (x_5) variables including the rotor position flux ρ given in equations 51, (35-36) and (52) respectively.

The main objective of this work is to provide a motor speed estimation without any mechanical sensor, and then drive it. Note that the speed sensor is only used in comparison of estimated speed with its measure. To validate our strategy we propose some tests into different conditions.

Figures 12 and 13 permit to validate accuracy of estimated speed compare to measured speed in high variation range. However, it is admit that at low and very low speed, estimated speed damages more and more, as we can see on figures 14 and 15.

Now we propose some dynamical test results. During acceleration and deceleration phases (c.f. 16) , estimated speed is steel working although there is small delay between x_5 and $\hat{x}_5$.

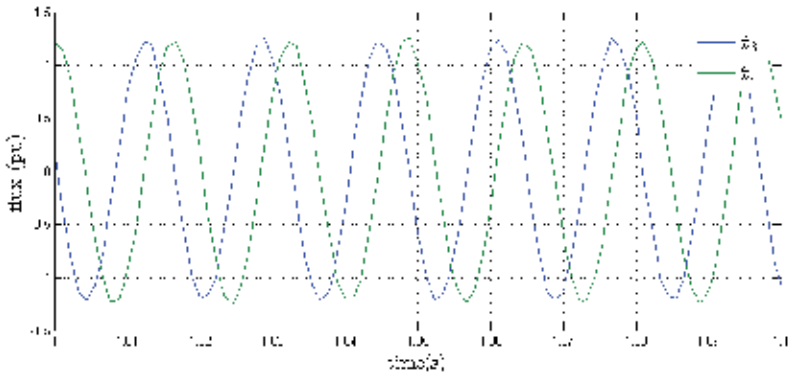

Figure 10. Flux Estimation: x_3 and x_4 during static phase.

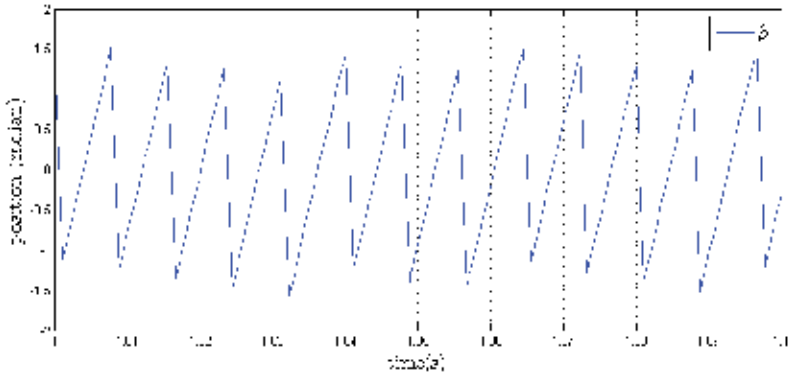

Figure 11. Estimated of rotor flux position: ρ.

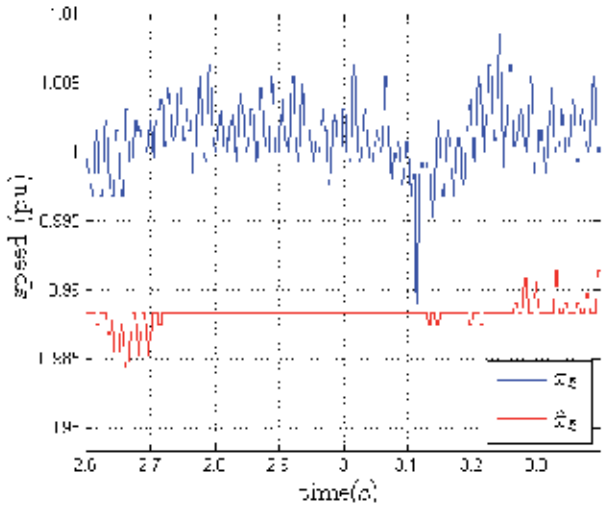

Figure 12. Measure and estimate of speed during static phase: x_5 and $\hat{x}_5$

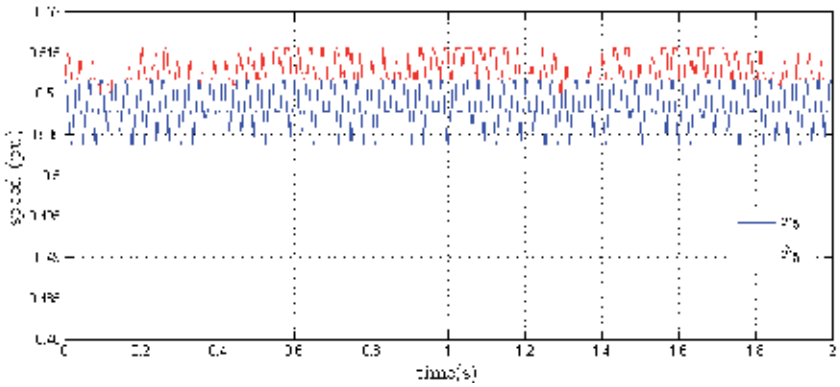

Figure 13. Measure and estimate of speed during static phase: x_5 and $\hat{x}_5$

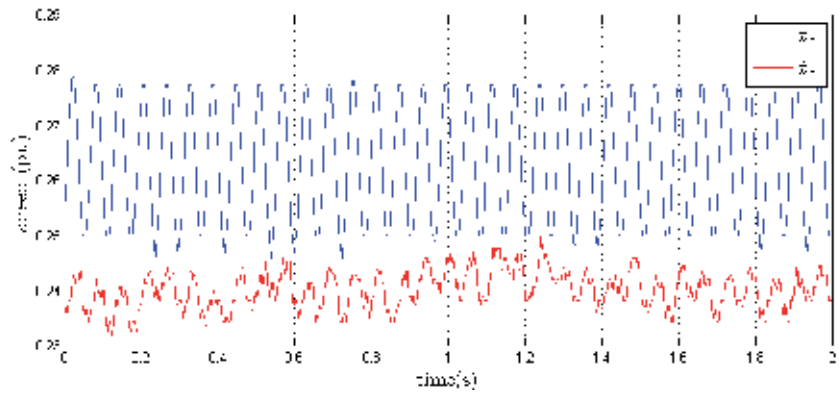

Figure 14. Measure and estimate of speed during static phase: x_5 and $\hat{x}_5$

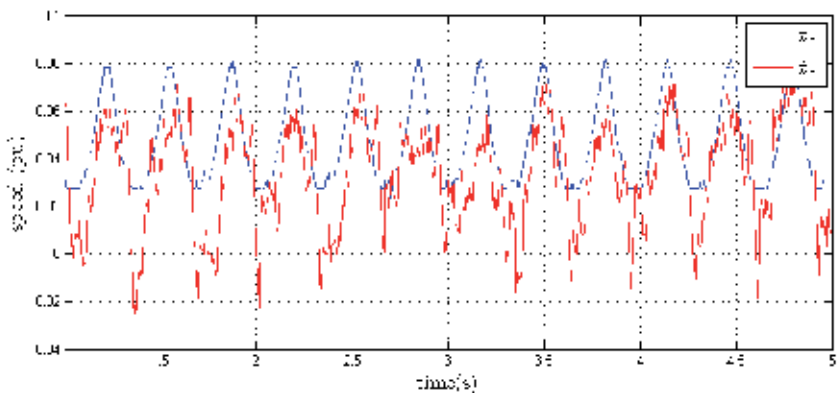

Figure 15. Measure and estimate of speed during static phase: x_5 and $\hat{x}_5$

During static phase operation we saw that at low and very low speed , speed observation does not work very well. However on figures (17) and (18) we cross 0 speed, we denote a small

divergence as small as the time to cross it; in fact this phenomenon underlines that speed is non observable with low current dynamic.

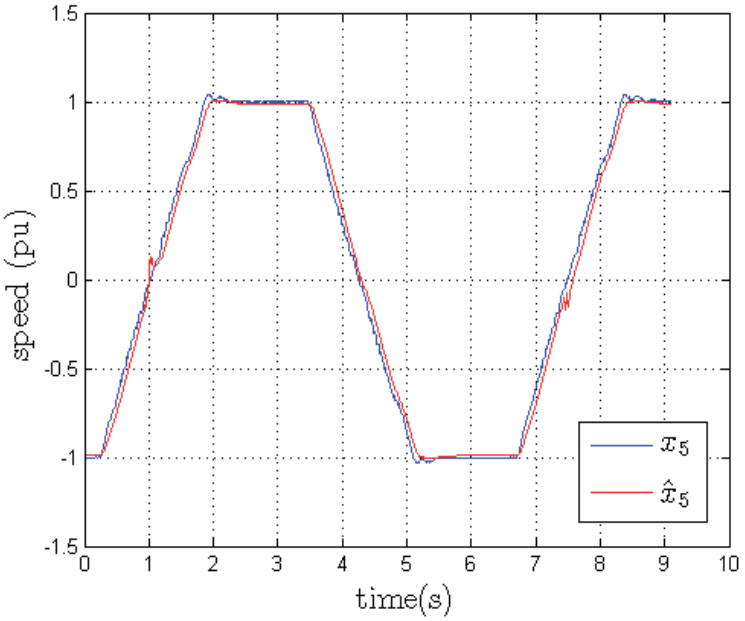

Figure 16. Measure and estimate of speed during variable phase: x_5 and $\hat{x}_5$

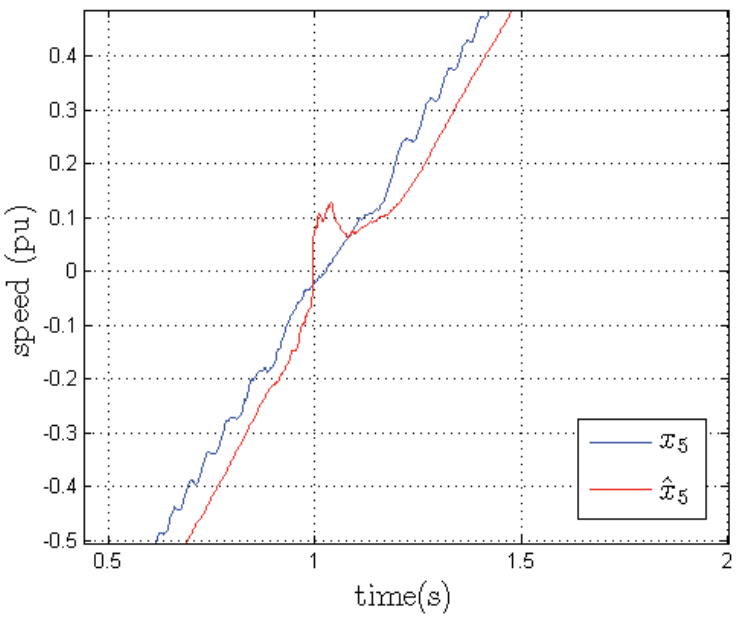

Figure 17. Measure and estimate of speed during acceleration phase: x_5 and $\hat{x}_5$

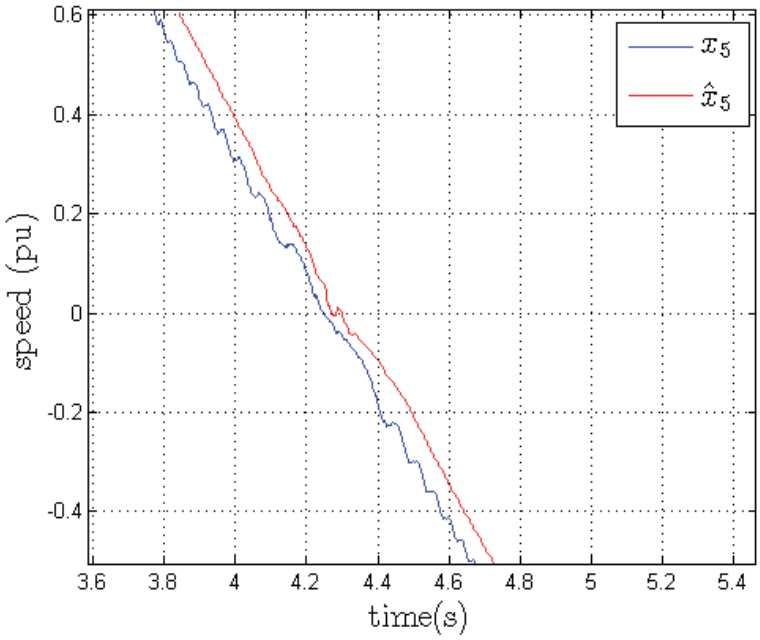

Figure 18. Measure and estimate of speed during deceleration phase: x_5 and $\hat{x}_5$

Figures 12 and 13 at high speed, show that speed approximation proposed in equation (51) work and permit to obtain magnitude and speed sign. This efficiency is also proved during dynamical phases as we can see on figure 16.

About this bad results, we have 2 arguments:

- Parameters error, mainly on stator and rotor resistance (R_S, R_R).
- Poor current dynamic, combined to digitizing error at low frequency working.

To overcome all this features, we propose to use an on-line resistor measurement of stator threw temperature.

6. Conclusion

Through this chapter an original method of observation without mechanical sensors for induction machine was introduced.

Designed for a embedded system (VAR-CNTRL) equipped with a fixed point DSP, we carried out various tests of validation.

We used concept of Sliding Mode through Super Twisting Algorithm, and oversampling method being based on the explicit Euler development. The contribution of this paper is mainly based on the applicability of the proposed observer for sensorless induction motor when a basic microprocessors are used in an industrial context.

At the time of the setting works of our strategy some technical constraints brought us to introduce a news strategy.

Thus the practical results permit us to do a first assessment:

- we validate our oversampling method introduced to overcome low speed data acquisition.
- we validate speed estimation during static and dynamic steps.
- we obtained an image of rotor flux(x_3, and x_4), and also rotor position.

Compared with mechanical sensor the precision provides by the observer on the size speed offer a precision inferior or equal to 5% in the operating speed range from: 25% to 100%.

In term of prospects, it possible to improve the threshold of operation in low mode (25% to 5%) by adaptation oversampling number to stator frequency value, indeed a larger sample number could improve approximation of the continuous system .

In next step some tests will done to validate:

- Validation of hardiness to load variation.
- Validation in closed loop.

About Observability loose at very low speed a first solution could be to switch with a speed estimator.

Author details

Sebastien Solvar, Malek Ghanes, Leonardo Amet, Jean-Pierre Barbot and Gaëtan Santomenna
ECS - Lab, ENSEA and GS Maintenance, France

7. References

[1] Aurora, C. & Ferrara, A. [2007]. A sliding mode observer for sensorless induction motor speed regulation, *International Journal of Systems Science* 38(11): 913–929.
[2] Bartolini, G., Ferrara, A. & Usani, E. [1998]. Chattering avoidance by second-order sliding mode control, *Automatic control, IEEE Transactions on* 43(2): 241–246.
[3] Canudas De Wit, C., Youssef, A., Barbot, J., Martin, P. & Malrait, F. [2000]. Observability conditions of induction motors at low frequencies, *Decision and Control, 2000. Proceedings of the 39th IEEE Conference on*, Vol. 3, IEEE, pp. 2044–2049.
[4] Chiasson, J. [2005]. *Modeling and high performance control of electric machines*, Vol. 24, Wiley-IEEE Press.
[5] Davila, J., Fridman, L. & Levant, A. [2005]. Second-order sliding-mode observer for mechanical systems, *IEEE Transactions on Automatic Control* Vol. 50(11): 1785–1789.
[6] Dib, A., Farza, M., MŠSaad, M., Dorléans, P. & Massieu, J. [2011]. High gain observer for sensorless induction motor, *World Congress*, Vol. 18, pp. 674–679.
[7] Floquet, T. & Barbot, J. [2007]. Super twisting algorithm-based step-by-step sliding mode observers for nonlinear systems with unknown inputs, *International Journal of Systems Science* 38(10): 803–815.
[8] Ghanes, M., Barbot, J., De Leon, J. & Glumineau, A. [2010]. A robust sensorless output feedback controller of the induction motor drives: new design and experimental validation, *International Journal of Control* 83(3): 484–497.
[9] Ghanes, M., De Leon, J. & Glumineau, A. [2006]. Observability study and observer-based interconnected form for sensorless induction motor, *Decision and Control, 2006 45th IEEE Conference on*, IEEE, pp. 1240–1245.

[10] Ghanes, M. & Zheng, G. [2009]. On sensorless induction motor drives: Sliding-mode observer and output feedback controller, *Industrial Electronics, IEEE Transactions on* 56(9): 3404–3413.
[11] Hilairet, M., Auger, F. & Berthelot, E. [2009]. Speed and rotor flux estimation of induction machines using a two-stage extended kalman filter, *Automatica* 45(8): 1819–1827.
[12] Holtz, J. [2006]. Sensorless control of induction machinesŮwith or without signal injection ?, *Industrial Electronics, IEEE Transactions on* 53(1): 7–30.
[13] Ibarra-Rojas, S., Moreno, J. & Espinosa-Pérez, G. [2004]. Global observability analysis of sensorless induction motors, *Automatica* 40(6): 1079–1085.
[14] Khalil, H., Strangas, E. & Jurkovic, S. [2009]. Speed observer and reduced nonlinear model for sensorless control of induction motors, *Control Systems Technology, IEEE Transactions on* 17(2): 327–339.
[15] Kubota, H., Matsuse, K. & Nakano, T. [1993]. Dsp-based speed adaptive flux observer of induction motor, *Industry Applications, IEEE Transactions on* 29(2): 344–348.
[16] Leppänen, V.-M. [2003]. *Low-Frequency Signal-Injection Method for Speed Sensorless Vector Control of Induction Motors*, Oxford University Press, ISBN 0-19-856465-1.
[17] Levant, A. [1998]. Robust exact differentiation via sliding mode technique, *Automatica* 34(3): 379–384.
[18] Levant, A. [2003]. Higher-order sliding modes, differentiation and output-feedback control, *International Journal of Control* 76(9-10): 924–941.
[19] Maiti, S., Verma, V., Chakraborty, C. & Hori, Y. [2012]. An adaptive speed sensorless induction motor drive with artificial neural network for stability enhancement, *IEEE Transactions on Industrial Informatics* .
[20] Perruquetti, W. & Barbot, J. [2002]. *Sliding mode control in engineering*, Vol. 11, CRC.
[21] Schauder, C. [1992]. Adaptive speed identification for vector control of induction motors without rotational transducers, *Industry applications, IEEE Transactions on* 28(5): 1054–1061.
[22] Vas, P. [1998]. *Sensorless vector and direct torque control*, Vol. 729, Oxford university press Oxford, UK.

Chapter 16

The Asymmetrical Dual Three-Phase Induction Machine and the MBPC in the Speed Control

Raúl Igmar Gregor Recalde

Additional information is available at the end of the chapter

http://dx.doi.org/10.5772/50559

1. Introduction

Recent research has focused on exploring the advantages of multiphase[1] machines over conventional three-phase systems, including lower torque pulsations, less DC-link current harmonics, higher overall system reliability, and better power distribution per phase [1]. Among these multiphase drives, the asymmetrical dual three-phase machines with two sets of three-phase stator windings spatially shifted by 30 electrical degrees and isolated neutral points is one of the most widely discussed topologies and found industrial application in more-electric aircraft, electrical and hybrid vehicles, ship propulsion, and wind power systems [2]. This asymmetrical dual three-phase machines is a continuous system which can be described by a set of differential equations. A methodology that simplifies the modeling is based on the vector space decomposition (VSD) theory introduced in [3] to transform the original six-dimensional space of the machine into three two-dimensional orthogonal subspaces in stationary reference frame $(\alpha - \beta)$, $(x - y)$ and $(z_1 - z_2)$. From the VSD approach, can be emphasized that the electromechanical energy conversion variables are mapped in the $(\alpha - \beta)$ subspace, meanwhile the current components in the $(x - y)$ subspace represent supply harmonics of the order $6n \pm 1$ $(n = 1, 3, 5, ...)$ and only produce losses, so consequently should be controlled to be as small as possible. The voltage vectors in the $(z_1 - z_2)$ are zero due to the separated neutral configuration of the machine, therefore this subspace has no influence on the control [4].

Model-based predictive control (MBPC) and multiphase drives have been explored together in [5, 6], showing that predictive control can provide enhanced performance for multiphase drives. In [7, 8], different variations of the predictive current control techniques are proposed to minimize the error between predicted and reference state variables, at the expense of increased switching frequency of the insulated-gate bipolar transistor (IGBTs). On the other hand are proposed control strategies based on sub-optimal solutions restricted the available voltage vectors for multiphase drive applications aiming at reducing the computing cost and

[1] The multiphase term, regards more than three phase windings placed in the same stator of the electric machine.

improving the drive performance [9]. This chapter wide the concept of the MBPC techniques to the speed control of a dual three-phase induction machine, by using an Kalman Filter (KF) to improve the estimation of states through an optimal estimation of the rotor current. The KF is an efficient recursive filter that estimates the internal state of a dynamic system from a series of noisy measurements. Its purpose is to use measurements that are observed over time that contain noise (random variations) and other inaccuracies (including modeling errors), and produce values that tend to be closer to the true values of the measurements and their associated calculated values. This feature is an attractive solution in the predictive control of induction machines based on the model, mainly if not precisely known internal parameters of the drive, and the measurement of the state variables are perturbed by gaussian noise.

The chapter includes simulation results of the current control based on a predictive model of the asymmetrical dual three-phase induction machine and proposes a new approach to speed control based on MBPC technique. The results provided confirm the feasibility of the speed control scheme for multi-phase machines. The rest of the chapter is organized as follows. Section 2 introduces an asymmetrical dual three-phase AC drive used for simulations. Section 3 details the general principles of the predictive current control method for AC drives. Section 4 shows the simulation results obtained from the inner loop of predictive current control and proposed a new approach to speed control for the dual three-phase induction machine, on the other hand presents a discussion of the obtained results from the proposed approach. The chapter ends with Section 5 where the conclusions are presented.

2. The asymmetrical dual three-phase AC drive

The asymmetrical dual three-phase induction machine is supplied by a 6-phase voltage source inverter (VSI) and a Dc Link, as shown in Figure 1. This six-phase machine is a continuous system which can be described by a set of differential equations. A methodology that simplifies the modeling is based on the vector space decomposition (VSD) theory introduced in [3] to transform the original six-dimensional space of the machine into three

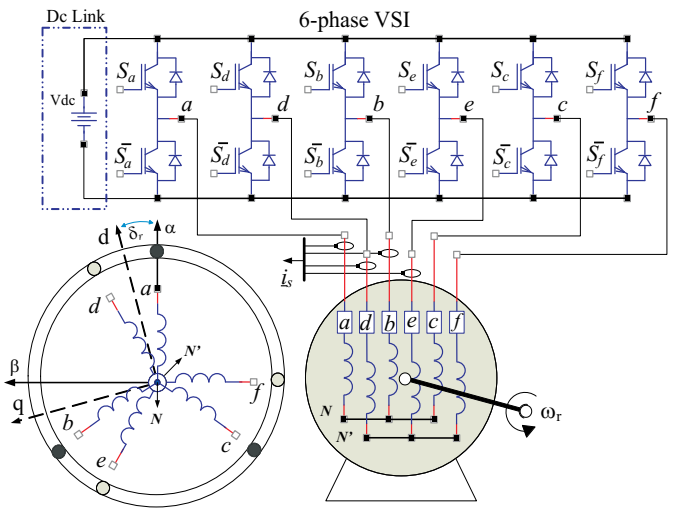

Figure 1. A general scheme of an asymmetrical dual three-phase drive

two-dimensional orthogonal subspaces in stationary reference frame $(\alpha - \beta)$, $(x - y)$ and $(z_1 - z_2)$, by means of a 6×6 transformation matrix using an amplitude invariant criterion:

$$\mathbf{T} = \frac{1}{3}\begin{bmatrix} 1 & \frac{\sqrt{3}}{2} & -\frac{1}{2} & -\frac{\sqrt{3}}{2} & -\frac{1}{2} & 0 \\ 0 & \frac{1}{2} & \frac{\sqrt{3}}{2} & \frac{1}{2} & -\frac{\sqrt{3}}{2} & -1 \\ 1 & -\frac{\sqrt{3}}{2} & -\frac{1}{2} & \frac{\sqrt{3}}{2} & -\frac{1}{2} & 0 \\ 0 & \frac{1}{2} & -\frac{\sqrt{3}}{2} & \frac{1}{2} & \frac{\sqrt{3}}{2} & -1 \\ 1 & 0 & 1 & 0 & 1 & 0 \\ 0 & 1 & 0 & 1 & 0 & 1 \end{bmatrix} \tag{1}$$

The VSI has a discrete nature and has a total number of $2^6 = 64$ different switching states defined by six switching functions corresponding to the six inverter legs $[S_a, S_d, S_b, S_e, S_c, S_f]$, where $\mathbf{S}_i \in \{0, 1\}$. The different switching states and the voltage of the DC link (Vdc) define the phase voltages which can in turn be mapped to the $(\alpha - \beta) - (x - y)$ space according to the VSD approach. Consequently, the 64 different on/off combinations of the six VSI legs lead to 64 space vectors in the $(\alpha - \beta)$ and $(x - y)$ subspaces. Figure 2 shows the active vectors in the $(\alpha - \beta)$ and $(x - y)$ subspaces, where each vector switching state is identified using the switching function by two octal numbers corresponding to the binary numbers $[S_a S_b S_c]$ and $[S_d S_e S_f]$, respectively. For the sake of conciseness, the 64 VSI switching vectors will be usually referred as voltage vectors, or just vectors, in what follows. It must be noted that the 64 possibilities imply only 49 different vectors in the $(\alpha - \beta) - (x - y)$ space. Nevertheless, redundant vectors should be considered as different vectors because they have a different impact on the switching frequency even though they generate identical torque and losses in the six-phase machine.

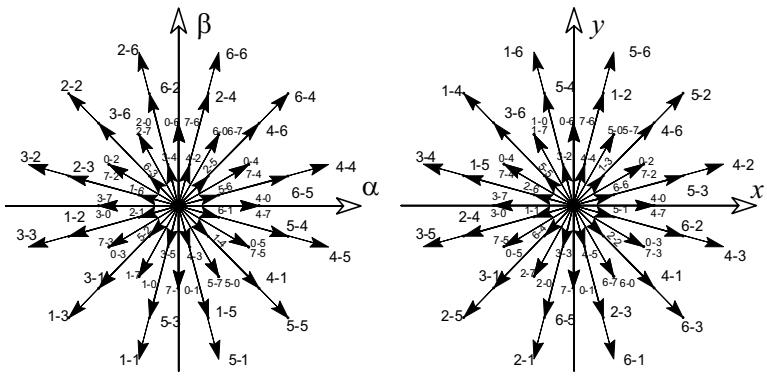

Figure 2. Voltage vectors and switching states in the $(\alpha - \beta)$ and $(x - y)$ subspaces for a 6-phase asymmetrical VSI

To represent the stationary reference frame $(\alpha - \beta)$ in dynamic reference $(d - q)$, a rotation transformation must be used. This transformation is given by:

$$\mathbf{T}_{dq} = \begin{bmatrix} cos\,(\delta_r) & -sin\,(\delta_r) \\ sin\,(\delta_r) & cos\,(\delta_r) \end{bmatrix} \tag{2}$$

where δ_r is the rotor angular position referred to the stator as shown in Figure 1.

2.1. Machine model in the $(\alpha - \beta)$ subspace

The asymmetrical dual three-phase machine model can be obtained using a specific and convenient choice of state-space variables, for example, stator and rotor currents. Thus the six-phase machine can be modelled in a stationary reference frame according to the VSD approach as:

$$[\mathbf{u}]_{\alpha\beta} = [\mathbf{G}] \frac{d}{dt} [\mathbf{x}]_{\alpha\beta} + [\mathbf{F}] [\mathbf{x}]_{\alpha\beta} \tag{3}$$

$$[\mathbf{u}]_{\alpha\beta} = \begin{bmatrix} u_{\alpha s} & u_{\beta s} & 0 & 0 \end{bmatrix}^T ; [\mathbf{x}]_{\alpha\beta} = \begin{bmatrix} i_{\alpha s} & i_{\beta s} & i_{\alpha r} & i_{\beta r} \end{bmatrix}^T \tag{4}$$

where $[\mathbf{u}]_{\alpha\beta}$ is the input vector, $[\mathbf{x}]_{\alpha\beta}$ is the state vector and $[\mathbf{F}]$ and $[\mathbf{G}]$ are matrices that define the dynamics of the electrical drive that for this set of state variables are:

$$[\mathbf{F}] = \begin{bmatrix} R_s & 0 & 0 & 0 \\ 0 & R_s & 0 & 0 \\ 0 & \omega_r \cdot L_m & R_r & \omega_r \cdot L_r \\ -\omega_r \cdot L_m & 0 & -\omega_r \cdot L_r & R_r \end{bmatrix} ; [\mathbf{G}] = \begin{bmatrix} L_s & 0 & L_m & 0 \\ 0 & L_s & 0 & L_m \\ L_m & 0 & L_r & 0 \\ 0 & L_m & 0 & L_r \end{bmatrix} \tag{5}$$

where ω_r is the rotor angular speed, and the electrical parameters of the machine are the stator and rotor resistances R_s, R_r, the stator and rotor inductances $L_s = L_{ls} + L_m$, $L_r = L_{lr} + L_m$, the stator and rotor leakage inductances L_{ls}, L_{lr} and the magnetization inductance L_m. Using selected state-space variables and amplitude invariant criterion in the transformation, the mechanical part of the drive is given by the following equations:

$$T_e = 3.P \left(\psi_{\beta r} i_{\alpha r} - \psi_{\alpha r} i_{\beta r} \right) \tag{6}$$

$$J_i \frac{d}{dt} \omega_r + B_i \omega_r = P \left(T_e - T_L \right) \tag{7}$$

where T_e is the generated torque, T_L the load torque, P the number of pair of poles, J_i the inertia coefficient, B_i the friction coefficient and $\psi_{\alpha\beta r}$ the rotor flux.

The $(\alpha - \beta)$[2] axes are selected in such a manner that they coincide with the plane of rotation of the airgap flux. Therefore, these variables will are associated with the production of the airgap flux in the machine and with the electromechanical energy conversion related [3].

2.2. Machine model in the $(x - y)$ subspace

Because the $(x - y)$ subspace is orthogonal to the $(\alpha - \beta)$ subspace, the projected variables in this subspace will do not contribute to the airgap flux, and therefore are not related to energy conversion. This model are limited only by the stator resistance and stator leakage inductance, as shown in the following equation:

$$\begin{bmatrix} u_{xs} \\ u_{ys} \end{bmatrix} = \begin{bmatrix} L_{ls} & 0 \\ 0 & L_{ls} \end{bmatrix} \frac{d}{dt} \begin{bmatrix} i_{xs} \\ i_{ys} \end{bmatrix} + \begin{bmatrix} R_s & 0 \\ 0 & R_s \end{bmatrix} \begin{bmatrix} i_{xs} \\ i_{ys} \end{bmatrix} \tag{8}$$

[2] It can be noted that $(\alpha - \beta)$ equations are similar to those of a three-phase machine while that, as will be seen in the following section, the $(x - y)$ equations do not link the rotor side and consequently do not influence the machine dynamics but are source of Joule losses in the machine.

3. Predictive model

The machine model must be discretized in order to be of use as a predictive model. Taking into account that the electromechanical energy conversion involves only quantities in the $(\alpha - \beta)$ subspace, the predictive model could be simplified, discarding the $(x - y)$ subspace. Assuming the asymmetrical dual three-phase induction machine model (see Equation 3) and using the following state components ($x_1 = i_{\alpha s},\ x_2 = i_{\beta s},\ x_3 = i_{\alpha r},\ x_4 = i_{\beta r}$), the resulting equations can be written as:

$$\begin{aligned}
\dot{x_1} &= c_3\left(R_r x_3 + \omega_r x_4 L_r + \omega_r x_2 L_m\right) + c_2\left(u_{\alpha s} - R_s x_1\right) \\
\dot{x_2} &= c_3\left(R_r x_4 - \omega_r x_3 L_r - \omega_r x_1 L_m\right) + c_2\left(u_{\beta s} - R_s x_2\right) \\
\dot{x_3} &= c_4\left(-R_r x_3 - \omega_r x_4 L_r - \omega_r x_2 L_m\right) + c_3\left(-u_{\alpha s} + R_s x_1\right) \\
\dot{x_4} &= c_4\left(-R_r x_4 + \omega_r x_3 L_r + \omega_r x_1 L_m\right) + c_3\left(-u_{\beta s} + R_s x_2\right)
\end{aligned} \tag{9}$$

where c_1-c_4 are constant coeficients defined as:

$$c_1 = L_s \cdot L_r - L_m^2,\ c_2 = \frac{L_r}{c_1},\ c_3 = \frac{L_m}{c_1},\ c_4 = \frac{L_s}{c_1} \tag{10}$$

Stator voltages are related to the control input signals through the inverter model. The simplest model has been selected for this case study for the sake of speeding up the optimization process. Then if the gating signals are arranged in vector $\mathbf{S} = \left[S_a,\ S_d,\ S_b,\ S_e,\ S_c,\ S_f\right] \in \mathbf{R}^6$, with $\mathbf{R} = \{0, 1\}$ the stator voltages are obtained from:

$$\mathbf{M} = \frac{1}{3}\begin{bmatrix} 2 & 0 & -1 & 0 & -1 & 0 \\ 0 & 2 & 0 & -1 & 0 & -1 \\ -1 & 0 & 2 & 0 & -1 & 0 \\ 0 & -1 & 0 & 2 & 0 & -1 \\ -1 & 0 & -1 & 0 & 2 & 0 \\ 0 & -1 & 0 & -1 & 0 & 2 \end{bmatrix} \cdot \mathbf{S}^T \tag{11}$$

An ideal inverter converts gating signals to stator voltages that can be projected to $(\alpha - \beta)$ and $(x - y)$ axes and gathered in a row vector $\mathbf{U}_{\alpha\beta xys}$ computed as:

$$\mathbf{U}_{\alpha\beta xys} = \left[u_{\alpha s},\ u_{\beta s},\ u_{xs},\ u_{ys},\ 0,\ 0\right]^T = Vdc \cdot \mathbf{T} \cdot \mathbf{M} \tag{12}$$

being Vdc the Dc Link voltage and superscript $(^T)$ indicates the transposed matrix. Combining Equations 9-12 a nonlinear set of equations arises that can be written in state space form:

$$\begin{aligned}
\dot{\mathbf{X}}(t) &= f\left(\mathbf{X}(t),\ \mathbf{U}(t)\right) \\
\mathbf{Y}(t) &= \mathbf{C}\mathbf{X}(t)
\end{aligned} \tag{13}$$

with state vector $\mathbf{X}(t) = \left[x_1,\ x_2,\ x_3,\ x_4\right]^T$, input vector $\mathbf{U}(t) = \left[u_{\alpha s},\ u_{\beta s}\right]$, and output vector $\mathbf{Y}(t) = \left[x_1,\ x_2\right]^T$. The components of vectorial function f and matrix $\mathbf{C}$ are obtained in a straightforward manner from Equation 9 and the definitions of state and output vector.

Model (Equation 13) must be discretized in order to be of use for the predictive controller. A forward Euler method is used to keep a low computational burden. As a consequence the resulting equations will have the needed digital control form, with predicted variables depending just on past values and not on present values of variables. This leads to the following equations:

$$\begin{aligned} \hat{\mathbf{X}}(k+1|k) &= \mathbf{X}(k) + T_m f\left(\mathbf{X}(k),\, \mathbf{U}(k)\right) \\ \mathbf{Y}(k) &= \mathbf{C}\mathbf{X}(k) \end{aligned} \tag{14}$$

denoting by (k) the current sample, T_m the sampling time and being $\hat{\mathbf{X}}(k+1|k)$ a prediction of the future next-sample state made at sample time (k).

3.1. Kalman Filter design

Kalman Filter is an optimal recursive estimation algorithm based on the state-space concepts and suitable for digital computer implementation. That is, it is an optimal estimator for computing the conditional mean and covariance of the probability distribution of the state of a linear stochastic system with uncorrelated gaussian process and measurement noise. The algorithm minimizes the estimate error of the states by utilizing knowledge of system and measurements dynamic, assuming statistics of system noises and measurement errors, considering initial condition information [10]. Considering uncorrelated gaussian process and measurement noise, Equations 14 can be written as:

$$\begin{aligned} \hat{\mathbf{X}}(k+1|k) &= \mathbf{A}\mathbf{X}(k) + \mathbf{B}\mathbf{U}(k) + \mathbf{H}\varpi(k) \\ \mathbf{Y}(k) &= \mathbf{C}\mathbf{X}(k) + \nu(k) \end{aligned} \tag{15}$$

the matrices **A**, **B** and **C** are obtained in a straightforward manner from Equation 14 and the definitions of state and output vector, **H** is the noise-weight matrix, $\varpi(k)$ is the process noise matrix, and $\nu(k)$ is the measurement noise matrix. The covariance matrices R_ϖ and R_ν of these noises are defined in function to the expected value $E\{\cdot\}$ as:

$$R_\varpi = cov(\varpi) = E\left\{\varpi \cdot \varpi^T\right\}; R_\nu = cov(\nu) = E\left\{\nu \cdot \nu^T\right\} \tag{16}$$

3.1.1. Reduced-order state estimation

In the state space description of Equation 14 only stator currents, voltages and mechanical speed are measured. Stator voltages are easily predicted from gating commands issued to the VSI, rotor current, however, is not directly measured. This difficulty can be overcome by means of estimating the rotor current using the concept of reduced-order estimators. The reduced-order estimator provide an estimate for only the unmeasured part of state vector, then, the evolution of states can be written as:

$$\begin{bmatrix} \mathbf{X}_a(k+1|k) \\ \cdots \\ \mathbf{X}_b(k+1|k) \end{bmatrix} = \begin{bmatrix} \overline{\mathbf{A}}_{11} & \vdots & \overline{\mathbf{A}}_{12} \\ \cdots & \cdots & \cdots \\ \overline{\mathbf{A}}_{21} & \vdots & \overline{\mathbf{A}}_{22} \end{bmatrix} \begin{bmatrix} \mathbf{X}_a(k) \\ \cdots \\ \mathbf{X}_b(k) \end{bmatrix} + \begin{bmatrix} \overline{\mathbf{B}}_1 \\ \cdots \\ \overline{\mathbf{B}}_2 \end{bmatrix} \mathbf{U}_{\alpha\beta s}(k)$$

$$\mathbf{Y}(k) = \begin{bmatrix} \overline{\mathbf{I}} \vdots \overline{\mathbf{0}} \end{bmatrix} \begin{bmatrix} \mathbf{X}_a(k) \\ \cdots \\ \mathbf{X}_b(k) \end{bmatrix} \tag{17}$$

where $\mathbf{I}$ is the identity matrix of order 2x2, $\mathbf{X}_a = \left[i_{\alpha s}(k)\ i_{\beta s}(k) \right]^T$ is the portion directly measured, which is $\mathbf{Y}(k)$, $\mathbf{X}_b = \left[i_{\alpha r}(k)\ i_{\beta r}(k) \right]^T$ is the remaining portion to be estimated, and $\overline{\mathbf{A}}$ and $\overline{\mathbf{B}}$ are matrices obtained in a straightforward manner from Equation 15 and are represented according to the following matrices:

$$\overline{\mathbf{A}} = \begin{bmatrix} (1 - T_m.c_2.R_s) & T_m.c_3.L_m.\omega_r & \vdots & T_m.c_3.R_r & T_m.c_3.L_r.\omega_r \\ -T_m.c_3.L_m.\omega_r & (1 - T_m.c_2.R_s) & \vdots & -T_m.c_3.L_r.\omega_r & T_m.c_3.R_r \\ \cdots & \cdots & \cdots & \cdots & \cdots \\ T_m.c_3.R_s & -T_m.c_4.L_m.\omega_r & \vdots & (1 - T_m.c_4.R_r) & -T_m.c_4.L_r.\omega_r \\ T_m.c_4.L_m.\omega_r & T_m.c_3.R_s & \vdots & T_m.c_4.L_r.\omega_r & (1 - T_m.c_4.R_r) \end{bmatrix}$$

$$\overline{\mathbf{B}} = \begin{bmatrix} T_m.c_2 & 0 \\ 0 & T_m.c_2 \\ \cdots & \cdots \\ -T_m.c_3 & 0 \\ 0 & -T_m.c_3 \end{bmatrix} \tag{18}$$

The portion describing the dynamics of the unmeasured states can be written as:

$$\mathbf{X}_b(k+1|k) = \overline{\mathbf{A}}_{22}\mathbf{X}_b(k) + \overline{\mathbf{A}}_{21}\mathbf{X}_a(k) + \overline{\mathbf{B}}_2\mathbf{U}_{\alpha\beta s}(k) \tag{19}$$

where the last two terms on the right are known and can be considered as an input into the $\mathbf{X}_b$ dinamics. The $\mathbf{X}_a$ portion may be expressed as:

$$\mathbf{X}_a(k+1|k) - \overline{\mathbf{A}}_{11}\mathbf{X}_a(k) - \overline{\mathbf{B}}_1\mathbf{U}_{\alpha\beta s}(k) = \overline{\mathbf{A}}_{12}\mathbf{X}_b(k) \tag{20}$$

Note in Equation 20 that this equation represent a relationship between a measured quantity on the left and the unknown state vector on the right. Therefore, the dynamics of the reduced-order estimator ecuations are:

$$\begin{aligned} \hat{\mathbf{X}}_b(k+1|k) = (\overline{\mathbf{A}}_{22} - \mathbf{K}_e\overline{\mathbf{A}}_{12})\hat{\mathbf{X}}_b(k) + \mathbf{K}_e\mathbf{Y}(k+1) + \\ (\overline{\mathbf{A}}_{21} - \mathbf{K}_e\overline{\mathbf{A}}_{11})\mathbf{Y}(k) + (\overline{\mathbf{B}}_2 - \mathbf{K}_e\overline{\mathbf{B}}_1)\mathbf{U}_{\alpha\beta s}(k) \end{aligned} \tag{21}$$

where, $\mathbf{K}_e$ represents the KF gain matrix based on the covariance of the noise.

3.1.2. Kalman Filter gain matrix evaluation

The KF gain matrix ($\mathbf{K}_e$) is recalculated at each sampling time recursive manner as:

$$\mathbf{K}_e(k) = \mathbf{\Gamma}(k) \cdot \mathbf{C}^T R_v \tag{22}$$

where $\mathbf{\Gamma}$ is the covariance of the new estimate and is a function of the old estimate covariance (φ) as follows:

$$\mathbf{\Gamma}(k) = \varphi(k) - \varphi(k) \cdot \mathbf{C}^T(\mathbf{C} \cdot \varphi(k) \cdot \mathbf{C}^T + R_v)^{-1} \cdot \mathbf{C} \cdot \varphi(k) \tag{23}$$

From the state equation which includes the process noise it is possible to obtain a correction of the covariance of the state estimate as:

$$\varphi(k+1) = \mathbf{A} \cdot \mathbf{\Gamma}(k) \cdot \mathbf{A}^T + \mathbf{H} \cdot R_\omega \cdot \mathbf{H}^T \tag{24}$$

This completes the required relations for the optimal state estimation. Thus $\mathbf{K}_e$ provides the minimum estimation errors, given a knowledge of the process noise magnitude (R_ω), the measurement noise magnitude (R_ν), and the covariance initial condition ($\varphi(0)$) [11].

3.2. Current control loop

The current control loop, based on the MBPC technique avoids the use of modulation techniques since a single switching vector is applied during the whole switching period. The MBPC technique selects the control actions through solving an optimization problem at each sampling period. A model of the real system, is used to predict its output. This prediction is carried out for each possible output, or switching vector, of the six-phase inverter to determine which one minimizes a defined cost function. The proposed scheme is shown in Figure 3.

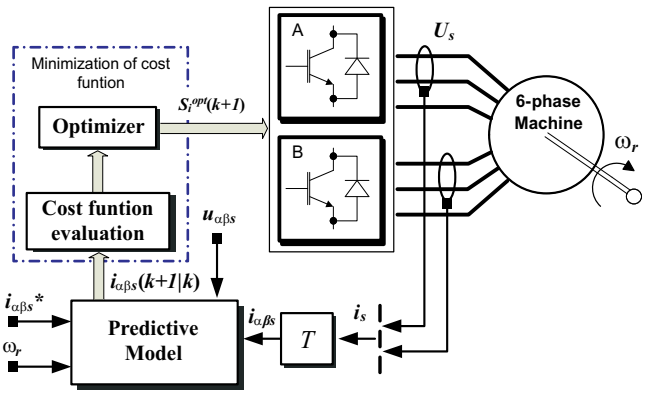

Figure 3. Current control loop based on the MBPC technique

3.2.1. Cost function

The cost function should include all aspects to be optimized. In the current predictive control applied to the asymmetrical dual three-phase induction machine, the most important feature to be optimized are the tracking errors of the stator currents in the $(\alpha - \beta)$ subspace for a next sampling time, since this variables are related to the electromechanical conversion. To minimize the prediction errors at each sampling time k it enough utilize a simple term as:

$$J = \| \hat{e}_{i\alpha s}(k+1|k) + \hat{e}_{i\beta s}(k+1|k) \|^2 \leftrightarrow \begin{cases} \hat{e}_{i\alpha s}(k+1|k) = i^*_{\alpha s}(k+1) - \hat{i}_{\alpha s}(k+1|k) \\ \hat{e}_{i\beta s}(k+1|k) = i^*_{\beta s}(k+1) - \hat{i}_{\beta s}(k+1|k) \end{cases} \tag{25}$$

where $\| \cdot \|$ denotes the vector modulus, i^*_s is a vector containing the reference for the stator currents and $\hat{i}_s(k+1|k)$ is the prediction of the stator currents calculated from measured and estimated states and the voltage vector $U_{\alpha\beta s}(k)$ as shown in Equation 20. Figure 4 (a) shows the all projection of the stator current predictions calculated from the prediction model. The current control selects the control vector that minimizes the cost function at each sampling time. Figure 4 (b) shows the selection of the optimal vector based on a minimization of prediction errors.

More complicated cost functions can be devised for instance to minimize harmonic content, VSI switching losses, torque and flux and/or active and reactive power. Also, in multi-phase

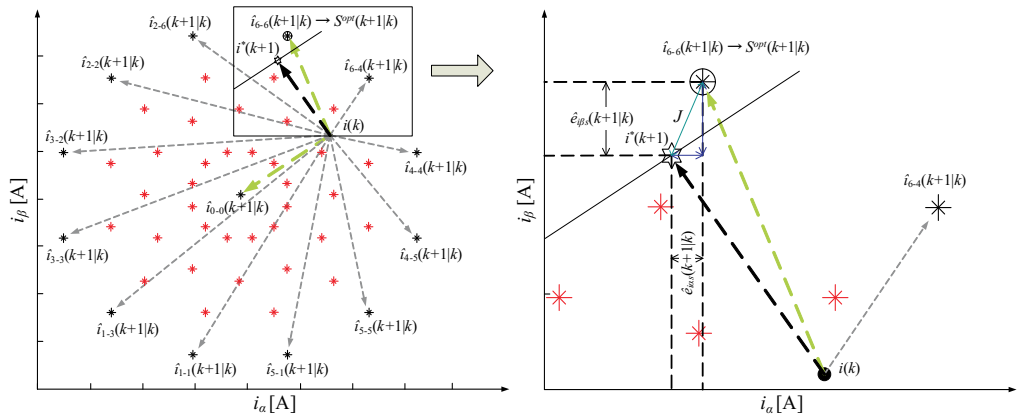

(a) Projection of the stator currents prediction in stationary reference frame $(\alpha - \beta)$

(b) Evaluation of the cost function (J) and selection of the optimal vector (S^{opt})

Figure 4. Minimization of tracking error in stator currents in stationary reference frame $(\alpha - \beta)$

drives stator current can be decomposed in subspaces in different ways. An appropriate decomposition allow to put more emphasis on harmonic reduction as will be shown in the case study for a six-phase motor drive [5, 12]. The more relevant cost functions are shown in Table 1. The superscript $(^*)$ denote the reference value and the terms involved in each cost function are detailed in the Table 2.

Controlled variables	Cost functions (J)
Currents (α-β) and harmonic $(x-y)$	$\|\|i_\alpha^* - i_\alpha\| + \|i_\beta^* - i_\beta\|\|^2 + \lambda.\|\|i_x^* - i_x\| + \|i_y^* - i_y\|\|$
Active and reactive power	$\|Q_{in}\| + \|P_{in}^* - P_{in}\|$
Torque and flux	$\|T_e^* - T_e\| + \lambda\|\|\psi_s^*\| - \|\psi_s\|\|$
Currents (α-β) and voltage balance	$\|\|i_\alpha^* - i_\alpha\| + \|i_\beta^* - i_\beta\| + \lambda.\|V_{c1} - V_{c2}\|$
Currents (α-β) and VSI switching losses	$\|\|i_\alpha^* - i_\alpha\| + \|i_\beta^* - i_\beta\|\| + \lambda.N_s$

Table 1. Possible cost functions in function to the controlled variables

Variable	Description
i_α	Measured α current
i_β	Measured β current
i_x	Measured x current
i_y	Measured y current
Q_{in}	Reactive power
P_{in}	Active power
T_e	Torque
ψ_s	Flux of the stator
λ	Weighting factor
V_{c1}, V_{c2}	Voltages on each capacitor (VSI balanced)
N_s	Number of switches

Table 2. Description of the terms involved in each cost function of the Table 1

3.2.2. Optimizer

The predictive model should be used 64 times to consider all possible voltage vectors. However, the redundancy of the switching states results in only 49 different vectors (48 active and 1 null) as shown on Figure 2. This consideration is commonly known as the optimal solution. The number of voltage vectors to evaluate the predictive model can be further reduced if only the 12 outer vectors (the largest ones) are considered. This assumption is commonly used if sinusoidal output voltage is required and it is not necessary to synthesize $(x-y)$ components. In this way, the optimizer can be implemented using only 13 possible stator voltage vectors[3]. This way of proceeding increases the speed at which the optimizer can be run, allowing decreasing the sampling time at the cost of losing optimality. A detailed study of the implications of considering the optimal solution can be found at [6]. For a generic multi-phase machine, where f is the number of phase and ε the search space (49 or 13 vectors), the control algorithm proposed produces the optimum gating signal combination S^{opt} as follows:

Algorithm 1 Proposed algorithm

comment: Compute the covariance matrix. Equation 23
$\mathbf{\Gamma}(k) = \varphi(k) - \varphi(k) \cdot \mathbf{C}^T (\mathbf{C} \cdot \varphi(k) \cdot \mathbf{C}^T + R_v)^{-1} \cdot \mathbf{C} \cdot \varphi(k)$
comment: Compute the KF gain matrix. Equation 22
$\mathbf{K}_e(k) = \mathbf{\Gamma}(k) \cdot \mathbf{C}^T R_v$
comment: Optimization algorithm
$J_o := \infty$, $i := 1$
while $i \leq \varepsilon$ **do**
  $\mathbf{S}_i \leftarrow \mathbf{S}_{i,j} \; \forall \, j = 1, ..., f$
  comment: Compute stator voltages. Equation 12
  $U_{\alpha\beta xys} = \left[u_{\alpha s},\, u_{\beta s},\, u_{xs},\, u_{ys},\, 0,\, 0 \right]^T = Vdc \cdot \mathbf{T} \cdot \mathbf{M}$
  comment: Compute a prediction of the state. Equation 15
  $\hat{\mathbf{X}}(k+1|k) = \mathbf{A}\mathbf{X}(k) + \mathbf{B}\mathbf{U}(k) + \mathbf{H}\varpi(k)$
  comment: Compute the cost function. Equation 25
  $J = \| \, \hat{e}_{i\alpha s}(k+1|k) + \hat{e}_{i\beta s}(k+1|k) \, \|^2$
  if $J < J_o$ **then**
    $J_o \leftarrow J$, $\mathbf{S}^{opt} \leftarrow \mathbf{S}_i$
  end if
  $i := i + 1$
end while
comment: Compute the correction of the covariance matrix. Equation 24
$\varphi(k+1) = \mathbf{A} \cdot \mathbf{\Gamma}(k) \cdot \mathbf{A}^T + \mathbf{H} \cdot R_\varpi \cdot \mathbf{H}^T$

4. Simulation results

A Matlab/Simulink simulation environment has been designed for the VSI-fed asynchronous asymmetrical dual three-phase induction machine, and simulations have been done to prove the efficiency of the scheme proposed. Numerical integration using fourth order Runge-Kutta

[3] 12 active, corresponding to the largest vectors in the $(\alpha-\beta)$ subspace and the smallest ones in the $(x-y)$ subspace plus a zero vector.

algorithm has been applied to compute the evolution of the state variables step by step in the time domain. Table 3 shows the electrical and mechanical parameters for the asymmetrical dual three-phase induction machine.

Parameter		Value
Stator resistance	R_s (Ω)	1.63
Rotor resistance	R_r (Ω)	1.08
Stator inductance	L_s (H)	0.2792
Rotor inductance	L_r (H)	0.2886
Mutual inductance	L_m (H)	0.2602
Inertia	J_i (kg.m^2)	0.109
Pairs of poles	P	3
Friction coefficient	B (kg.m^2/s)	0.021
Nominal frequency	ω_a (Hz)	50

Table 3. Parameters of the asymmetrical dual three-phase induction machine

Computer simulations allow valuing the effectiveness of the proposed control system under unload and full-load conditions, with respect to the mean squared error (MSE) of the speed and stator current tracking. In all cases is considered a sampling frequency of 6.5 kHz, and that the initial conditions of the covariance matrix ($\varphi(0)$), and the process and measurement noise, are known. The Kalman Filter has been started with the following initial conditions; $\varphi(0) = diag\left[1\ 1\ 1\ 1\right]$, in order to indicate that the initial uncertainty (rms) of the state variables is 1 A. Because $\varphi(k)$ is time varying, the KF gain is sensitive to this initial condition estimate during the initial transient, but the steady final values are not affected [11]. The magnitudes of the process noise (R_ω) and measurement noise (R_ν) are known and are generate using a Random Source block of the Simulink Signal Processing Blockset, assuming the following values, $R_\omega = 15 \times 10^{-3}$ and $R_\nu = 25 \times 10^{-3}$, respectively.

4.1. Efficiency of current control loop

A series of simulation tests are performed in order to verify the efficiency of current control loop in three points of operation of the machine. Figure 5 shows the current tracking in stationary reference frame $(\alpha - \beta)$ and $(x - y)$ subspaces considering sub-optimal solution in the optimization process (12 active and 1 null vectors). The predicted stator current in the α component is shown in the upper side (zoom graphs and green curves). For all cases of analysis efficiency is measured with respect to the MSE of the currents tracking in $(\alpha - \beta)$-$(x - y)$ subspaces and the total harmonic distortion (THD), defined as the ratio of the sum of the powers of all harmonic components to the power of the fundamental frequency, obtained from the Powergui-Continuous Simulink block. A 2.5 A reference stator current at 12 Hz is established for the case of Figure 5 (a). Figure 5 (b) shows the current tracking in the $(\alpha - \beta)$ and $(x - y)$ subspaces using a 2 A reference stator current at 18 Hz and Figure 5 (c) shows the current tracking in stationary reference frame using a 1.5 A reference stator current at 36 Hz. Table 4 summarizes the results of the three previous trials where are considered different amplitudes and angular frequencies for the reference current.

From the obtained results can be emphasized as follows:

Method	Test	MSE_α, MSE_β	MSE_x, MSE_y	THD_α, THD_β
MBPC	(a)	0.2105, 0.2322	0.9298, 0.9304	7.1330,7.5969
	(b)	0.1989, 0.2141	1.0957, 1.0885	10.3610, 11.8192
	(c)	0.2287, 0.2348	1.2266, 1.3102	15.8951, 17.4362

Table 4. Simulation results obtained from Figure 5

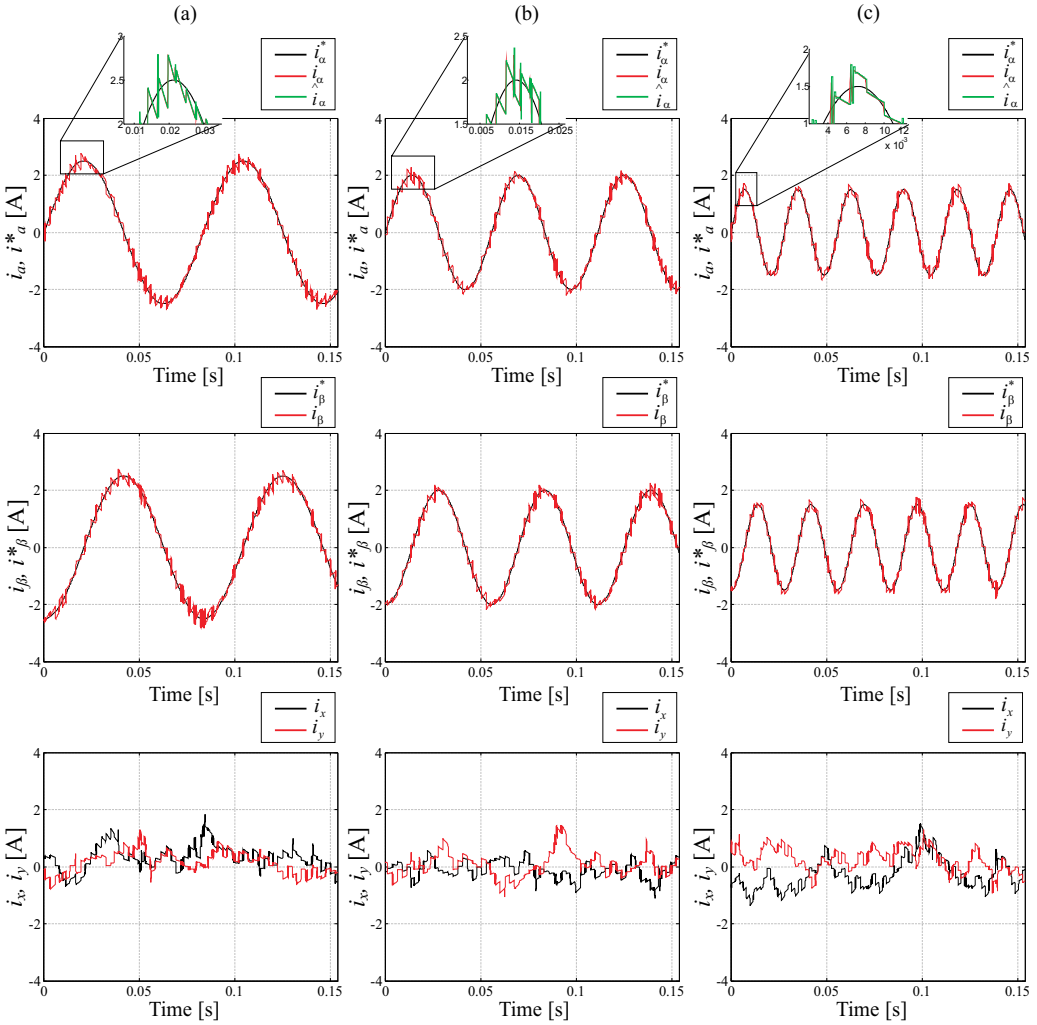

Figure 5. Stator current in $(\alpha - \beta)$ component tracking and $(x - y)$ current components. (a) 2.5 A (peak) current reference at 12 Hz. (b) 2 A current reference at 18 Hz and (c) 1.5 A current reference at 36 Hz

a. The MBPC is a flexible approach that, opposite to PWM based control methods, allows a straightforward generalization to different requirements only changing the cost function

b. The MBPC method is discontinuous technique, so the switching frequency is unknown. This feature reduces the switching losses (compared to continuous techniques) at expense of an increase in the harmonics of the stator current

c. As increases the frequency of the reference currents the switching frequency decreases, consequently there is a degradation in the THD of the stator currents as can be seen in Table 4

4.2. Proposed speed control method

The structure of the proposed speed control for the asymmetrical dual three-phase induction machine based on a KF is shown in Figure 6. The process of calculation of the slip frequency (ω_{sl}) is performed in the same manner as the Indirect Field Orientation methods, from the reference currents in dynamic reference frame (i^*_{ds}, i^*_{qs}) and the electrical parameters of the machine (R_r, L_r) [13, 14]. The inner loop of the current control, based on the MBPC selects control actions solving an optimization problem at each sampling period using a real system model to predict the outputs. As the rotor current can not be measured directly, it should be estimated using a reduced order estimator based on an optimal recursive estimation algorithm from the Equations 21-24.

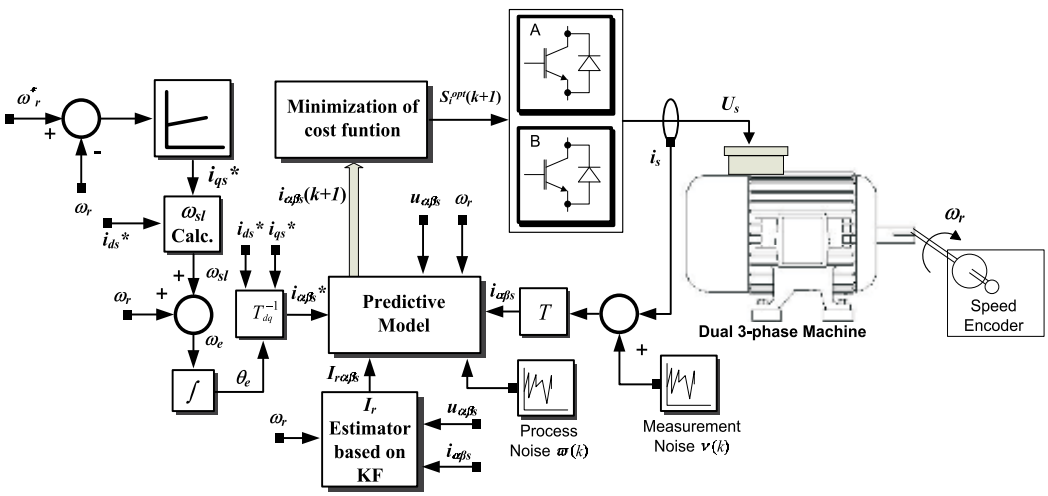

Figure 6. Proposed speed control technique based on KF for the asymmetrical dual three-phase induction machine

Different cost functions (J) can be used, to express different control criteria. The absolute current error, in stationary reference frame ($\alpha - \beta$) for the next sampling instant is normally used for computational simplicity. In this case, the cost function is defined as Equation 25, where i^*_s is the stator reference current and $i_{\alpha\beta}(k+1|k)$ is the predicted stator current which is computationally obtained using the predictive model. However, other cost functions can be established, including harmonics minimization, switching stress or VSI losses [6]. Proportional integral (PI) controller is used in the speed control loop, based on the indirect vector control schema because of its simplicity. In the indirect vector control scheme, PI speed controller is used to generate the reference current i^*_{ds} in dynamic reference frame. The current reference used by the predictive model is obtained from the calculation of the electric angle used to convert the current reference, originally in dynamic reference frame ($d - q$), to static reference frame ($\alpha - \beta$) as shown in Figure 6.

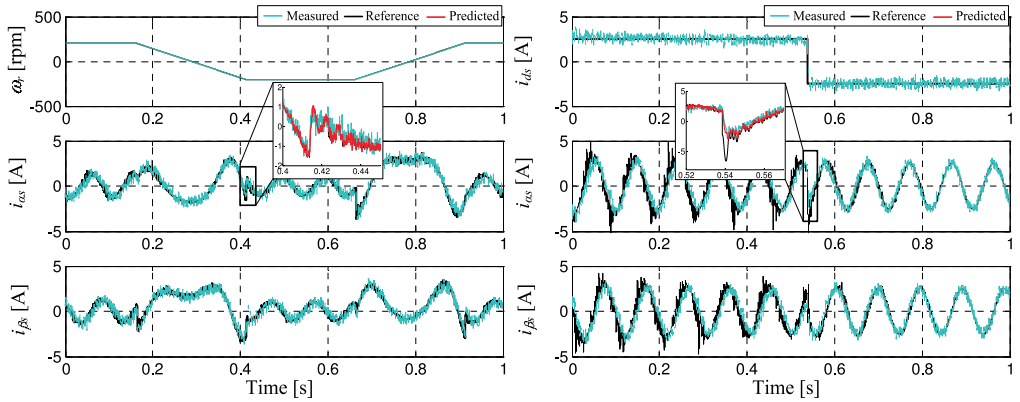

(a) Simulation results for a ±320 rpm step wave speed comand tracking

(b) Simulation results for a ±2.5 A step in the reference current comand tracking

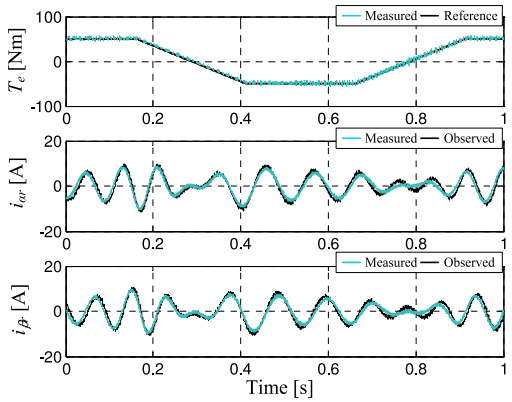

(c) Simulation results for a 50 Nm trapezoidal load

Figure 7. Simulation results for a proposed speed control. The predicted stator current in the α component is shown in the upper side (zoom graphs, red curves)

Figure 7 (a) shows simulation results for a 200 revolutions per minute (rpm) trapezoidal speed reference, if we consider a fixed current reference ($i_{ds}^{*} = 1$ A). The subscripts $(\alpha - \beta)$ represent quantities in the stationary frame reference of the stator currents. The measurement speed is fed back in the closed loop for speed regulation and a PI controller is used in the speed regulation loop as shown in Figure 6. The predicted stator current in the α component is shown in the upper side (zoom graph, red curve). Under these test conditions, the MSE in the speed and current tracking are 0.75 rpm and 0.15 A, respectively. Figure 7 (b) shows the step response for the induction machine to a change of ±2.5 A in the current reference (i_{ds}^{*} see Figure 6), if we consider a fixed speed reference ($\omega_r^{*} = 200$ rpm). In these simulation results, the subscripts $(\alpha - \beta)$ represent the stator current in stationary reference frame. Under these test conditions, the MSE in the stator current tracking are 0.1 A for the reference current (i_{ds}^{*}) and 0.18 A considering stationary reference frame. Finally, Figure 7 (c) shows a trapezoidal load application response, and the rotor current evolution (measured and observed) in stationary reference frame. These simulation results substantiate the expected

performance of the proposed algorithm, based on a Kalman Filter. The estimated rotor current converges to real values for these test conditions as shown in figures, proving that the observer performance is satisfactory.

5. Conclusions

In this chapter a new approach for the speed control of the asymmetrical dual three-phase induction machine has been proposed and evaluated. The speed control scheme uses an inner loop predictive current control based on the model, where the main advantage is the absence of modulation techniques. The MBPC is described using a state-space representation, where the rotor and stator current are the states variables. The proposed algorithm provides an optimal estimation of the rotor current in each sampling time in a recursive manner, even when internal parameters of the drive are not precisely known, and the measurements of the state variables are perturbed by gaussian noise. The theoretical development based on a Kalman Filter has been validated by simulations results. The method has proven to be efficient even when considering that the machine is operating under varying load regimes.

Acknowledgments

The author gratefully the Paraguay Government for the economical support provided by means of a Conacyt Grant (project 10INV01). Also, wishes to express his gratitude to the anonymous reviewers for their helpful comments and suggestions.

Author details

Raúl Igmar Gregor Recalde
Engineering Faculty of the National University of Asunción
Department of Power and Control Systems, Asunción-Paraguay

6. References

[1] Levi, E. (2008). Multiphase electric machines for variable-speed applications. *IEEE Transactions on Industrial Electronics*, Vol. 55, No. 5, (May 2008) page numbers (1893-1909), ISSN 0278-0046

[2] Bucknal R. & Ciaramella, K. (2010). On the Conceptual Design and Performance of a Matrix Converter for Marine Electric Propulsion. *IEEE Transactions on Power Electronics*, Vol. 25, No. 6, (June 2010) page numbers (1497-1508), ISSN 0885-8993

[3] Zhao Y. & Lipo, T. (1995). Space vector PWM control of dual three-phase induction machine using vector space decomposition. *IEEE Transactions on Industry Applications*, Vol. 31, No. 5, (October 1995) page numbers (1100-1109), ISSN 0093-9994

[4] Boglietti, A.; Bojoi, R.; Cavagnino, A.& Tenconi, A. (2008). Efficiency Analysis of PWM Inverter Fed Three-Phase and Dual Three-Phase High Frequency Induction Machines for Low/Medium Power Applications. *IEEE Transactions on Industrial Electronics*, Vol. 55, No. 5, (May 2008) page numbers (2015-2023), ISSN 0278-0046

[5] Arahal, M.; Barrero, F.; Toral, S.; Durán, M.; & Gregor, R. (2008). Multi-phase current control using finite-state model-predictive control. *Control Engineering Practice*, Vol. 17, No. 5, (October 2008) page numbers (579-587), ISSN 0967-0661

[6] Barrero, F.; Arahal, M.; Gregor, R.; Toral, S. & Durán, M. (2009). A proof of concept study of predictive current control for VSI driven asymmetrical dual three-phase AC machines. *IEEE Transactions on Industrial Electronics*, Vol. 56, No. 6, (June 2009) page numbers (1937-1954), ISSN 0278-0046

[7] Barrero, F.; Prieto, J.; Levi, E.; Gregor, R.; Toral, S.; Duran, M. & Jones, M. (2011). An Enhanced Predictive Current Control Method for Asymmetrical Six-phase Motor Drive. *IEEE Transactions on Industrial Electronics*, Vol. 58, No. 8, (Aug. 2011) page numbers (3242-3252), ISSN 0278-0046

[8] Gregor, R.; Barrero, F.; Toral, S.; Duran, M.; Arahal, M.; Prieto, J. & Mora, J. (2010). Predictive-space vector PWM current control method for asymmetrical dual three-phase induction motor drives. *IET Electric Power Applications*, Vol. 4, No. 1, (January 2010) page numbers (26-34), ISSN 1751-8660

[9] Duran, M.; Prieto, J.; Barrero, F. & Toral, S. (2011). Predictive Current Control of Dual Three-Phase Drives Using Restrained Search Techniques. *IEEE Transactions on Industrial Electronics*, Vol. 58, No. 8, (Aug. 2011) page numbers (3253-3263), ISSN 0278-0046

[10] Shi, K.L.; Chan, T.F.; Wong, Y.K. & Ho, S.L. (2002). Speed estimation of an induction motor drive using an optimized extended Kalman filter. *IEEE Transactions on Industrial Electronics*, Vol. 49, No. 1, (Feb. 2002) page numbers (124-133), ISSN 0278-0046

[11] Franklin, G.; Powell, J. & Workman, M. (1998). Optimal Estimation. The Kalman Filter, In: *Digital Control of Dynamic Systems*, Addison - Wesley, (Ed. 3rd), page numbers (389-392), ISBN 978-0-201-82054-6

[12] Vargas, R.; Cortes, P.; Ammann, U.; Rodriguez, J. & Pontt, J. (2007). Predictive Control of a Three-Phase Neutral-Point-Clamped Inverter. *Transactions on Industrial Electronics*, Vol. 54, No. 5,(Oct. 2007), page numbers (2697-2705), ISSN 0278-0046

[13] Ong, C.M. (1997). Indirect Field Orientation Methods, In: *Dynamic Simulation of Electric Machinery Using MatLab/Simulink*, Prentice Hall, page numbers (439-440), ISBN 978-0-137-23785-2

[14] Krause, P.; Wasynczuk, O. & Sudhoff, S. (2002). Indirect Rotor Field-Oriented Control, In: *Analysis of Electric Machinery and Drive Systems*, Wiley-IEEE Press, (Ed. 2nd) page numbers (550-554), ISBN 978-0-471-14326-0

Chapter 17

Evaluation of an Energy Loss-Minimization Algorithm for EVs Based on Induction Motor

Pedro Melo, Ricardo de Castro and Rui Esteves Araújo

Additional information is available at the end of the chapter

http://dx.doi.org/10.5772/52280

1. Introduction

This work addresses the problem of optimal selection of the flux level in induction motors used in electric vehicles (EVs). The basic function of a fully electric powertrain controller is to generate electric torque (force) which is required at any time by the driver. But, it is well-known that the flux level used in a controller for induction motors offers an extra degree of freedom that can be used to maximise energy efficiency. The induction motor is an efficient motor when working close to its rated operating point (Zeraoulia, Benbouzid et al. 2006). However, at light loads the efficiency is greatly reduced when magnetization flux is maintained at nominal value. In induction motor drives for EVs, where real operation conditions are significantly different from rated conditions, the energy saving control is crucial for improving the running distance per charge.

Due to the widespread use of induction motors, its efficiency optimization gave rise to a large number of research publications (Bazzi & Krein 2010). Algorithms for real-time implementation of loss-minimization methods are vital for designing intelligent and optimized EV controllers. Standard methods for induction motor control, including field-oriented control (FOC) or direct torque control (DTC), can be improved in efficiency by using loss minimization control. Basically, there are three different methods to improve the efficiency in induction motors: i) loss model based methods (which is considered in this work), ii) power measure based methods, also known as search controllers; and iii) hybrid controllers that combines the first two methods. The main goal of the present work is to investigate the potential benefits of loss minimization algorithms in EVs powered by induction motors. Accordingly, a detailed simulation case study will be provided which will show that, depending on the type of driving cycle, energy savings up to 12.5% can be achieved. The chapter is organized as follows: Section 2 reviews the basic concepts of rotor field oriented control (FOC). Section 3 introduces the loss minimization method based on a standard mathematical model of the induction motor and gives the value of the flux level

which maximizes the energy efficiency at given torque subject to voltage and currents limits. In Section 4 the developed EV non-causal simulation model (motor-to-wheel) is presented, while Section 5 includes the simulation results and its analysis for a set of standard driving cycles. Finally, Section 6 contains the main conclusions and some reference to future work.

2. Rotor FOC

In this study, a model based approach was selected for minimizing the induction motor losses (Lim & Nam 2004). This Loss Minimization Algorithm (LMA) was developed in d-q coordinates, considering an equivalent motor model in the synchronous reference frame, as described in section 3. In addition, as we will discuss in a later section, the induction motor controller is also based on rotor FOC. These reasons justify a brief review on induction motor rotor FOC. Figure 1 represents the basic concept of rotor FOC (based on Krishnan, 2001).

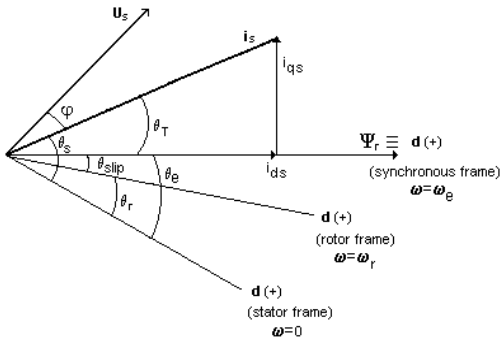

Figure 1. Rotor FOC principle for induction motors

Recall that, in the synchronous frame (ω_e), the rotor magnetic flux (Ψ_{rd}) is aligned with d axis, thus $\Psi_{rd} = \Psi_r$, $\Psi_{rq} = 0$. In the same reference frame, the stator current component i_{ds} is aligned with the rotor magnetic flux, controlling its value. On the other hand, i_{qs} (shifted $\pi/2$ electrical rad from i_{ds}) controls the motor electromagnetic torque:

$$\Psi_r = L_m i_{ds} \left(\text{steady} - \text{state}\right) \tag{1}$$

$$T_t\left(t\right) = K_t \Psi_r i_{qs} \tag{2}$$

From figure 1, it may be seen that i_{ds} and i_{qs} are, respectively, the d and q components of the space vector $\mathbf{i_s}$ in the synchronous reference frame. This way, from the control philosophy perspective, i_{ds} and i_{qs} regulation is implemented in this reference frame; however, from the control hardware perspective, i_{ds} and i_{qs} must be considered in stator reference phase-coordinates (i_a, i_b, i_c). To do that, it is mandatory to obtain i_{ds} and i_{dq} in the static d-q reference, which requires the information about $\theta_s=\theta_e+\theta_T$. The determination of θ_e is the main issue, since $\theta_T = \text{arctg}(i_{qs}/i_{ds})$; θ_e calculation can be accomplished through θ_{slip} and θ_r (see figure 1) – indirect FOC.

Since
$$\omega_{\text{slip}} = \omega_{\text{e}} - \omega_{\text{r}} = \frac{L_m}{L_r / R_r} \frac{i_{qs}}{\Psi_r} \tag{3}$$

θ_{slip} is given by:

$$\theta_{\text{slip}}(\text{t}) = \theta_{\text{slip}}(\text{t}_0) + \int_{t_0}^{t} \omega_{slip}\, dt \tag{4}$$

Knowing the instantaneous rotor speed ω_r, one have:

$$\theta_{\text{r}}(\text{t}) = \theta_{\text{r}}(\text{t}_0) + \int_{t_0}^{t} \omega_r dt \tag{5}$$

From figure 1:

$$\theta_{\text{e}}(\text{t}) = \theta_{\text{slip}}(\text{t}) + \theta_{\text{r}}(\text{t}) \tag{6}$$

3. Loss minimization by selecting flux references

The loss-minimization scheme demands the decrease or increase of the flux level depending on the torque. This means that the minimization algorithm selects the flux reference through the minimization of the copper and core losses while ensuring the desired torque requested by the driver. Different techniques for loss minimization in induction motor are presented in the literature (Bazzi & Krein 2010). Recently, (Lim & Nam 2004) proposed a LMA that features a major difference from previous works by taking into consideration the leakage inductance and the practical constrains on voltage and current in the high-speed region, which play a great role in EVs applications. This is an important difference from other works, like (Garcia et al., 1994), (Kioskeridis & Margaris, 1996), (Fernandez-Bernal et al., 2000), where leakage inductance are not considered (although similar motor loss models are included), leading to considerable result differences in the high-speed region. In addition, our work considers the optimization of both positive and negative torque generation with bounded constraints on both current and voltage.

3.1. The LMA method

The implemented method is based on the conventional induction motor model where the iron losses are represented by an equivalent resistance (R_m) modelling the iron losses, placed in parallel with the magnetizing inductance (L_m). A simplification is then considered, allowing a partial decoupling between R_m and L_m: the iron losses are represented by separated circuits with dependent voltage sources (V_{dm}^e and V_{qm}^e). Figure 2 shows the complete equivalent model in the synchronous reference frame.

Considering steady state analysis with low slip values (s) – rotor iron losses may be neglected –, the total motor losses (copper and iron ones) are given by (Lim & Nam 2004):

$$P_{loss} = R_d(\omega_e) i_{ds}^{e\,2} + R_q(\omega_e) i_{qs}^{e\,2} \tag{7}$$

$$R_d(\omega_e) = R_s + \frac{\omega_e^2 L^2{}_m}{R_m} \tag{8}$$

$$R_q(\omega_e) = R_s + \frac{R_r L_m^2}{L_r^2} + \frac{\omega_e^2 L^2{}_m L_{lr}^2}{R_m L_r^2} \tag{9}$$

Where:

i_{ds}^e : d-axis stator current in the synchronous reference frame;

i_{qs}^e : q-axis stator current in the synchronous reference frame;

ω_e : electrical angular frequency;

- R_s; R_r: stator and rotor resistances (respectively);
- R_m: equivalent stator iron losses resistance;
- L_r; L_{lr}: rotor total inductance and rotor leakage inductance (respectively);
- L_m: magnetizing inductance.

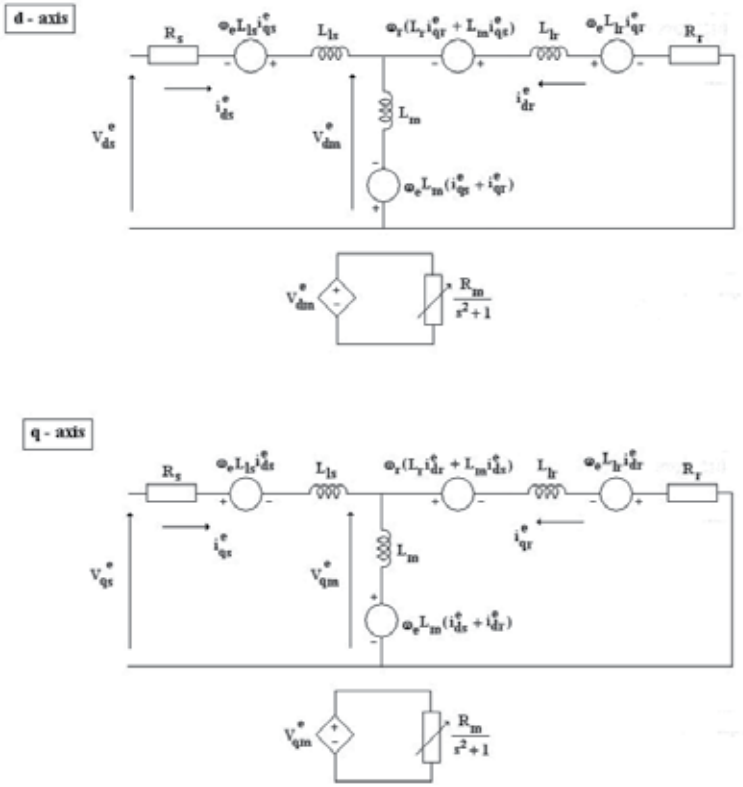

Figure 2. Simplified motor equivalent model (Lim & Nam 2004)

Note that $R_d(\omega_e)$ and $R_q(\omega_e)$ are the direct (d) and quadrature (q) components of the equivalent resistors representing the total losses. Voltage and current constraints (mentioned before) are defined by (neglecting stator resistor drop):

$$(\omega_e L_s i_{ds}^e)^2 + (\omega_e \sigma L_s i_{qs}^e)^2 \leq V_{max}^2 \tag{10}$$

$$i_{ds}^{e\,2} + i_{qs}^{e\,2} \leq I_{max}^2 \tag{11}$$

Where:

$$\sigma = 1 - L_m^2 / (L_s L_r) \tag{12}$$

σ: induction machine leakage coeficient; L_s: stator total inductance;

V_{max}; I_{max}: motor (or inverter) voltage and current limits, respectively;

An important observation is that voltage constraint depends on the considered ω_e.

The LMA´s goal is to achieve the optimal flux level that minimizes the motor total losses under voltage and current constraints. The motor rated flux level must also be taken into consideration, in order to avoid magnetic saturation. Moreover, the torque developed by the motor cannot be compromised by the LMA implementation. From the mathematical point of view, the LMA algorithm consists in:

$$\min P_{loss}(i_{ds}^e, i_{qs}^e)$$

$$\text{s.t.: (10), (11)}$$

$$i_{ds}^e \leq I_{dn} \tag{13}$$

$$T_e = K_t i_{ds}^e i_{qs}^e$$

Where:

I_{dn}: rated d-axis stator current

T_e: electromagnetic torque (steady-state), considering rotor FOC;

$$K_t = \frac{3}{2} p \frac{L_m^2}{L_r} \tag{14}$$

[p: pairs of magnetic poles]

3.1.1. Unconstrained optimization

In the (i_{ds}^e, i_{qs}^e) domain, the optimal flux solution for the region inside the inequality restrictions is achieved through Lagrange multipliers method, since only one restriction is active – the torque one

For one restriction only, the general problem is formulated as follows:

$$\nabla L(i_{ds}^{\ e}, i_{qs}^{\ e}, \lambda) = 0 \tag{15}$$

with: $$L(i_{ds}^{\ e}, i_{qs}^{\ e}, \lambda) = P_{loss}(i_{ds}^{\ e}, i_{qs}^{\ e}) + \lambda (T_e - K_t i_{ds}^{\ e} i_{qs}^{\ e}) \tag{16}$$

where $L(i_{ds}^e, i_{qs}^e, \lambda)$ is the lagrangian associated to the problem, λ is the Lagrange multiplier, $P_{loss}(i_{ds}^e, i_{qs}^e)$ is the cost function and T_e-$K_t i_{ds}^e i_{qs}^e$ is the restriction. Applying first-order optimal condition (15) gives the following equation system:

$$\frac{\partial L}{\partial i_{sq}^{\ e}} = 0 \qquad \frac{\partial L}{\partial i_{sq}^{\ e}} = 0 \qquad \frac{\partial L}{\partial \lambda} = 0 \tag{17}$$

yielding

$$i_{ds}^e = \left(\frac{T_e^2}{K_t^2} \frac{R_q(\omega_e)}{R_d(\omega_e)} \right)^{1/4} \; ; \; i_{qs}^e = \left(\frac{T_e^2}{K_t^2} \frac{R_d(\omega_e)}{R_q(\omega_e)} \right)^{1/4} \tag{18}$$

3.1.2. Constrained optimization

Previously, all the inequalities were considered inactive. In order to obtain the optimal solutions in each restriction boundary, the Lagrange multipliers method is applied for each inequality constraint activation (i.e. only "=" operator is valid), together with the torque one. This way, three non linear algebraic equation systems are defined for the inequality constraints. The optimal i_{ds}^e is given by these systems solutions, since it refers to regions on the border lines of the inequality restrictions.

Table 1 presents the solutions, in (i_{ds}^e, i_{qs}^e) plane, for interior points (zone 0) and for inequality restriction borders (zones 1, 2 and 3).

The voltage and current limits (V_{max}, I_{max} and I_{dn}) lead naturally to three regions of operation referred to as constant torque (low-speed), constant power (midrange speed) and constant power-speed (high-speed), as defined in (Novotny & Lipo, 1996). The transition between constant torque region and power region is characterized by the rated speed (ω_n), which is defined by the interception of inequality restrictions border lines:

$$(\omega_n L_s i_{ds}^e)^2 + (\omega_n \sigma L_s i_{qs}^e)^2 = V_{max}^2 \tag{19}$$

$$i_{ds}^{e\ 2} + i_{qs}^{e\ 2} = I_{max}^2 \tag{20}$$

$$i_{ds}^{e} = I_{dn} \tag{21}$$

Zone	Name	Active Constraints	Solution
0	LMA Operation in Interior Points	$T_e = K_t i_{ds}^e i_{qs}^e$	(18)
1	Max Torque Limit	$T_e = K_t i_{ds}^e i_{qs}^e$ $i_{ds}^e = I_{dn}$	$i_{ds}^e = I_{dn}$; $i_{qs}^e = \frac{T_e}{K_t I_{dn}}$
2	Max. Current Limit	$T_e = K_t i_{ds}^e i_{qs}^e$ $i_{ds}^{e\,2} + i_{qs}^{e\,2} = I_{max}^{\ 2}$	$i_{ds}^e = \left(\frac{I_{max}^2 - (I_{max}^4 - 4T_e^2 / K_t^2)^{1/2}}{2} \right)^{1/2}$ $i_{qs}^e = \left(\frac{I_{max}^2 + (I_{max}^4 - 4T_e^2 / K_t^2)^{1/2}}{2} \right)^{1/2}$
3	Max. Voltage Limit	$T_e = K_t i_{ds}^e i_{qs}^e$ $(\omega_e L_s i_{ds}^e)^2$ $+(\omega_e \sigma L_s i_{qs}^e)^2 = V_{max}^2$	$i_{ds}^e = \left(\frac{V_{max}^2 + (V_{max}^4 - 4\omega_e^4 \sigma^2 L_s^4 T_e^2 / K_t^2)^{1/2}}{2(\omega_e L_s)^2} \right)^{1/2}$ $i_{qs}^e = \left(\frac{V_{max}^2 - (V_{max}^4 - 4\omega_e^4 \sigma^2 L_s^4 T_e^2 / K_t^2)^{1/2}}{2(\omega_e L_s)^2} \right)^{1/2}$

Table 1. LMA optimized solutions

The calculated result is:

$$\omega_n = \frac{V_{max}}{L_s} \frac{1}{[I_{dn}^2 + \sigma^2 (I_{max}^2 - I_{dn}^2)]^{1/2}} \tag{22}$$

ω_c is the boundary speed between constant power and power-speed (P_{mec}*ω_e=constant) regions:

$$\omega_c = \frac{V_{max}}{I_{max} L_s} \left(\frac{\sigma^2 + 1}{2\sigma^2} \right)^{1/2} \tag{23}$$

For region 1, the maximum torque is limited by I_{dn} and I_{max}:

$$T_{m1} = K_t I_{dn} (I_{max}^2 - I_{dn}^2)^{1/2} \tag{24}$$

The maximum torque in region 2 is limited by V_{max} and I_{max}:

$$T_{m2} = K_t \frac{[(V_{max} / (\omega_e L_s))^2 - I_{max}^2 \sigma^2]^{1/2} [I_{max}^2 - (V_{max} / (\omega_e L_s))^2]^{1/2}}{1 - \sigma^2} \tag{25}$$

In region 3, the maximum torque is limited by V_{max}, but the current is smaller than I_{max}. So, the current limit does not interfere with T_{m3}:

$$T_{m3} = K_t \left(\frac{V_{max}}{\omega_e L_s} \right)^2 \frac{1}{2\sigma} \tag{26}$$

3.1.3. Optimal I_{ds} generation

For the zone in the (i_{ds}^e, i_{qs}^e) plane limited by restrictions (10), (11) and $i_{ds}^e \leq I_{dn}$, optimal result (18) is valid, meaning that:

$$i_{ds}^e = \left(\frac{R_q(\omega_e)}{R_d(\omega_e)} \right)^{1/2} i_{qs}^e \tag{27}$$

In the border lines of those restrictions, the previous relation can not be considered. So, for region 1, (18) is applied if:

$$i_{qs}^e \leq \left(\frac{R_d(\omega_e)}{R_q(\omega_e)} \right)^{1/2} * I_{dn} \tag{28}$$

The i_{qs}^e upper limit in (28) defines T_{p1}(see Figure 3):

$$T_{p1} = K_t \left(\frac{Rd(\omega_e)}{Rq(\omega_e)} \right)^{1/2} I_{dn}^2 \tag{29}$$

Of course, for: $$\left(\frac{Rd(\omega_e)}{Rq(\omega_e)} \right)^{1/2} * I_{dn} < i_{qs}^e \leq (I_{max}^2 - I_{dn}^2)^{1/2} \rightarrow i_{ds}^e = I_{dn} \tag{30}$$

For region 2, (18) can be considered, until the voltage limit (V_{max}) is achieved:

$$i_{qs}^e \leq \frac{V_{max} / (\omega_e L_s \sigma)}{[\sigma^{-2} + R_d(\omega_e) / R_q(\omega_e)]^{1/2}} \left(\frac{Rd(\omega_e)}{Rq(\omega_e)} \right)^{1/2} \tag{31}$$

This way, T_{p2} is given by the following expression:

$$T_{p2} = K_t \frac{V_{max}^2 [R_d(\omega_e) * R_d(\omega_e)]^{1/2}}{[\sigma^2 R_d(\omega_e) + R_q(\omega_e)](\omega_e L_s)^2} \tag{32}$$

Above this limit, i_{ds}^e (and i_{qs}^e) is given by zone 3 solution (table 1).

As stated before, only the voltage limit must be considered for region 3, which means that $T_{p3}= T_{p2}$. Of course, for this region one must consider $\omega_e > \omega_c$.

Figure 3 presents the paths for I_{ds}* generation in i_{ds}; i_{qs} coordinates (origin-T_p-T_m), considering the three described operation regions. Quadrants I and II are represented, in order to consider both motor and braking modes (optimal i_{ds} paths for quadrant II are symmetric to quadrant I paths).

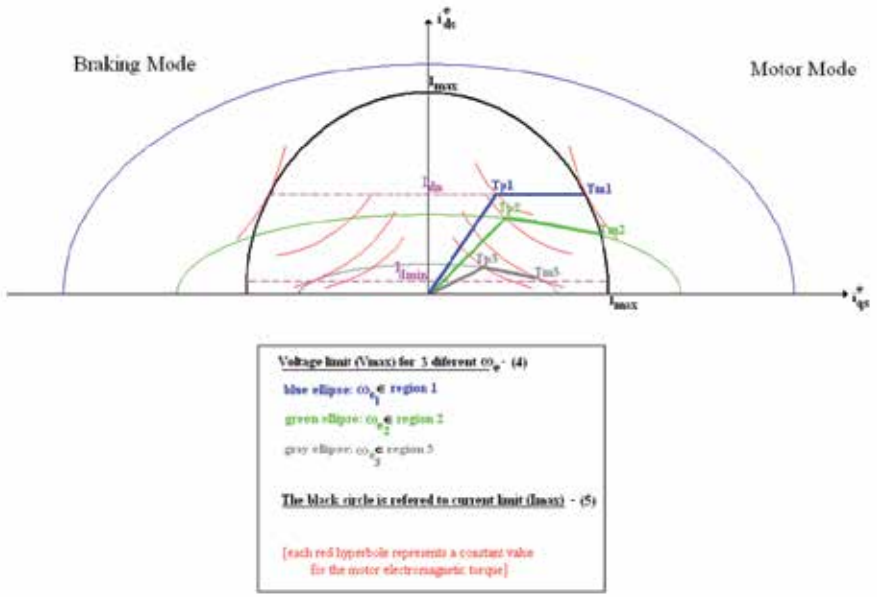

Figure 3. I_{ds}* paths for ω_{e1} (blue), ω_{e2} (green) and ω_{e3} (gray)

It is clear the linear evolution in the three regions (given by (27)), while in region 3, only voltage limit must be considered, since I_{max} is not reached. After that, in region 1, I_{dn} imposes the optimal path. In region 2 both current and voltage limits (i.e. I_{max} and V_{max}) restrict I_{ds} optimal path, while in region 3, I_{max} most probably is not reached.

3.2. Optimal I_{ds} generation for the simulated induction motor

In order to get some insight on LMA main features, a first set of results is presented in figures 4-6, based on an induction motor, with the following parameters:

[Rs; Rr] (Ω) [0,399; 0,3538]
[Ls; Lr] (H) [59,3; 60,4]*10^{-3}
[ls; lr] (H) [2,7; 3,8]*10^{-3}
Lm (H) 56,6*10^{-3}
Rm (Ω) 350
J(kg m^2) 0,089

Table 2. Induction Motor Parameters (9 kW; 60 Hz; 4 poles; 1750 rpm)

Figure 4 represents the optimal I_d generation for conventional approach, i.e. constant flux +field weakening (CF+FW), and the LMA approach.

Inspecting these results one can find that the LMA influence on I_d* is mostly visible for low torques (T<20 N.m). It is interesting to note that in the high speed zone (>2000 rpm), LMA and conventional flux regulation tend to present closer I_d* values, as the speed increases. Also, for high torque values (above 30 N.m) both approaches have similar performances.

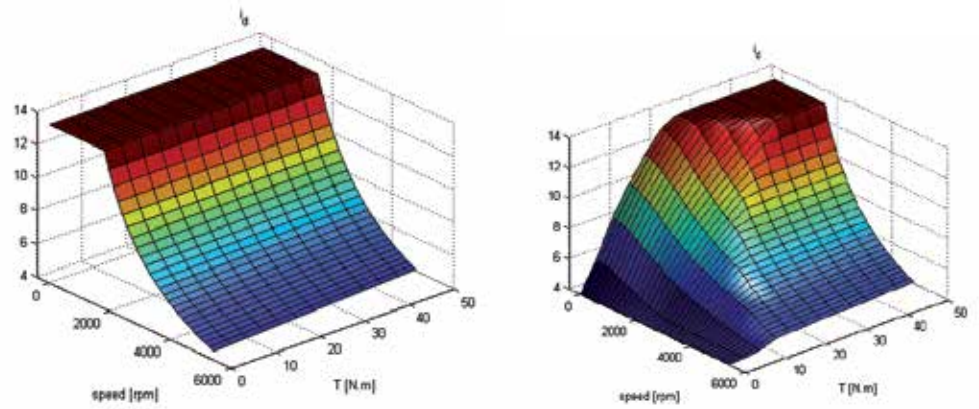

(a) (b)

Figure 4. I_{ds}* generations: a) CF+FW; b) LMA

From the above analysis, it is expectable that the differences in the generation of I_d* lead to different efficiencies curves of the induction motor, which is, indeed, observed in the maps illustrated in Figure 5.

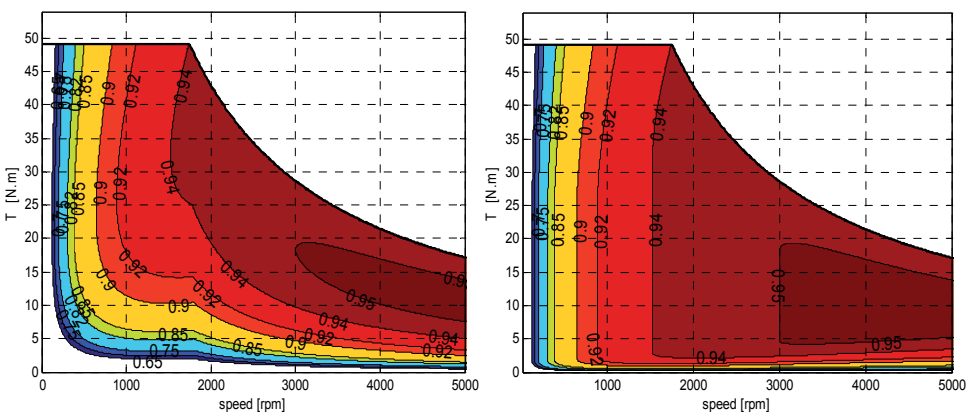

(a) (b)

Figure 5. Induction motor efficiency maps: a) CF+FW; b) LMA

A complementary perspective is presented in figure 6. It can be seen that the main LMA influence region is below 15 N.m (about 30% of motor nominal torque), with a slight behavior difference, according to n<2000 rpm or n>2000rpm: in the former case (coincident with the

constant torque zone), the LMA's efficiency gain is almost constant, while in the late case the energy savings decrease in a smooth way to zero.

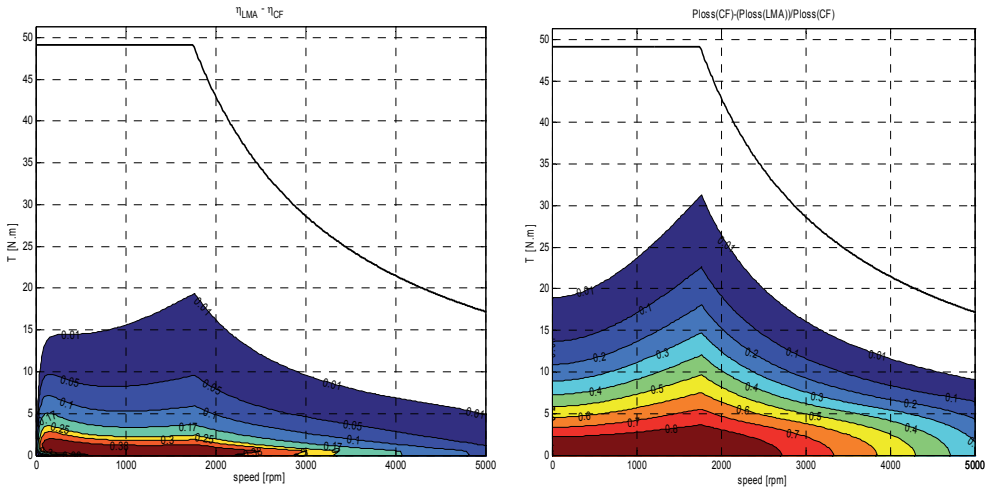

Figure 6. LMA Efficiency gain (a) and relative loss differences (b) compared to (CF+FW)

Naturally, LMA acts directly on motor iron losses, since it regulates I_{ds}. However, it has also an impact in motor copper losses, because it provides a better equilibrium between I_{ds} and I_{qs}, particularly in regions where I_{ds} regulation has wide limits. This can be seen in (7).

As a side-note, when considering the plane surfaces in figure 4 (for $I_{d\ max}$ and $I_{d\ min}$), interesting correlations can be made with figure 3, through ($I_{d\ max}$, $I_{d\ min}$) dashed lines and the torque hyperbolas (e.g. higher torques are provided by $I_{d\ min}$ as the speed grows).

4. Simulation model

To evaluate the LMA´s contributions to the EV energy consumption reduction, and comparing it to the conventional flux regulation, a simulation study was performed with four diferent driving cycles: ECE-R15, Europe: City, 11-Mode (Japan) and FTP-75. Simulation with other drive-cycles was also implemented, but results achieved with these four give a wide overview of LMA´s features. For that purpose, a Matlab/Simulink model was built, which is represented in figure 7.

Basically, I_d* is generated through (CF+FW) method or by the LMA – blocks (3a) and (3b), respectively. The induction motor is controlled by conventional rotor FOC (block 4); the motor model in block 5 is presented in section 4.4. The motor load and speed references are generated based on a particular drive cycle features (block 1), which includes the vehicle dynamic and mechanical transmission models. Finally, block 2 implements the speed controller (based on a proportional+integral(PI) control law) which generates the motor torque reference. In the following sections, the main model blocks are discribed.

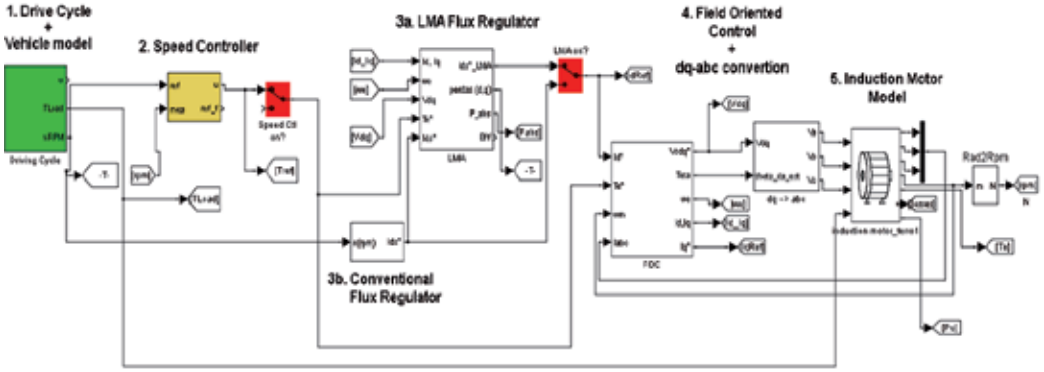

Figure 7. Global simulation model

4.1. Drive cycle+vehicle model

The drive cycles plus the vehicle and mechanical transmission models were implemented with the QuasiStatic Simulation Toolbox (QSS TB), based on Matlab/Simulink, developed by (Guzzella, Amstutz, 2005). The QSS TB library integrates a set of several elements, such as driving cycles, vehicle dynamics, internal combustion engine, electrical motor and mechanical transmisson. Batteries, supercapacitor and fuel cell are also included.

Essentially, it considers a backward (wheel-to-engine) quasi-satic causal model which, based on driving cycle speeds (at discrete times), calculates accelerations and determines the necessary forces, based on the vehicle features and an eventual mechanical transmission. The implemented model includes the QSS TB elements depicted in figure 8.

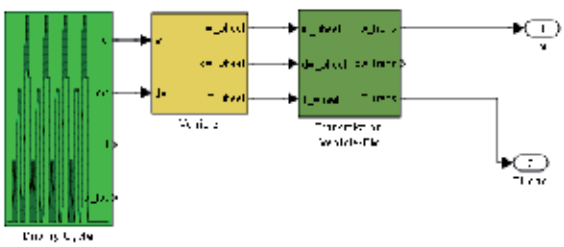

Figure 8. Drive cycle and vehicle/transmission models

The load power demanded to the induction motor ($T_{load}*\omega_r$) considers the drive cycle, vehicle dynamics (rolling and aerodynamic resistance, only in the plane) and also a mechanical transmission with a fixed gear ratio. The vehicle dynamics is modelled by the following equation:

$$M_t \frac{dv(t)}{dt} = F_d(t) - M_t g C_r - \frac{1}{2}\rho C_w A v(t)^2 \quad (33)$$

Where:
M_t - vehicle mass + equivalent mass of rotating parts;
v(t) – vehicle instantaneous longitudinal speed;
$F_d(t)$ – instantaneous driving force;
g – gravity acceleration;
Cr, Cw – rolling friction coefficient, aerodynamic drag coefficient;
ρ, A – air density; vehicle´s cross section.

Besides the inertia force, associated to vehicle displacement, the inertia of rotating parts (i.e., kinetic energy stored on it caused by rotational movement) should also be considered, since it is the motor(s) who supply it. This is considered in the "equivalent mass of rotating parts" M_t term (see Table 3). It should be noted that driving cycle block output speed (v) and acceleration (dv) are discrete values. The time step size default value is 1 s; however, in order to increase simulation accuracy, its value was fixed in 0,01 s.

Vehicle and transmission parameters are shown in Tables 3 and 4:

Total vehicle's mass (kg)	350
Rotating mass (%)	5
Vehicle´s cross section (m^2)	1,5
Wheel diameter (m)	0,3
Aerodynamic drag coefficient	0,3
Rolling friction coefficient	0,008

Table 3. Vehicle Parameters

Gear ratio	5
Efficiency (%)	98
Idling losses by friction (W)	10
Minimum wheel speed beyond which losses are generated (rad/s)	1

Table 4. Mechanical Transmission Parameters

4.2. Rotor flux setpoint generation

a. LMA

Figure 9 presents the developed LMA block set. R_d and R_q are inputs for the block regions "$w_e<w_n$" and "$w_e>w_n$". Basically, these two elements generate I_{ds}*, according to 3.1.3. As it was described, for zones in the (i_{ds}; i_{qs}) plane limited by restrictions (10), (11) and $i_{ds} \leq I_{dn}$, equation (27) is applied. For the border lines, the three defined regions must be considered: in region 1, I_{ds}* is restricted to its maximum allowable value (I_{dn}); for regions 2 and 3, only voltage limit is considered in I_{ds}* generation restriction. Since $T_{p2} = T_{p3}$, the same block can be used for generating I_{ds}* in these two regions.

Since the flux level should not decrease below a minimum value (I_{d_min}), in order to guarantee that $I_{d\_min} \leq I_{ds} \leq I_{dn}$, two saturation blocks are placed at "$w_e<w_n$" and "$w_e>w_n$" outputs.

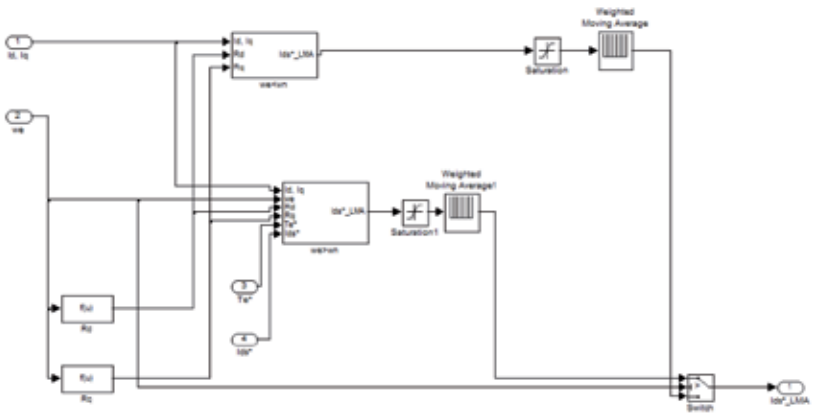

Figure 9. LMA block contents

Figure 10 shows the interior of "w_e<w_n" block.

As it can be seen, I_{ds}* is generated by (27), while I_{ds}<I_{dn}; after that I_{ds}*=I_{dn}. It should be noted that the absolute value of I_{qs} must be used, in order to consider both motor and braking modes.

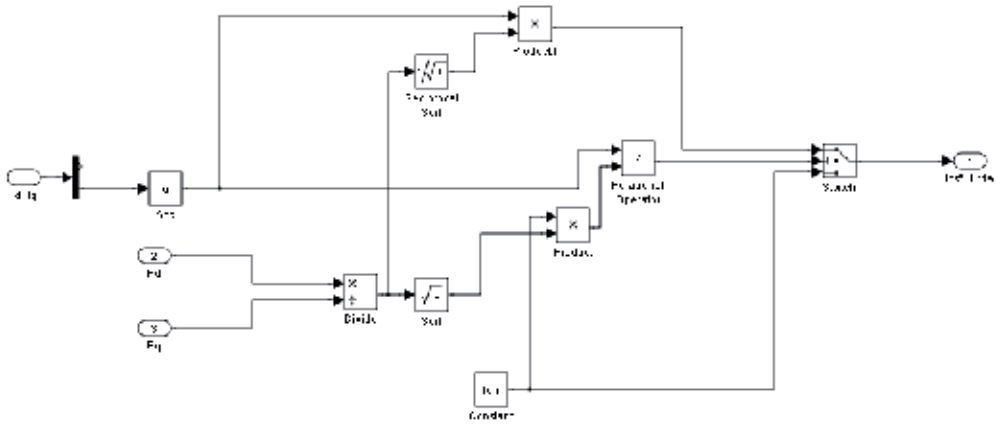

Figure 10. I_{ds}* generation in region 1 (blue path in figure 3)

The block "w_e>w_n" is represented in figure 11. Equation (27) regulates I_{ds}* generation until (31) is no longer true (notice that the absolute value of i_{qs} is compared to the product of "V_{max} restriction" by $(R_d/R_q)^{1/2}$). After that, I_{ds}* is given by zone 3 solution in table 1 (s_3)– "Id* for Vmax restriction border" block. It also should be pointed that when a load point overcomes the voltage limit, the result given by (s_3) is a complex value. In order to deal with this issue, for these situations I_{ds} is taken from the conventional flux regulator.

In contrast with the LMA, the conventional flux regulation (depicted as block (3b) in Figure 7) generates a I_{ds} setpoint according to the following strategy:

$$\begin{cases} I_{ds} = I_{dn} & n \le n_n \\ I_{ds} = n_n/n \cdot I_{dn} & n > n_n \end{cases} \tag{34}$$

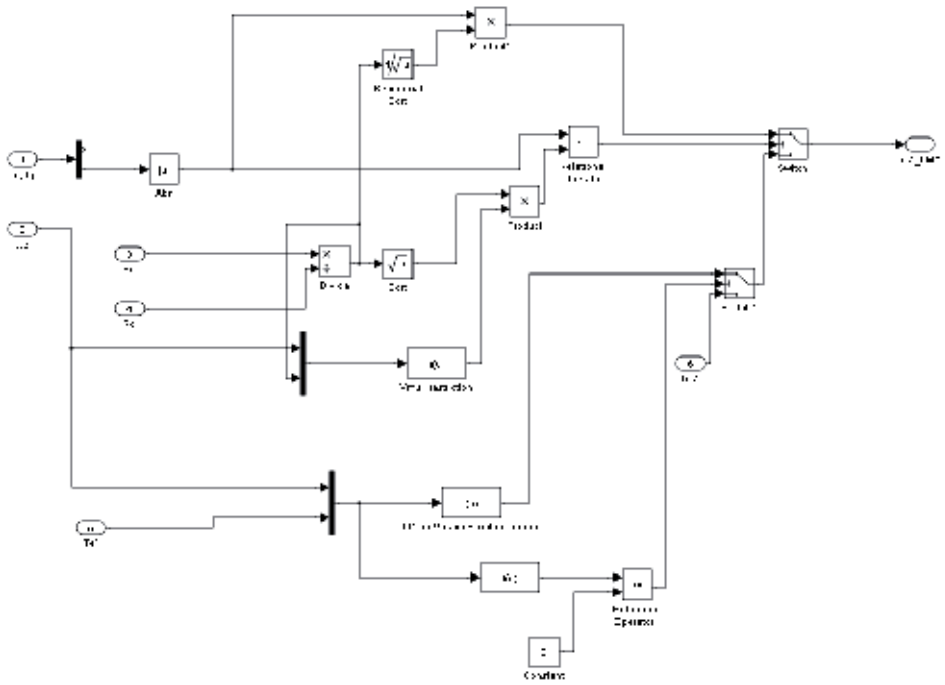

Figure 11. I_{ds}* generation for regions 2 and 3 (green and gray paths in figure 3)

4.3. Rotor indirect FOC

Figure 12 shows the block structure for indirect FOC.

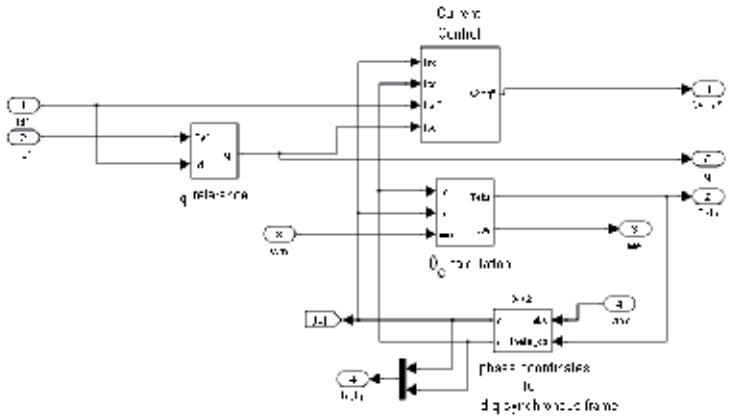

Figure 12. Rotor indirect FOC implementation

Equations (1) and (2) are the basis of "Iq reference" block. Equations (3)-(6) are implemented in "θ_e calculation" block (notice that $\omega_e=\omega_{slip} + \omega_r$). The bottom block considers the coordinates change of instantaneous stator currents, from phase domain to d-q synchronous frame. To do so, the following well known coordinate transformation matrix is applied:

$$\begin{bmatrix} i_{qs} \\ i_{ds} \end{bmatrix} = \frac{2}{3} \begin{bmatrix} \sin\theta_e & \sin(\theta_e - \frac{2}{3}\pi) & \sin(\theta_e + \frac{2}{3}\pi) \\ \cos\theta_e & \cos(\theta_e - \frac{2}{3}\pi) & \cos(\theta_e + \frac{2}{3}\pi) \end{bmatrix} \begin{bmatrix} i_{sa} \\ i_{sb} \\ i_{sc} \end{bmatrix} \quad (35)$$

The "Current Control" block generates stator reference voltage (V_{sdq}*) in synchronous frame (through PI´s current i_{ds} and i_{qs} controllers), which is applied to the motor model, in phase coordinates, in order to make the real instantaneous stator currents to achieve the reference values.

4.4. Induction motor model

Figure 13 presents the induction motor model considered in simulations, which also includes motor iron losses.

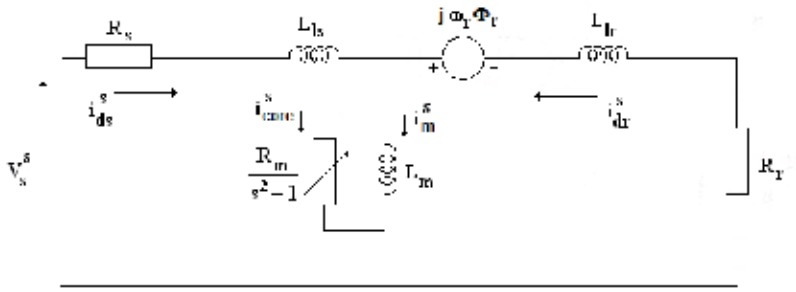

Figure 13. Induction motor model simulated (space vectors in stator reference frame)

When comparing this model to the one considered in LMA (figure 2), the major differences are in parallel (magnetizing) branch. Since core losses currents are not considered in the major circuit, it is expectable that the voltages (V^e_{dm} and V^e_{qm}) on the independent sources are larger compared to the parallel branch voltages in the equivalent model of figure 13. Since core losses are given by $((V^e_{dm})^2+(V^e_{qm})^2)/R_m$, it seems plausible to admit that the core losses in LMA model are higher than the ones in figure 13 model.

Figure 14 shows the simulink implementation of the considered induction motor model (block 5 in figure 7).

5. Simulation results and analysis

An important note is that simulation results were extracted through block 5 (see figure 7), where P_u is obtained directly through T_e*ω_r, based on the drive cycle reference values. In block 3a, Pu is achieved considering P_{ab}-p_{losses} (note that $P_{ab}=u_{sa}i_{sa}+u_{sb}i_{sb}+u_{sc}i_{sc}$, i.e. the sum of instantaneous power of motor phases a, b, c – see figure 14). Motor losses considered by LMA are based on equation (7). There are some differences in P_u values when block 5 or block 3a are considered, which seems to put in evidence the issue mentioned in 4.4.

For each drive cycle, results are presented following the same pattern: the first figure includes the main results for conventional flux regulation and LMA. The second figure

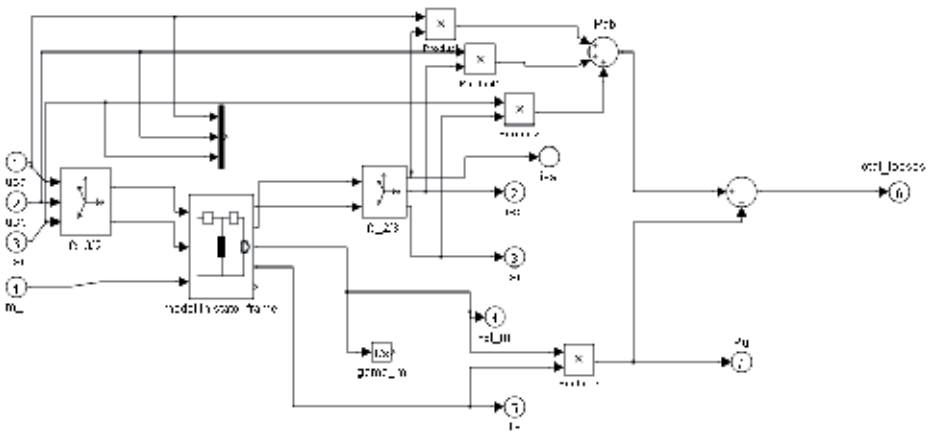

Figure 14. Induction motor model of figure 15 (stator d-q reference frame)

represents the load torque demanded by the drive cycle, while in the third one the motor limits and working points imposed by the drive cycle are illustrated, together with the most significant LMA´s efficiency gain zones. Finally, a table with LMA and conventional flux regulation energy performances is also presented.

From a general perspective, these results confirm the main LMA features, described in section 3.2 visible differences from conventional flux regulation occur for low load torque, particularly for relative low speeds. This agrees to the fact that in regions where I_{ds} has a large regulation flexibility, LMA and conventional flux regulation have clearly different performances.

5.1. ECE-R15

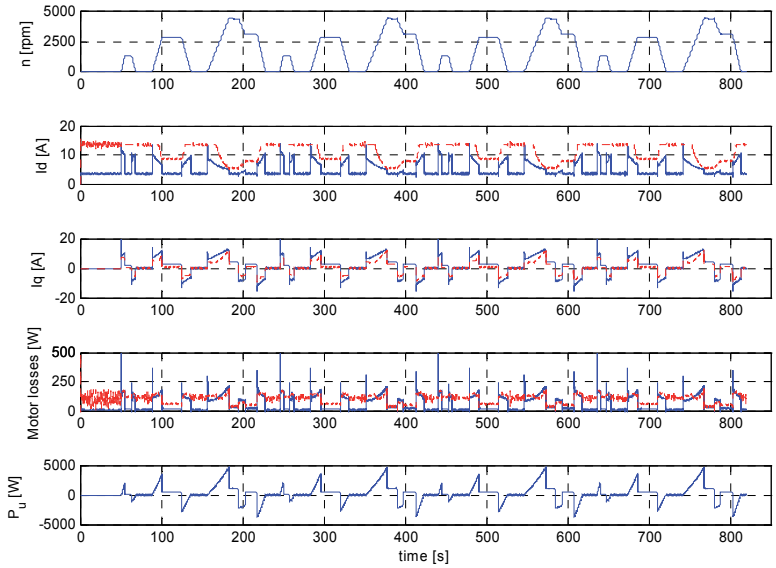

Figure 15. Drive-cycle; (I_d; I_q; Motor losses) – [blue:LMA; red dashed line: conventional regulation]; P_u

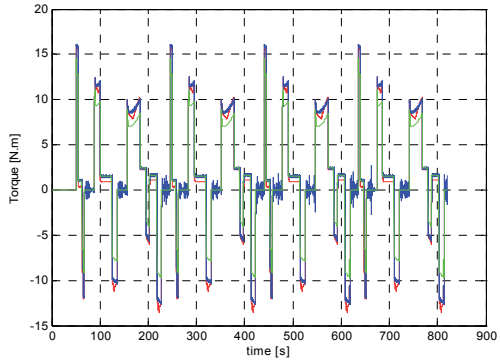

Figure 16. Torques [T_load (green); Te*(red); Te (blue)]

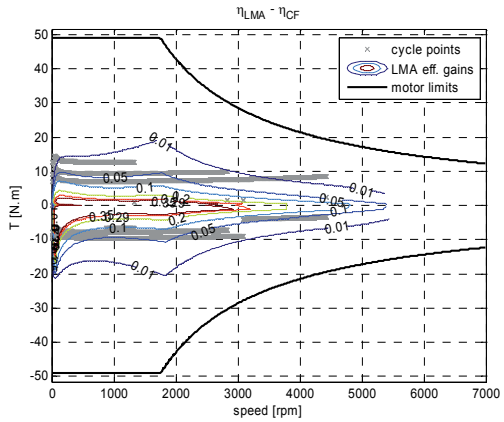

Figure 17. ECE-R15 drive cycle points over LMA efficiency curve gain

	Without LMA	With LMA
Eu (kJ)	221,8	221,5
Eab (kJ)	305,5	266,5
Motor losses (kJ)	83,7	45,0
Energy efficiency (%)	72,6	83,1

Table 5. ECE-R15 energy performances (Eu: energy supplied by the induction motor for the considered drive cycle; Eab: energy absorbed by the induction motor)

In almost 50% of the ECE-R15 drive cycle duration, motor speed is between 0 and 2000 rpm, with the motor torque among -13 Nm and 16 Nm (aprox.) – see figure 16. So, LMA inclusion allows significant loss reductions (table 5): with LMA, total losses are about 20% of E_u (energy supplied by the motor); without LMA, goes up to 38% of E_u. As expected, the main I_{ds} differences occur for n<2000 rpm, particularly for low torques (with LMA, smaller I_{ds} values are clearly visible). In a similar way, LMA performance in braking modes brings good results, since demanded torque has always low values. It should be pointed that when

the vehicle is immobilized (I_{qs}=0), LMA performance leads to very significant results (figure 15), since I_{ds} is regulated to its minimum value, while with conventional flux regulation, I_{ds} has its maximum value. In this case, motor iron losses are much higher when compared to the ones with LMA.

From an energy perspective, although LMA acts directly on the iron losses (since it regulates I_{ds}), it has also an impact in motor copper losses (as mentioned in section 3.2). Although for a given torque value, I_{qs} with LMA is higher than with conventional flux regulation (since I_{ds} is smaller), a better equilibrium between I_{ds} and I_{qs} is achieved with LMA. Since copper losses are also dependent on I_{ds}^2 and I_{qs}^2, the motor efficiency has a clear improvement in this drive cycle scenario, which may be seen from figure 17. Nevertheless, efficiency values are relative low, which is no surprise if one take into consideration the efficiency maps (figure 5) together with figure 17 (notice the efficiency (power) curve gains and cycle working points, particularly for n<2000 rpm).

5.2. Europe: City

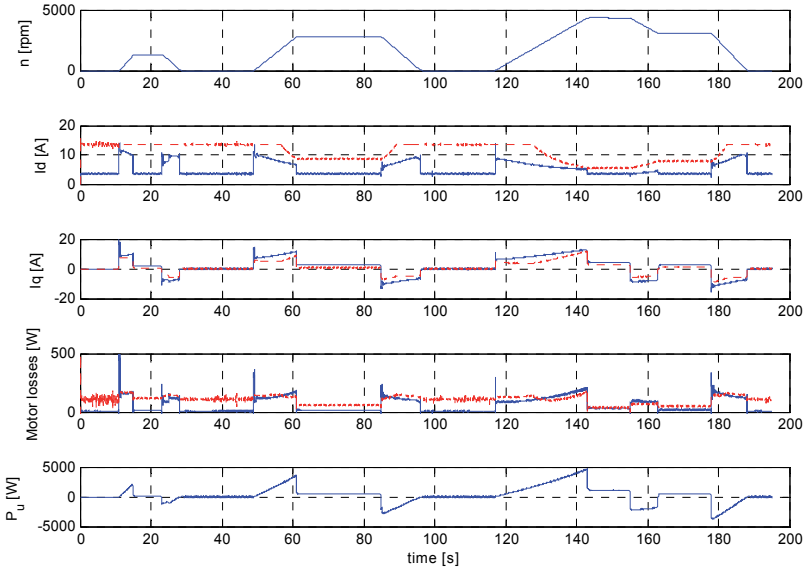

Figure 18. Drive-cycle; (Id; Iq; Motor losses) – [blue:LMA; red dashed line: conventional regulation]; P_u

For about 60% of total time of the "Europe: City" cycle, the vehicle speed is also below 2000 rpm, with the motor torque between -13 Nm and 16 Nm (aprox.). The vehicle is at rest for about 25% of the drive cycle duration. Basically, it puts the motor in the same (T,ω) working region as ECE-R15 (see figures 17 and 20). However, since it has a short time period (195 seg.), energy level demanded is much lower – the lowest one from the chosen drive cycle set. Similar relative energy losses are achieved: 20% for LMA and 36% without LMA of E_u (table 6). In both motor and braking modes, LMA most relevant results are in low speed – low torque region.

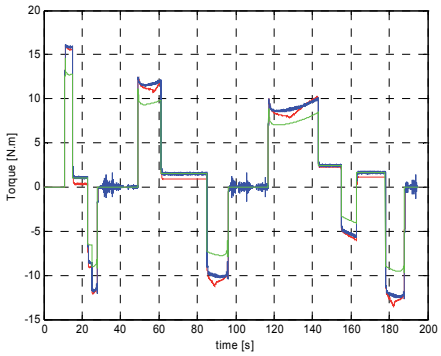

Figure 19. Torques [T_load (green); Te*(red); Te (blue)]

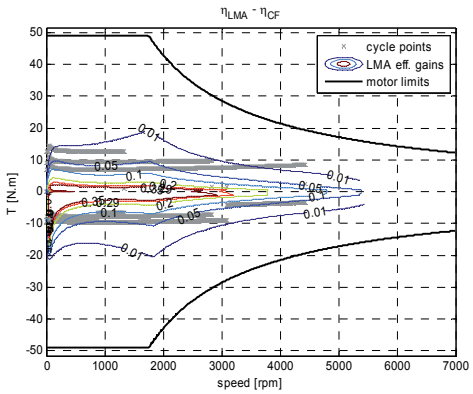

Figure 20. Europe: City drive cycle points over LMA efficiency curve gain

	Without LMA	With LMA
Eu (kJ)	55,5	55,4
Eab (kJ)	75,3	66,6
Motor losses (kJ)	19,8	11,2
Energy efficiency (%)	73,6	83,2

Table 6. Europe: City energy performances

The slightly efficiency increase for this cycle (when compared to ECE-R15) may be associated to the relative decrease of vehicle resting period (about 33% in ECE-R15).

5.3. 11 – Mode (Japan)

Drive cycle period where n<2000 rpm is relative short (<33%); the motor torque lies between 13 Nm and -10 Nm and the vehicle is immobilized a little less than 25% of the cycle duration. As expected, it´s in the initial resting time period and on the final 25 sec that I_{ds} values generated by the LMA are significantly different from the conventional flux I_{ds}

values. In other words, the motor losses difference are attached to these time periods, particularly to the resting one (figure 21). On the other drive cycle periods, motor losses are very similar (notice that in some intervals, LMA losses are slightly larger. This unexpected result is most probably related to the issue discussed in section 4.4).

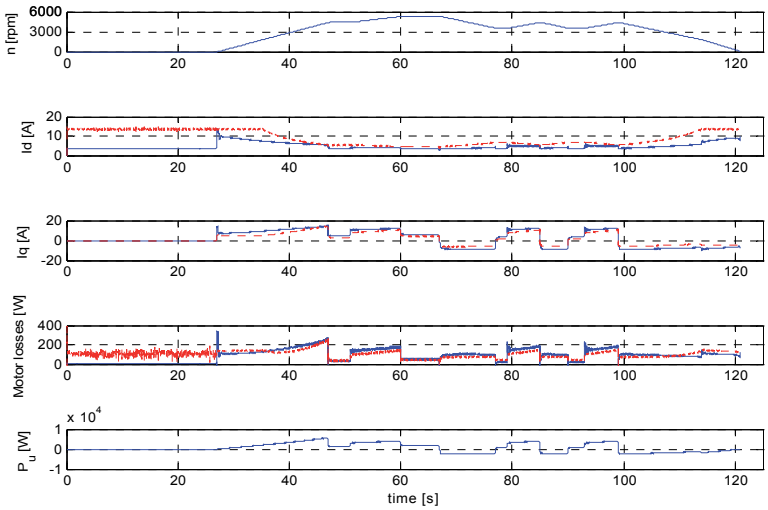

Figure 21. Drive-cycle; (Id; Iq; Motor losses) – [blue:LMA; red dashed line: conventional regulation]; P_u

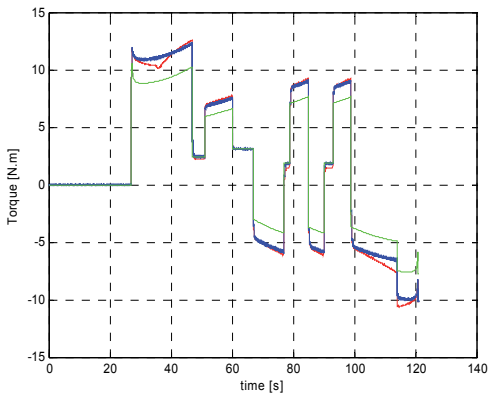

Figure 22. Torques [T_load (green); Te*(red); Te (blue)]

LMA total losses are about 14% of E_u, while conventional regulation losses are 16% of E_u. Although curve efficiency gains in figure 23 are referred to power efficiency, cycle working points somehow agree with efficiency energy gain achieved with LMA (table 7): for n> 2000 rpm there is a significant number of points between 1% and 5 % efficiency curves gain; also notice that some points are below 1% efficiency gain.

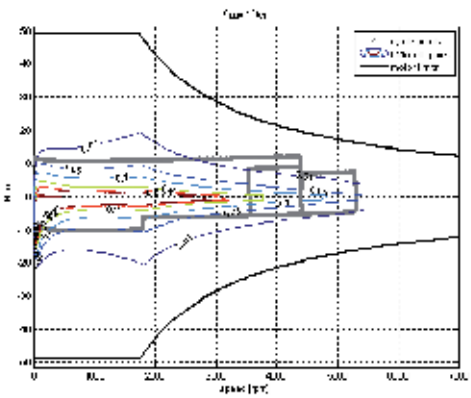

Figure 23. 11-Mode drive cycle points over LMA efficiency curve gain

	Without LMA	With LMA
Eu (kJ)	76,7	76,7
Eab (kJ)	89,3	87,5
Motor losses (kJ)	12,5	10,8
Energy efficiency (%)	86	87,6

Table 7. 11-Mode energy performances

5.4. FTP-75

For this drive cycle, the time period for which n<2000 rpm is shorter then the previous cycles. Motor torque limit is now -20 Nm and 25 Nm (aprox), while maximum speed is 8000 rpm. Frequent accelerations, as well as its long time period (1840 sec), make this cycle the most energy demanding. At the same time, pushes the motor to its limits: figure 24 shows that motor exceeds its nominal power between [200-300] s and later in the interval [1500-1700] sec. However, this overload (whose maximum instantaneous power is about 11 kW) occurs for a small number of intervals, each one with a very short existence. This way, it´s reasonable to assume that motor is not under electric hazardous working conditions. From a mechanical perspective, maximum speed - about 4 times motor nominal speed – is reached for relative short intervals, so one may assume that the motor (and the vehicle) will be safe in this working conditions.

Due to high speeds and relative high torque demand (figure 25), LMA shows a relative performance closer to the conventional regulation. As expected, relevant differences for I_d generation occur for relative low speed (basically, when the vehicle is at rest) and low torque values, e.g. intervals [50-200; 800-950] sec. – figures 25 and 26. With LMA and without it, motor losses are, respectively, 11,4% and 13,1% of E_u (table 8). Motor efficiency map (figure 5) explains the high efficiency values associated to this cycle, while the small efficiency gain achieved is according to figures 25 and 26.

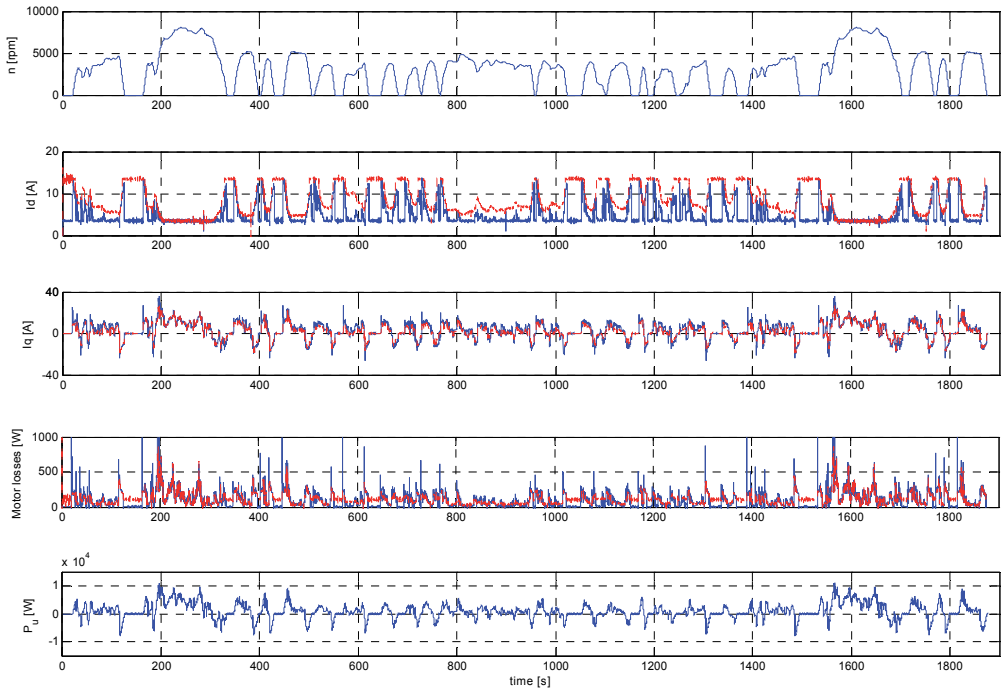

Figure 24. Drive-cycle; (Id*-red & Id-blue); (Iq*-red & Iq-blue); P_{ab} and motor losses (without LMA)

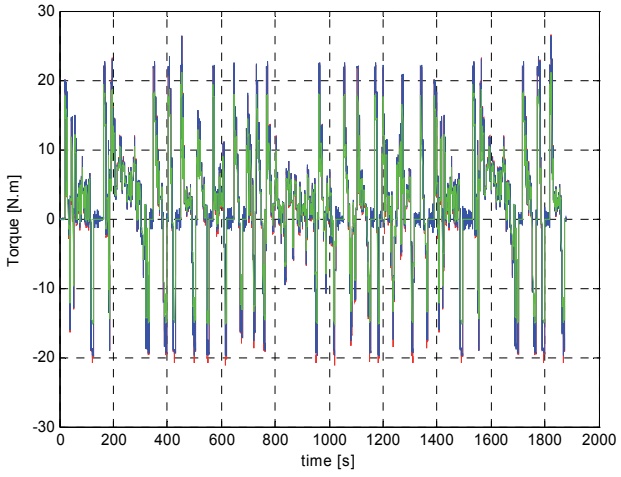

Figure 25. Torques [T_load (green); Te*(red); Te (blue)]

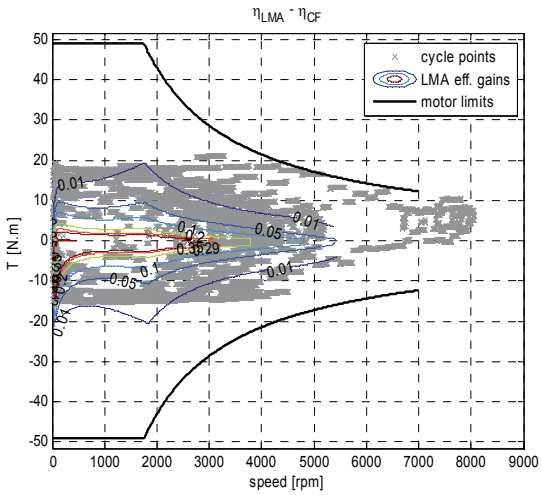

Figure 26. FTP-75 drive cycle points over LMA efficiency curve gain

	Without LMA	With LMA
Eu (kJ)	1716	1716
Eab (kJ)	1941	1910
Motor losses (kJ)	225,1	194,6
Energy efficiency (%)	88,4	89,8

Table 8. FTP-75 energy performances

Figures 27 and 28 present, respectively, induction motor energy consumption, efficiency and losses for each simulated drive cycle, with and without LMA.

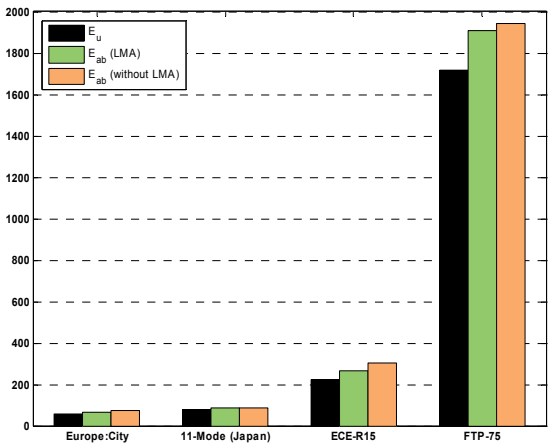

Figure 27. Drive-Cycles energy consumptions [kJ]

As a final remark, it is interesting to note that Europe:city and ECE-R15 have similar efficiency levels; also the same fact can be seen for 11-Mode and FTP-75.

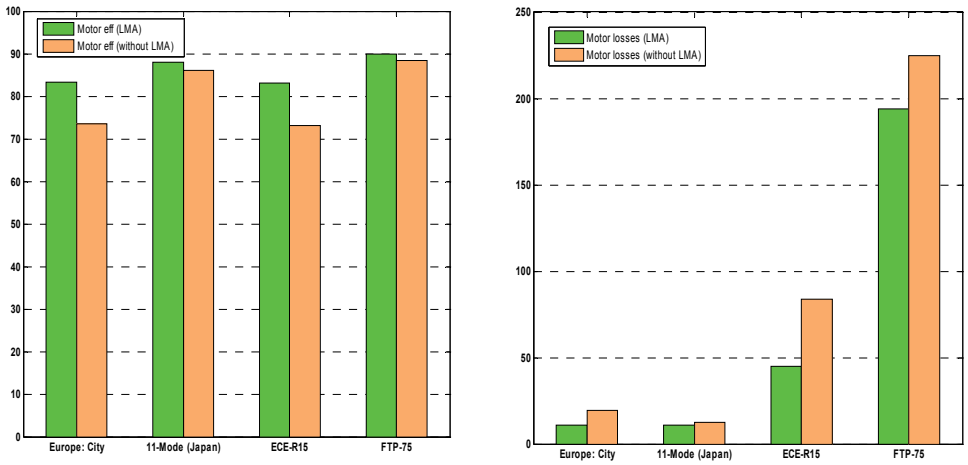

Figure 28. Drive-Cycles energy efficiency [%] (a) and motor losses [kJ] (b)

6. Conclusion

Induction motor drives for EVs are submitted to a large set of working conditions, quite different from rated ones. Motor energy saving is fundamental for improving EVs performances. Under the loss model based approach previously discussed (LMA), a set of simulation results was presented in this book chapter, aiming to improve the induction motor energy performance. Different standard driving cycle scenarios were considered in order to evaluate the chosen LMA features: compared to conventional flux regulation, the major improvements in motor efficiency are for low load torque, particularly for relative low speeds. These are the motor working points where its efficiency is tipically lower, which is an interesting LMA feature. This is in agreement to the fact that LMA action has a more significative impact on ECE-R15 and Europe:city efficiencies, as explained through figures 15,17 and 18, 20 analysis.

Due to LMA impact on iron losses (function of I_d), a possibility to be considered in future works is the impact of LMA on motors with higher power rates and/or high efficiency level motors, where the relative weights of iron and copper losses are different.

Author details

Pedro Melo
Polytechnic Institute of Porto, Portugal

Ricardo de Castro and Rui Esteves Araújo
Faculty of Engineering – University of Porto, Portugal

7. References

Bazzi, A., & Krein, P. (2010). Review of Methods for Real-Time Loss Minimization in Induction Machines. *IEEE Transactions on Industrial Applications,* Vol.41, No.6, pp. 2319-2328.

Fernandez-Bernal, F., Garcia-Cerrada, A., & Faure, R. (2000). Model-based loss minimization for DC and AC vector-controlled motors including core saturation. *IEEE Transactions on Industrial Applications,* Vol.36, No.3, pp. 755-763.

Garcia, G., Luis, J., Stephan, R., & Watanabe, E. (1994). An efficient controller for an adjustable speed induction motor drive. *IEEE Transactions on Industrial Electronics*, Vol.41, No.5, pp. 533-539.

Guzzella, L., & Amstutz, A. (2005), *The QSS Toolbox Manual*, Measurement and Control Laboratory –Swiss Federal Institute of Technology Zurich.

Kioskeridis, I., & Margaris, N. (1996). Loss minimization in induction motor adjustable-speed drives. *IEEE Transactions on Industrial Electronics,* Vol.43, No.1, pp. 226-231.

Krishnan, R. (2001). *Electric Motor Drives – Modeling, Analysis and Control* (1 edition), Prentice Hall, ISBN 13: 978-0130910141.

Lim, S. and K. Nam (2004). Loss-minimising control scheme for induction motors. I*EE Proceedings - Electric Power Applications,* Vol.151, No.4, pp. 385-397.

Novotny, D., Lipo, T. (1996). *Vector control and dynamics of AC drives,* Clarendon Press, Oxford, ISBN 9780198564393.

Zeraoulia, M., M. E. H. Benbouzid, et al. (2006). Electric Motor Drive Selection Issues for HEV Propulsion Systems: A Comparative Study. *IEEE Transactions on Vehicular Technology*, Vol.55, No.6, pp. 1756-1764.

Chapter 18

Sensorless Control of Induction Motor Supplied by Current Source Inverter

Marcin Morawiec

Additional information is available at the end of the chapter

http://dx.doi.org/10.5772/51133

1. Introduction

The circuits used for power conversion applied in drives with induction motor (IM) are classified into two groups: voltage source inverters (VSI) and current source inverters (CSI). The VSI were used more often than the CSI because of their better properties. Nowadays, the development of power electronics devices has enormous influence on applications of systems based on the CSI and creates new possibilities.

In the 1980s the current source inverters were the main commonly used electric machine feeding devices. Characteristic features of those drives were the motor electromagnetic torque pulsations, the voltage and current with large content of higher harmonics. The current source inverter was constructed of a thyristor bridge and large inductance and large commutation capacitors. Serious problems in such drive systems were unavoidable overvoltage cases during the thyristor commutation, as the current source inverter current is supplied in a cycle from a dc-link circuit to the machine phase winding. The thyristor CSI has been replaced by the transistor reverse blocking IGBT devices (RBIGBT), where the diode is series-connected and placed in one casing with transistor. The power transistors like RBIGBT or Silicon Carbide (SiC) used in the modern CSIs guarantee superior static and dynamic drive characteristics.

The electric drive development trends are focused on the high quality system. The use of current sources for the electric machine control ensures better drive properties than in case of voltage sources, where it may be necessary to use an additional passive filter at the inverter output. The Pulse width modulation (PWM) with properly chosen dc-link inductor and input-output capacitors result in sinusoidal inverter output currents and voltages. Methods of calculating proper inductance in dc-link were proposed in [Glab (Morawiec) M. et. al., 2005, Klonne A. & Fuchs W.F., 2003, 2004]. Properties of dc-link circuit of the Current Source Converter (CSC) force the utilization of two fully-controlled inverters to supply

system with electric motor. The first of them – CSI - generates the current output vector to supply the induction motor. The second one – Current Source Rectifier (CSR) - generates a DC voltage to supply a dc-link circuit. The strategy for controlling the output current vector of CSI can be realized in two ways [Glab (Morawiec) M. et. al., 2005, Klonne A. & Fuchs W.F., 2003, Kwak S. & Toliyat H.A., 2006]. First of them is based on changes of modulation index while the value of current in dc-link circuit remains constant [Klonne A. & Fuchs W.F., 2003]. The second method is based on changes of dc-link current. In this case the CSI is working with constant, maximum value of PWM modulation index. Control of modulation index in CSI is used in drive systems, where high dynamic of electromagnetic torque should be maintained [Klonne A. & Fuchs W.F., 2003]. High current in dc-link circuit is a reason for high power losses in CSI. The simplified control method is the scalar control: current to slip (I/s). This method is very simple to implement, but the drive system has average performance (only one controller is necessary, the current in dc-link is kept at constant value by PI controller).

The drive system quality is closely connected with the machine control algorithm. The space vector concept, introduced in 1959 by Kovacs and Racz, opened a new path in the electric machine mathematical modelling field. The international literature on the subject presents drive systems with the CSI feeding an induction motor with the control system based on the coordinate system orientation in relation to the rotor flux vector (FOC – Field Oriented Control). Such control consisted of the dc-link circuit current stabilization [Klonne A. & Fuchs W.F., 2003]. In such control systems the control variables are the inverter output current components. This control method is presented in [Nikolic Aleksandar B. & Jeftenic Borislav I.], where the authors analyze control system based on direct torque control. The control process where the control variable is the inverter output current may be called *current control* of an induction motor supplied by the CSI.

Another control method of a current source inverter fed induction motor is using the link circuit voltage and the motor slip as control variables. That type of control may be called *voltage control* of a CSI fed induction motor, as the dc-link circuit voltage and angular frequency of current vector are the control variables. Proposed control strategy bases on nonlinear multi-scalar control [Glab (Morawiec) M. et. al., 2005,]. The nonlinear control may result in better properties in case if the IM is fed by CSI. To achieve independent control of flux and rotor speed, new nonlinear control scheme is proposed. In this control method the inverter output currents are not controlled variables. The voltage in dc-link and pulsation of output current vector are the controlled variables which can be obtained by nonlinear transformations and are proposed by authors in [Krzeminski Z., 1987, Glab (Morawiec) M. et. al., 2005, 2007]. The multi-scalar model is named the extended one because the mathematical model contained dc-link current and output capacitors equations. This full mathematical model of induction machine with the CSI is used to derive new multi-scalar model. In proposed method the output current vector coefficients are not controlled variables. The output current vector and the flux vector are used to achieve new multi-scalar variables and new multi-scalar model. The control system structure may be supported on PI controllers and nonlinear decouplings or different controllers e.g. sliding mode controllers, the backstepping control method or fuzzy neural controller.

2. Structure of the drive system supplied by CSI or CSC

The simplified configuration of the drive system with the CSI is presented in the Fig. 1. The integral parts of the system are the inductor in dc-link and the output capacitors. In the Fig. 1 the structure with the chopper as an adjustable voltage source is presented.

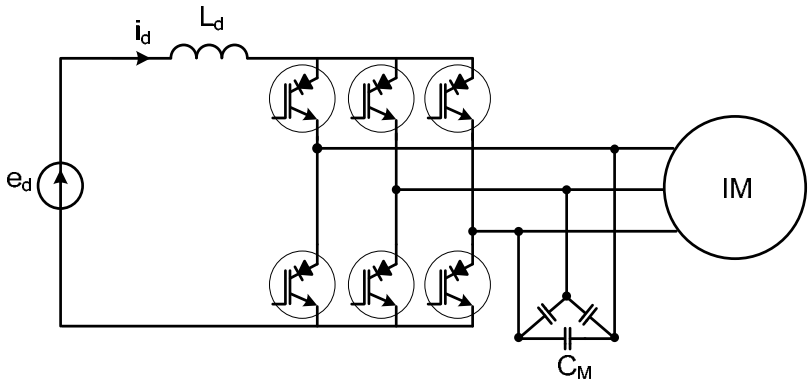

Figure 1. The CSI with the chopper

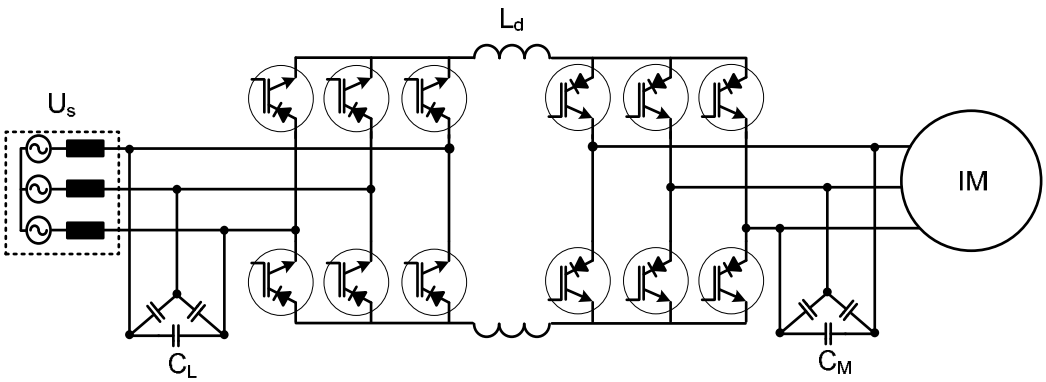

Figure 2. The Current source converter

The chopper with the small inductor L_d (a few mH) forms the large dynamic impedance of the current source. In the proposed system the transistors forms commutator which transforms DC current into AC current with constant modulation index. The current is controlled by voltage source e_d in dc-link. In this way the system with CSI remains voltage controlled and the differential equation for dc-link may be integrated with differential equation for the stator. The inductor limits current ripples during commutations of transistors. The transistors used in this structure are named the reverse blocking IGBT transistors (RBIGBT).

In order to avoid resonance problem the CSI or CSC structure parameters (input-output capacitors and inductor) ought to be properly chosen. The transistor CSI or CSC structures should guarantee sinusoidal stator current and voltage of IM if the parameters are selected by iteration algorithm.

2.1. The iteration algorithm selection of the inductor and input-output capacitors

The inductance in dc-link L_d may be calculated as a function of the integral versus time of the difference of input voltage e_d and output voltage u_d in dc-link [Glab (Morawiec) M. et. al., 2005, Klonne A. & Fuchs W.F., 2003, 2004]. Calculating an inductance from [Glab (Morawiec) M. et. al., 2005, Klonne A. & Fuchs W.F., 2003] may be not enough because of the resonance problem. The parameters could be determined by simple algorithm.

Two criteria are taken into account:

- Minimization of currents ripples in the system
- Minimization of size and weight.

The first criteria can be defined as:

$$w_i = \frac{\Delta i_{d\max}}{i_d}, \tag{1}$$

where

Δi_{dmax} is $\max(i_{dmax}(t_1) - i_{dmin}(t_2))$,

i_d is average value of dc-link current in one period.

The current ripples in dc-link has influence on output currents and commutation process. According to this, the w_i factor, THD_i stator and THD_u stator must be taken into account. Optimal value of inductance L_d and output C_M ensure performance of the drive system with sinusoidal output current and small THD. In Fig. 3 the iteration algorithm for choosing the inductor and capacitor is shown. In every step of iteration new values w_i, THD_i, THD_u are received. In every of these steps new values are compared with predetermined value w_{ip}, THD_{ip}, THD_{up} and:

N is number of iteration,

THD_i – stator current total harmonic distortion,

THD_u – stator voltage total harmonic distortion. Number of iteration is set for user.

In START the initial parameters are loaded. In block Set L_d inductance of the inductor is set. In Numerical process block the simulation is started. In next steps THD_i, THD_u and w_i coefficient are calculated. THD_i, THD_u and w_i coefficient are compared with predetermined value. If YES then C_M is setting, if NO the new value of L_d must be set. Comparison with predetermined value is specified as below:

$$\left\{\begin{array}{l} THD_{ip\max} \le THD_i(i) \le THD_{ip\min} \\ THD_{up\max} \le THD_u(i) \le THD_{up\min} \\ \Delta i_{dp\max} \le \Delta i_d(i) \le \Delta i_{dp\min} \end{array}\right\} \tag{2}$$

where

Δi_{dpmax} – maximum value for w_i coefficient,

Δi_{dpmin} – minimum value for w_i coefficient,

THD_{ipmax}, THD_{upmax} – maximum predetermined value of THD for range (ΔL_d, ΔC_M),

THD_{ipmin}, THD_{upmin} – minimum predetermined value of THD (ΔL_d, ΔC_M),

ΔL_d – interval of optimal value L_d,

ΔC_M – interval of optimal value C_M.

For optimal quality of stator current and voltage in a drive system THD_i ought to be about 1%, THD_u<2% and w_i<15% in numerical process. Estimated CSC parameters by the iteration algorithm are shown in Fig. 4 and 5 or Table 1.

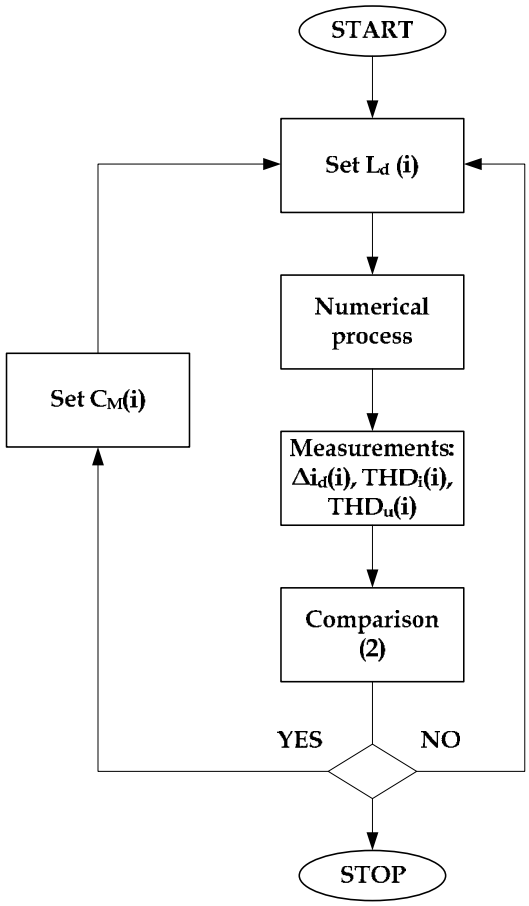

Figure 3. The iteration algorithm for selection of the inductor L_d an capacitors C_M

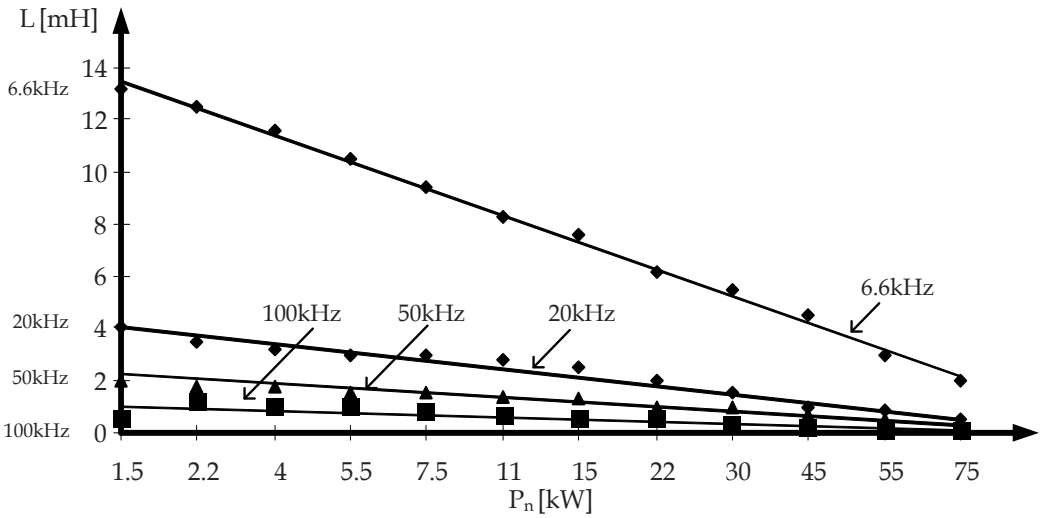

Figure 4. Inductor inductance from iteration algorithm, where P_n [kW] is nominal machine power for different transistors switching frequency [kHz]

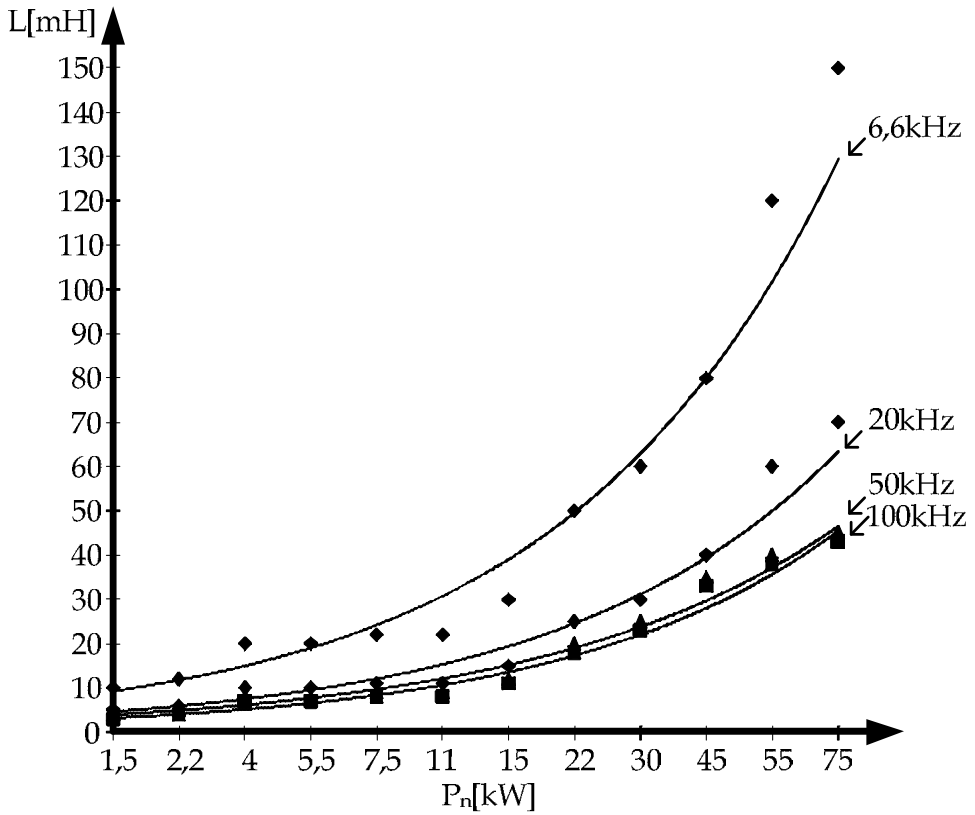

Figure 5. Capacitor capacitance from iteration algorithm where P_n [kW] is nominal machine power for different transistors switching frequency [kHz]

The value of AC side capacitors C_L ought to be about 25% higher than for C_M because of higher harmonics in supply network voltage:

$$C_L \approx 1{,}25 \cdot C_M \,. \tag{3}$$

P_n [kW]	L_d [mH]	C_M [μF]	C_L [μF]	P_n [kW]	L_d [mH]	C_M [μF]	C_L [μF]
1,5	13,2	10	10	15	7,6	30	35
2,2	12,5	12	12	22	6,2	50	60
4	11,6	20	20	30	5,5	60	70
5,5	10,5	20	20	45	4,5	80	90
7,5	9,4	22	22	55	3	120	150
11	8,3	22	25	75	2	150	200

Table 1. Estimated a CSC parameters

3. The mathematical model of IM supplied by CSC

3.1. Introduction to mathematical model

Differential equation for the dc-link is as follows

$$e_d = i_d R_d + L_d \frac{di_d}{d\tau} + u_d \,, \tag{4}$$

where: u_d is the inverter input voltage, R_d is the inductor resistance, L_d is the inductance, e_d is the control voltage in dc-link, i_d is the current in dc-link.

Equation (4) is used together with differential equation for the induction motor to derive the models of induction motor fed by the CSI.

The model of a squirrel-cage induction motor expressed as a set of differential equations for the stator-current and rotor-flux vector components presented in $\alpha\beta$ stationary coordinate system is as follows [Krzeminski Z., 1987]:

$$\frac{di_{s\alpha}}{d\tau} = -\frac{R_s L_r^2 + R_r L_m^2}{L_r w_\sigma} i_{s\alpha} + \frac{R_r L_m}{L_r w_\sigma} \psi_{r\alpha} + \omega_r \frac{L_m}{w_\sigma} \psi_{r\beta} + \frac{L_r}{w_\sigma} u_{s\alpha} \,, \tag{5}$$

$$\frac{di_{s\beta}}{d\tau} = -\frac{R_s L_r^2 + R_r L_m^2}{L_r w_\sigma} i_{s\beta} + \frac{R_r L_m}{L_r w_\sigma} \psi_{r\beta} - \omega_r \frac{L_m}{w_\sigma} \psi_{r\alpha} + \frac{L_r}{w_\sigma} u_{s\beta} \,, \tag{6}$$

$$\frac{d\psi_{r\alpha}}{d\tau} = -\frac{R_r}{L_r} \psi_{r\alpha} - \omega_r \psi_{r\beta} + \frac{R_r L_m}{L_r} i_{s\alpha} \,, \tag{7}$$

$$\frac{d\psi_{r\beta}}{d\tau} = -\frac{R_r}{L_r} \psi_{r\beta} + \omega_r \psi_{r\alpha} + \frac{R_r L_m}{L_r} i_{s\beta} \,, \tag{8}$$

$$\frac{d\omega_r}{d\tau} = \frac{L_m}{JL_r}(\psi_{r\alpha} i_{s\beta} - \psi_{r\beta} i_{s\alpha}) - \frac{1}{J} m_0, \tag{9}$$

where

R_r, R_s are the motor windings resistance, L_s, L_r, L_m are stator, rotor and mutual inductance, $u_{s\alpha}$, $u_{s\beta}$, $i_{s\alpha}$, $i_{s\beta}$, $\psi_{r\alpha}$, $\psi_{r\beta}$ are components of stator voltage, currents and rotor flux vectors, ω_r is the angular rotor velocity, J is the torque of inertia, m_0 is the load torque. All variables and parameters are in p. u.

3.2. The mathematical model of IM contains full drive system equations

The vector components of the rotor flux together with inverter output current are used to derive model of IM fed by the CSI. The model is developed using rotating reference frame *xy* with *x* axis orientated with output current vector. The *y* component of the output current vector is equal to zero.

The variables in the rotating reference frame are presented in Fig. 6.

The output current under assumption an ideal commutator can be expressed

$$i_f = K \cdot i_d, \tag{10}$$

where

K is the unitary commutation function (K=1).

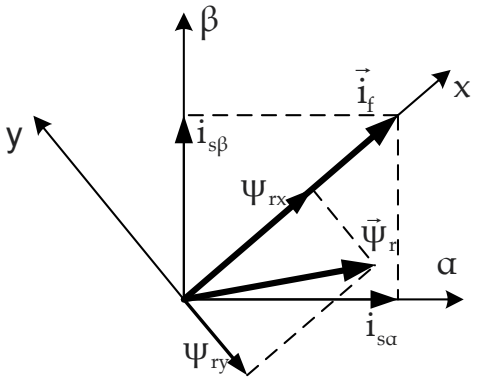

Figure 6. Variables in the rotating frame of references

If the commutation function is K=1 than

$$\left| i_f \right| \approx i_d. \tag{11}$$

The equation (12) results from (11) taking into account ideal commutator of the CSI, according to equation

$$\begin{aligned} p_{DClink} &= p_{AC\ motor\ side} \\ u_d i_d &= u_{sx} i_{fx} \end{aligned}, \tag{12}$$

where: u_d is the input six transistors bridge voltage, u_{sx} is the stator voltage component.

The full model of the drive system in rotating reference frame xy with x axis oriented with inverter output current vector is as follows

$$\frac{di_{sx}}{d\tau} = -\frac{R_s L_r^2 + R_r L_m^2}{L_r w_\sigma} i_{sx} + \frac{R_r L_m}{L_r w_\sigma} \psi_{rx} + \omega_i i_{sy} + \omega_r \frac{L_m}{w_\sigma} \psi_{ry} + \frac{L_r}{w_\sigma} u_{sx}, \tag{13}$$

$$\frac{di_{sy}}{d\tau} = -\frac{R_s L_r^2 + R_r L_m^2}{L_r w_\sigma} i_{sy} + \frac{R_r L_m}{L_r w_\sigma} \psi_{ry} - \omega_i i_{sx} - \omega_r \frac{L_m}{w_\sigma} \psi_{rx} + \frac{L_r}{w_\sigma} u_{sy}, \tag{14}$$

$$\frac{d\psi_{rx}}{d\tau} = -\frac{R_r}{L_r} \psi_{rx} + (\omega_i - \omega_r) \psi_{ry} + \frac{R_r L_m}{L_r} i_{sx}, \tag{15}$$

$$\frac{d\psi_{ry}}{d\tau} = -\frac{R_r}{L_r} \psi_{ry} - (\omega_i - \omega_r) \psi_{rx} + \frac{R_r L_m}{L_r} i_{sy}, \tag{16}$$

$$\frac{d\omega_r}{d\tau} = \frac{L_m}{J L_r} (\psi_{rx} i_{sy} - \psi_{ry} i_{sx}) - \frac{1}{J} m_0, \tag{17}$$

$$\frac{di_d}{d\tau} = \frac{e_d}{L_d} - \frac{R_d}{L_d} i_d - \frac{u_{sx}}{L_d}, \tag{18}$$

$$\frac{du_{sx}}{d\tau} = \frac{1}{C_M} (i_{fx} - i_{sx}) + \omega_i u_{sy}, \tag{19}$$

$$\frac{du_{sy}}{d\tau} = -\frac{1}{C_M} i_{sy} - \omega_i u_{sx}. \tag{20}$$

where: ω_i is angular frequency of vector $\vec{i}_f$, i_{sx}, i_{sy} are the capacitors currents.

4. The nonlinear multi-scalar voltage control of IM with PI controllers

4.1. The simplified Multi-scalar control

The Nonlinear multi-scalar control was presented by authors [Krzeminski Z., 1987, Glab (Morawiec) M. et. al., 2005, 2007]. This control in classical form based on PI controllers. The simplify multi-scalar control of IM supplied by CSC for different vector components ($\vec{\psi}_r, \vec{i}_s$), ($\vec{\psi}_s, \vec{i}_s$), ($\vec{\psi}_m, \vec{i}_s$) was presented in [Glab (Morawiec) M. et. al., 2005, 2007]. These multi-scalar

control structures give different dynamical and statical properties of IM supplied by CSI. In this chapter the simplified control is presented. The simplification is based on (11) and (12) equations. If the capacity C_M has small values (a few μF) the mathematical equations (19) - (20) can be ommitted and the output current vector in stationary state is $|i_f| \approx |i_s|$. Under this simplification, to achieve the decoupling between two control paths the multi-scalar model based control system was proposed [Krzeminski Z., 1987, Glab (Morawiec) M. et. al., 2005, 2007]. The variables for the multi-scalar model of IM are defined

$$x_{11} = \omega_r, \tag{21}$$

$$x_{12} = -i_d \psi_{ry}, \tag{22}$$

$$x_{21} = \psi_{rx}^2 + \psi_{ry}^2, \tag{23}$$

$$x_{22} = i_d \psi_{rx}, \tag{24}$$

where

x_{11} is the rotor speed, x_{12} is the variable proportional to electromagnetic torque, x_{21} is the square of rotor flux and x_{22} is the variable named magnetized variable [Krzeminski, 1987].

Assumption of such machine state variables may lead to improvement of the control system quality due to the fact that e.g. the x_{12} variable is directly the electromagnetic torque of the machine. In FOC control methods [Klonne A. & Fuchs W.F., 2003, 2004, Salo M. & Tuusa H. 2004] the electromagnetic torque is not directly but indirectly controlled (the i_{sq} stator current component). With the assumption of a constant rotor flux modulus, such a control conception is correct. The inaccuracy of the machine parameters, asymmetry or inadequately aligned control system may lead to couplings between control circuits.

The mathematical model for new state of variables (21) - (24) used (15) - (18) is expressed by differential equations:

$$\frac{dx_{11}}{d\tau} = \frac{L_m}{JL_r}(x_{12}) - \frac{1}{J} m_0, \tag{25}$$

$$\frac{dx_{12}}{d\tau} = -\frac{1}{T_i} x_{12} + \frac{1}{L_d} u_{sx} \psi_{ry} - \frac{R_r L_m}{L_r} i_{sy} i_d + v_1, \tag{26}$$

$$\frac{dx_{21}}{d\tau} = -2\frac{R_r}{L_r} x_{21} + 2R_r \frac{L_m}{L_r} x_{22}, \tag{27}$$

$$\frac{dx_{22}}{d\tau} = -\frac{1}{T_i} x_{22} + \frac{R_r L_m}{L_r} i_{sx} i_d + v_2. \tag{28}$$

The compensation of nonlinearities in differential equation leads to the following expressions for control variables v_1 and v_2 appearing in differential equations (27) - (28):

$$v_1 = \frac{R_r L_m}{L_r} i_{sy} i_d - \frac{u_{sx}}{L_d} \cdot \psi_{ry} + \frac{1}{T_i} m_1, \tag{29}$$

$$v_2 = -\frac{R_r L_m}{L_r} i_{sx} i_d + \frac{u_{sx}}{L_d} \cdot \psi_{rx} + \frac{1}{T_i} m_2, \tag{30}$$

where $m_{1,2}$ are the PI controllers output and

$$\frac{1}{T_i} = \frac{R_s}{L_r} + \frac{R_d}{L_d}. \tag{31}$$

The control variables are specified

$$e_d = -L_d \cdot \frac{\psi_{ry} v_1 - \psi_{rx} v_2}{x_{21}}, \tag{32}$$

$$\omega_i = \frac{\psi_{rx} v_1 + \psi_{ry} v_2}{i_d \cdot x_{21}} + x_{11}, \tag{33}$$

when $x_{21}, i_d \neq 0$.

The inverter control variables are: voltage e_d and the output current vector pulsation. The multi-scalar control of IM supplied by CSI was named voltage control because the control variable is voltage e_d in dc-link.

The decoupled two subsystems are obtained:

- electromagnetic subsystem

$$\frac{dx_{21}}{d\tau} = -2\frac{R_r}{L_r} x_{21} + 2\frac{R_r L_m}{L_r} x_{22}, \tag{34}$$

$$\frac{dx_{22}}{d\tau} = \frac{1}{T_i}(-x_{22} + m_2), \tag{35}$$

- electromechanical subsystem

$$\frac{dx_{11}}{d\tau} = \frac{L_m}{J L_r} x_{12} - \frac{1}{J} m_0, \tag{36}$$

$$\frac{dx_{12}}{d\tau} = \frac{1}{T_i}(-x_{12} + m_1). \tag{37}$$

4.2. The multi-scalar control with inverter mathematical model

The author in [Morawiec M., 2007] revealed stability proof of simplified multi-scalar control while the parameters of the CSI are optimal selected.

When the capacitance C_M is neglected the stator current vector $\vec{i}_s$ is about ~5% out of phase to $\vec{i}_f$ while nominal torque is set. Then the control variables and decoupling are not obtained precisely. The error is small than 2% because PI controllers improved it.

In order to compensate these errors the capacity C_M to mathematical model is applied.

From (19) - (20) in stationary state lead to dependences:

$$i_{sx} = i_{fx} + \omega_{if} C_M u_{sy} , \tag{38}$$

$$i_{sy} = -\omega_{if} C_M u_{sx} . \tag{39}$$

The new mathematical model of the drive system is obtained from (38) - (39) through differentiation it and used (15) - (16) in *xy* coordinate system:

$$\frac{di_{sx}}{d\tau} = -\frac{R_d}{L_d} i_d + \frac{1}{L_d} e_d - \frac{1}{L_d} u_x - \omega_{if} C_M i_{sy} - \omega_{if}^2 C_M^2 u_{sx} , \tag{40}$$

$$\frac{di_{sy}}{d\tau} = -\omega_{if} C_M i_d + \omega_{if} C_M i_{sx} - \omega_{if}^2 C_M^2 u_{sy} , \tag{41}$$

$$\frac{d\psi_{rx}}{d\tau} = -\frac{R_r}{L_r} \psi_{rx} + (\omega_{if} - \omega_r)\psi_{ry} + \frac{R_r L_m}{L_r} i_{sx} , \tag{42}$$

$$\frac{d\psi_{ry}}{d\tau} = -\frac{R_r}{L_r} \psi_{ry} - (\omega_{if} - \omega_r)\psi_{rx} + \frac{R_r L_m}{L_r} i_{sy} , \tag{43}$$

$$\frac{di_d}{d\tau} = -\frac{R_d}{L_d} i_d + \frac{1}{L_d} e_d - \frac{1}{L_d} u_{sx} , \tag{44}$$

$$\frac{du_{sx}}{d\tau} = \frac{1}{C_M}(i_{fx} - i_{sx}) + \omega_{if} u_{sy} , \tag{45}$$

$$\frac{du_{sy}}{d\tau} = -\frac{1}{C_M} i_{sy} - \omega_{if} u_{sx} . \tag{46}$$

Substituting (38) - (39) to multi-scalar variables [Krzeminski Z., 1987] one obtains:

$$x_{11} = \omega_r , \tag{47}$$

$$x_{12} = -i_{fx}\psi_{ry} - \omega_{if}C_M x_{32}\,, \tag{48}$$

$$x_{21} = \psi_{rx}^2 + \psi_{ry}^2\,, \tag{49}$$

$$x_{22} = i_{fx}\psi_{rx} + \omega_{if}C_M x_{31}\,, \tag{50}$$

and

$$x_{31} = \psi_{rx}u_{sy} - \psi_{ry}u_{sx}\,, \tag{51}$$

$$x_{32} = \psi_{rx}u_{sx} + \psi_{ry}u_{sy}\,. \tag{52}$$

The multi-scalar model for new multi-scalar variables has the form:

$$\frac{dx_{11}}{d\tau} = \frac{L_m}{JL_r}x_{12} - \frac{1}{J}m_0\,, \tag{53}$$

$$\frac{dx_{12}}{d\tau} = -\frac{1}{T_i}x_{12} + \frac{1}{L_d}u_{sx}\psi_{ry} - x_{11}x_{22} + v_1\,, \tag{54}$$

$$\frac{dx_{21}}{d\tau} = -2\frac{R_r}{L_r}x_{21} + 2R_r\frac{L_m}{L_r}x_{22}\,, \tag{55}$$

$$\frac{dx_{22}}{d\tau} = -\frac{1}{T_i}x_{22} - \frac{1}{L_d}u_{sx}\psi_{rx} + \frac{R_r L_m}{L_r}i_d^2 + x_{11}x_{12} + v_2\,, \tag{56}$$

where

$$v_1 = -\frac{1}{L_d}e_d\psi_{ry} + \omega_{if}\left(x_{22} - \frac{R_d}{L}C_M x_{32} - C_M\frac{R_r L_m}{L_r}p_s\right), \tag{57}$$

$$v_2 = \frac{1}{L_d}e_d\psi_{rx} + \omega_{if}\left(-x_{12} + \frac{R_d}{L}C_M x_{31} + C_M\frac{R_r L_m}{L_r}q_s\right), \tag{58}$$

$$q_s = i_{sx}u_{sy} - i_{sy}u_{sx}\,, \tag{59}$$

$$p_s = u_{sx}i_{sx} + u_{sy}i_{sy}\,. \tag{60}$$

The compensation of nonlinearities in differentials equation leads to the following expressions for control variables v_1 and v_2 appearing in differential equations (54), (56):

$$v_1 = \frac{1}{T_i}m_1 - \frac{1}{L_d}u_{sx}\psi_{ry} + x_{11}x_{22}\,, \tag{61}$$

$$v_2 = \frac{1}{T_i} m_2 + \frac{1}{L_d} u_{sx} \psi_{rx} - x_{11} x_{12} - \frac{R_r L_m}{L_r} i_d^2 , \tag{62}$$

and the control variables

$$e_d = L_d \frac{V_2 x_{41} - V_1 x_{42}}{\psi_{rx} x_{41} + \psi_{ry} x_{42}} , \tag{63}$$

$$\omega_i = \frac{V_1 \psi_{rx} + V_2 \psi_{ry}}{\psi_{rx} x_{41} + \psi_{ry} x_{42}} , \tag{64}$$

where

$$x_{41} = x_{22} - \frac{R_d}{L} C_M x_{32} - C_M \frac{R_r L_m}{L_r} p_s , \tag{65}$$

$$x_{42} = -x_{12} + \frac{R_d}{L} C_M x_{31} + C_M \frac{R_r L_m}{L_r} q_s , \tag{66}$$

$\frac{1}{T_i}$ is determined in (31).

The decoupled two subsystems are obtained as in (34) - (37).

4.3. The multi-scalar adaptive-backstepping control of an IM supplied by the CSI

The backstepping control can be appropriately written for an induction squirrel-cage machine supplied from a VSI. In literature the backstepping control is known for adaptation of selected machine parameters, written for an induction motor [Tan H. & Chang J., 1999, Young Ho Hwang, 2008]. In [Tan H. & Chang J., 1999, Young Ho Hwang, 2008] the authors defined the machine state variables in the dq coordinate system, oriented in accordance with the rotor flux vector (FOC). The control method presented in [Tan H. & Chang J., 1999, Young Ho Hwang, 2008] is based on control of the motor state variables: ω_r – rotor angular speed, rotor flux modulus and the stator current vector components: i_{sd} and i_{sq}. Selection of the new motor state variables, as in the case of multi-scalar control with linear PI regulators, leads to a different form of expressions describing the machine control and decoupling. The following state variables have been selected for the multi-scalar backstepping control

$$e_1 = x_{11}^* - x_{11} , \tag{67}$$

$$e_2 = x_{12}^* - x_{12} , \tag{68}$$

$$e_3 = x_{21}^* - x_{21} , \tag{69}$$

$$e_4 = \left(2R_r \frac{L_m}{L_r} x_{22} \right)^* - 2R_r \frac{L_m}{L_r} x_{22}, \tag{70}$$

where: x_{11}, x_{12}, x_{21} and x_{22} are defined in (47) - (50).

The e_4 tracking error is defined in (70), it does not influence on the control system properties and is only an accepted simplification in the format of decoupling variables.

Derivatives of the (67) - (70) errors take the form

$$\dot{e}_1 = \frac{L_m}{JL_r} e_2 - k_1 e_1 - \frac{\tilde{m}_0}{J}, \tag{71}$$

$$\dot{e}_2 = k_1 e_2 - k_1^2 \frac{JL_r}{L_m} e_1 + \frac{L_r}{L_m} \dot{\hat{m}}_0 + \frac{1}{T_i} x_{12} - \frac{1}{L_d} u_{sx} \psi_{ry} + x_{11} x_{22} + \frac{R_r L_m}{L_r} i_{sy} i_d - v_1, \tag{72}$$

$$\dot{e}_3 = -k_3 e_3 + e_4, \tag{73}$$

$$\begin{aligned} \dot{e}_4 = {} & -k_3^2 e_3 + k_3 e_4 - 4\left(\frac{R_r}{L_r}\right)^2 x_{21} + 4\left(\frac{R_r}{L_r}\right)^2 L_m x_{22} + 2\frac{R_r L_m}{L_r T_i} x_{22} + 2\frac{R_r L_m}{L_r L_d} u_{sx} \psi_{rx} - 2\left(\frac{R_r L_m}{L_r}\right)^2 i_{sx} i_d + \\ & -2\frac{R_r L_m}{L_r} x_{11} x_{12} - 2\frac{R_r L_m}{L_r} v_2 \end{aligned}. \tag{74}$$

The Lyapunov function derivative, with (71) – (74) taken into account, may be expressed as:

$$\begin{aligned} \dot{V} = {} & -k_1^2 e_1 - k_2^2 e_2 - k_3^2 e_3 - k_4^2 e_4 + e_2 (f_1 - v_1) + e_4 (f_2 - a_3 v_2) + \\ & + \tilde{m}_0 \left(-\frac{e_1}{J} - k_1 \frac{L_r}{L_m} e_2 + \frac{\dot{\hat{m}}_0}{\gamma} \right) \end{aligned}, \tag{75}$$

where

$$v_1 = -\frac{1}{L_d} e_d \psi_{ry} + \omega_{if} x_{41}, \tag{76}$$

$$v_2 = \frac{1}{L_d} e_d \psi_{rx} + \omega_{if} x_{42}, \tag{77}$$

$$\begin{aligned} f_1 = {} & \lim it_{12} \cdot e_1 \left(\frac{L_m}{JL_r} - k_1^2 \frac{JL_r}{L_m} \right) + k_2 e_2 + k_1 e_2 + \frac{L_r}{L_m} \dot{\hat{m}}_0 + \frac{1}{T_i} x_{12} - \frac{1}{L_d} u_{sx} \psi_{ry} + \\ & + x_{11} x_{22} \end{aligned}, \tag{78}$$

$$\begin{aligned} f_2 = {} & \lim it_{12} \cdot (e_3 - k_3^2 e_3) + k_4 e_4 + k_3 e_4 - 4\left(\frac{R_r}{L_r}\right)^2 x_{21} + 4\left(\frac{R_r}{L_r}\right)^2 L_m x_{22} + 2\frac{R_r L_m}{L_r T_i} x_{22} + \\ & + 2\frac{R_r L_m}{L_r L_d} u_{sx} \psi_{rx} - 2\left(\frac{R_r L_m}{L_r}\right)^2 i_d^2 - 2\frac{R_r L_m}{L_r} x_{11} x_{12} \end{aligned}, \tag{79}$$

$$a_3 = 2\frac{R_r L_m}{L_r}.$$

$limit_{12}$ – is a dynamic limitation in the motor speed control subsystem,

$limit_{22}$ – is a dynamic limitation in the rotor flux control subsystem,

$k_1 \ldots k_4$ and γ are the constant gains.

The control variables take the form:

$$e_d = L_d \frac{x_{41} f_2 - a_3 x_{42} f_1}{a_3(\psi_{rx} x_{41} + \psi_{ry} x_{42})}, \tag{80}$$

$$\omega_i = \frac{a_3 \psi_{rx} f_1 + \psi_{ry} f_2}{a_3(\psi_{rx} x_{41} + \psi_{ry} x_{42})}. \tag{81}$$

The inverter control variables are: voltage e_d and the output current vector pulsation. The two decoupled subsystems are obtained as in (34) - (37).

The load torque m_0 can be estimated from the formula:

$$\dot{\hat{m}}_0 = \gamma\left(\frac{e_1}{J} + k_1 \frac{L_r}{L_m} e_2\right). \tag{82}$$

4.4. Dynamic limitations of the reference variables

In control systems with the conventional linear controllers of the PI or PID type, the reference (or controller output) variable dynamics are limited to a constant value or dynamically changed by (83) - (84), depending on the drive working point.

Control systems where the control variables are determined from the Lyapunov function (like in backstepping control) have no limitations in the set variable control circuits. The reference variable dynamics may be limited by means of additional first order inertia elements (e.g. on the set speed signal).

The author of this paper has not come across a solution of the problem in the most significant backstepping control literature references, e.g. [Tan H. & Chang J., 1999, Young Ho Hwang, 2008]. In the quoted reference positions, the authors propose the use of an inertia elements on the set variable signals. Such approach is an intermediate method, not giving any rational control effects. The use of an inertia element on the reference signal, e.g. of the rotor angular speed, will slow down the reference electromagnetic torque reaction in proportion to the inertia element time-constant. In effect a "slow" build-up of the motor electromagnetic torque is obtained, which may be acceptable in some applications. In practice the aim is to limit the electromagnetic torque value without an impact on the build-up dynamics. Control systems with the Lyapunov function-based control without limitation

of the set variables are not suitable for direct adaptation in the drive systems. Therefore, a solution often quoted in literature is the use of a PI or PID speed controller at the torque control circuit input.

The set values of the x_{12}^{*}, x_{22}^{*} variables appearing in the e_2 and e_4 deviations can be dynamically limited and the dynamic limitations are defined by the expressions [Adamowicz M.; Guzinski J., 2005]:

$$x_{12\lim} = \sqrt{I_{s\max}^2 x_{21} - x_{22}^2}\,, \tag{83}$$

$$x_{22\lim} = f(U_{s\max}^2, I_{s\max}^2, x_{11})\,, \tag{84}$$

where

x_{12lim} – the set torque limitation,

x_{22lim} – the x_{22} variable limitation,

I_{smax} – maximum value of the stator current modulus,

U_{smax} – maximum value of the stator voltage modulus.

The above given expressions may be modified to:

$$x_{12\lim} = \sqrt{I_{s\max}^2 x_{21} - \frac{x_{21}^2}{L_m^2}}\,, \tag{85}$$

giving the relationship between the x_{21} variable, the stator current modulus I_{smax}, and the motor set torque limitation.

For the multi-scalar backstepping control, to the f_1 and f_2 variables the $limit_{12}$ and $limit_{22}$ variables were introduced; they assume the 0 or 1 value depending on the need of limiting the set variable.

Limitation of variables in the Lyapunov function-based control systems may be performed in the following way:

$$if\ \left(x_{12}^{*} > x_{12\lim}\right)\ then\ \begin{Bmatrix} \mathrm{limit}_{12} = 0, \\ e_2 = x_{12\lim} - x_{12} \end{Bmatrix}, \tag{86}$$

$$if\ \left(x_{12}^{*} < -x_{12\lim}\right)\ \text{then}\ \begin{Bmatrix} \mathrm{limit}_{12} = 0, \\ e_2 = -x_{12\lim} - x_{12} \end{Bmatrix}, \tag{87}$$

$$\text{else}\ \ \mathrm{limit}_{12} = 1\,,$$

$$if\ \left(x_{22}^{*} > x_{22\lim}\right)\ then\ \begin{Bmatrix} \mathrm{limit}_{22} = 0, \\ e_4 = x_{22\lim} - x_{22} \end{Bmatrix}, \tag{88}$$

$$if\ \left(x_{22}^{*} < -x_{22\lim}\right)\ \text{then}\ \begin{Bmatrix} \text{limit}_{22} = 0, \\ e_4 = -x_{22\lim} - x_{22} \end{Bmatrix}, \tag{89}$$

$$\text{else}\ \ \text{limit}_{22} = 1.$$

The dynamic limitations effected in accordance with expressions (83) – (84) limit properly the value of x_{12}^{*} and x_{22}^{*} variables without any interference in the reference signal build-up dynamics.

Fig. 7 presents the variable simulation diagrams. The backstepping control dynamic limitations were used.

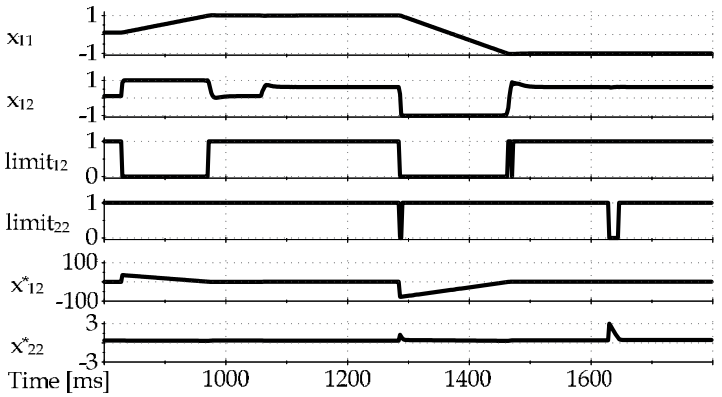

Figure 7. Diagrams of multi-scalar variables in the machine dynamic states, the $x_{12ogr} = 1.0$ and $x_{22ogr} = 0.74$ limitations were set for a drive system with an induction squirrel-cage machine supplied from a CSC-simulation diagrams, x^{*}_{12} – diagram of the machine set electromagnetic torque (without signal limitation), x^{*}_{22} – diagram of the x^{*}_{22} set signal (without limitation).

4.5. Impact of the dynamic limitation on the estimation of parameters

The use of a variable limitation algorithm may have a negative impact on the control system estimated parameters. This has a direct connected with the limited deviation values, which are then used in an adaptive parameter estimation. Such phenomenon is presented in Fig. 7. The estimated parameter in the control system is the motor load torque $\hat{m}_0$. The set electromagnetic torque is limited to the $x_{12lim} = 1.0$ value. Fig. 7 shows that the estimated load torque increases slowly in the intermediate states. Limitation of the set electromagnetic torque causes the limitation of deviation e_2, which in turn causes limited increase dynamics of the estimated load torque. The $\hat{m}_0$ value for $\text{limit}_{12} = 0$ in the dynamic states does not reach the real value of the load torque, which should be $\hat{m}_0 \approx x_{12}$. A large $\tilde{m}_0$ estimation error occurs in the intermediate states, which can be seen in Fig. 8. The estimation error in the intermediate states is $\tilde{m}_0 \neq 0$ because the torque limitation, introduced to the control system, is not compensated. The simulation and experimental tests have shown that the load torque estimation error in the intermediate state has an insignificant impact on the

speed control. Omitting $\hat{m}_0$ in the set torque x^*_{12} expression eliminates the intermediate state speed over-regulation. But absence of $\hat{m}_0$ in x^*_{12} for a steady state gives the deviation value $e_1 \neq 0$ and lack of full control over maintaining the rotor set angular speed. Compensation of the $limit_{12}$ limitation introduced to the control system is possible by installing a corrector in the rotor angular speed control circuit.

A corrector in the form of an e_1 signal integrating element was added to the set electromagnetic torque x^*_{12} signal. In this way a system reacting to the change of machine real load torque was obtained. The introduced correction minimizes the rotor angular speed deviation and the corrector signal may be treated as the estimated load torque value.

The correction element is determined by the expression:

$$KT_L = k_{e1} \int_{t_{k-1}}^{t_k} e_1 d\tau \,, \tag{90}$$

where

$t_{k-1} \ldots t_k$ is the e_1 signal integration range,

KT_L – correction element,

k_{e1} – is the correction element amplification.

The gain k_{e1} should be adjusted that the speed overregulation in the intermediate state does not exceed 5%:

$$0 < k_{e1} \leq 0{,}1 \cdot k_1 \,, \tag{91}$$

The correction element amplification must not be greater than k_1, or:

$$k_{e1} \leq k_1 \,. \tag{92}$$

For $k_{e1} > k_1$ the KT_L signal will become an oscillation element and may lead to the control system loss of stability.

The KT_L signal must be limited to the x_{12lim} value.

The x^*_{12} set value expression must be modified:

$$x^*_{12} = \frac{JL_r}{L_m} k_1 e_1 + KT_L \,, \tag{93}$$

where

$$\hat{m}_0 \approx KT_L \,. \tag{94}$$

The use of (93) in the angular speed control circuit improves the load torque estimation and eliminates the steady state speed error.

Fig. 9 presents the load torque (determined in (94)) estimation as well as x_{12} and the $limit_{12}$ limitations.

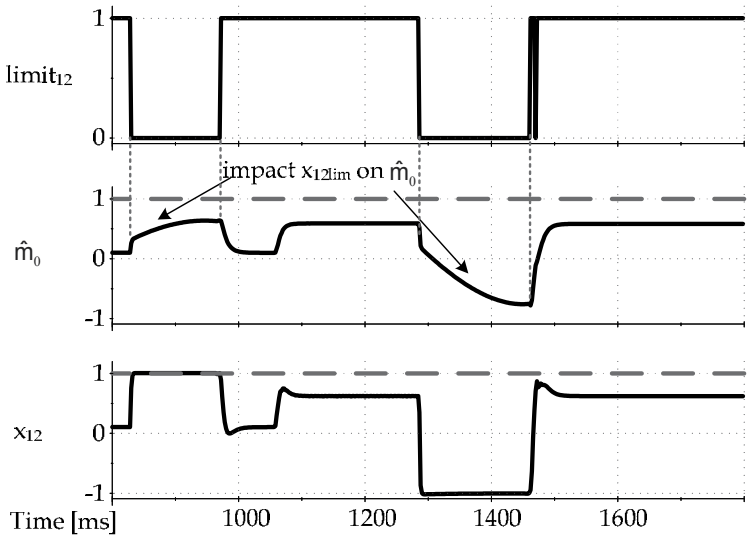

Figure 8. Impact of the electromagnetic torque limitation x_{12lim} on the estimated load torque $\hat{m}_0$ (82).

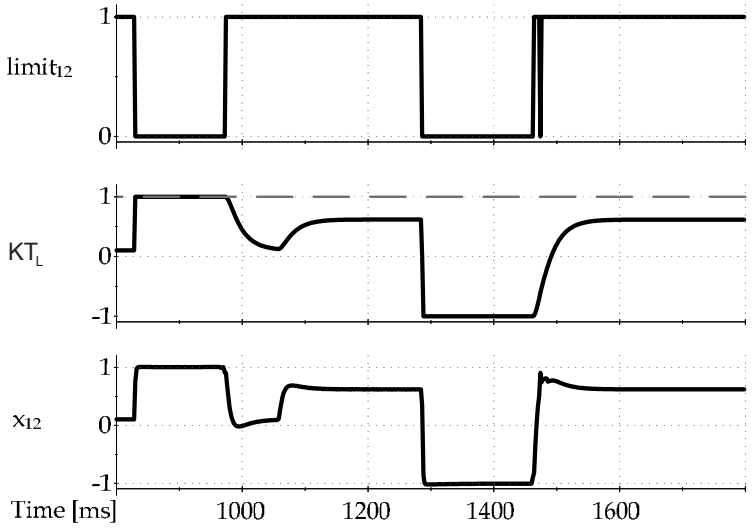

Figure 9. Diagrams of the $limit_{12}$ variable, KT_L load torque and electromagnetic torque x_{12}.

5. The nonlinear multi-scalar current control of induction machine

Conception of the CSI current control is based on forced components of the CSI output current. The dc-link circuit inductor could be modeled as the first order inertia element with the time constant T of a value equal to the dc-link circuit time constant value. The dc-link

equation may be introduced to the induction machine mathematical model to obtain the set CSI output current component. The time constant T is equal the inductance L_d, it can be written:

$$\frac{d\vec{i}_s}{dt} = \frac{1}{T}(\vec{i}_f - \vec{i}_s), \tag{95}$$

$$T = \frac{R_d}{L_d}. \tag{96}$$

5.1. The simplified multi-scalar current control of induction machine

The simplified version of the CSI output current control it is assumed that the output capacitors have negligibly small capacitance, so their impact on the drive system dynamics is small. Assuming that the cartesian coordinate system, where the mathematical model variables are defined, is associated with the CSI output current vector (which with this simplification is the machine stator current) the mathematical model can be obtained (95) and (42) - (43) equations).

The multi-scalar variables have the form

$$x_{11} = \omega_r, \tag{97}$$

$$x_{12} = -i_{sx}\psi_{rx}, \tag{98}$$

$$x_{21} = \psi_{rx}^2 + \psi_{ry}^2, \tag{99}$$

$$x_{22} = i_{sx}\psi_{rx}, \tag{100}$$

where

i_{sx} is treated as the output current vector component and $|i_f| \approx |i_s|$.

For those variables, the multi-scalar model has the form:

$$\frac{dx_{11}}{d\tau} = \frac{L_m}{JL_r}x_{12} - \frac{1}{J}m_0, \tag{101}$$

$$\frac{dx_{12}}{d\tau} = -\frac{1}{T_i}x_{12} + v_1, \tag{102}$$

$$\frac{dx_{21}}{d\tau} = -2\frac{R_r}{L_r}x_{21} - 2\frac{R_r L_m}{L_r}x_{22}, \tag{103}$$

$$\frac{dx_{22}}{d\tau} = -\frac{1}{T_i}x_{22} + \frac{R_r L_m}{L_r} i_d + v_2 \,. \tag{104}$$

Applying the linearization method, the following relations are obtained, where m_1 is the subordinated regulator output in the speed control line and m_2 is the subordinated regulator output in the flux control line

$$v_1 = \frac{1}{T_i} m_1 \,, \tag{105}$$

$$v_2 = \frac{1}{T_i} m_2 - \frac{R_r L_m}{L_r} i_d \,. \tag{106}$$

The control variables are modulus of the CSI output current and the output current vector pulsation, given by the following relations:

$$\left|\mathrm{i_f}\right| = T \frac{v_2 \psi_{rx} - v_1 \psi_{ry}}{x_{21} \psi_{ry}} \,, \tag{107}$$

$$\omega_i = \frac{v_1 + v_2}{x_{21} i_{sx}} + x_{11} \,. \tag{108}$$

where: L_d –inductance, T_i– the system time constant.

5.2. The multi-scalar current control of induction machine

The current control analysis presented in the preceding sections does not take the CSI output capacitors into account. Such simplification may be applied because of the small impact of the capacitors upon the control variables (the machine stator current and voltage are measured). The capacitor model will have a positive impact on the control system dynamics.

The output capacitor relations have the form:

$$\frac{d\vec{\mathrm{u}}_s}{dt} = \frac{1}{C_M}(\vec{\mathrm{i}}_f - \vec{\mathrm{i}}_s) \,, \tag{109}$$

where: $\vec{\mathrm{u}}_s$ is the capacitor voltage vector, $\vec{\mathrm{i}}_f$ is the current source inverter output current vector, $\vec{\mathrm{i}}_s$ is the stator current vector.

Using the approximation method, relation (38) may be written as follows:

$$\frac{\vec{\mathrm{u}}_s(k) - \vec{\mathrm{u}}_s(k-1)}{T_{imp}} = \frac{1}{C_M}\left[\vec{\mathrm{i}}_f(k) - \vec{\mathrm{i}}_s(k)\right] . \tag{110}$$

Deriving $\mathbf{u}_s(k)$ from (38), the motor stator voltage is obtained as a function of the output current, stator current and stator voltage, in the form:

$$\vec{u}_s(k) = \frac{T_{imp}}{C_M}\left[\vec{i}_f(k) - \vec{i}_s(k)\right] + \vec{u}_s(k-1), \tag{111}$$

where

$\vec{u}_s(k)$ is the stator voltage vector at the k-th moment, T_{imp} - sampling period.

In the equations (5) - (9) representing the cage induction motor mathematical model the stator current vector components are appeared but the direct control variables do not. The motor stator current vector components cannot be the control variables because the multi-scalar model relations are derived from them. This is a different situation than with the FOC control. The FOC control is based on the machine stator current components described in a coordinate system associated with the rotor flux and the stator current components are the control variables. Therefore, control variables must be introduced into the mathematical model (5) - (9). The control may be introduced considering the machine currents (5) - (6) and equation (95) written for the $\alpha\beta$ components and describing the dc-link circuit dynamics. Adding the respective sides of equations (5) and (95) and equations (6) and (95), where equation (95) must be written with the ($\alpha\beta$) components – the mathematical model of the drive system fed by the CSI is obtained:

$$\frac{di_{s\alpha}}{d\tau} = -\frac{R_s L_r^2 T + R_r L_m^2 T + L_r w_\sigma}{2L_r w_\sigma T} i_{s\alpha} + \frac{R_r L_m}{2L_r w_\sigma}\psi_{r\alpha} + \omega_r \frac{L_m}{2w_\sigma}\psi_{r\alpha} + \frac{L_r}{2w_\sigma}u_{s\alpha} + \frac{1}{2T}i_{f\alpha}, \tag{112}$$

$$\frac{di_{s\beta}}{d\tau} = -\frac{R_s L_r^2 T + R_r L_m^2 T + L_r w_\sigma}{2L_r w_\sigma T} i_{s\beta} + \frac{R_r L_m}{2L_r w_\sigma}\psi_{r\beta} - \omega_r \frac{L_m}{2w_\sigma}\psi_{r\alpha} + \frac{L_r}{2w_\sigma}u_{s\beta} + \frac{1}{2T}i_{f\beta}, \tag{113}$$

and equations (7) - (8).

The multi-scalar variables are assumed like in [Krzeminski Z., 1987]:

$$x_{11} = \omega_r, \tag{114}$$

$$x_{12} = \psi_{r\alpha} i_{s\beta} - \psi_{r\beta} i_{s\alpha}, \tag{115}$$

$$x_{21} = \psi_{r\alpha}^2 + \psi_{r\beta}^2, \tag{116}$$

$$x_{22} = \psi_{r\alpha} i_{s\alpha} + \psi_{r\beta} i_{s\beta}. \tag{117}$$

Introducing the multi-scalar variables (114) - (117), the multi-scalar model of an IM fed by the CSI is obtained:

$$\frac{dx_{12}}{d\tau} = -\frac{1}{2T_i}x_{12} - x_{11}x_{22} - x_{11}x_{22}\frac{L_m}{2w_\sigma} + \frac{L_r}{2w_\sigma}(u_{s\beta}\psi_{r\alpha} - u_{s\alpha}\psi_{r\beta}) + v_1, \tag{118}$$

$$\frac{dx_{22}}{d\tau} = -\frac{1}{2T_i}x_{22} + x_{11}x_{12} + \frac{R_r L_m}{2L_r w_\sigma}x_{21} + \frac{R_r L_m}{2L_r}i_{s\alpha}^2 + \frac{L_r}{2w_\sigma}(\psi_{r\alpha}u_{s\alpha} + \psi_{r\beta}u_{s\beta}) + v_2, \tag{119}$$

where

$$v_1 = \frac{1}{2T}\psi_{r\alpha}i_{f\beta} - \frac{1}{2T}\psi_{r\beta}i_{f\alpha}, \tag{120}$$

$$v_2 = \frac{1}{2T}\psi_{r\alpha}i_{f\alpha} + \frac{1}{2T}\psi_{r\beta}i_{f\beta}. \tag{121}$$

Applying the linearization method to (118) - (119), the following expressions are obtained:

$$v_1 = \frac{1}{2T_i}m_1 + x_{11}x_{22} + \frac{L_m}{2w_\sigma}x_{11}x_{21} + \frac{L_r}{2w_\sigma}\left[u_{s\beta}(k-1)\psi_{r\alpha} - u_{s\alpha}(k-1)\psi_{r\beta}\right] - a_1 x_{12}, \tag{122}$$

$$v_2 = \frac{1}{2T_i}m_2 - x_{11}x_{21} - \frac{R_r L_m}{2w_\sigma L_r}x_{21} - \frac{R_r L_m}{2L_r}i_{s\alpha}^2 - \frac{L_r}{2w_\sigma}\left[u_{s\alpha}(k-1)\psi_{r\alpha} + u_{s\beta}(k-1)\psi_{r\beta}\right] + a_1 x_{22}, \tag{123}$$

where

$$v_1 = a_1\left[i_{f\beta}\psi_{r\alpha} - i_{f\alpha}\psi_{r\beta}\right], \tag{124}$$

$$v_2 = -a_1\left[i_{f\alpha}\psi_{r\alpha} + i_{f\beta}\psi_{r\beta}\right]. \tag{125}$$

The control variables take the form

$$i_{f\alpha} = a_2\frac{\psi_{r\alpha}v_2 - \psi_{r\beta}v_1}{x_{21}}, \tag{126}$$

$$i_{f\beta} = a_2\frac{\psi_{r\alpha}v_1 + \psi_{r\beta}v_2}{x_{21}}, \tag{127}$$

where

$$a_1 = \frac{L_r T_{imp}}{2w_\sigma C_M}, \tag{128}$$

$$a_2 = a_1 + \frac{1}{2T}. \tag{129}$$

The time constant T_i for simplified for both control method is given

$$T_i = \frac{w_\sigma L_r T}{R_s L_r^2 T + R_r L_m^2 T + L_r w_\sigma}, \tag{130}$$

5.3. Generalized multi-scalar control of induction machine supplied by CSI or VSI

A cage induction machine fed by the CSI may be controlled in the same way as with the voltage source inverter (VSI). The generalized control is provided by an IM multi-scalar model formulated for the VSI machine control [Krzeminski Z., 1987]. The (114) - (117) multi-scalar variables and additional u_1 and u_2 variables are used

$$u_1 = \psi_{r\alpha} u_{s\beta} - \psi_{r\beta} u_{s\alpha}, \tag{131}$$

$$u_2 = \psi_{r\alpha} u_{s\alpha} + \psi_{r\beta} u_{s\beta}, \tag{132}$$

which are a scalar and vector product of the stator voltage and rotor flux vectors.

The multi-scalar model feedback linearization leads to defining the nonlinear decouplings [Krzeminski Z., 1987]:

$$U_1^* = \frac{w_\sigma}{L_r}\left[x_{11}(x_{22} + \frac{L_m}{w_\sigma} x_{21}) + \frac{1}{T_v} m_1 \right], \tag{133}$$

$$U_2^* = \frac{w_\sigma}{L_r}[-x_{11} x_{12} - \frac{R_r L_m}{L_r} i_s^2 - \frac{R_r L_m}{L_r w_\sigma} x_{21} + \frac{1}{T_v} m_2]. \tag{134}$$

The control variables for an IM supplied by the VSI have the form [Krzeminski Z., 1987]:

$$u_{s\alpha}^* = \frac{\psi_{r\alpha} U_2^* - \psi_{r\beta} U_1^*}{x_{21}}, \tag{135}$$

$$u_{s\beta}^* = \frac{\psi_{r\alpha} U_1^* + \psi_{r\beta} U_2^*}{x_{21}}. \tag{136}$$

The controls (135) - (136) are reference variables treated as input to space vector modulator when the IM is supplied by the VSI.

On the other side, when the IM is fed by the CSI, calculation of the derivatives of (131) - (132) multi-scalar variables yields the following relations:

$$\frac{du_1}{d\tau} = -\frac{R_r}{L_r} u_1 - x_{11} u_2 + \frac{R_r L_m}{L_r} q_s - \frac{1}{C_M} x_{12} + v_{11}, \tag{137}$$

$$\frac{du_2}{d\tau} = -\frac{R_r}{L_r}u_2 + x_{11}u_1 + \frac{R_r L_m}{L_r}p_s + \frac{1}{C_M}x_{22} + v_{22}, \tag{138}$$

where p_s and q_s are defined in (59) - (60).

By feedback linearization of the system of equations, one obtains

$$v_{11} = -\frac{R_r}{L_r}v_{p1} - \frac{R_r L_m}{L_r}q_s + \frac{1}{C_M}x_{12} + x_{11}u_2, \tag{139}$$

$$v_{22} = -\frac{R_r}{L_r}v_{p2} - \frac{R_r L_m}{L_r}p_s + \frac{1}{C_M}x_{22} - x_{11}u_1, \tag{140}$$

where

v_{p1} and v_{p2} are the output of subordinated PI controllers.

The control variables of the IM fed by the CSI have the form:

$$i_{f\alpha} = -C_M \frac{v_{11}\psi_{r\beta} - v_{22}\psi_{r\alpha}}{x_{21}}, \tag{141}$$

$$i_{f\beta} = C_M \frac{v_{11}\psi_{r\alpha} + v_{22}\psi_{r\beta}}{x_{21}}. \tag{142}$$

As a result, two feedback loops and linear subsystems are obtained (Fig. 15).

6. The speed observer backstepping

General conception of the adaptive control with backstepping is presented in references [Payam A. F. & Dehkordi B. M. 2006, Krstic M.; Kanellakopoulos I.; & Kokotovic P. 1995]. In [Krstic M.; Kanellakopoulos I.; & Kokotovic P. 1995] the adaptive back integration observer stability is proved and the stability range is given.

Proceeding in accordance with the adaptive estimator with backstepping conception, one can derive formulae for the observer, where only the state variables will be estimated as well as the rotor angular speed as an additional estimation parameter.

Treating the stator current vector components $\hat{i}_{s\alpha,\beta}$ as the observer output variables (as in [Payam A. F. & Dehkordi B. M. 2006, Krstic M.; Kanellakopoulos I.; & Kokotovic P. 1995]) and $v_{\alpha,\beta}$ as the new input variables, which will be determined by the backstepping method, one obtains:

$$\frac{d\hat{i}_{s\alpha}}{d\tau} = -a_1\hat{i}_{s\alpha} + a_5\hat{\psi}_{r\alpha} + \hat{\omega}_r a_4\hat{\psi}_{r\beta} + a_6 u_{s\alpha} + v_\alpha, \tag{143}$$

$$\frac{d\hat{i}_{s\beta}}{d\tau} = -a_1\hat{i}_{s\beta} + a_5\hat{\psi}_{r\beta} - \hat{\omega}_r a_4\hat{\psi}_{r\alpha} + a_6 u_{s\beta} + v_\beta\,, \tag{144}$$

$$\frac{d\hat{\psi}_{r\alpha}}{d\tau} = -\frac{R_r}{L_r}\hat{\psi}_{r\alpha} - \hat{\omega}_r\hat{\psi}_{r\beta} + \frac{R_r L_m}{L_r}\hat{i}_{s\alpha}\,, \tag{145}$$

$$\frac{d\hat{\psi}_{r\beta}}{d\tau} = -\frac{R_r}{L_r}\hat{\psi}_{r\beta} + \hat{\omega}_r\hat{\psi}_{r\alpha} + \frac{R_r L_m}{L_r}\hat{i}_{s\beta}\,. \tag{146}$$

In accordance to the backstepping method, the virtual control must be determined together with the observer stabilizing variables. In that purpose, the new ς_α and ς_β variables have been introduced and linked with the stator current estimation deviations (the integral backstepping structure [Krstic M.; Kanellakopoulos I.; & Kokotovic P. 1995]):

$$\frac{d\tilde{\varsigma}_a}{d\tau} = \tilde{i}_{s\alpha}\,, \tag{147}$$

$$\frac{d\tilde{\varsigma}_b}{d\tau} = \tilde{i}_{s\beta}\,. \tag{148}$$

The stator current vector component deviations are treated as the subsystem control variables [Payam A. F. & Dehkordi B. M. 2006, Krstic M.; Kanellakopoulos I.; & Kokotovic P. 1995]. Adding and deducting the stabilizing functions, one obtains:

$$\frac{d\tilde{\varsigma}_\alpha}{d\tau} = \tilde{i}_{s\alpha} - \sigma_\alpha + \sigma_\beta\,, \tag{149}$$

$$\frac{d\tilde{\varsigma}_\beta}{d\tau} = \tilde{i}_{s\beta} - \sigma_\alpha + \sigma_\beta\,, \tag{150}$$

where

$$\sigma_\alpha = -c_1\tilde{\varsigma}_\alpha\,,\ \sigma_\beta = -c_1\tilde{\varsigma}_\beta\,, \tag{151}$$

by introducing the deviation defining variable, one obtains:

$$z_\alpha = \tilde{i}_{s\alpha} + c_1\tilde{\varsigma}_\alpha\,, \tag{152}$$

$$z_\beta = \tilde{i}_{s\beta} + c_1\tilde{\varsigma}_\beta\,. \tag{153}$$

Transformation of (152) - (153) leads to:

$$\frac{d\tilde{\varsigma}_\alpha}{d\tau} = z_\alpha - c_1\tilde{\varsigma}_\alpha \tag{154}$$

$$\frac{d\tilde{\varsigma}_\beta}{d\tau} = z_\beta - c_1\tilde{\varsigma}_\beta \,. \tag{155}$$

Calculation of the (152) - (153) deviation derivatives gives:

$$\dot{z}_\alpha = a_5\tilde{\psi}_{r\alpha} + a_4\left[\hat{\omega}_r\tilde{\psi}_{r\beta} + \tilde{\omega}_r(\hat{\psi}_{r\beta} - \tilde{\psi}_{r\beta})\right] + v_\alpha + c_1\tilde{i}_{s\alpha}\,, \tag{156}$$

$$\dot{z}_\beta = a_5\tilde{\psi}_{r\beta} - a_4\left[\hat{\omega}_r\tilde{\psi}_{r\alpha} + \tilde{\omega}_r(\hat{\psi}_{r\alpha} - \tilde{\psi}_{r\alpha})\right] + v_\beta + c_1\tilde{i}_{s\beta}\,. \tag{157}$$

By selecting the following Lyapunov function

$$V = \tilde{\varsigma}_\alpha^2 + \tilde{\varsigma}_\beta^2 + z_\alpha^2 + z_\beta^2 + \tilde{\psi}_{r\alpha}^2 + \tilde{\psi}_{r\beta}^2 + \frac{1}{\gamma}\tilde{\omega}_r^2\,, \tag{158}$$

calculating the derivative and substituting the respective expressions, new correction elements can be determined, treated in the speed observer backstepping as the input variables. The Lyapunov function is determined for the dynamics of the $\varsigma_{\alpha,\beta}$, $z_{\alpha,\beta}$ variables and for the rotor flux components. Calculating the (158) derivative, one obtains:

$$\begin{aligned}\dot{V} = {} & -c_1\tilde{\varsigma}_\alpha{}^2 - c_1\tilde{\varsigma}_\beta{}^2 - c_2z_\alpha^2 - c_2z_\beta^2 - \frac{R_r}{L_r}\tilde{\psi}_{r\alpha}^2 - \frac{R_r}{L_r}\tilde{\psi}_{r\beta}^2 + z_\alpha(a_5\tilde{\psi}_{r\alpha} + \hat{\omega}_r a_4\tilde{\psi}_{r\beta} + \tilde{\omega}_r a_4(\hat{\psi}_{r\beta} - \tilde{\psi}_{r\beta}) + \\ & + v_\alpha + c_1\tilde{i}_{s\alpha} + c_2z_\alpha + \tilde{\varsigma}_\alpha) + z_\beta(a_5\tilde{\psi}_{r\beta} - \hat{\omega}_r a_4\tilde{\psi}_{r\alpha} - \tilde{\omega}_r a_4(\hat{\psi}_{r\alpha} - \tilde{\psi}_{r\alpha}) + v_\beta + c_1\tilde{i}_{s\beta} + c_2z_\beta + \tilde{\varsigma}_\beta) + \\ & \tilde{\psi}_{r\alpha}(-\frac{R_r}{L_r}\tilde{\psi}_{r\alpha} - \hat{\omega}_r\tilde{\psi}_{r\beta} - \tilde{\omega}_r(\hat{\psi}_{r\beta} - \tilde{\psi}_{r\beta})) + \tilde{\psi}_{r\beta}(-\frac{R_r}{L_r}\tilde{\psi}_{r\beta} + \hat{\omega}_r\tilde{\psi}_{r\alpha} + \tilde{\omega}_r(\hat{\psi}_{r\alpha} - \tilde{\psi}_{r\alpha})).\end{aligned} \tag{159}$$

The input variables $v_{\alpha,\beta}$, resulting directly from (159), should include the estimated variables and the estimation deviations:

$$v_\alpha = -a_5\tilde{\psi}_{r\alpha} - \hat{\omega}_r a_4\tilde{\psi}_{r\beta} - c_1\tilde{i}_{s\alpha} - c_2z_\alpha - \tilde{\varsigma}_\alpha\,, \tag{160}$$

$$v_\beta = -a_5\tilde{\psi}_{r\beta} + \hat{\omega}_r a_4\tilde{\psi}_{r\alpha} - c_1\tilde{i}_{s\beta} - c_2z_\beta - \tilde{\varsigma}_\beta\,. \tag{161}$$

Taking (160) - (161) into account, the deviation derivatives may be written in the form:

$$\dot{z}_\alpha = \tilde{\omega}_r a_4(\hat{\psi}_{r\beta} - \tilde{\psi}_{r\beta}) - c_2z_\alpha - \tilde{\varsigma}_\alpha\,, \tag{162}$$

$$\dot{z}_\beta = -\tilde{\omega}_r a_4(\hat{\psi}_{r\alpha} - \tilde{\psi}_{r\alpha}) - c_2z_\beta - \tilde{\varsigma}_\beta\,. \tag{163}$$

Using (162) - (163), the Lyapunov function may be written as follows:

$$\dot{V} = -c_1\tilde{\varsigma}_\alpha{}^2 - c_1\tilde{\varsigma}_\beta{}^2 - c_2z_\alpha^2 - c_2z_\beta^2 + \tilde{\omega}_r a_4\left[z_\alpha(\hat{\psi}_{r\beta} - \tilde{\psi}_{r\beta}) - z_\beta(\hat{\psi}_{r\alpha} - \tilde{\psi}_{r\alpha}) + \frac{1}{\gamma}\dot{\hat{\omega}}_r\right]. \tag{164}$$

The observer, defined by the (143) - (146) and (154) - (155) equations, is a backstepping type estimator.

In the (160) - (163) expressions the rotor flux deviations appear, which may be neglected without any change to the observer properties (143) - (146). Besides, the $\tilde{\varsigma}_{\alpha,\beta}$ deviations in (160) - (161) may be zero, thus lowering the observer order. Assuming the simplifications, one obtains

$$v_\alpha = -c_1\tilde{i}_{s\alpha} - c_2 z_\alpha\,, \tag{165}$$

$$v_\beta = -c_1\tilde{i}_{s\beta} - c_2 z_\beta\,, \tag{166}$$

and

$$\dot{\hat{\omega}}_r = \gamma a_4\left(z_\beta\hat{\psi}_{r\alpha} - z_\alpha\hat{\psi}_{r\beta}\right). \tag{167}$$

where

c_1, c_2, γ are constant gains,

$$a_4 = \frac{L_m}{w_\sigma}\,,\ a_5 = \frac{R_r L_m}{L_r w_\sigma}\,,\ a_6 = \frac{L_r}{w_\sigma}\,.$$

In Fig. 10, 11 the backstepping speed observer test is shown. When the load torque is set to ~-0.1 p.u. the rotor speed in backstepping observer is more precisely estimated than e.g. Krzeminski's speed observer.

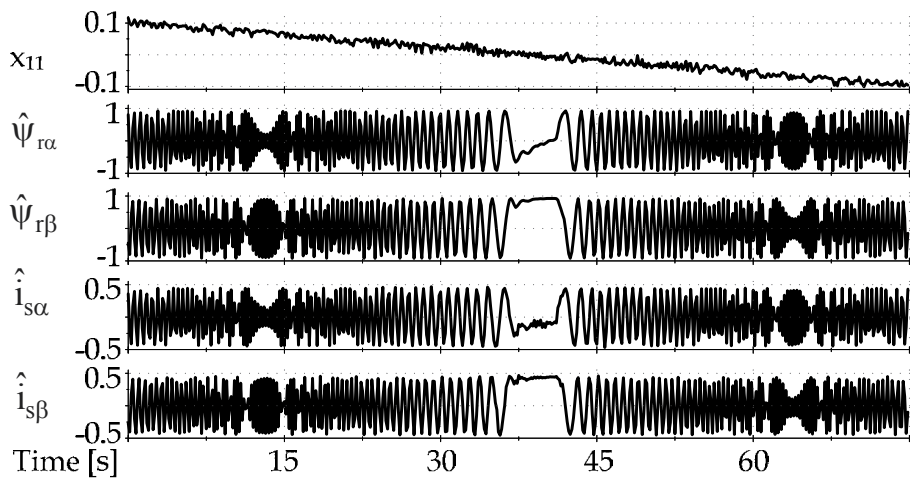

Figure 10. The Speed observer test: the estimated rotor speed x_{11} is changed from 0.1 to -0.1 p.u., the rotor flux and stator current coefficients are shown

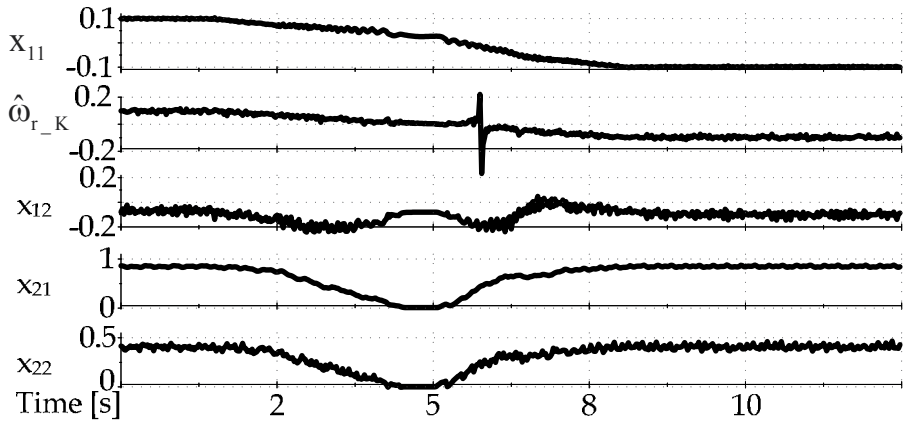

Figure 11. The Speed observer test: the estimated rotor speed x_{11} in backstepping observer is changed from 0.1 to -0.1 p.u., the estimated rotor speed $\hat{\omega}_{r\_K}$ by Krzeminski's speed observer [Krzeminski Z., 1999] and the multi-scalar variable: x_{12}, x_{21}, x_{22} are shown . The load torque m_0 is set to -0.1 p.u.

7. The control system structures

In Fig. 12 and Fig. 14 the voltage and current multi-scalar control system structure is shown. These structures are based on four PI controllers and contain: the modulator, the speed observer and decouplings blocks .

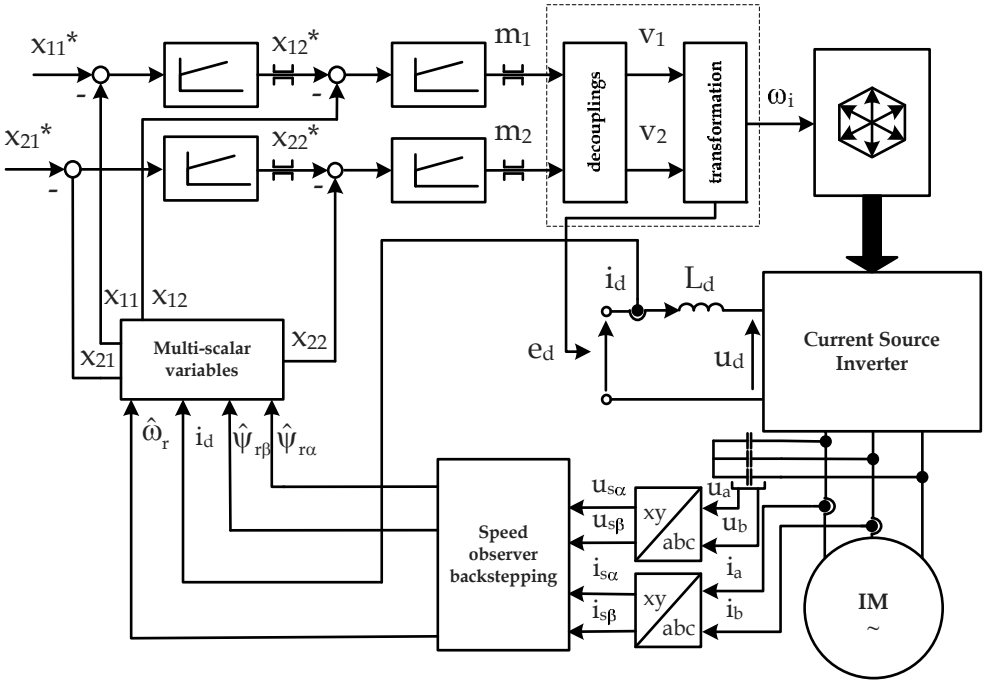

Figure 12. The voltage multi-scalar control system structure

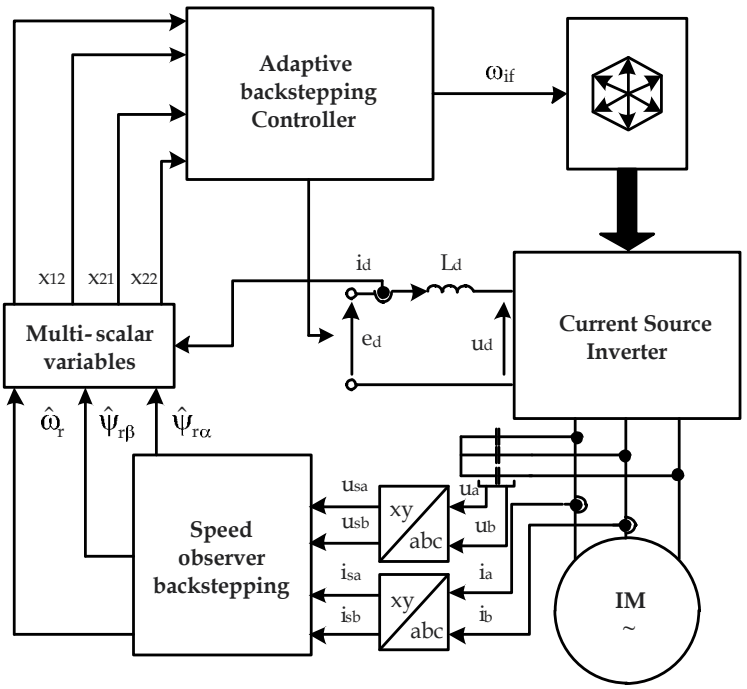

Figure 13. The voltage multi-scalar adaptive backstepping control system structure

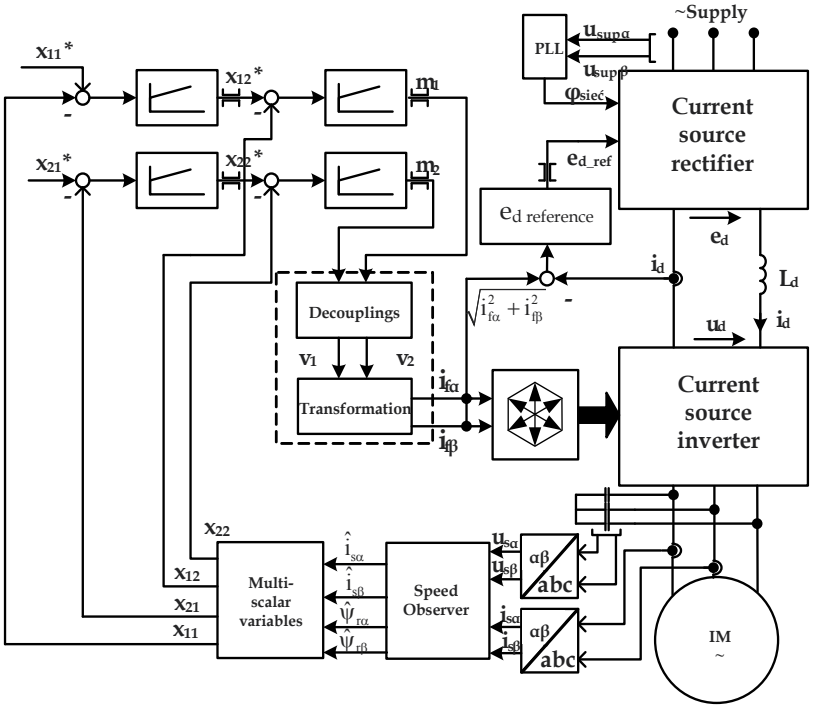

Figure 14. The current multi-scalar control system structure.

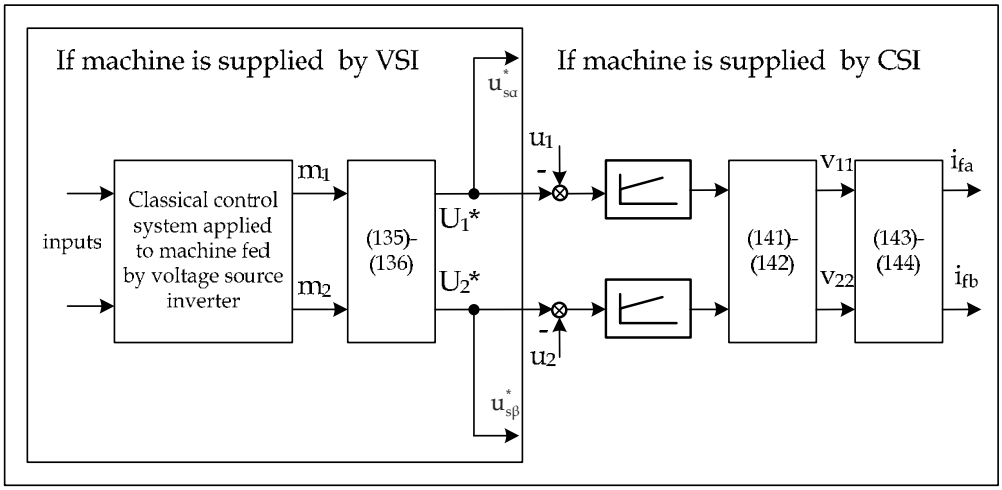

Figure 15. Generalized Multi-scalar Control System of Induction Machine supplied by CSI or VSI.

In Fig. 14 the e_{d_ref} value is determined in e_d reference block. The e_d reference block can be PI current controller or other controller.

In Fig. 13 the voltage multi-scalar adaptive backstepping control system structure is shown.

In Fig. 15 generalized multi-scalar control system structure is presented. This control structure is divided into two parts: the control system of IM fed by VSI and the control system of IM fed by CSI.

8. Experimental verification of the control systems

The tests were carried out in a 5.5 kW drive system. The motor parameters are given in Table 2 and the main per unit values in Table 3. In Fig. 16, 17 motor start-up and reverse for control system presented in chapter 4.1-4.2 are shown. In Fig. 18, 19 motor start-up and reverse for control system presented in chapter 5 are shown. Fig. 20,21 presents the same steady state like previous but for adaptive backstepping control system (chapter 4.3). Fig. 22 presents diagram of stator currents and voltages when motor is starting up for voltage control system (chapter 4.3). In Fig. 23 load torque setting to 0.7 p.u. for current control is presented. In Fig. 24, 25 the i_d current and the sinusoidal stator voltage and stator current are presented.

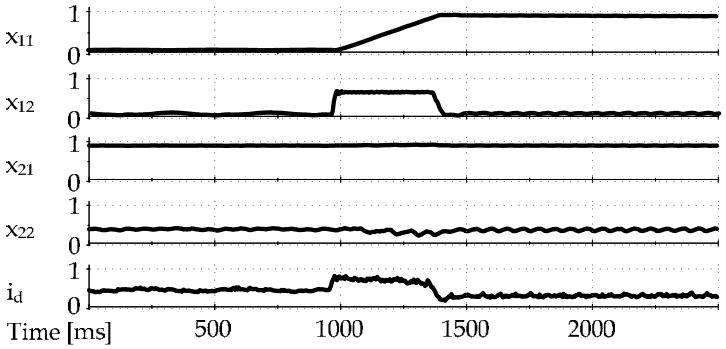

Figure 16. Motor start-up (chapter 4.1- 4.2)

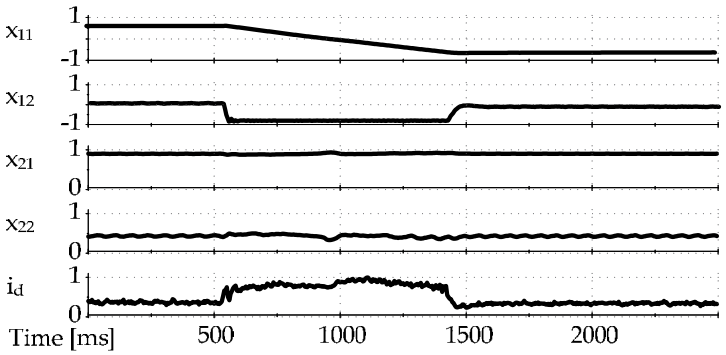

Figure 17. Motor reverse (chapter 4.1- 4.2)

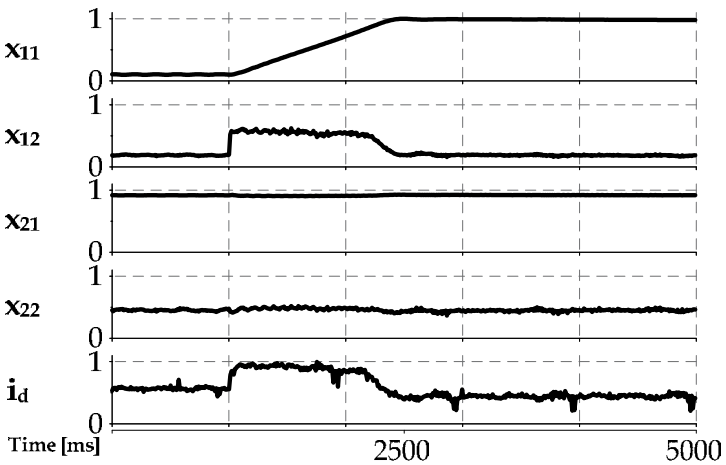

Figure 18. Motor start-up (chapter 5)

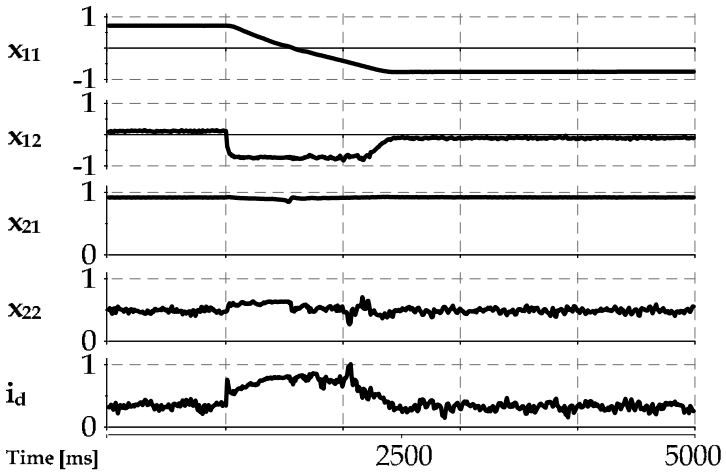

Figure 19. Motor reverse (chapter 5)

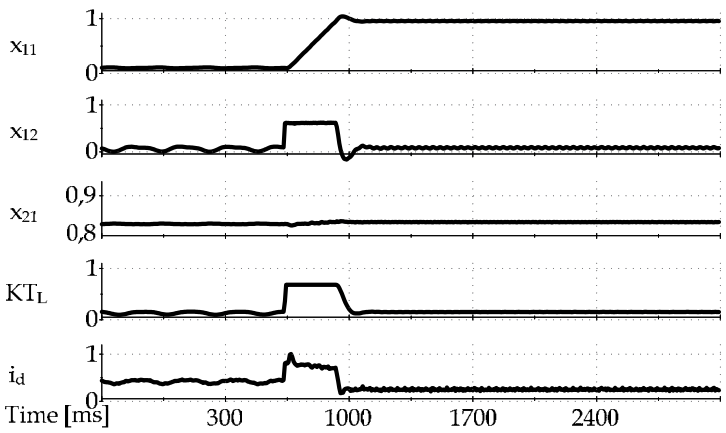

Figure 21. Motor start-up (chapter 4.3)

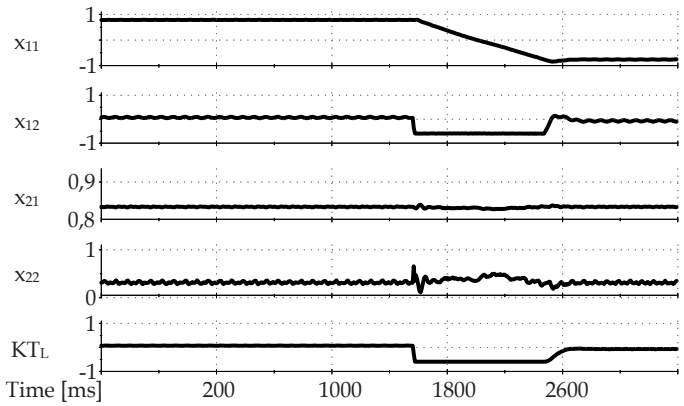

Figure 21. Motor reverse (chapter 4.3)

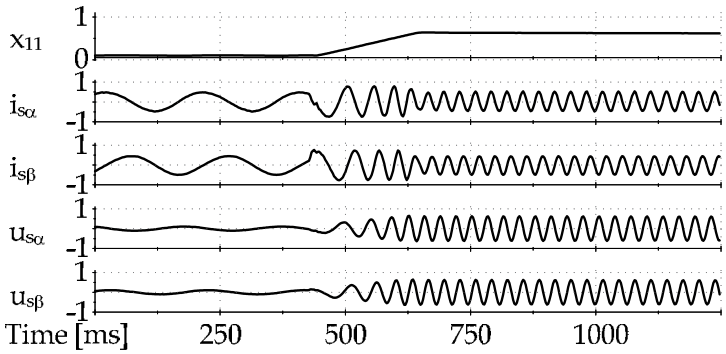

Figure 22. The currents and voltages

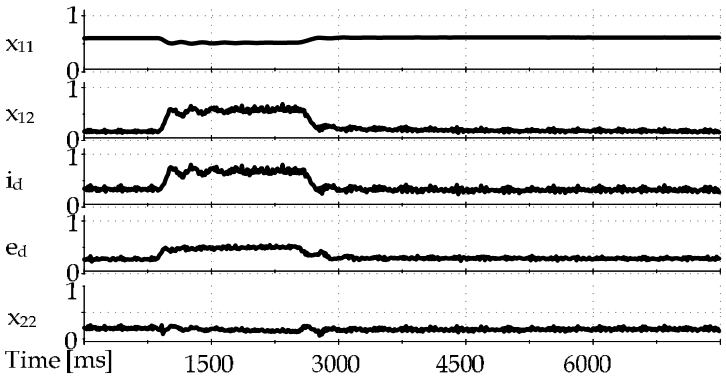

Figure 23. Load torque is set to 0.7 p.u. (chapter 5)

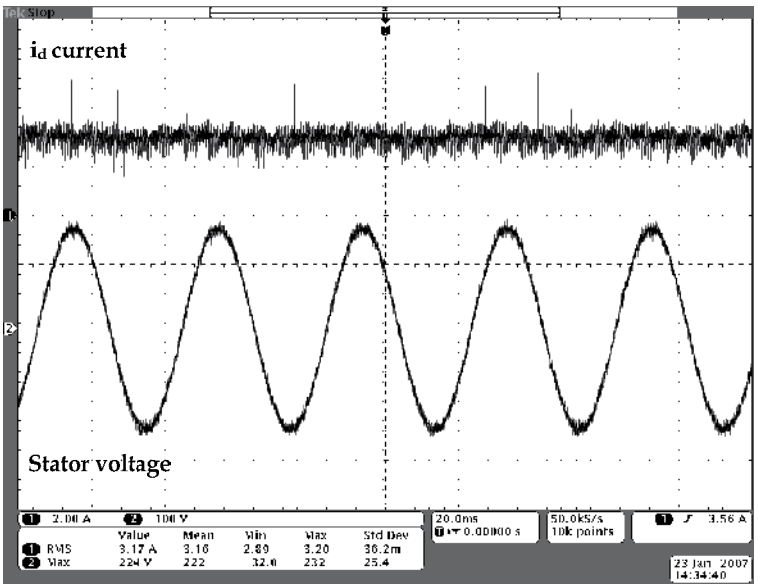

Figure 24. i_d current and the stator voltage

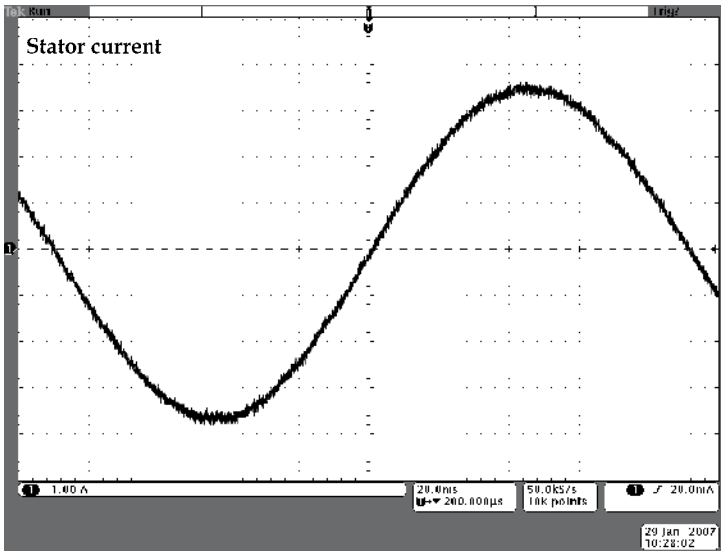

Figure 25. The stator current in stationary state.

where:

x_{11} is the rotor speed, x_{12} is the variable proportional to electromagnetic torque, x_{21} is the square of rotor flux and x_{22} is the additional variables, i_d is the dc-link current, $u_{s\alpha,\beta}$ are the capacitor voltage components, KTL is correction element (load torque), $i_{s\alpha,\beta}$ are the stator current components.

9. Conclusion

In this chapter two approaches to control of induction machine supplied by current source converter are presented. The first of them is voltage multi-scalar control based on PI controllers or backstepping controller. The voltage approach seems to be a better solution than the second one: current control, because the control system structure is more simple than the current control structure. The voltage in dc-link is the control variables obtained directly from decouplings. The current in dc-link is not kept at constant value but its value depend on induction machine working point. The current control gives higher losses in dc-link and higher transistor power losses than the voltage control. The power losses can be minimized by modulation index control method but the control system is more complicated. Both control systems lead to decoupling control path and sinusoidal stator current and voltage when space vector modulation of transistors is applied.

PARAMETER	VALUE
P_n (motor power)	5.5 kW
U_n (phase to phase voltage)	400 V
I_n (current)	10.9 A
J (interia)	0.0045 kgm^2
n_n (rotor speed)	1500 rpm
PARAMETER	PER UNIT VALUES
R_s (stator resist.)	0.045
R_r (rotor resist.)	0.055
L_m (mutual-flux induct.)	1.95
L_s (stator induct.)	2.05
L_r (rotor induct.)	2.05
Current Source Converter	
C (capacitor in dc-link)	0.1
R_d (inductor resist.)	0.002
$C_{M,L}$ (input-output caps)	0.2

Table 2. The motor drive system parameters

DEFINITION	DESCRIPTION
$U_b = \sqrt{3}U_n$	base voltage
$I_b = I_n$	base current
$z_b = U_b / I_b$	base impedance

Table 3. Definition of per unit values

Author details

Marcin Morawiec
Gdansk University of Technology, Faculty of Electrical and Control Engineering, Poland

10. References

Adamowicz M.; Guzinski J.; Minimum-time minimum-loss speed sensorless control of induction motors under nonlinear control, *Compatibility in Power Electronics 2005*.

Bassi E.; Benzi F.P.; Bolognani S.; Buja G.S., A field orientation scheme for current-fed induction motor drives based on the torque angle closed-loop control, *IEEE Transactions on Industry Applications, Volume 28, Issue 5, Sept.-Oct. 1992 Pages: 1038 – 1044.*

Glab (Morawiec) M.; Krzeminski Z. & Włas M., The PWM current source inverter with IGBT transistors and multiscalar model control system, *11th European Conference on Power Electronics and Applications, IEEE 2005.*

Glab (Morawiec) M.; Krzeminski Z.; Lewicki A., Multiscalar control of induction machine supplied by current source inverter, *PCIM 2007, Nuremberg* 2007.

Fuschs F. & Kloenne A. dc-link and Dynamic Performance Features of PWM IGBT Current Source Converter Induction Machine Drives with Respect to Industrial Requirements, *IPEMC 2004, Vol. 3, 14-16 August 2004.*

Kwak S.; Toliyat H.A., A Current Source Inverter With Advanced External Circuit and Control Method, *IEEE Transactions on Industry Applications, Volume 42, Issue 6, Nov.-dec. 2006 Pages: 1496 – 1507.*

Klonne A. & Fuchs W.F., High dynamic performance of a PWM current source converter induction machine drive, *EPE 2003, Toulouse*.

Krstic M.; Kanellakopoulos I.; & Kokotovic P., Nonlinear and Adaptive Control Design, *John Wiley & Sons, 1995.*

Krzeminski Z., A new speed observer for control system of induction motor. IEEE Int. Conference on Power Electronics and Drive Systems, *PESC'99, Hong Kong, 1999.*

Krzeminski Z., Nonlinear control of induction motor, *Proceedings of the 10th IFAC World Congress, Munich 1987.*

Morawiec M., Sensorless control of induction machine supplied by current source inverter , *PhD Thesis, Gdansk University of Technology 2007.*

Nikolic Aleksandar B., Jeftenic Borislav I.: Improvements in Direct Torque Control of Induction Motor Supplied by CSI, *IEEE Industrial Electronics, IECON 2006 - 32nd Annual Conference on Industrial Electronics.*

Payam A. F.; Dehkordi B. M.; Nonlinear sliding-mode controller for sensorless speed control of DC servo motor using adaptive backstepping observer, *International Conference on Power Electr., PEDES '06, 2006.*

Salo M.; Tuusa H., Vector-controlled PWM current-source-inverter-fed induction motor drive with a new stator current control method, *IEEE Transactions on Industrial Electronics, Volume 52, Issue 2, April 2005 Pages: 523 – 531.*

Tan H.; & Chang J.; Adaptive Backstepping control of induction motor with uncertainties, *in Proc. the American control conference, California, June 1999, pp. 1-5.*

Young Ho Hwang; Ki Kwang Park; Hai Won Yang; Robust adaptive backstepping control for efficiency optimization of induction motors with uncertainties, *ISIE 2008.*

Chapter 19

Minimizing Torque-Ripple in Inverter-Fed Induction Motor Using Harmonic Elimination PWM Technique

Ouahid Bouchhida, Mohamed Seghir Boucherit and Abederrezzek Cherifi

Additional information is available at the end of the chapter

http://dx.doi.org/10.5772/37883

1. Introduction

Vector control has been widely used for the high-performance drive of the induction motor. As in DC motor, torque control of the induction motor is achieved by controlling torque and flux components independently. Vector control techniques can be separated into two categories: direct and indirect flux vector orientation control schemes. For direct control methods, the flux vector is obtained by using stator terminal quantities, while indirect methods use the machine slip frequency to achieve field orientation.

The overall performance of field-oriented-controlled induction motor drive systems is directly related to the performance of current control. Therefore, decoupling the control scheme is required by compensation of the coupling effect between q-axis and d-axis current dynamics (Jung et al., 1999; Lin et al., 2000; Suwankawin et al., 2002).

The PWM is the interface between the control block of the electrical drive and its associated electrical motor (fig.1). This function controls the voltage or the current inverter (VSI or CSI) of the drive. The performance of the system is influenced by the PWM that becomes therefore an essential element of the system. A few problems of our days concerning the variable speed system are related to the conventional PWM: inverter switching losses, acoustical noise, and voltages harmonics (fig.2).

Harmonic elimination and control in inverter applications have been researched since the early 1960's (Bouchhida et al., 2007, 2008; Czarkowski et al., 2002; García et al., 2003; Meghriche et al., 2004, 2005; Villarreal-Ortiz et al., 2005; Wells et al., 2004). The majority of these papers consider the harmonic elimination problem in the context of either a balanced connected load or a single phase inverter application. Typically, many papers have focused

on finding solutions and have given little attention to which solution is optimal in an application context.

A pre-calculated PWM approach has been developed to minimize the harmonic ratio within the inverter output voltage (Bouchhida et al., 2007, 2008; Bouchhida, 2008, 2011). Several other techniques were proposed in order to reduce harmonic currents and voltages. Some benefit of harmonic reduction is a decrease of eddy currents and hysterisis losses. That increase of the life span of the machine winding insulation. The proposed approach is integrated within different control strategies of induction machine.

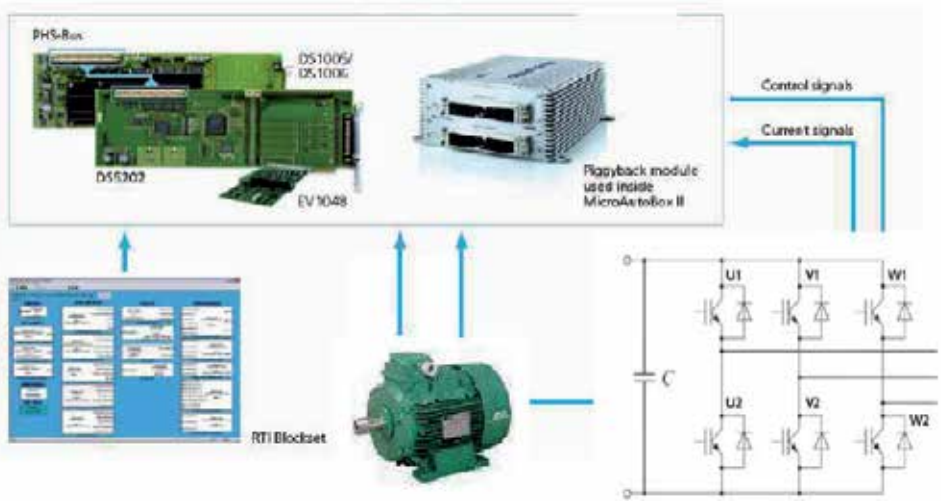

Figure 1. Global scheme of the Induction machine control

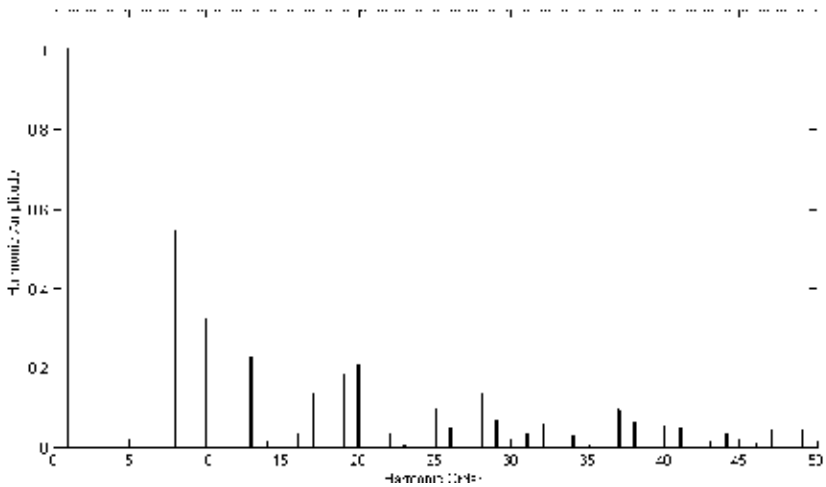

Figure 2. Harmonic spectrum of the PWM inverter output voltage.

A novel harmonic elimination pulse width modulated (PWM) strategy for three-phase inverter is presented in this chapter. The torque ripple of the induction motor can be

significantly reduced by the new PWM technique. The three-phase inverter is associated with a passive LC filter. The commutation angles are predetermined off-line and stored in the microcontroller memory in order to speed up the online control of the induction motors. Pre-calculated switching is modelled to cancel the greater part of low-order harmonics and to keep a single-pole DC voltage across the polarized capacitors. A passive LC filter is designed to cancel the high-order harmonics. This approach allows substantial reduction of the harmonic ratio in the AC main output voltage without increasing the number of switches per period. Consequently, the duties of the semiconductor power switches are alleviated. The effectiveness of the new harmonic elimination PWM technique for reducing torque-ripple in inverter-fed induction motors is confirmed by simulation results. To show the validity of our approach, DSP-based experimental results are presented.

2. New three-phase inverter model

Figure 3 shows the new structure of the three-phase inverter, with E being the dc input voltage and $U_{12\text{-}out}=V_{C1}-V_{C2}$, $U_{23\text{-}out}=V_{C2}-V_{C3}$ and $U_{31\text{-}out}=V_{C3}-V_{C1}$ are the ac output voltage obtained via a three LC filter. R represents the internal inductors resistance. Q_i and Q'_i (i=1,2,3) are the semiconductor switches. It is worth to mention that transistors Q_i and Q'_i undergo complementary switching states. V_{C1}, V_{C2} and V_{C3} are the inverter filtered output voltages taken across capacitors C_1, C_2 and C_3 respectively.

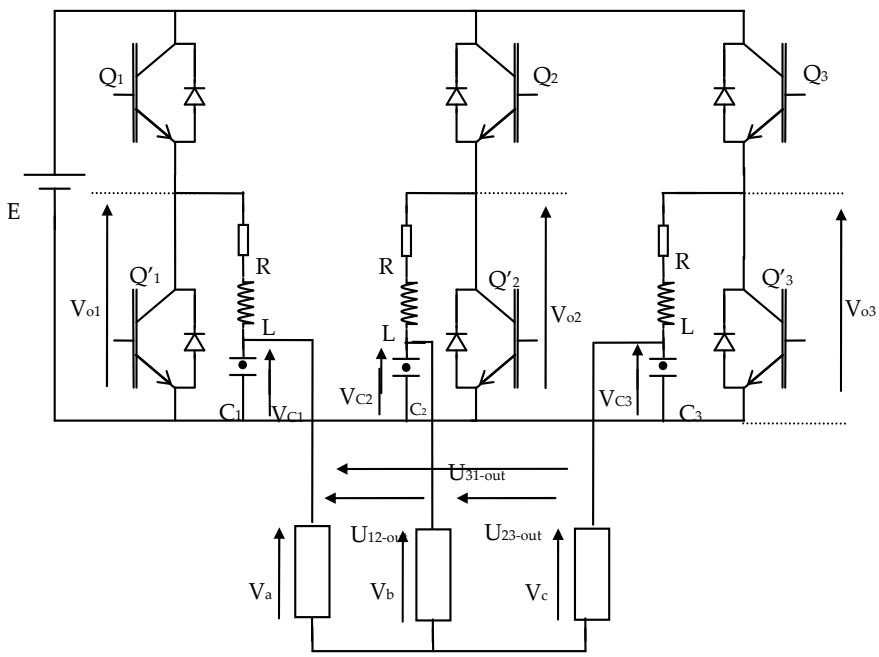

Figure 3. New three-phase inverter model.

2.1. Harmonic analysis

In ideal case, the non filtered three inverter output voltage V_{o1}, V_{o2} and V_{o3} is desired to be:

$$\begin{cases} V_{o1-ideal} = \frac{E}{2}[1+\cos\alpha] \\ V_{o2-ideal} = \frac{E}{2}[1+\cos(\alpha-\frac{2}{3}\pi)] \\ V_{o3-ideal} = \frac{E}{2}[1+\cos(\alpha-\frac{4}{3}\pi)] \end{cases} \quad (1)$$

With: $\alpha=\omega t$, and ω is the angular frequency.

The relative Fourier harmonic coefficients of (1), with respect to E, are given by (2.1) or more explicitly by (2.2).

$$d_k^i = \frac{1}{E}\frac{1}{\pi}\int_{-\pi}^{+\pi} V_{oi-ideal}.\cos(k\alpha)d\alpha \quad (2.1)$$

$$d_0^i = 1,\ d_1^i = \frac{1}{2},\ d_k^i = 0 \text{ , for } k \in [2,\infty[\quad (2.2)$$

With index i is the phase number.

However, in practice, the non filtered inverter output voltage V_{o1} (V_{o2}, V_{o3}) is a series of positive impulses (see Fig. 4): 0 when Q'_1 (Q'_2, Q'_3) is on and E when Q'_1(Q'_2, Q'_3) is off, so that voltage of capacitor C_1 (C_2, C_3) is always a null or a positive value. In this case, the relative Fourier harmonic coefficients, with respect to E, are given by (3).

$$a_k^1 = \frac{2}{k\pi}\sum_{i=0}^{N_\alpha} \sin k\alpha_i(-1)^{i+1} \quad (3)$$

Where:

k is the harmonic order

α_i are the switching angles

N_α is the number of α_i per half period

The other inverter outputs V_{o2} and V_{o3} are obtained by phase shifting V_{o1} with 2/3 π, 4/3 π, respectively as illustrated in fig. 4 for N_α=5.

The objective is to determine the switching angles α_i so as to obtain the best possible match between the inverter output V_{o1} and $V_{o1\text{-ideal}}$.

For this purpose, we have to compare their respective harmonics. A perfect matching is achieved only when an infinite number of harmonics is considered as given by (4).

$$\frac{2}{k\pi}\sum_{i=0}^{N_\alpha} sin\, k\alpha_i(-1)^{i+1} = d_k \text{, for } k \in \left[0,\infty\right[\tag{4}$$

In practice, the number of harmonics N that can be identical is limited. Thus, a nonlinear system of N+1 equations having N_α unknowns is obtained as:

$$a_k = \frac{2}{k\pi}\sum_{i=0}^{N_\alpha} sin\, k\alpha_i(-1)^{i+1} = d_k \text{, for } k \in \left[0,N\right] \tag{5}$$

To solve the nonlinear system (5), we propose to use the genetic algorithms, to determine the switching angles α_i (Bäck, 1996; Davis, 1991). The optimal switching angles family are listed in table I.

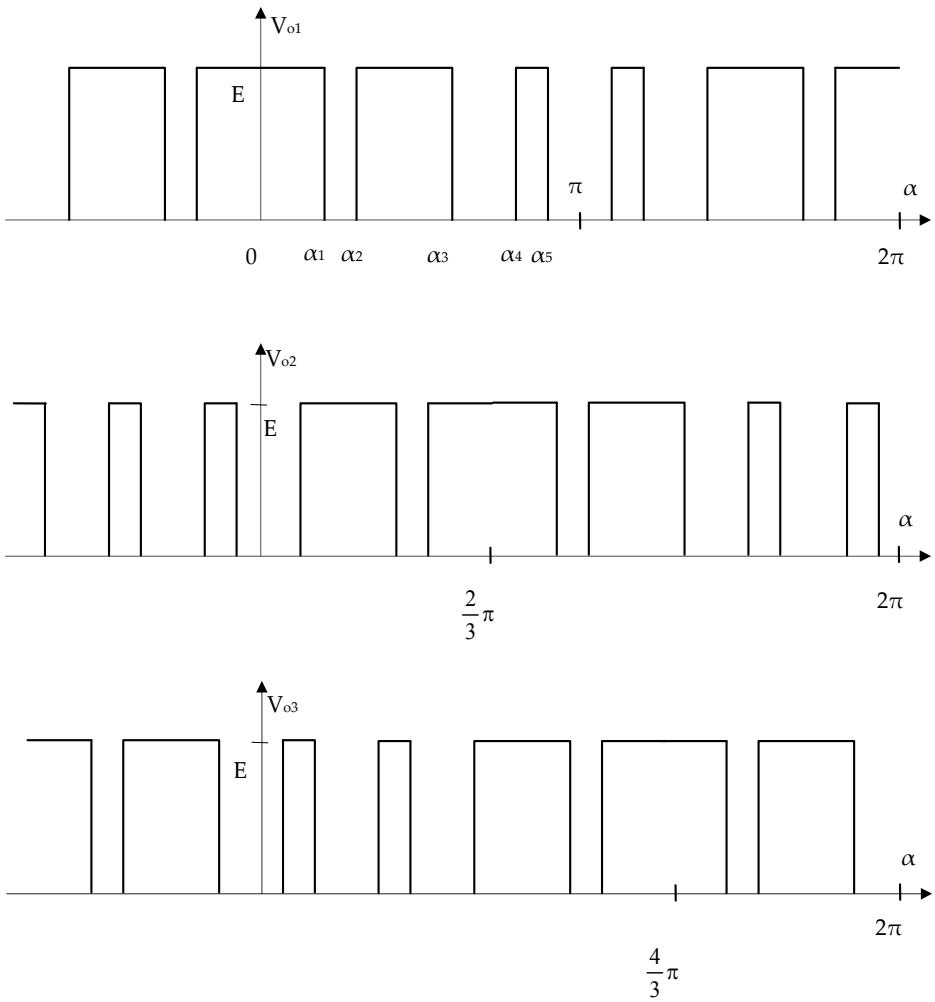

Figure 4. Inverter direct outputs representation for Nα=5.

Family	symbol	Angles (radians)	Angles (degrees)
N_α=3	α1	0.817809468	46.8570309622392
	α2	1.009144336	57.8197113723319
	α3	1.911639657	109.528884295936
N_α=5	α1	1.051000076	60.2178686227288
	α2	1.346257127	77.1348515165077
	α3	1.689593122	96.8065549849324
	α4	2.374938655	136.073961533976
	α5	2.47770082	141.961799882103
N_α=7	α1	0.52422984	30.0361573268184
	α2	0.57159284	32.7498573318965
	α3	1.14918972	65.8437208158208
	α4	1.41548576	81.1013600088678
	α5	1.66041537	95.134792939653
	α6	2.16577455	124.089741091845
	α7	2.29821202	131.677849172236
N_α=9	α1	0.43157781	24.7275870444989
	α2	0.45713212	26.1917411558679
	α3	0.70162245	40.2000051966286
	α4	0.77452452	44.3769861253959
	α5	0.96140142	55.0842437838843
	α6	1.09916539	62.9775378338511
	α7	1.21595592	69.6691422899472
	α8	1.45409688	83.3136142271409
	α9	1.64220075	94.0911720882184

Table 1. Optimal switching angles family with genetic algorithms

2.2. Dynamic LC filter behavior

Considering the inverter direct output fundamental, the LC filter transfer function is given by:

$$\bar{T} = \frac{\bar{V}_{C1}}{\bar{V}_{o1}} = \frac{1}{1 - LC\omega^2 + jRC\omega} \tag{6}$$

From (6), one can notice that for ω=0, $\bar{T}$ =1, meaning that the mean value (dc part) of the input voltage is not altered by the filter. Consequently, the inverter dc output part is entirely transferred to capacitor C_1. The same conclusion can be drawn for capacitor C_2 and C_3.

Letting $x = \omega\sqrt{LC}$ and $y = R\sqrt{\frac{C}{L}}$, the filter transfer function can rewritten as:

$$\bar{T} = \frac{\bar{V}_{C1}}{\bar{V}_{o1}} = \frac{1}{1 - x^2 + jxy} \tag{7}$$

For a given harmonic component of order k, the LC filter transfer function T_k is obtained by replacing ω with kω as:

$$\overline{T}_k = \left(\frac{\overline{V}_{C1}}{\overline{V}_{o1}} \right)_k = \frac{1}{1 - x^2k^2 + jkxy} \tag{8}$$

Assuming that the filter L and C components are not saturated, and using the superposition principle, we obtain the inverter filtered output voltages V_{C1}, V_{C2} and V_{C3}, taken across capacitors C_1, C_2 and C_3 as given by (9.1), (9.2) and (9.3) respectively:

$$V_{C1} = E(\frac{a_0}{2} + \sum_{k=1}^{N} a_k T_k \cos(k\alpha + \varphi_k)) \tag{9.1}$$

$$V_{C2} = E(\frac{a_0}{2} + \sum_{k=1}^{N} a_k T_k \cos[k(\alpha - \frac{2}{3}\pi) + \varphi_k]) \tag{9.2}$$

$$V_{C3} = E(\frac{a_0}{2} + \sum_{k=1}^{N} a_k T_k \cos[k(\alpha - \frac{4}{3}\pi) + \varphi_k]) \tag{9.3}$$

T_k and φ_k are the k^{th} order magnitude and phase components of the LC filter transfer function respectively.

Each k harmonic term of the inverter output voltage has a frequency of kω and an amplitude equal to a_kT_k, Where a_k is the amplitude of the k^{th} order harmonic of V_{o1}.

The transfer function magnitude and phase are given, respectively, by:

$$\left|\overline{T}_k\right| = T_k = \frac{1}{\sqrt{(1 - x^2k^2)^2 + y^2x^2k^2}} \tag{10}$$

$$\varphi_k = -arctan\frac{kxy}{1 - x^2k^2} \tag{11}$$

The maximum value T_{max} of T_k , obtained when $\frac{dT}{dx} = 0$, can be expressed by:

$$T_{max} = \frac{\frac{1}{y^2}}{\sqrt{\frac{1}{y^2} - \frac{1}{4}}} \tag{12}$$

In which case, (12) corresponds to a maximum angular frequency, this last is given by:

$$\omega_{max} = \frac{\sqrt{2}}{RC}\sqrt{1 - \frac{y^2}{2}} \tag{13}$$

The maximum angular frequency ω_{max} exists if, and only if, $y < \sqrt{2}$. The filter transfer function will exhibit a peak value then decreases towards zero. As consequence, the fundamental, as well as the harmonics, are amplified, this leads to undesirable situation, as illustrated in fig.5.

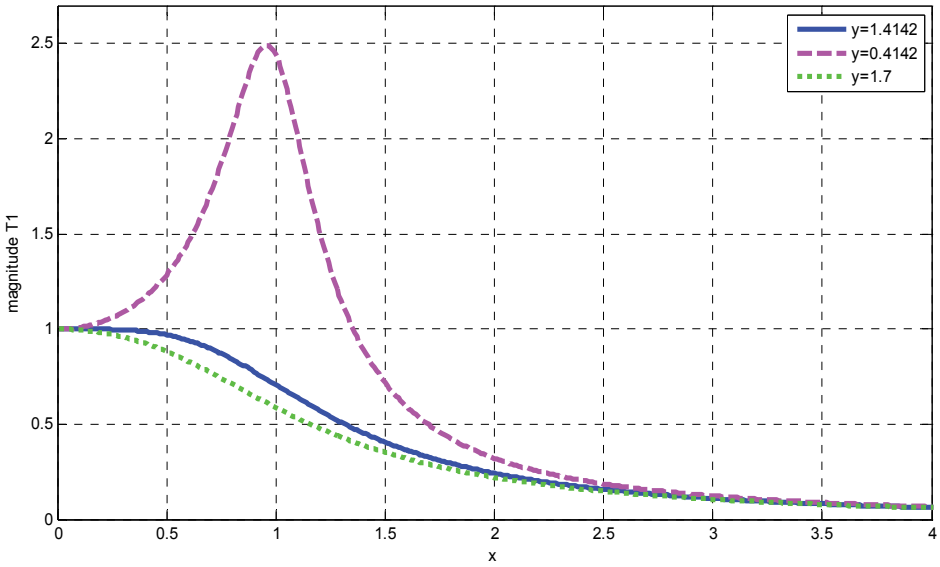

Figure 5. LC filter transfer function magnitude for the fundamental.

If (14) is satisfied, the filter transfer function will exhibit a damped behaviour.

$$y = R\sqrt{\frac{C}{L}} > \sqrt{2} \tag{14}$$

This condition matches both practical convenience and system objectives.

2.3. Harmonic rate calculation

Using (1) to (3), the non filtered inverter output voltages V_{o1}, V_{o2} and V_{o3} can be expressed as

$$V_{o1} = \frac{E}{2}(1 + cos\,\omega t) + a_5 cos\,5\omega t + a_6 cos\,6\omega t + \ldots \tag{15.1}$$

$$V_{o2} = \frac{E}{2}[1 + cos(\omega t - \frac{2}{3}\pi)] + a_5 cos\,5(\omega t - \frac{2}{3}\pi) + a_6 cos\,6(\omega t - \frac{2}{3}\pi) + \ldots \tag{15.2}$$

$$V_{o3} = \frac{E}{2}[1 + cos(\omega t - \frac{4}{3}\pi)] + a_5 cos\,5(\omega t - \frac{4}{3}\pi) + a_6 cos\,6(\omega t - \frac{4}{3}\pi) + \ldots \tag{15.3}$$

Taking into consideration the filter transfer function, we get the expressions (16), (17) and (18) for V_{C1}, V_{C2} and V_{C3} respectively.

$$V_{C1} = \frac{E}{2}[1 + a_1.T_1.cos(\alpha + \varphi_1) + a_8.T_8.cos(8.\alpha + \varphi_8) + a_{10}.T_{10}.cos(10.\alpha + \varphi_{13}) + ... \quad (16)$$

$$V_{C2} = \frac{E}{2}[1 + a_1.T_1.cos([\alpha - \frac{2}{3}\pi] + \varphi_1) + a_8.T_8.cos(8[\alpha - \frac{2}{3}\pi] + \varphi_8) + a_{10}.T_{10}.cos(10[\alpha - \frac{2}{3}\pi] + \varphi_{10}) + ... \quad (17)$$

$$V_{C3} = \frac{E}{2}[1 + a_1.T_1.cos([\alpha - \frac{4}{3}\pi] + \varphi_1) + a_8.T_8.cos(8[\alpha - \frac{4}{3}\pi] + \varphi_8) + a_{10}.T_{10}.cos(10[\alpha - \frac{4}{3}\pi] + \varphi_{10}) + ... \quad (18)$$

Using (15), (16), (17) and (18), we get the three inverter filtered output voltages expressions as:

$$\begin{cases} U_{12-out} = E\frac{\sqrt{3}}{2}\left[a_1 T_1 cos(\alpha + \beta_1) + \sum_{\substack{k=8 \\ k=3n+1 \\ k=3n+2}}^{\infty} a_k T_k cos(k\alpha + \beta_k) \right] \\ U_{23-out} = E\frac{\sqrt{3}}{2}\left[a_1 T_1 cos(\alpha + \beta_1 - \frac{2}{3}\pi) + \sum_{\substack{k=8 \\ k=3n+1 \\ k=3n+2}}^{\infty} a_k T_k cos(k\alpha + \beta_k - \frac{2}{3}\pi) \right] \\ U_{31-out} = E\frac{\sqrt{3}}{2}\left[a_1 T_1 cos(\alpha + \beta_1 - \frac{4}{3}\pi) + \sum_{\substack{k=8 \\ k=3n+1 \\ k=3n+2}}^{\infty} a_k T_k cos(k\alpha + \beta_k - \frac{4}{3}\pi) \right] \end{cases} \quad (19)$$

with: $\beta_k = \varphi_k + \frac{\pi}{6}$.

From the precedent fig. 3, and for each lever, the equations with the currents and the voltages can be written in the following form (Bouchhida et al., 2007, 2008; Bouchhida, 2008, 2011).

- Currents equations

$$\begin{cases} \frac{dv_{C1}}{dt} = \frac{1}{C_1}(i_1 - i_{1ch}) \\ \frac{dv_{C2}}{dt} = \frac{1}{C_2}(i_2 - i_{2ch}) \\ \frac{dv_{C3}}{dt} = \frac{1}{C_3}(i_3 - i_{3ch}) \end{cases} \quad (20)$$

- Voltages equations:

$$\begin{cases} \dfrac{di_1}{dt} = (V_{o1} - R_1.i_1 - v_{C1}).\dfrac{1}{L_1} \\ \dfrac{di_2}{dt} = (V_{o2} - R_2.i_2 - v_{C2}).\dfrac{1}{L_2} \\ \dfrac{di_3}{dt} = (V_{o3} - R_3.i_3 - v_{C3}).\dfrac{1}{L_3} \end{cases} \tag{21}$$

These equations are put in following matric form:

$$\frac{d}{dt}\begin{bmatrix} v_C \\ I \end{bmatrix} = \begin{bmatrix} \mathbf{0_{3\times3}} & \dfrac{\mathbf{1}}{\mathbf{C}} \times \mathbf{I_{3\times3}} \\ -\dfrac{\mathbf{1}}{\mathbf{L}} \times \mathbf{I_{3\times3}} & -\mathbf{R} \times \mathbf{I_{3\times3}} \end{bmatrix} \begin{bmatrix} v_c \\ I \end{bmatrix} + \begin{bmatrix} -\dfrac{1}{C} \times I_{3\times3} & 0_{3\times3} \\ 0_{3\times3} & \dfrac{1}{L} \times I_{3\times3} \end{bmatrix} \begin{bmatrix} i_{ch} \\ V_o \end{bmatrix} \tag{22}$$

with : $v_C = \begin{bmatrix} v_{C1} \\ v_{C2} \\ v_{C3} \end{bmatrix}$; $I = \begin{bmatrix} i_1 \\ i_2 \\ i_3 \end{bmatrix}$; $v_o = \begin{bmatrix} v_{o1} \\ v_{o2} \\ v_{o3} \end{bmatrix}$

3. Indirect field- oriented induction motor drive

The dynamic electrical equations of the induction machine can be expressed in the d-q synchronous reference frame as:

$$\begin{cases} \dfrac{di_{ds}}{dt} = -\dfrac{1}{\sigma L_s}(R_s + R_r \dfrac{M_{sr}^2}{L_r^2})i_{ds} + \omega_s i_{qs} + \dfrac{M_{sr}R_r}{\sigma L_s L_r^2}\psi_{dr} + \dfrac{M_{sr}}{\sigma L_s L_r}\psi_{qr}\omega_r + \dfrac{1}{\sigma L_s}V_{ds} \\ \dfrac{di_{qs}}{dt} = -\omega_s i_{ds} - \dfrac{1}{\sigma L_s}(R_s + R_r \dfrac{M_{sr}^2}{L_r^2})i_{qs} - \dfrac{M_{sr}}{\sigma L_s L_r}\psi_{dr}\omega_r + \dfrac{M_{sr}R_r}{\sigma L_s L_r^2}\psi_{qr} + \dfrac{1}{\sigma L_s}V_{qs} \\ \dfrac{d\psi_{dr}}{dt} = \dfrac{M_{sr}R_r}{L_r}i_{ds} - \dfrac{R_r}{L_r}\psi_{dr} + \omega_g\psi_{qr} \\ \dfrac{d\psi_{qr}}{dt} = \dfrac{M_{sr}R_r}{L_r}i_{qs} - \omega_g\psi_{dr} - \dfrac{R_r}{L_r}\psi_{qr} \end{cases} \tag{23}$$

$$\frac{d\Omega_r}{dt} = -\frac{f}{j}\Omega_r - \frac{1}{j}(C_{em} - C_r) \tag{24}$$

$$\Omega_r = \frac{\omega_r}{p} \tag{25}$$

$$C_{em} = p\frac{M_{sr}}{L_r}(\psi_{dr}i_{qs} - \psi_{qr}i_{ds}) \tag{26}$$

Where:

V_{ds} , V_{qs} : d-axis and q-axis stator voltages;

i_{ds} , i_{qs} : d-axis and q-axis stator currents;

ψ_{dr} ,ψ_{qr} : d-axis and q-axis rotor flux linkages;

R_s , R_r : stator and rotor resistances;

L_s , L_r : stator and rotor inductances;

M_{sr} : mutual inductance

ω_s ,ω_r : electrical stator and rotor angular speed

ω_g : slip speed ωg=(ωs-ωr)

Ω_r : mechanical rotor angular speed

C_r , C_{em} : external load torque and motor torque

j , f : inertia constant and motor damping ratio

p : number of pole pairs

σ : leakage coefficient, ($\sigma = 1 - \frac{M_{sr}^2}{L_s L_r}$)

Equation (23) represents the dynamic of the motor mechanical side and (26) describes the electromagnetic torque provided on the rotor. The model of a three phase squirrel cage induction motor in the synchronous reference frame, whose axis d is aligned with the rotor flux vector, ($\psi_{dr}=\psi_r$ and $\psi_{qr}=0$), can be expressed as:

$$\frac{di_{ds}}{dt} = -\gamma i_{ds} + \omega_s i_{qs} + \frac{K}{T_r}\psi_{dr} + \frac{1}{\sigma L_s}V_{ds} \tag{27}$$

$$\frac{di_{qs}}{dt} = -\omega_s i_{ds} - \gamma i_{qs} - p\Omega K\psi_{dr} + \frac{1}{\sigma L_s}V_{ds} \tag{28}$$

$$\frac{d\psi_{dr}}{dt} = \frac{M_{sr}}{T_r} i_{ds} - \frac{1}{T_r}\psi_{dr} \tag{29}$$

$$\frac{d\dot{\psi}_{qr}}{dt} = \frac{M_{sr}}{T_r} i_{qs} - (\omega_s - p\Omega)\psi_{dr} \tag{30}$$

$$\frac{d\dot{\Omega}}{dt} = \frac{pM_{sr}}{JL_r}(\psi_{dr} i_{qs}) - \frac{C_r}{J} - f\,\Omega \tag{31}$$

With: $T_r = \frac{L_r}{R_r}$, $K = \frac{M_{sr}}{\sigma L_s L_r}$, $\gamma = \frac{R_s}{\sigma L_s} + \frac{R_r M_{sr}^2}{\sigma L_s L_r^2}$.

The bloc diagram of the proposed indirect field-oriented induction motor drive is shown in fig.6. Speed information, obtained by encoder feedback, enables computation of the torque reference using a PI controller. The reference flux is set constant in nominal speed. For higher speeds, rotor flux must be weakened.

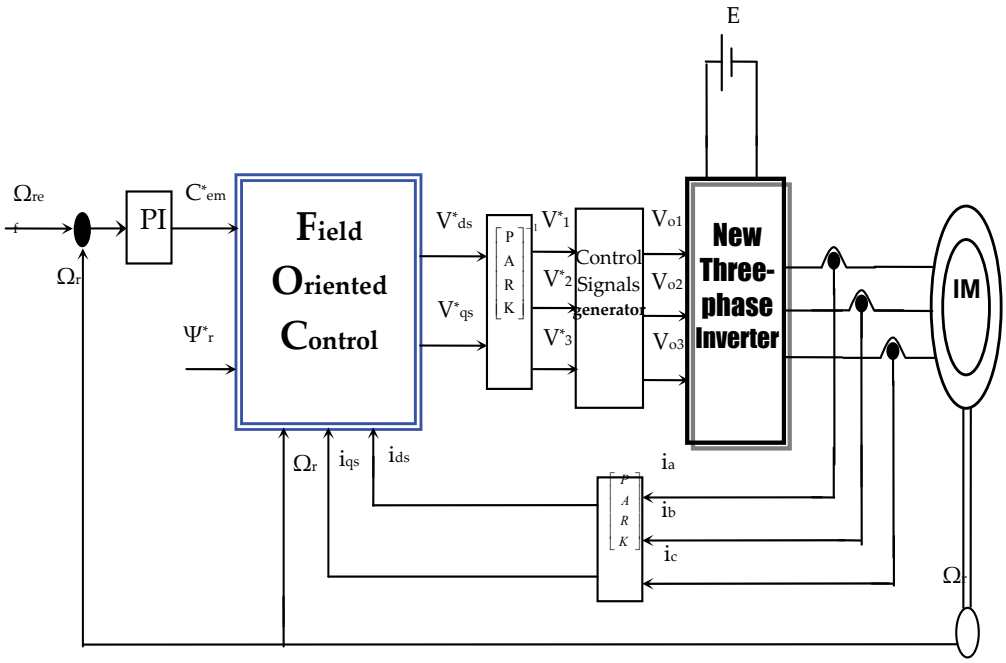

Figure 6. Block diagram of the proposed indirect field oriented induction motor drive system.

4. Simulation results

To demonstrate the performance of a new tree-phase inverter, we simulated three filtered inverter output voltages. Two frequency values are imposed on the inverter, starting with a frequency of 50 Hz, then at time t=0.06(s) the frequency is changed to 60Hz. The three filtered inverter output voltages are illustrated in (figure 7.a) which clearly shows that the three voltages are perfectly sinusoidal and follow the ideal values with a transient time of

0.012(s). The harmonic spectrum of the filtered output voltage is shown in (figure 7.b). In order to compare the performance of the new three-phase inverter with the conventional PWM inverter, the output voltage of the latter, where a modulation index of 35 was used, is shown in (figure 8.a) and its harmonic spectrum is presented in (figure 8.b).

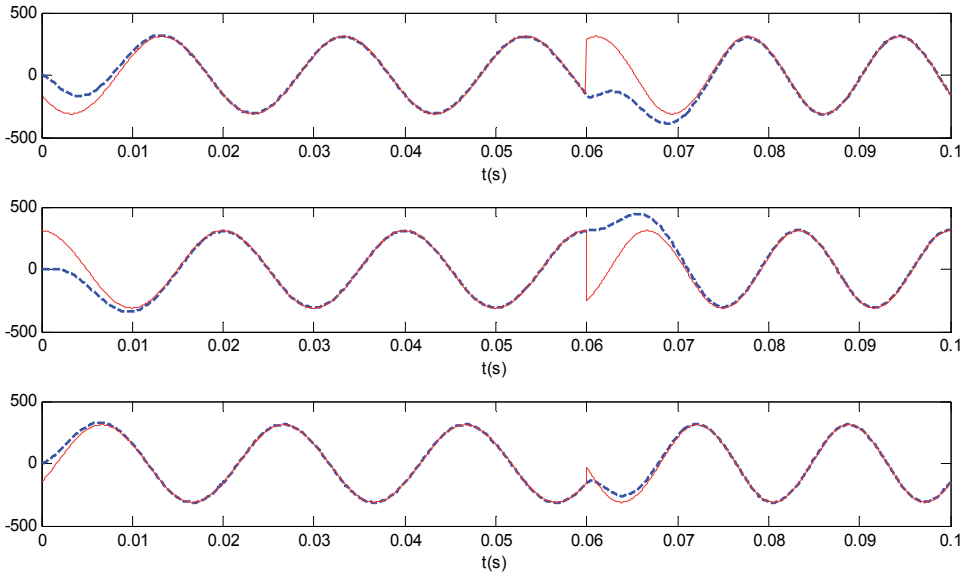

('---' filtered output voltage) ('—' ideal output voltage)

(a)

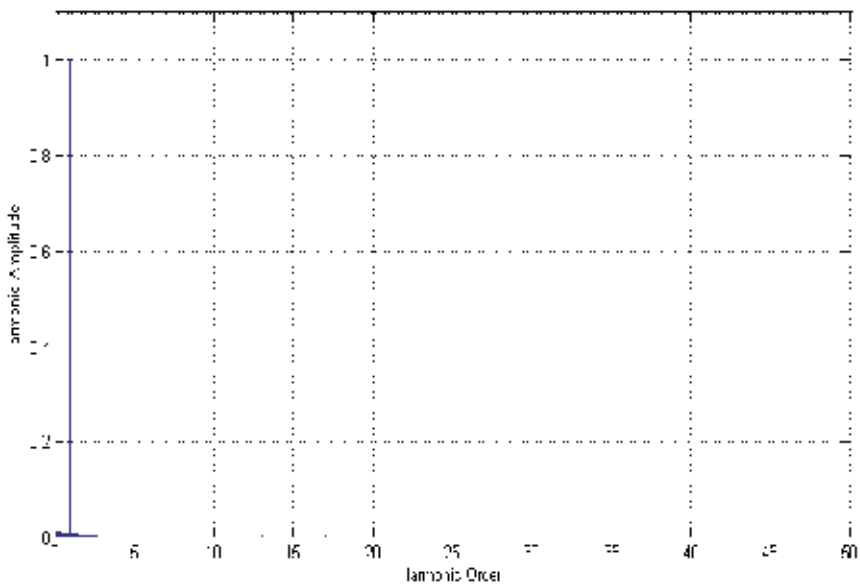

(b)

Figure 7. (a) Three filtered inverter outputs voltages.(b) Harmonic spectrum of the filtered output voltage.

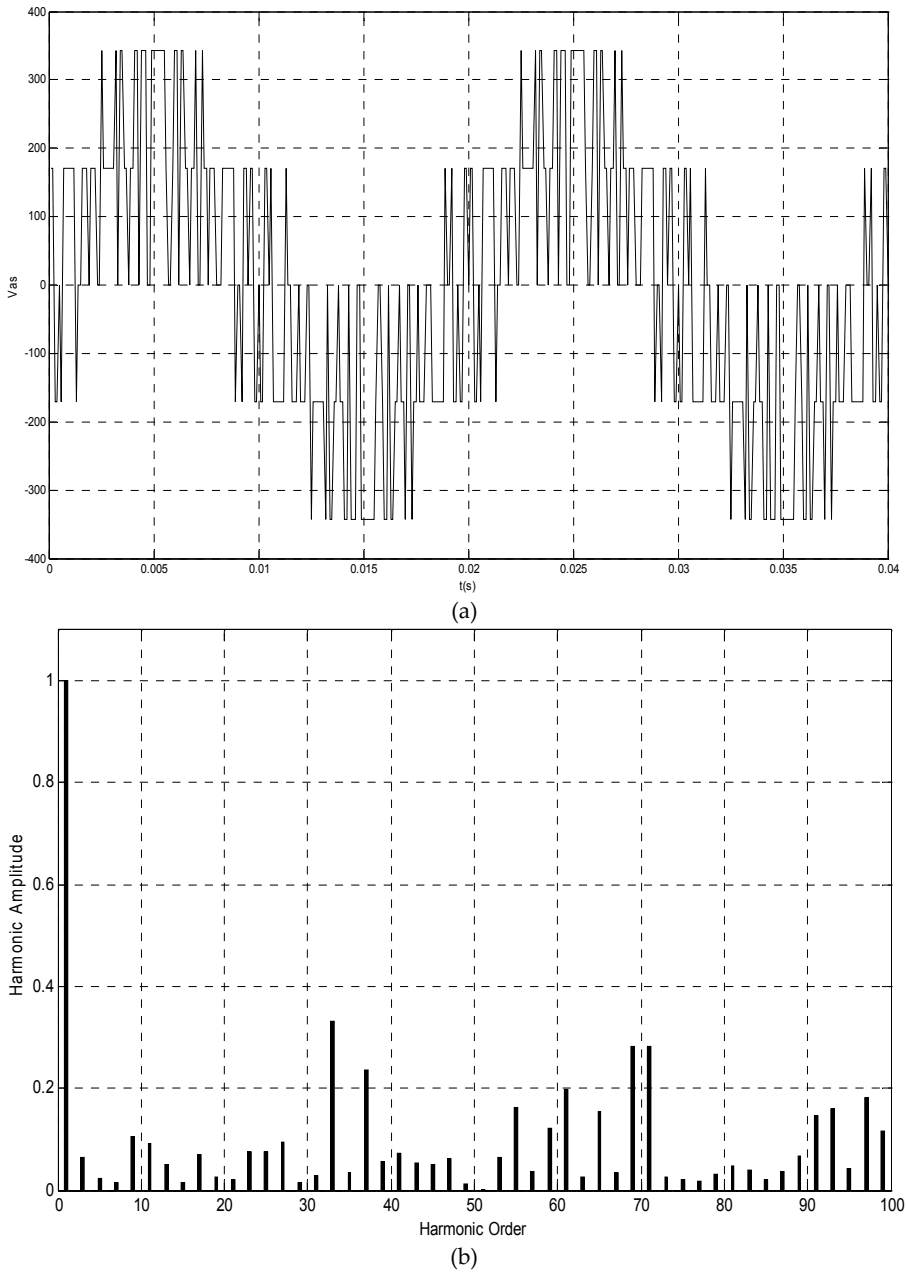

Figure 8. (a) PWM inverter output voltage (b) Harmonic spectrum of thePWM inverter output voltage.

We carried out two simulations of the field-oriented control for induction motor drives with speed regulation using the new structure of the three phase inverter in the first simulation (figure 9.a) and the conventional PWM (figure 9.b) inverter in the second simulation. The instruction speed is set to 100 (rad/sec) for both simulations. During the period between 1.3(s) and 2.3(s), a resistive torque equal to 10 (N.m) (i.e the nominal torque) is applied.

In order to illustrate the effectiveness of the proposed inverter, the torque response obtained by using the proposed and the conventional PWM inverters are shown in (figure 10.a) and (figure 10.b), respectively. The obtained results clearly show that the conventional PWM inverter generates more oscillations in the torque than the proposed structure (figure 11). Moreover, the switching frequency of the proposed inverter is dramatically reduced (see (figure 12.a)) when compared to its counterpart in the conventional PWM inverter (see figure 12.b). Therefore, the proposed inverter gives a better dynamic response than the conventional PWM inverter.

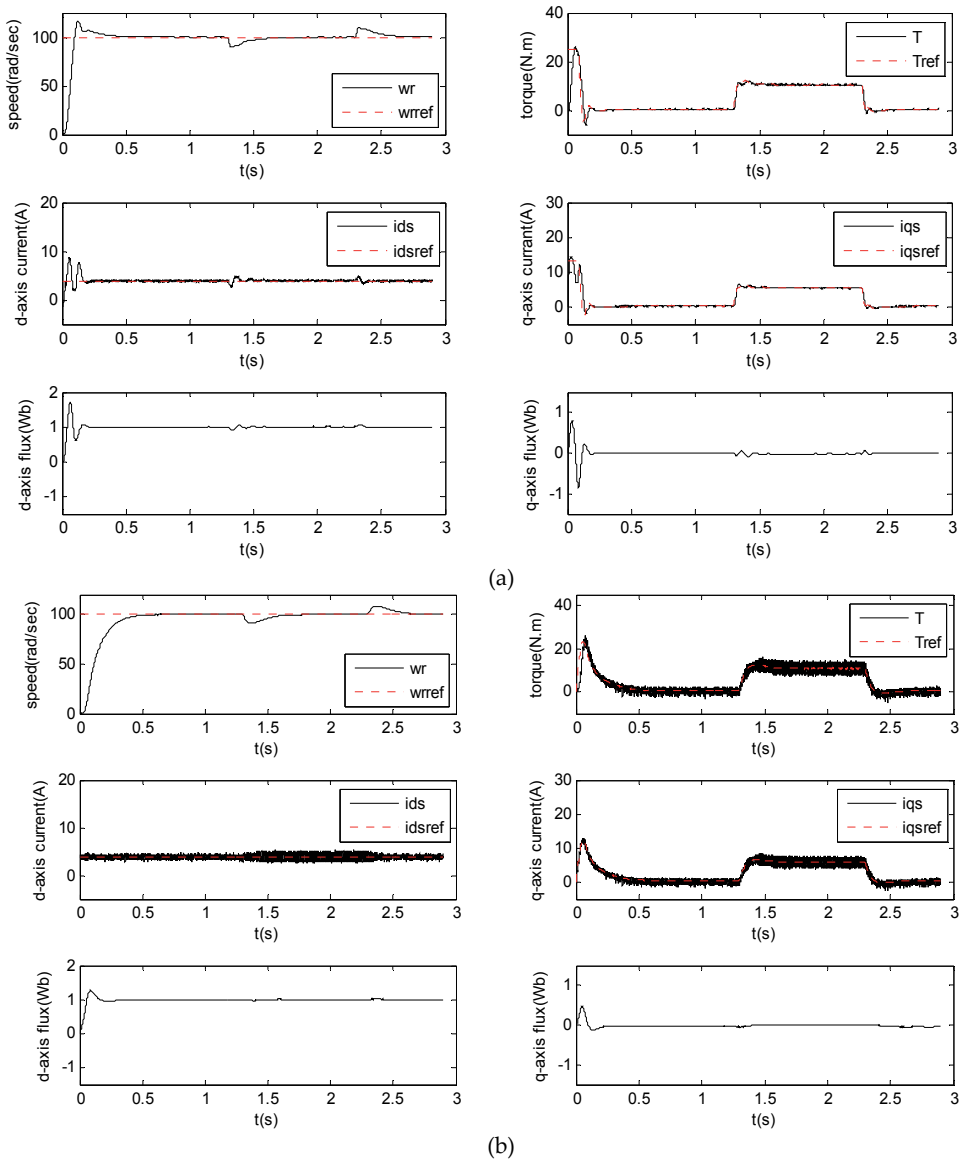

Figure 9. (a) Simulation results of the indirect field-oriented control for proposed inverters (b) Simulation results of the indirect field-oriented control for conventional PWM inverters

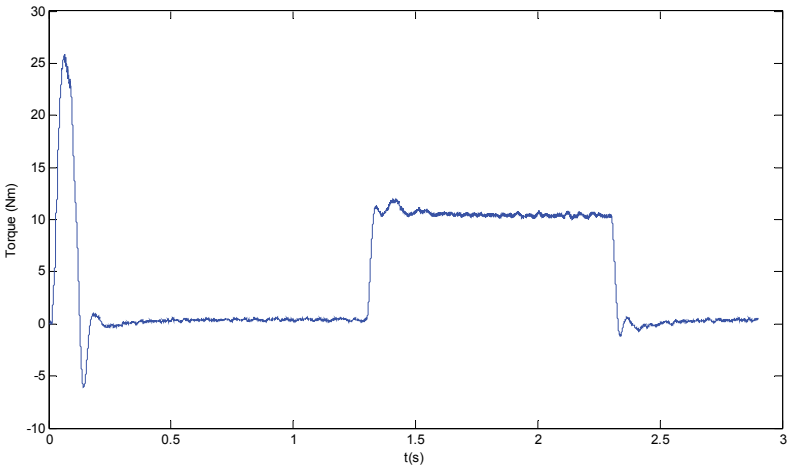

(a)

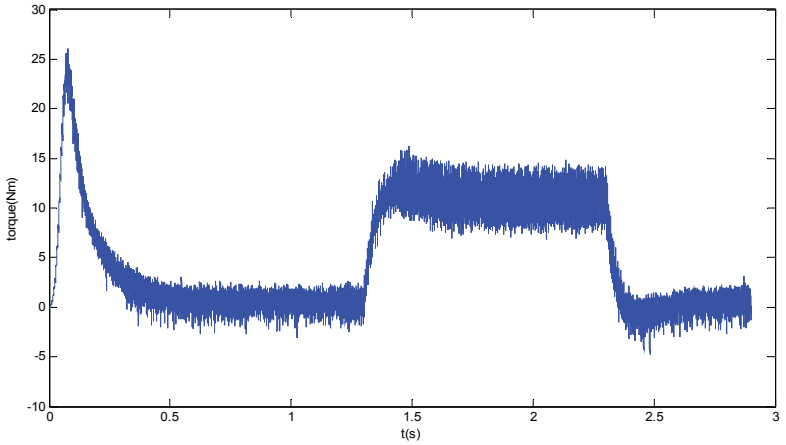

(b)

Figure 10. (a) Torque response for proposed inverters (b)Torque response for conventional PWM inverters

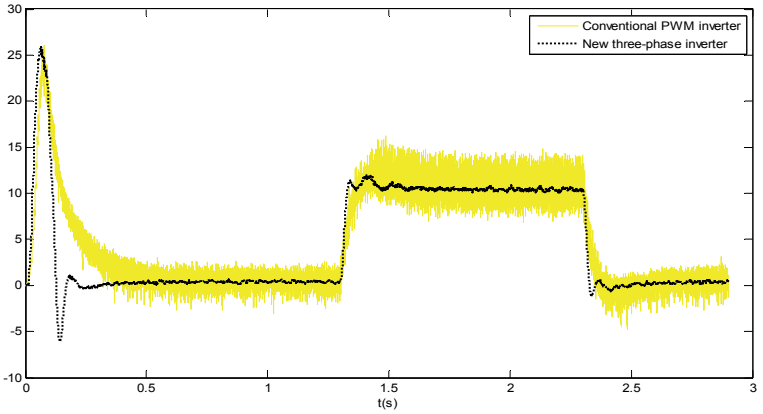

Figure 11. Torque response for proposed and conventional PWM inverters

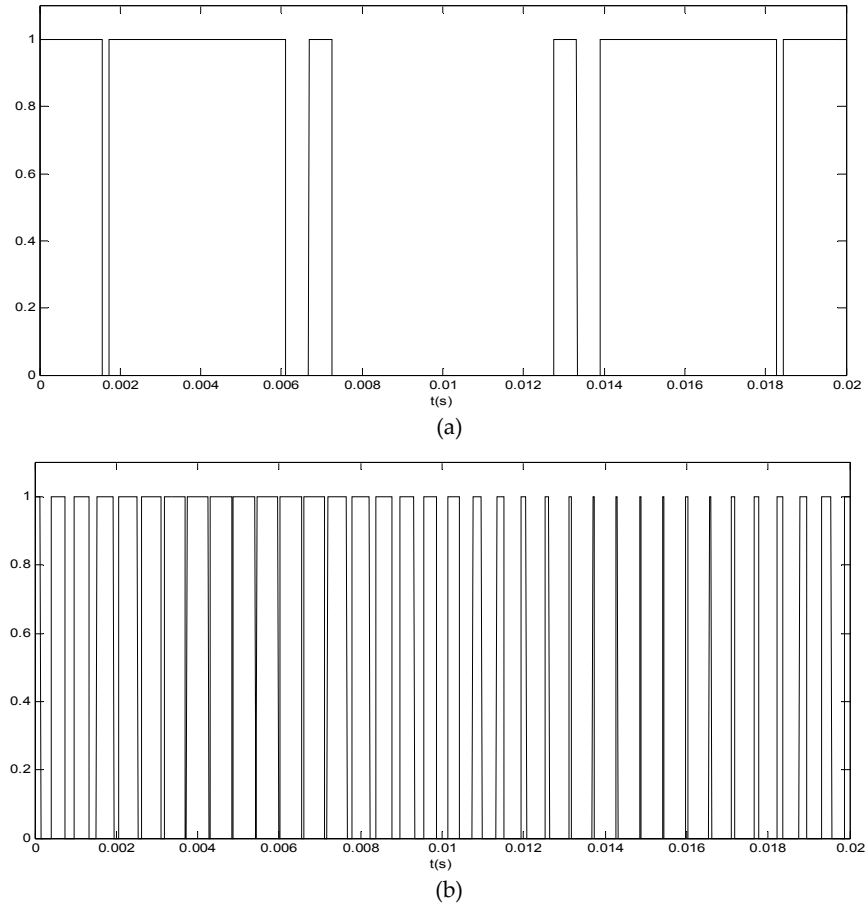

Figure 12. (a) Switching frequency for proposed inverters (b) Switching frequency for conventional PWM inverters

5. Experimental setup

The experimental setup was realized based on the DS1103 TMS320F240 dSPACE kit (dSPACE, 2006a, 2006b, 2006c, 2006d, 2006e). Figure 13 gives the global scheme of the experimental setup. This kit allows real time implementation of inverter and induction motor IM speed drive, it includes several functions such as Analog/Digital converters and digital signal filtering. In order to run the application the control algorithm must be written in C language. Then, we use the RTW and RTI packages to compile and load the algorithm on processor. To visualize and adjust the control parameters in real time we use the software control-desk which allows conducting the process by the computer.

The novel single phase inverter structure for pre-calculated switching is based on the use of IGBT (1000V/25A) with 10 kHz as switching frequency. The switching angles are predetermined off-line using Genetic Algorithms and stored in the card memory in order to speed up the programme running. The non-filtered inverter output voltages are first

designed in Simulink/Matlab, then, the Real-Time Workshop is used to automatically generate optimized C code for real time application. Afterward, the interface between Simulink/Matlab and the Digital Signal Processor (DSP) (DS1103 of dSPACE) allows the control algorithm to be run on the hardware.

The master bit I/O is used to generate the required 2 gate signals, and a several Analog-to-Digital converters (ADCs) are used for the sensed line-currents, capacitors voltage, and output voltage. An optical interface board is also designed in order to isolate the entire DSP master bit I/O and ADCs. The block diagram of the experimental plant is given in figure 14

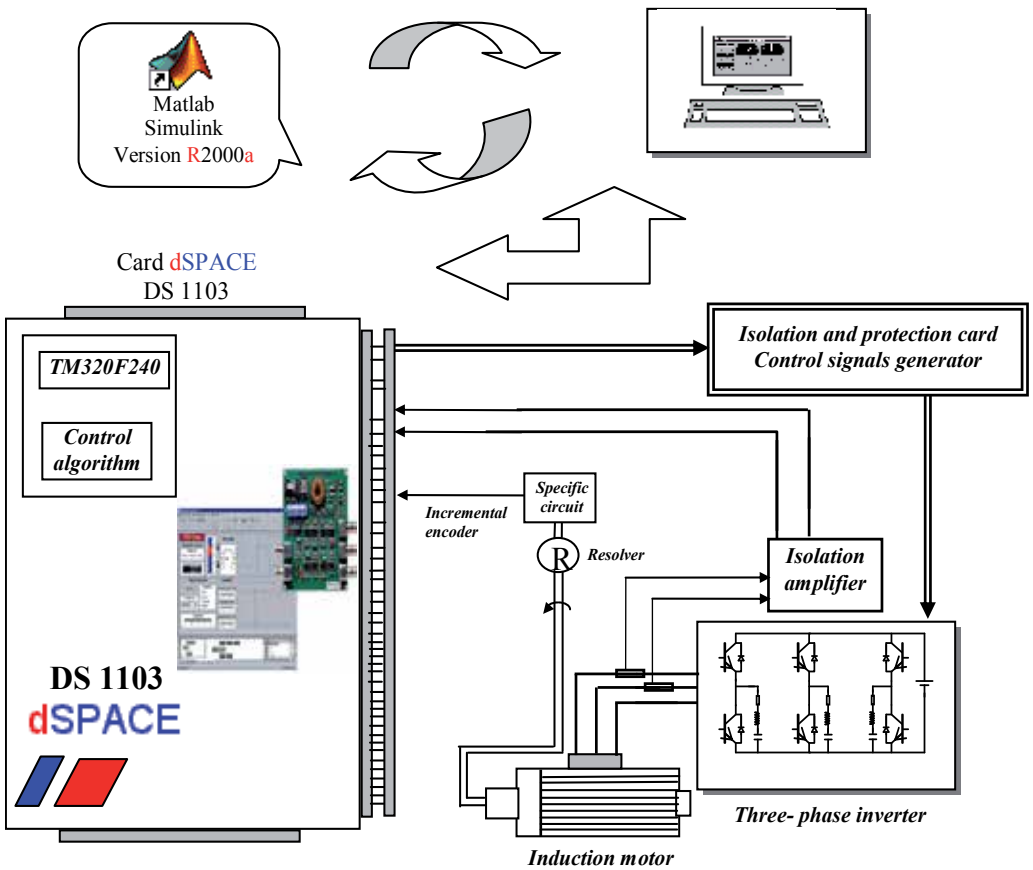

Figure 13. Global scheme of the experimental setup

6. Experimental evaluation

Figure 15 shows the experimental filtered inverter output voltage (V_{C1}-V_{C2}) for frequency value equal 50 Hz. The filtered inverter output voltage is perfectly sinusoidal. The experimental result in Figure 16 shows the torque response obtained by using the proposed PCPWM inverter: during the period between 0.65 sec and 1.95 sec, a load torque equal to 13 (N.m) is applied. The torque ripple of the induction motor is dramatically reduced.

Figure 14. Snapshot of the laboratory experimental setup

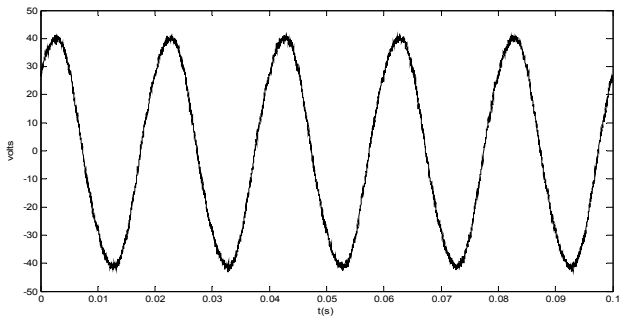

Figure 15. Experimental inverter filtered output voltage.

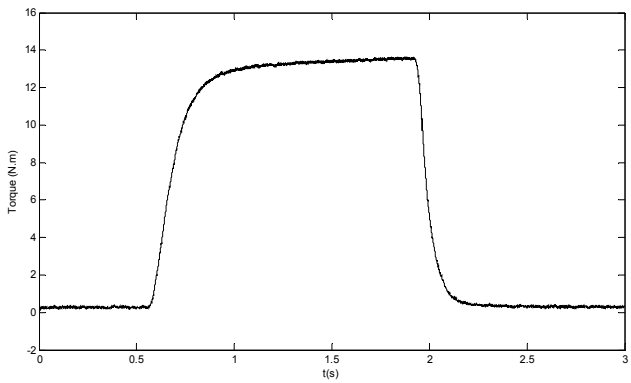

Figure 16. Experimental torque response for proposed PCPWM inverters

Moreover, as shown in Figure 17, the experimental switching frequency of the proposed PCPWM inverter is very less compared to the conventional PWM inverter one Figure 18. As a consequence, the proposed inverter provides higher dynamic response than the conventional PWM inverter in vector controlled induction motor applications.

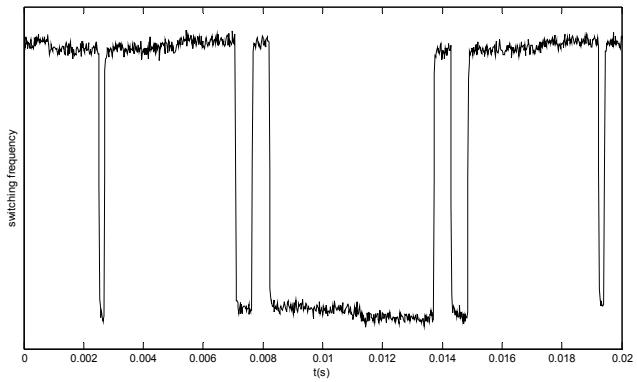

Figure 17. Experimental switching frequency for proposed PCPWM inverters

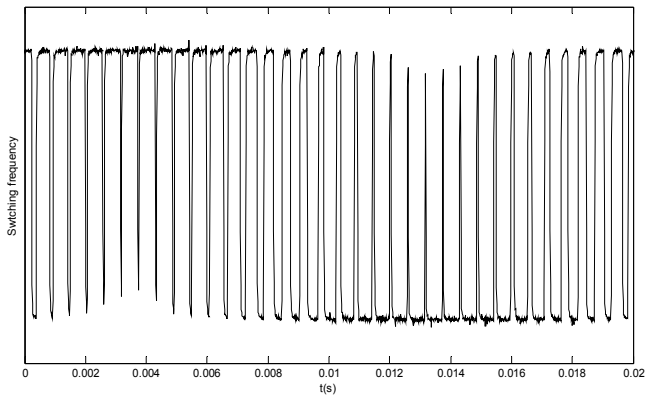

Figure 18. Experimental switching frequency for conventional PWM inverters

7. Conclusion

A three-phase inverter model was developed by combining pre-calculated switching angles and a passive filter to eliminate inverter output harmonics. The inverter model needs a nonlinear system of equations for the switching angles computation. The proposed inverter model succeeds to substantially reduce the harmonics while using polarized capacitors. The reduced number of switching angles provides more reliability and increases system components life time. Moreover, the proposed inverter design and control simplicity could be used as a cost effective solution to harmonics reduction problem. The torque ripple of the induction motor is dramatically reduced by the PCPWM inverter. The global scheme of the experimental setup has been implemented. The obtained experimental results exhibit good matching with the theoretical values. It is shown that the proposed PCPWM has better tracking performance as compared with the conventional PWM.

Author details

Ouahid Bouchhida
Université Docteur Yahia Farès de Médéa, Département Génie Electrique, Algérie

Mohamed Seghir Boucherit
Ecole Nationale Polytechnique, Département Génie Electrique, Algérie

Abederrezzek Cherifi
IUT Mantes-en-Yvelines, France

Appendix

The squirrel cage induction motor data are:

Symbol	Quantity	Value
P_n	Rated power	1.5 KW
V_n	Rated line voltage	220/380 V
C_n	Rated load torque	10 Nm
P	No. of pole pair	2
R_s	Stator resistance	5.62 Ω
R_r	Rotor resistance	4.37 Ω
M_{sr}	Mutual inductance	0.46 H
L_s	Stator leakage inductance	0.48 H
L_r	Rotor leakae inductance	0.48 H
I_n	Rated current	6.4/3.7 A
Ω_n	Motor speed	1480 tr/min
f	Viscosity coefficient	0.001136 N.m.s/rd
J	Moment of inertia	0.0049 kg.m²
C_1, C_2, C_3	Capacitance	10 mF
L	Inductance	0.5 mH
R	Internal inductor resistance	0.5Ω

8. References

Bäck, T. (1996). *Evolutionary Algorithms in Theory and Practice*, Oxford University Press, 1996

Bouchhida, O.; Cherifi, A. & Boucherit, M.S. (2007). Novel harmonic elimination PWM Technique for reducing Torque–Ripple in Inverter-fed Induction motor. *Archives of Electrical Engineering (AEE)*, Vol. 56, No.3-4, (Mar. 2007), 197-212.

Bouchhida, O.; Benmansour, K.; Cherifi, A. & Boucherit, M.S. (2008). Low switching-frequency and novel harmonic elimination for three-phase inverter', *Proceedings of the Fifth International Multi-Conference on Systems, Signals and Devices SSD08, IEEE*, Philadelphia University Amman Jordan, July 2008.

Bouchhida, O. (2008). *Contribution à l'Optimisation de Structure des Convertisseurs pour la Commande des Machines Asynchrones: Réalisation expérimentale*. thèse de Doctorat, Ecole Nationale polytechnique ENP d'Alger, Algérie

Bouchhida, O. (2011). *Etude et Optimisation des Performances d'Onduleur Monophasé et Triphasé à Commutation Pré-Calculée*. Habilitation Universitaire, Université Saad D'hleb Blida, Algérie

Czarkowski, D.; Chudnovsky, D.; Chudnovsky, G. & Selesnick, I. (2002). Solving the optimal PWM problem for Single-phase inverters. *IEEE Transactions Circuits Syst*. I, Vol. 49, (April 2002), 465-475

Davis, L. (1991). *The Handbook of Genetic Algorithms*, Van Nostrand & Reinhold, 1991

dSPACE (2006a). *DS1103 PPC Controller Board, Feature, Realise 5.1*, dSPACE digital signal processing and control engineering, Germany

dSPACE (2006b). *How to implement user-specific functions on the DS1103 slave DSP (TMS320F240).* dSPACE digital signal processing and control engineering GmbH, Germany

dSPACE (2006c). *DS1103 PPC Controller Board, Hardware Installation and Configuration, Realise 5.1*, dSPACE digital signal processing and control engineering, Germany

dSPACE (2006d). *DS1103 PPC Controller Board RTI Reference, Realise 5.1*, dSPACE digital signal processing and control engineering, Germany

dSPACE (2006e). *DS1103 PPC Controller Board RTLib Reference, Realise 5.1*, dSPACE digital signal processing and control engineering, Germany

García, O.; Martínez-Avial, M.D.; Cobos, A.; Uceda, J.; González, J. & Navas, A. (2003). Harmonic reducer converter. *IEEE Transactions on Industrial Electronics*, Vol. 50, No. 2, (April 2003), 322–327

Jung, J. & Nam, K. (1999). A dynamic decoupling control scheme for high speed operation of induction motors. *IEEE Transaction on Industrial Electronics, V*ol.46, No. 1, (Feb 1999), 100–110.

Lin, F.J.; Wai, R.J.; Lin, C.H.; & Liu, D.C. (2000). Decoupling stator-flux oriented induction motor drive with fuzzy neural network uncertainly observer. *IEEE Transaction on Industrial Electronics*, Vol.47, No.2, (Apr 2000), 356–367.

Meghriche, K.; Chikhi, F. & Cherifi, A. (2004). A new switching angle determination method for three leg inverter, *Proceedings of International IEEE Mechatronics and Robotics MechRob-2004*, 378–382, Aachen, Germany, September 2004

Meghriche, K.; Mansouri, O. & Cherifi, A. (2005). On the use of pre-calculated switching angles to design a new single phase static PFC inverter, *Proceedings of the 31st IEEE IECON'05*, 906–911, Raleigh North-Carolina, November 2005.

Suwankawin, S. ; & Sangwongwanich, S. (2002). A speed sensorless IM drive with decoupling control and stability analysis of speed estimation. *IEEE Transaction on Industrial Electronics*, Vol. 49, No. 2, (Apr 2002), 444–455.

Villarreal-Ortiz, R.A.; Hernández-Angeles, M.; Fuerte-Esquivel, C.R. & Villanueva-Chávez, R.O. (2005). Centroid PWM technique for inverter harmonics elimination. *IEEE Transactions on Industrial Electronics*, Vol. 20, No. 2, (April 2005), 1209–1210

Wells, J.R.; Nee, B.M.; Chapman, P.L. & Krein, P.T. (2004). Optimal Harmonic elimination control, *Proceedings of the 35th Annual IEEE Power Electronics Specialists Conference*, 4214-4219, Aachen, Germany, 2004.

Chapter 20

Predictive Maintenance by Electrical Signature Analysis to Induction Motors

Erik Leandro Bonaldi, Levy Ely de Lacerda de Oliveira,
Jonas Guedes Borges da Silva, Germano Lambert-Torresm
and Luiz Eduardo Borges da Silva

Additional information is available at the end of the chapter

http://dx.doi.org/10.5772/48045

1. Introduction

Industries always try to increase the reliability of their productive process. In this context, predictive maintenance performs a fundamental role in order to reach high availability and reliability concerning their pieces of equipment. Predictive maintenance can be understood as the action on the equipment, system or installations based on the previous knowledge about the operation condition or performance, obtained by means of parameters previously determined (Bonaldi et al, 2007).

Since the induction motors are the center of the vast majority of the industrial processes, this chapter gives total emphasis to the failure analysis and identification of this kind of electrical machine. Like all the rotating machines, the induction motors are exposed to many different adversities such as thermal and environmental stresses and mechanical damages, which demand maximum attention (Lambert-Torres et al., 2003). Usually, in industries, attention must be even larger since the downtime costs are very high. High and medium voltage induction motors are highly used in industrial processes. Many of them are strategic to the productive process and, because of that, looking for solutions that minimize the failure statistics is mandatory. In most cases, these motors are highly reliable and extremely expensive, forcing the company to operate without a stand-by.

Many predictive techniques are applied to these motors to reduce the number of unplanned outage. The most common techniques applied to fault detection in induction motors are: vibration analysis, acoustical analysis, speed oscillations, partial discharges, circuit analysis, etc. The analyses based on mechanical concepts are established, but the techniques based on electrical signature analysis are being introduced only now. Because of that status, the application of Electrical Signature Analysis (ESA) to industries is the concern of this chapter.

The industries currently look for products and outside services for predictive maintenance. In many cases, the outside service company or even the industrial plant predictive group make mistakes that can compromise the whole condition monitoring and failure diagnosis process.

In this increasing demand for prediction technology, a specific technique referred as Electrical Signature Analysis (ESA) is calling more and more attention of industries. Considering this context, this chapter intends to disseminate important concepts to guide companies that have their own predictive group or want to hire consultants or specialized service to obtain good results through general predictive maintenance practices and, especially through electrical signature analysis.

Figure 1 presents the comparative between vibration analysis and ESA (considering Motor Current Signature Analysis (MCSA), Extended Park's Vector Approach (EPVA) and Instantaneous Power Signature Analysis (IPSA)), showing which technique is more recommended to a specific kind of problem in a determined part of the rotating drive train. One can say that those techniques are complementary.

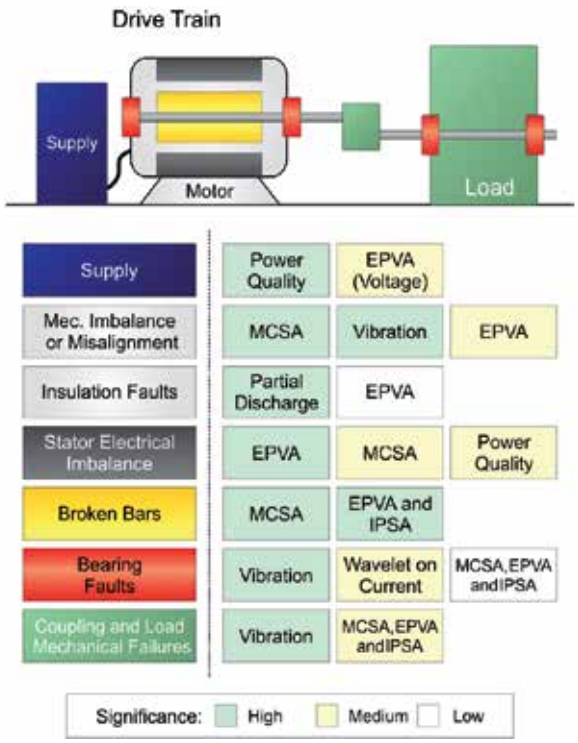

Figure 1. Comparison of predictive maintenance techniques

The main objective of this chapter is to present a procedure to acquire and analyze electrical signals for condition monitoring of electrical machines through motor current signature analysis in order to get the best possible results in an industrial environment. As secondary

contributions, the chapter intends to disseminate important concepts to guide companies that have their own predictive group or want to hire consultants or specialized service to obtain good results through general predictive maintenance practices and, especially through electrical signature analysis. For this purpose, the chapter presents a discussion between condition monitoring and troubleshooting, pointing the differences between both approaches and the main benefits and problems involved with each one.

The result of the proposed discussion in this chapter is a procedure of acquisition and analysis, which is presented at the end of the chapter and intends to be a reference to be used by industries that have a plan to have ESA as a monitoring condition tool for electrical machines.

2. Considerations about maintenance

The motors are the center of the majority of the industrial production processes. Therefore, these machines deserve concerns to increase the reliability of the productive process. In this sense, many techniques have been developed for an on-line motor monitoring of the behavior and performance.

Monitoring condition of electric machines is an evaluation continuous process of the health of equipment during all its useful life. The main function of a monitoring predictive system is to recognize the development of failures in an initial state. For the maintenance department, each failure must be detected as soon as possible in order to promote a programmed stop of the machine.

The process of continuous monitoring of the condition of vital electric machines for the production process brings significant benefits for the company. The main benefits are: bigger efficiency of the productive process, reduction of the losses for not-programmed stops, increase of the useful life of the equipment, and build a historical of failure (Legowski et al., 1996; Tavner et al., 1997; Thomson & Fenger, 2001).

A continuous monitoring system must observe parameters that give to the maintenance team trustworthy information for the decision-making. The more usual monitored parameters are: voltage and current of the stator; temperature of the nucleus; level of vibration; instantaneous power; level of contamination in the lubricant of the rolling; speed of rotation; flow of escape; and so on.

In such a way, it can be noticed that this area of the technology demands knowledge of the functioning of electric machines, instrumentation, microprocessors, processing of signal, analysis of materials, chemical analysis, analysis of vibrations, etc.

2.1. Classification of the maintenance activities

"Maintenance" can be understood as the action to repair or to execute services in equipment and systems. It can have its activities classified in four main groups:

a. Corrective maintenance: this is the most primary form of maintenance. It occurs after a failure carried out. Usually, it becomes the unavailable equipment for use. Many disadvantages of this type of maintenance are clear. As examples, the systematic occurrence of not-programmed stops, lesser time of useful life for the machine, bigger consumption of energy (since with the presence of the failure the motor needs more current keeping the constant torque) can be cited.
b. Preventive maintenance: this is the name that receives a set of actions developed with the intention of preventing the occurrence of unsatisfactory conditions, and consequently, reducing the number of corrective actions. When preventive maintenance plan is elaborated, a set of technical measurements must be created in order to increase the machine reliability and decrease the total cost of the maintenance. A preventive maintenance program can still choose for one of the three types of activities: continuous monitoring; periodic measurements; or predictive techniques.
c. Predictive maintenance: as it can see previously, the predictive maintenance can be a sub-area of the preventive maintenance. However, the predictive maintenance presents some proper characteristics as:

- Support in not invasive techniques, that is, it is not necessary to stop the operation of the machine for its application
- Elimination of corrective maintenance;
- Not consideration of information as the durability of components;
- On-line or off-line can be effected through techniques.

d. Systematic maintenance: characterized for the substitution of components of the equipment or for the substitution of the equipment as a whole (Bonaldi et al., 2007).

2.2. Status of predictive maintenance

Usually, industries have the vast majority of their condition monitoring programs based on the mechanical parameters analysis. The most common methods applied are: Vibration Analysis, Acoustical Analysis, Shock Pulse and Speed Fluctuations. Other techniques involving mechanical concepts are also applied such as temperature monitoring, oil and gases analysis, etc.

When involving electrical concepts, intrusive methods are more common used in industries such as surge test, polarization index, hipot tester, motor circuit analysis (MCA), etc. These techniques are more correctly classified as preventive maintenance, being performed at planned outages.

Concerning motor condition monitoring through non-intrusive electrical methods in Brazil, one can observe more often the RMS voltage and current monitoring. For example, broken bars produce current oscillations that can be observed through an ampere-meter installed in the electric panel. But, again, it is not possible to separate load oscillations from broken bars.

This way, a more reliable program to detect electrical and mechanical problems must consider the introduction of new condition monitoring tools, mainly those related to electrical signature that has been neglected until now. Since the petrochemical industry constantly aims to increase the process reliability and operational continuity, a very

interesting and little explored field surfaces, which is the introduction of predictive maintenance techniques based on electrical signature analysis.

3. Common failures in three-phase induction motors

Consider the following brief description of the most common failures that can be avoided through the adoption of condition monitoring methods:

a. Bearings Faults: can be caused by incorrect lubrication, mechanical stresses, incorrect assembling, misalignment, etc. They can affect all the bearing parts such as inner and outer races, cage and balls or rolls.
b. Stator Winding Faults: normally a consequence of overheating, contamination, project errors, etc., possibly causing shorted turns, shorted coils (same phase), phase to phase, phase or coil to ground and single phasing. Such failures cause stator electrical imbalance as well as variations in the current harmonic content. Mechanical problems can also occur in the stator such as loosen edges, but this is statistically less frequent.
c. Rotor Faults: usually caused by broken bars or broke end rings, rotor misalignment and imbalance.

Faults in the coupling (pulley, belt and gear mesh) and in the attached load also can be diagnosed. The failures are also related to the petrochemical process different characteristics. For example, at off-shore plants, the motors start directly from the mains. This demands high start currents and causes pulsating torques which contributes to the origin of rotor and stator faults. Furthermore, outdoors motors present more incidence of failure than indoor motors. The same statistic holds for high voltage motors and high speed motors when compared with low voltage motors and low speed motors.

3.1. Abnormalities in three-phase induction motors

The main focus of problems in three-phase induction motors are in the stator and the supports. The main causes of failures are: superheating, imperfections in the isolation, mechanical bearings and electric failures. Figure 2a presents a division of the failures in three-phase induction motors with squirrel steamer and power of 100 HP or higher (Bonnett & Soukup, 1992).

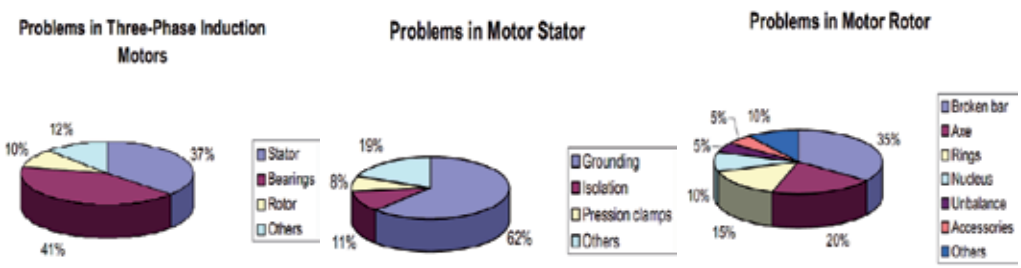

(a) (b) (c)

Figure 2. Problems in: (a) Three-Phase Induction Motors, (b) Motor Stator, and (c) Motor Rotor.

In one hand, the main source of electrical problems in induction motor is in stator that totalizes 37% of the total of failures. Figure 2b details different type of problems in the motor stators. In the other hand, problems in the motor rotor totalize 10% of the total of motor failures, and they are shown in Figure 2c.

3.2. Relation between motor specification and failure mechanism

Many failures can be deriving of incorrect specifications. The specification of a motor must consider the mechanical and electric conditions, and the environment in which the machine goes to work. The monitored parameters are affected by these operational conditions. In terms of the mechanical conditions, the failures appear as resulted of the behavior of the load. Amongst the main problems they are distinguished:

- Successive overloads that can cause superheating and/or damages to the bearing;
- Pulsing load that can cause damages to the bearing;
- Repeated departures that can damage the machine bearing;
- Vibration that can be transmitted to the machine causing damages to the bearing.

In terms of the electric conditions, the failures can result of the electrical power system characteristics or the load feeder by the motor. Amongst the main problems they are distinguished:

- Slow fluctuations of voltage being able to cause loss of stop power and of the machine.
- Brusque fluctuations of voltage being able to cause failure in the isolation.

In terms of the environment conditions, the failures can result of the characteristics of the process in which the machine is being used. Amongst the main problems they are distinguished:

- High temperatures that can cause the deterioration of isolation.
- Humidity and pollution that can respectively cause imperfections and contamination of the isolation.

Thus, it is clear that the failures that occur in electric machines depend on the type of machine and the environment where it is working. What it is really important to observe it is that the failure mechanism happens in gradual way, from an initial defect up to real failure. The time of propagation of the failure depends on some factors. However, the major parts of the failures present initial pointers of its presences and are exactly in these initial indications that the predictive maintenance must act (Bonaldi et al., 2003).

4. Electrical signature analysis overview

Electrical Signature Analysis (ESA) is the general term for a set of electrical machine condition monitoring techniques through the analysis of electrical signals such as current and voltage. These techniques are: Current Signature Analysis (CSA), Voltage Signature Analysis (VSA), Extended Park's Vector Approach (EPVA), Instantaneous Power Signature

Analysis (IPSA), among others. The electrical motor of the rotating system under analysis is analyzed for the failure diagnosis purposes, acting as a transducer in this process. Variations in the voltage and current signals are analyzed in relation to some failure patterns.

The industrial application of ESA techniques aims to improve the equipment reliability once those techniques imply greater robustness to the diagnosis. The expected results are: downtime reduction, increase in the machine availability, maintenance costs reduction, better management and planning of maintenance, etc.

The inherent benefits in ESA are: non-intrusive; it does not demand sensors installed in the rotating drive train; it is not necessary to be suited for classified areas (the sensors can be installed in the motor control centre (MCC) free of explosive mixtures); it presents high capability of remote monitoring, reducing the human exposure to risks; it can be applied to any induction motor without power restriction; it presents sensitivity to detect mechanical failures in the motor and load, electrical failures in the stator and problems in the mains, etc.

For these reasons, one recommends the application of these techniques (together with the mechanical approaches) in order to prevent catastrophic failures; improve the safety and the reliability of the productive process; reduce the downtime, improve the condition monitoring of motors installed in places of difficult access and improve the motor management in the maintenance context for reliability purposes.

Among the several ESA techniques, two of them are considered in this chapter: MCSA and EPVA.

The stator line current spectral analysis has been widely used recently for the purpose of diagnosing problems in induction machines. This technique is known as Motor Current Signature Analysis (MCSA) and the current signal can be easily acquired from one phase of the motor supply without interruption of the machine operation. In MCSA the current signal is processed in order to obtain the frequency spectrum usually referred to as current signature. By means of the motor signature, one can identify the magnitude and frequency of each individual component that constitutes the signal of the motor. This characteristic permits identifying patterns in the signature in order to differentiate healthy motors from unhealthy ones and point where the failures happen. Although it is important to say that the diagnosis is something extremely complicated, e.g., the decision of stopping or not the productive process based on the current spectrum indications is always not elementary and demands experience and knowledge of the process.

4.1. Current and voltage signature analysis

CSA – Current Signature Analysis or VSA – Voltage Signature Analysis techniques are used to generate analyses and trend of electric machines dynamically. They aim to detect predictive problems in a rotating electric machine, such as: problems in the stator winding, rotor problems, problems on the engagement, problems in bound load, efficiency and system load; problems in the bearing, among others. It may initially cause a certain

astonishment that the electrical signals contain information in addition to the electrical characteristics of the machine under supervision, but they work for mechanical defects as a transducer, allowing the electrical signals (voltage and/or current) can carry information of electrical and mechanical problems until the power panel of the machine.

The signs of current and/or voltage of one or three phases of the machine produce, after analyzed, the *signature of machine*, i.e., its operating pattern. This signature is composed of magnitudes of frequencies of each individual component extracted from their signals of current or voltage. This isolated fact itself is an advantage, as it allows the monitoring of the evolution of the magnitudes of the frequencies, which can denote some sort of evolution of operating conditions of the machinery. The response that the user of such a system needs to know is whether your machine is "healthy" or not, and that part of the machine the failure might occur.

This analysis (diagnosis) is not something easy to be done, because it involves a set of comparisons with previously stored patterns and own "history" of the machine under analysis. In this instant, normally a specialist is called to produce the final diagnosis, generating the command when stopping the machine.

4.2. Motor Current Signature Analysis (MCSA)

MCSA is the technique used to analyze and monitor the trend of dynamic energized systems. The appropriate analysis of the results of applying predictive technique helps in identifying problems in stator winding, rotor problems, problems in the coupling, problems in attached load, efficiency and system load, problems in the bearing, among others.

This technique uses the induction motor as a transducer, allowing the user to evaluate the electrical and mechanical condition from the panel and consists primarily in monitoring of one of the three phases of the supply current of the motor. A simple and sufficient system for the implementation of the technique is presented in the Figure 3a.

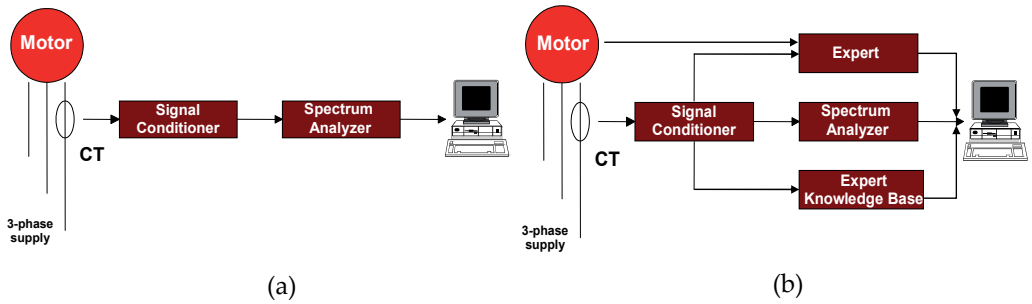

Figure 3. Basic System for Spectral Analysis of the Current

Thus, the current signal of one of the phases of the motor is analyzed to produce the power spectrum, usually referred to as motor signature. The goal is to get this signature to identify the magnitude and frequency of each individual component that integrates the motor

current signal. This allows that patterns in current signature be identified to differentiate "healthy" motors from “unhealthy” ones and even detect in which part of machine failure should occur.

However, it is important to note that the diagnosis is something extremely complicated, i.e. the definition of stopping or not the production process in view of the indications of the power spectrum is always difficult and requires experience and knowledge of the process. This time, it is important to consider the expert knowledge and the data history of the behavior of the set (motor, transmission system and load). For this reason, an automatic diagnostic system that combines the data history of the motor to the attention of specialist is a niche market quite promising. This way, the automatic diagnosis and analysis system is no longer as simple as the model shown in Figure 3a and can be represented by the new elements in Figure 3b.

The Fast Fourier Transform (FFT) is the main tool employed, however some systems employ in conjunction with other techniques to increase the ability of fault detection since signal acquisition, through processing, up to the diagnostic step. Among the most important issues related to acquisition of signals and the FFT include:

a. **Frequency range:** the frequency response is typically required in MCSA 5 kHz. This way, the bandwith of the transducers used must be at least 10 kHz.
b. **Nyquist theorem:** this theorem states that for any signal to be reconstructed without significant losses must be removed samples with twice the maximum frequency of the signal. In practice it uses 10 times the maximum frequency and ensures excellent accuracy.
c. **Resolution:** spectral lines resolution, i.e. the distance between two spectral is given by (1):

$$\Delta f = \frac{f_s}{N} \tag{1}$$

Where Δf is the spectral resolution, f_s is the sampling frequency used, and N is the number of samples.

Other important issues are related to the own operation of induction motors. The first one is the induction motor synchronous speed that is given by (2):

$$N_S = \frac{f_1}{p} \tag{2}$$

Where f_1 represents the power frequency, N_s is the velocity of the rotating field, and p is the number of motor pole pairs.

From the synchronous speed, two important concepts for the current signature analysis can be presented: the slip speed and the slip. In MCSA is important to note that the rotor speed is always less than the synchronous speed. The frequency of the induced currents in the rotor is a function of frequency and power slip. When operating without load, the rotor rotates at a speed close to the synchronous speed. In this case, torque should be just

sufficient to overcome friction and ventilation. The difference between the rotor speed (*Nr*) and the synchronous speed (*Ns*) is named as slip speed (N_{Slip}):

$$N_{Slip} = N_s - N_r \tag{3}$$

When mechanical load is attached to the rotor demanding torque the rotor speed decreases. In this turn, the slip speed increases and also the current in the rotor to provide more torque. As the load increases, the rotor continues having reduced its speed relative to synchronous speed. This phenomenon is known as motor slip, denoted by *s*.

$$s = \frac{\left(N_s - N_r\right)}{N_s} \tag{4}$$

Another important definition refers to slip frequency. The frequency induced in the rotor is correctly set to slip frequency and is given by:

$$f_2 = \left(N_s - N_r\right) \cdot p \tag{5}$$

As noted, the rotor frequency is directly proportional to the slip speed and the number of pair of poles. Thus:

$$s \cdot N_S = N_S - N_r \text{ and } p \cdot N_S = f_1 \text{ then } f_2 = s \cdot f_1 \tag{6}$$

This is a very important result for MCSA once the current frequency is rotor slip function. The characteristic frequencies are well known. The patterns of these failures are presented below.

The stator line current spectral analysis has been widely used recently for the purpose of diagnosing problems in induction machine. This technique is known as MCSA and the current signal can be easily acquired from one phase of the motor supply without interruption of the machine operation. In MCSA the current signal is processed in order to obtain the frequency spectrum usually referred to current signature. By means of the motor signature, one can identify the magnitude and frequency of each individual component that constitutes the signal of the motor. This characteristic allows identifying patterns in the signature in order to differentiate healthy motors from unhealthy ones. Mechanical failures such as rotor imbalance, shaft misalignment, broken bars and bearing problems are common in induction machines applications and commonly discussed or presented when talking about MCSA. Another very important cause of poor functioning of induction motor is load mechanical failure. When a mechanical failure is present either in the motor, or in the transmission system or in the attached load, the frequency spectrum of the line current, in other words, the motor signature, becomes different from that of a non-faulted machine.

When a mechanical failure occurs in the attached load of an induction motor, multiples rotational frequencies appear in the stator current due to the load torque oscillation (Benbouzid, 2000). These frequencies are related to the constructive characteristics of the load and the transmission system, and an abnormal value of a given frequency expresses a

specific failure, and more, the severity of this failure. The frequency component that appears in the stator current spectrum can be expressed by:

$$f_{lf} = f_1 \pm \kappa f_r \tag{7}$$

Where f_{lf} is the characteristic frequency of the load fault, f_1 is the supply frequency, κ is the constant resulting from the drive train constructive characteristics and f_r is the motor rotational frequency.

It is known that when a mechanical failure has developed in the load, it generates an additional torque (T_{1f}). Thus, the overall load torque (T_{load}) can be represented by an invariable component (T_{const}) plus this additional variable component which varies periodically at a characteristic frequency ω_{lf} in (8)

$$T_{load}(t) = T_{const} + T_{lf}\cos(\omega_{lf}t) \tag{8}$$

Where T_{lf} is the amplitude of the load torque oscillation caused by the load mechanical failure and $\omega_{lf} = 2\pi f_{lft}$. Also, the torque relates to the rotational frequency (ω_r) can be expressed by:

$$T(t) = T_{motor}(t) - T_{load}(t) = J\frac{d\omega_r(t)}{dt} \tag{9}$$

Where J is the total inertia of machine and load. Thus:

$$J\frac{d\omega_r(t)}{dt} = T_{motor}(t) - T_{const} - T_{lf}\cos\left(\omega_{lf}t\right) \tag{10}$$

In steady state, $T_{motor} = T_{const}$ and:

$$\frac{d\omega_r(t)}{dt} = -\frac{1}{J}\left(T_{lf}\cos\left(\omega_{lf}t\right)\right) \text{and } \omega_r(t) = -\frac{T_{lf}}{J}\int\cos\left(\omega_{lf}\right)dt + Const. \tag{11}$$

Then

$$\omega_r(t) = -\frac{T_{lf}}{J\omega_{lf}}\sin\left(\omega_{lf}t\right) + \omega_{r0} \tag{12}$$

Observing (12), the mechanical speed consists of a constant component ω_{r0} and a component which varies according to a sinusoidal signal. Then, the integration of mechanical speed results in the mechanical rotor position $\theta_r(t)$:

$$\theta_r(t) = \frac{T_{lf}}{J\omega_{lf}^2}\cos\left(\omega_{lf}t\right) + \omega_{r0}t \tag{13}$$

The rotor position oscillations act on the magneto motive force (MMF). In normal conditions, the MMF referred to as the rotor ($F_{r(R)}$) can be expressed by (14).

$$F_r^{(R)}(\theta',t) = F_r \cos(p\theta' - s\omega_1 t) \tag{14}$$

Where θ' is the mechanical angle in the rotor reference frame, p is the number of pole pairs, ω_1 is the synchronous speed, s is the motor slip, and F_r is the rotor MMF.

Figure 4 shows a phasorial diagram for the rotor MMF (R axes) referred to the stator frame (S axes), the difference can be expressed by the angle θ'.

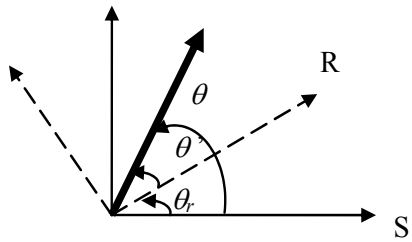

Figure 4. Phasorial diagram of the rotor MMF referred to the stator frame

According the Figure 4 and Equation (14) and replacing (13) in (15), it results in:

$$\theta = \theta' + \theta_r \text{ and } F_r(\theta,t) = F_r \cos[p(\theta - \theta_r) - s\omega_1 t] \tag{15}$$

$$F_r(\theta,t) = F_r \cos\left(p\theta - p\omega_{r0}t - \frac{pT_{lf}}{J\omega_{lf}^2}\cos(\omega_{lf}t) - s\omega_1 t \right) \tag{16}$$

Doing $\beta = pT_{lf} / J\omega_{lf}^2$ and using the relation $\omega_{r0} = (1-s)\omega_1 / p$, it produces:

$$F_r(\theta,t) = F_r \cos\left(p\theta - \omega_1 t - \beta\cos(\omega_{lf}t) \right) \tag{17}$$

Where β is the modulation index and generally β<<1.

At this point, it is important to notice that the term $\beta\cos(\omega_{lf}t)$ means a phase modulation. The failure does not have direct effect on stator MMF which can be expressed by:

$$F_s(\theta,t) = F_s \cos(p\theta - \omega_1 t - \varphi_s) \tag{18}$$

Where φ_s is the initial phase between rotor and stator MMFs.

Supposing for the sake of simplicity the value of the air gap permeance Λ constant (because slotting effects and eccentricity were neglected), the air gap flux density B can be expressed by the product of total MMF and Λ:

$$B(\theta,t) = \left[F_s(\theta,t) + F_r(\theta,t)\right]\Lambda \text{ and}$$

$$B(\theta,t) = B_s \cos\left(p\theta - \omega_1 t - \varphi_s\right) + B_r \cos\left(p\theta - \omega_1 t - \beta\cos\left(\omega_{lf} t\right)\right) \tag{19}$$

As the flux $\varphi(t)$ is obtained by the integration of the flux density $B(\theta,t)$, then all phase modulation existing in the flux density also exists in the flux $\varphi(t)$. It is important to explain that the winding structure affects only the flux amplitude and not its frequencies. Thus:

$$\varphi(t) = \varphi_s \cos\left(\omega_1 t - \varphi_s\right) + \varphi_r \cos\left(\omega_1 t - \beta\cos\left(\omega_{lf} t\right)\right) \tag{20}$$

The relationship between the flux and the current is given by the equation (21).

$$V(t) = R_s I(t) + \frac{d\varphi(t)}{dt} \tag{21}$$

Where R_s is the stator resistance. Thus,

$$I(t) = \frac{V(t)}{R_s} - \frac{1}{R_s}\frac{d\varphi(t)}{dt} \tag{22}$$

And as:

$$\begin{aligned}\frac{d\varphi(t)}{dt} = &-\omega_1\varphi_s \sin\left(\omega_1 t + \varphi_s\right) - \omega_1\varphi_r \sin\left(\omega_1 t + \beta\cos\left(\omega_{lf} t\right)\right) \\ &+ \omega_{lf}\beta\varphi_r \sin\left(\omega_1 t + \beta\cos\left(\omega_{lf} t\right)\right)\sin\left(\omega_{lf} t\right)\end{aligned} \tag{23}$$

With the last term being neglected once $\beta \ll 1$. Finally:

$$I(t) = \underbrace{\frac{V(t)}{R_s} + \frac{1}{R_s}\omega_1\varphi_s \sin\left(\omega_1 t + \varphi_s\right)}_{\text{Stator}} + \underbrace{\frac{1}{R_s}\omega_1\varphi_r \sin\left(\omega_1 t + \beta\cos\left(\omega_{lf} t\right)\right)}_{\text{Rotor}} \tag{24}$$

$$I(t) = \underbrace{I_{st}\sin\left(\omega_1 t + \varphi_s\right)}_{i_{st}} + \underbrace{I_{rt}\sin\left(\omega_1 t + \beta\cos\left(\omega_{lf} t\right)\right)}_{i_{rt}} \tag{25}$$

Notice that the term i_{st} results from stator MMF and it is not influenced by the torque oscillation, and the term i_{rt} results from the rotor MMF and presents phase modulation due to torque oscillations. And also, when the motor is healthy β is null.

Considering the component i_{rt} with phase modulation in (14) given in its complex form:

$$i_{rt}(t) = I_{rt} e^{j\left(\omega_1 t + \beta\cos\left(\omega_{lf} t\right)\right)} \tag{26}$$

Applying a Discrete Fourier Transform (DFT) in (26), as well known from communications theory, it can be expressed by (27).

$$I_{rt}(f) = I_{rt}\sum_{n=-\infty}^{\infty} j^n J_n(\beta)\delta\left(f-\left(f_1+nf_{lf}\right)\right) \tag{27}$$

Where J_n denotes the nth-order Bessel function of first kind and $\delta(f)$ is the Dirac delta function. Since β is so small, the Bessel functions of order $n \geq 2$ can be neglected.

Finally, the Power Spectral Density (PSD) of the stator current, considering the approximations used, is given by:

$$\left|I(f)\right| = \left(I_{st} + I_{rt}J_0(\beta)\right)\delta\left(f-f_1\right) + I_{rt}J_1(\beta)\delta f - \left(f_1 \pm f_{lf}\right) \tag{28}$$

It is clear that the phase modulation leads to sideband components of the fundamental at $f_1 \pm f_{lf}$ as it happens in an amplitude modulation. Considering all the development accomplished in this section and the result in (28), the load failure patterns can be presented.

4.3. Voltage Signature Analysis (VSA)

The technique of Voltage Signature Analysis follows the same strategy of analysis of the current signature; however the signal is analyzed from the voltage supply of the motor. This technique is most often used in analysis of generating units. In the case of motors, it can be usefully employed in cases of problems from the motor power and the analysis of electric stator imbalance in conjunction with the analysis of the current signature. It can be used also to know the origin of certain components in the power spectrum, that is, it can be used to infer if the source of the component comes from the mains or has its origin in the array itself.

4.4. Instantaneous Power Signature Analysis (IPSA)

The analysis of the instantaneous power is another failure analysis technique based on spectral analysis. The big difference between this technique and MCSA and VSA is that it considers the information present in voltage and current signals of a motor phase concurrently and demodulated fault component appears under the name of Characteristic Frequency. Considering an ideal three phase system, instant power $p(t)$ is given by:

$$p(t) = v_{LL}(t)i_L(t) \tag{29}$$

Where v_{LL} is the voltage between two terminals of the motor and i_L is the current entering one of these terminals. And, a motor under normal conditions, i.e. without breakdowns, and constant velocity, one has:

$$v_{LL}(t) = \sqrt{2}V_{LL}\cos(\omega t) \tag{30}$$

$$i_{L,0}(t) = \sqrt{2} I_L \cos\left(\omega t - \varphi - \frac{\pi}{6}\right) \tag{31}$$

$$p_0 = v_{LL}(t) i_{L,0}(t) = V_{LL} I_L \left[\cos\left(2\omega t - \varphi - \frac{\pi}{6}\right) + \cos\left(\varphi + \frac{\pi}{6}\right)\right] \tag{32}$$

Where V_{LL} and I_L are the RMS values of voltage and current line, ω is the angular frequency and φ is the phase angle of the motor load.

Let's consider now the presence of a mechanical fault in the drive train, resulting in the appearance of motor torque oscillations accompanied by surges of speed and slip, which in turn result in modulations in the current spectrum.

For simplicity, it is considered that the failure cause only an amplitude modulation on the stream of the stator by deleting the effect on stage. It could also prove that phase modulations, in function of torque oscillations, appear in current as amplitude modulations by processed result from similar functions to the Bessel functions. The modulated current i_L can be expressed by:

$$\begin{aligned} i_L &= i_{L,0}(t)\left[1 + M\cos(\omega_f t)\right] \\ &= i_{L,0}(t) + \frac{MI_L}{\sqrt{2}}\left\{\cos\left[\left(\omega + \omega_f\right)t - \varphi - \frac{\pi}{6}\right] + \cos\left[\left(\omega + \omega_f\right)t - \varphi - \frac{\pi}{6}\right]\right\} \end{aligned} \tag{33}$$

Where M is the index modulation and ω_f is the angular frequency of the failure.

The expression of instant power results in:

$$\begin{aligned} p(t) = p_0(t) + \frac{MV_{LL}I_L}{2}\Bigg\{&\cos\left[\left(2\omega + \omega_f\right)t - \varphi - \frac{\pi}{6}\right] + \cos\left[\left(2\omega - \omega_f\right)t - \varphi - \frac{\pi}{6}\right] + \\ &+2\cos\left(\varphi + \frac{\varphi}{6}\right)\cos\left(\omega_f t\right)\Bigg\} \end{aligned} \tag{34}$$

Besides the fundamental component $2\omega/2\pi$ and the lateral bands in $(2\omega \pm \omega_f)/2\pi$, the spectrum of instantaneous power contains an additional component directly related to the modulation caused by failure. This component is named as **Characteristic Component** and can be used as information for the diagnosis of the condition of the machine.

The following simulation which considers a motor current modulation originated by an alleged mechanical failure whose frequency characteristic is of 15 Hz. Note the Figure 5 that the spectrum of voltage does not have any type of modulation, since the current spectrum has lateral bands apart from 15 Hz fundamental's (located at 60 Hz). The instantaneous power spectrum has the fundamental frequency in 120 Hz with modulations of 15 Hz at 105 and 135 Hz, besides presenting the fault feature component in isolated 15 Hz.

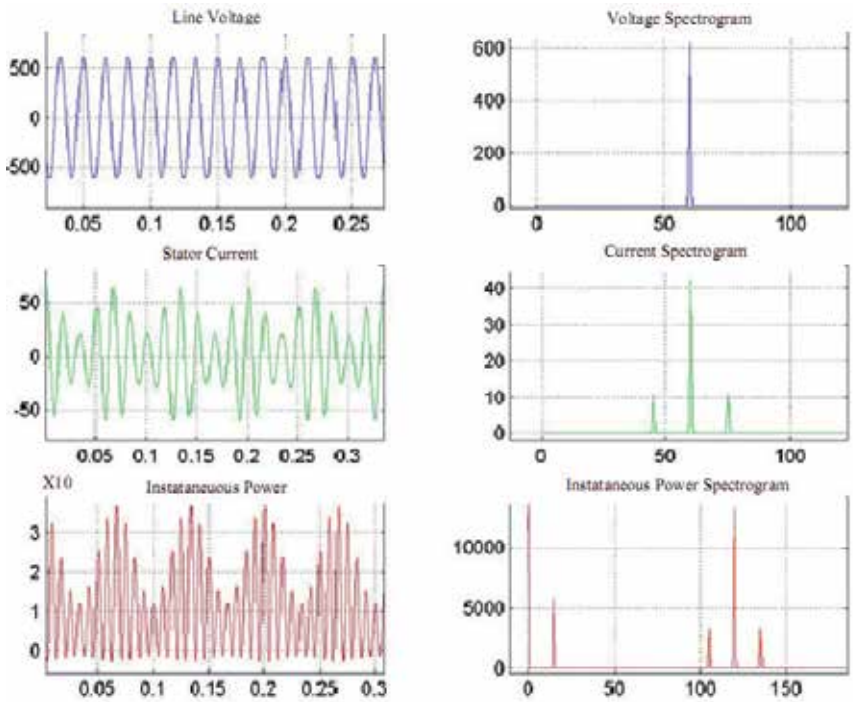

Figure 5. Fault Simulation in 15 Hz and the respective spectra of voltage, current and instant power

4.5. Enhanced Park's Vector Approach (EPVA)

The first research involving the use of Park's vector method for the diagnosis of failures in motors such as short circuit between turns, airgap eccentricity and broken bars, etc.(Cardoso & Saraiva, 1993). At first, the proposed damage detection was based only on the distortion suffered by circle of Park on the emergence and on the aggravation of the damage. More recently, the technique has been improved (now named EPVA) and may be described as following steps. The three phases of currents in a motor can be described by:

$$i_A = i_M \cos(\omega t - \alpha) \tag{35}$$

$$i_B = i_M \cos\left(\omega t - \alpha - \frac{2\pi}{3}\right) \tag{36}$$

$$i_C = i_M \cos\left(\omega t - \alpha + \frac{2\pi}{3}\right) \tag{37}$$

Where i_M is the peak value of the supply current, ω is the angular frequency in rad/s, α the is the initial phase angle in rad, t is the time variable; and i_A, i_B and i_C are respectively the currents in the phases A, B and C. The current components of the Park's vector are given by:

$$i_D = \left(\frac{\sqrt{2}}{\sqrt{3}}\right) i_A - \left(\frac{1}{\sqrt{6}}\right) i_B - \left(\frac{1}{\sqrt{6}}\right) i_C \text{ and } i_Q = \left(\frac{1}{\sqrt{2}}\right) i_B - \left(\frac{1}{\sqrt{2}}\right) i_C \tag{38}$$

Ideally:

$$i_D = \left(\frac{\sqrt{6}}{2}\right) i_M \cos(\omega t - \alpha) \text{and } i_Q = \left(\frac{\sqrt{6}}{2}\right) i_M sen(\omega t - \alpha) \tag{39}$$

Graphically, ideal conditions generate a perfect Park circle centered at the origin of coordinates, as shown in Figure 6.

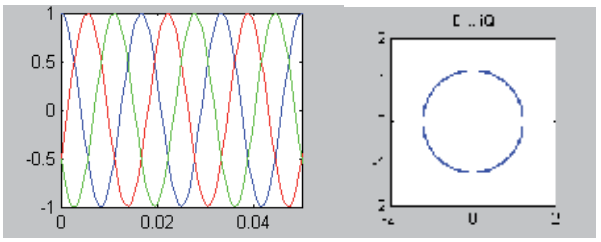

Figure 6. Signals in time and Park circle

Under abnormal conditions of operation, i.e. when the emergence of mechanical or electrical failure, the previous equations are no longer valid and the circle of Park passes to suffer distortions. As these changes in the circle of Park are difficult to be measured, was proposed by EPVA method of observation of spectrum of Park's vector module. The advantage of EPVA technique combines the simplicity of the previous method (analysis of the Park's circle) with spectral analysis capability. In addition, the fundamental component of the motor power is automatically subtracted from the spectrum by Park transformation, causing the failure characteristics components appear prominently. The most important point is the fact that the technique considers the three phases of current, generating a more significant spectrum by encompass information from three phases. This feature is extremely useful in cases where failure can only be detected if considered the three phases. This is the case of unbalanced electric motor fuelled in open loop.

When there is an unbalanced voltage supply, the motor currents can be represented by:

$$i_A = i_d \cos(\omega t - \alpha_d) + i_i \cos(\omega t - \beta_i) \tag{40}$$

$$i_B = i_d \cos\left(\omega t - \alpha_d - \frac{2\pi}{3}\right) + i_i \cos\left(\omega t - \beta_i + \frac{2\pi}{3}\right) \tag{41}$$

$$i_C = i_d \cos\left(\omega t - \alpha_d + \frac{2\pi}{3}\right) + i_i \cos\left(\omega t - \beta_i - \frac{2\pi}{3}\right) \tag{42}$$

Where i_d is the maximum value of the current direct sequence, i_i is the maximum value of reverse sequence current, α_d is the current initial phase angle direct sequence in rad, and β_i is the initial phase angle reverse sequence current in rad. In the Park's vector:

$$i_D = \left(\frac{\sqrt{3}}{\sqrt{2}}\right)\left(i_d \cos(\omega t - \alpha_d) + i_i \cos(\omega t - \beta_i)\right) \text{and } i_Q = \left(\frac{\sqrt{3}}{\sqrt{2}}\right)\left(i_d \sin(\omega t - \alpha_d) - i_i \sin(\omega t - \beta_i)\right) \quad (43)$$

And the square of the Park's vector module is given by:

$$\left|i_D + j i_Q\right|^2 = \left(\frac{3}{2}\right)\left(i_d{}^2 + i_i{}^2\right) + 3 i_d i_i \cos(2\omega t - \alpha_d - \beta_i) \quad (44)$$

Now, just applying the FFT to the square of the Park's vector module and observe that this is composed by a DC level plus one additional term located at twice the supply frequency. It is exactly this additional term that indicates the emergence and intensification of stator electrical asymmetries. Let's the example shown in Figure 7a which is considered an unbalanced feed; and also, the Park circle passes to resemble an ellipse and arises in the spectrum the component located at twice the supply frequency, as shown in Figure 7 b and c. Thus, the whole process can be represented by the elements of Figure 8.

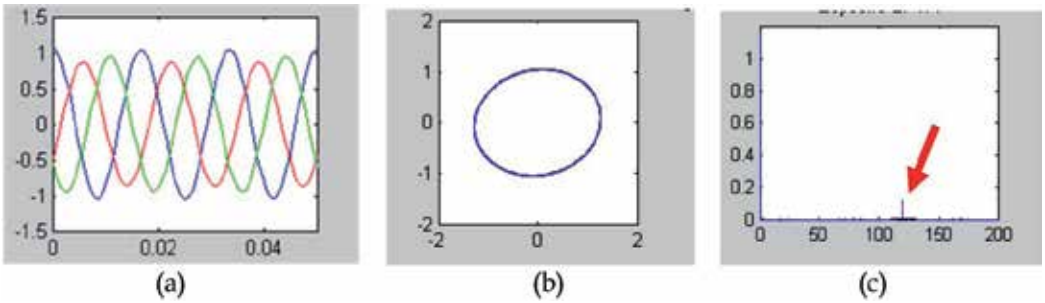

Figure 7. Imbalance between the phases, Park circle distorted and presence of the component at twice the supply frequency

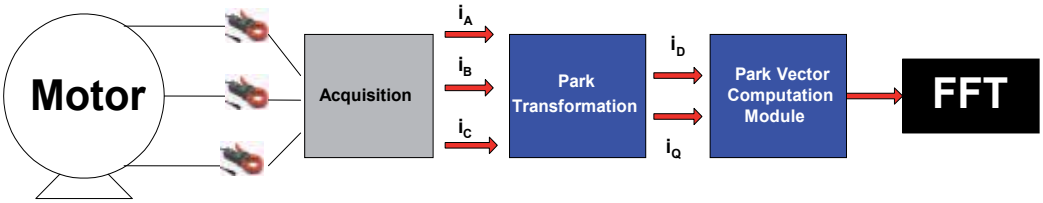

Figure 8. Block Diagram of the EPVA technique

This demonstrates the effectiveness of the component located at twice the supply frequency (in this case 120 Hz) of the EPVA monitoring to diagnosis short circuit between turns. The test procedure was the following: used the Marathon motor failures Simulator Spectra Quest

in which *taps* was inserted to the gradual introduction of imbalance in power depending on the insertion of short. Figure 9a presents the characteristics of the motor and the *taps* as to the short are introduced.

Tests have been made in the conditions of non-faulted motor (no imbalance) and five severities of short circuit generating imbalances of 1.2 V, 1.8 V, V, V 5.4 6.7 and 8.5 V. Figure 9b shows the overlap of the spectra of the motor in normal condition (in red) and motor in the worst condition of imbalance (8.5 V) highlighting the component twice the power frequency in the spectrum of Park vector module.

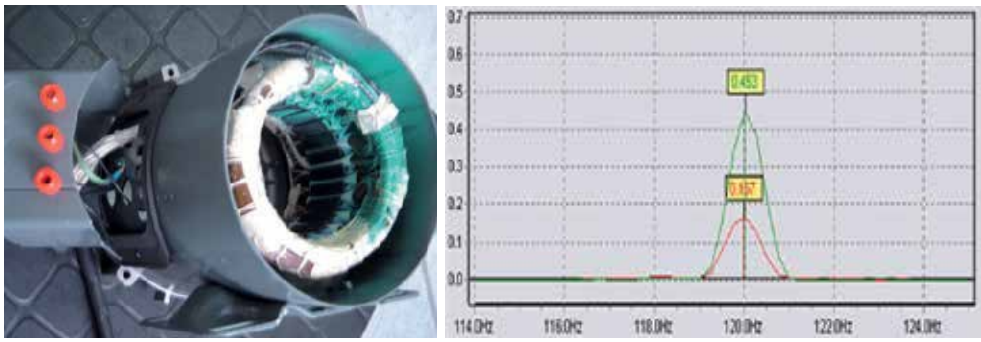

(a) (b)

Figure 9. Featured for the inserted short-circuit and spectrum of Park vector module

The current trend curve (shown in Figure 10) demonstrates a general growth of electric unbalance component EPVA with increasing the short circuit. Each three points of the curve represent a condition of normal severity, starting and advancing to severity 1 (1.2 V), 2 (1.8 V), 3 (5.4 V), 4 (6.7 v) and 5 (V 8.5). Severity 4 presents amplitude less than Severity 3 due to a change in the equilibrium condition of input voltage shown in the trend curve in tension (shown in Figure 10), being thus possible to separate the effects of those supply imbalances caused by short circuits and other anomalies.

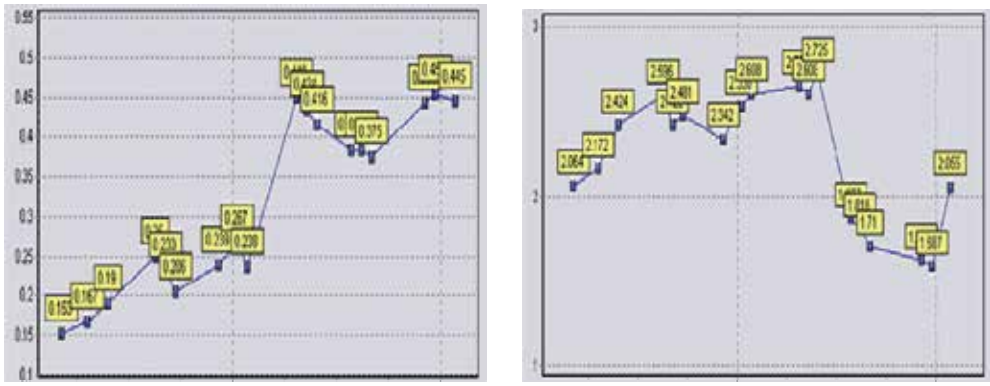

Figure 10. Trend curve to the imbalance component: (a) for current and (b) for voltage

5. Patterns of failures

A fault in any part of the machine is a decrease in this part performance when compared with the minimum requirements specified. Thus the fault results from natural wear, project errors, incorrect installation, poor use or a combination of all of them. If the fault is not identified in time and increases, failure may ensue (Thorsen & Dalva, 1999). Therefore, failure is the reason why the machine breaks down. This way, one tries to identify the fault before it becomes a failure, even when it is incipient.

5.1. Rotor failure patterns

This section shows the failure patterns for rotor problems.

1. Broken Bar: it is the rotor most common problem and the better known pattern. Figure 11 presents this failure pattern, where *f* is the supply fundamental frequency and *s* is the motor slip.

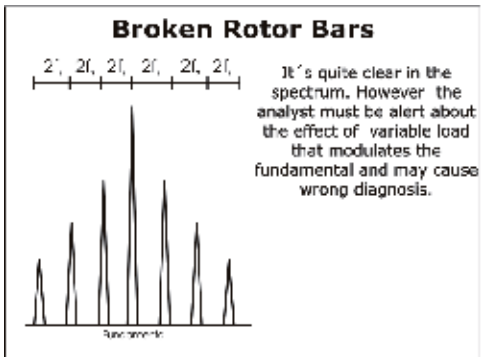

Figure 11. Broken bar pattern

2. Air gap Eccentricity: it is the condition in which the air gap doesn't present a uniform distance between the rotor and stator, resulting in a region of maximum air gap and another region of minimum air gap. There are two kinds of air gap eccentricity: static and dynamic. Figure 12 shows the patterns for both kinds, where f_1 is the supply fundamental frequency, R is number of rotor bars, and CF is the center frequency.

a. Static Eccentricity: the minimal radial air gap position is fixed in the space. The stator core is bowed or there is an incorrect positioning between the rotor and the stator generated as a consequence of misalignment. Besides those possibilities, constructive aspects permit an inherent level of eccentricity due to the tolerances of the manufacturing process.
b. Dynamic Eccentricity: the minimum air gap turns with the rotor. The main causes are: rotor outer diameter is not concentric, rotor thermal bent, bearing problems, rotor or load imbalance.

Mechanical problems such as rotor misalignment and imbalance can be also inferred in the low spectrum through the analysis of the rotational frequency sidebands. Figure 13 shows this pattern, where f_r is rotational frequency.

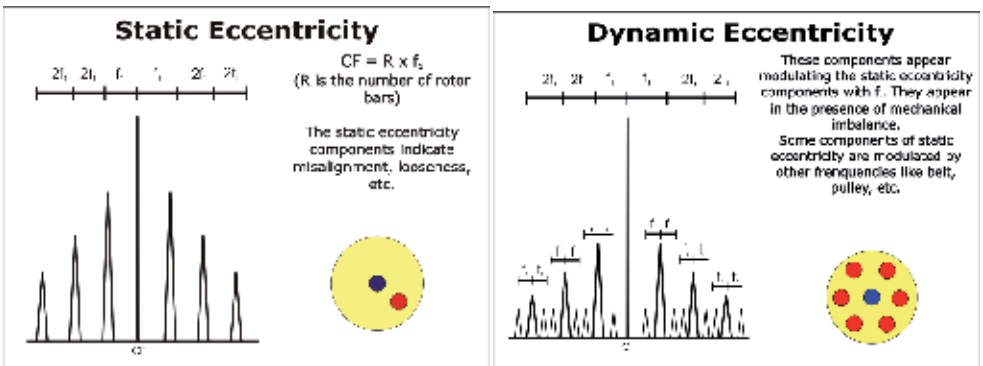

Figure 12. Static and Dynamic Eccentricities patterns

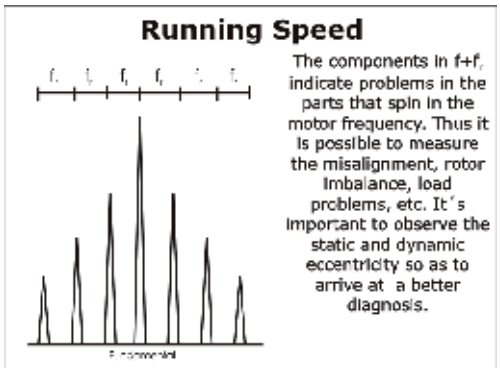

Figure 13. Rotational frequency pattern

5.2. Stator failure patterns

Most induction motor stator failures are related to the windings. The occurrence of failures in the stator core is less frequent. In spite of being rare, this last problem can cause considerable damages to the machine (Borges da Silva et al., 2009).

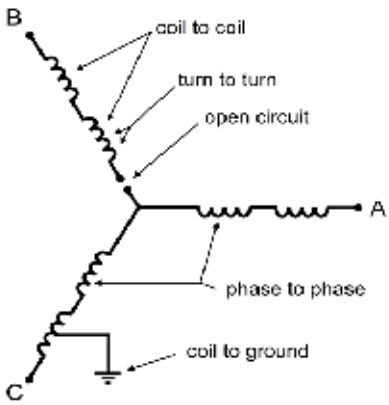

Figure 14. Stator winding failure modes

The failures related to the stator windings present a diversified set of possible manifestations according to the Figure 14. It is possible to notice their simultaneous occurrence. There are MCSA patterns for the detection of these failures, but EPVA is the most recommended technique to detect electrical imbalance in motors without direct torque control.

5.3. Bearing failure patterns

The monitoring of bearing damages is very important in predictive maintenance program since these problems account for 40% of the total amount of failures in an induction motor (Schoen et al., 1995). Many papers have recommended current signature analysis for the diagnosis of bearing faults, although it is important to register that this is an area that can be more explored and improved, tracking earlier fault detection.

There are several causes for bearing damages. Since this is not the objective of this work, the chapter presents just the characteristic components of failure in the outer and inner races, and rolling elements. The pattern is given by the Figure 15; where FBPFO is the rolling element characteristic frequency, FBPFI is the inner race characteristic frequency, FBSF is the outer race characteristic frequency, FFTF is the cage characteristic frequency, PD is the bearing pitch diameter, BD is the ball bearing diameter, β is the contact angle, n is the number of rolling elements, and Fr is the rotational speed.

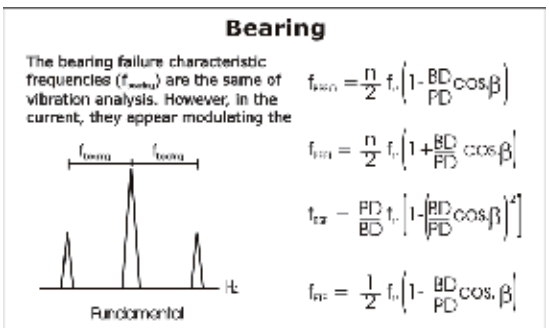

Figure 15. Bearing failure modes

5.4. Load failure patterns

The vast majority of the published papers about failure monitoring via current spectrum analysis presents the failure patterns related to broken bars and air gap eccentricity. This chapter presents a very meaningful contribution to the previous works since it adds new patterns related to the attached load. All the patterns have been tested, first through controlled laboratory tests and later through industrial cases. The failure patterns can be divided in three groups: motor failure, transmission system failure and attached load failure. By using the induction motor as a transducer, one can monitor the complete drive train, i.e., motor, transmission system and attached load, so as to increase the reliability of productive system.

5.4.1. Transmission System Failure

The MCSA monitors the frequency components related to pulleys (motor pulley and load pulley), belts and gear mesh. It has been observed that load problems can reflect in the transmission system frequency components. This characteristic is one more way of detecting mechanical load failures to be used in addition to the load characteristic frequency components.

1. **Pulleys**: by analyzing the rotational frequency one can detect problems related to the motor pulley. When there is no change in the speed, it is not possible to distinguish the damaged pulley from the healthy one since they have the same rotational frequency. But when a speed transformation is present, one can monitor the load pulley and the attached load through the pattern presented in Figure 16. In this case, f_{lf} is equal to f_{pulley}, and f_{pulley} is the load pulley characteristic frequency given by (45).

$$f_{pulley} = \frac{D_{motor\_pulley} \times f_r}{D_{load\_pulley}} \tag{45}$$

Where f_r is the rotational frequency, D_{motor_pulley} is the diameter of the motor pulley and D_{load_pulley} is the diameter of the load pulley. The sideband components of the fundamental are at $f_1 \pm f_p$.

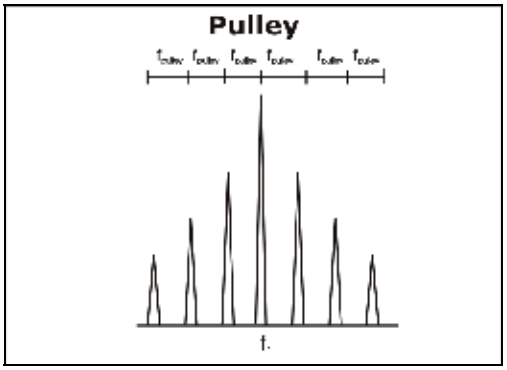

Figure 16. Load Pulley Pattern

The most common problems are eccentric pulley, pulley with mechanical looseness and unbalanced pulley. Problems related to the load can also reflect in the same frequencies. When this happens, the analyst himself must cross pieces of information from other spectrum regions so as to arrive at a reliable conclusion.

2. **Belts**: the first step when monitoring the belt characteristic frequency components is to calculate the belt frequency (f_b). In this case, f_{lf} is equal to f_b, and f_b is the belt characteristic frequency given by (46).

$$f_b = \frac{D_{motor\_pulley} \times \pi \times f_r}{L_{belt}} \tag{46}$$

Where L_{belt} is the belt length

This way the sideband components of the fundamental are at $f_1 \pm f_b$. After calculating this frequency, it is enough to follow the pattern presented in Figure 17 and follow up the tendency curve in order to diagnose problems in this transmission system element.

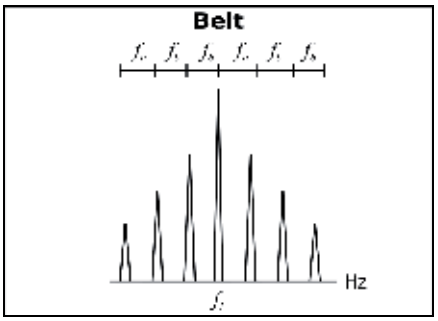

Figure 17. Belt Failure Pattern

Besides diagnosing problems such as loosen belt, broken belt or too taut belt, one can analyze problems originating in the load. In case of load failure, the vibration levels in the belts increase considerably and result in higher amplitudes for the belt characteristic frequencies.

3. **Gear Mesh**: in this case, two spectrum regions must be monitored. The first one, in a lower frequency band, shows punctual failure in the gear (for instance, a broken tooth). These frequencies are related to the rotational frequencies before and after the speed transformation. This way the sideband components of the fundamental are at $f_1 \pm f_{r1}$ and $f_1 \pm f_{r2}$ respectively. Where f_{r1} is the rotational frequency before the speed transformation and f_{r2} is the rotational frequency after the speed transformation. The second spectrum region of interest shows distributed failures in the gear. They are known as gear mesh frequency (f_g) and can be calculated by multiplying the rotational shaft speed by the gear teeth number Figure 18a illustrates this situation, and Figure 18b shows the sideband components of the fundamental are at $f_1 \pm f_g$.

$$f_g = n \cdot f_{r1} = N \cdot f_{r2} \tag{47}$$

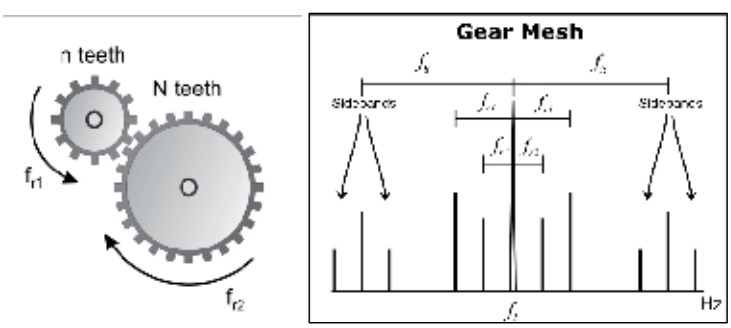

Figure 18. Gear features: (a) gear mesh, and (b) gear mesh failure pattern

5.4.2. Attached load failure

As seen previously, a load fault reflects in the motor stator current by means of torque oscillations. This chapter presents in this section three different kinds of loads and their respective patterns. Other load types result in different patterns but the fundamental sequence is always the same: define the characteristic frequencies from the constructive data, find their presence in the motor current signature due to torque oscillations from load faults, analyze the tendency curve and diagnose the fault.

1. **Centrifugal Pumps:** for the analysis of centrifugal pumps one has to consider the pump rotational frequency (f_{r_pump}) and the vane pass frequency (f_{vp}) that is given by:

$$f_{vp} = n \cdot f_{r\_pump} \tag{48}$$

Where n is the number of pump vanes.

The analysis of the pump rotational frequency (f_{r_pump}) indicates problems related to misalignment or pump imbalance. In this case, f_{lf} is equal to f_{r_pump} and the sideband components of the fundamental are at $f_1 \pm f_{r\_pump}$. On the other hand, the increase of the amplitudes of vane passing frequency indicates problems inside the pump, such as vane deterioration. Now the sideband components of the fundamental are at $f_1 \pm f_{vp}$. Figure 19 shows the pattern for these frequencies.

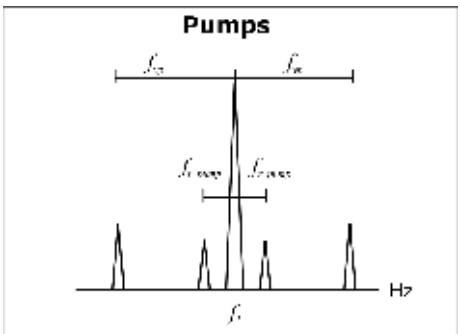

Figure 19. Centrifugal pump failure pattern

In addition to those frequencies one has to monitor the increase of saliencies close to the supply frequency. These frequencies are characteristic of pump signature and also can indicate pump problems.

2. **Screw Compressor:** the complete set motor, gear mesh and screw compressor can be monitored by means of MCSA satisfactorily. The motor and the gear mesh can be analyzed according to the patterns presented previously. Figure 20a shows the scheme of a screw compressor. Where N is the motor gear teeth number, n is the compressor gear teeth number, L_m is the male screw lobules number, L_f is the female screw lobules number, F_r is the motor rotational frequency, F_{r1} is the male screw rotational frequency, F_{r2} is the female screw rotational frequency and F_p is the pulsation frequency. The screw compressor failure spectral pattern is presented in Figure 20b.

The screw compressor analysis takes into consideration three characteristic frequencies:

a. Male screw rotational frequency: in this case, $f_{lf} = f_{r1}$ and f_{r1} is the male screw rotational frequency given by (51). The sideband components of the fundamental are at $f_1 \pm f_{r1}$.

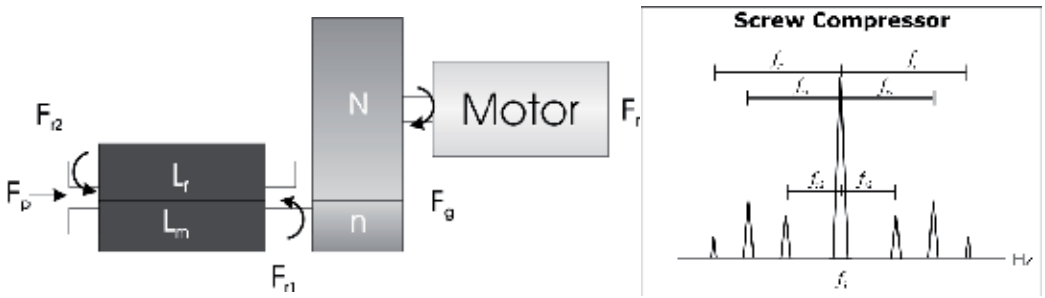

Figure 20. Screw compressor: (a) schematic and (b) failure spectral pattern

$$f_{r1} = \frac{N}{n} \cdot f_r \tag{49}$$

b. Female screw rotational frequency: in this case, f_{lf} is equal to f_{r2} and f_{r2} is the female screw rotational frequency given by (50). The sideband components of the fundamental are at $f_1 \pm f_{r2}$.

$$f_{r2} = \frac{L_m}{L_f} \cdot f_{r1} \tag{50}$$

c. Pulsation frequency: in this case, f_{lf} is equal to f_p and f_p is the pulsation frequency given by (51). The sideband components of the fundamental are at $f_1 \pm f_p$.

$$f_p = L_m \cdot f_{r1} = L_f \cdot f_{r2} \tag{51}$$

When the screw compressor has two stages, it is enough to apply the same reasoning for the second stage of compression. Since the speed transformations are different, the characteristic component of each stage can be separated in the spectrum.

3. **Fans:** in the same way of pumps, fan failure analysis considers the fan rotational frequency and the blade passing frequency (f_{bp}):

$$f_{bp} = N_b \times f_{r\_fan} \tag{52}$$

Where N_b is the number of blades and f_{r_fan} is the fan rotational frequency.

Analyzing the rotational frequency (f_{r_fan}), problems related to misalignment or fan imbalance can be detected. When, f_{lf} is equal to f_{r_fan} and the sideband components of the fundamental are at $f_1 \pm f_{r\_fan}$. Also, the increase of the amplitudes of blade passing frequency

indicates problems like blade deterioration or break. The sideband components of the fundamental are given by $f_1 \pm f_{bp}$. Figure 21 shows the fan failure patterns.

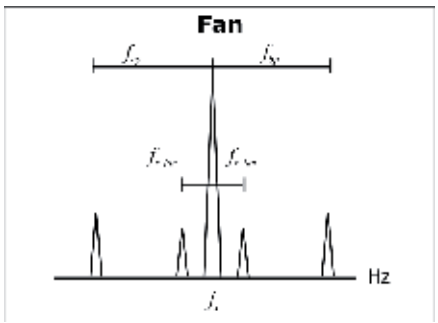

Figure 21. Fan failure pattern

6. Elements of a monitoring system for predictive maintenance

A sophisticated monitoring system can read the entrances of hundreds of sensors and execute mathematical operations and process a diagnosis. Currently, the diagnosis is gotten, most of the time, using artificial intelligence techniques (Lambert-Torres et al. 2009).

Considering the previous statements, a monitoring system can be divided in four main stages: (a) transduction of the interest signals; (b) acquisition of the data; (c) processing of the acquired data; and (d) diagnosis. Figure 22 presents a pictorial form of this process.

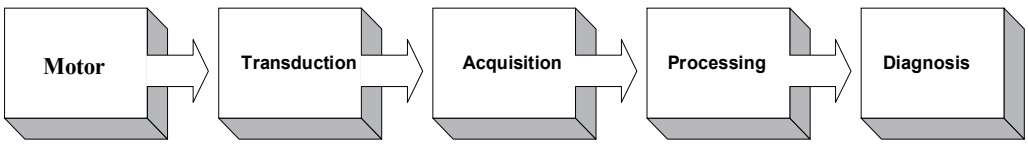

Figure 22. Steps of the Monitoring Process

6.1. Transduction

A transducer is a piece of equipment that has in its entrance an input value to be monitored (current, voltage, acceleration, temperature, etc), whereas in its output it has a signal that is conditioned and envoy to the acquisition system and processing. The main transducers used in the monitoring processing of electric machines are:

- For measurement of temperature: they are the three main methods of measurement of temperature: thermocouple, thermister, and RTD (Resistance Temperature Detection).
- For the measurement of vibration: two types of transducers for the vibration analysis exist: the absolute transducers or with contact and the relative ones or without contact. The absolute transducers measure the real movement of the machine, whereas the relative ones measure the movement of an element of the machine in relation to the other element. The accelerometer is the main and more used existing absolute sensor in the market.

- For measurement of force: the most common is the strain gauge, that it is a device that understands a resistance that has its modified size and transversal area in function of the application of a force. Then, the force can be measured through the variation of the resistance.
- For measurement of electric and magnetic values: the electric values are measured from transforming of voltage and current those always are presented as part of the protection system. However, it can still have the necessity an extra measure, the density of magnetic flow in the machine, using itself a hall-effect device.

6.2. Data acquisition

The data acquisition is a stage with fundamental importance; because it needs to guarantee the integrity and precision of the collected data. The precision of the data demanded of the acquisition is determined by the future mathematical manipulations that are applied to the data set. The collection and the transmission of the data must be made in order to minimize to the maximum the effect of the noise, being become the sufficiently consistent data. In complex systems with many entrances, it is oriented that the processing system is remote, that is, located to a certain distance of the inspected process. Figure 23 presents an example where some motors are being monitored. A group of adjacent machines is connected to a point of collection of data that digitalize the signal and sends for the remote central office of processing and diagnosis.

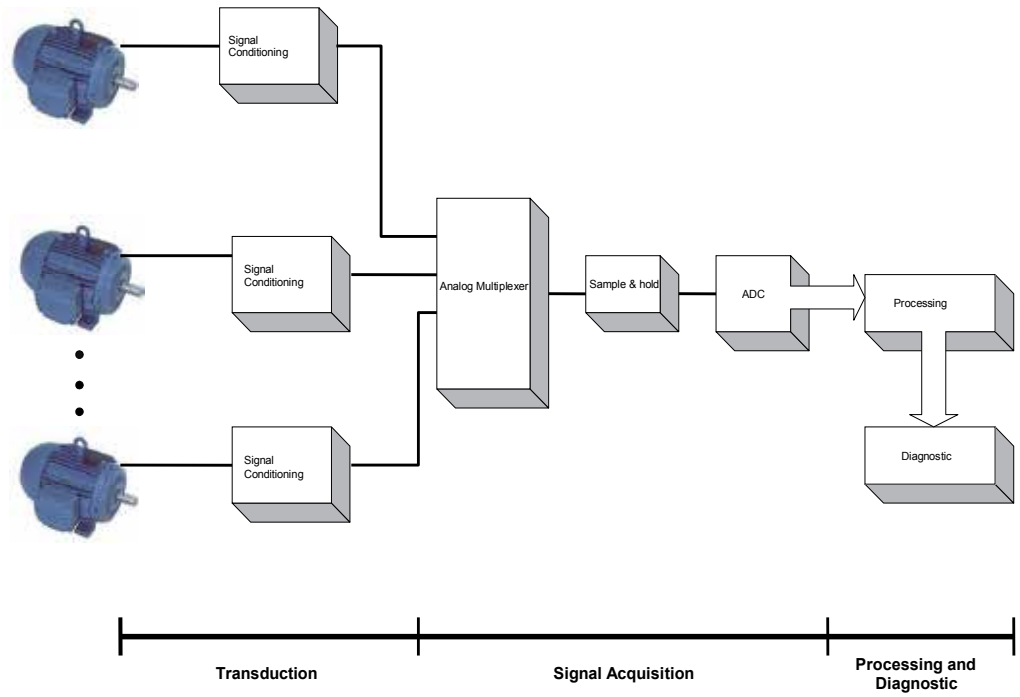

Figure 23. Example of a Monitoring System

The multiplexer is essential when a great number of channels must be monitored. Moreover, it also is recommended for a small number of channels, since it allows the use of only one converter A/D. Already converter A/D is the heart of the acquisition system and must be specified in function of the time of conversion and precision.

6.3. Processing

The task of the processing must be to catch the collected data and to manipulate them and/or to transform them, aiming at the agreement of these for the system of diagnosis in a faster and easier form. The processing can be done on-line or off-line. The choice depends on the process that are being monitored and on the speed with that the characteristics of interest of this process modify themselves.

There are different techniques of processing to monitor electric machines. One of the simplest of them, it examines the amplitude of the signal of entrance of the function in the time, and compares it with a predetermined value. Elaborated techniques are currently possible due to the new computers, such as: spectral analysis, correlation, averages, cepstral, envelope analysis, etc.

6.4. Diagnosis

Diagnosis is the part most critical of the system, because it involves decisions and consequently money. Currently, many techniques of artificial intelligence as expert systems and neural nets are being used (Lambert-Torres et al., 2009).

7. Implementation in a real-case predictive maintenance

A Brazilian petroleum company has decided to implement electrical signature analysis through a remote condition monitoring system named Preditor (PS Solutions, 2011). The communication is based on Ethernet network. Each hardware has been plugged in this network has an IP address and through the motor configuration the software knows exactly where each signal comes from. This way it is possible to monitor the motor condition from a remote office with a group of expert analysts or to count on the automatic support of the software.

Among the induction motors monitored, an example of electrical imbalance was chosen. Motor nameplate features are 250 CV, 2400 V, 70 A, 505 RPM, 14 poles, and attached to a reciprocating compressor. The remote system software has indicated electrical imbalance based on EPVA signature. Figure 24 presents the stator electrical imbalance signature and tendency curve for this motor.

One can observe from the figure above that the electrical imbalance was around 5.7%. For an idea of magnitude, all the other motors presented an electrical imbalance around 1%. The motor history was tracked and the maintenance department detected a set of defective coils in one phase. These coils were by-passed, which caused the imbalance, as shown in Figure 25.

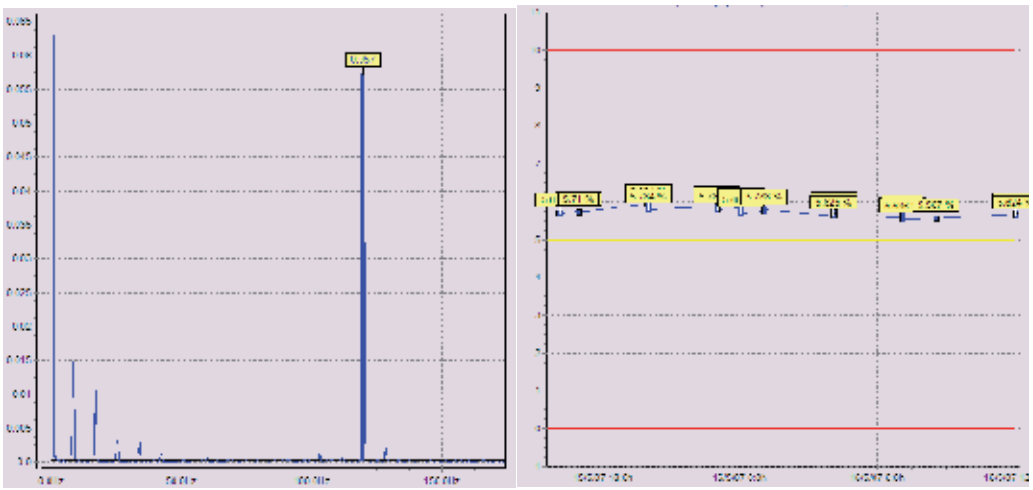

Figure 24. Stator electrical imbalance signature and tendency curve

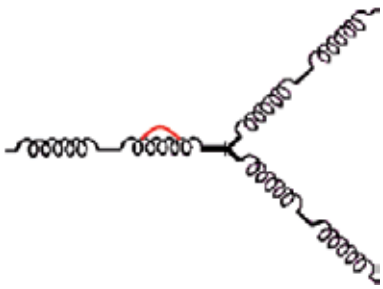

Figure 25. Set of defective coils by-passed

After all the implementing job, one can say that the remote system based on electrical signature analysis is an effective alternative for rotating machines monitoring since the system fits the refineries safety rules. It still allows the non-intrusive monitoring, avoiding exposing the workers to electrical shock and arcs, confined spaces and eliminating the necessity of job permissions and risk analysis for signal acquiring (which implies in cost reduction). The electrical failure dynamic monitoring presents a good potential to increase the industries process reliability. Besides, the techniques also allow the tracking of mechanical components, which is an interesting tool to detect mechanical faults in machines located in places of difficult access.

In 2006, a petroleum refinery experienced an unplanned outage in its Coker Unit caused by the breakage of some rotor bars in the induction motor of the decoking pump which damaged the rotor and the stator of the motor as can be seen in the picture below. The damaged motor had the following features: Poles – 4, Rated Power – 1700 kW, Rated Voltage – 13.8 kV, Shaft Height – 500 mm, and Hazardous Area – Free zone. Although it is not possible to operate without the decoking pump, there is not a standby motor because of its high reliability and cost. Figure 26 shows the stator and rotor damages.

Figure 26. Stator and Rotor Damages

After the event, the motor was sent to be repaired, but the first information was that it would take 70 days to be fixed. Since this deadline would compromise the refinery production plan, the refinery's maintenance team started looking for a similar motor. In normal conditions, it was not possible to find a better solution, than to wait for 70 days (considering the purchase of a new motor it would take, at least, 6 months). Luckily, a motor was found in a factory with the following features: Poles – 4, Rated Power – 1656 kW, and Rated Voltage – 4.16 kV, Shaft Height – 450 mm, and Hazardous Area – Free zone.

Considering that the refining process is based on pumps and compressors, the engineers noticed that the unique parameter that should be exactly the same was the number of poles. To the others, the following analysis was done:

- Rated Power – Since the original motor does not operate at its rated power, it was possible to use the similar motor;
- Rated Voltage – the refinery had a voltage transformer in stock (4.16/13.8 kW), that could be used to supply the rated voltage to the similar motor;
- Shaft Height – the original motor shaft was higher than the similar one, but this could be solved easily by adapting the skid.

Besides, considering that the decoking pump had been installed in a non hazardous area, the similar motor completely met the requirement to be installed. Then, after a short negotiation, an agreement was made between the oil company and the motor manufacturer, where the similar motor was rented to be adapted, while the manufacturer made another motor to replace the original one. While the similar motor was in its way to the refinery, all possible and necessary electrical and mechanical work to fit this motor to the site was in process. When the similar motor arrived, the maintenance team spent only one day to replace the motor. Six days after the outage, the Coker Unit started over.

8. Cost analysis

Based on the Brazilian Petroleum Company experience reported above, in terms of costs, it is very easy to demonstrate the benefits of having an ESA system installed together with a motor management.

Considering that 1 day without production means losses of US$ 300,000.00, we would have US$ 21,000,000.00 in 70 days. However, as we found a motor to be adapted, we had just 6 days of losses (US$ 1,800,000.00). If we had an ESA System installed monitoring this motor, we could realize in advance that the motor was developing a failure. As we said before, some refineries have similar motors that could be adapted. So, in that case, it would be possible to plan the replacement, sending the motor, and making the adaptations and stopping the production for only 1 day, i.e. losses of US$ 300,000.00.

9. Conclusions

The industries currently look for products and outside services for predictive maintenance. In many cases, the outside service company or even the industrial plant predictive group make mistakes that can compromise the whole condition monitoring and failure diagnosis process. In this increasing demand for prediction technology, a specific technique referred as Electrical Signature Analysis (ESA) is calling more and more attention of industries.

Considering this context, the presented chapter intends to disseminate important concepts to guide companies that have their own predictive group or want to hire consultants or specialized service to obtain good results through general predictive maintenance practices and, especially through electrical signature analysis.

The result of the proposed discussion in this chapter is a procedure of acquisition and analysis, which is presented at the end of the chapter and intends to be a reference to be used by industries that have a plan to have MCSA as a monitoring condition tool for electrical machines.

Author details

Erik Leandro Bonaldi, Levy Ely de Lacerda de Oliveira,
Jonas Guedes Borges da Silva and Germano Lambert-Torres
PS Solutions, Brazil

Luiz Eduardo Borges da Silva
Itajuba Federal University, Brazil

Acknowledgement

The academic authors would like to express their thanks for CNPq, CAPES, FINEP and FAPEMIG for support this work.

10. References

Benbouzid, M.H. (2000). A Review of Induction Motors Signature Analysis as a Medium for Faults Detection, *IEEE Transactions on Industrial Electronics*, Vol.47, No.5, (October 2000), pp. 984-993, ISSN 0278-0046.

Bonaldi, E.L., Borges da Silva, L.E., Lambert-Torres, G. de Oliviera, L.E.L. (2003). A Rough Sets Based Classifier for Induction Motors Fault Diagnosis, *WSEAS Transactions on Systems*, Vol.2, No.2, (April 2003), pp. 320-327, ISSN 109-2777.

Bonaldi, E.L., de Oliviera, L.E.L., Lambert-Torres, G. & Borges da Silva, L.E. (2007). Proposing a Procedure for the Application of Motor Current Signature Analysis on Predictive Maintenance of Induction Motors, *Proceedings of the 20th International Congress & Exhibition on Condition Monitoring and Diagnosis Monitoring Management - COMADEM 2007*, Faro, Portugal, Jun. 13-15, 2007.

Bonnett, A.H., & Soukup, G.C. (1992). Cause and Analysis of Stator and Rotor Failures in Three-Phase Squirrel-Cage Induction Motors, *IEEE Transactions on Industrial Electronics*, Vol.28, No.4, (July/August 1992), pp. 921-937, ISSN 0278-0046.

Borges da Silva, L.E., Lambert-Torres, G., Santos, D.E., Bonaldi, E.L., de Oliveira, L.E.L. & Borges da Silva, J.G. (2009). An Application of MSCA on Predictive Maintenance of TermoPE's Induction Motors, *Revista Ciências Exatas*, Vol. 15, No. 2, (July 2009), pp. 100-108, ISSN 1516-2893.

Cardoso, A.J.M. & Saraiva, E.S. (1993). Computer-Aided Detection of Airgap Eccentricity in Operating Three-Phase Induction Motors by Park's Vectors Approach, *IEEE Transactions on Industry Applications*, Vol.29, No.5, (Sept/Oct 1993), ISSN 0093-9994.

Lambert-Torres, G., Bonaldi, E.L., Borges da Silva, L.E. & de Oliviera, L.E.L. (2003). An Intelligent Classifier for Induction Motors Fault Diagnosis, *Proceedings of the International Conference on Intelligent System Applications to Power Systems - ISAP'2003*, Paper 084, Lemnos, Greece, Aug. 31 – Sept. 3, 2003.

Lambert-Torres, G., Abe, J.M., da Silva Filho, J.I. & Martins, H.G. (2009). *Advances in Technological Applications of Logical and Intelligent Systems*, IOS Press, ISBN 978-1-58603-963-3, Amsterdam, The Netherlands.

Legowski, S.F., Sadrul Ula, A.H.M., & Trzynadlowski, A.M. (1996). Instantaneous Power as a Medium for the Signature Analysis of Induction Motors. *IEEE Transactions on Industry Applications*, Vol.32, No.4, (July/August 1996), pp. 904-909, ISSN 0093-9994.

PS Solutions. (October 2011). Predictor, Available from www.pssolucoes.com.br, visited on 22/10/2011.

Schoen, R.R., Habetler, T.G., Kamram, F. & Bartheld, R.G. (1995). Motor Bearing Damage Detection Using Stator Current Monitoring, *IEEE Transactions on Industrial Electronics*, Vol.31, No.6, (Nov/Dec 1995), pp. 1274-1279, ISSN 0278-0046.

Tavner, P.J., Ran, L., Penman, J. & Sedding, H. (1987). *Condition Monitoring of Rotating Electrical Machines*, The Institution of Engineering and Technology – IET, 2nd Edition, ISBN 978-0863417412, London, UK.

Thomson, W.T., & Fenger, M. (2001). Current Signature Analysis to Detect Induction Motor Faults, *IEEE Industry Applications Magazine*, Vol.7, No.4, (July 2001), pp. 26-34, ISSN 1077-2618.

Thorsen, O.V. & Dalva, M. (1999). Failure Identification and Analysis for High-Voltage Induction Motors in the Petrochemical Industry, *IEEE Transactions on Industry Applications*, Vol.35, No.4, (July/August 1999), pp. 810-817, ISSN 0093-9994.

Chapter 21

Rotor Cage Fault Detection in Induction Motors by Motor Current Demodulation Analysis

Ivan Jaksch

Additional information is available at the end of the chapter

http://dx.doi.org/10.5772/47811

1. Introduction

Rotor cage faults as broken rotor bars, increased bars resistance and end-ring faults can be caused by thermal stresses, due to overload, overheating and thus mechanical stresses, magnetic stresses and dynamic stresses due to shaft torques. Environmental stresses as contamination or abrasion also contributes to the rotor cage faults. The rotor cage faults can also lead to the shaft vibration and thus bearing failures and air gap dynamic eccentricity.

Various rotor cage faults detection techniques for induction motors (IM) have been proposed during the last two decades. One of these is a widely used Motor Current Signature Analysis (MCSA) representing namely the direct spectral analysis of stator current (Thomson & Fenger, 2001; Jung et.al, 2006). MCSA can be combined with other methods as stray flux detection and a radial and axial vibration analysis. MCSA is still an open research topic, namely in the region of higher harmonics.

Strongly nonstationary working conditions as start-up current analysis require the application of methods generally called Joint Time Frequency Analysis (JTFA). These methods are Short Time Fourier Transform, Continuous Wavelet Transform (Cusido et.al, 2008; Riera-Guasp, 2008), Discrete Wavelet Transform (Kia et. al., 2009), Wigner Distribution (Blödt et al., 2008), etc. The fundamental of the wavelet analysis is the stator current decomposition into a determined number of detailed and approximation components and their pattern recognition. Wavelet analysis can be combined with other methods as a torsional vibration (Kia et. al., 2009).

The Vienna monitoring method –VMM (Kral et. al, 2008) is a rotor fault detection method based on instantaneous torque evaluation determined by voltage and current models. Other introduced methods for IM rotor fault diagnostics are multivariable monitoring (Concari et.al, 2008), artificial neural networks and neural network modeling (Su & Chong, 2007), fuzzy based approach (Zidani et. al., 2008), wavelet analysis together with hidden Markov

models (Lebaroud & Clerc, 2008), pendulous oscillation of rotor magnetic field (Mirafzal & Demerdash, 2005), vibration analysis (Dorrell et al., 1977) etc. A review of diagnostic techniques has been presented in several publications (Nandi et. al., 2005; Bellini et. al., 2008; Zhang et. al., 2011).

We can see that today it is not a problem to find rotor faults. What still remains a problem is to exactly and unambiguously determine fault indicator and its fault severity with a defined measurement uncertainty under changing motor parameters - various loads and inertia. Ideally the fault indicator should be independent on IM load. The examination of the various load influence on the fault indicator changes is very important especially in the industrial applications, where the keeping the same motor loads is often difficult. It has to be known what range of parameter changes are allowed for the keeping of the fault indicator constancy. As it is not known, at repeated measurements with different fault indicators, it is not clear, if the reason is due to the varied (deteriorating) IM faults or due to IM changing parameters. What is also important is the repeatability of the measurement with the same result. The third problem is a preferably simplicity and easy implementation of the methods for practical use in industry. Introduced new demodulation methods fulfill most of these requirements.

Dynamic rotor faults of IM, namely rotor broken bars and dynamic or combined eccentricity, cause a distortion of the rotor bars current distribution, and thus they cause periodical dynamic changes related to IM rotation frequency f_r in the rotor magnetic field and consequently torque oscillation and therefore stator current modulation. The complex stator current analysis and experiments based on simultaneous amplitude and phase demodulation techniques proved that the stator current at rotor faults consists both of amplitude modulation (AM) and phase modulation (PM). AM and PM are combined into the Joint Amplitude Phase Modulation (JAPM). Amplitude and phase modulating currents are in certain relations, both in their amplitudes and mutual phases, dependent on motor load, inertia and also on IM working conditions.

Motor Current Demodulation Analysis - MCDA comes out from the fundamental principle which arises at dynamic rotor faults - IM stator current modulation. The basic idea of MCDA is to extract only those currents from the whole stator current which are directly induced and caused by rotor faults, and to investigate only these fault currents in the time and frequency domain. At health IM these currents do not exist, practically are near zero.

The demodulation is a process, how to gain back the information about the time course of modulating signal from modulated signal. Outputs of demodulation methods are, therefore, the direct time courses of modulating i.e. fault currents. The spectrum of a fault current does not contain any sideband components, fault frequencies are determined directly and only one spectral peak represents the fault indicator. The great advantage of MCDA is its easy use in industrial diagnostics.

Most of the present diagnostic methods, both for stationary and non-stationary (Joint Time-Frequency Analysis) IM working conditions, use full IM current analysis methods for rotor fault detection. Just MCDA proved the complexity of the IM current at dynamic rotor faults and therefore the dependence of fault indicators based on full IM current on IM

working conditions. It is mostly various IM loads which changes PM and great inertia or insufficient IM feeding which change an angle φ between AM and PM and therefore cause the dependence. These rotor fault indicators dependence cannot be removed.

2. The analysis of IM current and current signature at rotor faults

The widely used rotor fault detection technique - MCSA is presented in a large number of publications. This approach analyses whole IM stator current uses the spectral low and high slip pole frequency $2sf_1$ sidebands a_{APL}, a_{APH} around the supply frequency f_1 for broken bars detection (Bellini et. al., 2001). According to this theory, magnetic rotor asymmetry causes a backward rotating field and formation of a current component a_{APL} at the low sideband frequency f_1-f_{sp}. The consequent torque and speed oscillation cause the occurrence of a new component a_{APH} at the high sideband frequency f_1+f_{sp}. First, the only low sideband spectral magnitude was taken as a fault indicator for broken bars. Later a new diagnostic index was introduced as a sum of the two spectral sideband components a_{APL}+a_{APH}.

Presented theory of the spectral low a_{APL} and high a_{APH} sidebands origination and formation and broken bars detection is quite different from MCSA theory. The theory comes from general modulation principles and exactly determinates both sidebands origination including the equations for a_{APL}, a_{APH} computation.

An exact detailed analysis of the stator current content at broken bars from the view of the complex air-gap rotor electromagnetic field analysis representing simultaneous stator current AM and PM, their mutual relation and changes at different load and inertia moment, and their formation to the MCS a_{APL} and a_{APH} magnitudes has been missing so far.

2.1. Broken bars stator current modulation and its contribution to the MCS formation

Introduced theory and rotor fault analysis and diagnostics come from the basic principle when periodical changes in rotor magnetomotive force (MMF) cause the periodical changes of IM stator current amplitude and phase, and thus the stator current AM and PM.

Broken rotor bars, as an electric fault, cause the rotor asymmetry, the distortion of the rotor current distribution, rotor current pulsation and its amplitude modulation by the slip frequency f_{slip}. Rotor bars current amplitude changes are transformed to stator current on slip pole frequency f_{sp} and appears here as a stator current AM. This modulation can be interpreted as a primary modulation.

Rotor bars current amplitude changes cause the changes in force on coils moving in a magnetic field. The force can be obtained from the vector cross product of the current vector and the flux density vector $F_x = NI\ \upsilon\phi/\upsilon x$, where NI is MMF, ϕ is linked magnetic flux and x is the force direction. Subsequently, the total force on a current carrying rotor coils (bars), moving in a magnetic field, changes and electromagnetic torque oscillation appears. Torsion vibration also can appear. Oscillating torque causes periodical changes in the rotating phase angle and therefore the stator current PM. This modulation can be interpreted as a

subsequent or secondary modulation, so PM cannot originate without AM and JAPM always exists. The JAPM can be interpreted as a stator current modulation by a complex modulating vector which changes both its amplitude and phase. Angular speed oscillation as the derivation of phase oscillation also appears.

The frequency of periodical changes is a slip pole frequency f_{sp} (suffix$_{sp}$) which is independent on the number of motor poles

$$f_{sp} = pf_{slip} = psf_{sync} = ps2f_l / p = 2sf_l = 2f_l - f_r p \tag{1}$$

For better understanding of a real IM state, which comes in IM current at dynamic rotor faults and for the explanation of a_{APL} and a_{APH} origination and formation from AM and PM, the properties of AM and PM have to be firstly well known. So the basic properties of AM and PM will be firstly presented before the explanation of the real IM state - JAMP.

2.1.1. Amplitude modulation-AM

AM is clearly visible from the time course of an IM current amplitude which is not stable, but changes according to the modulating current amplitude. It can be clearly seen as the IM current time course envelope already from about 2% deep of modulation I_{spa}/I_l representing approximately 2 broken bars.

Spectrum of AM (suffix $_A$) is derived from the Euler formula $cos(\omega t)=½(exp(j\omega t)+exp(-j\omega t))$ expressing the decomposition of a harmonic signal into the pair of rotating vectors (phasors) -Fig.1. Phasors' amplitudes are the half of the original harmonic signal amplitude; one rotates positive direction, the other rotates negative direction.

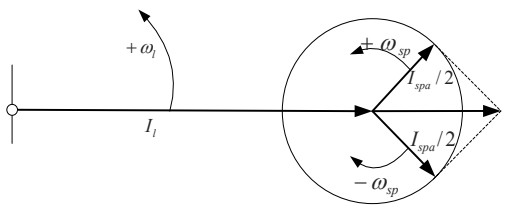

Figure 1. Vector representation of AM for broken bars

Spectra of modulated signals are always connected with two sidebands peaks around the carrier signal spectral peak. AM appears in the autospectrum of the modulated signal as three peaks: one at the carrier frequency with the magnitude equal to the amplitude of carrier signal and two sidebands spaced by modulating frequency from the carrier frequency each of them with the half amplitude of the modulating signal.

For broken bars there are two sideband components at low and high frequency $f_{L,H}$ and their low and high sidebands magnitudes a_{AL}, a_{AH} have the same size a_A which equals the half of the amplitude of the modulating current I_{spa}

$$f_{L,H} = f_l \pm f_{sp} \qquad a_A = a_{AL} = a_{AH} = I_{spa} / 2 \tag{2}$$

2.1.2. Phase modulation-PM

Unlike AM, PM is not observable from the stator current time course at so small modulation indexes to 0.15. PM can be visible as stator current time course compression and decompression from modulation indexes greater than 2, which are approximately 10 times higher than the usual modulation indexes at broken bars.

The spectrum of phase modulation (suffix $_P$) is dependent on the modulation index size. If the modulation index is greater than *1*, the PM spectrum consists of many side components, if it is lower than *0.4*, the spectrum contains only a few side components. The spectral magnitudes computation of phase-modulated signals requires the use of the Bessel functions J_i, $i=1, 2,..,M$ (Randall, 1987).

The real modulation indexes at rotor faults, expressed by I_{spp}, are very low about to max. *0.15* at large rotor faults and in this case the stator current autospectrum contains only two significant sideband components $J_1(I_{spp})$ with the same magnitudes $a_{PL,H} = a_P$ equal to the half of the I_{spp} multiplied by phase current amplitude I_l. (Bessel functions are not needed).

$$f_{L,H} = f_l \pm f_{sp} \qquad a_P = a_{PL} = a_{PH} = I_l I_{spp} / 2 \tag{3}$$

The result is that the autospectrum of PM current looks the same as the autospectrum of AM current. But the substantial difference is in the initial phases of sidebands magnitudes at $f_l - f_{sp}$ and $f_l + f_{sp}$ frequencies, Table 1., 2nd row, bold, and Fig.2. Spectral sideband magnitudes a_{PL}, a_{PH} increase both owing to I_{spp} and also owing to I_l, unlike at AM, see (2).

Component frequency	f_l-2f_{sp}	f_l-f_{sp}	f_l	f_l+f_{sp}	f_l+2f_{sp}
Initial phase	$\pi-2\phi$	$\boldsymbol{\pi/2-\varphi}$	0	$\boldsymbol{\pi/2+\varphi}$	$\pi+2\varphi$
Component amplitude	$J_2(I_{spp})$	$J_1(I_{spp})$	$J_0(I_{spp})$	$J_1(I_{spp})$	$J_2(I_{spp})$

Table 1. Frequencies and phases of the first 2 sidebands components of PM

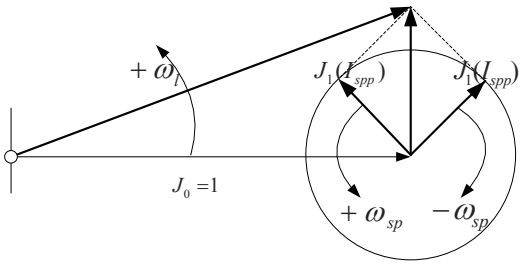

Figure 2. Vector representation of PM for broken bars

Table 1 and Fig.2 show that the initial phase of Bessel function J_1 is $\pi/2$ so the resulting vector of PM is perpendicular to the resulting vector of AM. The initial phase shift for the component at f_l+f_{sp} is the original phase shift $+\varphi$ of the modulating signal, the initial phase for the component at f_l+f_{sp} is $-\varphi$ (a highlight and bold in Table 1, middle row).

2.1.3. JAPM and MCS–the real motor state at broken bars

This type of modulation expresses exactly the real motor state at broken bars. Both AM and PM have the same frequencies and their amplitudes and phase shifts between them are in certain relations depending on IM load and inertia. Providing sinusoidal currents, the IM current of healthy motor $i_a=I_l \cos(\omega_l t)$ changes at rotor broken bars to

$$i_a = \left(I_l + I_{spa}\cos\omega_{sp}t\right)\cos(\omega_l t - I_{spp}\cos(\omega_{sp}t + \varphi)) \tag{4}$$

which contains both AM and PM. Amplitude modulating current $i_{AM} = I_{spa}\cos\omega_{sp}t$, phase modulating current $i_{PM} = -I_{spp}\cos(\omega_{sp}t + \varphi)$. The term I_{spa}/I_l represents the deep of modulation of AM and I_{spp} represents the modulation index of PM.

At low inertia and normal and stable working conditions the AM and PM currents have exactly opposite phases $\varphi_0=\pi$, $\varphi=0$. This results from the IM torque-speed characteristic, where torque changes induced by MMF changes induce opposite changes in speed.

The necessary condition for both MCS low a_{APL} and high a_{APH} autospectral magnitudes equality is the mutual perpendicularity of vectors forming AM and PM, Fig.1, 2 and Table 1. It occurs only in the case of exactly coincident or exactly opposite phases of AM and PM.

Since the necessary condition is fulfilled, the resulting low a_{APL} and high a_{APH} autospectral sideband magnitudes of JAPM have the same size given by (5).

$$a_{APL} = a_{APH} = \sqrt{a_A^2 + a_P^2} \tag{5}$$

Unfortunately from sideband magnitudes a_{APL}, a_{APH}, which are the results of the widely used MCS, the contribution of AM and PM cannot be found out. Only demodulation techniques can find them.

Increasing IM load causes the increase of IM current I_l. Previous investigations and experiments (Jaksch & Zalud, 2010) proved also an increasing oscillation of rotor magnetic field at f_{sp} with increasing load which means the increase of I_{spp}. It means consequently the increase of a_{APL}, a_{APH} according to (3) at the same rotor fault size (dash line in Fig.3). The result is that PM is the main reason of a_{APL}, a_{APH} dependence on IM load.

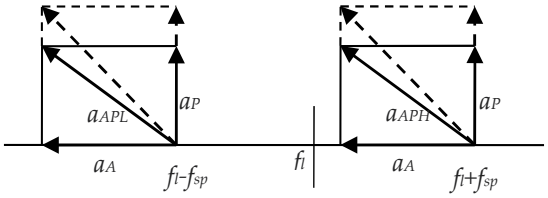

Figure 3. The formation of MCS a_{APL}, a_{APH} at broken bars from JAPM, φ=0, increasing motor load means the increase of PM –dash line.

Generally the inertia influences dynamic behavior of systems. Great inertia causes the increase of the mechanical time constant of the motor rotating system and therefore the delay $-\varphi$ (φ <0) of PM behind AM on f_{sp}. IM current spectrum symmetry and a_{APL}, a_{APH} equality disappears. The initial phase shift for the positive component at $f_l + f_{sp}$ frequency is $+\varphi$, see bold in Table I, and therefore a_{APH} decreases, the initial phases shift for the negative component at $f_l - f_{sp}$ is $-\varphi$ and therefore the a_{APL} increases -Fig.4. The angle between AM and PM modulation vectors is not $\pi/2$, (5) is not valid and the resulting a_{APL}, a_{APH}, are the vector sum of AM and PM rotating vectors.

Spectral magnitudes $a_{APL,H}$ of MCS can be computed according to the modified cosine low.

$$a_{APL,H} = \sqrt{a_A^2 + a_P^2 - 2a_A a_P \sin(\mp\varphi)} \tag{6}$$

For φ=0 this general equation for MCS computation, equation (6) changes to equation (5).

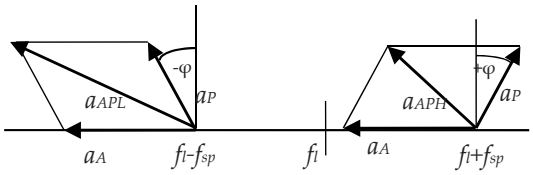

Figure 4. The formation of MCS a_{APL}, a_{APH} at broken bars from JAPM at great inertia, φ= -π/6

In the case of the extremely large inertia the shift between AM and PM is almost φ= -π/2. The result is that only the low spectral sideband component appears, see (6), with and the right sideband component is almost zero. The result is only theoretical.

The same comes in the case of overloaded and insufficiently fed IM by the voltage substantially lower than nominal AC voltage, which can be named as "abnormal working condition", when PM cannot follow AM and φ<0. In all other cases of normal IM working condition a_{APL}, a_{APH} should be the same size, in the range of possible Digital signal processing (DSP) errors.

Based on the JAMP the phenomena which appear in dynamic motor modes like start-up or breaking and their formation to a_{APL} and a_{APH} can be explained.

2.2. Dynamic eccentricity IM current modulation

The rotor cage faults can also lead to the mechanical stresses, shaft torques, bearing failures and therefore air gap dynamic eccentricity (Joksimovic, 2005; Drif & Cardoso, 2008). So the dynamic eccentricity, as a mechanical fault, closely relates to the rotor cage faults. Dynamic eccentricity is the condition of the unequal air gap between the stator and rotor caused namely by loose or bent rotor, worn bearing etc. IM current analysis is the base method, but the vibration as the cause of unbalance and the torsional vibration as the cause of the torque oscillation can be also performed as supporting method, but IM current related detection

methods in most cases give very good results. Relative dynamic eccentricity is defined as the ratio of the difference between the rotor and the stator center to the difference between the stator and the rotor radius. The values of dynamic eccentricity are 0-1 or 0-100%.

Dynamic or combined eccentricity and subsequently the air gap alternation changes the rotor electromagnetic field ones per IM revolution, so the modulating frequency is the rotation frequency f_r (suffix $_r$). IM spectrum contains two sidebands around f_l.

$$f_{L,H} = f_l \pm f_r \tag{7}$$

Spectrum of demodulated current contains peaks on direct frequencies f_r. The air gap changes do not contain stepping changes and the change usually pass subsequently during one revolution, so modulating current is often almost harmonic and contains only small higher harmonics, unlike modulating current for broken bars.

Providing sinusoidal currents, the motor current of healthy motor $i_a=I_l \cos(\omega_l t)$ changes at rotor dynamic eccentricity to

$$i_a = \left(I_l + I_{ra}\cos\omega_r t\right)\cos(\omega_l t - I_{rp}\cos(\omega_r t)) \tag{8}$$

which contains both AM and PM.

2.3. The influence of the time varying load

Until now the modulations caused by the internal IM rotor faults were solved providing IM different, but constant load when MCDA spectrum contains two significant peaks on f_{sp} and f_r , see Fig.6. In the case of the external periodical harmonic time varying load, which varies with the frequency $f_{load} < f_l$, both additional AM and PM of IM current arise on the f_{load} frequency. It can come e.g. in the case when IM drives machines with various machine cycles e.g. textile machines, machine tools etc. (In the case of the speed reducing devices as gearbox transmissions, the gear-ratio has to be counted for f_{load} determination).

In the IM full current spectrum - MCS two additional spectral sidebands peaks appear on frequencies $f_l \pm f_{load}$. In MCDA spectrum the time varying load appears as a one spectral peak on f_{load} with the magnitude proportional to a load torque difference which can be expressed as an I_{load}. So together 3 significant spectral peaks on f_{sp}, f_r and f_{load} appear in MCDA spectrum of IM with rotor faults. The AM can be also observed in the time course of IM current as the stator current envelope or in the time course of amplitude demodulated current.

If f_{load} equals exactly f_{sp} or f_r the rotor faults diagnostics is not correct because the resulting spectral magnitudes are the vector sum of the corresponding modulating amplitudes. The situation when $f_{load}=f_r$ can come when IM directly drives a machine with uneven load during one revolution e.g. a cam mounted on the main shaft. But practically it is a minimal probability that f_{load} equals f_{sp} or f_r. The minimal difference between f_{load} and f_{sp} or f_r is at Hanning window approximately 4 discrete step Δf. Usually used acquisition time is $T= 4s$, $\Delta f=1/T= 0.25$ Hz, so a minimal difference between external f_{load} and rotor faults frequencies f_{sp},

f_r is roughly 1Hz for the rotor fault diagnostic not influenced by the time varying load. The f_{sp} computation from f_r (1), enables the differentiation and subsequently the omission of an additional disturbing spectral peak on f_{load}.

Small external time varying load can be also caused by the fault of IM driven devices as a gearbox. In MCDA spectrum another peak appears and by the allocation of this peak frequency to the gearbox relevant mechanism frequency, the device fault can be identified.

3. Demodulation methods for rotor faults

Generally, the demodulation methods extract the original AM and PM signals using special computation methods. Now the demodulated signals are original modulating signals.

Demodulation methods can be used without precarious presumption whether the signal is modulated or not and in the case of no modulation, the demodulation results are zeros (PM) or constants (AM) and by removing DC also zeros.

For the determination of the modulated signal instantaneous amplitude and phase, a complex analytical signal has to be defined and created. An analytical complex signal created by mathematical formula is the base for the demodulation analysis. The most used methods are Hilbert transform, Hilbert-Huang transform or quadrate mixing. For 3-phase motors rotor faults a new method based on the space transform was developed.

The rotor fault amplitude demodulation extracts the original AM current. The AM current appears in stator current as an envelope of this current -Fig.5. Therefore the amplitude demodulation is known as an envelope analysis (Jaksch, 2003). It is the base for dynamic rotor fault diagnostics.

At broken bars, phase demodulation extracts PM current I_{spp} [A] which, as an argument of harmonic function (4), really represents the phase angle ripple or phase swinging [rad]. The phase demodulation gives the time course of the instantaneous swinging angle or instantaneous angular speed and represents a huge tool for the research of the rotor magnetic field oscillation, sensor-less angular speed, speed variation or other irregularities.

The demodulation analysis should be used for band pass filtered signals with the center in a carrier frequency and span corresponding to the maximal modulating frequency. Spectrum of demodulated current outside this bandwidth is shifted by a carrier frequency towards to the low frequencies. For IM rotor faults the carrier frequency is usually a supply frequency f_1 and the maximal modulating frequency is f_r, so the basic bandwidth $0\text{-}2f_1$ is suitable. In the case when analog bandwidth $0\text{-}2f_1$ cannot be kept it is possible to use higher bandwidths, but Shannon sampling theorem has to be strictly kept and demodulated spectrum must be evaluated only in the range of $0\text{-}f_1$ because for higher frequencies is not valid.

Higher order harmonics of supply current and also modulating broken bar current should appear as sideband components at frequencies $f_{k,l} = kf_1 \pm 2ls f_1$, $k=3,5,7$, $l= 1,2,3$ where k represents the index for stator current harmonics and l represents the index for broken bar

sideband current harmonics. Because of the interaction of time harmonics with a space harmonics, a saturation related permeance harmonics together with phase shifts of AM and PM means that some sidebands harmonics are suppressed and only certain ones can appear, so the above introduced formula is not generally valid.

Demodulation in the region of higher *k*-harmonics of the supply frequency requires the shift of the supply carrier frequency kf_1 to zero before the demodulation. It means the spectral frequency resolution Δf increasing which is often called Band Selectable Fourier Analysis (BSFA) or Zoom. Dynamic signal analyzers are equipped with this function (zoom mode) and a maximal Δf = 1mHz. However, this analysis has a little practical sense, because of above mentioned problems with higher order harmonics. In addition the modulating currents there usually have smaller amplitudes.

3.1. The demodulation using Hilbert transformation

The Hilbert transform (Bendat, 1989) is a well-known tool which enables to create an artificial complex signal $H(t)= x(t)+jy(t)$, called analytical signal, from a real input signal $x(t)$. The real part $x(t)$ of the analytical signal $H(t)$ is the original signal – stator current, the imaginary part $jy(t)$ represents the Hilbert transform of a real part $x(t)$. The absolute value $magH(t)$ representing amplitude demodulation and the phase $\beta(t)$ representing phase demodulation can be computed according to (9), (10).

$$magH(t) = \sqrt{x^2(t) + y^2(t)} \tag{9}$$

$$\beta(t) = \arctan(y(t) / x(t)) \quad in < -\pi, \pi > \tag{10}$$

The amplitude demodulation computation is quite easy and can be used for continual monitoring and diagnostics in real time.

Phase determination $\beta(t)$ [rad] from a complex number position holds only in the range $<-\pi, \pi>$ and if the phase overlaps these limits, it is necessary to unwrap it and moreover to remove the phase trend component which increases by2π every revolution with the increase of the common phase carrier signal (Randall, 1987). The computation of phase demodulation is a little difficult comparing to amplitude demodulation, but generally there is usually no problem with the phase demodulation computation.

3.2. The demodulation using space transformation

The space (Park) transform, based on the physical motor model, is used primarily for the motor vector control. A three phase i_a, i_b, i_c, $i_a(t)=I_1 \cos(\omega t)$ system is expressed in one space current vector $\boldsymbol{i}= K_s (i_a + a\, i_b + a^2 i_c)$, $a= e^{j2\pi/3}$ projected to the complex *d-q* plane (11).

From the 3 possible choices of K_s: $K_s = 1$ - amplitude invariance, $K_s = sqrt(2/3)$- power invariance, K_s=2/3 is used. In this case the additional recomputation coefficient between phase currents and transformed currents does not have to be used.

$$i_d(t) = (2/3)i_a(t) - (1/3)i_b(t) - (1/3)i_c(t)$$
$$i_q(t) = (\sqrt{3}/3)i_b(t) - (\sqrt{3}/3)i_c(t) \quad (11)$$

Space transform was firstly also used for the demodulation (Jaksch, 2003). From the viewpoint of the means necessary for the demodulation process, space vector $P(t)=i_d(t)+ji_q(t)$ represents a complex analytical signal computed from three three currents i_a, i_b, i_c similarly like the Hilbert transform creates the artificial complex signal $H(t)$ from one phase current.

The absolute value $magP(t)=sqrt(i_d^2(t)+i_q^2(t))$ forms the amplitude demodulation, $\beta(t) = arctan\ (i_q(t)/\ i_d\ (t))$ forms the phase demodulation.

3.3. The comparison of both demodulation methods

The space transform requires 3 currents measurement, but only simple computation (11) and no other transformation for the complex analytical signal determination. On the contrary Hilbert transform needs only one current measurement, but $jy(t)$ computation.

The space transform creates the analytical signal from 3 currents. In order to obtain the same sizes of fault indicators as from Hilbert transform, (11), using K_s=2/3 must be kept.

Small differences between Hilbert and space transforms can occur in the following cases:

- The violation of the exact phase shift $a=e^{j2\pi/3}$ between IM phase currents (space transform supposes exact shift $2\pi/3$).
- Power feeding voltage unbalance or great stator fault, which can cause greater IM currents unbalance.

The maximum error should not be greater than in the range of several percent. The experiment showed - see Table II., Table III, I_{spaH}, I_{spaP} that the differences are up to 5 %.

Amplitude demodulation can be implemented also by the other techniques resulting also from the three phase IM feeding system as an apparent power magnitude or a squared stator current space vector magnitude. However these methods are more complicated than the space transformation method and in addition the results of these methods are in units and dimensions which are not comparable with the Hilbert transform results.

4. Simulation results

Various simulations have been performed. The main aim of the simulation was the verification of (5), (6) for the IM current MCS - a_{APL}, a_{APH} computation, namely the influence of angle φ on the sizes of a_{APL}, a_{APH}. The verification of the equality of MCDA fault indicators (lower window in Fig. 5) with input data values I_{spa}, I_{ra} also has been performed.

As it was previously derived in the section 2, the IM current of healthy motor $i_a=I_l\ cos(\omega_l t)$ changes at dynamic rotor faults - rotor broken bars and dynamic eccentricity to

$$i_a = \left(I_l + I_{spa}\cos\omega_{sp}t + I_{ra}\cos\omega_r t\right)\cos(\omega_l t - I_{spp}\cos(\omega_{sp}t + \varphi) - I_{rp}\cos(\omega_r t)) \quad (12)$$

Input data for the simulation result from (12). Simulation values of I_l, I_{spa}, I_{spp}, I_{ra}, I_{rp}, φ start from the measurement, but various values can also be used. Other data processing is the same as in experiments. Hilbert transform, (9), (10) was used for the IM current amplitude and phase demodulation. The values for a_{APL}, a_{APH} (2nd window in Fig.5) were compared to the values computed from (3),(6). Full identity with the theory was found.

The simulation was also used for the case where angle φ is positive and $a_{APL} < a_{APH}$. But this IM state is not stable and can come only in IM dynamic regime.

Simulation results are depicted in Fig.5. Note that the time course of amplitude demodulated current follows the envelope of IM current – compare the window 3 to the window 1. Time course of amplitude and phase demodulation (windows 3, 4) shows small ripple at the beginning - t=0, given by nonsequenced modulating current in time window.

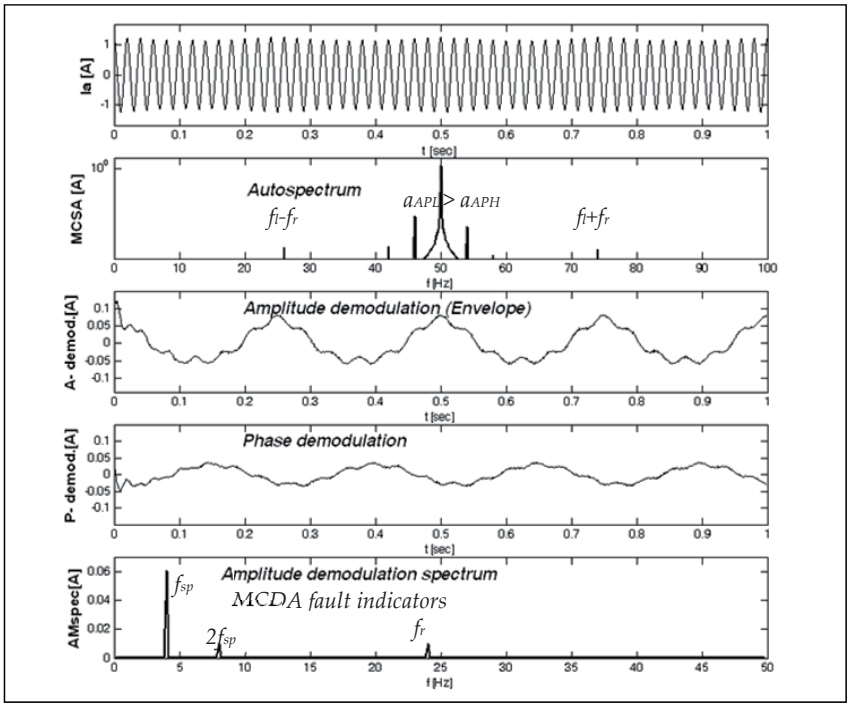

Figure 5. The demodulation analysis of stator current, 4-poles motor 0.75 kW, 2 broken bars, great inertia - φ <0, low dynamic eccentricity. Simulation results.

5. Experimental results

The main aim of the experiments was to verify the introduced theory of JAPM, to verify the both fault indicators I_{spa}, I_{ra} changes at different IM load and to verify the influence of the time varying load.

Two sorts of IM were used for the experiments.

The first IM was SIEMENS type 1LA7083-2AA10, 1.1 kW, two-pole, rated revolutions 2850 min^{-1}, I_{nom}=2.4A, n_{rb} =23, air gap dimension=0.25 mm, health motor, 1 interrupted rotor bar and 2 contiguous interrupted rotor bars, both 3 rotors were balanced with factory set-up dynamic eccentricity (setting the exact value of dynamic eccentricity is at so small air gap very difficult). The 2nd IM was SIEMENS type 1LA 7083-4AA10, 0.75 kW, four-pole motor, I_{nom} = 1.8A, n_{rb} =26, balanced rotor and rotor with 2 contiguous interrupted rotor bars.

Various motors and fault rotors used in experiments were manufactured directly at Siemens Electromotor. Motors were tested at 25%, 50%, 75% and 85% of the full load according to the motor load record from Siemens. The changes in the broken bar fault indicator I_{spa} was also tested in the low load range from no load to 20% of full load.

The experiments were based on Bruel&Kjaer PULSE 20 bits dynamic signal analyzer (DSA) based on the frequency filtration and decimation principle. All channels are sampled simultaneously. FFT analyzer was set on the base band mode, frequency span 100Hz, 400 frequency lines, Δf =0.25Hz, Hanning window, continuous RMS exponential averaging with 75% overlapping. For the experiment of I_{spa} changes at very low load the measuring time T= 32s, Δf =0.03125Hz was used.

To find out the possible differences in both introduced demodulation methods, both Hilbert and space transform were simultaneously evaluated in the real time.

The experiments results were verified by 16 channels PC measurement system based on two 8 channels, 24-bit DSA NI 4472B from National Instruments setting in the lowest possible frequency range 1kHz.

To obtain the maximal measurement accuracy the possible errors in Digital Signal Processing (DSP) should be avoided. Sampling theorem with full agreement between the sampling frequency and surveyed analog frequency band should be strictly kept. At the violation of sampling theorem, signal frequencies higher than Nyquist frequency f_N are tilted - masked to the basic frequency region from $0\text{-}f_N$ and they can create there aliasing frequencies or interfere with regular frequencies, changing their amplitudes. Masking can come through many higher bands of the sampling frequency. Unlike dynamic signal analyzers, simple PC cards and scopes are usually not equipped with anti aliasing filters.

The measurement acquisition time T should be optimally set. Spectral frequency resolution Δf is a reciprocal value of the acquisition window T, $\Delta f = 1/T$.

A great DSP error, both in frequency and magnitude, occurs if the analog frequency of the examined signal is exactly in the centre of Δf. In the case of a rectangular window, the spectral magnitude decline is $sinc(\pi/2)=2/\pi=0.636=-3.92\ dB$, representing 36% fault in magnitude! In the case of Hanning window the decline is $(3/\pi - 1/(3\pi))=0.848=-1.43\ dB$. If the low analog sideband frequency $f_1\text{-}f_{sp}$ is nearer to the discrete spectral frequency than the high sideband frequency f_1+f_{sp}, the a_{APL} can be higher than a_{APH} and vice versa. The optimal acquisition time should be longer than 1sec. e.g. 4sec. with Δf = 0.25Hz. In the case of very low load, the minimal acquisition time 8 sec with Δf = 0.125Hz can be used for the accurate f_{sp} detection and for the decrease of DSP errors probability.

Spectrum averaging, which lowers stator current non-stationary errors, should be always used for the error minimization. FFT computation time is substantially shorter than the acquisition time, so the start of a new acquisition and a new averaging can start earlier than the end of the previous acquisition time. This process is called overlapping. It is expressed in percent of the acquisition time in the range of 0% - no overlapping- to max, when the new acquisition starts immediately at the end of previous FFT. The overlapping implementation (programming) is easy. Overlapping more than 50% is recommended.

Spectrum of demodulated current does not contain any sidebands components, it is transparent and easy readable and only one simple spectral peak is the fault indicator.

The fault indicator I_{spa} [A] for broken bars is the amplitude of the amplitude modulating current on fault frequency f_{sp} so the spectral magnitude of amplitude demodulated IM current on f_{sp}, see Fig.6, 4rd window from the top. The fault indicator I_{ra} [A] for dynamic eccentricity is the amplitude of the amplitude modulating current on fault frequency f_r so the spectral magnitude of amplitude demodulated IM current on f_r, Fig.6, 4rd window.

Fault indicators clearly show the rotor faults but do not show the real fault severity. I_{spa} and I_{ra} amplitudes considerably differ with the IM power.

Fault severity dimensionless coefficients $k_{sp,}$ k_r [%] are fault indicators normalized by a constant value - motor rated current I_{nom}

$$k_{sp} = I_{spa} / I_{nom} \tag{13}$$

$$k_r = I_{ra} / I_{nom} \tag{14}$$

where fault indicators I_{spa}, I_{ra} are expressed in RMS.

In order to keep the independence of fault severity coefficients of the different load, the normalizing value must be a constant. Therefore the coefficients $k_{sp,}$ k_r as the basic evaluating tool for the assessment of fault severity and for the state of rotor bars was suggested.

Five various experiments, presented in paragraphs 5.1 to 5.5, covering different IM states, time varying load and IM energized from inverters were performed.

5.1. The results of MCDA fault indicators for broken bars at different IM load

The complex stator current analysis using simultaneous amplitude and phase demodulation of the two-pole IM is depicted in Fig. 6 – individual windows from above: stator current autospectrum i.e. MCS, AM fault current extracted from the stator current by the amplitude demodulation (9), PM fault current extracted from the stator current by the phase demodulation (10). Corresponding spectra are depicted in the 4th and 5th windows. The time courses of AM and also PM clearly show fault currents with 2 dominating frequencies f_{sp} and f_r which are better seen in the corresponding spectra. It is clearly seen that the phases of AM and PM at f_{sp} are exactly opposite, compare 2nd window to 3rd window from the top.

MCDA fault indicators are depicted in 4th window from the top.

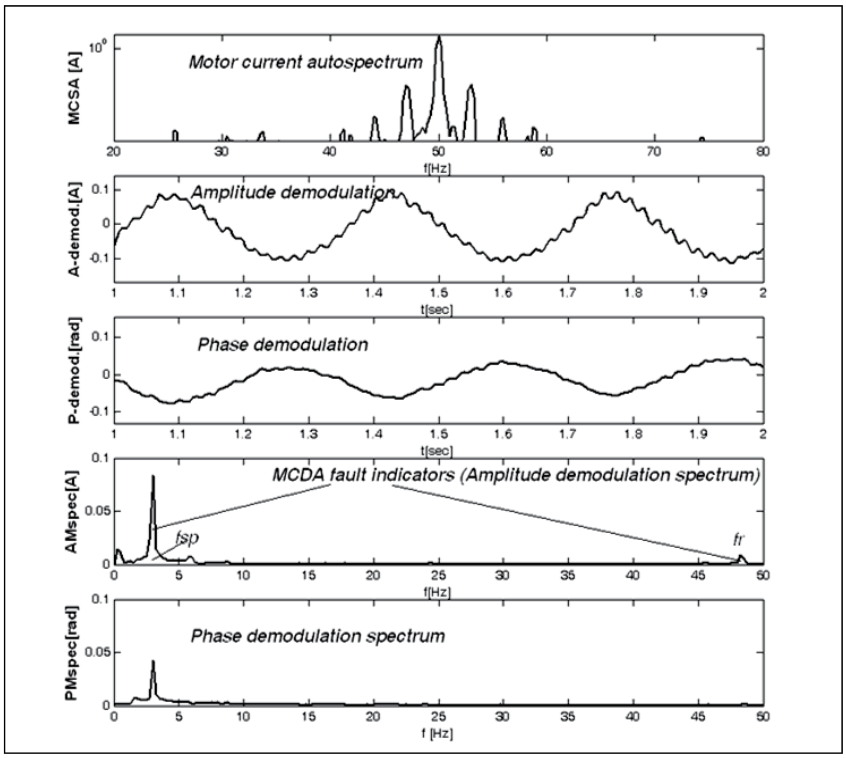

Figure 6. Complex demodulation analysis of IM current, 2-poles 1.1.kW motor, 75% of full load

Demodulation methods suppress large I_1 and therefore the relatively accurate linear scale for spectrum can be used, but for the observation of higher harmonics of f_{sp} a logarithmic scale also can be used.

Equation (5) which pays only under steady conditions and low inertia, was verified. The full agreement with the theory of a_{APL} and a_{APH} equality was found in the range of possible a_{APL}, a_{APH} variations, which can be in the range of ± 2.5dB.

There are two reasons for the a_{APL} and a_{APH} variation:

1. The non-stationarity of IM current. The rotor analog current is not a fully stationary signal and therefore the phase shift φ between AM and PM may not be exactly zero and due to small dynamic changes it can oscillate around zero and therefore causes changes in a_{APL} and a_{APH} according to (6). Linear or exponential spectrum averaging lowers this error.
2. DSP errors. DSP errors come owing to the finite Δf which was described in detail in the previous part of this section 5.

The shortened experimental results are briefly summarized in Table 2 (suffix$_H$ for the demodulation using Hilbert transform, suffix$_P$ for the demodulation using space transform) for 2-pole motors and Table 3 for 4-pole motors.

Motor state		25% load	50% load	75% load	85% load
2-poles	f_r [Hz]	48.95	48.6	48.1	47.6
1.1.kW	f_{sp} [Hz]	1.99	2.8	3.8	4.62
Health	I_{spaP} [mA]	9.4	9.5	9.3	8.5
motor	I_{spaH} [mA]	9.5	9.6	9.6	8.2
	k_{sp} [%]	0.28	0.29	0.28	0.25
1	I_{spaP} [mA]	35	40	39	39
interrupted	I_{spaH} [mA]	36	41	40	39
rotor bar	k_{sp}[%]	1.11	1.28	1.26	1.25
2 contin.	I_{spaP} [mA]	69	78	79	77
interrupted	I_{spaH} [mA]	67	75	77	76
rotor bars	k_{sp}[%]	1.93	1.98	1.95	2.01
Dynamic ecc.	I_{raP}[mA]	3.9	3.9	3.9	3.5
Balanced	I_{raH}[mA]	3.8	3.9	4.1	3.3
rotor	k_r[%]	0.15	0.15	0.16	0.13

Table 2. Fault Indicators and fault severity coefficients for broken bars and dynamic eccentricity, Hilbert and Space Transforms, 2- poles IM

Motor state		25% load	50% load	75% load	85% load
4- poles	f_r [Hz]	24.56	24.41	24.21	24.12
0.75 kW	f_{sp} [Hz]	1.73	2.3	3.1	3.45
Health	I_{spaP} [mA]	3.3	3.4	3.4	3.3
motor	I_{spaH} [mA]	3.4	3.3	3.4	3.2
	k_{sp} [%]	0.18	0.18	0.18	0.17
2 contin.	I_{spaP} [mA]	37	41	43	42
interrupted	I_{spaH} [mA]	38	42	43	41
Rotor bars	k_{sp}[%]	1.46	1.68	1.70	1.68
Balanced	I_{raP}[mA]	5.1	5.4	5.3	4.9
rotor	I_{raH}[mA]	5.2	5.5	5.4	4.9
	k_r[%]	0.28	0.28	0.27	0.26

Table 3. Fault Indicators and fault severity coefficients for broken bars and dynamic eccentricity, Hilbert and Space Transforms, 4- poles IM

5.1.1. The experimental results discussion

The experiments proved the correctness of JAPM theory and the correctness of the used demodulation techniques.

The experiments show that broken bar AM is almost insensitive to the motor load. The I_{spa} changes are in the range of 11% within the interval between 25 – 85% and in the range of 7 % in the interval 50 – 85%. The same holds for the fault severity coefficient k_{sp} because the denominator in (13) is a constant value. The values of fault indicator for 2 continuous rotor bars are almost twice greater then indicators for 1 broken bar.

At no load and at low load below 20 % of full load I_{spa} decreases- see Table 5. Therefore for the industrial diagnostics the recommended load range is from 20% of load to the full load. For more accurate diagnostics, the range from 25% of load to the full load is recommended.

Fault severity coefficient k_{sp} for 2 broken bars at 4-poles motor are little smaller in comparison with 2-poles motor owing to a greater number of rotor bars n_{rb} - 26 on 23.

Healthy motor shows some residual modulation, due to irregularities in rotor bars layout, but k_{sp} were not at all measurements greater than 0.3 %.

The acceptable limits for k_{sp}, should be experimentally stated for various motor types because they can differ. Namely the sizes of k_{sp} for large IM can have different acceptable limits.

The values of fault severity coefficient k_r for dynamic eccentricity slightly decrease with increasing load. Over the 85% of full load the decrease is slightly greater. The values of I_{ra} at a factory balanced rotor are still sufficient for a sensorless rotor electromagnetic field speed and speed irregularities measurement (Jaksch & Zalud, 2010). PM for rotor eccentricity slightly decreases with increasing load unlike PM for broken bars.

Two introduced demodulation methods for dynamic rotor fault detection - Hilbert and space transforms - give the same results and both can be used for rotor fault diagnostic. Both measurement systems - Bruel&Kjaer PULSE and NI 4472B give the same fault indicators.

5.2. The comparison of AM and PM at different loads

The second experiment examined the spectral magnitudes of amplitude and phase demodulated IM current on f_{sp} at different loads, together with the comparison of the MCSA low sideband a_{APL} on f_1-f_{sp}. The results are depicted in Fig.7 -9 and summarized in Table 4.

2-poles IM, 1.1 kW 2 broken bars	25% load	50% load	75% load	85% load
AM - MCDA fault indicator I_{spa} [mA]	70	77	78	78
PM [mrad]	24	33	44	49
Low sideband a_{APL} [mA]	36	44	46	48

Table 4. AM and PM, 2 broken bars, at different IM load in comparison to low sideband a_{APL}

The experiment proved the theory that PM substantially increases with increasing load (2nd row in Table 4 and peaks in circles on f_{sp} in lower window in Fig.7 to Fig.9).

PM increases 2.2 times within the interval between 25 - 85%. The increase of PM spectral magnitude a_P is caused both by I_1 increase at increasing load and also by I_{spp} increase, (3). It is the real cause of MCS fault indicators a_{APL} and a_{APH} increasing with increasing load, Fig.3 and (5).

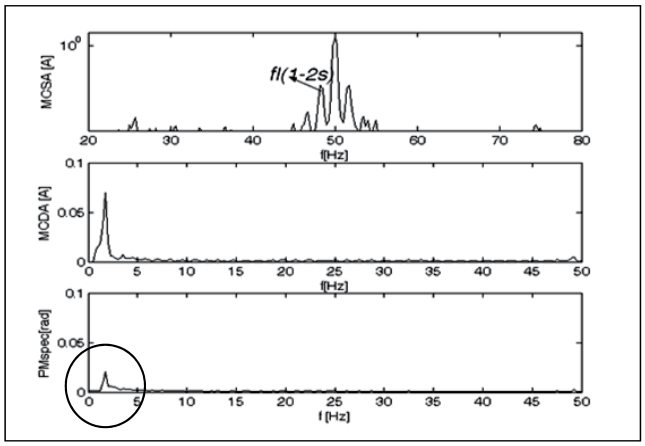

Figure 7. IM spectrum, spectrum of amplitude and phase demodulated current, 25% of full load

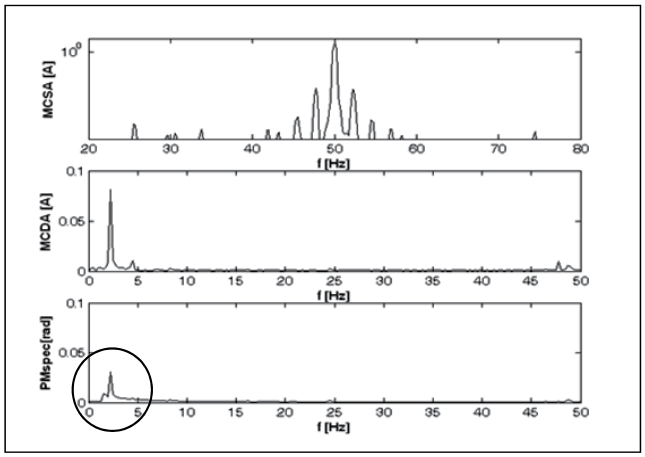

Figure 8. IM spectrum, spectrum of amplitude and phase demodulated current, 50% of full load

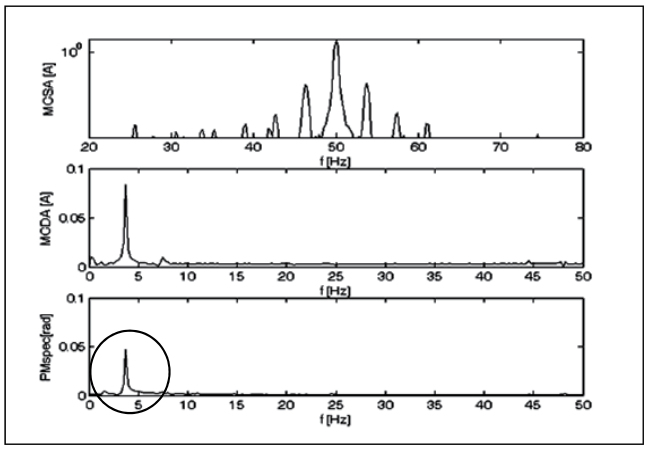

Figure 9. IM spectrum, spectrum of amplitude and phase demodulated current, 85% of full load

5.3. The analysis of indicator I_{spa} at very low load from no load to 20 % of full load

The 3rd experiment analyses the changes of I_{spa} in the range of no load to 20 % of full load. Table 5 shows the MCDA broken bars fault indicator I_{spa} decline under 20% of full load. For very low load at s=0.44%, f_{sp}=0.44 Hz the I_{spa} for 2 broken bars decreases to I_{spa}=31mA, which is approximately the half of its nominal value and it corresponds to I_{spa} for 1 broken bar (Table 2), so great confusion in broken bar diagnostics may come.

s[%]	0.21	0.37	0.44	0.69	0.94	1.16	1.37
f_{sp} [Hz]	0.21	0.37	0.44	0.69	0.94	1.16	1.37
I_{spaH} [mA]	19	25	31	37	47	56	69

Table 5. I_{spa} changes from no load to 20% of full load, 2 broken bars, 1.1.kW IM

The decrease of I_{spp} representing PM, and therefore the decrease of MCSA fault indicators a_{APL}, a_{APH} under 20% are substantially faster than the decrease of MCDA fault indicator I_{spa} (Fig.7–Fig.9, PM in circles).

5.4. IM rotor fault diagnostics at time varying load

The aim of 4th experiment was to verify presented theory of the time varying load and its influence on MCDA fault indicator I_{spa}. The time varying load frequency f_{load} = 4 Hz was chosen very near to the broken bars fault indicator frequency f_{sp} =1.9 Hz.

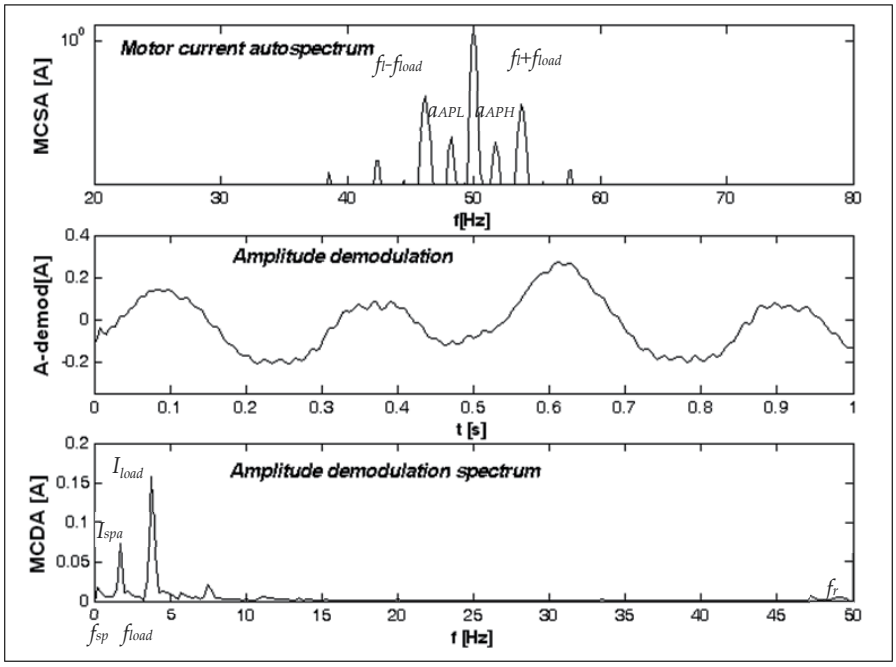

Figure 10. Windows from above: MCS, time course of amplitude demodulated current, and its MCDA spectrum, 25% of full load.

Experimental results are depicted in Fig.10. Additional two new spectral sidebands appear on frequencies $f_1 \pm f_{load}$ in MCSA spectrum-upper window and one new spectral peak appears on f_{load} in MCDA spectrum –lower window.

The time course of amplitude demodulated current, so the time course of amplitude modulating (i.e. fault) current is depicted in the middle window. The sum of three harmonic with the fundamental amplitudes I_{spa}, I_{load} and I_r and corresponding frequencies f_{sp}, f_{load} and small ripple from f_r is clearly visible.

The broken bar fault indicator I_{spa} did not change its amplitude (compare with Fig.7). The important conclusion is that the size of MCDA fault indicator I_{spa} is not influenced by the time varying load.

5.5. IM energized from inverters

The last experiment examined two-pole IM with 2 broken bars energized from inverters. Two PWM open-loop inverters were used. The measurements were made at low inertia and at a stable motor load.

In the first measurement, an inverter was properly rated. In this case, the results correspond to the results for IMs energized from line. The MCS $a_{APL} = a_{APH}$ and time course of AM and PM was completely opposite.

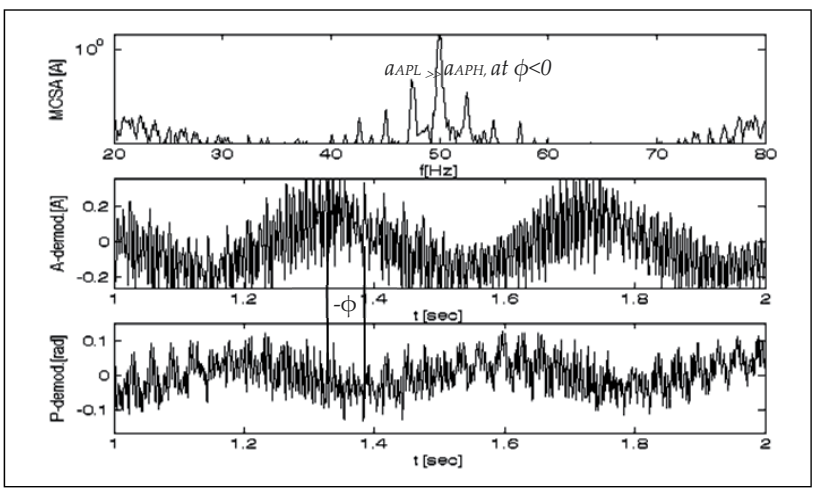

Figure 11. Inverter fed IM, low DC-link and overloaded, low inertia, 75% of full load, MCS, time course of amplitude and phase demodulated current, PM delays $-\varphi$ behind AM.

In the second measurement another inverter was not properly rated and its DC-link voltage was only 400V. IM was fed by lower voltage apps. 185V and therefore was overloaded. In

this case the MCS $a_{APL} > a_{APH}$ appeared (the same phenomenon which can appear at great inertia). The demodulation detected PM delay $-\varphi$ behind AM -see Fig.11 and validated the explanation of $a_{APL} > a_{APH}$ in Fig.4., and also the correctness of (6).

This phenomenon of PM delay behind AM at low inertia appears when an AC source is not properly dimensioned, its feeding voltage is lower than nominal voltage and therefore it is not able to fully excite IM.

It can be concluded that continual increasing of a_{APL} above a_{APH} (out of the range of possible a_{APL} and a_{APH} variations± 2.5dB) generally means, that IM working conditions are out of the normal.

6. Demodulation analysis versus direct analysis

The presented MCDA and following AM and PM synthesis to the full IM current fault indicators a_{APL}, a_{APH} (6) enables the comparison of the demodulation analysis to the direct full IM current analysis.

The IM stator current demodulation analysis enables to find out the complex changes in the rotor electromagnetic field and MMF. Based on this analysis the new method MCDA was introduced. MCDA comes from the basic fundamental which occurs at dynamic rotor faults – JAPM. MCDA senses the whole stator current, but before the further evaluation as spectral analysis, it extracts time courses of fault currents directly induced by dynamic rotor faults. Anything more accurate than the extraction and direct processing of fault currents cannot exist.

The phase demodulation extracts PM current and can be used for the research of rotor magnetic field changes and oscillation and for the sensorless speed measurement. PM is not very suitable for rotor fault diagnostics, because the fault indicators are dependent on motor load.

The amplitude demodulation extracts AM fault current. AM is from 20% of full load almost independent of motor load and it is the base for rotor fault diagnostics not dependent on different load and inertia. Broken bar and dynamic eccentricity fault indicators are simple spectral peaks at direct fault frequencies f_{sp}, f_r (no sidebands). The amplitude demodulation can be easily implemented continually in a real time.

MCDA is a clear, very simple and reliable method and it is very useful for industrial application both for diagnostics and also for IM continual monitoring.

Methods of the direct analysis of IM current sense and subsequently process the full IM current. The great disadvantage of the direct IM current analysis is that its fault indicators a_{APL}, a_{APH} are dependent on IM load and inertia moment. The second disadvantage is that fault frequencies cannot be determined directly, but as a difference from f_1, which can change. The third disadvantage is the lower resolution both in frequency and amplitude.

Great differences between the magnitudes of the main spectral peak on f_i and the sidebands magnitudes a_{APL}, a_{APH} requires the use of logarithmic or dB scale.

The presented demodulation analysis of IM current proved that IM current at dynamic rotor faults is not so simple and inwardly contains JAPM. Simply to say stator current consists of 3 parts - stator current of health motor, amplitude modulating current and phase modulating current (12). Just JAPM is the main reason for of the full current based fault indicators dependences on motor load and inertia.

The demodulation analysis exactly established the reasons for a_{APL} and a_{APH} formation and developed equations for their computation (5), (6). Consequently the MCDA has allowed a complete explanation of both MCS load and inertia dependences: MCS fault indicators a_{APL}, a_{APH} actually consist of 3 variables - AM, PM and φ, (6). PM increases with the increasing load (Fig.7-9, Table 4) and therefore causes the increase of both a_{APL} and a_{APH}. Great inertia or poorly fed IM causes that the angle φ changes from zero values to negative values and therefore $a_{APL} > a_{APH}$ (6). The summation or averaging of a_{APL} and a_{APH} is inaccurate, because the equation (6) is not a linear function.

The processing and direct analysis of the whole stator current does not enable the distinction of the individual AM, PM and φ contribution to the a_{APL} and a_{APH} and the result is the continual dependence of MCSA a_{APL} and a_{APH} fault indicators on IM load and inertia. No improvements and sophistication of the measurement and evaluation methods can reduce this dependence. Logarithmic or dB scale has to be used for a_{APL} and a_{APH} displaying. It together means the low resolution both in amplitudes and frequencies.

7. Conclusion

Dynamic rotor faults cause dynamic changes of rotor electromagnetic field and MMF and therefore the motor current AM and PM together creating JAPM.

Based on this theory, the new diagnostic method MCDA was developed. Basic properties of AM and PM at rotor faults were presented. The analyses of IM current and current signature at rotor faults together with mathematical equations for low and high autospectral magnitudes computation were derived. These equations were verified by simulation and experimentally and the possible low and high autospectral magnitudes variation due to IM current nonstationarity and DSP errors were discussed.

Two demodulation methods based on Hilbert transform and space transform are presented. Space transform gives the same results as Hilbert transform.

The phase demodulation extracts the fault PM current. PM can be used for the research of rotor magnetic field phase changes and oscillation and for the sensorless rotor magnetic field speed measurement. PM fault indicators are dependent on the motor load.

The amplitude demodulation extracts the fault AM current. The simple spectral peaks at fault frequencies f_{sp} and f_r are the dynamic rotor faults indicators almost independent on IM

load and inertia. It was also proved that MCDA fault indicators are not influenced by the time varying load.

The presented diagnostic method is very clear and can be easily used for a reliable rotor faults diagnostics in a real time or for continual IM monitoring.

Author details

Ivan Jaksch
Technical university of Liberec, Czech Republic

Acknowledgement

The author gratefully acknowledges the contributions of the Grant Agency of Czech Republic.

Appendix

Nomenclature

AM	Amplitude Modulation
PM	Phase Modulation
JAPM	Joint Amplitude Phase Modulation
MCDA	Motor Current Demodulation Analysis
MCS	Motor Current Signature -a_{APL}, a_{APH}
IM	Induction motor
a_{AL}, a_{AH}	Low and high spectral magnitudes of AM
a_{PL}, a_{PH}	Low and high spectral magnitudes of PM
a_{APL}, a_{APH}	Low and high spec. mag. of MCS at JAPM –real motor state
f_{sp}	Slip pole frequency – $2sf_l$
f_r	Motor rotation frequency
f_l	Motor supply frequency
f_{load}	Time varying load frequency
$f_{L,H}$	Low and high spectral sidebands frequencies
$H(t)$	Analytical signal created by Hilbert transform
I_l	Induction motor current amplitude
I_{nom}	Induction motor nominal current amplitude
$i_d(t)$, $i_q(t)$	Real and imaginary part of space vector
I_{spa}	AM current amplitude at f_{sp} frequency, **broken bars fault indicator**
I_{spp}	PM current amplitude at f_{sp} frequency

I_{ra}	AM current amplitude at f_r frequency, dynamic eccentricity fault indicator
I_{rp}	PM current amplitude at f_r frequency
I_{load}	AM current amplitude at f_{load} frequency,
$J_i(I_{spp})$	i^{th}-order Bessel function of the first kind
$k_{sp,}$	Fault severity coefficient for broken bars
k_r	Fault severity coefficient for dynamic eccentricity
$magH(t)$	Absolute value of the complex analytical signal
n_{rb}	Number of rotor bars
p	Number of motor poles
$P(t)$	Analytical signal from the space vector
s	Per unit slip
$\beta(t)$	Phase of the complex analytical signal
φ	Phase angle of PM in reference to AM at broken bars

8. References

Bellini, A., Filippeti, F., Tassoni, C. & Kliman, G.B. (2001). Quantitative evaluation of induction motor broken bars by means of electrical signature analysis. *IEEE Transactions on industry applications,* vol. 37 pp. *1248-1255.*

Bellini, A., Filippetti, F., Tassoni, C. & Capolino, G.-A. (2008) Advances in Diagnostic Techniques for Induction Machines, *IEEE Trans. on Industrial. Electronics,* vol. 55, pp 4109-4126.

Bendat, J.S. (1989). *The Hilbert Transform*, Bruel &Kjaer Publication BT0008-11, DK 2850, Naerum, Denmark.

Blödt, M., Bonacci, D., Regnier, J., Chabert, M. & Faucher, J. (2008). On-line monitoring of mechanical faults in variable-speed induction motor drives using Wigner distribution, *IEEE Transactions on Industrial Electronics.,* vol. 55, no. 2, pp. 522–533

Concari, C., Franceschini, G. & Tassoni, C. (2008). Differential Diagnosis Based on Multivariable Monitoring to Assess Induction Machine Rotor Conditions, *IEEE Transactions on Industrial Electronics,* vol. 55, no. 12, pp. 4156-4166.

Cusido, J., Romeral, J.A., Ortega, J.A., Rosero, A. & Garcia Espinosa A. (2008). Fault Detection in Induction Machines Using Power Spectral Density in Wavelet Decomposition, *IEEE Transactions on Industrial Electronics,vol.55,* no.2, pp.633-643

Dorrell, D. G., Thomson, W. T. & Roach, S. (1997). Analysis of airgap flux, current, and vibration signals as a function of the combination of static and dynamic airgap eccentricity in 3-phase induction motors, *IEEE Transactions on Industrial Application.*, vol. 33, no. 1, pp. 24–34.

Drif, M. & Cardoso, A.J.M. (2008). Airgap-Eccentricity Fault Diagnosis, in Three-Phase Induction Motors, by the Complex Apparent Power Signature Analysis, *IEEE Trans. on Industrial Electronics,* vol. 55, no. 3, pp. 1404-1410, March 2008.

Jaksch, I. (2003). Faults diagnosis of three-phase induction motors using envelope analysis, *Proceedings of 4th IEEE International Symposium on Diagnostics for Electric Machines, Power Electronics and Drives,* ISBN 0-7803-7838-5, pp. 289–295, Atlanta, USA, 9/2003

Jaksch, I. & Zalud, J. (2010). Rotor Fault Detection of Induction Motors by Sensorless Irregularity Revolution Analysis, *Proceedings of XIX International Conference on Electric Machines,* ISBN 978-1-4244-4175-4, Paper number RF-001511, Rome, 9/2010.

Joksimovic, G. M. (2005) Dynamic simulation of cage induction machine with air gap eccentricity, *Proceedings of Institute. Elect. Eng.—Electric Power Appl.*, vol. 152, no. 4, pp. 803–811.

Jung, J.H., Lee, J.J. &. Kwon B. H. (2006). Online Diagnosis of Induction Motors Using MCSA. *Transactions on Industrial Electronics*, vol.53, no.6, pp.1842-1852..

Kia, S.H., Henao, H. & Capolino, G.-A. (2009). Diagnosis of broken bar fault in induction machines using discrete wavelet transform without slip estimation, *IEEE Transactions on Industry Applications,* vol. 45, no. 4, pp. 1395-1404.

Kia, S.H.; Henao, H.& Capolino, G. (2010). Torsional vibration Assesment Using Induction Machine Electromagnetic Torque Oscillation, *IEEE Trans. on Ind. electronics*, vol. 57, pp. 209-219.

Kral, C., Pirker, F., Pascoli, G. & Kapeller, H. (2008). Robust Rotor Fault Detection by Means of the Vienna Monitoring Method and a Parameter Tracking Technique, *IEEE Transactions on industrial electronics,* vol. 55, pp. 4229-4237

Lebaroud, G. & Clerc, A. (2008). Classification of Induction Machine Faults by Optimal Time–Frequency Representations, *IEEE Trans. on Industrial Electronics,* vol. 55, no. 12, pp. 4290-4298.

Mirafzal,B. & Demerdash, N. (2005). Effects of Load Magnitude on Diagnosing Broken Bar Faults in Induction Motors Using the Pendulous Oscillation of the Rotor Magnetic Field Orientation, *IEEE Transactions on industry applications,* vol. 41, pp. 771-783.

Nandi, S., Toliyat, H. A. & Li, X. (2005). Condition monitoring and fault diagnosis of electrical motors - A review, *IEEE Transactions on Energy Conversion*., vol. 20, no. 4, pp. 719–729.

Randall, R.B. (1987). *Frequency analysis,* Bruel&Kjaer Publication, ISBN 87 8735 14 0

Riera-Guasp, M., Antonino-Daviu J. A., Roger-Folch J. & Molina Palomares, M. P. (2008). The use of the wavelet approximation signal as a tool for the diagnosis of rotor bar failures, *IEEE Trans. Industrial Appl*., vol. 44, no. 3, pp. 716–726.

Su, H. &. Chong, K. T. (2007). Induction machine condition monitoring using neural network modeling, *IEEE Transactions on Ind. Electronics*, vol. 54, no. 1, pp. 241–249.

Thomson, W. & Fenger, M. (2001). Current signature analysis to detect induction motor faults. *IEEE Industry Application Magazine.*, vol. 7, no. 4, pp. 26–34.

Zhang, P, Du, Y., Habetler, T. G. & Lu B. (2011). A Survey of Condition Monitoring and Protection Methods for Medium-Voltage Induction Motors, *Transactions on Industry application,* vol.47, pp.34-46

Zidani, F., Diallo, D., Benbouzid, M.E.H. & Nait-Said, R. (2008). A Fuzzy-Based Approach for the Diagnosis of Fault Modes in a Voltage-Fed PWM Inverter Induction Motor Drive, , *IEEE Transactions on Industrial Electronics*, vol.55, no.2, pp.586-593

Edited by Prof. Rui Esteves Araújo

Motivated by the need of energy-efficiency improvements, process optimization, soft-start capability and numerous other environmental benefits, it may be desirable to operate induction motors for many applications at continuously adjustable speeds. The induction motor drives can provide high productivity with energy efficiency in different industrial applications and are the basis for modern automation. This book provides an account of this developing subject through such topics as modelling, noise, control techniques used for high-performance applications and diagnostics. Compiled from contributions by international researchers, this is not a textbook, but the result is an interesting exploration of this technology, that provides a combination of theory, implementation issues and practical examples.

ISBN 978-953-51-6267-4

Photo by aquatarkus / iStock

IntechOpen